Proceedings of the 15th Australian Space Research Conference Canberra September 29 - October 1, 2015

Australian Space Research Conference Series

1st Edition
Published in Australia in 2016 by
National Space Society of Australia Ltd
GPO Box 7048
Sydney NSW 2001
Fax: 61 (02) 9988-0262
email: nssa@nssa.com.au
website: http://www.nssa.com.au

ISBN 13: 978-0-9775740-9-4
Editors: Wayne Short and Graziella Caprarelli

Distributed on DVD

Preface to the Proceedings

The Australian Space Research Conference (2015), held at the UNSW - Canberra Campus (ACT, Australia) from September 29 to October 1, 2015 (http://www.nssa.com.au/15asrc/), was a very successful event, where over 150 papers from Australian and international groups working in the field of space research, business, policy and culture, were presented. Following the conference some of the works were submitted as full-length papers. These proceedings collect the papers accepted after a rigorous process of peer-review.

Each paper published in these proceedings has been peer-reviewed by at least two assessors selected by the Chair of the Program Committee with inputs from members of the committee, and revised by the authors accordingly. Final decisions to accept or reject manuscripts in their submitted or revised form were taken by the Editor of these proceedings in consultation with the Editor-in-Chief.

More than 40 scientists, engineers and space professionals from Australian and international organizations participated in the peer-review process, with several referees assessing and providing feed-back on more than one manuscript. We list below (in alphabetical order) only the referees who agreed to be identified:

Ramon Brasser (Earth-Life Science Institute, Japan); Adrian Brown (SETI Institute, USA); David Bruce (University of South Australia, Australia); Iver Cairns (The University of Sydney, Australia); Graziella Caprarelli (University of South Australia, Australia; International Research School of Planetary Sciences, Italy); Luca Casagrande (Australian National University, Australia); Jonathan Clarke (Mars Society Australia, Australia); Miguel Angel de Pablo Hernandez (Universidad de Alcalá, Spain); Jason Held (Saber Astronautics, Australia, USA); Andrew Lambert (UNSW ADFA-Canberra, Australia); Lenard Pederick (DSTG, Australia); Monica Pondrelli (International Research School of Planetary Sciences, Italy); Josh Richards (MarsOne Astronaut Candidate, Australia); Tracy Rushmer (Macquarie University, Australia); Richard Samuel (Australian Space Research Institute, Australia); Richard Schwarz (University of Vienna, Austria); Michael Smart (University of Queensland, Australia).

To all the other reviewers who asked to remain anonymous, but who also responded enthusiastically to our invitation to assess and provided timely reviews, we express our gratitude and special

acknowledgments for their generous support: they are highly regarded experts in their disciplines, affiliated to universities, and research and professional organizations all over the world.
All reviewers made constructive criticism and suggestions that greatly improved the manuscripts and contributed to the quality of these proceeding. Responsibility for the published content remains with the authors of the papers, as well as the intellectual property of the work described. The publisher retains copyright over the published Proceedings. Papers appear in these Conference Proceedings with authors' permission.

We thank the University of NSW – Canberra, for providing the venue and conference facilities, the ASRC 2015 Organizing Committee chaired by Iver Cairns and Wayne Short, the UNSW Canberra members of the Local Organizing Committee chaired by Russell Boyce, the members of the Program Committee chaired by Graziella Caprarelli, and all the members of the Australian Space Research Community for giving generously of their time, suggestions, and efforts. The Australian Academy of Science, Mars Society Australia, and Lockheed Martin co-sponsored various conference events.
We trust that you will find the 2015 Conference Proceedings enjoyable and informative.

Graziella Caprarelli
(Editor, 15th ASRC Proceedings; Chair, ASRC 2015 Program Committee)
Wayne Short
(Editor-in-Chief, ASRC Proceedings)

July 2016

Conference Background

The Australian Space Research Conference (ASRC) is the focus of scientific cooperation and discussion in Australia on research relating to space. It is a peer reviewed forum for space scientists, engineers, educators, and workers in Industry and Government.

The conference is of relevance to a very broad cross section of the space community, and therefore generates an enlightening and timely exchange of ideas and perspectives. The scope of the conference covers fundamental and applied research that that can be done from space and space-based platforms, and includes the following:

- **Space science**, including space and atmospheric physics, remote sensing from space, planetary sciences, astrobiology and life sciences, and space-based astronomy and astrophysics ;
- **Space engineering**, including communications, navigation, space operations, propulsion and spacecraft design, testing, and implmentation ;
- **Space industry ;**
- **Space archeology and Indigenous sky knowledge;**
- **Space situational awareness ;**
- **Current and future Australian space projects ;**
- **Government, International relations and law ; and**
- **Education and outreach.**

The 15th ASRC was held at the University of New South Wales (Canberra Campus) during September 29 to October 1, 2014. The Conference was opened by Nobel Prize winner Professor Brian Schmidt.

The conference included a comprehensive program of plenary talks and special sessions on the national context for space the foci and the programs of Australian Government units with interests in space. In addition, the program contained a special planetary science session, with a strong preponderance of projects involving the Mars Society of Australia. The program also contained multiple sessions of invited and contributed presentations, both oral and poster, on Propulsion, Planetary Science, Earth Observation and GNSS, Space Capabilities, Space Physics, Space Situational Awareness, Space Technology, Space Archeology, Education and Outreach, and Indigenous Sky Knowledge.

Appendix A lists all abstracts accepted for presentation at the conference. A call for abstracts was issued in March 2015 and researchers were invited to submit abstracts intended for presentation at the conference. Following the conference itself, a call for written papers was issued in October 2015: this invited presenters to submit a formal written papers for this Proceedings that covered their conference presentations.

Table of Contents

List of Proceedings Papers

The National Space Society of Australia is the coming together of like-minded space enthusiasts who share a vision for the future in which there is an ambitious and vigorous space program leading to eventual space settlement.

To this end the National Space Society (worldwide) promotes interest in space exploration, research, development and habitation through events such as science and business conferences, speaking to the press, public outreach events, speaking engagements with community groups and schools, and other pro-active events. We do this to stimulate advancement and development of space and related applications and technologies and by bringing together people from government, industry and all walks of life for the free exchange of information.

As a non-profit organisation, the National Space Society of Australia draws its strength from an enthusiastic membership who contributes their time and effort to assist the Society in pursuit of its goals.

For more information, and to become a member:

http://www.nssa.com.au

Ad Astra!
Wayne Short
NSSA President

The National Committee for Space and Radio Science (NCSRS) is chartered by the Australian Academy of Science to foster space science, to link Australian space scientists together and to their international colleagues, and to advise the Academy's Council on policy for science in general and space and radio science in particular. The NCSRS was formed in 2012 by combining the former National Committee for Space Science (NCSS) and the National Committee for Radio Science (NCRS). The NCSRS web page can be reached at

https://www.science.org.au/committee/space-and-radio-science

NCSRS believes that ASRC meetings provide a natural venue to link Australian space scientists and foster the associated science, two of its core goals. As well as ASRC, NCSRS is also sponsoring the VSSEC – NASA Australian Space Prize.

This is the fifth ASRC meeting following launch of the first Decadal Plan for Australian Space Science. NCSRS encourages people to work together to accomplish the Plan's vision: "Build Australia a long term, productive presence in Space via world-leading innovative space science and technology, strong education and outreach, and international collaborations."

2015 ASRC Program Committee

Jeremy Bailey (UNSW Australia)

Russell Boyce (UNSW Australia, Canberra)

Iver Cairns (Deputy Chair, University of Sydney)

Graziella Caprarelli (Chair, University of South Australia)

Jonathan Clarke (Mars Society of Australia)

Andrew Dempster (UNSW Australia)

Alice Gorman (Finders University)

Duane Hamacher (UNSW Australia)

Trevor Harris (Defence Science and Technology Group, Department of Defence)

Isabelle Kingsley (POWERHOUSE Museum)

Alexey Kondyurin (University of Sydney)

Philippe Lorrain (UNSW Australia, Canberra)

Flavia Tata Nardini (Launchbox Australia)

Carol Oliver (UNSW Australia)

Tim Parsons (Delta V SpaceHub)

Chris Rizos (UNSW Australia)

Roy Sach

Richard Samuel (Australian Space Research Institute)

Wayne Short (NSSA)

Michael Smart (University of Queensland)

Kefei Zhang (RMIT University)

2015 ASRC Organising Committee

Russell Boyce
UNSW Australia (Canberra)
Chair, local organising committee

Cheryl Brown
Australian Centre for Space Engineering Research, UNSW Australia
Conference Secretariat

Iver Cairns
University of Sydney
Co-Chair ASRC 2015
Deputy Chair, ASRC Program Committee

Graziella Caprarelli
University of South Australia
Chair, ASRC Program Committee

Aditya Chopra
Australian National University

Jonathan Clarke
Mars Society Australia

Alice Gorman
Flinders University

Jonathan Horner
University of Southern Queensland

Philippe Lorrain
UNSW Australia (Canberra)

Wayne Short
Co Chair ASSC 2015
President, NSSA

Conference Plenary Speakers

Professor Russell Boyce
University NSW (Canberra)
"Near-Earth Space Physics : the science to underpin Space Situational Awareness"

Professor Iver H. Cairns
University of Sydney
"*Solving the `Type II Solar Radio Burst Problem' and Predicting Space Weather"*

Dr Grant Haulser
Geoscience Australia
"GNSS Activities in Australia - Strengthening Capability and Resilience"

Dr Gail Higginbottom
Australian National University, University of Adelaide
"Origins of Standing Stone Astronomy in Britain"

Dr Ed Kruzins
CSIRO Director NASA Operations and Canberra Deep Space Communication Complex
"Options for Australian Payloads and Cubesats with NASA"

Conference Plenary Speakers

Dr Naomi Mathers
Australian National University
"The Advanced Instrumentation and Technology Centre (AITC): A National Facility Supporting Astronomy and Space Activities in Australia"

Professor Fredrick Menk
University of Newcastle
"Magnetoseismology: Ground-based remote sensing of Earth's magnetosphere"

Professor Ross Taylor
Australian National University
"Why can't a planet be more like a star"

Professor Martin van Kranendonk
University of of New South Wales – Australian Centre for Astrobiology
"Early Earth and the making of Mankind: Astrobiology in our own backyard"

15th ASRC Conference Program
September 29 – October 1

TIME	TUESDAY			WEDNESDAY			THURSDAY			TIME
8:00	Registration			Registration			Registration			8:00
8:30										8:30
9:00	Opening / Plenaries			Plenaries			Plenaries			9:00
10:00				Mars Symposium	Satellite Platforms	SSA Workshop (1)				10:00
10:30	Break			Break			Break			10:30
11:00	National Context			Mars Symposium (con'td) Space Projects	Satellite Platforms (cont'd) Space Industry	SSA Workshop (1) (cont'd)	Space and Atmospheric Physics	Earth Astro-Biology	Hist/Med/Social	11:00
11:15										11:15
11:30									HOT TOPIC: Off Earth Mining	11:30
12:00										12:00
12:30							Lunch	Lunch (12:20)	Lunch (12:45)	12:30
13:00	Lunch / Poster Session 1			Lunch	(13:15) Lunch	Lunch	Poster Session 2			13:00
13:30									Education	13:30
14:00				Plenary Talk						14:00
14:30	Space and Atmospheric Physics	Remote Sensing	Archaeo-astronomy/ Indigenous Sky	Moon	Satellite Subsystems	SSA Workshop (2)	Space Engineering	Planets		14:30
15:00										15:00
16:00	(16:05) Break	Break	Break	(16:10) Break	(16:15) Break	Break	Break			16:00
16:30	Space and Atmospheric Physics	GNSS	Small Objects SS / Meteorites	Decadal Plan Mid-Term Review Town Hall Meeting			Closing remarks / Prize Giving Ceremony			16:30
17:15										17:15
18:00	Cocktail Reception			Gala Dinner			Mars Society Dave Cooper Public Talk			18:00
19:00										19:00
19:30	Close									19:30
20:30				Close			Close			20:30
22:00										22:00

The Gender Balance of the Australian Space Research Community: A Snapshot From The 15th ASRC, 2015

Jonathan Horner[1,2], Alice Gorman[3], Ann Cairns[4,5,6] and Wayne Short[6]

[1] *Computational Engineering and Science Research Centre, University of Southern Queensland, Toowoomba, Queensland 4350, Australia*
[2] *Australian Centre for Astrobiology, UNSW Australia, Sydney, New South Wales 2052, Australia*
[3] *Department of Archaeology, Flinders University, GPO Box 2100, Adelaide, South Australia 5001, Australia*
[4] *New South Wales Department of Education, New South Wales, Australia*
[5] *Division of Information Technology, Engineering and the Environment, University of South Australia, GPO Box 2471, Adelaide, South Australia, 5001, Australia*
[6] *National Space Society of Australia Ltd, GPO Box 7048, Sydney, New South Wales, 2001, Australia*

Summary: In recent years, the striking gender imbalance in the physical sciences has been a topic for much debate. National bodies and professional societies in the astronomical and space sciences are now taking active steps to understand and address this imbalance. In order to begin this process in the Australian Space Research community, we must first understand the current state of play. In this work, we therefore present a short 'snapshot' of the current gender balance in our community, as observed at the 15th Australian Space Research Conference.

We find that, at this year's conference, male attendees outnumbered female attendees by a ratio of 3:1 (24% female). This gender balance was repeated in the distribution of conference talks and plenary presentations (25 and 22% female, respectively). Of the thirteen posters presented at the conference, twelve were presented by men (92%), a pattern repeated in the awards for the best student presentations (seven male recipients vs one female). The program and organising committees for the meeting fairly represented the gender balance of the conference attendees (28% and 30% female, respectively). These figures provide a baseline for monitoring future progress in increasing the participation of women in the field. They also suggest that the real barrier is not speaking, but in enabling conference attendance and retaining female scientists through their careers – in other words, addressing and repairing the 'leaky pipeline'.

Keywords: Women in STEM, gender equity, space sciences,

Introduction

In the past few years, the pervasive imbalance between the number of men and women studying and working in STEM (Science, Technology, Engineering and Maths) fields has become the subject of wide debate. Traditionally, women were supposed to be more suited to 'soft' disciplines such as biological and social sciences. Whether this was argued to be a result of differing interests or ability, it amounted to the same thing: a 'chilly climate' for women who did choose to enter STEM fields. Women have struggled to gain employment, promotion and pay at equal rates to their male

counterparts. Researchers such as Cordelia Fine ([1]) have effectively debunked studies purporting to characterise female cognitive development as inimical to mathematical or physical reasoning. Nonetheless, beliefs about the inferior intellectual capacity of women abound in both unconscious and explicitly expressed forms, as described below [2]:

> Two stereotypes are prevalent: girls are not as good as boys in math, and scientific work is better suited to boys and men. As early as elementary school, children are aware of these stereotypes and can express stereotypical beliefs about which science courses are suitable for females and males.

Increasingly, STEM communities are refusing to accept these persistent stereotypes as 'natural', and are actively working to redress past discrimination. As a result, a number of initiatives have been launched to attempt to build equity in those subjects from kindergarten through to senior levels in academia and industry. Notable among these is the Athena SWAN charter in the UK, which was launched in 2005 to *'encourage and recognise commitment to advancing the careers of women in science, technology, engineering, maths and medicine (STEMM) employment in higher education and research'*[1] [3].

So successful has the Athena SWAN Charter been that Australian science organisations have initiated their own schemes, based on the Athena SWAN model. The Australian Academy of Science launched its pilot of the 'Science in Australia Gender Equity' scheme, SAGE, in 2015 ([4]). At the time of writing, SAGE has already been joined by 32 Australian institutions, including more than half of all Australia's Universities. The Women in Astronomy Chapter of the Astronomical Society of Australia has also taken a leading role. In addition to running annual workshops for the Astronomical community to build equity, in 2014 the Chapter launched the *Pleiades Awards*, directly inspired by the Athena SWAN program. The awards are given to Astronomy groups in Australia with a demonstrated commitment to equity in their workplaces [5].

One of the first steps any community can make to address questions of equity is to understand the state of play – to obtain a snapshot of the gender balance in their discipline as a starting point, and to see whether the distribution of conference presentations, organising committees, and particularly awards and plenary talks are a fair representation of the gender balance of the community. To this end, a number of studies have been carried out in Australia, the UK and the US, to determine the balance of the astronomical community in those countries. For example, in [6] the authors examine the gender balance at the UK's annual National Astronomy Meeting. In that work, they take inspiration from [7], who carried out a study of the talks at the 223rd American Astronomical Society meeting, presenting data on the gender of speakers, session chairs, and also those who asked questions.

At the 223rd AAS meeting, 225 talks were sampled, with 78 (35%) being presented by women. This was in broad agreement with the gender balance of conference attendees. One area that they did note a significant departure from the gender balance of attendees was in the gender of those asking questions at the end of talks. When the talks were chaired by a man, 80% of the questions asked came from male members of the audience, with only 20% coming from the female members. By contrast, when the session chairs were female, the gender balance of questions (66% male, 34% female) was the same as that as conference attendees.

[1] For more information on the Athena SWAN Charter, we direct the interested reader to http://www.ecu.ac.uk/equality-charters/athena-swan/ .

Following a similar methodology, [6] found that 28% of the attendees of the 2014 National Astronomy Meeting were female, a gender balance reflected fairly in the oral presentations and session chairs at that meeting. They found that, despite this, the same pattern emerged – women were under-represented among the questions asked after the talks, when compared to the gender balance of the conference itself.

These studies suggest that the number of female presenters at the conferences reflects the number of female delegates. The main problem is then that the number of delegates and presenters falls far below the equivalent categories for men – something that often reflects the gender balance of the broader community.

At the 14th Australian Space Research Conference in 2014, a lunchtime discussion meeting was held to examine questions of gender equity in the Australian space research community. Topics covered included the importance of mentors and role models, and cultural barriers to networking, such as venues which may not suit women (such as pubs and saunas). This was repeated at the 15th Australian Space Research Conference, at which it was suggested that the compilation of statistics on the gender balance at that conference would be a useful first step in understanding that balance in our community. In this work, we therefore present a snapshot of the gender balance at that conference, based on the attendees and conference program.

The Gender Distribution of the 15th Australian Space Research Conference

The Australian space research community is a diverse group that intersects with a variety of fields such as astronomy, physics, engineering, geospatial sciences, education and heritage. A typical conference is attended by around 120 – 200 people, and a special effort is made to attract students through offering volunteer opportunities and student prizes. Each conference features around nine plenary talks, spread over the three days of the conference. Non-plenary sessions feature up to three parallel streams. Sessions cover propulsion systems, remote sensing, planetary science, archaeoastronomy, Indigenous sky knowledge, space archaeology, space physics, satellite systems, habitation and space medicine, space mission architecture, orbital debris, space environment, and STEM education.

Before we can begin to address any inequity in the Australian Space Research community, it is vital that we get a feel for the current state of play. As the idea to undertake this study was born of a meeting towards the end of the conference, it was not possible to survey the conference attendees in advance, or to repeat the excellent work of [6] and [7]. We therefore present a post-hoc analysis of the gender balance at the recent 15th Australian Space Research Conference.

To do this, we took the list of conference attendees and the conference program, and determined the gender of each person listed based on personal knowledge of the individuals concerned. Where an individual was not personally known to us, we searched for their details online, on their professional websites, or the homepages of their institutions or employers. We acknowledge the limitation that this might not necessarily represent the personal gender identification of individual delegates, and hope in

future that such information might be obtained through an anonymised survey as part of the conference registration process.

In Table 1, we present the results obtained in this manner. In total, 191 people attended the conference, giving a total of 129 oral presentations. Across the meeting, there were nine plenary talks, and thirteen posters. We were not able to obtain a breakdown of the gender of conference attendees/presenters as a function of their career stage – this, again, is something we would look to obtain at future meetings.

Table 1: The gender distribution across the 15th Australian Space Research Conference.

	Male	Female	Total
Delegates	145 75.9%	46 24.1%	191
Talks	89 74.8%	30 25.2%	129
Posters	12 92.3%	1 7.7%	13
Plenary Presentations	7 77.8%	2 22.2%	9
Student Awards	7 87.5%	1 12.5%	8
Program Committee	13 72.2%	5 27.8%	18
Organising Committee	7 70%	3 30%	10

The proportions of male and female delegates who presented a paper, plenary or poster compared to those simply attending the conference were also broadly similar. Of the male delegates, 74% presented out of the 145; the figure for women was 71%.

In Figure 1, we present the distribution of conference attendees (left) and conference speakers (right), based on the data in Table 1. It is immediately clear that the two distributions are essentially identical – with the gender distribution of speakers mirroring that of the attendees. The program and conference organising committees had essentially the same gender distribution as the conference attendees (Figure 2). The same was true of the plenary speakers at the meeting (Figure 3), with seven male speakers and two female speakers.

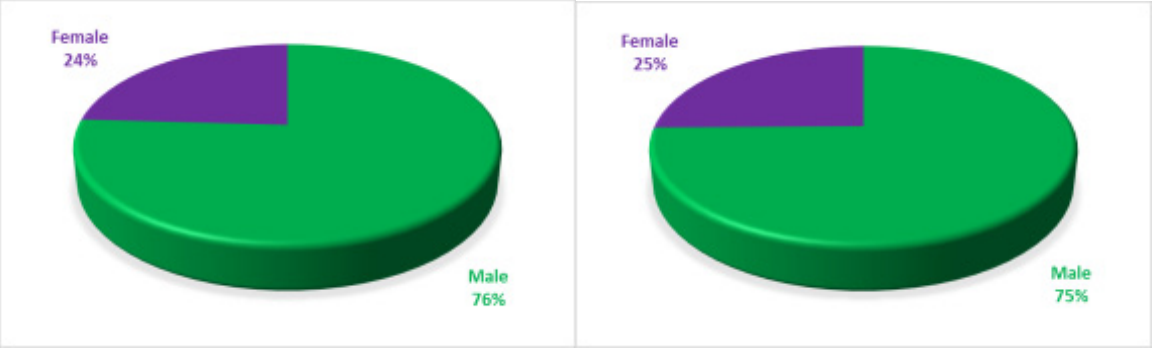

Figure 1: The gender distribution of delegates (left; 191 total) and speakers (right; 129 total) at the 15th Australian Space Research Conference.

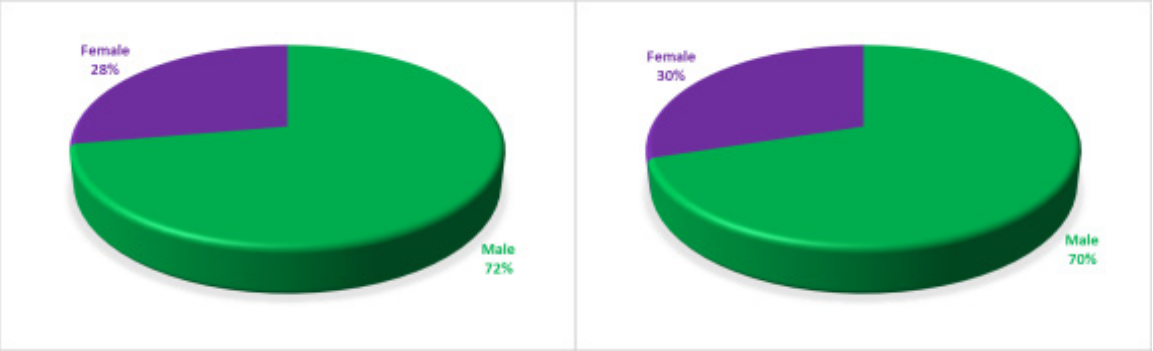

Figure 2: The gender distribution of the program committee (left; 18 members) and organising committee (right; 10 total) at the 15th Australian Space Research Conference.

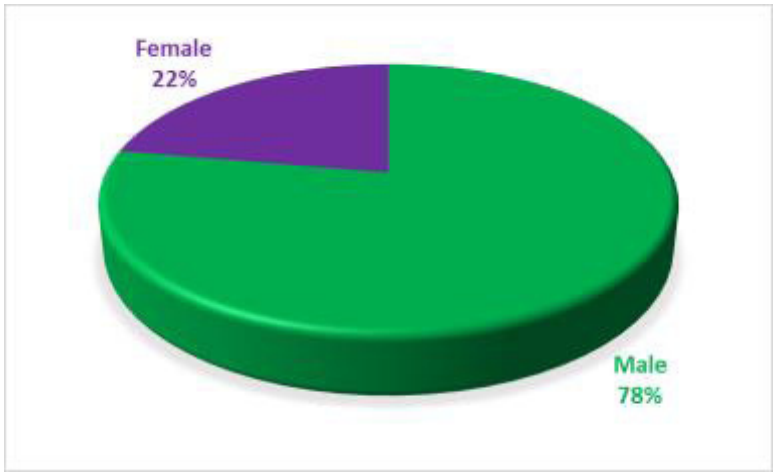

Figure 3: The gender distribution of plenary presentations at the 15th Australian Space Research Conference.

Whilst the distribution of both invited and submitted talks was in line with the overall gender distribution of conference delegates, the same is not true of the posters presented at the conference (12 male, one female) or the prizes awarded for the best undergraduate and postgraduate student presentations (seven male, one female). These figures are presented in Figure 4. Although the female percentage in both cases is lower than the overall gender balance of the conference, we note that in both cases the number of participants is so small that the difference is not strongly statistically significant.

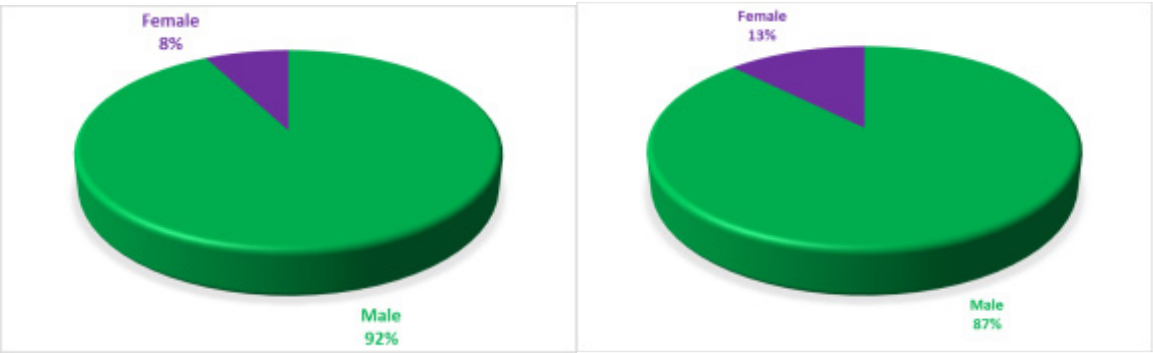

Figure 4: The gender distribution of posters presented (left; 13 total) and prizes award (right; 8 total) at the 15th Australian Space Research Conference. The number of prizes presented to female attendees was markedly smaller than the percentage of conference attendees that were female, but not strongly statistically significant.

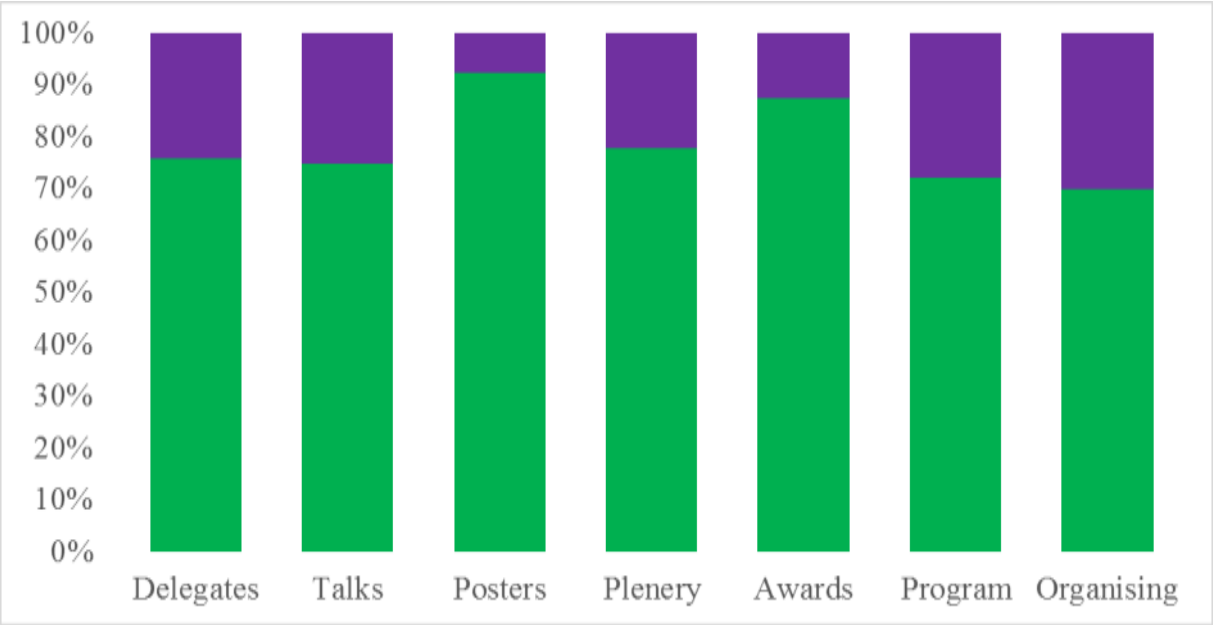

Figure 5: The gender balance across all facets of the 15th Australian Space Research Conference. Here, green = male and purple = female. From left to right, the columns show the gender balance of: the conference delegates as a whole; the talks presented; the posters presented; the plenery presentations; the student awards; the program committee and the organising committee.

Figure 5 presents the gender balance across the conference in the form of a bar chart, allowing the distributions in each category to be directly compared. The paucity of posters presented by women, and the male-dominated student awards clearly stand out from the overall trend of ~25% female participation at the meeting.

These results, taking into account the limitations identified, are consistent with the two studies described above. The number of female/male presenters is in direct proportion to the number of female/male delegates. This suggests that the immediate problem to be addressed is increasing the number of women attending the conference.

Current and Future Initiatives

In order to begin to address the clear gender imbalance within the Australian Space Research Community, lunchtime discussion meetings were held at both the 14th and 15th conferences. These meetings, which were well attended (~30 attendees in 2015) featured an open and wide-ranging discussion, covering many of the factors that are thought to contribute both to the early-career gender imbalance in our field, and the ongoing 'leaky pipeline' that has been recognised as exacerbating that imbalance towards later career stages (see e.g. Slide 6 in http://www.mso.anu.edu.au/wia-workshop-2014/presentations/WiA_workshop2014_demographics.pdf).

Several ideas have been highlighted that might help to effect long-term change, and to help make our community and conferences more equitable. These would benefit everybody – both male and female – but might help to address some of the issues that drive the 'leaky pipeline'. They include:

- The provision of childcare at the conference for delegates;
- The option to attend the conference remotely (i.e. via streaming) for those who can't attend in person;
- The organisation of networking sessions during the daytime, for those who can't attend evening events;
- Aiming to increase the fraction of female plenary speakers above parity with the current demographic distribution of attendees;
- Inviting a plenary speaker to talk on the topic of equity in space science;
- Increasing the visibility of female space scientists online by creating Wikipedia and Scimex profiles[2];
- Creating a repository of information on women working in space science (such as pictures, CVs and biographies), to provide a teaching resource.

The first four recommendations reflect the fact that women are more likely to be the primary carers of children, elderly parents or relatives, and partners, and thus less mobile, without additional support, when it comes to attending conferences.

Although no data are available to us about the gender distribution of attendees and speakers as a function of their career stage, our anecdotal observations through the course of the conference suggest that the gender balance among early-career researchers at the conference is far closer to parity. Addressing the 'leaky pipeline' to ensure that the female early-career researchers have the same opportunities for advancement as male early-career researchers is a challenge that goes beyond the remit of our conference – but taking some small measures to increase the exposure of female ECR and MCRs, and to highlight the success of strong female role models, can help to address the issue that "You can't be what you can't see".

One suggestion that was made after the conference finished was that future equity discussion meetings should possibly be embedded within the main conference program, rather than held as lunchtime splinter events, to ensure the best possible exposure and participation.

Conclusions

[2] Scimex (https://www.scimex.org/) is a media database maintained by the Australian Science Media Centre.

In recent years, the gender imbalance in the physical sciences has become the subject of much discussion. Globally, the STEM community is taking steps to understand and address inequity in the field – and it is recognised that a vital first step in that process is to obtain and track statistics on the gender balance as a function of time, both at conferences and in the community as a whole[3].

For that reason, we have carried out a simple post-hoc analysis of the gender balance of the 15th Australian Space Research conference, in order to assess the current 'state of play'. Of 191 conference attendees, 46 were female (24%). Of a total of 129 oral presentations, 30 were given by women (25%). The balance of the plenary presentations (seven male, two female), and the program and organising committees (13:5 and 7:3 male:female, respectively) were all consistent with this roughly 3:1 male:female balance. By contrast, the poster presentations were strongly male dominated (twelve to one), as were the prizes awarded for the best student presentations (seven to one). This provides us with some baseline figures to use for comparison in subsequent years.

Future research may explore gendered factors in the questions addressed formally to a speaker after their presentations, both in terms of the speaker's gender, and those asking the questions, as discussed by [6] and [7]. It would also be useful to compare career stage, to investigate the observation that there was a higher proportion of ECR women at the conference. Posters are frequently a pathway for students to more fully participate, and it is noteworthy that there was only one poster by a women out of the 12 at the 2015 ASRC. As noted, this number is not statistically significant, but perhaps flags the need to obtain further data. On the other hand, this may also be due to conscious action to increase speaking opportunities for women.

Our results show that when women attend a conference such as the ASRC, they participate as actively in presenting their research as do male delegates. The problem, therefore, lies in increasing the number of women attending the conference. Recommendations arising from the 2015 meeting emphasised the necessity for childcare and other flexible attendance options. Currently these are not automatically provided as part of the conference logistics and are something for the organising and program committees to consider.

Most studies of gender balance in conferences focus on the number of female vs male speakers on panels or in invited talks (e.g. [8]). The solutions proposed are generally around identifying emerging all-male line-ups and ensuring that more women are invited before the line-ups are finalised. These discussions, however, rarely address the number of women in the general conference sessions. The ASRC currently solicits papers in a general call-out in which people self-select. It is at this stage that we need to increase the number of women submitting abstracts.

While it is not possible to solve society-wide biases that work against women in STEM with a study of this nature, the small steps taken here to understand gender inequity in the context of the Australian Space Research community offers some ways forward.

Acknowledgements

[3] See, for example, the compilation of statistics hosted on the website of the Astronomical Society of Australia's Women in Astronomy chapter, at http://asawomeninastronomy.org/statistics/

JH is supported by USQ's Strategic Research Fund: the STARWINDS project. The authors thank Marcia Tanner of the Mars Society of Australia, who took notes at the 2014 meeting.

References

1. Fine, C., "Delusions of gender: How our minds, society, and neurosexism create difference.", 2010, New York: W. W. Norton.

2. Hill, Catherine, Christianne Corbett, and Andresse St Rose 2010 Why So Few? Women in Science, Technology, Engineering, and Mathematics. AAUW: Washington DC http://files.eric.ed.gov/fulltext/ED509653.pdf

3. Quote sourced from http://www.ecu.ac.uk/equality-charters/athena-swan/ , accessed on 28th October 2015.

4. Details of the SAGE scheme can be found on the Australian Academy of Science's website, at https://www.science.org.au/SAGE/Pilot

5. Details of the Pleiades Award scheme can be found on the homepage of the Women In Astronomy Chapter, at http://asawomeninastronomy.org/the-pleiades-awards/

6. Pritchard, J., Masters, K., Allen, J., Contenta, F., Huckvale, L., Wilkins, S. and Zocchi, A., "Asking gender questions: Results from a survey of gender and question asking among UK Astronomers at NAM2014", *Astronomy and Geophysics*, 2014, 55, 6.8 – 6.12

7. Davenport, J. R. A., Fouesneau, M., Grand, E., Hagen, A., Poppenhaeger, K. and Watkins, L., 2014, arXiv:1403.3091; paper available on the arXiv website at http://arxiv.org/pdf/1403.3091v1.pdf

8. Casadevall A. and Handelsman J., "The presence of female conveners correlates with a higher proportion of female speakers at scientific symposia", mBio, 2014, 5(1):e00846-13. doi:10.1128/mBio.00846-13

Additional Resources

The Women In Astronomy blogspot contains a collection of excellent posts by a number of academics on a variety of topics to do with equity and gender bias. http://womeninastronomy.blogspot.com.au/

The Astronomical Society of Australia's Women in Astronomy Chapter maintains a website at http://asawomeninastronomy.org/. Of particular interest are the details of the annual Women in Astronomy Workshops, which can be found here: http://asawomeninastronomy.org/meetings/. Many of the materials from those meetings are hosted on the relevant webpages and can be freely downloaded.

The ‘Project Implicit’ Implicit Bias tests are a fascinating tool that highlights our implicit associations. These cover a wide variety of topics, from broad fields such as age, sexuality and religion, to more specifically focussed topics such as Gender-Science. They can be found here: https://implicit.harvard.edu/implicit/selectatest.html

Launching Melbourne into the Final Frontier

Troy McCann, Robert Mearns, Anton Tarasenko, Martin Lawrence, Nicola Ojerholm and Stan Skafidas

The University of Melbourne Space Program, The University of Melbourne, Victoria, 3053, Australia

Summary: Currently, communications systems take up a significant proportion of both mass and power budgets in deep space spacecraft, increasing their size, and consequently energy requirements and propulsion system complexity. In the near future, as both space exploration and other space-based industries develop, long-range communication will be required. Specialised whole earth orbiting satellite networks for providing communication between Earth and deep space assets will enable better more reliable communication.

The University of Melbourne Space Program is a student run program with the ambitious long-term vision of developing an intra-solar system communications network for both space based industry and scientific research. In order to achieve this, the UMSP is currently prototyping a CubeSat based platform.

Unlike larger satellites, CubeSat are uniquely suited for our long-term vision; their small size facilitates the rapid and inexpensive prototyping, which can then be integrated into earth wide aperture mesh networks.

Mesh networks relaying data between orbiting CubeSat, will permit the creation of advanced large aperture receive stations bigger than ambitious projects like the square kilometre array.

Utilising these small satellites, however, introduces many challenges in miniaturising and integrating pointing, power, low integration time, and high-gain dish technologies into such a small form-factor. Although the program is in its infancy, our first CubeSat aims to address some of these challenges.

Keywords: nanosatellite, CubeSat, satellite constellation, academic program, project management, student project

Introduction

The University of Melbourne Space Program (UMSP) is a team of over 100 ambitious and creative students at The University of Melbourne. Members come from a range of schools and faculties but share a passion for technology and innovation, and all hope to play a key role in the establishment and expansion of the Australian space industry.

The UMSP is currently designing and testing a range of different technologies with the vision to create innovative nano-satellites, to address limitations of existing methods and systems of space based telecommunications between Earth and remote devices. This paper will explore the existing space industry, the development of the UMSP to date, and the future direction of the program.

Background

Historic and contemporary methods of planetary exploration have favoured single asset missions over a multi-agent scalable approach. The driving factor behind this is cost and engineering constraints including launch mass, asset communications, and autonomy. However, to facilitate greater access to remote regions of planetary bodies and potential sites of astrobiological interest – including magmatic-driven uplift, hydrothermal activity or recent aqueous activity – autonomous missions will be necessary [1]. Furthermore, the way for future human exploration and off-earth industries, such as asteroid capture and mining, will be paved by extensive robotic missions.

Traditional single asset missions are insufficient for these future endeavours, requiring the development of multi-agent robotic missions [2] [3]. A common problem among the proposed methods of swarm exploration is that each agent of the swarm has a limited communication range. This means agents acting alone are unsuitable for a Direct-To-Earth link, leading to agents relying on a central node, typically the lander, to perform earth communications. Though this method shows distinct benefits over a single asset, it still suffers from a lack of redundancy in communication channels. Additionally, central nodes can be prohibitively expensive.

A “tier-scalable” methodology in which each successive tier operates within a decreased range and scope has been proposed in "Next-generation robotic planetary reconnaissance missions: A paradigm shift,",[4]. The lowest of these, a ground-based tier, comprised of either miniaturised traditional rovers, or cheaper mass-produced robots such as those discussed in "A preliminary design for a spherical microrover for planetary exploration",[2], and “A Concept Mission: Microbots for Large-Scale Planetary Surface and Subsurface Exploration”, [3], would serve a very small area around the drop zone with a limited sensor suite. A number of these drop-zones would be chosen for each area of scientific interest. For those bodies with a sufficiently dense atmosphere, each drop-zone would be marshalled by agents within an airborne tier, with each agent serving as both command and control for the nearest drop-zone as well as the communication link between the ground assets and the space-borne tier. When there is insufficient atmosphere to support an airborne tier, these roles are taken over by the space-borne tier. This final tier serves as the interaction point between Earth and all other assets. While the methodology suggested by [4] calls only for a few agents within the space-borne tier, limiting the size of this network would limit the potential redundancy of communication channels as well as the potential data through-put.

The major bottleneck in current planetary exploration missions is data-throughput. The Mars Reconnaissance Orbiter (MRO) fills its 160GB on-board storage within 1.5 hours, while relaying this data takes upwards of 8 hours to transmit in its entirety. In addition, the MRO often served as a communication link between various surface missions and Earth. This added data transmission burden limited the data collection capabilities of the orbiter. For future exploration, and prospecting missions for extraterrestrial resources, methodologies such as that proposed by [4] have great potential. However, a few sparse agents within a space-borne tier responsible for data relay from all ground assets, air-borne assets in addition to carrying out their own data collection, would be hard pressed to accomplish the data transmission requirements. Looking into the future, the potential for off earth mining as an example of extraterrestrial industry will be limited by the ability to reliably command vast numbers of autonomous units simultaneously [5]. Utilising a few centralised orbiting communications platforms will simply not be feasible.

Due to the deficiencies inherent in using a few large and expensive command and control relay satellites to service a vast number of ground and airborne assets, a similar approach to the distributed ground exploration, presents significant promise. Using a large number of small, relatively simple and low cost communication satellites, a mesh network can be formed in orbit around the entire planetary or asteroid body. Due to the self-healing possibility of mesh networks, the loss of individual nodes presents little danger to the overall mission success. In addition, orbital mesh networks provide opportunities to leverage the changing network topology to increase the signal to noise ratio and reduce error rate in transmissions between Earth and multiple different nodes in the network.

Similar opportunities exist for communication networks in Geosynchronous Earth Orbit(GEO). Currently, many missions within GEO utilise NASA's Space Network (SN), a communication network consisting of several ground stations and six geostationary Tracking and Data Relay Satellites (TDRS) with two more stationed on orbit for redundant backup. These satellites are capable of tracking and communicating with any craft within GEO, ensuring constant contact with the ground. Unfortunately, the cost of replacement TDRS is becoming prohibitive for NASA. NASA's inability to procure replacements and launch vehicles due to budgetary constraints is outlined in [6]. This has resulted in four of the required six TDRS operating past their designed end of life. TDRS-3 is operating over fifteen years past its designed end of life, and while still fully operational, its inevitable loss poses significant concerns. With an expansion in the number of future NASA and NASA supported missions into GEO, the capabilities of the current TDRS Space Network will be insufficient [6].

NASA's Deep Space Network (DSN) suffers from similar concerns. Currently, the network is insufficiently equipped to facilitate the predicted expansion of deep space exploration missions [7]. The three current stations are slated for extension under the DSN Aperture Enhancement Project. However, due to budgetary constraints this project has consistently been pushed back, leaving its future in doubt.

While the future capabilities of both the TDRS and DSN are uncertain, the future loads on these networks, and those like them, are predicted to at least double in the short-term [8] and ultimately, dramatically increase. Utilising a space-based mesh network presents an alternative to traditional commercial and government networks; a number of ground station installations communicate with either individual assets or small orbiting networks, similar in manner to the SN and DSN. These current networks rely on a few large, costly and complex assets to maintain contact with ongoing missions. Though these methods have been sufficient to date, due to the predicted expansion of space-exploration and space industry, the ability to communicate with many more remote assets simultaneously will be required. Though this could be achieved by expanding the number of current ground-stations, a mesh-network of small, relatively cheap nodes presents the opportunity to scale the capabilities of the network more efficiently than when using fewer more complex ground or orbital nodes. Within a network with only a few nodes, as in the case of those like the DSN and TDRS, each node must be purpose built and highly reliable while still carrying a large fraction of the total load. These factors drive up the development and manufacturing cost of each node, be it on earth or in orbit. The current estimated cost of replacing a single TDRS satellite is US $500 million, [6]. In comparison, a mesh-network with many simple nodes allows for the reliability of the network to be distributed across nodes, while each node only needs to carry a small fraction of the total load. This topology would require far more nodes than a traditional network for the same load, however, this allows economies of scale to kick in, reducing the cost of each node. Having these nodes in orbit will allow for greater flexibility in positioning and pointing as network requirements change, than would the equivalent number of terrestrial nodes.

The development of nano-satellites as nodes within a mesh network capable of taking on the burden of interplanetary communications presents significant challenges. These include increasing the pointing capabilities of nano-satellites into the arc-second range, improving the power harvesting and storage technology available to support high power transmission from a small form-factor as well as the inclusion of high-gain antennas into the small mass and volume requirements of nano-satellites. In addition, the development of collaboration techniques between nodes to facilitate aperture synthesis, spatial division of communication packets, division and recombination of communication packets for spatially separated transmission and recombination of redundant transmission paths present exciting research paths to develop the capabilities of planetary communication mesh networks. In light of these opportunities, the University of Melbourne has established a space research program. Although, there was a successful student project to develop a single satellite at the University of Melbourne in the 1960's, Australis Oscar V. The scope of the current program goes beyond this; joining student satellite development, like that of BlueSat at UNSW with dedicated research.

In the decades following the world's first forays into space, Australia's involvement in the space sector waned from that of a forerunner [9] [10] [11] to a minor participant, with only 15 satellites launched to date. Australia is now the only Organisation for Economic Co-Operation and Development (OECD) nation lacking a space agency [12], despite Earth observation satellites benefiting the Australian economy by approximately $4 billion in 2015, up from $3.3 billion in the years 2008 and 2009 [13]. Despite a lack of sufficient support for a local space industry, Australia benefits from free data generously provided and generated by the space activities of other nations, including Algeria, Indonesia, Malaysia, Morocco, Nigeria and Singapore [14].

The *Space Activities Act 1998* (Commonwealth) ('the *Act*') ratified Australia's obligations as a signatory to the *Outer Space Treaty 1967* [15] and *Liability Convention 1972* [16]. The *Act* sought to enable private organisations to launch large satellites into Earth from Australian launch sites. However, these requirements were conceived in the context of large corporations launching only a few satellites, and a large corporation's ability to satisfy those requirements. Due to the lack of development of Australian launch capabilities and the emergence of nano-

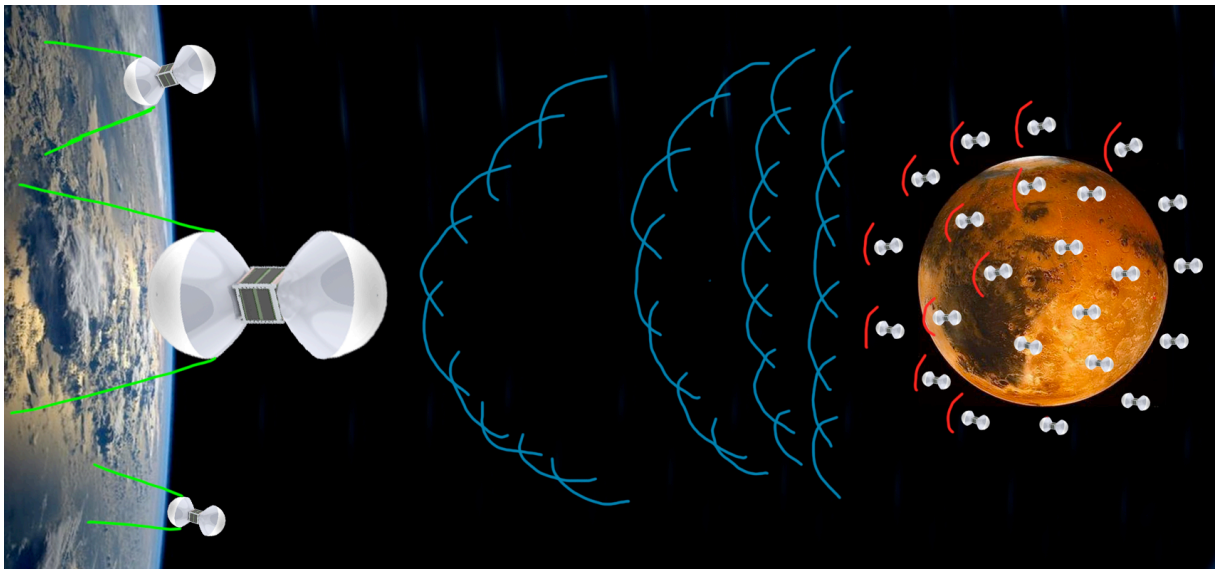

Figure 1. *Graphic depicting a conceptual example of small scale satellite clusters forming planet wide aperture synthesis and phased array telecommunications. A cluster of satellites around Mars or other celestial bodies may relay signals between other bodies utilizing these techniques, resulting in a transmission with the same angular resolution as an antenna of equal size of the entire body.*

satellites, something unforeseen at the time of legislation, these regulations are no longer suited to the climate. As a consequence, the *Act* presents significant obstacles in the establishment of space programs at universities throughout Australia. At the time of writing, this fact has been acknowledged by the federal government, and as such, the *Act* is currently under review.

Program Overview

Despite the significant roadblocks faced by such a program, the UMSP was formed in late 2014 to begin the research and development process of realising a nano-satellite based interplanetary communication network. It is hoped that the program and the development of its missions will lead to a cost-effective method of addressing the future requirements and short-comings of existing systems outlined above. A university program such as the UMSP will allow the freedom to pursue these goals without the commercial constraints industry programs must operate under.

Despite the freedom allowed by a student based satellite program, they suffer from unique challenges in comparison to industry programs. The inability to recruit a veteran workforce with existing knowledge in the desired areas, high turn-over of students as they finish their courses, and the volunteer nature of the work force all combine to create an environment which, if improperly managed, is not conducive to lengthy projects, such as the development of satellites.

Surveys of university CubeSat programs, including [17], [18], [19], [20], [21], and [22], have revealed the common pitfalls of these programs including insufficient communication between sub-teams, scope creep, and mismatched rates of progress among different sub-teams.

To address these challenges, the UMSP consists of two separate but integral branches, the engineering and operations branches [Figure 2]. While the engineering processes and product development of a CubeSat is the focus of many university CubeSat programs, other aspects are oft overlooked. The following non-STEM areas were identified as vital for the long-term survival of the program and the accomplishment of its goals:

1. Academic Development
2. Advancement (Sponsorship and Industry relations)
3. Finance
4. Information and Communications Technology
5. Legal
6. Marketing and Communications
7. Project Monitoring and Management

An executive committee, consisting of four members, leads the two branches. The Managing Director provides ultimate accountability for the program, and ensures that the Executive Committee remains effective and functional. The Operations Director is accountable for direction of the Operations branch, and as such provides direction to the operations coordinators. Similarly, the Engineering Director is accountable for the direction and progress of the Engineering branch. Finally, the Leadership Director assists the various team leaders of the engineering and operation branches with maintaining an agile culture of motivated individuals.

To maintain transparency and reduce any potential disengagement caused by a large organisation or tall hierarchy, all team leaders and members of the executive committee are

equally responsible for directing the program towards an inclusive, professional and productive culture.

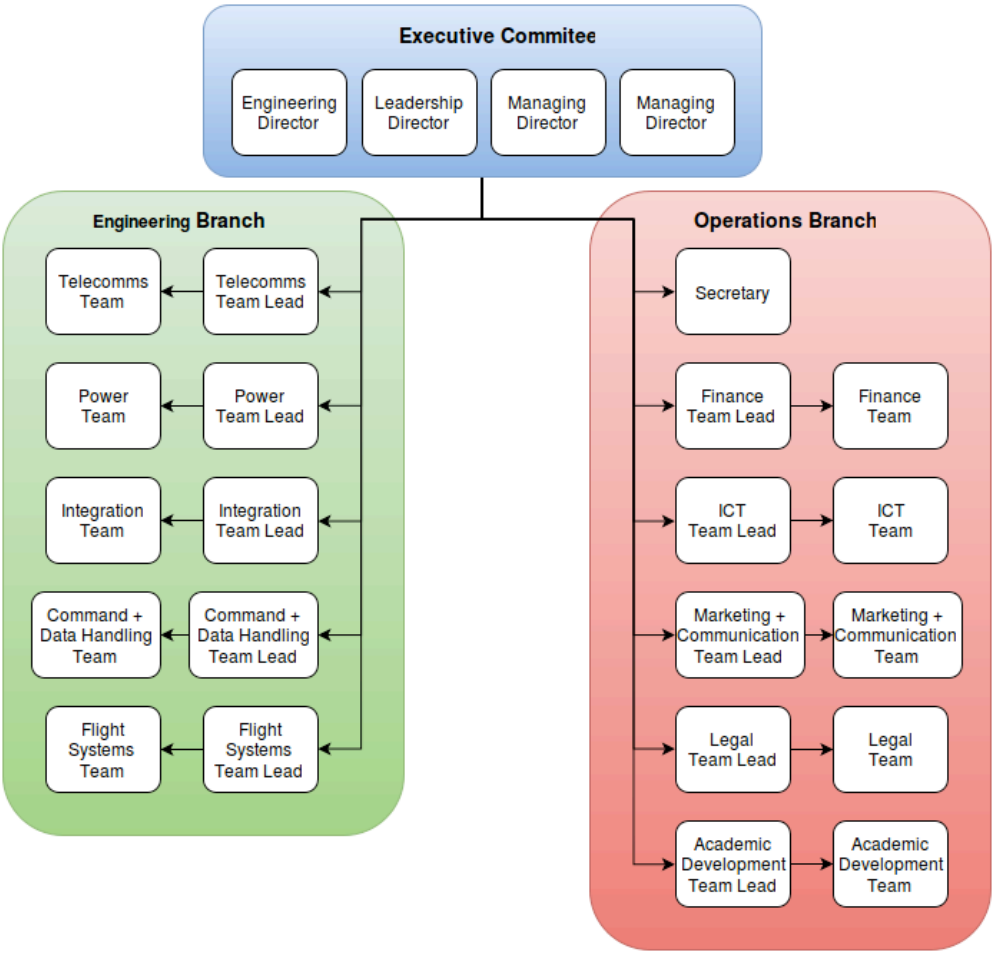

Figure 2. *Organisational Architecture of the University of Melbourne Space Program*

Engineering Branch

The primary branch of the UMSP consists of five groups responsible for the design, testing and implementation of the satellites. Collaboration and innovation by these groups is essential to the success of the program.

Several technological areas have been identified as key to the development of technologies capable of performing in an orbital-based aperture synthesis mesh network. These areas correspond to the five groups involved in the engineering branch of the UMSP: flight systems, flight vehicle (general), flight vehicle (operating systems), communications and power systems. Mission progression within the program will be determined by the successive testing of technologies in these areas [Figure 3.a]. Relevant research will be decided by mission requirements.

The first 1U CubeSat (a 100x100x100mm^3 satellite with a mass less than 1.33kg) ('CS-1') will be a test bed for each of the satellite subsystems to verify their design and functionality in a space environment. The second 1U CubeSat ('CS-2') will serve as a test bed for a deployable high-gain parabolic antenna suitable for nano-satellites, with following missions to build on these capabilities [Figure 3.a]. Each mission will be followed by a program review period, during which the mission objectives and timelines will be reassessed, as well as an

analysis of the effectiveness of the design methodology and organisational structure of the mission team.

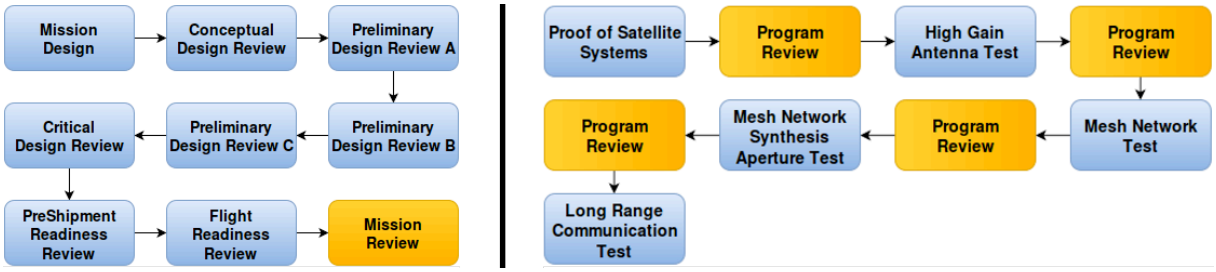

Figure 3*Left: Mission Design and Review Stages Right: Planned Program Missions and Review*

Within a single mission the prototypical series of Conceptual Design Review, Preliminary Design Review A, B and C, Critical Design Review, Pre-shipment Readiness Review and Flight Readiness Review [23] will be followed [Figure 3.b]. In addition, a mission review, independent of each program review, will be conducted at the conclusion of the operational life of the craft to assess system performance and make recommendations for future missions.

To overcome some of the challenges inherent in a student program, an agile Scrum methodology has been adopted [24] [25]. This methodology uses a system of strict length, short work periods termed 'sprints'. Prior to the commencement of each sprint a 'sprint planning' session is held where any requirement changes are identified, the list of required tasks is updated, and the scope of work for this sprint are decided upon. Clear, tangible outcomes for each sprint are also identified. This methodology will allow frequent reassessment of design criteria and objectives as the team develops their knowledge. Furthermore, short sprint periods will facilitate the restructuring of timelines around the team's course requirements.

One source, [24] suggests that the scrum methodology is best suited to team divisions where there is very little overlap in responsibilities between teams and the interfaces between them is well defined. To this end, the prototypical system division has been altered for the first mission to present a clearer delineation between teams and more accurately reflect the utilisation of a standardised form factor [Figure 4]. Examples of this include the rationalisation behind the thermal control sub-team being folded into the integration sub-team and the creation of the flight systems team. Due to the small form factor and limited power of a CubeSat, thermal control is more closely tied to the relative positioning of components and passive cooling elements than to the design of an entire system, and hence falls under systems integration. The flight systems comprises the typical attitude control systems, navigation and guidance, as well as sensor suites for all other subsystems. By separating the design and implementation of a sensor network from the interpretation and application of the collected data, the amount of work being replicated by disparate teams is minimised.

The interfaces between each team are well defined, with volume, mass, power, bandwidth and computation budgets being managed by their corresponding teams. The inclusion of a dedicated integration sub-team to ensure physical, electrical and thermal interference is minimised, during the development of each system rather than post development, will foster ongoing communication between teams and sub-teams. In addition, during planning, sub-teams are encouraged to work in conjunction with both the integration team and other sub-teams to define system interactions. It is hoped that these two methods will foster significant intra-team communication, ameliorating a common pitfall of student-based programs.

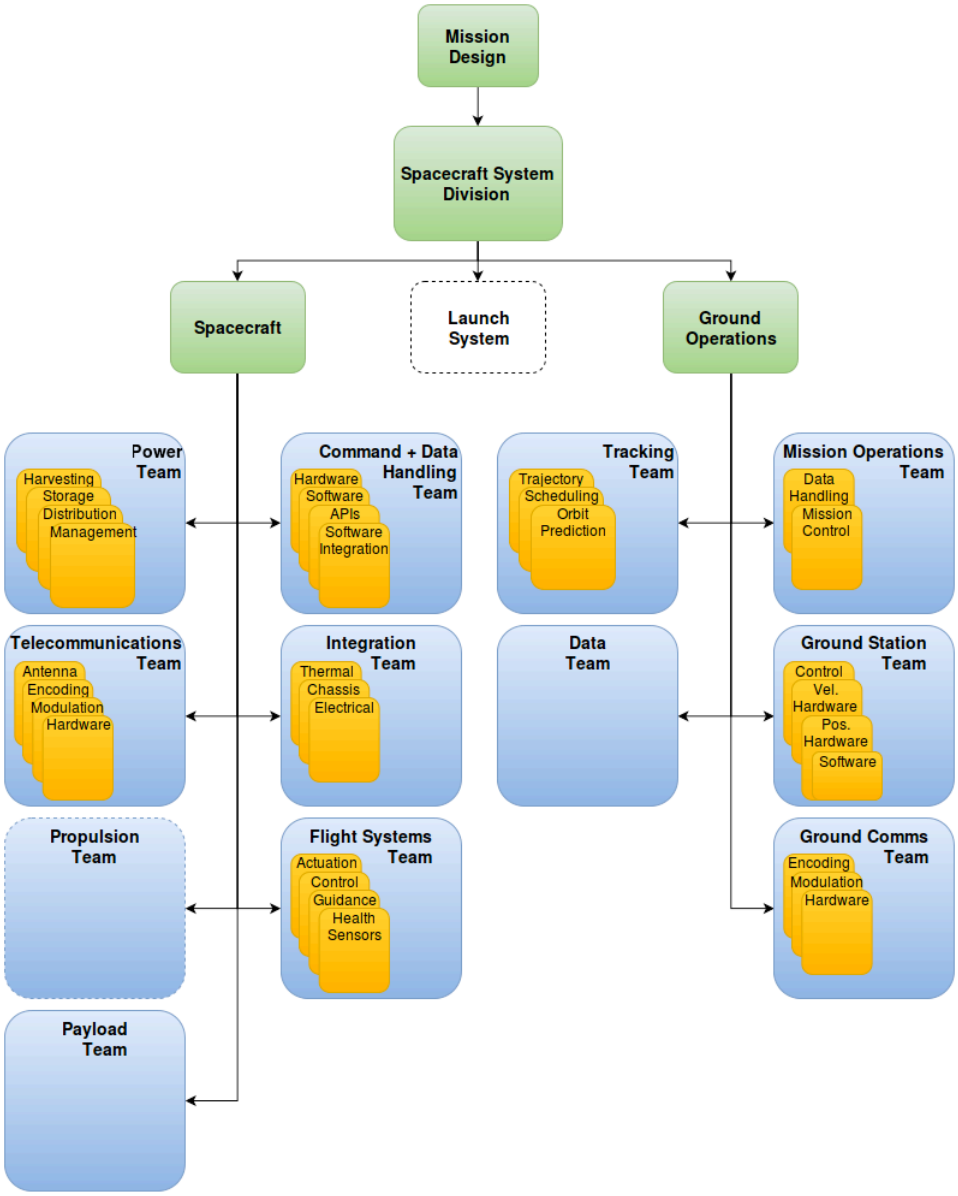

Figure 4: First Mission System Division

Prior to the commencement of each mission, management members will develop a detailed list of milestones for each subsystem. These milestones will form the basis of each sprint within the scrum methodology. During the course of each sprint, the team leaders will monitor the progress of each subsystem team and any unexpected obstacles will be referred to the Engineering Director. Prior to the commencement of the next sprint, the overall mission timeline will be reconsidered according to these obstacles.

It is expected that students will be part of the program for an average of two years, with each mission predicted to last between two and five years. Therefore, sufficient handover will be required to ensure that missions continue to run smoothly throughout membership changes. To accommodate a sufficient handover, it is proposed that each team leader be shadowed by a deputy for the duration of their leadership, with both leader and deputy taking part in all aspects of sprint planning, resource management and design work. At the end of a mission year, the deputy will take over leadership and they will in turn be shadowed. In this manner, it

is hoped that the long-term vision of the program will be instilled in each successive leadership group.

Furthermore, each member of the program is encouraged to maintain an online lab book detailing decisions and processes used throughout a sprint. At the culmination of each sprint, a brief report of the progress made will be required. It is hoped that these procedures will be sufficient to ensure developmental knowledge is maintained throughout membership transitions. The above procedures and methodology will be evaluated following the first mission for efficacy and efficiency.

Operations Branch

To support the Engineering Branch, the Operations Branch encompasses those areas not directly related to the production of each mission but nevertheless vital to its success. The non-STEM areas identified above as critical to the efficacy of the UMSP fall under the purview of the Operations Branch, and have been divided between the teams.

Operations members are drawn from non-STEM schools and faculties throughout the university, including the Melbourne Law School, Melbourne Business School and the Melbourne Graduate School of Education. By incorporating these disparate faculties, members of both branches will have the opportunity to work with colleagues from different areas and develop those professional skills vital to a successful career.

Ultimately, these operational areas will produce valuable research and development vital to the success of the UMSP and the wider Australian space industry. Potential areas of research include Australian space policy reform, exploration of off-earth resource rights, financial support of Australian space industries, development of financial models of extra-terrestrial industries, and the development of youth education programs dedicated to fostering future STEM graduates.

Academic Development

While the lab books and leadership transition procedures will record developmental knowledge of each mission, they will not be sufficient to increase the knowledge base of new members. Consequently, academic and professional development of UMSP members is a core aspect of the program. This will serve multiple beneficial purposes, but critically it will result in members with superior theoretical, practical and professional experience.

The academic development team is dedicated to two primary areas. The first, development of program members, seeks to increase the knowledge and skill base of new and junior members. The second area aims to develop outreach workshops for school students to increase interest in the space sector, with the goal of encouraging more students to enter STEM pathways [26]. The academic development team is working with the marketing and communications team to develop this outreach program.

With respect to the first area, it has been identified that many graduating students lack both practical and professional experience. While many students place great emphasis on their academic transcript for employment opportunities, many employers place equal if not greater value on demonstrations of practical and professional experience. Engineers Australia, as the accreditation body for engineers in Australia, seeks to foster these skills, and as such requires demonstrations of practical and professional experience in accredited engineering courses. The Stage 1 Competency Standard for Professional Engineers [15] details three primary

competencies as: Knowledge and skill base, Engineering application ability, Professional and personal attributes. The program seeks to foster the development of these competencies for both engineering students and those from other faculties, through the application of program management methodologies, frequent skills workshops and regular design reviews throughout the satellite design.

Skills workshops are frequently held on topics pertaining to both professional and engineering skills, especially those overlooked in coursework. Skills workshops run by the UMSP include: the use of and best practice when using Git, Kanban methodology, project initialisation including work breakdowns and risk assessment, budgeting procedures, soldering skills and basic PCB layout. In addition workshops specific to satellite design and concepts such as, mission design, orbital mechanics, subsystem parameter estimations and communication channel fundamentals. Through these and other skills workshops the knowledge and skill base of program members will be greatly increased.

Legal

As the launch of an Australian satellite is an international endeavour, the expedient navigation of all necessary regulations, including launch and export licensing and communication regulations, is critical to the success of any mission. Developing knowledge and experience of these policies and regulations has been identified as a major objective for the program. To achieve this, the legal team is formed of a team of Juris Doctor students with the following primary responsibilities:

- Identify how the *Act* will affect the intentions of the UMSP;
- Develop a plan to mitigate any potential delays; and
- Work closely with the telecommunications engineering teams to understand and navigate any regulations relating to RF spectrum licencing with the Australian Communications and Media Authority (ACMA) and the International Telecommunications Union (ITU).

The legal team will participate in all discussions necessitating legal considerations, including the negotiation of contracts and memorandums of understanding.

The legal team is also tasked with establishing contacts within the legal fraternity with expertise on topics of space law both locally and internationally. It is hoped that through the efforts of the program and the legal team, opportunities for study and research into space law within the University of Melbourne will broaden.

As a result of participation in the program, Juris Doctor students will be able to develop a greater understanding of those areas of law not widely practiced in Australia, and develop practical and professional skills in an industry setting unlikely to be replicated in work experience. At the time of writing, the legal team is contributing towards the federal government review of the *Act*.

Marketing and Communications

Marketing and Communications is tasked with maintaining healthy internal and external relations through organising events, establishing a positive image, and contributing to the advancement of the program. The surveys of university CubeSat programs discussed in the first section of this paper revealed that such projects are susceptible to student disengagement over the long term and as coursework commitments mount. Though the agile scrum methodology goes some way to combating this inevitable aspect of student programs, the Marketing and Communications team organises internal social events to provide a positive

social outlet for members and between teams, stimulating member engagement and cross team relationships.

One highly coordinated project being undertaken by the Academic Development, Marketing and Communications and members of various engineering teams is the development of a 'build-your-own-satellite' workshop. This 'Papersat-1' workshop is being designed to cater for varying levels of audiences, and will be used for training and orienting new UMSP members in an engaging series of sessions, as well as for public outreach amongst audiences from primary school to undergraduate students.

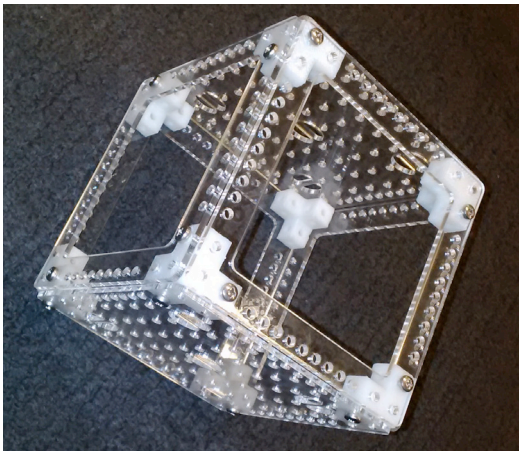

Figure 5: Final chassis design for the Papersat-1 workshop

The final responsibility of the Marketing and Communications team is developing partnerships with external organisations. The design of an attractive brand, careful curation of social media, distribution of media, hosting public lectures, organising radio interviews and attending trade shows has proven to be effective at raising brand awareness. This increased awareness can then be capitalised upon when approaching external organisations for investment or partnership. Many student run engineering projects necessitate external sponsorships in order to establish a sustainable project. It has been identified that many of these groups insufficiently plan for the two-way relationship required in such relationships, and particularly as a project draws to its conclusion. This results in great difficulty in maintaining relationships and forming new ones. To avoid this, a detailed external relations plan has been created, focusing on the supply of well-rounded high-performing graduate students as a potential resource for industry sponsors.

Information and Communications Technology

A common pattern with many student operated engineering projects is a resistance to the consistent utilisation of project management principles and tools. In order to maximise the adoption of principles outlined previously, a set of tools was carefully selected for use within the UMSP. The ICT team are responsible for the installation, maintenance, training and support of these tools in order to establish utilisation as a part of the organisational culture. The following tools assist with collaboration, planning and maintaining documentation and records:

- Collaboration – *Slack*: A messenger client with inbuilt support for collaborative work flows and hooks for common software development tools.
- Planning – *Trello*: A web based planning tool, allowing for the detailed planning of sprints and longer term objectives, with the ability to track subtasks throughout the

sprint.

- Documentation – *GitLab* (Gollem Wiki): A simple to use wiki based documentation system
- Storage – *GitLab* (Git Version Control System) An open source version control platform allowing for private hosting of documentation and design archives.

Conclusion

There has been significant work on nano-satellite or similar, mesh networks by both commercial entities, most notably Google's project Loon and SpaceX's space internet network, and research groups such as those at the University of Surrey, California Polytechnic and the University of Florida. These organisations have focused on the potential for nano-satellite networks to service remote areas or for distributed space and earth monitoring missions. However, the potential for these networks to be utilised for data relay over both earth orbit and interplanetary scales has not been examined. We have established a student run program devoted to contributing to the development of interplanetary communication networks. An organisational structure and agile work flow methodology has been instituted to work towards these objectives. While the development and review of critical missions is managed by the engineering branch of the program, an additional operational branch supports the development of both the program and its members. Graduating members of the program will leave with developed professional and personal skills, and the knowledge base to contribute towards developing nano-satellite based mesh networks.

Acknowledgements

We owe a massive thank you to all of the members of the UMSP; the efforts of whom, this paper represents. The program is only possible because of the dedication and contributions of each and every one of you. What you all have achieved in less than a year so far requires significant congratulations. The authors of this paper each look forward to continuing to make history with you in 2016.

References

[1] T. Reichardt, "Planetary Exploration: a job for the droids?," *Nature,* no. 428, pp. 888-890, 2004.

[2] F. C. Bruhn and e. al, "A preliminary design for a spherical microrover for planetary exploration," *Acta Astro,* no. 63, pp. 618-631, 2008.

[3] S. Dubowsky, "A Concept Mission: Microbots for Large-Scale Planetary Surface and Subsurface Exploration," *STAIF,* 2005.

[4] W. Fink, "Next-generation robotic planetary reconnaissance missions: A paradigm shift," *Planetary and Space Science,* no. 53, pp. 1419-1426.

[5] D. Latimer, "Excavation in Space: A Survey of Automation Technologies," *Rob. Inst. & Civ. Eng., Carnegie Melon Univ.,* 2001.

[6] NASA, "Space Communications and Navigation: NASA's Management of the Space Network," *NASA Office of Inspector General,* no. 18, 2014.

[7] NASA, "NASA's Management of The Deep Space Network," *NASA Office of Inspector General,* no. 13, 2015.

[8] B. Preston, A Vision for the Next Generation Deep Space Network, NASA, 2006.

[9] Herald, "A Place In Space For Us," *Herald,* 14 April 1966.

[10] T. Australian, "U.S. to launch our first satellite," *The Australian,* 15 April 1966.

[11] Defence Science and Technology Group, "WRESAT — WEAPONS RESEARCH ESTABLISHMENT SATELLITE," [Online]. Available: http://www.dsto.defence.gov.au/innovation/wresat-%E2%80%94-weapons-research-establishment-satellite. [Accessed 1 11 2015].

[12] Australian Senate Standing Committee on Economics, "Lost in Space? Setting a new direction for Australia's space science and industry sector," 12 November 2008. [Online]. Available: http://www.aph.gov.au/Parliamentary_Business/Committees/Senate/Economics/Completed_inquiries/2008-10/space_08/report/index. [Accessed 1 November 2015].

[13] ACIL Tasman, "The economic value of earth observation from space: A review of the value to Australia of Earth observation from space," 2010.

[14] A. Dempster, "Australia's satellite scarcity leaves us vulnerable," 7 August 2012. [Online]. Available: http://www.abc.net.au/news/2012-08-07/dempster-space-technology/4179922. [Accessed 1 November 2015].

[15] Office for Outer Space Affairs, United Nations, "Treaty on Principles Governing the Activities of States in the Exploration and Use of Outer Space, including the Moon and Other Celestial Bodies," 1966. [Online]. Available: http://www.unoosa.org/oosa/en/ourwork/spacelaw/treaties/introouterspacetreaty.html. [Accessed 1 November 2015].

[16] Office for Outer Space Affairs, United Nations, "Convention on International Liability for Damage Caused by Space Objects," 1971. [Online]. Available: http://www.unoosa.org/oosa/en/ourwork/spacelaw/treaties/introliability-convention.html. [Accessed 1 November 2015].

[17] T. N. Woods, Miniature X-ray Solar Spectrometer (MinXSS) CubeSat Mission, NASA, 2013.

[18] T. H. Nguyen, "Finishing BLUEsat: Lessons learnt from 15 years of managing an undergraduate space engineering project," *Proc. Austr. Space Science Conf.,* 2013.

[19] M. Swartwout, "AC 2011-1151: Significance Of Student-Built Spacecraft Design Programs – It's Impact On Spacecraft Engineering Education Over Last Ten Years," *Proc. American Society for Engineering Education Annual Conference,* 2011.

[20] C. D. Abadi, "Product and Process: an Innovative Approach for a Student Satellite Program from the Systems Engineering Point of View," *Proc. USU Conference on Small SAtellites,* 2001.

[21] T. Hoge, "Norwegian Student Satellite Program - ANSAT," *Proc. AIAA/USU Conference on Small Satellites,* 2008.

[22] K. M. Brumbaugh and E. G. Lightsey, "Application of Risk Management to University CubeSat Missions," *Journal of Small Satellites,* vol. 2, no. 1, p. 1470160, 2013.

[23] C. Brown, Elements of Spacecraft Design, Reston VA: AIAA, 2002.

[24] L. Rising and N. S. Janoff, "The Scrum Software Development Process for Small Teams," *IEEE Softw.,* no. Jul./Aug., pp. 26-33, 2000.

[25] C. L. Rich, "The success Factors of Running Scrum: A Qualitative Perspective," *Journal of Software Engineering and Applications,* no. 6, p. 367, 2012.

[26] Australian Council of Learned Academies, "STEM: Country Comparisons," 2013.

The Case for Mining Asteroids

Author: Gabi Hobbs[1]

[1]U.N.S.W. Canberra, Australia

Summary: Human rights, space exploration, ethics and law are long-term key steps for human development. Asteroids provide a viable stage for extraterrestrial mining, providing material requirements for a burgeoning space race. As a necessary step in understanding our future life in space, ethicists must define asteroid ethics in order to clarify the necessity and the limits of asteroid mining, due to the fact that many asteroids orbit closer to Earth than the Moon. This ethics relates to all asteroids, including those located in the Main Asteroid Belt and the Kuiper Belt because despite their variety, no asteroid can be treated as a lawless frontier and an ethical hierarchy for best-suitable asteroids should be followed when mining, before any space mining law is ratified. This classification will probably be based on the asteroid's proximity to Earth and will be similar to other ethical decisions such as the ethical differences between the International Space Station, the future asteroidal habitats and the colonies on other planets. They need to advocate against extreme positions such as human indulgence with its resource overspending and also against the standards of 'love for outer space', which lobbies against space mining based on moral values. While the some people think space mining should be done with any ethical considerations based for instance on the utilitarian idea that there are millions of asteroids in our solar system, this doesn't legitimize humanity to destroy unique environments based on 'infinite'-resources idea, when, in fact, asteroids are just vast territories. The other extreme position promotes no mining at all based on illogical claims such as religious motivations like 'man's dominion only over the Earth, rocks have souls' or based on radical environmental rights and aesthetic considerations which claim man should not step foot in outer space since it is a pristine place. The shift to asteroids will help ethicists contribute to a balanced space decision-making. The Earth's experience has demonstrated that a discussion on mining involves ethical value-approaches, competition between governments, and clashes among profit-driven companies. All these factors will come into play when humans will employ technology to mine asteroids. Multinational cooperation, on the other hand, has proven that ethical standards have been already set in place for specialists of various areas of science and of different countries to interact positively. We all have much to learn about mutual cooperation - an essential step for a pro-exploration culture. Without resource mining, colonisation of outer space is impossible.

1. Introduction

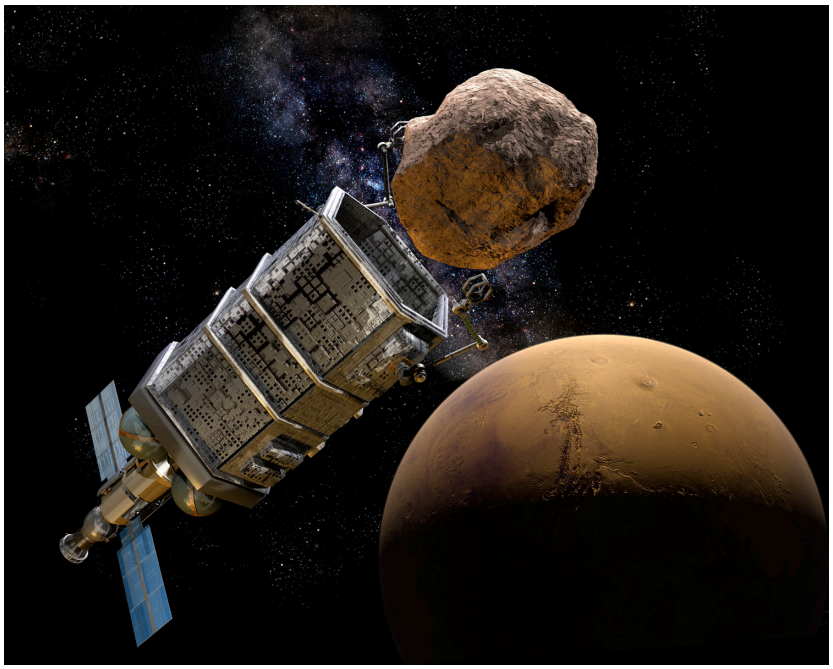

Fig. 1 An artistic depiction of an autonomous probe capturing an asteroid near Mars for mining of its raw materials (stevenhobbsphoto.com.au)

Is now the time for humans to go beyond the Moon? Asteroid mining seems to be the next compelling goal for humans, the first phase in colonising outer-space (Fig. 1). Mining in space will surely happen and there is pressure to allow it. Why are ethics so important? Should asteroids mining be permitted? How exactly can we reach an answer for this ethical question?

If humanity is to encourage ethical development amongst the future space mining parties, it must do so deliberately. Ethics should contribute to shaping a vision to outline space mining objectives and boundaries. With low gravity, undiluted solar energy [1, 2] and a vast, untapped source of raw materials [3], asteroids have plenty to offer to the troubled inhabitants of planet Earth. Whether humanity mines or not asteroids to suit its needs, is a choice to make, like any daily choice and in this sense the urgent dilemma humanity faces is the NEAs' destruction and not so much the mining distant asteroids in the Main Asteroid Belt (MAB). In order to choose wisely, we need to articulate alternative possibilities of how the future can unfold in relation to our history. In this paper I focus on why we should mine asteroids and show that asteroid mining is a key step in space exploration. I begin with a brief explanation of asteroids, followed by an explanation of technical terms. This is then followed by a discussion of some methods for mining, a definition of asteroid mining ethics, and the reasons in favour and against mining of asteroids. I conclude with suggestions for the future, and summarize the argument outlined in the introduction: asteroid mining is an essential step for a pro-exploration culture based on an ethical value-approach and also on competition.

1.1. Asteroids

Asteroids are small rocky bodies less than 1,000 km in diameter [4]. They are defined as Near Earth Objects or Near Earth Asteroids (NEOs or NEAs) when estimating their close proximity to Earth or Potentially Hazardous Asteroids (PHAs) when defined based on parameters measuring the object's potential to make threatening close approaches to the Earth [5, 6]. Forty percent of NEAs have a cometary origin [7, 8]. More than $1.5x10^6$ asteroids were already known in 2015 and probably many more about will be discovered in the future. NEAs are asteroids whose orbit is close to, but do not cross, the Earth's orbit.
Some of them appear to be rocky, while others seem to be metallic and yet may have water ice inside [9]. We currently have the technology to mine asteroids. Decades ago, Pioneers 10 & 11 and Voyager 1 & 2 have long demonstrated that spacecraft can pass unscathed through regions of great asteroid density and use different techniques [10, 11] to travel beyond our Solar System. In my opinion, these exploratory probes have developed a pathway to reaching the deep space, since they were the first explorers to navigate the MAB and the first to encounter asteroids and hazardous solar radiation, significantly higher than that found in the Earth or the Moon's orbit [12, 13]. Additionally, we currently have advanced mining technology like the already tested bio-mining [14], great robot design and sophisticated space instruments [15, 16, 17].

1.2. Economic Factors

The human enthusiasm for asteroid mining is due to the economic factor foreseen for this century by many private entrepreneurs such as: Deep Space Industries and Planetary Resources [18, 19, 20].These two U.S. companies proposing mining the NEAs have proposed criteria regarding what asteroids are desirable to mine (i.e. their twelve-asteroid list) [21, 22, 23, 24], and the suggestion of a limit of 10 m in diameter and of 500 km/s velocity seems like a reasonable definition to apply as an internationally acceptable standard to define an asteroid which could possibly be destroyed in order to profit from the usage of its minerals. However, the tracking of a NEA and its dismantling in the Earth's or the Moon's orbit is yet to be tested. Despite skeptic views regarding the unprofitability of asteroids [25], most scientists

believe that, despite their diminished quantity on Earth [26, 27], Rare-Earth-Resources (RER) are found abundantly on asteroids [28, 29]. Such examples are free metal granules of lanthanide found predominantly in the planetary mantle and core [30], thus extremely hard to access on Earth [31] and also new minerals such as purple putnisite discovered in 2014 [32]. In our Solar System, many asteroids have the potential to have pure minerals in their regolith that would be viable for mining [31, 32]. Although most studied asteroids (the NEAs) are of class C (carbonaceous or chondrite) [33], there is enough evidence to suggest that the NEAs also include class S (silicate) and class M (metallic) asteroids [34]. These last ones are of great interest due to various mixtures of metals and silicates during the asteroidal separation from its original planetoid [35, 36, 37]. Thus, the real drive for asteroid mining would be the 'gold rush' for asteroidal resources for class M asteroids [38, 39, 40].

1.3. Methods and Risks of Asteroid Mining

Several methods of asteroid mining have been proposed, of which most prominent are:
a) sending robots to extract minerals or to capture gases such as helium (He_3), b) bio-mining, and c) asteroid tracking and capture parts of asteroids. While tracking an asteroid means researching and selecting the best candidates for mining, its capture involves changing its orbit using mechanical or nuclear technology and putting it in the Earth's orbit or in one of the Lagrange Points where its rotation would cancel itself. [41]
Bio-mining is a technique already tested on Earth as a sustainable treatment of ores and of mine waste, providing an alternative supply of metals such as copper, zinc, nickel and gold [42]. Bio-mining in space raises two ethical dilemmas: the dilemma of sending microorganisms into space (forward contamination) and bringing back foreign bacteria or viruses (backwards contamination) [43]. Both asteroid-mining private companies Deep Space Industries and Planetary Resources are considering bio-mining asteroids [44] with CubeSats - small probes yet to be developed and sent from a mother ship on promising nearby asteroids. This project is planned to start in the 3-4 years and with mainstream mining commencing in 15-20 years.

The plan to send CubeSats to inject a low-temperature fluid laden with bacteria through cracks and fissures generated by the injection process [45] is problematic for many reasons. We don't yet know how well this mining approach will work in space since we are unaware of the effects of living metal-processing microbes within a vacuum environment, nor the limits of such metabolized life in such a hostile place. It will be extremely unethical for space miners to willingly contaminate an entire or a part of an asteroid with foreign life because life could spread into other possible inhabited worlds, for instance through comet collision with that bio-mined asteroid. Similarly, mining accidents could involuntarily contaminate asteroids unplanned for mining and thus not scheduled for de-contamination after the activity ceases on the nearby mined asteroid. Secondly, terrestrial bacteria and microbes could thrive in space and even change their properties and thus negatively affect our own planet [46]. The usage of bacteria in itself is not immoral as long as humans keep it contained and destroy the microbes after bio-mining. Thus, before any mining of an asteroid commences, the asteroid needs to be searched for life and/or fossils, because this process needs to be carried out in accordance with the non-contamination and humanity's common heritage principles for 'terra nullius' set by the international legal system [47, 48].

Although bio-mining processes might be a jump in processing high valuable resources, this kind of chemical interference is similar to terraforming Mars. This poses ethical problems because of the multiple changes the planet would suffer in the event of implanting new

ecosystems such as the creation of new atmosphere and the introduction of animal and plant species which might suffer genetic mutations. The process of introducing foreign life is an ethical dilemma which humans could solve by bio-mining at a small scale in order to determine its full effects. Engaging in asteroid mining using robots will reduce liability of this type of mission since it won't risk human lives [49, 50]. Notwithstanding the pressure of losing personnel and thus the fear of bad reputation on Earth, mining companies will be willing to take greater risks on landing on difficult asteroids since crewed missions will not actually land on a fast-spinning asteroid.

Another viable alternative, seen as the cheapest option for most entrepreneurs [51], is to capture an asteroid and move it into the Earth or the Moon's orbit. Breaking up an asteroid or capturing He_3 in the MAB causes little disruption in space because MAB is filled with asteroids of different dimensions. In contrast with the MAB, the Earth's orbit is already full and tracking an asteroid in it could be environmentally dangerous. This is due to 'free fall' or asteroidal micro-gravity which may make regolith re-enter over Earth – especially in case of an accident during the dismantling phase. Mining an asteroid close to home could present irreversible effects such as change of Earth's orbit and possibly the disruption of our fragile terrestrial ecosystem.

Therefore, for a cheaper, safer and more convenient option of asteroid mining, we should send small cubesats to conduct mining although it might take more time – up to two or three decades. The reason for this is that it is better for the process to take longer due to safety reasons since the public interest prevails over those of a company/government [52]. If we want the mining to be achieved more safely we may need mine one of Mars' moons.

1.4. Asteroids Mining Ethics

There are no clear approaches to directly define and detail space mining ethics. The dominant ethical requirements for an asteroid mining industry will require the need to be 'objective', meaning not having a detached view, but a cooperative approach in order to manage wisely both earthly and space resources. Just as on Earth where all human activities are governed by ethics, humans must develop an asteroid ethic. There are multiple reasons why we cannot regard asteroids as simply barren surfaces which can be used as we wish (i.e. mining limits to current technological capacity to investigate them and ethical limits similar to those on Earth such as archaeological, paleontological, Indigenous community-based factors). Thus, we must develop an asteroid ethics which allows for responsible use of these celestial bodies.

The human future in space depends on present ethics. The future expansion is not only in the hands of some issue-motivated groups such as environmentalists, but in the hands of humanity as a whole. Fulfilling life's potential at all costs would be unethical [53] and raises questions regarding how life is valued – whether merit is judged based on the level at which lives contribute to others or by some other means. The process in which the present is different from the past does not make present ethics limited or dependent on the past. Thus, asteroid ethics should not focus only on utilitarian or deontological arguments of duty, purpose or value. However real and important they might be, these arguments don't provide defensible reasons for acting because mining asteroids will not be done only according to the main two principles governing ethical professional conduct (the interest of public and that of clients), but it will also be performed in the interest of future generations and for future unknown benefits.

71]. Similar to small human communities' overseeing morality and usage of resources in a region, nations would not agree to permit trivial and frivolous use of space resources after proper deliberations [72, 73].
4) Space mining is a financially viable investment for companies because it will open a new market for diverse, complex products in fields such as robotics (i.e. cubesats, satellites), energy access and consumption, medicine and planetary defence to avoid from asteroid impact.
5) The technology to access asteroidal resources is here and if properly deployed, space mining will no longer be in the realms of science fiction. Instead, space mining will be attractive and affordable to those countries which choose to be actively involved in space industry and also constantly educate citizens in space exploration [74, 75, 76].
6) Another possible secondary benefit of asteroid mining could be the linguistic factor with the development of a new terms and language used by space miners [77]. A space mining community could develop its own linguistic conventions and culture whose diversity will indirectly benefit humanity in literature, art and music. A terrestrial analogue has been the enrichment of Australian language, culture and art following a historic move from white Australia policy to a multicultural society [78, 79].

Non-viable arguments
Some writers have suggested that mining asteroids will end all human conflicts [80] because this will provide virtually unlimited resources, which is a highly unlikely situation, since not all conflicts are ones over resources (with ideological conflicts being very important in the world today). Making territorial conflicts obsolete [81] is an illusion and an irrational suggestion. While there is life, there is both evil [80] and altruism [82], as proven by social studies on human behaviour [83, 84, 85]. Human ethics must be founded on life and experience, which means space values also need to come 'from below' and not 'from above' rules, in the sense that asteroid ethics have to be applied ethics [86] in order to reflect a correct human conduct in the mining field and in all areas of space life. I believe the suggestions regarding asteroid mining ending major conflicts, political cheating, social turmoil and other forms of violence such as nuclear threat, authoritarianism or extreme ideologies abusing human rights [87, 88, 89] are unrealistic because the abolition of evil is impossible according to Immanuel Kant who regarded evil as a personal challenge every human must overcome. Thus terrorism, starvation or inequality between social classes will not disappear if human society benefits from space mining. Nor will states' wealth will become equal even in a democratic society which not necessarily acts in the best interest of its citizens [91].

The problem with these main reasons is that even if we have the technology for a successful mining expedition, at present, no tests have yet been performed in tracking small asteroids or 'safe-altering' their orbits. In addition, there haven't been any mining tests in zero-gravity mining. Tracking an asteroid even into the Moon's orbit – not necessarily into our planet's orbit already full of debris and satellites, could cause a future domino effect if accidents occur and therefore an international war may be inevitable. This means possible inadvertent change of the Moon's orbit through ongoing asteroid gravity capture, which could then destabilise Earth's tides and climate. If an asteroidal disaster occurs, the international influence of mining states involved will have great significance for terrestrial peace because one of the main objectives of peace process is to change perceptions by focusing on the issues underlining conflicts through an issue-based approach [92]. Thus, rather than nations using armed conflicts to resolve differences perceived as irreconcilable on particular issues, mining nations will have the resources and experience to forge compromises in order to answer

future disputes without the recourse to armed violence. Additionally, since modern war uses products manufactured from RER used to manufacture sophisticated communication technology, a focus on economic issues will open new opportunities for conflict resolution [93] because wealth or economy in general plays a dual role in war-to-peace transitions by addressing the past (the means and ends of past disputes) and by shaping the present (the vision of a new society [94]). An asteroidal conflict started between a space power and a small state (such as Equatorial nations – already angered - see the Bogota Declaration) will have a lesser impact on the world's stability - unlike a dispute between states like China or Russia which could easily start a world conflict. Future property claims over certain asteroids, disputes over orbit borders or market fluctuations could turn sour and challenge states' status. In my opinion, space-faring nations need the support of small developing nations in order to mine asteroids because we live in a global era when strong economies can be impacted by the insolvency of one country (i.e. the Greek economy) and also regional conflicts over territorial claims can change the borders of a nation (i.e. the Spitzbergen Islands off the Norwegian coast [95] and Moldova, part of former U.S.S.R., now democratic mostly due to the Romanian language, culture and history [96]).

Should we regulate the use of asteroids to protect it for future generations, or should we simply continue the 'laissez faire' attitude of previous generations? Since space exploration and space industry in particular are much riskier than anything we experience on Earth, asteroid mining should be prioritized according to a benefit-risk balance, meaning each asteroid would be individually considered and mined separately because their resources and location vary greatly.

3. Main Arguments Against Asteroid Mining

Asteroid exploration is set for a bright future despite all opposition to asteroid mining because there are many agencies investigating it for its great benefits, like NASA, ESA, Japan Space Agency.

1) Opponents claim that tracking asteroids in the Earth's orbit is likely to cause the asteroid to hit the Earth, endanger humans, fauna and flora, contaminate ecosystems with foreign life and disrupt life as we know it. However, because asteroid mining doesn't need to rely on tracking asteroids into the Earth's orbit and it doesn't necessarily imply mining disasters such as terrestrial ones (i.e. those in Inner Mongolia where Chinese profit comes at a high environmental price: the huge wasteland near the city of Baotou), most people don't consider asteroid mining morally wrong.

2) Another objection to space mining regards the supposed inexistence of sophisticated methods (such as waste recycling) for asteroid mining to be a winner or a front-runner for the global earthly economy. Some people condemn space mining industry for not having the intent to use space debris and inoperative satellites for fuel or not having enough 'green' programs in place to recycle future space products obtained from the asteroidal regolith [97]. This scrutiny is unjustified because this industry is still in its infancy, about to deliver spectacular results and overcome great future difficulties. All mining endeavours present unforseen situations and nothing is perfect - not even in engineering design and thus any ethical position needs to be critically evaluated from different perspectives which might include the future unforseen mining contributions for the human flourishing in space.

3) Asteroids are also considered by some ethicists as pristine environments and thus in need for protection as 'wilderness areas' [98, 99]. I believe this rule should apply for particular asteroids which have been proven to be inhabited by a form of life, similar to terrestrial

future disputes without the recourse to armed violence. Additionally, since modern war uses products manufactured from RER used to manufacture sophisticated communication technology, a focus on economic issues will open new opportunities for conflict resolution [93] because wealth or economy in general plays a dual role in war-to-peace transitions by addressing the past (the means and ends of past disputes) and by shaping the present (the vision of a new society [94]). An asteroidal conflict started between a space power and a small state (such as Equatorial nations – already angered - see the Bogota Declaration) will have a lesser impact on the world's stability - unlike a dispute between states like China or Russia which could easily start a world conflict. Future property claims over certain asteroids, disputes over orbit borders or market fluctuations could turn sour and challenge states' status. In my opinion, space-faring nations need the support of small developing nations in order to mine asteroids because we live in a global era when strong economies can be impacted by the insolvency of one country (i.e. the Greek economy) and also regional conflicts over territorial claims can change the borders of a nation (i.e. the Spitzbergen Islands off the Norwegian coast [95] and Moldova, part of former U.S.S.R., now democratic mostly due to the Romanian language, culture and history [96]).

Should we regulate the use of asteroids to protect it for future generations, or should we simply continue the 'laissez faire' attitude of previous generations? Since space exploration and space industry in particular are much riskier than anything we experience on Earth, asteroid mining should be prioritized according to a benefit-risk balance, meaning each asteroid would be individually considered and mined separately because their resources and location vary greatly.

3. Main Arguments Against Asteroid Mining

Asteroid exploration is set for a bright future despite all opposition to asteroid mining because there are many agencies investigating it for its great benefits, like NASA, ESA, Japan Space Agency.

1) Opponents claim that tracking asteroids in the Earth's orbit is likely to cause the asteroid to hit the Earth, endanger humans, fauna and flora, contaminate ecosystems with foreign life and disrupt life as we know it. However, because asteroid mining doesn't need to rely on tracking asteroids into the Earth's orbit and it doesn't necessarily imply mining disasters such as terrestrial ones (i.e. those in Inner Mongolia where Chinese profit comes at a high environmental price: the huge wasteland near the city of Baotou), most people don't consider asteroid mining morally wrong.

2) Another objection to space mining regards the supposed inexistence of sophisticated methods (such as waste recycling) for asteroid mining to be a winner or a front-runner for the global earthly economy. Some people condemn space mining industry for not having the intent to use space debris and inoperative satellites for fuel or not having enough 'green' programs in place to recycle future space products obtained from the asteroidal regolith [97]. This scrutiny is unjustified because this industry is still in its infancy, about to deliver spectacular results and overcome great future difficulties. All mining endeavours present unforseen situations and nothing is perfect - not even in engineering design and thus any ethical position needs to be critically evaluated from different perspectives which might include the future unforseen mining contributions for the human flourishing in space.

3) Asteroids are also considered by some ethicists as pristine environments and thus in need for protection as 'wilderness areas' [98, 99]. I believe this rule should apply for particular asteroids which have been proven to be inhabited by a form of life, similar to terrestrial

national reserves and parks where special care is offered to endangered plant or animal species, for instance. At present, there is no life or aesthetic and cultural value considered by humanity to support this claim.
4) According to many scientists, asteroids offer great scientific benefits such as clues to the origin of life on Earth. Some people believe that by mining/destroying them we prevent future research in this area. However scientific experiments are to be done before each mine starts.
5) Some people are in favour of Arctic and Antarctic mining, considered to cost much less. In many scientists' view [100], however, if mined, these zones may release methane gas found under the thick ice layers found at each of the poles and thus raise global temperatures and affect the ozone layer. Another potential peril is ocean contamination with smelting products– inexistent danger in space. Thus, asteroid mining is preferable because mining RER will have a lesser impact on the Earth's environment than terrestrial mining.
6) Some people have argued that space resources ought to be evenly distributed amongst all countries. Sharing in resources and profits without any contribution is unethical no matter how rich or advanced the sharing company or country might be because of the economic changes which take place and which are closely connected with the phenomenon of increasing returns - the oldest theory in economics [101]. Another reason is the fluctuation in the behaviour of populations which plays an important and controversial role in evolutionary biology – the Fisher's principle. [102]. I consider the equal distribution of space resources or humanity's role of overseeing the interest of a private client or country as wrong due to the competition principle which drives the mining industry at present [103, 104, 105, 106, 107] and also due to present international wealth balance's instability [108]. In modern economics, despite collaboration and joined operations between mining companies, mining companies have the tendency to follow their own economic interests, usually with no final collaborative engagement or common identification towards a unified mining industry. Thus, competitiveness is not achieved by focusing on one parameter, but actively and extensively pursued on a group of pertinent issues (i.e. human resource investment, innovation and manufacturing processes and so on) [109]. Additionally, at the international level, a country's dominance in the world is changed by many different factors apart from the economical parameter [110]. Wider societal factors will play their part in humanity's future circular economy which has much to do with mining processes, design of consumer products and recycling of waste in the fight to protect Earth and outer space [111]. Nevertheless, deliberate national choices in sharing resources are not unethical [112] if supported through referendum and should be encouraged based on humanitarian aid principles such as royalties on leases delivering funds to help developing countries. The ideal goal of space ethics, including asteroid ethics as a science, is to objectively justify the proposed set of principles which will be fundamental enough to hold for all particular situations [113, 114], including mining processes and resource delivery.

Objections to these arguments

Most of these values refer to abstract notions and are not really practical in real life where competition and desire for a quick gain mark modern society. Since this opposition relies mainly on earthly mining disaster-arguments, we shouldn't consider asteroid mining to be intrinsically morally wrong. The idea that asteroids have intrinsic value in themselves only as a whole is incorrect because, as a parallel, our Earth is not valuable only as a planet, but due to each of its unique ecosystems [115, 116]. Similarly, an asteroid should be valued as a whole and in parts. Additionally, present space law or lack of law should not stop us from mining because law has never been an obstacle for great inventions.

The current international law system doesn't cover space mining. Despite the lack of present regulations, a parallel with earthly mines carefully preserving items of historical significance such as fossils or artefacts applies to asteroid mines because looking for alien life before and during future excavations should always be a priority. Nevertheless, asteroid mining will be governed by principles such as 1) human rights of freedom and open access, and freedom of information; 2) fair competition, private property rights, and minimal state based on the OST principles of transparency which will deny a private company to keep asteroidal information commercial-in-confidence and will prevent a nation from hiding classified mining information; and 3) the priorities of leadership and national security in world of affairs" – extremely important in the development of international asteroid policy.

Asteroid mining will also have legal implications with the need for an Asteroid Treaty. In my opinion, until space settlements have their own government in place, the best option for space mining conflicts is an improved OST legal system with an International Asteroid Treaty for all main space powers to agree upon in order to avoid future conflicts and legalise usage and ownership of asteroids. This treaty will be similar to the Madrid Agreement of 2002 which clarified the legal regime governing Antarctica. My argument for not using the international sea or air systems as a guide is based on the fact that there are huge differences between sea and air benefits (i.e. fishing, travel) and the usage of asteroids and that the Sovereignty Principle for asteroids and the private ownership of a company are both guaranteed on behalf of that country's signatory status to the United Nations (U.N.) space policy. Additionally, there is no need for a state to enforce a space policy, rather a U.N. engagement. Thus, USA's Asteroid Bill (May 2015) is irrelevant because the OST covers the space law regarding these space bodies. Further studies of the legal issues of asteroid mining will be the subject of future work.

I strongly believe that due to the huge risks and costs nobody will mine asteroids unless private property is guaranteed. Although mining NEAs could be managed efficiently through a system of leases by the U.N. [117], no terrestrial international organism will enforce its regulations for the MAB asteroids due to the vast distance or at least not at present due to inexistent legal jurisdiction areas for specific asteroidal families. Declaring sovereignty on asteroids and releasing asteroid lease titles should be tasks dealt by an international body of the U.N. and according to an Asteroid International Agreement. Most space miners will be registered within a parent state and, thus, easily identifiable. In my opinion, the odd 'pirate' ventures with no state of registry will be made liable by supplementary norms of this treaty. And if this system fails, then the state regulations should apply for each space mining company or multilateral state agreement in case of a multinational company, if in place.

4. Suggestions for Asteroid Mining

Without the back-up plan of seeking new RER, found abundantly on asteroids, the future global economy will suffer greatly. In my opinion, all mining should be performed responsibly, without destroying the environment by humans or robotic technologies as it might take away the 'future unknown asteroid experience' a human might have when visiting asteroids. During the incoming decades, due to its known benefits, asteroid mining will be conducted within certain limits stated by a future asteroid ethics which will greatly help the enforcement of legal regulations. The ethical behaviour in space will be hallmark for space industry since humanity assumes that the OST principles will be respected by the future space industry and that unethical space behaviour will be strongly condemned by the international

community, maybe much more severely than wrong terrestrial actions due possibly to greater impacts on environment and human lives.

The need to protect asteroids is mainly due to the fact that humans will not be able to live in a hostile climate for a long time unless they use resources such as those found inside asteroidal regolith and also due to the possibility of life that might exist on them. Space exploration equals asteroid mining and its main reasons, such as humans' unique sense of curiosity, capacity to 'project oneself beyond the immediate boundaries of space and time' and exploration mission or desire, also apply to space mining. Although I agree with these important reasons for asteroid mining, I consider that the greatest benefit is the opening of new possibilities of exploration, greatly enhancing humanity's ability to go beyond its physical and intellectual limits. In addition, such missions invite international cooperation in multiple fields: hardware design, mineral delivery, commercial exploitation, planetary defence against asteroidal impact, engineering deflection of dangerous planetoids, geological, psychological and legal research.

Taken together, with all its main economic benefit, asteroid mining will demonstrate great human cooperation as never seen before. It will be the greatest scientific achievement, more valuable than humanity's first step on the Moon because we have something larger to gain in mining asteroids: not just the preservation of our species, the study of our evolution or the safeguard for our environment. Space mining will require various people of different backgrounds coming together towards a common purpose: the opening of a new frontier which will enlarge human opportunities on Earth and in the far-land which many will come to call 'home'. During history, societies which took risks and extended themselves beyond their borders are known as non-stagnant worlds [118, 119] and increase the chances for success for successful peace, prosperity and progress. Asteroid mining will be such a milestone for human future in space due to multi-national operations which guarantee cooperation, and not necessarily peace (i.e. despite its role in human progress, International Space Station ISS has not guaranteed peace).

Unlike Mars or the Moon, the need to protect asteroids from human ruin is immediate, as private companies will likely mine them within the next generation. Nevertheless, there will clearly be no great magnitude of asteroid extraction soon and it will always happen in connection with to the Earth's climate's destruction. The future usage of asteroid minerals depends on their profitability on the earthly markets and will be a stepping stone in the creation of a space settlement. The uniqueness of products which result will be according to the characteristics of such mined asteroids. The operating costs will have a huge impact at first knowing the high price for space equipment and the high risk for human space involvement.

I don't believe market fluctuations will have a great impact on the value of asteroidal resources, knowing how expensive and rare He_3 and strategic metals are on Earth. Space minerals are expected not be subject to market fluctuations as international markets are generally not subject to cyclical fluctuations due to unchanged tastes and habits [120]. Also the fact that the mining industry will happen at a small scale due to immense investments needed, infant technologies (i.e. biomining, nanotechnology, hydrometallurgy for treating RER ores or concentrates) and inexistent qualified space mining personnel will temper market fluctuations. Similar to climate resources (i.e. sun, sea, sand supply), the value of space minerals varies in time and space. However, unlike other market commodities, they will probably not be affected by markets' fluctuations due to their demand, geographical

supply and abundance for the future [121]. Another reason for the value of space mining investments not to be subject to market variations is the great return of these shares which will drive a low market risk [122]. Due to their high demand and terrestrial scarcity, these pure minerals will continue to be expensive for a long time without a wide price fluctuation or at least less wide than that of terrestrial supplies. Nevertheless, due to possible alteration of global/regional terrestrial resources' usage, markets and regulatory mechanisms are needed for an equitable and sustainable allocation of space resources [123, 124] because it is crucially important to move from a current capitalist understanding of the world towards an ecological understanding [125]. Additionally, more than economic and legal reasons (such as the synergy between the public and private sector), testing the equipment will be the most critical step towards the feasibility of asteroid mining (i.e. unlike NASA's risks, Russia's repetitive testing brought back a higher rate of success [126]).

All these previous arguments are important as they provide a clear set of ethical thinking for establishing reasons for mining and for setting clear asteroid land marks and space mining regulations for future asteroid mines before human and robotic presence are established on them. A cosmocentric ethic enunciated for the protection of asteroids and the recognition of space private property will be a powerful incentive given to governments to sign an international asteroid treaty to settle in outer space. This treaty must be an active timely legal tool with practical examples, not a simple list of postulates.

5. Future Directions

Asteroid mining will maximise the choices available to us and to future generations because of its various benefits. It will help humanity to take a responsible environmental position regarding the Earth due to new technologies and withdrawal from the Artic mining. In addition, it will teach us to avoid a potential asteroidal impact because experience in asteroid mining will allow for changing an asteroidal orbit and destroy it, if necessary. Although self-interested reasons should never have priority over moral reasons, some rational compromise between self-interested reasons and human welfare is to be reached in this ethical decision of asteroid mining.

Fig. 2 An artistic depiction of human and robotic mining on a NEA (stevenhobbsphoto.com.au)

Conclusion

Throughout history humanity has been driven by a sense of adventure and curiosity to explore, including extreme environments such as the poles and the Himalayan Mountains. I believe that there are decades in the history of a nation when challenges occur. To miss them is to miss the whole meaning of progress, of an era. Thus, asteroid mining is such a challenge because we risk great peril if we can't predict how to answer to problem of resource depletion and explore new possibilities to further our innovations within space exploration. Humanity should be careful about retreating from space mining because if we are reluctant to turn our back upon asteroids and we will deny all capability to colonise space and to manifest our presence beyond Earth.

Acknowledgments

I am extremely indebted to my professor, Stephen Coleman of U.N.S.W., for his help, constant motivation and invaluable inspiration. Additionally, I express all many thanks to the anonymous reviewer of this paper and especially to Prof. Graziella Caprarelli of University of South Australia for her invaluable review and great scientific suggestions regarding the cosmochemistry and the geochemistry of asteroids.

References

1. Bãdescu, Viorel, Asteroids: Prospective Energy and Material Resources, Springer Science & Business Media, 2013.

2. Tony & Schwartz, James S.J., Some Ethical Constraints on near-Earth Resource Exploitation, www.academia.edu/17490769/Some.Ethical_Constraints_on_Near-Earth_Resource_Exploitation as read on 12/05/15- asteroids are called 'peaks of eternal light', 'places of uninterrupted sunlight' due to extremely powerful solar energy concentrated on asteroidal regolith.

3. Resources in Abundance, in *Sky at Night: Stairway to Heaven*, pp. 68, 2009.

4. Liou, J.; Malhotra, R., Depletion of the Outer Asteroid Belt, *Science,* No. 275, pp. 375-377, 1997.

5. Benner, L., Goldstone Radar Observation Planning: Asteroid Radar Research, *JPL/California Institute of Technology*, 2014.

6. Chesley, S.R.; Chodas, P.W. & al., Quantifying the Risk Posed by Potential Earth Impacts, *Icarus* No. 159, pp. 423-432, 2002.

7 . Wetherill, G.B., Where the Apollo Objects come from? *Icarus*, No. 76, pp.1-18, 1988.

8. Number disputed by Luu, Jane, Comets Disguised as Asteroids, *Publications of the Astronomical Society of the Pacific*, Vol. 106, pp 43, 1994.

9. Supra Note 8.

10. Fimmel, Richard O.; Van Allen; James & Burgess; Eric, Pioneer: The First to Jupiter, Saturn and Beyond, *National Aeronautics and Space Administration*, U.S. Government Printing Office, Washington D.C., 1980.

11. Murphy, Guy, Mars: A Survival Guide, ABC Books, pp. 32-37, 2010.

12. Durante, Marco, Space Radiation Protection: Destination Mars, Life Sciences, in *Space Research*, Vol. 1, pp. 2-9, 2014.

13. Coca, James, Space Invaders – Asteroids, Mars and Radiation, 2013 on the website www.forbes.com as retrieved on 19/07/15.

14. http://deepindustries.com/mission/ and http://planetaryresources.com, read 23/04/15.

15. Thermal blankets made out of kapton to release and retain heat according to Sheedy, Chris, Star turn, UNSW Magazine, Summer 15/16, Graph of Eight, Australia, 2015.

16. Book of Robots: Discover the Amazing Androids Changing the World, in How It Works Bookazine Series, Imagine Publishing, Sydney, pp. 19 &22 & 100, 2015

17. Supra Note 1.

18. Mazanek, D.D.; Merill, R.G.; Brophy, J.P.; Mueller, R.P., Asteroid direct Mission Concept: A Bold Approach for Utilizing Space Resources, Acta Astronautica, Elsevier, 2015.

19. Lewicki, C.; Diamandis, P.; Anderson, E., Planetary Resources – the Asteroid Mining Company, 2014 as read on 10/10/14 on www.mdpi.com/2078-1547/5/2/224/pdf

20. Tronchetti, F., Private Property rights on Asteroid Resources: Assessing the Legality of the Asteroids Act, *Space Policy*, No 33, Elsevier, 2015.

21. www.marssociety.org, on the website accessed 12/06/15.

22. Listner, Michael: Space Property Rights: It's Time, and Here's Where to Start on www.permanent.com

23. Elvis, Martin, How Many Ore-bearing Asteroids?, *Planetary and Space Science*, No. 91, pp. 20-26, 2014 Elvis estimates that there are only 10 NEAs suitable for platinum-group metal mining and 9,000 NEAs suitable for water extraction.

24. Szoka, Berin & Dunstan, James, Space Law: Is Asteroid Mining Legal?, as accesses on www.wired.com/2012/05/opinion-asteroidmining on 01/10/15

25. Henbest, Nigel, Striking it Rich in the Sky, *New Scientist*, Vol. 94, No. 1306, 20 May 1982.

26. Steven Siceloff, Study: Asteroids Provide Sustainable Resource, 2013, on the website www.nasa.gov/mission_pages/asteroids/news/asteroidmining.html, accessed 27/07/15.

27. Massari, Stefania; Ruberti, Marcello, Rare Earth Elements as Critical Raw Materials: Focus on international Markets and Future Strategies, Resources Policy, No. 38, pp. 36-43, 2013.

28. Kargel, J. S., Market Value of Asteroidal Precious Metals in an Age of Diminishing Terrestrial Resources, *Proceedings of Space, American Society of Civil Engineers*, pp 10, 1996,. and www.permament.com/lunar-and-asteroid-mining-company.html, as read on 12 May 2015.

29. Baxter, Stephen, Our Future In Space, Focus, No 214, pp. 32, Apr. 2010 and Galliot, Jai, Commercial Space Exploration: Ethics, Policy and Governance, Ashgate Publishing Ltd., 2015.

30. Hamblin, W. Kenneth; Christiansen, Eric H., Exploring the Planets, Chap. 8. *Meteorites and Asteroids: Small Bodies of the Inner Solar System*, Macmillan Publishing Co., New York, pp. 273-280, 1990.

31. Barrera Bello, Elixir William, Lanthanide-Based Dieletric Nanoparticles for Upconversion Luminescence, Doctoral Thesis, Universitat Rovira I Virgili, Tarragona, 2013.

32. Shaw, David, Missing Minerals, *Double Helix, CSIRO*, pp. 6, Dec 2015.

33. Dunn, T.L.; McCoy, T.J.; Sunshine, J.M.; McSween Jr., H.Y., A Coordinated Spectral, Mineralogical, and Compositional Study of Ordinary Chondrites, *Icarus*, No. 208, pp. 789-797, 2010 and Vita-Finzi, Claudio & Fortes, Dominic; Planetary Geology: An Introduction, Dunedin Academic Press Ltd , pp. 14-15, 2013.

34. Dunn, T.L.; Burbine, T.H.; Bottke, W.F.; Clark, J.P., Mineralogies and Source Regions of Near-Earth Asteroids*, Icarus*, No 222, pp. 273-282, 2012.

35. i.e. Iotokawa, once considered to be ordinary chondrite –unmelted origin , [according to Binzel, R.P.; Thomas, C.A.; DeMero, F.E.; Tokunaga, A.; Rivkin, A.S.; Bus, S.J., The MIT-Hawaii-IRTF Joint Campaign for NEO Spectral Reconnaissance, Lunar Planet, *Science*, No. 37, pp. 1491, 2006] has now its composition confirmed as of primitive achondrite origin, [according to Nakamura, T. et. al., Preliminary Examination of Habayusa Asteroidal Samples: Mineralogy and Mineral-Chemistry, Japan, Geoscience Union Meeting, 2011].

36. Trial Harbour, Strahan, Port Davey, Bruny Island, Marrawah, Naracoopa, Cape Barren Island, Rheban and the King River delta.

37. Bottrill, R.S., Rare Earthly Ta, Nb and Sc Minerals reported in Tasmania, Tasmanian Geological Survey Record No 7, 2001 as read on the 12/10/15 www.mrt.tas.gov.au/dominfo/download/UR2001_07UR2001_07.pdf The terrestrial analogue of the Tasmanian RER, like highly valuable tantalum, niobium and scandium discovered in alluvial conglomerates, makes us understand how little we know about RER deposits – present not only in igneous rocks like basalt or granite of volcanic rock, but also in sedimentary rocks

38. Elvis, Martin, Let's Mine Asteroids – for science and profit, *Nature*, No 549, Vol. 485, 2012.

39. Jones, Tom, Snaring a Piece of the Sky, *Aerospace America*, pp. 18-20, 2012.

40. Parker, Russ, Energy Supplies in Crisis, *David West Books*, New York, 2009.

41. www.neo.jpl.nasa.gov and www.en.wikipedia.org/wiki/Asteroid_capture, website accessed on 10/03/15

42. http://deepindustries.com/mission/ and http://planetaryresources.com, read 23/04/15.

43. Fogg, Martyn, The Ethical Dimension of Space Settlement, *Space Policy,* No. 16, pp. 205-211, 2000.

44. Healey, Justin ,The Cloning Debate, *Issues in Society*, Vol. 188, The Spinney Press, pp. 1-2 & 6-10, 2003.

45. Wall, Mike, Asteroid Miners May Get Help from Munching Microbes, Jan 2015, on www.space-com/28320-asteroid-mining-bacteria-microbes.html, website accessed 20/04/15.

46. Butler, Jeb, Unearthly Microbes and the Laws Designed to Resist Them, *Georgia Law Review,* Vol. 41, pp. 1363 & 1368-1369, 2007.

47. Rathman, Kim Alane, The Common Heritage Principle and the United States Commercialisation of Outer Space, PhD, Graduate Theological Union, pp. 183-184, 1996.

48. Dodirina, Catherine, Who Owns Outer Space? Accessed on 12/05/15, on the website www.eandt.theiet.org/magazine/2010/11/who-owns-outer-space.cfm

49. Clarke, Jonathan, Outback Mars, in *Australian Sky & Telescope: The Essential Magazine of Astronomy*, No. 83, 2015, pp.18-20, 2015.

50. Clarke, Jonathan; Held, Jason M.; Dahl, Astrid; Wheaton, Nicolette & the Arkaroola Mars Robot Challenge Expeditioners, Field Robotics, Astrobiology and Mars Analogue Research on the Arkaroola Mars Robot Challenge Expedition, *Proceedings from the 14th Australian Space Research Conference*, pp. 237-249, 2014.

51. Scheeres, D.J. & Schweickart, R.L., The Mechanics of Moving Asteroids, *Proceedings of the Planetary Defence Conference*, AIAA, Orange County, California, 2004.

52. Alger, Philip L.; Christensen, N.A.; Olmsted, Sterling P., Ethical Problems in Engineering, *John Wiley & Sons Inc.*, N.Y., U.S.A., pp. 1-3, 1965.

53. Cave, Peter - Beyond Experiences or Appearances, *Oneworld Publications*, Sydney, pp. 67, 2015.

54. McQuaid, Kim, Earthly Environmentalism and The Space Exploration Movement, 1960-1990: *A Study in Irresolution*, *Space Policy*, No. 26, pp. 163-173, 2010.

55. Nacu, Ion, Un Posibil Impact al Asteroidului 'Apophis' cu Pamantul in Anul 2036, *Fizica si Tehnologiile Moderne, Vol. 6, No. 1-2*, Chisinau, pp. 34-39, 2008.

56. Aron, Jacob, Exponential Growth, *New Scientist,* No. 3051, pp. 34-35, Dec 2015.

57. Shapiro, I.I.; A'Hearn, M. & al., Defending Planet Earth: Near-Earth Object Surveys and Hazard Mitigation Strategies, in *National Research Council*, No. 153, Washington D.C., 2010.

58. Anker, Peder, The Ecological Colonisation of Space, *Environmental History,* No.10, pp. 239-268, 2000.

59. Phillips, Ellen; Skyner, Ed; Moore, Gillian; Gray, Ilse & Staples, Mary (ed.), Voyage through the Universe: The Far Planets, *Long-Time Books*, Amsterdam, pp. 138, 1990.

60. Chesley, S.R.; Chodas, P.W. & al., Quantifying the Risk Posed by Potential Earth Impacts, *Icarus,* No. 159*,* pp 423-432, 2002.

61. Strategic Importance of Australia's Uranium Resources, Paladin Resources Ltd, Submission No. 47, 2005, website accessed 01/05/15 www.aphref.aph.au_house_commitee_isr_uranium.report_chapter9.pdf

62. www.industry.gov.au/Office-of-theChief-Economist/News/media-releases/Pages/ Resource-depletion-masks-Australian-mining-productivity-growth.aspx, as read on 01/05/15

63. www.web.mit.edu/12.00/www/m2016/finalwebsite/elements/ree.html, website accessed 01/05/15.

64. Long, G., The Geology or Rare Earth Elements, 2010, www.geology.com/usgs/ree-geology/, website accessed 20/05/15.

65. www.static.businessinsider.com, as read 22/06/15.

66. Sonter, Michael J., The Technical and Economic Feasibility of Mining the Near-Earth Asteroids, the 49th International Astronautical Congress, Sep-Oct 1998, Melbourne, Australia, on www.spacefuture.com, as read on 20/06/15.

67. www.progressivehumanism.com as accessed on the 01/10/15

68. www.theguardian.com/science/2015/may/14/early-men-women-equal-scientists, website accessed on the 01/10/15

69. www.bighistoryproject.com/chapter4 Chapter 4: Humans accessed on the 01/10/15

70. Diamond, Jared, The Worst Mistake in the History of Human Race, 1999 accessed on the 01/10/15 on www.discoverymagazine.com/1987/may/02-the-worst-mistake-in-the-history-of-the-human-race

71. Bedwell, Theodore Cleveland & Stronghold, Hubertus, *Bioastronautics and the Exploration of Space*, U.S. Air Force, Aerospace Medical Division, 1965.

72. Milligan, Tony & Schwartz, James S.J., Some Ethical Constraints on near-Earth Resource Exploitation, www.academia.edu/17490769/Some.Ethical_Constraints_on_Near-Earth_Resource_Exploitation as read on 12/05/15. These authors believe the scientific benefits overweight the economic gain, which is questionable because one might argue that terraforming asteroids leads to a betterment of humanity and needs to be put into practice as soon as possible after the scientific secrets have been revealed since Earth will not be a habitable planet indefinitely.

73. Read more on the moral reasons for terraforming in Supra Notes 43 and 58.

74. Zubrin, Robert, The Case for Mars Conference, A.N.U. Public Talk, Canberra, on 23/03/2015.

75. David, Leonard, Is Asteroid Mining Possible? Study Says Yes for 2,6 Billions, 2012 on www.space.com/15405-asteroidf-mining-feasible-study.html, as accessed on 01/09/15 regarding the 02/04/2012 study of Keck Institute for Space Studies (KISS) of the California Institute in Pasadena

76. William, Robyn, Bold Ambition drive More Countries in Space Exploration, 2015 quoting Erica Vowles' study of 2014 on www.abc.net.au, as accessed in 02/04/15

77. Auer, Peter, Language and Space: An International Handbook of Linguistic Variation. Theories and Methods, Walter de Gruyter, London, 2010.

78. Chow, Benjamin (ex-chairman of the Council for Multicultural Australia), The Challenges of Immigration & Integration in Australia and The European Union, , *National Europe Centre Paper*, No. 61, University of Sydney , Sydney, Australia, 2003, as read on 26/01/16, on the website https://digitalcollections.anu.edu.au/bitstream/1885/41480/3/chow.pdf

79. Bastian, Brock, Immigration, Multiculturalism and the Changing Face of Australia, School of Psychology, University of Queensland, Brisbane , Australia, 2012 as accessed on the website www.uq.edu.au on 27/01/16 and Bastian, B. & Haslam, N., Immigration from the perspective of hosts and immigrants: Roles of psychological essentialism and social identity, *Asian Journal of Social Psychology*, No.11, Issue 2, pp. 127-140, 2008.

80. http://www.newrepublic.com/article/117815/space-mining-will-not-solve-earths-conflict-over-natural-resources

81. www.moonexpress.com, as read on 22/05/15.

82. Jean-Paul Sartre, L'Existentialisme est un Humanisme, Nagel, Paris, 1949.

83. Szalavitz, Maia, Is Human Nature Fundamentally Selfish or Altruistic?, 2012, as accessed on 26/01/16 http://healthland.time.com/2012/10/08/is-human-nature-fundamentally-selfish-or-altruistic/

84. Hinde, Robert A., Bending the Rules: The Flexibility of Absolutes in Modern Life, *Oxford University Press*, 2008.

85. Vardy, Peter & Grosch, Paul, The Puzzle of Ethics, *Harper Collins Publishers,* 1999.

86. Anastaplo, George, But Not Philosophy: Seven Introductions to Non-Western Thought, *Lexington Books,* Lanham, Boulder, N.Y & Oxford, 2002. He gives the great example of the Noble Prize, pp. 226-227

87. Preston, Noel, Understanding Ethics, 3rd Edition, *The Federation Press,* Leichhardt, N.S.W., Australia, pp. 7-15, 2014 about human capacity to choose among values in chapter 1 The Ethical Challenge.

88. www.ohchr.org/en/NewsEvents/Pages/DisplayNews.aspx?NewsID=15789&LangID=E.

89. Bertrand Badie, Bertrand; Berg-Schlosser, Dirk & Morlino, Leonardo (ed.), *International Encyclopaedia of Political Science SAGE Publications*, pp. 1189, 2011.

90. Young, Frederic C., Labor Relations in Space: An Essay in Extraterrestrial Business Ethics, Philosophical Problems of Space Exploration, *Oxford University Press*, pp 128-129, 1988.

91. i.e. Romanian floods in 2006 when Southern villages were sacrificed to prevent damage in Bucharest www. srfa.ro, as accessed on 01/10/15

92. Wennmann, Achim, Sharing Natural Resource Wealth during War-to-Peace Transitions, in High-Value Natural Resource and Peacebuiliding, Lujala P. & Rustad, S.A., Earthscan (ed.), London, pp. 228, 2012.

93. Idem, Hoeffler, Anke & Collier, Paul, High-Value Natural Resources, Development and Conflict: Channels of Causation, 2012.

94. Zartman, I.W., Looking Forward and Looking Backward on Negotiation Theory, in *Peace versus Justice: Negotiation forward – and backward - looking outcomes,* Zartman, I.W. & Kremeyuk, V. (ed.), Rowman and Littlefield, MD, U.K., 2005.

95. Ederington, L. Benjamin, Property as a Natural Institution: The Separation of Property from Sovereignty, in *the American University International Law Review*, No. 13, Issue 2, pp. 284-288, 1997.

96. Scorpan, Costin, Istoria României: Enciclopedia Comparată a Istoriei Politice a Românilor, Nemira, 1997.

97. www.bbcnews.com, retrieved on 27/02/15.

98. Light, Andrew -The Moral Journey of Environmentalism: From Wilderness to Place, in Moore, Steven (ed.), *Pragmatic Sustainability: Theoretical and Practical Tools*, Routledge Press, London, pp. 6, 2010.

99. Clarke, Jonathan, A Simple Land Use Policy for Mars, in D. A. Cockell, Charles S. (ed.), *Mars Analog Research*, Vol. 11, Science and Technology Series: A supplement to Advances in the Astronautical Sciences, pp. 307, 2006.

100. Lowell, Thomas, Scientists Ride Ice Islands on Artic Odysseys, *National Geographic,* Vol. 128, No.5, pp. 671-691, 1965.

101. Metcalfe, J.S., Competition, Fisher's Principle and Increasing Returns in the Selection Process, *Journal of Evolutionary Economics*, No. 4, pp. 327, 1994.

102. Idem, pp. 329-346. The eminent evolutionary biologist R.A. Fisher's Principle states that the concept of selection plays a fundamental role in explaining the changing importance over time of different patterns of behaviour within a population: patterns of change are premised on patterns of differential or mean behaviour, such as collecting the fruits of someone else's work.

103. i.e. the demand for gas, a cleaner and greener energy alternative to coal has contributed to a major mining development in Western Australia, through Deloitte company Heber, Alex, LNG to drive 'super growth' in Australia, 2013, as accessed on 01/11/15 on http://www.australianmining.com.au/news/lng-to-drive-super-growth-in-australia

104. http://www.minerals.org.au/corporate/about_the_minerals_industry, website accessed on 20/01/16

105. Carbonnier, G., Les Négociations Multi-Parties Prenantes: L'Exemple de l'Initiative de Transparence des Industries Extractives, *Relations Internationales* No. 136, pp. 101-113, 2008.

106. Bannon, I & Collier, P. (ed.), Natural Resources and Violent Conflict: Options and Actions, World Bank, Washington D.C., 2003

107. Collier, P; Elliott, H.Hegre; Hoeffler, A.; Reymal-Querol, M.; Sambanis, N., Breaking the Conflict Trap: Civil War and Development Policy, World Bank, Washington D.C., 2003

108. See more on inefficient space regulations in Landry, Benjamin David, A Tragedy of the Anticommons: The Economic Inefficiencies of Space Law, as read on 14 May 2015 on http://ir.lawnet.fordham.edu/cgi/viewcontent.cgi?article=4770&context=flr

109. http://www.industryupdate.com.au/article/competition-drives-converging-industrial-sector as accessed on 28/11/15.

110. Bennett, J., Conflict Prevention and Revenue-Sharing Regimes, *U.N. Global Compact*, N.Y., 2002.

111. Smith, Michael, Virtuous Circles, *Royal Society of Chemistry News*, Dec 2015 on www.rsc.org, as accessed 22/12/15.

112. Supra Note 92.

113. Supra Note 43.

114. Farber, Marvin, Basic issues of Philosophy: Experience, Reality and Human Values, *Harper Torhbooks*, N.Y., Evanston & London, pp.258, 1968.

115. www.environment-ecology.com

116. Warren, Mary Anne, Moral Status: Obligations to persons and Other Living Things, Clarendon Press, Oxford, 1997.

117. Supra Note 72. Milligan and Schwartz' proposed regulatory system for the careful management of space resources is both practical and rational: '*an ideal licensing regime'* based on '*societal value* of exploitation and *independent* scientific and environmental oversight'.

118. Bury, John Bagnell, The Idea of Progress: An Inquiry Into Its Origin and Growth, *Courier Corporation*, U.K., 1987.

119. Gay, Geneva, The Relationship between Multicultural and Democratic Education, pp 5-11, 2010 on doi://10.1080/00377999709603738 as accessed in 01/11/15

120. Fine, Ben, Labour Market Theory: A Constructive Reassessment, *Routledge*, pp. 40-41, 2002.

121. Scott, Daniel; Hall, C. Michael; Gosling, Stefan, Tourism and Climate Change: Impacts, Adaptation and Mitigation, *Routledge*, pp. 54-55, 2012.

122. Pailwar, Veena Keshav, Economic Environment of Business, PHi Learning Pvt. Ltd., pp. 276-277, 2011.

123. Supra Note 72.

125. Williamson, Mark, Space Ethics and Protection of the Space Environment, *Space Policy*, No. 19, pp. 47–52, 2003.

126. Nieuwenhuis, Paul, Ecology Precedes Economy, *New Scientist*, No. 3051, pp. 52, Dec 2015.

126. www.nasa.gov/pdf/602090main.44s_international_life_support.pdf, read on 20/07/15.

If you build it, will they come?
Price & Demand in the Space Transportation Industry

Matthew P. Richardson

Nova Systems,
Suite 33, 192 Breakfast Creek Road, Newstead, QLD, 4006, Australia

Summary: Lowering space launch costs is widely seen as crucial to the long-term development of the space industry. However, many proposals for reducing these costs make use of an unspoken underlying assumption: that reducing launch costs will stimulate demand. Such a significant assumption warrants investigation, in order to test its validity. To this end, a census of all commercial LEO and GEO launch activities from 1997 to 2014 has been completed. Average annual unit launch costs (in USD/kg) and total annual demand (measured as total payload mass delivered to orbit) have been determined for all commercial launch systems over this period. This data was used in a non-linear regression analysis to establish a model for the relationship between launch costs and demand. The model is used to estimate how much of the variance in demand is attributable to cost, and to establish Price Elasticity of Demand (a measure of the behaviour of demand relative to price) for the space transportation industry. The model is also assessed as a general tool for use in space economics analysis and research. The results indicate that there is a significant correlation between price and demand, with price accounting for around two thirds of the observed variance in demand. Furthermore, the model indicates that demand is highly elastic relative to price. However, while the model fits the existing data well, it would be unviable for extrapolation outside the existing data set. Even with this caveat, the results indicate that there is a strong correlation between price and demand. Therefore, efforts to reduce launch costs should stimulate demand, and the aforementioned assumption is valid.

Keywords: Space Transportation, Space Economics, Price Elasticity of Demand.

Introduction

The excessive cost of launching payloads into space is widely considered to be one of the most significant barriers to growth in the space industry, with costs typically exceeding thousands of United States Dollars (USD) per kilogram of payload delivered to orbit [1]. Low-cost space transportation solutions, such as Reusable Launch Vehicles, are often proposed to reduce launch costs. However, in justifying the business case for these solutions, it is often assumed that lowering launch costs will stimulate demand to levels at which the return on investment for the development of these low-cost solutions is acceptable. This may not be the case – if demand is inelastic in comparison to price for space transportation services, then reductions in launch costs will not have a significant impact on demand. On the other hand, if demand is elastic, then reductions in launch costs should have the desired effect of stimulating demand. This paper details the results of a statistical analysis designed to test this assumption of elasticity using space launch industry data covering the past 18 years. The primary aims of this analysis are to determine if there is a statistically significant correlation between price and demand for space transportation services, and if this relationship exists, to determine of the relationship is elastic or inelastic. It should be noted that historical data, such as that which is used in

this analysis, may not accurately predict future trends, especially where disruptive technologies, such as low-cost space transportation, could have a significant impact on the market.

Data Collection

For the purposes of this study, only the relationship between price and demand is considered. Other factors, such as supply rates and macroeconomic drivers may also influence demand. However, data required to measure these factors was not available from the sources used in this analysis, and their inclusion would not significantly improve the outcomes of this study, which focuses explicitly on the impact of reducing costs on demand for space transportation. As such, while it is important to acknowledge these factors, and perhaps consider them in a more comprehensive economic model of the space transportation industry, measuring the impact of other variables on space transportation demand is outside the scope of this study.

A census of all commercial launch events from 1997 to 2014 was conducted, using launch data from the United States Federal Aviation Administration (FAA) Commercial Space Transportation Year in Review reports [2]. In order to determine the nature of the relationship between price and demand, total annual demand (in kilograms of payload to be delivered to orbit) was compared to average annual price (in USD per kilogram of payload to be delivered to orbit) for each individual launch system. Determining price and demand on a "per kilogram" basis allows for fair comparison of large and small capacity launch systems. Furthermore, comparing launch systems on an annualized basis allows for fair comparison of systems with a shorter commercial service history (such as the SpaceX Falcon 9) with systems which have a longer commercial service history (such as the Ariane 5).

Non-commercial (government) launches may not be strongly influenced by price – other factors, such as political concerns, could take priority. As such, this analysis focuses commercial launch events only, as defined by the FAA. Inflation factors were applied to the historical data using figures from the United States Bureau of Labor Statistics [3]. Payload deliveries to both Low-Earth Orbit (LEO) and Geostationary Orbit (GEO) were considered in this analysis. GEO payloads were converted to a LEO equivalent by dividing the payload mass by the launch vehicle GEO payload capacity, then multiplying this value by the launch vehicle LEO payload capacity. This compensates for the reduced payload capacity associated with the higher delta-V requirements for a GEO launch, and allows for LEO and GEO launches to be compared directly.

The FAA reports provided information on launch systems, dates, and payload descriptions and launch costs. However, payload masses, which were required for both total annual payload and average annual price calculations, were only included in FAA quarterly reports until 2000 [4]. As such, payload values were obtained from a wide variety of sources, including Government and NGO databases [5] [6] [7] [8], space agencies [9] [10] [11] [13] [13] [14] [15] [16] [17] [18], launch service providers [19] [20] [21] [22] [23] [24] [25] [26] [27], academic papers & technical reports [28] [29] [30] [31] [32] [33], news articles [34] [35], conference presentations [36] [37] [38] , manufacturers [39] [40] and other service providers [41].

The collected data was processed and 163 data points were produced. Each data point reflects the total payload delivered to orbit (in kilograms) by a particular launch system in a calendar year, and the average price (in USD per kilogram) of delivering these payloads to orbit in the respective year. These data points are plotted in Fig. 1.

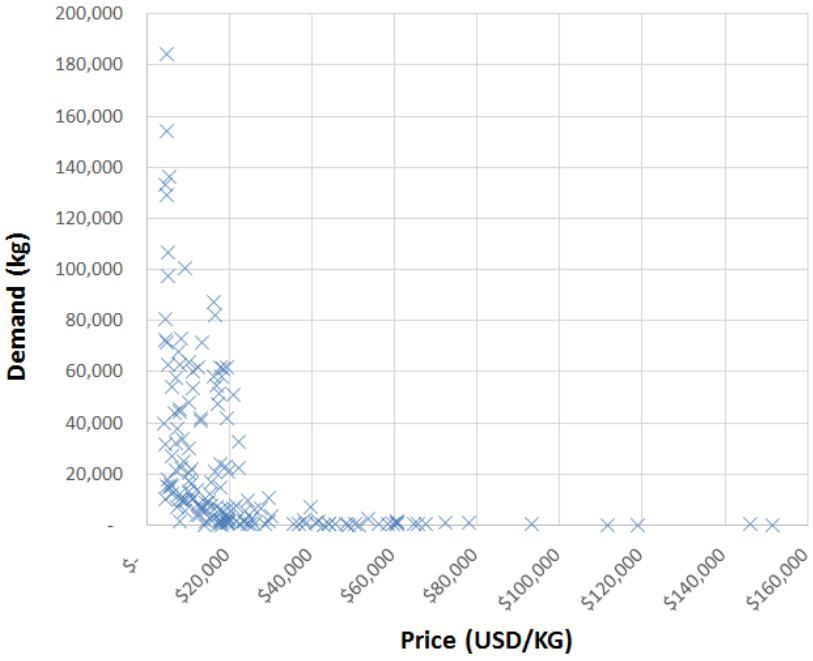

Fig. 1: Collected Data

Regression Analysis

In order to establish whether a correlation exists between price and demand, several different transformations were performed on the data, including both inversion of the data and conversion to a logarithmic scale, and regression analyses were preformed to establish a modelling function. It was determined that simple inversion of the data and linear regression led to the best correlation between the data and the function (as measured by the R^2). As such, a regression analysis has been performed on the data set shown in Fig. 1. This data set is obviously not conducive to a linear regression. As such, the data was linearized through inversion of the demand values. This process of inversion revealed two significant outliers which are not visible in Fig. 1. These outliers can be seen in the inverted data set as shown in Fig. 2.

Fig. 2: Inverted Data (outliers circled in red)

Both outliers correspond to a single launch event each. Both launches were conducted under similar circumstances. The Shtil and Volna rockets were launched in 1998 and 2005, respectively. Both these launches were essentially retired Submarine-Launched Ballistic Missiles (SLBM's) owned by the Russian Navy, with small LEO payload capacities sold on the commercial market [42]. The launches were offered at extremely low cost, probably not fully recovering the cost of SLBM's modifications required for space launch. Furthermore, opportunities for launching payloads under these circumstances only arise through the operations of another stakeholder (i.e. disposal of the Russian Navy's SLBM's). In this sense, although these launches were classified as "commercial" by the FAA, and represent an innovative method for recycling and disposal of military hardware, such launches do not meet the true definition of a commercial launch for two primary reasons: the price is unsustainable for profitable commercial operations, as it does not reflect the total cost of developing and manufacturing the launch vehicle, and availability is constrained by SLBM disposal schedules, such that increases in demand could not necessarily be met through increased supply. For these reasons, these outliers have been removed from this analysis as they are not considered to be true commercial launches.

With the outliers removed, the data set is more amenable to a linear regression, as shown in Fig. 3. With the regression analysis performed, the regression trend line is also shown in Fig. 3. A regression slope hypothesis test was performed in order to determine if a correlation existed between price and demand. A significance level of $p = 0.01$ was selected for the hypothesis test. With the two outliers removed, there were 161 data points in the regression analysis, equating to 160 degrees of freedom for the hypothesis test. For a two-tailed regression slope test with $p = 0.01$ and 160 degrees of freedom, the minimum t-score for the hypothesis test is ±2.623 [43].

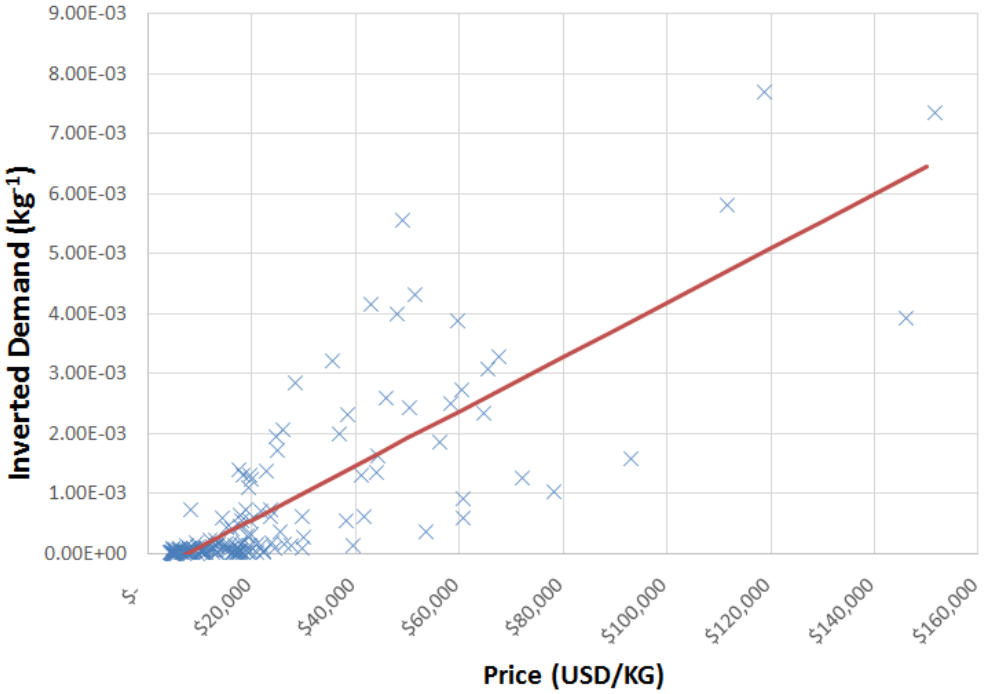

Fig. 3: Inverted Data with regression slope shown

Results

The regression slope shown in Fig. 3 has an R^2 value of 0.663. The result of the regression slope hypothesis test described in the previous section was a t-score of -3.928. This is outside the bounds of minimum score of ± 2.623. As such, it can be said with a 99% level of confidence that there is a statistically significant correlation between price and demand. With the likely presence of a correlation between price and demand established, a price-demand function can be established by inverting the regression slope function. The price-demand function is shown graphically in Fig. 4, along with the original data set for comparison. The equation for the price-demand function is also shown in Eqn. 1, where D = Total Annual Demand (kg) and P = Average Annual Price (USD/kg).

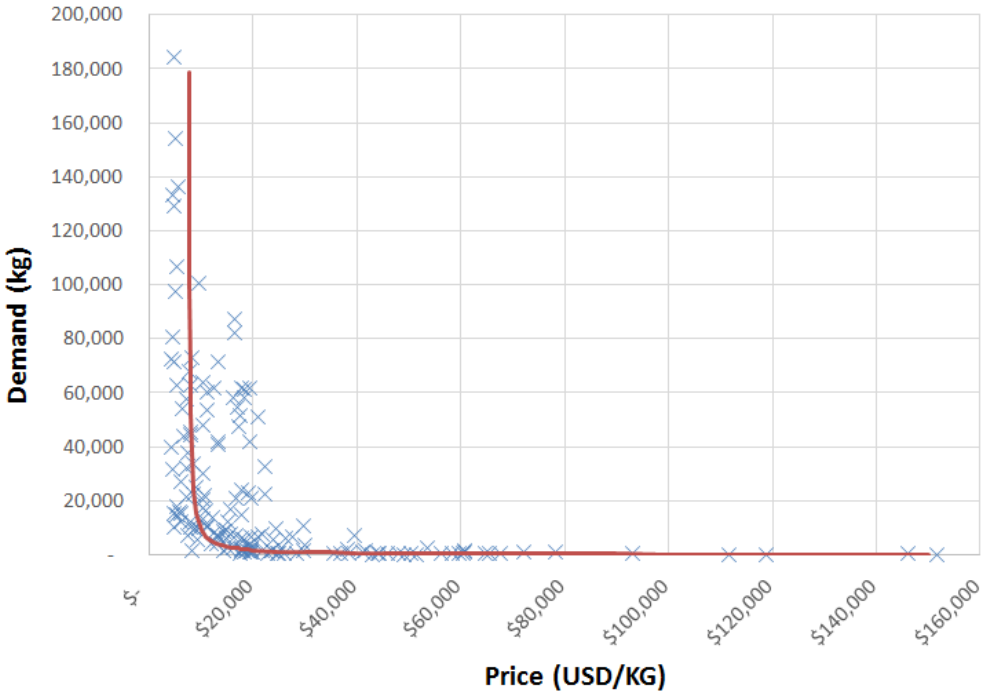

Fig. 4: Price-Demand Function

$$D = [P \times \{4.239 \times 10^{-8}\} - \{2.874 \times 10^{-4}\}]^{-1} \quad (1)$$

With the relationship between price and demand established and verified, the elasticity of the price-demand function needs to be tested. Price elasticity is calculated as a percentage change in demand over a percentage change in price. If this value is less than -1, demand is elastic. If the value is between 1 and 0, demand is inelastic. Price elasticity was tested for all values of the function shown in Fig. 4 (from P = \$7,700 USD/kg to P = \$150,000 USD/kg) in \$100 USD/kg increments. The highest value of price elasticity was determined to be -1.133 at P = \$150,000 USD/kg. Conversely, the lowest value of price elasticity was -63.039 at P = \$7,700 USD/kg. Elasticity was found to increase with decreases in price between these two values.

Conclusions

The results of this investigation indicate that there is a statistically significant correlation between price and demand. Furthermore, the R^2 value of 0.663 indicates that the regression function accounts for approximately 66% of the observed variance in demand. There are likely other factors which impact demand, such as prevailing economic conditions or new satellite technology. Introducing these factors into a multivariate demand function may account for more variance and increase the accuracy of the function, but such an investigation is beyond the scope of this analysis, as the primary focus of this investigation is the relationship between price and demand.

The price-demand function described in this paper has been developed to maximise correlation with available data. As such, the model is not ideal for extrapolation beyond the available data set. For example, the price-demand function reaches a vertical asymptote at a price value of \$7,576 USD/kg, which would indicate that demand effectively become infinite at this price point. While the function fits the data well, this example indicates that using this function to extrapolate to lower prices

in order to establish the impact on demand will yield unrealistic results. As such, extrapolation of the function for purposes outside of this analysis is not recommended.

The results of the price elasticity of demand analysis indicate that demand for space launch services is indeed elastic for changes in price. Furthermore, this elasticity increases as price decreases, suggesting that further reductions in price will have an ever more significant effect on demand. This result validates the assumption that driving down launch costs will stimulate demand for space launch services, and serves to justify the business case for investment on low-cost space transportation systems and technologies.

References

1. Woodcock, G.R., "Technological Barriers to Space Settlement", *Ad Astra*, Vol. 13, No. 1, 2001, pp. 20-23.

2. FAA, "Reports and studies – Year in review", 1998-2014, retrieved from www.faa.gov/about/office_org/headquarters_offices/ast/reports_studies/year_review

3. Bureau of Labor Statistics, "CPI Inflation calculator", 2015, retrieved from www.bls.gov/data/inflation_calculator.htm

4. FAA, "Quarterly Launch Reports", 1997-2000, retrieved from www.faa.gov/about/office_org/headquarters_offices/ast/reports_studies/quarterly_launch/

5. Union of Concerned Scientists, "UCS satellite database", published 2014, retrieved from www.ucsusa.org/satellite_database

6. Union of Concerned Scientists, "UCS satellite database", published 2015, retrieved from www.ucsusa.org/satellite_database

7. National Space Science Data Center, "Master Catalog Search – Spacecraft Query", 2014, retrieved from http://nssdc.gsfc.nasa.gov/nmc/SpacecraftQuery.jsp

8. ESA, "EO Portal – Satellite Missions Database", 2015, retrieved from https://directory.eoportal.org/

9. NASA, "Mir Hardware Heritage – Part 1: Soyuz", 2013, retrieved from http://spaceflight.nasa.gov/history/shuttle-mir/references/r-documents-mirhh.htm

10. ESA, "Our Activities", 2015, retrieved from http://www.esa.int/Our_Activities

11. JAXA, "Press Releases – 2006", 2006, retrieved from http://global.jaxa.jp/press/2006/index_e.html

12. NASA, "SpaceX CRS-4 – Fourth Commercial Resupply Services Flight to the International Space Station", 2014, retrieved from http://www.nasa.gov/sites/default/files/files/SpaceX_CRS-4_Mission_Overview-1.pdf

13. NASA, "Orion Flight Test – Exploration Flight Test-1 Press Kit, 2014, retrieved from http://www.nasa.gov/sites/default/files/files/JSC_OrionEFT-1_PressKit_accessible.pdf

14. NASA, "SpinSat (SpinSat) - 10.21.15", 2015, retrieved from http://www.nasa.gov/mission_pages/station/research/experiments/1019.html

15. NASA, "Orbital-2 Mission to the International Space Station", 2014, retrieved from http://www.nasa.gov/sites/default/files/files/Orb2_PRESS_KIT.pdf

16. NASA, "Orbital CRS-3 Mission Overview", 2014, retrieved from http://www.nasa.gov/sites/default/files/files/Orbital_CRS3_mission_overview.pdf

17. NASA, "ISS On-Orbit Status Report", 2013, retrieved from https://blogs.nasa.gov/stationreport/2013/09/18/

18. NASA, "NanoRacks-UAPSAT-1 (NanoRacks-UAPSAT-1) - 08.27.15", 2015, retrieved from www.nasa.gov/mission_pages/station/research/experiments/1331.html

19. Arianespace, "Launch kit – 2000-2005 Archive", 2015, retrieved from http://arianespace.com/news-launch-kits/2000-2005-archive.asp

20. Arianespace, "Launch kit – 2013-2014 Archive", 2015, retrieved from http://arianespace.com/news-launch-kits/2000-2005-archive.asp

21. International Launch Services, "News Releases", 2015, retrieved from http://www.ilslaunch.com/newsroom/news-releases

22. International Launch Services, "Proton Launch Archives", 2015, retrieved from http://www.ilslaunch.com/mission-control/proton-launch-archives

23. Orbital ATK, "Communications Satellites", 2015, retrieved from https://www.orbitalatk.com/space-systems/commercial-satellites/communications-satellites/

24. Sea Launch, "News & Events – Prior Years", 2013, retrieved from http://www.sea-launch.com/news/11330

25. Boeing, "Boeing-Built Communications Satellite Launched from Florida", 2004, retrieved from http://boeing.mediaroom.com/index.php?s=20295&item=126134&mobile=No

26. ISC Kosmotras, "ISCK documents", retrieved from http://www.kosmotras.ru/en/docs_mkk/

27. SpaceX, "SpaceX Successfully Launches Falcon 1 into Orbit", 2008, Retrieved from http://www.spacex.com/press/2012/12/19/spacex-successfully-launches-falcon-1-orbit

28. Swartwout, M.K., "Student-Built Gossamer Spacecraft: Why Aren't There More (Yet)?", *50th AIAA/ASME/ASCE/AHS/ASC Structures, Structural Dynamics, and Materials Conference*, Palm Springs, California, USA, May 4-7, 2009, doi:10.2514/6.2009-2158.

29. Tito, D.A., Anderson, G., Carrico, J.P., Clark, J., Finger, B., Lantz, G.A., Loucks, M.E., MacCallum, T., Poynter, J., Squire, T.H., Worden, S.P., "Feasibility analysis for a manned mars free-return mission in 2018", *IEEE Aerospace Conference 2013*, March 2-9, 2013, pp.1-18.

30. Burmistrov, V.B. Parkhomenko, N.N., Shargorodsky, V.D., Vasiliev, V.P., "REFLECTOR, LARETS and METEOR-3M(1) what did we learn from tracking campaign results", http://cddis.nasa.gov/lw14/docs/papers/tar3a_vbm.pdf

31. Biddy, C. , Svitek, T., "LightSail-1 Solar Sail Design and Qualification", *Proceedings of the 41st Aerospace Mechanisms Symposium*, JPL, California, USA, May 16-18, 2012, pp. 451-463.

32. Cosmogia, "Dove 3 Orbital Debris Assessment Report (ODAR)", 2012, retrieved from https://apps.fcc.gov/els/GetAtt.html?id=130310&x=

33. Southern Stars, "SkyCube Orbital Debris Assessment Report (ODAR)", 2013, retrieved from http://www.southernstars.com/skycube/files/SkyCube%20ODAR.pdf

34. Shamah, D., "Israeli high-school kids build life-saving satellite", 2014, retrieved from http://www.timesofisrael.com/israeli-high-school-kids-build-life-saving-satellite/

35. Rodino, A., "National Satellite Plan: Argentina's presence in space", 2015, retrieved from http://www.acercandonaciones.com/news/plan-nacional-satelital-la-presencia-argentina-en-el-espacio.html

36. Leveque, K. & Oltrogge, D., "An Evaluation of CubeSat Orbital Decay", *2011 Cubesat Developers Workshop*, San Luis Obispo, California, USA, April 20-22, 2011, retrieved from http://mstl.atl.calpoly.edu/~bklofas/Presentations/DevelopersWorkshop2011/2_MacGillivray_Welcome.pdf

37. Kalnins, I., "Small satellites from an industry perspective", retrieved from http://www.space-lt.eu/failai/Prezentacijos/Indulis%20Kalnins_Small%20satellites%20from%20an%20industry%20perspective.pdf

38. Unisec Global, "Satellite Litsat-1", retrieved from http://www.unisec-global.org/pdf/uniglo2/UNIGLO2_Day1/Student/1_1018_Lithuania.pdf

39. Surrey Satellite Technology, "UK-DMC-1", retrieved from http://www.sstl.co.uk/Missions/UK-DMC-1-Launched-2003/UK-DMC-1/UK-DMC-1-The-Mission

40. Surrey Satellite Technology, retrieved from "NigeriaSat-1" , http://www.sst-us.com/missions/nigeriasat-1--launched-2003/nigeriasat-1/nigeriasat-1--the-mission

41. AGI, “Launch Updates”, 2011, retrieved from http://www.agi.com/media-center/launch-notifications/view-launch-notification.aspx?id=36

42. Harvey, B., “The Rebirth of the Russian Space Program – 50 Years after Sputnik, New Frontiers”, Springer Science & Business Media, Berlin, 2007.

43. Gerstman, B.B., “t Tables”, 2007, retrieved from www.sjsu.edu/faculty/gerstman/StatPrimer/t-table.pdf

Carrying a Torch for Dust in Binary Star Systems

Daniel V. Cotton, Jonathan P. Marshall, Kimberly Bott, Lucyna Kedziora-Chudczer and Jeremy Bailey

School of Physics, University of New South Wales, NSW 2052, Australia

Summary: Young stars are frequently observed to host circumstellar disks, within which their attendant planetary systems are formed. Scattered light imaging of these proto-planetary disks reveals a rich variety of structures including spirals, gaps and clumps. Self-consistent modelling of both imaging and multi-wavelength photometry enables the best interpretation of the location and size distribution of disks' dust.

Epsilon Sagittarii is an unusual star system. It is a binary system with a B9.5III primary that is also believed to host a debris disk in an unstable configuration. Recent polarimetric measurements of the system with the High Precision Polarimetric Instrument (HIPPI) revealed an unexpectedly high fractional linear polarisation, one greater than the fractional infrared excess of the system. Here we develop a spectral energy distribution model for the system and use this as a basis for radiative transfer modelling of its polarisation with the RADMC-3D software package. The measured polarisation can be reproduced for grain sizes around 2.0 μm.

Keywords: Polarimetry, Debris Disk, Binary Star.

Introduction

Astronomical Polarimetry

Within the Solar System polarimetry was most famously used to identify the Venusian clouds as being a composition of H_2SO_4-H_2O particles of various sizes [1]. Venus is particularly well suited to this type of work because it presents a large range of phase angles to Earth in a short time frame, in contrast to the outer planets. Polarimetry is also used to learn more about particle size, composition and porosity of airless bodies like comets and asteroids [2]. Polarisation in these systems is phase and colour dependent with the maximum polarisation known to vary inversely with albedo [2]. Such determinations constitute complicated inverse value problems but are nevertheless pursued for the unique information they can provide.

The integrated light from the disc of a star is typically unpolarised; this is a result of the cancellation by circular symmetry of limb polarisation. For us to see polarisation from a star system requires that the circular symmetry be broken, or polarisation generated by scattering and absorption from surrounding gas and/or dust or another atmosphere. In this case it is possible to determine the size and composition of the scattering particles just as for Solar System bodies.

The HIPPI survey of Southern bright stars

We have recently completed and published [3] a short polarimetric survey of the brightest stars in the Southern hemisphere using the HIgh Precision Polarimetric Instrument (HIPPI) [4]. HIPPI is one of a new generation of parts-per-million polarimeters. The predecessor to HIPPI, PlanetPol [5], conducted a similar survey in the Northern hemisphere [6]. The unprecedented precision of these

two instruments in fractional polarisation – more than an order of magnitude more precise than previous instruments used for such surveys – enabled the identification of a plethora of polarigenic phenomena.

Stellar types identified with elevated levels of polarisation included: late giants, Ap stars, Be stars, close binaries as well as ordinary B-type stars (particularly earlier types) [3], such that polarised stars were most prominent at the extremes of the H-R diagram. The signals from most main sequence stars are polarised only by the interstellar medium. The alignment of elongated grains within the interstellar medium by magnetic fields or otherwise acts to polarise light. Within the local hot bubble, a region largely devoid of gas and dust close to the Sun, this interstellar polarisation is small; ranging between ~$2x10^{-7}$ pc^{-1} in parts of the Northern hemisphere to ~$3x10^{-6}$ pc^{-1} at some Southern declinations [3] (although we have since tentatively identified a small localised region of the Southern sky with interstellar polarisation perhaps double this (Marshall et al., unpublished data), this doesn't appear to be the norm). Amongst main sequence stars, those known to harbour debris disks exhibited slightly elevated levels of polarisation.

Dust grains in circumstellar disks polarise light by scattering and absorption processes. Polarisation seen by aperture polarimetry – where the aperture takes in the central star as well as the whole/a large portion of the disk – has been reported at levels of ~0.1 to 2% ([7] and references therein).

Debris Disks

Circumstellar debris disks around evolved, main sequence stars are the dusty remnants of planet formation processes [8, 9]. They are composed of bodies spanning micron-sized dust grains to kilometre-sized asteroids. The larger bodies (beyond ~ mm-cm sizes) cannot be directly observed, but we infer their presence due to the short lifetime of dust grains under the influence of radiation forces [10, 11] in comparison to that of the host star. Often, the presence of circumstellar dust is revealed by the measurement of excess emission from a system, above that expected from the stellar photosphere alone, at infrared wavelengths.

From multi-wavelength modelling of the excess emission we derive a temperature (radial distance) for the dust [8], i.e. cool disks are detectable at long wavelengths, whereas warm/hot disks have signatures at increasingly shorter wavelengths. Broadly speaking, debris disks are either warm asteroid-belt analogues, or cool Edgeworth-Kuiper belt analogues (e.g. [12]). The incidence varies with spectral type; around FGK (sun-like) stars, the incidence of cool debris disks is 20+/-2% [13], and slightly higher for A stars at ~ 30% [14]. The observations are limited by instrumental sensitivity. At shorter wavelengths, where the photosphere is a greater contribution to the total emission, the contrast between star and disk drops such that only 2% of FGK stars are known to host disks [15]. Likewise, determining the presence of a faint warm belt in the presence of a bright cool belt is also tricky [16].

The architectures of debris systems derived solely from the excess are subject to inherent degeneracies in the modelling process (e.g. between dust grain size and temperature). For example, a simple blackbody approximation underestimates the disk extent for FGK stars by a factor of 4-5 (e.g. [17, 18]). Using spatially resolved imaging as an additional constraint weakens the degeneracy and allows a much better constraint on the dust properties to be derived [19, 20]. Images of the disk continuum at infrared wavelengths are limited by the angular resolution offered by space telescopes. Imaging a disk in scattered light with ground-based 10m-class telescopes (or interferometers) provides both the high spatial resolution imaging, and a measure of the scattering properties of the

dust grains - information that cannot be gleaned by alternative means. However, most debris disks are tenuous, and the relationship between continuum excess and scattered light brightness is weak [21].

Polarimetric imaging using the high-contrast adaptive optics instrument GPI has provided new insights into the structure and architecture of several systems [22-25]. Tracing the polarisation of the disk as a function of its radial extent and orientation allows a unique determination of the disk alignment, and greater insight into the dust properties throughout the disk rather than in aggregate. Aperture polarimetry with e.g. HIPPI [4] can provide similar or even better sensitivity to polarisation induced by circumstellar dust, but without the spatial information, useful in cases where this would be unobtainable in any case e.g. for asteroid belts around more distant stars, or 'hot dust' disks.

Epsilon Sagittarii

System

The inspiration for the present paper is ε Sgr (HIP 90185); it is unusual for a debris disk system on two counts, firstly it has a spectral type of B9.5III, and secondly it is a binary system where the secondary is separated from the primary on a similar scale to the debris disk. It is this second property that makes ε Sgr particularly interesting, for it has the potential to produce an asymmetry in the scattered light seen in our aperture and thus a polarisation signal beyond what might be expected from the disk otherwise.

ε Sgr A is 3.52 M_{Sun} star of spectral type B9.5III. The secondary, ε Sgr B, has a mass of 0.95 M_{Sun} [26] and orbits at 106 AU from the primary [27]. Rhee et al. [28] have reported an excess of 4.5×10^{-6} from *IRAS* 60 μm data, indicating a debris disk centred at 155 AU [27]. Consequently Rodriguez and Zuckerman [27] list ε Sgr as one of nine known dynamically unstable binary/multiple debris disk systems, with only a 0.2% probability that uncertainties in inclination and orbit actually place the secondary outside the unstable zone. The excesses derived from *Spitzer* data at 13 μm and 31 μm [29, 30] are greater than that at 60 μm from *IRAS*, which implies a closer debris disk. Below we develop a spectral energy distribution model with this and other data. Both the cited references and our model assume a circumprimary debris disk, however it should be mentioned that a circumsecondary system like that described by Rodigas et al. [31] for HD 142527 may also be a possibility. Regardless of the true nature of the system we feel that the assumed geometry for ε Sgr represents an interesting case for investigation of the effects of a secondary on the observable features of a debris disk system.

Polarimetry

A linear polarisation measurement of $162.9 \pm 4.4 \times 10^{-6}$ for ε Sgr was obtained with the HIPPI instrument operating in the SDSS g' band (effective wavelength 462 nm) on 1/9/2014 [3]. HIPPI has an aperture of 6.7", which would place the secondary within the aperture, and the centre of the debris disk on the edge of it. However, seeing at the time of the observation was ~4", meaning that a significant contribution from the outer part of the disk can be counted on.

Based on the maximum interstellar polarisation we observed during the bright star survey we would not expect more interstellar polarisation than $\sim 132 \times 10^{-6}$ for a star at 44 pc in the South, meaning that at least $\sim 30 \times 10^{-6}$ is intrinsic to the system – more than would be expected from the infrared excess (Marshall et al., in prep). In the particular case of ε Sgr, the nearest star that we've measured that

we expect to have only interstellar polarisation is the A2.5V star ζ Sgr. It has an interstellar polarisation corresponding to 1.03×10^{-6} pc^{-1} [3]. Assuming a linear increase in polarisation with distance this suggests an interstellar contribution of only 45×10^{-6} for ε Sgr. However ζ Sgr and ε Sgr are separated by 10 degrees and 17.9 pc, and even though the magnitude of interstellar polarisation appears to vary fairly smoothly near to the Sun this calculation should be considered as potentially indicative only.

It should also be noted that ε Sgr B was found as a result of a search of late-B stars showing high X-ray fluxes [26]. Some X-ray binaries have been found to show variable polarisation [32] which may be an alternative explanation for the polarisation observed. However, such detections have been rare, and generally for much stronger X-ray sources. Indeed the X-ray activity might be an indication of dust accretion onto the secondary, which is another scenario suggested for HD 142527 [31].

Modelling Procedure and Results

Spectral Energy Distribution

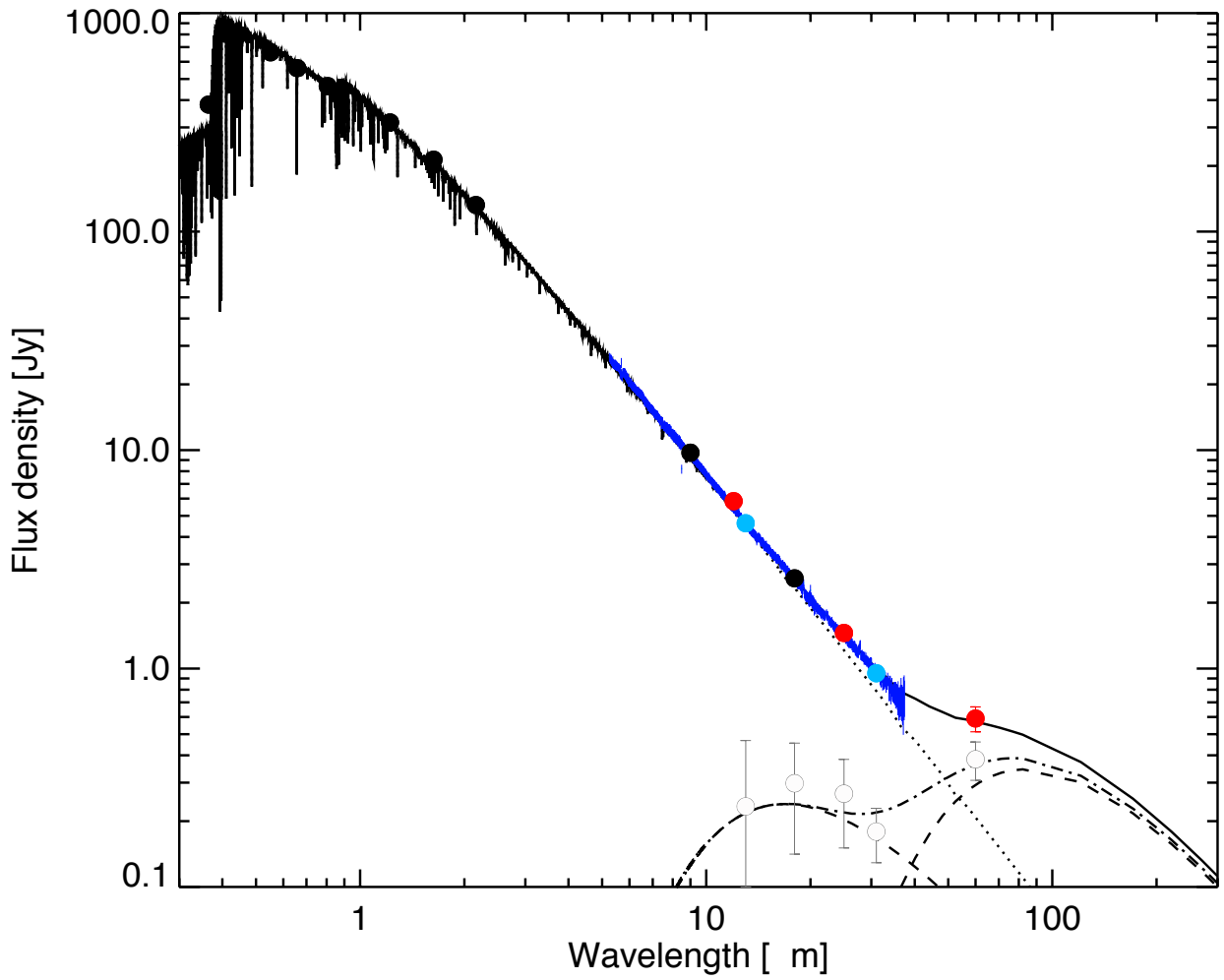

Fig 1: ε Sgr SED. Black data points are ancillary optical, near- and mid-infrared photometry. The dark blue line is the Spitzer IRS spectrum, and the light blue data points are fluxes derived from the spectrum at 13 and 31 μm. Red data points are IRAS photometry. Hollow data points denote the excess at mid- and far-infrared wavelengths. 1-sigma uncertainties are shown as error bars. The dotted line is the stellar photosphere, combining both primary and secondary

components, the dashed lines are the disk components, the dot-dash line is the sum of the disk components, and the solid line is the total star + disk model.

Fig 1 shows the modelled spectral energy distribution (SED). We modelled the spectral energy distribution of the system using two blackbody components and obtained a fractional excess of 75×10^{-6}, which is more consistent with what we would expect based on the polarisation measured. The quality of this value is strongly dependent on the assumptions made regarding the temperature of the cold component and the stellar photosphere contribution.

The contribution of the stellar binary to the total emission was represented by a pair of NEXTGEN stellar atmosphere models [33, 34]. The primary (B9.5III) was modelled with T_{eff} = 9800 K, log g = 3.5, and R* = 3.7 Rsol, whilst the secondary (K5) was modelled with T_{eff} = 5600 K, log g = 4.5, and R* = 1.1 Rsol. The stellar radii are derived from a least squares fit to the photometry based on the stellar models used, which are appropriate for the spectral types. Both stars were assumed to have solar metallicity. The combined stellar SEDs were scaled to optical and near-infrared photometry taken from *HIPPARCOS* [35], 2MASS [36], and WISE [37].

The disk model was approximated as a pair of blackbodies. This approach was motivated by the rising slope of the IRS spectrum at mid-infrared wavelengths combined with the strong excess at 60 μm, indicating the possible presence of two dust components. In our model the two dust components are fitted simultaneously using a least-squares approach, weighted by the photometric uncertainties. We find the best-fit temperature for the cold component, fitted to the 31 and 60 μm data points, to be 60±10 K ($L_{ir}/L_* = 7.4 \times 10^{-5}$), and the warm component, fitted to the mid-infrared excess, was found to have a best-fit temperature of 300±50 K ($L_{ir}/L_* = 1.3 \times 10^{-6}$). We note that a single, warmer disk model does not replicate the shape of the IRS spectrum and IRAS 60 μm data satisfactorily. Due to the absence of longer wavelength data constraining the peak of the cold emission, the total fractional excess is subject to large uncertainties.

Radiative Transfer and Polarisation

To estimate the disk polarisation we use RADMC-3D [38], a three-dimensional radiative transfer modelling code, to handle the scattering and polarisation of a given dust composition and disk structure. We assume that the disk architecture is a ring of uniform volume density of dust centred 120 AU from ε Sgr A with a diameter of 20 AU. The ring is wedge shaped with a narrow opening angle of 5 deg. The geometry of the system is shown in Fig 2. The dust composition used in our models is astronomical silicate [39]. The SED model used blackbodies to fit the excess but here we adopt a realistic grain model. To reconcile these two approaches, the emission from the RADMC-3D model, using the architecture inferred from the SED model, is scaled by an arbitrary amount to match the observed excess emission i.e. the dust mass, number density, etc. is scaled to achieve the same excess.

Using the DDSCAT code [40] we calculate the Mueller matrix elements for an ensemble model of the dust assuming a single grain size within the disk. A power law distribution would be consistent with a steady-state collisional cascade [41], and such is an approach we intend to take with further work, but here we are predominantly interested in the potential scale of the effect and so have taken a simpler approach for the sake of expediency. These matrix elements, along with the absorption and scattering efficiencies are then used as input to RADMC-3D to compute the disk model. Output from the disk model consists of four images tracing the Stokes parameters *I*, *Q*, *U* and *V* at 550 nm (which is the centre of the standard Johnson V band), of which we present *Q* and *U*. The models

below in Fig 3 through Fig 5 illustrate the expected polarisation from ε Sgr as a function of system inclination, geometry and dust grain size. Note that the RADMC-3D polarisation co-ordinate system is rotated 90 degrees such that positive Q aligns with the x-axis.

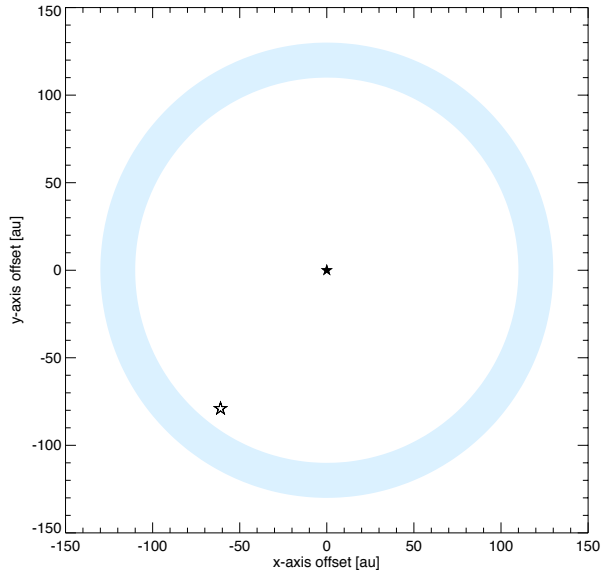

Fig 2: A schematic layout of the ε Sgr system as modelled. We have assumed a narrow, 20 AU, annulus for the disk in addition to known system parameters. In the latter polarisation maps the x- and y-axis units of 1 to 100 correspond to the -150 to 150 AU range shown here.

Table 1: Integrated polarisation for each geometry and grain size modelled. (0.1 μm sized grains were also tested but with no appreciable polarisation signal in any geometry.)

Particle Size (mm)	ε Sgr B PA (deg)	Inclination (deg)	Q (x10^{-6})	U (x10^{-6})	P (x10^{-6})
0.5 (Small)	0	0	-0.4	0.0	**0.4**
		60	0.6	0.0	**0.6**
		90	1.0	0.0	**1.0**
	90	0	0.4	0.0	**0.4**
		60	1.6	1.1	**1.9**
		90	2.5	0.1	**2.5**
1.0 (Medium)	0	0	-0.2	-0.1	**0.2**
		60	-12.0	0.0	**12.0**
		90	-12.3	0.0	**12.3**
	90	0	0.0	0.1	**0.1**
		60	-14.3	-4.2	**14.9**
		90	-15.2	0.6	**15.2**
2.0 (Large)	0	0	-16.0	-0.6	**16.0**
		60	-12.0	-0.1	**12.0**
		90	-12.3	0.0	**12.3**
	90	0	16.0	-0.2	**16.0**
		60	-110.0	-39.0	**116.7**
		90	-200.0	71.0	**212.2**

For inclinations other than 0 degrees, the position angle of the secondary is affecting the polarisation that we see, this can be seen by comparison of Fig 3 and Fig 4. Here greater polarisations are generated for ε Sgr B at a position angle (PA) of 90 degrees. This is a manifestation of asymmetry of the system from the perspective of the observer. Here we also see more significant polarisations in the *U* Stokes parameter. Again this is a result of asymmetry, but here it is brought on by the directionality of Mie scattering, i.e. there is greater forward scattering for the larger grains, and when the disk is inclined this manifests in *U*.

The single grain sizes tested here are on the same scale as the wavelength of light. Consequently there is a "ringing" effect superimposed on trends with grain size. Nevertheless, in Fig 5 we can see the result of increased forward scattering with increased grain size where the polarisation in *Q* near the secondary goes from mostly positive to mostly negative.

The most striking feature of Fig 3 through Fig 5 is the impact of the secondary on the polarisation map – intense fractional polarisation is localised near the secondary. Table 1 presents the total polarisation for the system in each geometry and for each grain size tested. It shows that the total polarisation is consistently larger when the secondary is off-centre and an asymmetry induced in the integrated system. Furthermore, Table 1 reveals that for the largest grains tested the polarisation produced is comparable to the polarisation measured by HIPPI for ε Sgr, and is greater than the infrared excess of the system.

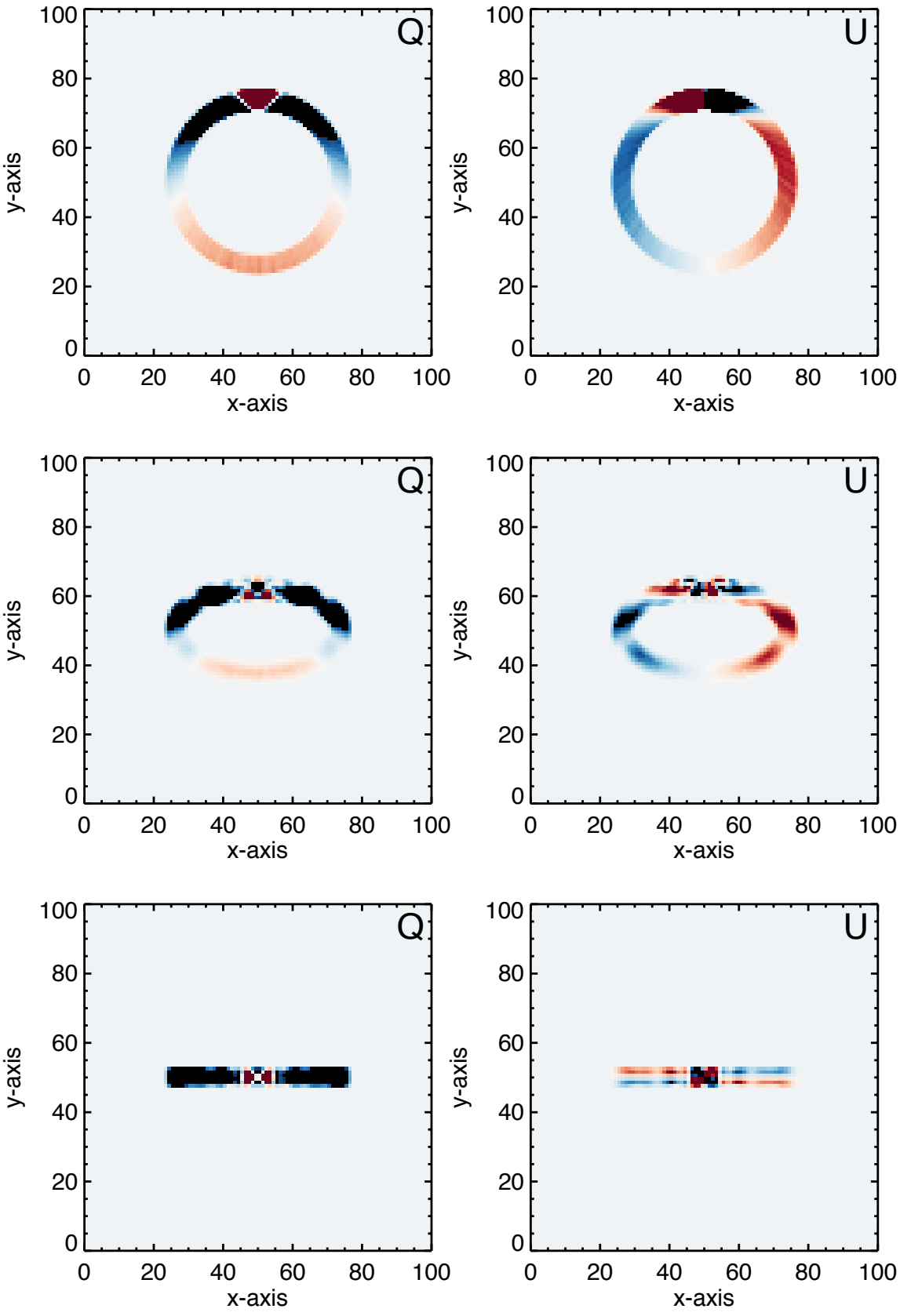

Fig 3: Polarisation maps (fractional Q *and* U*) of the ε Sgr disk at three inclinations (0, 60 and 90 deg, top to bottom) and for 1 μm sized dust grains. The secondary is positioned at 0 deg in the viewing plane. The magnitude of the colour scale is arbitrary but runs from positive red through white to negative blue, where negative* Q *is N-S on the diagram.*

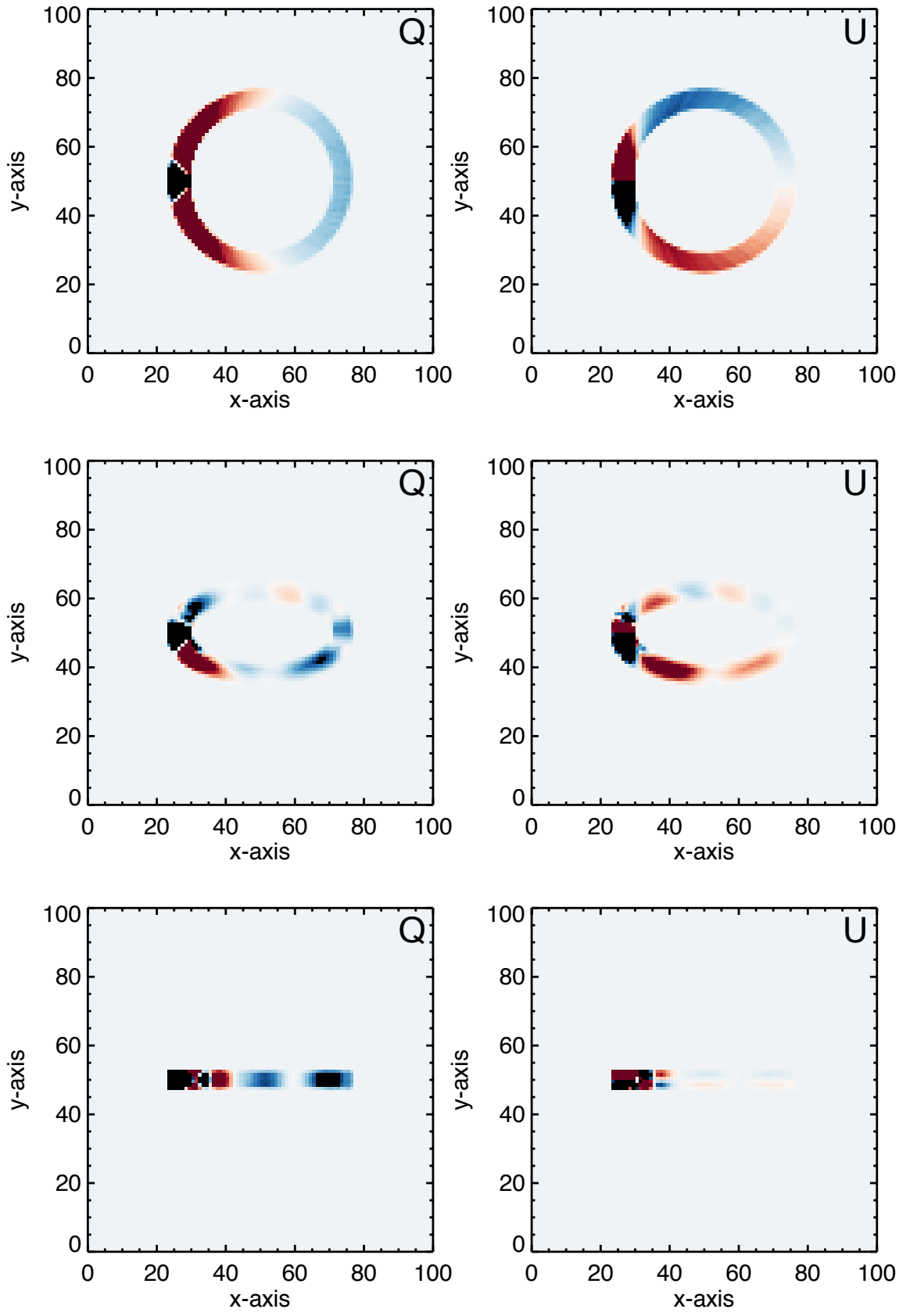

Fig 4: Polarisation maps (fractional Q *and* U*) of the ε Sgr disk at three inclinations (0, 60 and 90 deg, top to bottom) and for 1 μm sized dust grains. The secondary is positioned at 90 deg in the viewing plane. The magnitude of the colour scale is arbitrary but runs from positive red through white to negative blue, where negative* Q *is N-S on the diagram.*

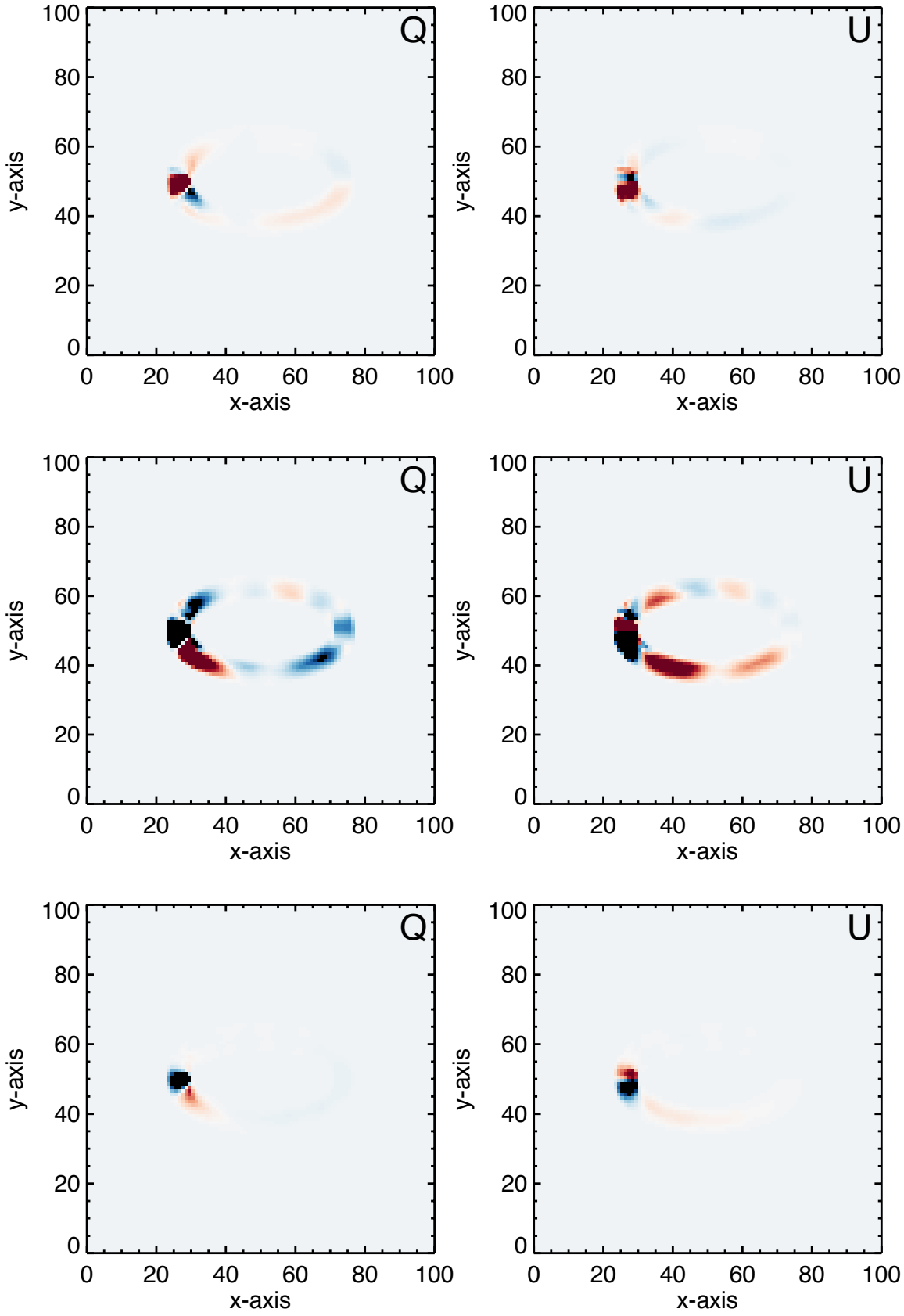

Fig 5: Polarisation maps (fractional Q *and* U*) of the ε Sgr disk at 60 deg inclination for three different dust grain sizes (0.5, 1.0 and 2.0 μm, top to bottom). The secondary is positioned at 90 deg in the viewing plane. The colour scale presented here is qualitative, with the scale for the large grains reduced by a factor of 100 compared to the small and medium sized grains to accommodate a larger dynamic range.*

Discussion and Conclusions

The calculations performed here are simplistic and may not accurately reflect the detailed geometry of the ε Sgr system. We have modelled only spherical grains, whereas real dust grains are irregular in size and thus would generate larger degrees of polarisation. Additionally, the (detectable) grains in the disk will not be single-sized but will have a distribution of sizes from the blow-out radius up to mm. The *blow-out radius* – the radius of the largest grains blown out of the system by a stellar wind – is a function of the stellar luminosity, with a larger blow-out radius for dust around more luminous stars [11]. For ε Sgr B the blow out radius might be as small as 0.5 μm, but as ε Sgr A is a giant and close we'd expect the smallest grains near the secondary to be larger than that. For a system such as this, with a 4 L_{Sun} primary, ~ 10 μm would be a typical size. The grain sizes tested are therefore fairly realistic. Smaller grains may be present in the system, produced in on-going collisions, but will be swiftly removed. It is noted by Rodriguez and Zuckerman [27] that the disk is unlikely to be stable given the architecture they infer from the available photometry, and perturbation of the disk by the secondary star would be one source of dynamical excitement driving collisions between bodies within the disk. A full model of the dynamical stability of circumbinary or circumsecondary disk architectures is beyond the scope of this work.

The larger grain sizes we modelled produced a level of polarisation greater than the infrared excess of the system. The magnitude of the polarisation produced being similar to what was measured for the system. The position angle of the system was measured in March 1999 to be 142.3 [26]. The measured polarisation angle was 38.1±0.8, which, neglecting the uncertainty, is a difference of 104.2 degrees. The polarisation produced by the models in the more favourable geometry for the larger grains is mostly negative Q, which is 90 degrees different to the secondary PA. Our modelling suggests the deviation from 90 degrees could be due to the inclination of the system, but it could also be a result of motion of the secondary since 1999 – if the system is face on (0 degree inclination) this could be as much as 11 degrees. This shows us that the large degree of polarisation measured could plausibly be due simply to the debris disk's interaction with the binary star system, without the need to invoke other polarisation mechanisms.

Further Work

The disk here is assumed to be smooth and radially symmetric. Future work will include an investigation of the effect of the addition of one or more clumps into the disk. Should such structure produce a significant effect then there is potential for using the secondary as a torch to illuminate progressive sections of the debris disk. Such a technique could be useful for more distant systems where imaging polarimetry is not possible.

ε Sgr B is a redder star than ε Sgr A, we would therefore expect a stronger polarisation signal at redder wavelengths. However, effects to do with the grain size distribution may offset this. In addition to looking at more realistic size distributions we also intend to carry out the calculations in a greater range of wavelengths and probe the ε Sgr system with multi-band polarimetry to inform and test the modelling.

References:

1. Hansen, J.E. and Hovenier, J.W., "Interpretation of the Polarization of Venus," *Journal of the Atmospheric Sciences*, Iss. 4, vol. 31, pp. 1137-1160, 1974.

2. Zubko, E., Videen, G., Shkuratov, Y., Muinonen, K. and Yamamoto, T., "The Umov effect for agglomerated particles with varying structure " *LPICo*, vol. 1667, pp. 6008, 2012.
3. Cotton, D.V., Bailey, J., Kedziora-Chudczer, L., Bott, K., Lucas, P.W., Hough, J.H. and Marshall, J.P., "The linear polarisation of southern bright stars measured at the parts-per-million level," *MNRAS*, Iss. 2, vol. 455, pp. 1607-1628, 2015.
4. Bailey, J., Kedziora-Chudczer, L., Cotton, D.V., Bott, K., Hough, J.H. and Lucas, P.W., "A high-sensitivity polarimeter using a ferro-electric liquid crystal modulator," *MNRAS*, vol. 449, pp. 3064-3073, 2015.
5. Hough, J.H., Lucas, P.W., Bailey, J.A., Tamura, M., Hirst, E., Harrison, D. and Bartholomew-Biggs, M., "PlanetPol: A Very High Sensitivity Polarimeter," *PASP*, vol. 118, pp. 1302-1318, 2006.
6. Bailey, J., Lucas, P.W. and Hough, J.H., "The linear polarization of nearby bright stars measured at the parts per million level," *MNRAS*, vol. 405, pp. 2570-2578, 2010.
7. García, L. and Gómez, M., "Optical polarization of solar type stars with debris disks," *RMxAA*, vol. 51, pp. 3-12, 2015.
8. Wyatt, M.C., "Evolution of Debris Disks," *ARA&A*, vol. 46, pp. 339-383, 2008.
9. Matthews, B.C., Krivov, A.V., Wyatt, M.C., Bryden, G. and Eiroa, C., "Observations, Modeling, and Theory of Debris Disks," presented at Protostars and Planets VI, 2014.
10. Backman, D.E. and Paresce, F., "Main-sequence stars with circumstellar solid material - The VEGA phenomenon," presented at Protostars and Planets III, 1993.
11. Burns, J.A., Lamy, P.L. and Soter, S., "Radiation forces on small particles in the solar system," *Icarus*, Iss. 1, vol. 40, pp. 1-48, 1979.
12. Morales, F.Y., Rieke, G.H., Werner, M.W., Bryden, G., Stapelfeldt, K.R. and Su, K.Y.L., "Common Warm Dust Temperatures Around Main-sequence Stars," *ApJL*, vol. 730, pp. L29, 2011.
13. Eiroa, C., Marshall, J.P., Mora, A., Montesinos, B., Absil, O., et al., "DUst around NEarby Stars. The survey observational results," *A&A*, vol. 555, pp. A11, 2013.
14. Thureau, N.D., Greaves, J.S., Matthews, B.C., Kennedy, G., Phillips, N., et al., "An unbiased study of debris discs around A-type stars with Herschel," *MNRAS*, vol. 445, pp. 2558-2573, 2014.
15. Trilling, D.E., Bryden, G., Beichman, C.A., Rieke, G.H., Su, K.Y.L., et al., "Debris Disks around Sun-like Stars," *ApJ*, Iss. 2, vol. 674, pp. 1086, 2008.
16. Kennedy, G.M. and Wyatt, M.C., "Do two-temperature debris discs have multiple belts?," *MNRAS*, Iss. 4, vol. 444, pp. 3162-3182, 2014.
17. Booth, M., Kennedy, G., Sibthorpe, B., Matthews, B.C., Wyatt, M.C., et al., "Resolved debris discs around A stars in the Herschel DEBRIS survey," *MNRAS*, Iss. 2, vol. 428, pp. 1263-1280, 2013.
18. Pawellek, N., Krivov, A.V., Marshall, J.P., Montesinos, B., Ábrahám, P., Moór, A., Bryden, G. and Eiroa, C., "Disk Radii and Grain Sizes in Herschel-resolved Debris Disks," *ApJ*, Iss. 1, vol. 792, pp. 65, 2014.
19. Krivov, A.V., "Debris disks: seeing dust, thinking of planetesimals and planets," *Research in Astronomy and Astrophysics*, Iss. 5, vol. 10, pp. 383, 2010.
20. Marshall, J.P., Kirchschlager, F., Ertel, S., Augereau, J.-C., Kennedy, G.M., et al., "Interpreting the extended emission around three nearby debris disc host stars," *A&A*, vol. 570, pp. A114, 2014.
21. Schneider, G., Grady, C.A., Hines, D.C., Stark, C.C., Debes, J.H., et al., "Probing for Exoplanets Hiding in Dusty Debris Disks: Disk Imaging, Characterization, and Exploration with HST/STIS Multi-roll Coronagraphy," *AJ*, vol. 148, pp. 59, 2014.
22. Perrin, M., D., Duchene, G., Millar-Blanchaer, M., Fitzgerald, M.P., Graham, J.R., et al., "Polarimetry with the Gemini Planet Imager: Methods, Performance at First Light, and the Circumstellar Ring around HR 4796A," *ApJ*, Iss. 2, vol. 799, pp. 182, 2015.
23. Millar-Blanchaer, M.A., Graham, J.R., Pueyo, L., Kalas, P., Dawson, R.I., et al., "Beta Pictoris' Inner Disk in Polarized Light and New Orbital Parameters for Beta Pictoris b," *ApJ*, Iss. 1, vol. 811, pp. 18, 2015.

24. Wang, J.J., Graham, J.R., Pueyo, L., Nielsen, E.L., Millar-Blanchaer, M., et al., "Gemini Planet Imager Observations of the AU Microscopii Debris Disk: Asymmetries within One Arcsecond," *ApJL*, Iss. 2, vol. 811, pp. L19, 2015.
25. Rodigas, T.J., Stark, C.C., Weinberger, A., Debes, J.H., Hinz, P.M., et al., "On the Morphology and Chemical Composition of the HR 4796A Debris Disk," *ApJ*, Iss. 2, vol. 798, pp. 96, 2015.
26. Hubrig, S., Le Mignant, D., North, P. and Krautter, J., "Search for low-mass PMS companions around X-ray selected late B stars," *A&A*, vol. 372, pp. 152-164, 2001.
27. Rodriguez, D.R. and Zuckerman, B., "Binaries among Debris Disk Stars," *ApJ*, vol. 745, pp. 147, 2012.
28. Rhee, J.H., Song, I., Zuckerman, B. and McElwain, M., "Characterization of Dusty Debris Disks: The IRAS and Hipparcos Catalogs," *ApJ*, vol. 660, pp. 1556-1571, 2007.
29. Mittal, T., Chen, C.H., Jang-Condell, H., Manoj, P., Sargent, B.A., Watson, D.M. and Lisse, C.M., "The Spitzer Infrared Spectrograph Debris Disk Catalog. II. Silicate Feature Analysis of Unresolved Targets," *ApJ*, vol. 798, pp. 87, 2015.
30. Chen, C.H., Mittal, T., Kuchner, M., Forrest, W.J., Lisse, C.M., Manoj, P., Sargent, B.A. and Watson, D.M., "The Spitzer Infrared Spectrograph Debris Disk Catalog. I. Continuum Analysis of Unresolved Targets," *The Astrophysical Journal Supplement*, vol. 211, pp. 25, 2014.
31. Rodigas, T.J., Follette, K.B., Weinberger, A., Close, L. and Hines, D.C., "Polarized Light Imaging of the HD 142527 Transition Disk with the Gemini Planet Imager: Dust around the Close-in Companion," *ApJL*, vol. 791, pp. L37, 2014.
32. Clarke, D., "Stellar Polarimetry," Wiley-VCH Verlag GmbH & Co. KGaA, Weinheim., 2010.
33. Hauschildt, P.H., Allard, F., Ferguson, J., Baron, E. and Alexander, D.R., "The NEXTGEN Model Atmosphere Grid. II. Spherically Symmetric Model Atmospheres for Giant Stars with Effective Temperatures between 3000 and 6800 K," *ApJ*, Iss. 2, vol. 525, pp. 871, 1999.
34. Hauschildt, P.H., Allard, F. and Baron, E., "The NextGen Model Atmosphere Grid for $3000 \leq$ Teff $\leq 10{,}000$ K," *ApJ*, Iss. 1, vol. 512, pp. 377, 1999.
35. Perryman, M.A.C., Lindegren, L., Kovalevsky, J., Hoeg, E., Bastian, U., et al., "The HIPPARCOS Catalogue," *A&A*, vol. 323, pp. L49-L52, 1997.
36. Skrutskie, M.F., Cutri, R.M., Stiening, R., Weinberg, M.D., Schneider, S., et al., "The Two Micron All Sky Survey (2MASS)," *AJ*, Iss. 2, vol. 131, pp. 1163, 2006.
37. Wright, E.L., Eisenhardt, P.R.M., Mainzer, A.K., Ressler, M.E., Cutri, R.M., et al., "The Wide-field Infrared Survey Explorer (WISE): Mission Description and Initial On-orbit Performance," *AJ*, Iss. 6, vol. 140, pp. 1868, 2010.
38. Dullemond, C.P., "RADMC-3D: A multi-purpose radiative transfer tool." Astrophysics Source Code Library, 2012.
39. Draine, B.T., "Scattering by Interstellar Dust Grains. I. Optical and Ultraviolet," *ApJ*, Iss. 2, vol. 598, pp. 1017, 2003.
40. Choliy, V.Y., "The discrete dipole approximation code DDSCAT.C++: features, limitations and plans," *Advances in Astronomy and Space Physics*, vol. 3, pp. 66-70, 2013.
41. Dohnanyi, J.S., "Collisional model of asteroids and their debris," *Journal of Geophysical Research*, Iss. 10, vol. 74, pp. 2531-2554, 1969.

The Kilodegree Extremely Little Telescope: Searching for Transiting Exoplanets in the Northern and Southern Sky

Jack Soutter[1], Jonti Horner[1,2], Joshua Pepper[3,4] and the KELT Science Team

[1] *University of Southern Queensland West St, Toowoomba QLD 4350, Australia*
[2] *Australian Centre for Astrobiology, UNSW Australia, Sydney, NSW 2052, Australia*
[3] *Department of Physics and Astronomy, Vanderbilt University, Nashville, TN 37235, USA*
[4] *Department of Physics, Lehigh University, Bethlehem, PA 18015, USA*

Summary: The Kilodegree Extremely Little Telescope (KELT) survey is a ground-based program designed to search for transiting exoplanets orbiting relatively bright stars. To achieve this, the KELT Science Team operates two planet search facilities - KELT-North, at Winer Observatory, Arizona, and KELT-South, at the South African Astronomical Observatory. The telescopes used at these observatories have particularly wide fields of view, allowing KELT to study a large number of potential exoplanet host stars. One of the major advantages of targeting bright stars is that the exoplanet candidates detected can be easily followed up by small, ground-based observatories distributed around the world. This paper will provide a brief overview of the KELT-North and KELT-South surveys, the follow-up observations performed by the KELT Follow-up Collaboration, and the exoplanet discoveries confirmed thus far, before concluding with a brief discussion of the future for the KELT program.

Keywords: KELT, exoplanet, transit, survey

Introduction

Since the discovery of the first exoplanets, over two decades ago (e.g. [1][2][3]) the field of extrasolar planetary science has experienced rapid growth. That growth has been driven by two main factors. The first is the ever-lengthening temporal baseline over which observations have been carried out, which is allowing the discovery of ever more distant planets, primarily through the Radial Velocity method[1], including the detection of the first 'Jupiter Analogues' around other stars (e.g. [4][5][6]). The second factor is the development of new technologies, tools, and programs that allow the study of an ever-greater number of stars in a variety of different manners (e.g. [7][8][9]). The influence of these new programs is perhaps best illustrated by the success of the Kepler mission [10][11][12], which has, to date, discovered 1030 planets[2].

When it comes to exoplanet surveys, two techniques greatly dominate the catalogue of discovered planets: Radial-Velocity (RV) and transit photometry. RV observations look for the subtle variations in a star's spectrum caused by the gravitational pull of orbiting bodies [13]. In contrast, the transit photometry method instead analyses a star looking for a drop of its visual brightness, caused by an

[1] The discussion of the various techniques used to discover planets around other stars is beyond the scope of this work – but we direct the interested reader to [13] for more details.

[2] The tally of planets discovered by the Kepler spacecraft continues to rise rapidly – the value of 1030 confirmed planets was obtained from the Kepler website, http://kepler.nasa.gov, on 18th November 2015, at which time Kepler had a further 4696 candidate planets awaiting confirmation.

exoplanet transiting in front of the star's disc [8]. While RV surveys have resulted in a large number of discoveries, they remain limited to the brightest stars in the night sky, with current technological limitations of stellar spectroscopy on the telescopes involved typically preventing RV surveys from observing many stars with an apparent visual magnitude fainter than ~8 without prohibitively long observations. Surveys searching for transiting exoplanets, on the other hand, only require photometric observations of stars, and as such are well suited for ground-based surveys that simultaneously target large numbers of fainter stars[3] [14].

For this reason, recent years have seen a proliferation in wide-field exoplanet transit surveys. In addition to KELT, the HATNet [15] and SuperWASP [16] programs have been running for several years, and have made a number of interesting discoveries in both the northern and southern skies [17][18]. The KELT survey, which operates in both hemispheres, typically targets stars brighter than those observed by other transit observation programs. To do this, the KELT surveys use two small, wide-field telescopes located in the southern and northern hemispheres to provide a rich supply of possible exoplanet hosting stars within the range of $8 < V < 12$ mag [19][20].

One of the great benefits of targeting bright stars with a transit survey such as KELT is that any planets found can then be followed up using other small astronomical facilities, allowing their accurate characterisation. To this end, the KELT science team incorporates a network of follow-up facilities located around the world, to facilitate timely and detailed follow-up observations.

The process of following up KELT discoveries typically involves two discrete steps. The first is confirmation follow-up. Here, the observed dips in a star's brightness due to the potential transit of a planet are used to create an ephemeris, and thereby predict the timings of future transits. The telescopes in the follow-up network can then target the potential planet-hosting star at the right time, and hopefully confirm that it dims as expected. This confirmation process takes place before the potential existence of the planet is widely publicised, and allows the KELT team to better characterise the orbit of the planet prior to its announcement.

Once the target has been confirmed as an exoplanet candidate, the true benefit of the brightness of the host star comes into play – with a bright host, a plethora of additional characterisation observations are possible. Observing future transits with larger telescopes allows the diameter of the newly discovered planet to be determined, and since the stars are bright, it is possible to also obtain measurements of the star's radial velocity variations – which allow the mass of the planet to be determined. By combining these observations, then, we are able to calculate the density of the planet in question, allowing us to determine whether it is most likely rocky or gaseous. Beyond this, further follow-up observations can allow the nature of the planet to be studied in still more detail. For example, measurements of the planet host star's radial velocity *during a transit* enable the measurement of the Rossiter-McLaughlin effect [21][22], allowing the determination of the orientation of the planet's orbit with respect to the spin axis of its host star. If sufficiently detailed spectra of the star can be obtained during either primary or secondary transit, the broad atmospheric composition of the planet can be determined [23][24].

[3] It is worth noting that while photometric data is perfect for analysing exoplanet candidature, it alone can not be used for confirmation. Additional radial velocity measurements are required for confirmation and characterisation. This is the reason that many of the Kepler spacecraft's detections are listed as exoplanet candidates rather than confirmed exoplanets.

In the following section, we provide a basic overview of the KELT survey, before moving on to a discussion of the follow-up process and partners. We then summarise some of KELT's key discoveries to date, before concluding with a short discussion of the future goals of the KELT program.

The KELT survey

The KELT program was launched in 2005, with the installation of the KELT-North telescope at Winer Observatory, Arizona. After that telescope had been successfully operating for several years, the KELT-South telescope was installed, at the South African Astronomical Observatory in Sutherland, South Africa. Both telescopes have operated almost continually since their installation, whenever the weather was suitable, and have allowed a large database of potential exoplanet candidates to be assembled. In order to follow-up on the objects in the catalogue, a significant number of other observatories have been engaged in the KELT program, as described below.

Optical assembly

The KELT project uses two similar optical assemblies in the northern and southern hemisphere to perform its wide-field survey. The optical assembly of each survey instrument consists of a CCD detector and a wide-field camera lens mounted on a robotic telescope mount, as shown in Figure 1.

Both the KELT-North and KELT-South detectors are equipped with a Mamyia 645 80mm f/1.9 medium-format manual focus lens with a 42mm aperture, which provides a 26° x 26° field of view, which corresponds to an image scale of approximately 23" $pixel^{-1}$ [19][20]. KELT-North and KELT-South also use similar CCD detectors; KELT-North uses an Apogee AP16E with 4096 x 4096 9µm pixels, while KELT-South operates using an Apogee U16M with 4096 x 4096 9µm pixels (both models use Kodak KAF-16801 front-illuminated CCDs). Both cameras are mounted on German-equatorial Paramount ME Robotic Telescope mounts.

KELT Locations

The KELT telescopes are located in both the southern and northern hemispheres to allow for complete sky coverage over the course of the year. The KELT-North telescope is housed at the Irvin M. Winer Memorial Mobile Observatory in Sonoita, Arizona. The site is located at N 31°39'53", W 110°36'03" at an elevation of 1515m. The KELT-South telescope is located in Sutherland, South Africa at the South African Astronomical Observatory (32°22'46" S, 20°38'48" E, elevation 1760m). Both locations yield relatively consistent clear skies, yielding an observing up-time of approximately 60% and 70%, respectively. The locations of the two KELT telescopes can be seen in Figure 2, below.

Figure 1: The KELT-South telescope located at the South African Astronomical Observatory in Sutherland, South Africa. The telescope is fully automated, and designed such that the dome opens and observations proceed only when conditions are appropriate. (Image courtesy of Dr Joshua Pepper, Vanderbilt University)

Observations and Data Reduction

Both KELT telescopes are designed to operate robotically on any night when the weather is suitable; with winds not exceeding the loading limit of the instrument, no heavy cloud cover, etc. If the conditions are suitable, the roof will open and the telescope will observe. It will observe a number of pre-selected fields across the sky, firstobserving all visible fields east of the local meridian, and then preforming a meridian flip and continuing the process to the west of the meridian. That process is repeated until dawn.

After the images are taken, the data is transferred online back to Ohio State (for KELT-North), and Vanderbilt University (for KELT-South). The data is then processed so that it can be added to a combined KELT candidate database, incorporating data and candidates from both telescopes.

Any images of low quality are removed based on their high background sky count, which is typically caused by excessive moonlight or cloud cover. After the compromised data has been removed, basic data reduction is performed through the subtraction of dark and bias images from the flat field images and raw data, a process that is followed by flat fielding. The final two automated steps involve the use of the astrometry software package from astrometry.net [25], which overlays a world coordinate system (WCS) into the .fits data files. Once the images have been properly calibrated, the

final step is to generate light-curves for each star. This is accomplished by performing image subtractions using a heavy modified version of the ISIS imaging package [26]. The ISIS package performs spatial recognition and aligns each image to a reference before creating a differenced image. These images allow for precise flux measurements and the creation of accurate light-curves. This information is then added to the KELT database to be accessed by the follow-up team.

Follow-Up Partners

As stated above, the KELT survey is designed to detect giant planets in orbits close to their host stars, and to target main-sequence stars with an apparent visual magnitude between 8 and 10. This has two major upsides.

First, it allows for exoplanet detection around stars that are fainter than those typically targeted by Radial Velocity planet search programs. Fainter stars require significantly longer exposures, and, fainter than ninth magnitude, such exposures become prohibitive when attempting to carry out a large survey. However, should planets be found around stars in this magnitude range (eighth to tenth), radial velocity follow-up observations are relatively straightforward. When the requirement to observe many stars many times is removed, resources can be efficiently allocated to observe the single target over longer periods, once there is evidence of an existing exoplanet. This means that the planets detected by KELT are ideally placed for the perfect combination of observational techniques – if a planet can be observed by both radial velocity and transit observations, a far more complete characterisation is possible than for planets observed by only one method.

Secondly, the relative brightness of the KELT target stars allows for timely photometric follow-up with small ground-based telescopes, and KELT can therefore take advantage of small observatories hosted by their partner institutions. In order to best make use of this ever-growing catalogue of planet candidates, and achieve timely confirmation and publication of their results, the KELT team have built a large collaborative network with partner institutions that operate their own observatories scattered around the planet. This collection of collaborators makes up the wider KELT Follow-up Team. There are currently over 30 observatories across both hemispheres that make up that team, and provide the KELT project with photometric and (where appropriate) RV follow-up observations.

There are typically hundreds of exoplanet candidates in the KELT database at any one given time, meaning that any observatory in the KELT network will have at least 2-3 viable targets every night. This density of targets allows for constant follow-up observations to be carried out year round, allowing for the removal of false-positives from the database and to refine the transit timing of any legitimate exoplanets. This widely distributed approach is already yielding great results, with a number of planet discoveries already published, and several more in preparation.

Figure 2: Locations of the KELT-North and KELT-South telescopes (marked in red), and the various observatories around the world that provide KELT with follow-up photometry (marked in blue). Images courtesy of Joshua Pepper, Vanderbilt University and Google Maps.

Discoveries

The KELT survey has already discovered and published a number of exoplanets. Here, we present a concise overview of some of KELT's discoveries to date.

KELT-1b

The first planet-sized object to be discovered by the KELT project, KELT-1b is a highly irradiated, transiting brown dwarf[4] orbiting its companion at a semi-major axis of only 0.02466±0.00016 au. Following the detection of the transits of KELT-1b, a program of spectroscopic, radial velocity and photometric follow-up was carried out by the KELT team, which resulted in a detailed characterisation of the object. As a result of that follow-up work, we know that KELT-1b weighs in at ~27M_J, placing it firmly within the brown-dwarf mass range. The follow-up observations also revealed that the orbit of KELT-1b is not significantly inclined to its host's equator, being consistent with zero obliquity, and suggest that the parent star is tidally locked to the orbit of KELT-1b. Finally, the follow-up observations also revealed the possible presence of an M-dwarf companion to the primary star, located at a separation of 588 milliarcseconds. Full details of the discovery, and the follow-up work carried out, can be found in [27].

[4] Brown dwarfs are objects that tread the line between stars and planets. The dividing line between an object being considered a planet and a brown dwarf lies at the Deuterium burning limit, at roughly 13 times the mass of Jupiter. In theory, the temperature and pressure in the core of such an object should be high enough for them to undergo a short period of Deuterium fusion, without ever reaching the conditions required to fuse Hydrogen. The dividing line between brown dwarfs and stars lies at the Hydrogen burning limit, at ~80 times Jupiter's mass. The official classification can be found at [28] and [29].

KELT-2Ab

KELT-2Ab is a hot Jupiter (~1.52M_J) in orbit around the primary star of the HD 42176 binary system, a late F-type star. At the time of its discovery, the mass and radius of KELT-2Ab placed it in a unique position amongst planets discovered orbiting bright stars. Indeed, it was the only known transiting planet in the mass range 1.2M_J and 3M_J orbiting such a bright star (V≈ 8.7). In many other ways, however, the planet is fairly unremarkable, being a fairly typical hot Jupiter (orbital period of just over four days, and slightly more massive and larger than Jupiter). During the follow-up observations of KELT-2Ab, the science team was also able to demonstrate for the first time that KELT-2A and KELT-2B were gravitationally bound to each other as a binary system, which in turn allowed them to infer that KELT-2B, the secondary star in the system, must be an early K-dwarf. Full details of the discovery and follow-up of KELT-2B can be found in [30].

KELT-3b

The third confirmed exoplanet from the KELT survey was KELT-3b ([31]), an inflated hot Jupiter with a mass of ~1.48M_J and a semi-major axis of ~0.041 au. The host star itself is a late F-type star with a visual magnitude of 9.8. While KELT-3b is a typical Hot Jupiter there is an interesting comparison between its host star and the planet-hosting star of HAT-P-2. The two stars have near identical masses, radii, metallicities, temperatures and ages. However, the two stars display vastly different rotational velocities, with KELT-3 rotating approximately half as quickly as HAT-P-2.

This difference in the rotational velocity of two stars that are otherwise almost identical may well have something to do with the nature of their planets. HAT-P-2b is significantly more massive than KELT-3b, and so the faster spin rate of HAT-P-2 (which is still longer than the orbital period of its planet) might feasibly be related to tidal star-planet interaction, particularly since the mass of the companion is likely comparable to the mass of the host's convective envelope [32]. In addition, like KELT-2Ab, there are suggestions that KELT-3 might well have a common proper motion companion – although its binary has not yet been definitively confirmed. Given that one of the proposed mechanisms by which hot-Jupiters could be created involves distant perturbations from massive companion objects, and evolution through a combination of Kozai-resonant oscillation and tidal-damping, the presence of companions in hot-Jupiter systems is always an interesting observation.

KELT-4Ab

KELT-4Ab is an inflated hot-Jupiter that orbits the brightest component of a hierarchical triple stellar system ([33]). In other words, KELT-4Ab orbits around KELT-4A, an F-star that is somewhat more massive and hotter than our Sun. Based on the Washington Double Star Catalog ([34]), KELT-4 had been identified as a common proper motion binary, with the components separated by 1.5” (following observations by [35] in 1973). The KELT follow-up program carried out Adaptive Optics observations of the system using the Keck II telescope in 2012. These revealed that the secondary companion (KELT-4B) was actually itself double, a binary separated by just ~49 mas, which the discoverers estimate to be twin K-stars, with T_{eff} ~ 4300 K.

As such, KELT-4Ab is just the third known transiting planet within such a hierarchical triple system. Due to the nature of the system, it is natural to consider whether Kozai-resonant interactions between KELT-4Ab and the KELT-4BC binary pair could have helped to drive the planet into its

current tight orbit about KELT-4A. [33] detail calculations examining this question, and show that such migration is certainly feasible for all eccentricites of the KELT-4A – BC orbit, although there is a sub-section of orbital element space in which such interactions could not engineer sufficient Kozai-resonant effects on the planet's orbit (namely those with low/moderate eccentricites and a near-coplanar planet-binary orbital architecture). Future radial-velocity observations to measure the Rossiter-McLaughlin effect for this system will be of great interest, since any mis-alignment between the rotation of the star and the orbit of its planet could be indicative of such a migration history.

KELT-6b

The least massive of all of the KELT discoveries to date, KELT-6b is a hot Saturn (~0.43M_J) orbiting around a metal-poor ([Fe/H] = -0.28), V=10.38, late F-type host star ([36]). KELT-6b is very similar to the well-studied exoplanet HD 209458b, other than for the metal-poor nature of its host star. As with the other planets detected by the KELT survey, KELT-6 is among the twenty brightest stars currently confirmed to host exoplanets, making it an excellent target for current and future characterisation work.

KELT-7b

KELT-7b is a relatively typical, somewhat inflated, hot-Jupiter (~1.28M_J, ~1.53R_J; [37]). Of the planets found to date by the KELT program, KELT-7b orbits the brightest star. Its host is significantly more massive and hotter than the Sun (~1.54 $M_\odot$, T_{eff}~6789 K). Furthermore, the host is a rapid rotated (~73 km s^{-1}), which enhances the strength of the Rossiter-McLaughlin effect. As a result, follow-up observations have revealed that the planet's orbit is well aligned to the plane of the star's oblate equator. Given the planet's relatively small orbital distance, the high luminosity and temperature of its host, and the planet's large 'puffed-up' radius, coupled to the brightness of the star as seen from Earth, KELT-7b is an ideal target for future follow-up and characterisation work.

KELT-8b

KELT-8b is one of the most inflated known transiting exoplanets ([38]). It orbits its host star (HD 343246) on a slightly eccentric (e ~0.035) orbit with radius ~ 0.0457 au. Despite being somewhat less massive than Jupiter (M ~0.867 M_J), the planet is significantly larger than our own giant, with radius ~1.86 R_J, giving inferred density of just ~0.167 g cm^{-3}!

KELT-8 (HD 343246) is significantly more massive than the Sun (M ~1.211 $M_\odot$), and is also more metal rich ([Fe/H] ~+0.272). It is thought to be mildly evolved, with the result that it is also larger than the Sun (R ~ 1.67 $R_\odot$), a factor that might play some role in the planet's degree of inflation. As with KELT-7b, the planet's large size means that it is an ideal candidate for follow-up spectroscopic observations to study its atmospheric composition.

KELT-10b

KELT-10b the latest confirmed exoplanet published by the KELT survey team [39], and the first confirmed exoplanet resulting from the KELT-South project. KELT-10b is a highly inflated, sub-Jupiter mass (~0.69M_J) planet with a semi-major axis of ~0.0529au. Its host star is sub-giant,

slightly more massive than the Sun, and it seems likely that the planet is doomed. Analysis of the evolution of KELT-10 suggests that the star will devour KELT-10b as it leaves its current sub-giant phase, at some point in the next billion years.

KELT-14b and KELT-15b

The newest additions to the KELT family are two hot Jupiters detected by the KELT-South survey, and announced in a submitted paper posted on arXiv in late September [40]. KELT-14b is an independent discovery of WASP-122b, and illustrates the competitive and complementary nature of exoplanet transit surveys. It has an inferred mass slightly greater than that of Jupiter ($M \sim 1.196\ M_J$), and is somewhat inflated, with a radius of ~1.52 R_J. It orbits a host star that is somewhat more massive and metal rich than the Sun, and is thought to be close to leaving the main sequence. KELT-15b is yet another inflated hot Jupiter, orbiting a G0 star of approximately the same age as the Sun (~4.6 Gyr). That star, once again, is more massive than our own, at ~1.181 solar masses, and is again thought to be close to leaving the main sequence. It is thought that both planets should be observable in emission at their secondary eclipses, which makes them exciting targets for future atmospheric characterisation.

KELT in the Future

At this time, over twelve hundred transiting exoplanets have been discovered. The Kepler space satellite discovered the bulk of these, with over one thousand confirmed discoveries to date [10]. Ground-based transit surveys like KELT have also been highly productive, contributing over two hundred planets to the total, a number that will rise in coming years. The transiting planets orbiting bright stars that KELT is discovering are especially valuable due to their accessibility to observations that can characterize their dynamics, energetics, and atmospheres.

In 2017, NASA will be launching the TESS satellite [41], which will scan almost the entire sky over a two-year period, carrying out observations with much higher photometric precision than can be achieved by ground-based telescopes. The TESS program is designed to target stars with I-band magnitudes in the range 4 – 13, and will observe those starts across intervals ranging between one month and one year, depending on their ecliptic latitude. As a result, TESS is expected to discover all transiting planets orbiting those stars with periods less than ten days. For stars closer to the ecliptic poles, TESS' completeness will extend to periods of aboutforty days, or more.

TESS will discover most transiting planets orbiting bright stars as seen from Earth.. Nevertheless, KELT will remain useful for a number of other science goals. These include the discovery and characterisation of eclipsing binary and other periodic variable stars. In addition, TESS will mostly be confined to observing relatively short-period behaviour, while KELT already boasts a 10-year baseline of observations. As a result, KELT will be capable of detecting much longer-term variability in its target stars. The on-going ability of KELT to monitor the sky will continue to be helpful for the characterisation of bright transient events, like supernovae [42].

Furthermore, the worldwide follow-up network assembled for KELT is well positioned to support the upcoming TESS mission, to serve a similar purpose in vetting and confirming many of the TESS planet candidates. The next three years will see a transition among this collaboration from a focus on

KELT follow-up to TESS follow-up. At the same time, however, a great quantity of KELT data will remain, and continue to be taken, that can be exploited for a variety of science goals.

Looking further into the future, the next generation of space-based exoplanet search and characterisation programs are currently in development, with proposed missions such as CHEOPS [43], WFIRST [44] and TWINKLE [45] being planned for the coming decade. By placing Australia at the forefront of exoplanet discovery and characterisation, dedicated programs such as the KELT-South survey and the recently funded MINERVA-Australis (a partner to the northern hemisphere MINERVA [46]) are laying the ground work for our future participation on the global stage. The planets discovered by those future missions will require follow-up observations to be carried out on a 24 hour basis, and Australia is ideally positioned to give almost unique longitude and latitude coverage of the night sky. As a result, these facilities will be pivotal in future work, and Australian researchers will be heavily involved in the international teams that are developing those projects.

Acknowledgements

JH is supported by USQ's Strategic Research Fund: the STARWINDS project.

References

1. Wolszczan, A. and Frail, D. A., "A planetary system around the millisecond pulsar PSR1257 +12", *Nature*, 1992, 355, pp. 145 - 147

2. Mayor, M. and Queloz, D., "A Jupiter-mass companion to a solar-type star", *Nature*, 1995, 378, pp. 355-359

3. Butler, R. P. and Marcy, G. W., "A Planet Orbiting 47 Ursae Majoris", *The Astrophysical Journal*, 1996, 464, L153

4. Butler, R. P., Wright, J. T., Marcy, G. W. et al., "Catalog of Nearby Exoplanets", *The Astrophysical Journal*, 2006, 646, pp. 505 - 522

5. Wittenmyer, R. A., Tuomi, M., Butler, R. P. et al., "GJ 832c: A Super-Earth in the Habitable Zone", *The Astrophysical Journal*, 2014, 791, article id. 114

6. Wittenmyer, R. A., Horner, J., Tinney, C. G. et al., "The Anglo-Australian Planet Search. XXIII. Two New Jupiter Analogs", *The Astrophysical Journal*, 2014, 783, article id. 103

7. Bond, U., Udalski, A., Jaroszyński, R. et al., "OGLE 2003-BLG-235/MOA 2003-BLG-53: A Planetary Microlensing Event", *The Astrophysical Journal*, 2004, 606, L155 – L158

8. Charbonneau, D., Brown, T. M., Latham, D. W. and Mayor, M., "Detection of Planetary Transits Across a Sun-like Star", *The Astrophysical Journal*, 2000, 529, L45 – L48

9. Marois, C., Macintosh, B., Barman, T., Zuckerman, B., Song, I., Patience, J., Lafrenière, D. and Doyon, R., "Direct Imaging of Multiple Planets Orbiting the Star HR 8799", *Science*, 2008, 322, p. 1348

10. Borucki, W. J., Koch, D. G., Basri, G. et al., "Characteristics of Planetary Candidates Observed by Kepler. II. Analysis of the First Four Months of Data", *The Astrophysical Journal*, 2011, 736, article id. 19

11. The latest tally of confirmed Kepler discoveries, and a wide variety of information about the mission, can be found at the Kepler science page, http://kepler.nasa.gov , which was accessed on 18th November 2015 to obtain the latest tally of confirmed Kepler planets.

12. Mullally, F., Coughlin, J. L., Thompson, S. E. et al., "Planetary Candidates Observed by Kepler. VI. Planet Sample from Q1 – Q16 (47 Months)", *The Astrophysical Journal Supplement Series*, 2015, 217, article id. 31

13. Perryman, M., "The Exoplanet Handbook", 2014*, Cambridge University Press, Cambridge UK*.

14. Pepper, J., Gould, A., DePoy, D, L. "Using All-Sky Surveys to Find Planetary Transits", *Acta Astronomica,* 2003, 53, p213

15. Bakos, G., Noyes, R. W., Kovács, G. et al. "Wide- field Millimagnitude Photometry with the HAT: A Tool for Extrasolar Planet Detection". *Publications of the Astronomical Society of the Pacific,* 2004, 116, p266

16. Pollacco, D. L., Skillen, I., Collier, C. et al."The WASP Project and the Superwasp Cameras".*Publications of the Astronomical Society of the Pacific*, 2006, 118, p1407.

17. Bakos, G., Kovács, G., Torres, G. et al. "HD147506b: A Supermassive Planet in an Eccentric Orbit Transiting a Bright Star", *The Astrophysical Journal,* 2007, 607, p826

18. Hebb, L., Collier-Cameron, A., Loeillet, B. et al. "WASP-12b: The Hottest Transiting Exoplanet Yet Discovered" *The Astrophysical Journal,* 2009, 693, p1920

19. Pepper, J., Pogge, R, W., DePoy, D, L. et al, "The Kilodegree Extremely Little Telescope (KELT): A Small Robotic Telescope for Large Area Synoptic Surveys", *The Publication of the Astronomical Society of the Pacific*, 2007, 119, p923

20. Pepper, J., Kuhn, R, B., Siverd, R. et al, "The KELT-South Telescope", *The Publication of the Astronomical Society of the Pacific*, 2012, 124, p230

21. Snellen, I, A , G. "A New Method for Probing the Atmospheres of Transiting Exoplanets" *Monthly Notices of the Royal Astronomical Society,* 2004, 353, L1-L6

22. Yasuiro, O., Atsushi, T., Yasushi, S. "The Rossiter-McLaughlin Effect and Analytic Radial Velocity Curves for Transiting Extrasolar Planetary Systems", *The Astrophysical Journal,* 2005, 622, p1118

23. Charbonneau, D., Brown, T. M., Noyes, R, W. et al "Detection of an Extrasolar Planet Atmosphere", *The Astrophysical Journal,* 2002, 568, p377

24. Vidal-Madjar, A., Lecavelier des Etangs, A., Desert, J-M., et al "An Extended Upper Atmosphere Around the Extrasolar Planet HD209458b" *Nature,* 422, p143

25. Lang, L., David, W. H., Keir, M. et al., "Astrometry.net: Blind astrometric calibration of arbitrary astronomical images", *The Astrophysical Journal*, 2010, 139, 5, pp 1782-1800

26. Alard, C., Lupton, R, H,. "A Method for Optimal Image Subtraction", *The Astronomical Journal*, 1998, 503, 1, pp 325-331

27. Siverd, R, J., Beatty, T, G., Pepper, J. et al. "KELT-1b: A Strongly Irradiated, Highly Inflated, Short Period, 27 Jupiter-mass Companion Transiting a Mid-F Star", *The Astrophysical Journal,* 2012, 761, p 123

28. Spiegel, D, S., Burrows A and, Milsom, J, A. "The Deuterium-Burning Mass Limit for Brown Dwarves and Giant Planets" *The Astrophysical Journal,* 2011, 727, p9

29: Burrows, A., Marley, M., Hubbard, W, B. et al. "A Nongray Theory of Extrasolar Giant Planets and Brown Dwarfs", *The Astrophysical Journal,* 1997, 491, p856

30. Beatty, T, G., Pepper, J., Siverd, R. et al. "KELT-2Ab: A Hot Jupiter Transiting the Bright (V = 8.77) Primary Star of a Binary System" *The Astrophysical Journal,* 2012, 756, p39

31. Pepper, J., Siverd, R., Beatty, T, G. et al. "KELT-3b: A Hot Jupiter Transiting a V = 9.8 Late-F Star", *The Astrophysical Journal,* 2013, 773, p64

32. Mengel, M. W., Fares, R., Marsden, S. C. et al., "The Evolving Magnetic Topology of τ-Boötis", *Monthly Notices of the Royal Astronomical Society*, 2016, *submitted*

33. Eastman, J. D., Beatty, T. G., Siverd, R. J. et al., "KELT-4Ab: An inflated Hot Jupiter transiting the bright (V~10) component of a hierarchical triple", *The Astronomical Journal*, 2016, *submitted*, arXiv:1510.00015

34. Mason, B. D., Wycoff, G. L., Hartkopf, W. I., Douglass, G. G. and Worley, C. E., "The 2001 US Naval Observatory Double Star CD-ROM. I. The Washington Double Star Catalog", *The Astronomical Journal*, 2001, 122, pp. 3466 - 3471

35. Couteau, P., "New double stars (9^{th} series) discovered at Nice", *Astronomy and Astrophysics Supplement*, 1973, 10, p. 273

36. Collins, K, A., Eastman, J, D., Beatty, T, G. et al. "KELT-6b: A P ~ 7.9 Day Hot Saturn Transiting a Metal-poor Star with a Long-period Companion", *The Astrophysical Journal,* 2014, 147, p39

37. Bieryla, A., Collins, K., Beatty, T. G. et al., "KELT-7b: A Hot Jupiter Transiting a Bright V = 8.54 Rapidly Rotating F-star", *The Astronomical Journal*, 2015, 150, id. 12

38. Fulton, B. J., Collins, K. A., Gaudi, B. S. et al., "KELT-8b: A Highly Inflated Transiting Hot Jupiter and a New Technique for Extracting High-precision Radial Velocities from Noisy Spectra", *The Astrophysical Journal*, 2015, 810, id. 30

39. Kuhn, R. B., Rodriguez, J. E., Collins, K. A. et al., "KELT-10b: The First Transiting Exoplanet from the KELT-South Survey – A Hot Sub-Jupiter Transiting a V = 10.7 Early G-Star", *Monthly Notices of the Royal Astronomical Society*, 2016, *in press*, arXiv:1509.02323

40. Rodriguez, J. E., Colon, K. D., Stassun, K. G. et al., "KELT-14b and KELT-15b: An Independent Discovery of WASP-122b and a New Hot Jupiter", *The Astronomical Journal*, 2016, *submitted*, arXiv: 1509.08953

41. Ricker, G. R., Winn, J. N., Vanderspek, R. et al., "Transiting Exoplanet Survey Satellite (TESS)", *Journal of Astronomical Telescopes, Instruments, and Systems*, 2015, 1, id. 014003

42. Siverd, R. J., Goobar, A., Stassun, K. G. and Pepper, J., "Observations of the M82 SN 2014J with the Kilodegree Extremely Little Telescope", *The Astrophysical Journal*, 2015, 799, id. 105

43. Broeg, C., Fortier, D., Ehrenreich, Y. et al., "CHEOPS: A Transit Photometry Mission for ESA's Small Mission Programme", *Hot Planets and Cool Stars*, 2013,47, id 03005

44. Spergel, D., Gehrels, N., Breckinridge, J. et al., "WFIRST-2.4: What Every Astronomer Should Know", *ArXiv e-prints*, 2013, arXiv 1305.5425

45. Twinkle – A Mission to Unravel the Story of Planets in Our Galaxy 2015, Twinkle Space Mission, viewed 25 February 2016, <http://www.twinkle-spacemission.co.uk>

46. Swift, J. J., Bottom, M., Johnson, J. A. et al., "Miniature Exoplanet Radial Velocity Array (MINERVA) I. Design, Commissioning, and First Science Results", *The Journal of Astronomical Telescope, Instrument, and Systems*, 2015, 1, id. 027002

The influence of Jupiter, Mars and Venus on Earth's orbital evolution

Jonathan Horner[1,2], James B. Gilmore[2], and Dave Waltham[3]

[1] *Computational Engineering and Science Research Centre, University of Southern Queensland, Toowoomba, Queensland 4350, Australia*
[2] *Australian Centre for Astrobiology, UNSW Australia, Sydney, New South Wales 2052, Australia*
[3] *Department of Earth Sciences, Royal Holloway, University of London*

Summary: In the coming years, it is likely that the first potentially Earth-like planets will be discovered orbiting other stars. Once found, the characterisation of those planets will play a vital role in determining which will be chosen as the first targets for the search for life beyond the Solar System. We must thus be able to gauge the relative importance of the various factors proposed to influence potential planetary habitability, in order to best focus that search.

One of the plethora of factors to be considered in that process is the climatic variability of the exo-Earths in question. In the Solar System, the Earth's long-term climate is driven by several factors, including the modifying influence of life on our atmosphere, and the temporal evolution of solar luminosity. The gravitational influence of the other planets in the Solar System adds an extra complication, driving the Milankovitch cycles that are thought to have caused the on-going series of glacial and interglacial periods that have dominated Earth's climate for the past few million years.

Here we present preliminary results of three suites of integrations that together examine the influence of Solar System architecture on the Earth's Milankovitch cycles. We consider separately the influence of the planets Jupiter, Mars and Venus, each of which contributes to the forcing of Earth's orbital evolution. Our results illustrate how small changes to the architecture of a given planetary system can result in marked changes in the potential habitability of the planets therein, and are an important first step in developing a means by which the nature of climate variability on planets beyond our Solar System can be characterised.

Keywords: Astrobiology, Exoplanets, Exo-Earths, Habitability, Climate change, Jupiter, Mars, Venus, Milankovitch cycles

Introduction

The question of whether we are alone in the universe is one that has long fascinated humankind. In the early to mid-twentieth century, speculation abounded as to the possibility of complex and advanced life on our nearest planetary neighbours – Mars and Venus (e.g. [1][2][3]). Some authors even went so far as to speculate on the forms that Martian and Venusian life might take (e.g. [4]).

With the dawn of the space age, and the advent of the first missions to other planets, it soon became abundantly clear that neither Mars nor Venus could host advanced life[1]. The Mariner 9 spacecraft

[1] In broad terms, advanced life is here taken to mean macroscopic, rather than microscopic life.

revealed Mars to be an arid world, cold and desolate (e.g. [5][6]), whilst the Venera missions showed Venus to be less habitable still, with a surface hot enough to melt lead (e.g. [7][8]). The observations of Mars suggested a past that might once have been wetter and warmer than the present (e.g. [9]), but neither planet offered hope for the discovery of contemporaneous advanced life.

In the past two decades, the question of life elsewhere has once again become the topic of serious discussion. Within our Solar System, the discovery of liquid water in a variety of locations has reawakened the possibility that microscopic life could find habitats beyond the Earth. Observations taken by the Galileo orbiter indicate the presence of sub-surface oceans on the Jovian satellites Europa ([10][11]), Ganymede ([12]), and Calisto ([13][14]). Similarly, and more surprisingly, the Cassini orbiter has found striking evidence of liquid water on the small Saturnian moon, Enceladus (e.g. [15][16]). Once again, however, the most promising target for the search for life in the Solar system seems to be Mars, with recent observations confirming the presence of water-based salty liquid brine on the planet's surface ([17]). However, despite this, there remains some debate over the modern habitability of Mars, as a consequence of its harsh surface conditions (e.g. [91]).

At the same time, we have seen the discovery of the first exoplanets. At first, in the mid-to-late 1990s, the planets found were nothing like the Earth – behemoths comparable in mass to, or more massive than, Jupiter, but orbiting at a fraction of Jupiter's orbital radius (e.g. [18][19][20]). As time has passed, however, the techniques used to search for planets have improved, and the temporal baselines of the searches have grown longer. Taken in concert, these advances have allowed astronomers to discover more distant giant planets, analogous to those in our own Solar System (e.g. [21][22][23]), and also to find ever smaller planets orbiting stars like the Sun (e.g. [24][25][26]).

As a result of the new techniques and instruments available to astronomers, including the exceptionally productive Kepler spacecraft, it is becoming increasingly clear that small planets far outnumber larger ones (e.g. [27][28][29]. A number of new exoplanet search programs will soon begin that will build on this knowledge, greatly increasing the number of small exoplanets known. In the next decade, new space-based surveys (the Kepler K2 mission [30][31], TESS [32], and PLATO [33]) will be complemented by observations taken by dedicated ground based facilities, such as MINERVA ([34]), NRES ([35]), and the newly announced MINERVA-Australis, to be constructed in 2016 at the University of Southern Queensland's Mt. Kent Observatory.

In the coming years, it is likely that these new exoplanet search programs will discover the first truly Earth-like planets orbiting nearby stars – planets of comparable size and mass to our own, orbiting at a distance from their host star that would allow liquid water to be present and stable on their surface. Once we cross this threshold, the search for life beyond the Solar System will move from the 'needle-in-a-haystack' search for evidence of intelligent aliens (SETI, e.g. [36][37][38]) to the systematic search for biomarkers on known Earth-like planets (e.g. [39][40]). However, the observations needed to characterise the newly discovered planets, and to search for any evidence of life upon them, will be incredibly challenging, and will require highly detailed and time consuming observations (e.g. [41][42]). It will therefore be critically important to determine the most promising targets for such observations, in order to maximise our chances of a positive and timely outcome. But how will that selection process be carried out?

Clearly, the ease with which a given target can be observed will play an important role – but beyond that, it is likely that the potential habitability of the planets discovered will be assessed prior to their being chosen for detailed further study. It is thought that a wide variety of factors combine to render one planet more (or less) habitable than another (e.g. [43], and references therein). Among many

other factors, the stability of the climate on the planets in question will clearly play an important role in determining the most promising target to study in the search for life elsewhere.

It is well established that the Earth's climate has exhibited significant variability throughout its history. At times, our planet has been far warmer than today (such as during the late Permian and early Triassic periods, some 250 million years ago; [44]), whilst at others it was significantly colder (such as the famous 'Snowball Earth' episodes, thought to have occurred on several occasions through Earth's history – e.g. [45][46]).

These climatic variations have been driven by a wide variety of factors. Earth's climate has been strongly affected by the configuration of the continents (e.g. hot, dry conditions when there was a supercontinent [85]; biological evolution (e.g. substantial draw-down of CO2 from the atmosphere following the first appearance of land-plants [86]); volcanism (e.g. the end-Permian mass-extinction [87]); impacts (e.g. the possible effect of an asteroid collision at the end of the Cretaceous [88][89]); and the steady increase in solar luminosity through time [90].

In addition to these long-term changes, and those driven by stochastic, unpredictable events, the Earth also experiences periodic climatic variation on relatively rapid geological timescales. Perhaps the best demonstration of such variability is that of the last few million years, which have been characterised by a series of glacial and interglacial periods (e.g. [47]). The cause of this semi-periodic behaviour are the Milankovitch cycles (e.g. [48][49]) – variability in the Earth's orbital eccentricity, obliquity and the timing of seasons relative to perihelion passage, driven by the gravitational influence of the Solar System's other planets.

Although the scale of Earth's climatic variability in the last few million years seems relatively dramatic, the variations in Earth's orbit that have driven that variability are actually rather small. The Earth's obliquity (the angle between its equatorial and orbital planes) varies by just over two degrees, whilst its eccentricity rarely ranges higher than ~0.06 (as can be seen in Figure 1 of [54]). It is certainly possible to imagine scenarios where an exo-Earth that might otherwise be highly promising as a target for the search for life would be driven to far greater excursions in eccentricity and inclination than is the Earth, without rendering its orbit sufficiently dynamically unstable as to render the system untenable.

The Milankovitch cycles of the planet Mercury, for example, can drive the planet's orbital eccentricity as high as 0.45 ([50][51]). If that were to be replicated for an otherwise habitable exo-Earth, that planet would experience epochs at which its orbital distance would vary by a factor of almost three from pericentre to apocentre. That would, in turn, result in the amount of flux received by a given region of its surface from its host star varying by almost nine times – something that might preclude, or severely hinder, the development of even the most basic forms of life[2].

Unlike the other processes that drive climate change, therefore, the Milankovitch cycles of a given planet will be unique to that world, driven by the gravitational influence of the other planets in the system. As a result, this offers the potential that the study of the Milankovitch cycles in newly discovered exoplanetary systems could form an important part of a procedure for identifying the most promisingly habitable worlds for further study.

[2] We note that the impact of the Milankovitch cycles would likely be diminished for life in the deep ocean relative to life on land.

This idea was examined by [52] in the context of our Solar System using a simple analytic approach, examining (among other things) the degree to which the architecture of our Solar System is unusual in the small scale of Earth's Milankovitch cycles. That work suggested that the Earth experiences unusually low Milankovitch frequencies when compared to similar systems with alternative architectures. We note, however, that the analytic model used in that work was unable to account for the influence of resonant effects and direct encounters between planets, and so serves more as the seed of an interesting idea, rather than strong indication of our Solar System's uniqueness. To build on that work, we therefore decided to carry out a similar study that fully models the interactions between the planets involved, as a first step in building a technique to help direct the search for life.

In this paper, we build upon our presentations at the two previous Australian Space Research Conferences ([53][54]), in which we examined the role played by Jupiter in determining the scale and frequency of Earth's Milankovitch cycles. Here, we compare the results of detailed *n*-body integrations that model Jupiter's influence on the amplitude and frequency of Earth's orbital oscillations to new simulations that model the influence of the Earth's nearest planetary neighbours, Mars and Venus.

In the next section, we detail our simulations, recapping those performed to determine Jupiter's influence, and summarising our new runs modelling the effects of Venus and Mars. We then present our preliminary results, before concluding with a discussion of the results and our plans for future work.

The Simulations

In order to examine how the Earth's Milankovitch cycles change as a function of the Solar System's architecture, we use a modified version of the Hybrid integrator within the *n*-body dynamics package MERCURY ([55]). In its default form, MERCURY neglects relativistic effects, calculating the orbital evolution of objects in a purely Newtonian manner. For most applications (e.g. [56][57][58]), this is no impediment – and performing simulations using a Newtonian rather than relativistic formulism allows the code to run significantly faster than would otherwise be the case. However, the assumption that relativistic effects do not significantly affect the evolution of objects begins to break down as one approaches sufficiently close to massive bodies such as the Sun – as is well illustrated by the failure of Newton's gravitation to explain the precession rate of Mercury's perihelion (e.g. [59][60]).

Here, we use a modified version of MERCURY that implements a user-defined force to take account of the first-order post-Newtonian relativistic correction ([61]). We have performed tests of the modified code, and have confirmed that it accurately replicates the evolution of Mercury's orbit. The addition of the user-defined force causes the code to run somewhat slower than would otherwise be the case – but thanks to recent advances in the computational power available for us, this has not proved to be too great an impediment.

We have used our code to carry out three suites of *n*-body integrations, using the *Katana* supercomputing cluster at the University of New South Wales, and the *Epic* supercomputing cluster, now retired, hosted by iVEC in Western Australia. The three suites of integrations are setup, where possible, in identical manners. They ran for a period of ten million years in to the future, from initial conditions based on the NASA DE431 ephemeris [62]. In order to maximise the accuracy of the

simulations, an integration time-step of 1 day was used. The orbital elements of each of the planets are output at 1,000-year intervals for every simulation.

The first, and most detailed, suite of integrations was that which examined the influence of Jupiter's orbit on Earth's Milankovitch cycles. For these simulations, the preliminary results of which we presented in [54], we tested 159,201 unique versions of our Solar System. In those simulations, the initial orbits of all the planets except Jupiter were held fixed at their DE431 values. By contrast, the semi-major axis and eccentricity of Jupiter's orbit was varied systematically through the runs, such that a 399 x 399 grid of solutions were tested in semi-major axis – eccentricity space. The semi-major axis values tested for Jupiter spanned a region of 4 au, centred on the DE431 value of a = 5.203102 au, and were distributed evenly throughout the range. The eccentricities considered were evenly distributed between circular orbits (e = 0.0) and those with moderate eccentricity (e = 0.4).

Given the wide range of Jovian orbits considered, we anticipated that at least some of the solutions tested would prove to be dynamically unfeasible – as has often be found when testing the proposed orbits of newly discovered exoplanetary systems (e.g. [63][64][65]). To address this issue, if any of the planets collided with one another, fell into the Sun, or reached a barycentric distance of 40 au, the simulations were halted, and the time at which the event happened was recorded.

These simulations allowed us to create maps showing how the Earth's orbital elements varied with time as a function of Jupiter's initial orbital semi-major axis and eccentricity, as well as allowing us to map out the regions of instability where Jupiter tore the Solar System asunder. These maps build on our earlier work studying the stability of Solar System and exoplanetary orbits (e.g. [66][67]), and provide a visual guide to the manner in which Earth's Milankovitch cycles are modified by Jupiter's orbital characteristics.

We have now complemented these simulations of Jupiter's influence by examining the influence of Mars and Venus on the Earth's orbital evolution. These new simulations each considered 39,601 different orbits for the planet in question. For both planets, we tested 199 unique values of eccentricity spread evenly between 0.0 and 0.3. At each of these eccentricities, we tested 199 unique values of semi-major axis, centred on the DE431 values for the planet's orbit. For Mars, the semi-major axes chosen were therefore centred on 1.524 au, and ranged as far as 0.45 au on either side of that value (i.e. ranging from 1.074 To 1.974 au). For Venus, the semi-major axes centred on 0.723 au, and ranged 0.277 au on either side of that value (for a range between 0.446 and 1.000 au).

We are currently in the process of taking the numerical results of these simulations (the orbital elements of the Earth across the three suites of integrations) and using them as input for simple climate models (e.g. [68]). Those calculations for our Jupiter simulations are almost complete, and we anticipate that the full analysis will be ready in the near future.

Preliminary results

In order to directly compare the influence of Jupiter, Mars and Venus on Earth's Milankovitch cycles, we present here the root-mean-square rates of change of the Earth's orbital inclination and eccentricity over the ten million year period integrated in this work. Regions plotted in black are

those where the Solar System was rendered unstable within the ten million year timeframe of our simulations by the initial architecture chosen. Figure 1 presents the rate of change of Earth's orbital eccentricity as a function of the chosen planet's semi-major axis and eccentricity, whilst Figure 2 presents the rate of change of its inclination with the planet's semi-major axis and eccentricity.

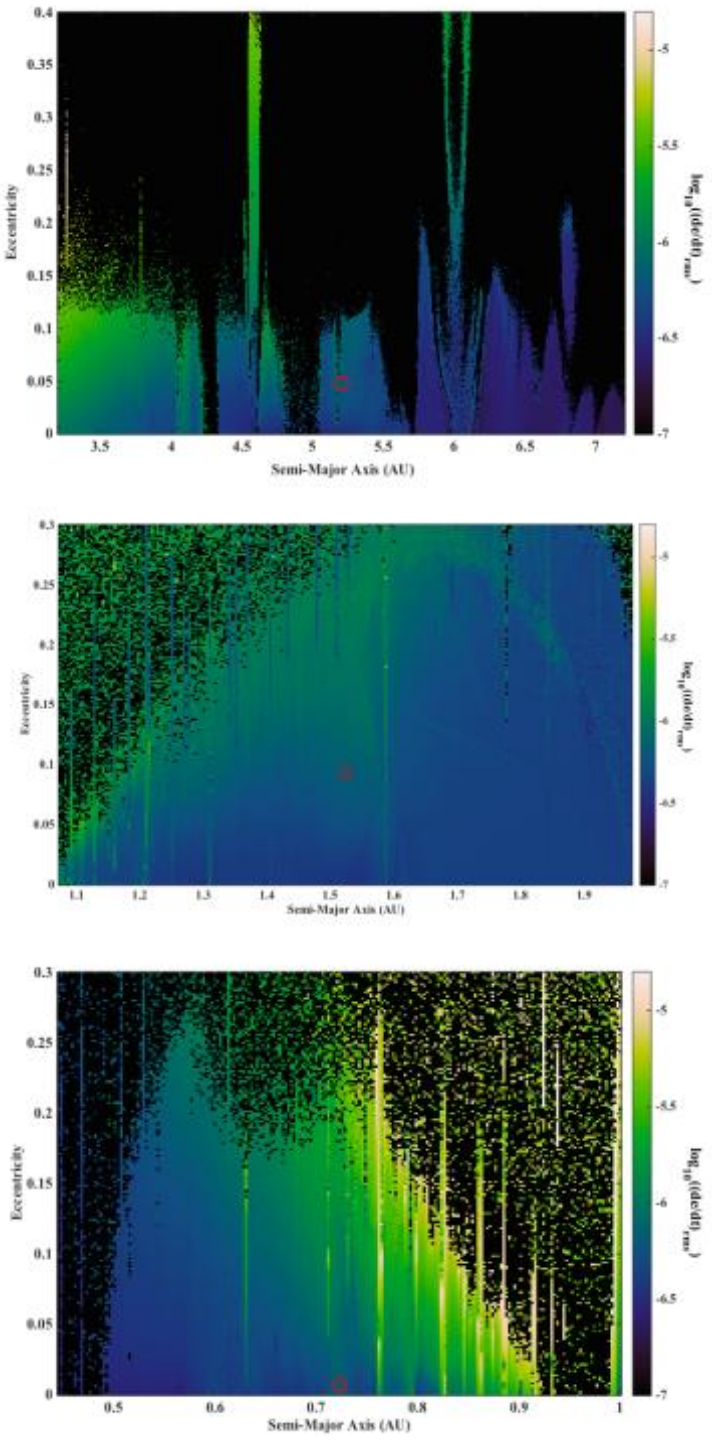

Figure 1: The root-mean-square rate of change of Earth's orbital eccentricity over a ten million year period, plotted on a logarithmic scale, to illustrate the influence of the Solar System's architecture on our planet's Milankovitch cycles. The top panel shows the variability as a function of Jupiter's initial semi-major axis and eccentricity, with the variability as a function of Mars and Venus' orbits being plotted in the centre and lower panels, respectively. Regions in black are those for which the Solar System was rendered dynamically unstable by

the chosen architecture, with planets either colliding with one another, being thrown into the Sun, or reaching a barycentric distance of 40 au (for Jupiter) or 1000 au (Venus and Mars). The orbit of the planet in our own Solar System lies at the centre of the hollow red circle.

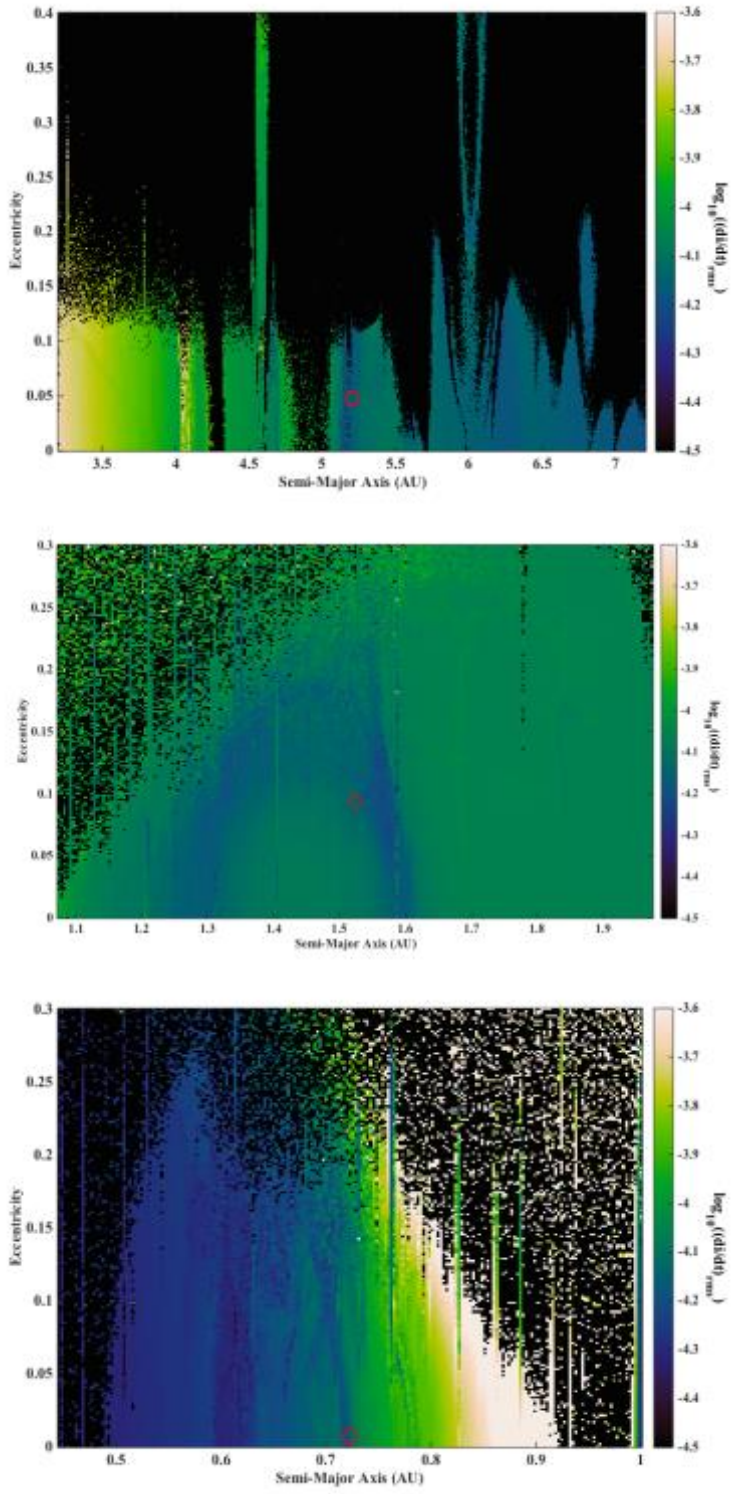

Figure 2: The root-mean-square rate of change of Earth's orbital inclination over ten million years, on a logarithmic scale, as a function of the initial orbit of Jupiter (top), Mars (middle) and Venus (bottom). The regions shown in black are those where the Solar System become unstable within the ten million year runtime, with planets being ejected, colliding with one

another, or being thrown into the Sun. As before, the hollow red circle denotes the orbit of the planet in question in our own Solar System.

Discussion and Conclusions

Several things are immediately apparent when one compares the influence of Jupiter, Mars and Venus on the Earth's orbital evolution (Figures 1 and 2). The first is how moving the three planets impacts the stability of the Solar System. As we noted in [54], the Solar System's stability is strongly dependent on Jupiter's initial orbit, with only a relatively small change in the planet's orbit being enough to destabilise the entire Solar System.

The same, to an extent, is true of Venus – if placed on an orbit with a perihelion distance less than ~0.485 au, Venus comes close enough to Mercury that the two undergo strong gravitational interaction, destabilising the Solar System. Similarly, if Venus' aphelion exceeds ~0.92 au, it strongly interacts with the Earth, again leading to the Solar System's disintegration. This result is not hugely surprising. Indeed, [69] studied the effect of tightly-packing planets on their orbital stability, and found that two planet systems are typically stable so long as the planets therein are separated by more than $2\sqrt{3}$ times their mutual Hill radius, where for low eccentricity orbits the mutual Hill radius is defined as:

$$R_H = \left[\frac{(m_1 + m_2)}{3M}\right]^{1/3}\left[\frac{(a_1 + a_2)}{2}\right] \quad [1].$$

Here m_1 *and* m_2 are the masses of the two planets in question, M is the mass of the central star, and a_1 and a_2 are the semi-major axes of the orbits of the two planets. In the case of Earth and Venus, we find that when Venus is at 0.92 au from the Sun, with the Earth at perihelion at ~0.98 au, their *instantaneous* mutual Hill radius is 0.012 au. Therefore, the two planets are separated by just approximately five mutual Hill radii, only slightly more than the $2\sqrt{3}$ Hill radii noted by [69]. Accordingly, the boundary between unstable and stable regimes in the region ~0.75 – 0.92 au tends to follow the line of constant aphelion distance meeting this criterion. It should be noted, too, that the values plotted for the semi-major axis and inclination of Venus (and Mars and Jupiter, in the other plots), are the instantaneous values at the start of the simulations – and it is quite feasible that planets which start out separated by more than these $2\sqrt{3}$ Hill radii will occasionally experience periods that offer encounters closer than this distance. For this reason, the boundary between stable and unstable regimes does not perfectly follow a line of constant Venutian aphelion, but instead tends along that line, with a certain amount of noise and fluctuation.

An exception to these regions of stability and instability resulting from close approaches occurs when Venus is placed at the location of mean-motion resonances with either Earth or Mercury, which can be seen as the striking vertical features in both figures (albeit most pronounced in Figure 1). Perhaps the most interesting of these regions of resonant stability is the one in the vicinity of the Earth's orbit, around 1 au from the Sun. Here, Venus and Earth can remain dynamically stable, and are most likely trapped in mutual 1:1 resonance – in other words, Venus is acting as a Trojan companion to the Earth. Such companions are widely observed in our own Solar System (e.g. the Jovian and Neptunian Trojans, [70][71][72][73]), and the existence of planet-mass Trojans has been suggested

as a means by which potentially habitable worlds could be found in planetary systems with hot- or warm-Jupiters (e.g. [74][75][76]).

Such papers usually discuss the existence of Trojan companions that are far less massive than the planet with which they share an orbit – just as is the case for the Trojan companions to the Solar System's planets. However, [77] considered the question of whether planets of similar or equal mass could survive as mutual Trojan companions. They found that mutually resonant planets could remain dynamically stable so long as their combined mass did not exceed ~1/26th of the mass of their host star. As such, our result that Venus and Earth *could* form a dynamically stable Trojan couple is not perhaps that surprising – but it is certainly interesting to consider, and opens up an additional direction for further study in the future. Namely – would the existence of a Trojan companion render the climate of a given planet too unstable for the evolution of detectable life? Whilst our results offer no definitive conclusions to the answer to this problem, it is clear that the stable 1:1 resonant solutions in our simulations featured variability in orbital inclination and eccentricity far more rapid than are experienced within our current Solar System. For this case, at least, it might therefore be to consider those solutions less habitable than our own Earth – but significantly more work would be required to extend this to a general argument for all Trojan scenarios.

In the case of Mars, far less instability is seen. Once again, though, it is clear that moving Mars too close to the orbit of the Earth will render the system unstable (region leftward of a line of constant perihelion ~1.06 au). Even above this line, though, a significant number of solutions survive for the 10 Myr of our simulations. This might well be an artefact of the 1000 au ejection criteria used in the simulations for Mars, however – and we intend to re-run those simulations in the near future using a 40 au ejection distance to match our work with Jupiter.

The influence of mean-motion resonances can be clearly seen in the plots detailing Mars' influence. To the outer edge of those plots, unstable solutions are found near a = 2 au. This instability is the result of the influence of the 4:1 mean-motion resonance with Jupiter, which is centred at 2.06 au, and is the cause of a broad Kirkwood gap in the asteroid belt (e.g. [78]). The influence of a less disruptive mean-motion resonance can be seen at ~1.587 au, in the form of a vertical stream of slightly accelerated variability in Earth's eccentricity evolution (Figure 1, middle plot). This is the location of the 2:1 mean-motion resonance between Earth and Mars.

Whilst the effect of resonances between Earth and Mars is somewhat understated in both Figure 1 and Figure 2, resonant interactions between Earth and Venus have a far stronger influence on the rate of change of Earth's orbit. This is not unsurprising – Venus is almost eight times more massive than Mars, and not hugely less massive than the Earth – so with all else equal, one would expect it to more strongly perturb our planet. This is borne out in the strength of the resonant perturbations on Earth visible in the lower panel of Figure 1, and the broader region of instability caused by Venus and Earth undergoing close approaches. Mars, the less massive of the two planets, can approach Earth slightly closer than Venus before destabilising the Solar System.

Beyond these observations on broad stability, a further surprising result is clear from our simulations. When moved away from its current location, Venus can induce far more rapid shifts in both Earth's orbital eccentricity (Figure 1) and inclination (Figure 2) than are observed for our simulations of Jupiter's influence. Before we leap to the conclusion that Venus actually has a greater influence on Earth's climate than does Jupiter, we need here to include the caveat that, even in the most extreme

scenarios tested, Jupiter remained far beyond Earth's orbit, at ~3.2 au from the Sun. It would be interesting to see how Jupiter would affect Earth's inclination and eccentricity were it moved further inward – though obviously it would eventually destabilise the system were it moved sufficiently far inward!

Whilst the influence of Venus on Earth's eccentricity evolution is strongest when resonant interactions come into play, it is interesting to observe that the same is not true for its influence on Earth's orbital inclination. The more closely Venus and Earth approach one another, the more rapidly the inclination of Earth's orbit is driven to change. This behaviour is strikingly illustrated towards the right-hand edge of the stability region in the lower panel of Figure 2.

Aside from those regions where close approaches or resonant interactions begin to render the Solar System unstable, our results show that Mars has a far less significant impact on the orbital evolution of the Earth than either Venus or Jupiter. The plots in Figures 1 and 2 all span the same range in inclination and eccentricity variability – and the variation seen across the bulk of the Martian simulations is lower than that for either Venus or Jupiter. Mean motion resonances (vertical strips in the plots) do induce some variability, and the eccentricity and inclination plots also reveal subtle variations – the 'breaking wave' in Figure 1, and the prominence-like loop in Figure 2. These are most likely the result of secular interactions between the planets, but are relatively minor features compared to the strong variability resulting from the other two planets.

In the coming year, we intend to pair our simulations of Venus, Mars and Jupiter's influence with climate models, which will incorporate the precession of the Earth's axis, allowing us to determine the variability of the Earth's obliquity in our simulations. The obliquity variability is the key dynamical parameter in translating the ongoing perturbations on Earth's motion into the resulting climatic variability, and will feed directly into our climate models.

Beyond that work, we have begun a suite of integrations that will examine how Earth's initial orbit influences its Milankovitch cycles. In those simulations, we hold the initial orbits of the other planet fixed, as described in this work, and instead move the Earth within the Solar System. Those simulations are currently underway on UNSW Australia's *Katana* supercomputing cluster, and will bring the first phase of our study of planetary architecture and climate stability to a close.

Taken in concert, our work will help us to uncover the degree to which fine tuning in planetary architecture can impact the climate, and potential habitability, of planets like the Earth. In doing so, it will give us a feel for how 'unusual' the Earth's climatic variability is. A core tenant of the 'Rare Earth' philosophy (e.g. [79]) is that the Earth is unusually fortunate in its properties – almost a fluke of nature that just happens to be a safe haven in an inimical cosmos. It suggests that, for example, the impact rate at Earth is far lower than it would be were the giant planet Jupiter not present – in other words, that without our good fortune in having a giant protector, we would not be here. Whilst that particular aspect of the hypothesis has since been effectively demolished (see e.g. [56][80][81][82][83][84]), the idea underpinning the thesis remains under debate. Is the Earth unusually quiescent? Would most other 'Earths' be far less habitable than our own? Once we bring together climate modelling with our *n*-body simulations, we will begin to get a feel for just how precarious is Earth's climate, in the context of the architecture of our own planetary system.

Beyond this, however, our work will build a framework by which the climatic variability of newly discovered exoEarths can be estimated – once such planets are found. Whilst this is far from the only consideration when it comes to determining the suitability of those planets as targets in the search for life, it will still provide a useful datum – potentially helping to rule out some otherwise promising targets, allowing observers to instead focus their efforts at more promising worlds.

Acknowledgements

JH is supported by USQ's Strategic Research Fund: the STARWINDS project. The work was supported by iVEC through the use of advanced computing resources located at the Murdoch University, in Western Australia. The authors wish to thank A/Prof Ramon Brasser and the anonymous second referee of this work, whose feedback greatly helped to improve the clarity and flow of the paper.

References

1. Henkel, F. W., "Venus as the Abode of Life", *Popular Astronomy*, 1909, 17, pp. 412 - 417

2. Lowell, P., "Mars as the Abode of Life", Published 1908 in New York by Macmillan, 338 pages; available online at https://archive.org/details/marsabodeoflife00loweiala (accessed Wednesday 4th November 2015)

3. Hamilton, G. H., "Mars as a living planet", *The Scientific Monthly*, 1921, 13, pp. 376 - 379

4. Duckwall, W. E., "Life on Mars", *Popular Astronomy*, 1941, 49, 479 – 484

5. Hanel, R., Conrath, B., Hovis, W., Kunde, V., Lowman, P., Maguire, W., Pearl, J., Pirraglia, J., Prabhakara, C., Schlachman, B., Levin, G., Straat, P. and Burke, T., "Investigation of the Martian Environment by Infrared Spectroscopy on Mariner 9 (A 5. 2)", *Icarus*, 1972, 17, pp. 423 – 442

6. Conrath, B., Curran, R., Hanel, R., Kunde, V., Maguire, W., Pearl, J., Pirraglia, J., Welker, J. and Burke, T., "Atmospheric and surface properties of Mars obtained by infrared spectroscopy on Mariner 9", *Journal of Geophysical Research*, 1973, 78, pp. 4267 - 4278

7. Avduevsky, V. S., Marov, M. Ya., Rozhdestvensky, M. K., Borodin, N. F. and Kerzhanovich, V. V., "Soft Landing of Venera 7 on the Venus Surface and Preliminary Results of Investigations of the Venus Atmosphere", *Journal of the Atmospheric Sciences*, 1971, 28, pp. 263 - 269

8. Marov, M. Ya., "Venus: A Perspective at the Beginning of Planetary Evolution", *Icarus*, 1972, 16, pp. 415 – 461

9. Sagan, C., Toon, O. B. and Gierasch, P. J., "Climatic Change on Mars", *Science*, 1973, 181, pp. 1045 – 1049

10. Carr, M. H., Belton, M. J. S., Chapman, C. R., Davies, M. E., Geissler, P., Greenberg, R., McEwen, A. S., Tufts, B. R., Greeley, R., Sullivan, R., Head, J. W., Pappalardo, R. T., Klaasen, K. P., Johnson, T. V., Kaufman, J., Senske, D., Moore, J., Neukum, G., Schubert, G., Burns, J. A., Thomas, P. and Veverka, J., "Evidence for a subsurface ocean on Europa", *Nature*, 1998, 391, p. 363

11. Kivelson, M. G., Khurana, K. K., Russel, C. T., Volwerk, M., Walker, R. J. and Zimmer, C., "Galileo Magnetometer Measurements: A Stronger Case for a Subsurface Ocean at Europa", *Science*, 2000, 5483, pp. 1340 - 1343

12. Kivelson, M. G., Khurana, K. K. and Volwerk, M., "The Permanent and Inductive Magnetic Moments of Ganymede", *Icarus*, 2002, 157, pp. 507 - 522

13. Khurana, K. K., Kivelson, M. G., Stevenson, D. J., Schubert, G., Russell, C. T., Walker, R. J. and Polanskey, C., "Induced magnetic fields as evidence for subsurface oceans in Europa and Callisto", *Nature*, 1998, 395, pp. 777 - 780

14. Zimmer, C., Khurana, K. K. and Kivelson, M. G., "Subsurface Oceans on Europa and Callisto: Constraints from Galileo Magnetometer Observations", *Icarus*, 2000, 147, pp. 329 - 347

15. Porco, C. C., Helfenstein, P., Thomas, P. C., Ingersoll, A. P., Wisdom, J., West, R., Neukum, G., Denk, T., Wagner, R., Roatsch, T., Kieffer, S., Turtle, E., McEwen, A., Johnson, T. V., Rathbun, J., Veverka, J., Wilson, D., Perry, J., Spitale, J., Brahic, A., Burns, J. A., Del Genio, A. D., Dones, L., Murray, C. D. and Squyres, S., "Cassini Observes the Active South Pole of Enceladus", *Science,* 2006, 311, pp. 1393 - 1401

16. Waite, J. H., Jr., Lewis, W. S., Magee, B. A., Lunine, J. I., McKinnon, W. B., Glein, C. R., Mousis, O., Young, D. T., Brockwell, T., Westlake, J., Nguyen, M.-J., Teolis, B. D., Niemann, H. B., McNutt, R. L., Perry, M. and Ip, W.-H., "Liquid water on Enceladus from observations of ammonia and ^{40}Ar in the plume", *Nature*, 2009, 460, pp. 487 - 490

17. Ojha, L., Wilhelm, M. B., Murchie, S. L., McEwen, A. S., Wray, J. J., Hanley, J., Massé, M. and Chojnacki, M., "Spectral evidence for hydrated salts in recurring slope lineae on Mars", *Nature Geoscience*, 2015, doi:10.1038/ngeo2546

18. Mayor, M. and Queloz, D., "A Jupiter-mass companion to a solar-type star", *Nature*, 1995, 378, 355-359

19. Marcy, G. W. and Butler, R. P., "A Planetary Companion to 70 Virginis", *Astrophysical Journal Letters*, 1996, 464, L147

20. Butler, R. P. and Marcy, G. W., "A Planet Orbiting 47 Ursae Majoris", *Astrophysical Journal Letters*, 1996, 464, L153

21. Boisse, I., Pepe, F., Perrier, C., Queloz, D., Bonfils, X., Bouchy, F., Santos, N. C., Arnold, L., Beuzit, J.-L., Díaz, R. F., Delfosse, X., Eggenberger, A., Ehrenreich, D., Forveille, T.,

Hébrard, G., Lagrange, A.-M., Lovis, C., Mayor, M., Moutou, C., Naef, D., Santerne, A., Ségransan, D., Sivan, J.-P. and Udry, S., "The SOPHIE search for northern extrasolar planets. V. Follow-up of ELODIE candidates: Jupiter-analogs around Sun-like stars", *Astronomy and Astrophysics*, 2012, 545, id. A55

22. Wittenmyer, R. A., Tinney, C. G., Horner, J., Butler, R. P., Jones, H. R. A., O'Toole, S. J., Bailey, J., Carter, B. D., Salter, G. S. and Wright, D., "Observing Strategies for the Detection of Jupiter Analogs", *Publications of the Astronomical Society of the Pacific*, 2013, 125, pp. 351 - 356

23. Wittenmyer, R. A., Horner, J., Tinney, C. G., Butler, R. P., Jones, H. R. A., Tuomi, M., Salter, G. S., Carter, B. D., Koch, F. E., O'Toole, S. J., Bailey, J. and Wright, D., "The Anglo-Australian Planet Search. XXIII. Two New Jupiter Analogs", *The Astrophysical Journal*, 2014, 783, id. 103

24. Delfosse, X., Bonfils, X., Forveille, T., Udry, S., Mayor, M., Bouchy, F., Gillon, M., Lovis, C., Neves, V., Pepe, F., Perrier, C., Queloz, D., Santos, N. C. and Ségransan, D., "The HARPS search for southern extra-solar planets. XXXIII. Super-Earths around the M-dwarf neighbors Gl 433 and Gl 667C", *Astronomy and Astrophysics*, 2013, 553, id. A8

25. Wittenmyer, R. A., Tuomi, M., Butler, R. P., Jones, H. R. A., Anglada-Escudé, G., Horner, J., Tinney, C. G., Marshall, J. P., Carter, B. D., Bailey, J., Salter, G. S., O'Toole, S. J., Wright, D., Crane, J. D., Schectman, S. A., Arriagada, P., Thompson, I., Minniti, D., Jenkins, J. S. and Diaz, M., "GJ 832c: A Super-Earth in the Habitable Zone", *The Astrophysical Journal*, 2014, 791, id. 114

26. Jenkins, J. M., Twicken, J. D., Batalha, N. M., Caldwell, D. A., Cochran, W. D., Endl, M., Latham, D. W., Esquerdo, G. A., Seader, S., Bieryla, A., Petigura, E., Ciardi, D. R., Marcy, G. W., Isaacson, H., Huber, D., Rowe, J. F., Torres, G., Bryson, S. T., Buchhave, L., Ramirez, I., Wolfgang, A., Li, J., Campbell, J. R., Tenenbaum, P., S,erfer, D., Henze, C. E., Catanzarite, J. H., Gillil,, R. L. and Borucki, W. J., "Discovery and Validation of Kepler-452b: A 1.6 $R_{\oplus}$ Super Earth Exoplanet in the Habitable Zone of a G2 Star", *The Astronomical Journal*, 2015, 150, id. 56

27. Wittenmyer, R. A., Tinney, C. G., Butler, R. P., O'Toole, S. J., Jones, H. R. A., Carter, B., D., Bailey, J. and Horner, J., "The Frequency of Low-mass Exoplanets. III. Toward $\eta_{\oplus}$ at Short Periods", *The Astrophysical Journal*, 2011, 738, id 81

28. Fressin, F., Torres, G., Charbonneau, D., Bryson, S. T., Christiansen, J., Dressing, C. D., Jenkins, J. M., Walkowicz, L. M. and Batalha, N. M., "The False Positive Rate of Kepler and the Occurrence of Planets", *The Astrophysical Journal*, 2013, 766, id. 81

29. Batalha, N. M., "Exploring exoplanet populations with NASA's Kepler Mission", *Proceedings of the National Academy of Sciences*, 2014, 111, pp. 12647 – 12654

30. Howell, S. B., Sobeck, C., Haas, M., Still, M., Barclay, T., Mullally, F., Troeltzsch, J., Aigrain, S., Bryson, S. T., Caldwell, D., Chaplin, W. J., Cochran, W. D., Huber, D., Marcy, G. W.,

Miglio, A., Najita, J. R., Smith, M., Twicken, J. D. and Fortney, J. J., "The K2 Mission: Characterization and Early Results", *Publications of the Astronomical Society of the Pacific*, 2014, 126, 938

31. Foreman-Mackey, D., Montet, B. T., Hogg, D. W., Morton, T. D., Wang, D. and Schölkopf, B., "A Systematic Search for Transiting Planets in the K2 Data", *The Astrophysical Journal*, 2015, 806, id. 215

32. Ricker, G. R., Winn, J. N., Vanderspek, R., Latham, D. W., Bakos, G. \'A., Bean, J. L., Berta-Thompson, Z. K., Brown, T. M., Buchhave, L., Butler, N. R., Butler, R. P., Chaplin, W. J., Charbonneau, D., Christensen-Dalsgaard, J., Clampin, M., Deming, D., Doty, J., De Lee, N., Dressing, C., Dunham, E. W., Endl, M., Fressin, F., Ge, J., Henning, T., Holman, M. J., Howard, A. W., Ida, S., Jenkins, J., Jernigan, G., Johnson, J. A., Kaltenegger, L., Kawai, N., Kjeldsen, H., Laughlin, G., Levine, A. M., Lin, D., Lissauer, J. J., MacQueen, P., Marcy, G., McCullough, P. R., Morton, T. D., Narita, N., Paegert, M., Palle, E., Pepe, F., Pepper, J., Quirrenbach, A., Rinehart, S. A., Sasselov, D., Sato, B., Seager, S., Sozzetti, A., Stassun, K. G., Sullivan, P., Szentgyorgyi, A., Torres, G., Udry, S. and Villasenor, J., "Transiting Exoplanet Survey Satellite (TESS)", *Proceedings of the SPIE*, 2014, 9143, id. 914320

33. Rauer, H., Catala, C., Aerts, C., Appourchaux, T., Benz, W., Brandeker, A., Christensen-Dalsgaard, J., Deleuil, M., Gizon, L., Goupil, M.-J., Güdel, M., Janot-Pacheco, E., Mas-Hesse, M., Pagano, I., Piotto, G., Pollacco, D., Santos, Ċ., Smith, A., Suárez, J.-C., Szabó, R., Udry, S., Adibekyan, V., Alibert, Y., Almenara, J.-M., Amaro-Seoane, P., Eiff, M. Ammler-von, Asplund, M., Antonello, E., Barnes, S., Baudin, F., Belkacem, K., Bergemann, M., Bihain, G., Birch, A. C., Bonfils, X., Boisse, I., Bonomo, A. S., Borsa, F., Brandão, I. M., Brocato, E., Brun, S., Burleigh, M., Burston, R., Cabrera, J., Cassisi, S., Chaplin, W., Charpinet, S., Chiappini, C., Church, R. P., Csizmadia, Sz., Cunha, M., Damasso, M., Davies, M. B., Deeg, H. J., Díaz, R. F., Dreizler, S., Dreyer, C., Eggenberger, P., Ehrenreich, D., Eigmüller, P., Erikson, A., Farmer, R., Feltzing, S., de Oliveira Fialho, F., Figueira, P., Forveille, T., Fridlund, M., García, R. A., Giommi, P., Giuffrida, G., Godolt, M., Gomes da Silva, J., Granzer, T., Grenfell, J. L., Grotsch-Noels, A., Günther, E., Haswell, C. A., Hatzes, A. P., Hébrard, G., Hekker, S., Helled, R., Heng, K., Jenkins, J. M., Johansen, A., Khodachenko, M. L., Kislyakova, K. G., Kley, W., Kolb, U., Krivova, N., Kupka, F., Lammer, H., Lanza, A. F., Lebreton, Y., Magrin, D., Marcos-Arenal, P., Marrese, P. M., Marques, J. P., Martins, J., Mathis, S., Mathur, S., Messina, S., Miglio, A., Montalban, J., Montalto, M., Monteiro, M. J. P. F. G., Moradi, H., Moravveji, E., Mordasini, C., Morel, T., Mortier, A., Nascimbeni, V., Nelson, R. P., Nielsen, M. B., Noack, L., Norton, A. J., Ofir, A., Oshagh, M., Ouazzani, R.-M., Pápics, P., Parro, V. C., Petit, P., Plez, B., Poretti, E., Quirrenbach, A., Ragazzoni, R., Raimondo, G., Rainer, M., Reese, D. R., Redmer, R., Reffert, S., Rojas-Ayala, B., Roxburgh, I. W., Salmon, S., Santerne, A., Schneider, J., Schou, J., Schuh, S., Schunker, H., Silva-Valio, A., Silvotti, R., Skillen, I., Snellen, I., Sohl, F., Sousa, S. G., Sozzetti, A., Stello, D., Strassmeier, K. G., Švanda, M., Szabó, Gy. M., Tkachenko, A., Valencia, D., Van Grootel, V., Vauclair, S. D., Ventura, P., Wagner, F. W., Walton, N. A., Weingrill, J., Werner, S. C., Wheatley, P. J. and Zwintz, K., "The PLATO 2.0 mission", *Experimental Astronomy*, 2014, 38, pp. 249-330

34. Swift, J. J., Bottom, M., Johnson, J. A., Wright, J. T., McCrady, N., Wittenmyer, R. A., Plavchan, P., Riddle, R., Muirhead, P. S., Herzig, E., Myles, J., Blake, C. H., Eastman, J., Beatty, T. G., Lin, B., Zhao, M., Gardner, P., Falco, E., Criswell, S., Nava, C., Robinson, C., Sliski, D. H., Hedrick, R., Ivarsen, K., Hjelstrom, A., de Vera, J. and Szentgyorgyi, A., "Miniature Exoplanet Radial Velocity Array (MINERVA) I. Design, Commissioning, and First Science Results", *Journal of Astronomical Telescopes, Instrumentation and Systems*, 2015, 1, id 027002

35. Eastman, J. D., Brown, T. M., Hygelund, J., van Eyken, J., Tufts, J. R. and Barnes, S., "NRES: the network of robotic Echelle spectrographs", *Proceedings of the SPIE*, 2014, 9147, id. 914716

36. Tarter, J., "The Search for Extraterrestrial Intelligence (SETI)", *Annual Review of Astronomy and Astrophysics*, 2001, 39, pp. 511 - 548

37. Turnbull, M. C. and Tarter, J., "Target Selection for SETI. I. A Catalog of Nearby Habitable Stellar Systems", *The Astrophysical Journal Supplement Series*, 2003, 145, pp. 181 - 198

38. Merali, Z., "Search for extraterrestrial intelligence gets a $100-million boost", *Nature*, 2015, 523, pp. 392 - 393

39. Kaltenegger, L., Selsis, F., Fridlund, M., Lammer, H., Beichman, C., Danchi, W., Eiroa, C., Henning, T., Herbst, T., Léger, A., Liseau, R., Lunine, J., Paresce, F., Penny, A., Quirrenbach, A., Röttgering, H., Schneider, J., Stam, D., Tinetti, G., White, G. J., "Deciphering Spectral Fingerprints of Habitable Exoplanets", *Astrobiology*, 2010, 10, pp. 89 - 102

40. Snellen, I. A. G., de Kok, R. J., le Poole, R., Brogi, M. and Birkby, J., "Finding Extraterrestrial Life Using Ground-based High-dispersion Spectroscopy", *The Astrophysical Journal*, 2013, 764, id. 182

41. Arnold, L., "Earthshine Observation of Vegetation and Implication for Life Detection on Other Planets. A Review of 2001 – 2006 Works", *Space Science Reviews*, 2008, 135, pp. 323 – 333

42. Kawahara, H., Matsuo, T., Takami, M., Fujii, Y., Kotani, T., Murakami, N., Tamura, M. and Guyon, O., "Can Ground-based Telescopes Detect the Oxygen 1.27 μm Absorption Feature as a Biomarker in Exoplanets?", *The Astrophysical Journal*, 2012, 758, id. 13

43. Horner, J. and Jones, B. W., "Determining habitability: which exoEarths should we search for life?", *International Journal of Astrobiology*, 2010, 9, pp. 273 – 291

44. Preto, N., Kustatscher, E. and Wignall, P. B., "Triassic climates – State of the art and perspectives", *Paleogeography, Paleoclimatology, Paleoecology*,2010, 290, pp. 1 – 10

45. Hoffman, P. F., Kaufman, A. J., Halverson, G. P. and Schrag, D. P., "A Neoproterozoic Snowball Earth", *Science*, 1998, 281, pp. 1342 – 1346

46. Pierrehumbert, R. T., Abbot, D. S., Voigt, A. and Koll, D., "Climate of the Neoproterozoic", *Annual Review of Earth and Planetary Sciences*, 2011, 39, pp. 417 – 460

47 Augustin, L., Barbante, C., Barnes, P. R. F., Marc Barnola, J., Bigler, M., Castellano, E., Cattani, O., Chappellaz, J., Dahl-Jensen, D., Delmonte, B., Dreyfus, G., Durand, G., Falourd, S., Fischer, H., Flückiger, J., Hansson, M. E., Huybrechts, P., Jugie, G., Johnsen, S. J., Jouzel, J., Kaufmann, P., Kipfstuhl, J., Lambert, F., Lipenkov, V. Y., Littot, G. C., Longinelli, A., Lorrain, R., Maggi, V., Masson-Delmotte, V., Miller, H., Mulvaney, R., Oerlemans, J., Oerter, H., Orombelli, G., Parrenin, F., Peel, D. A., Petit, J.-R., Raynaud, D., Ritz, C., Ruth, U., Schwander, J., Siegenthaler, U., Souchez, R., Stauffer, B., Peder Steffensen, J., Stenni, B., Stocker, T. F., Tabacco, I. E., Udisti, R., van de Wal, R. S. W., van den Broeke, M., Weiss, J., Wilhelms, F., Winther, J.-G., Wolff, E. W. and Zucchelli, M., "Eight glacial cycles from an Antarctic ice core", *Nature,* 2004, 429, pp. 623 - 628

48. Hays, J. D., Imbrie, J. and Shackleton, N. J., "Variations in the Earth's Orbit: Pacemaker of the Ice Ages", *Science*, 1976, 194, pp. 1121-1132

49. Roe, G., "In defense of Milankovitch", *Geophysical Review Letters*, 2006, 33, L24703

50. Strom, R. G., Sprague, A. L., "Exploring Mercury: the iron planet", eds. Strom, R. G., Sprague, A. L., Springer-Praxis Books in Astronomy and Space Sciences, London (UK): Springer, Chichester (UK): Praxis Publishing. ISBN 1-85233-731-1, 2003

51. Correia, A. C. M., Laskar, J., , "Mercury's capture into the 3/2 spin–orbit resonance including the effect of core–mantle friction", *Icarus*, 2009, 201, pp. 1 – 11

52. Waltham, D., "Testing Anthropic Selection: A Climate Change Example", *Astrobiology*, 2011, 11, pp. 105 - 111

53. Horner, J., Waltham, D. and Koch, F. E., "The role of Jupiter in driving Earth's orbital evolution", *Proceedings of the 13th annual Australian Space Science Conference*, ISBN 13: 978-0-9775740-7-0, eds. Wayne Short and Iver Cairns, 2014, pp. 117 – 128

54. Horner, J., Gilmore, J. B. and Waltham, D., "The role of Jupiter in driving Earth's orbital evolution: An update", *Proceedings of the 14th annual Australian Space Research Conference*, ISBN 13: 978-0-9775740-8-7, eds. Wayne Short and Iver Cairns, 2015, pp. 25 – 38

55. Chambers, J. E., "A hybrid symplectic integrator that permits close encounters between massive bodies", *Monthly Notices of the Royal Astronomical Society*, 1999, 304, pp. 793 – 799

56. Horner, J. and Jones, B. W., "Jupiter – friend or foe? II: the Centaurs", *International Journal of Astrobiology*, 2009, 8, pp. 75 - 80

57. Horner, J. and Lykawka, P. S., "2001 QR_{322}: a dynamically unstable Neptune Trojan?", *Monthly Notices of the Royal Astronomical Society*, 405, pp. 49 - 56

58. Wittenmyer, R. A., Horner, J., Marshall, J. P., "On the dynamical stability of the proposed planetary system orbiting NSVS 14256825", *Monthly Notices of the Royal Astronomical Society*", 2013, 431, pp. 2150 – 2154

59. Clemence, G. M., "The Relativity Effect in Planetary Motions", *Reviews of Modern Physics*, 1947, 19, pp. 361 - 364

60. Nobili, A. M. and Will, C. M., "The real value of Mercury's perihelion advance", *Nature*, 1986, 320, pp. 39 – 41

61. Gilmore, J. B. and Ross, A., "Effective field theory calculation of second post-Newtonian binary dynamics", *Physical Review D*, 2008, 78, 124021

62. Folkner, W. M., Williams, J. G., Boggs, D. H., Park, R. S. and Kuchynka, P., "The Planetary and Lunar Ephemerides DE430 and DE431", *The Interplanetary Network Progress Report,* 2014, 42, pp. 1 - 81

63. Horner, J., Marshall, J. P., Wittenmyer, R. A. and Tinney, C. G., "A dynamical analysis of the proposed HU Aquarii planetary system", *Monthly Notices of the Royal Astronomical Society*, 2011, 416, pp. 11 – 15

64. Horner, J., Hinse, T. C., Wittenmyer, R. A., Marshall, J. P. and Tinney, C. G., "A dynamical analysis of the proposed circumbinary HW Virginis planetary system", *Monthly Notices of the Royal Astronomical Society*, 2012, 427, pp. 2812 – 2823

65. Horner, J., Wittenmyer, R. A., Hinse, T. C., Marshall, J. P., Mustill, A. J. and Tinney, C. G., "A detailed dynamical investigation of the proposed QS Virginis planetary system", *Monthly Notices of the Royal Astronomical Society*, 2013, 435, pp. 2033 – 2039

66. Horner, J., Lykawka, P. S., Bannister, M. T. and Francis, P., "2008 LC_{18}: a potentially unstable Neptune Trojan", *Monthly Notices of the Royal Astronomical Society*, 2012, 422, pp. 2145 – 2151

67. Horner, J., Wittenmyer, R. A., Hinse, T. C. and Tinney, C. G., "A detailed investigation of the proposed NN Serpentis planetary system", *Monthly Notices of the Royal Astronomical Society*, 2012, 425, pp. 749 – 756

68. Gilmore, J. B., "How reliable are latitudinal energy balance models for habitability calculations when using Earth's radiative properties?", *Monthly Notices of the Royal Astronomical Society*, 2014, 440, pp. 1435 – 1445

69. Gladman, B., "Dynamics of systems of two close planets", *Icarus*, 1993, 106, p. 247

70. Levison, H. F., Shoemaker, E. M. and Shoemaker, C. S., "Dynamical evolution of Jupiter's Trojan asteroids", *Nature*, 1997, 385, pp. 42 - 44

71. Horner, J., Müller, T. G and Lykawka, P. S., "(1173) Anchises – thermophysical and dynamical studies of a dynamically unstable Jovian Trojan", *Monthly Notices of the Royal Astronomical Society*, 2012, 423, pp. 2587 – 2596

72. Sheppard, S. S. and Trujillo, C. A., "A Thick Cloud of Neptune Trojans and Their Colors", *Science*, 2006, 313, pp. 511 - 514

73. Lykawka, P. S., Horner, J., Jones, B. W. and Mukai, T., "Origin and dynamical evolution of Neptune Trojans – II. Long-term evolution", *Monthly Notices of the Royal Astronomical Society*, 2011, 412, pp. 537 – 550

74. Dvorak, R., Pilat-Lohinger, E., Schwarz, R. and Freistetter, F., "Extrasolar Trojan planets close to habitable zones", *Astronomy & Astrophysics*, 2004, 426, pp. 37 -

75. Schwarz, R., Süli, Á, Dvorak, R. and Pilat-Lohinger, E., "Stability of Trojan planets in multi-planetary systems. Stability of Trojan planets in different dynamical systems", *Celestial Mechanics and Dynamical Astronomy*, 2009, 104, pp. 69 - 84

76. Tinney, C. G., Wittenmyer, R. A., Butler, R. P., Jones, H. R. A., O'Toole, S. J., Bailey, J. A., Carter, B. D. and Horner, J., "The Anglo-Australian Planet Search. XXI. A Gas-giant Planet in a One Year Orbit and the Habitability of Gas-giant Satellites", *The Astrophysical Journal*, 2011, 732, id. 31

77. Laughlin, G. and Chambers, J. E., "Extrasolar Trojans: The Viability and Detectability of Planets in the 1:1 Resonance", *The Astronomical Journal*, 2002, 124, pp. 592 - 600

78. Moons, M. and Morbidelli, A., "Secular Resonances in Mean Motion Commensurabilities: The 4/1, 3/1, 5/2 and 7/3 Cases", *Icarus*, 1995, 114, pp. 33 – 50

79. Ward, P. and Brownlee, D., "Rare earth: why complex life is uncommon in the universe", 2000, Peter Ward, Donald Brownlee, New York : Copernicus

80. Laakso, T., Rantala, J. and Kaasalainen, M., "Gravitational scattering by giant planets", *Astronomy and Astrophysics*, 2006, 456, 1, pp. 373 - 378

81. Horner, J. and Jones, B. W., "Jupiter friend or foe? I: The asteroids", *International Journal of Astrobiology*, 2008, 7, pp. 251 – 261

82. Horner, J., Jones, B. W. and Chambers, J., "Jupiter – friend or foe? III: the Oort cloud comets", *International Journal of Astrobiology*, 2010, 9, pp. 1 - 10

83. Horner, J. and Jones, B. W., "Jupiter – friend or foe? IV: the influence of orbital eccentricity and inclination", *International Journal of Astrobiology*, 2012, 11, 3, pp. 147 – 156

84. Grazier, K. R., "Jupiter: Cosmic Jekyll and Hyde", *Astrobiology*, 2016, 16, 1, pp. 23 - 28

85. Goddéris, Y., Donnadieu, Y., Lefebvre, V., Le Hir, G. and Nardin, E., "Tectonic control of continental weathering, atmospheric CO_2, and climate over Phanerozoic times", *Comptes rendus – Géoscience*, 2012, 344, 11-12, pp. 652 – 662

86. Berner, R. A., "Paleozoic Atmospheric CO_2: Importance of Solar Radiation and Plant Evolution", *Science*, 1993, 261, 4117, pp. 68 – 70

87. Kiehl, J. T. and Shields, C. A., "Climate simulation of the latest Permian: Implications for mass extinction", *Geology*, 2005, 33, 9, 757

88. Alvarez, L. W., Alvarez, W., Asaro, F. and Michel, H. V., "Extraterrestrial Cause for the Cretaceous-Tertiary Extinction", *Science,* 1980, 208, 4448, pp. 1095 - 1108

89. Schulte, P., Alegret, L., Arenillas, I., Arz, J. A., Barton, P. J., Bown, P. R., Bralower, T. J., Christeson, G. L., Claeys, P., Cockell, C. S., Collins, G. S., Deutsch, A., Goldin, T. J., Goto, K., Grajales-Nishimura, J. M., Grieve, R. A. F., Gulick, S. P. S., Johnson, K. R., Kiessling, W., Koeberl, C., Kring, D. A., MacLeod, K. G., Matsui, T., Melosh, J., Montanari, A., Morgan, J. V., Neal, C. R., Nichols, D. J., Norris, R. D., Pierazzo, E., Ravizza, G., Rebolledo-Vieyra, M., Reimold, W. U., Robin, E., Salge, T., Speijer, R. P., Sweet, A. R., Urrutia-Fucugauchi, J., Vajda, V., Whalen, M. T. and Willumsen, P. S., "The Chicxulub Asteroid Impact and Mass Extinction at the Cretaceous-Paleogene Boundary", *Science*, 2010, 327, 5970, pp. 1214 –

90. Waltham, D., "On the absence of solar evolution-driven warming through the Phanerozoic", *Terra Nova*, 2014, 26, pp. 282 – 286

91. Atreya, S. K., Wong, A. –H., Renno, N. O., Farrell, W. M., Delory, G. T., Sentman, D. D., Cummer, S. A., Marshall, J. R., Rafkin, S. C. R. and Catling, D. C., "Oxidant Enhancement in Martian Dust Devils and Storms: Implications for Life and Habitability", *Astrobiology*, 2006, 6, 3, pp. 439 - 450

2001 QR_{322} – an update on Neptune's first unstable Trojan companion

Jonti Horner[1,2], Patryk Sofia Lykawka[3]

[1] *Computational Engineering and Science Research Centre, University of Southern Queensland, Toowoomba, Queensland 4350, Australia*
[2] *Australian Centre for Astrobiology, UNSW Australia, Sydney, New South Wales 2052, Australia*
[3] *Astronomy Group, School of Interdisciplinary Social and Human Sciences, Kinki University Shinkamikosaka 228-3, Higashiosaka-shi, Osaka, 577-0813, Japan*

Summary: The Neptune Trojans are the most recent addition to the panoply of Solar system small body populations. The orbit of the first discovered member, 2001 QR_{322}, was investigated shortly after its discovery, based on early observations of the object, and it was found to be dynamically stable on timescales comparable to the age of the Solar system.

As further observations were obtained of the object over the following years, the best-fit solution for its orbit changed. We therefore carried out a new study of 2001 QR_{322}'s orbit in 2010, finding that it lay on the boundary between dynamically stable and unstable regions in Neptune's Trojan cloud, and concluding that further observations were needed to determine the true stability of the object's orbit.

Here we follow up on that earlier work, and present the preliminary results of a dynamical study using an updated fit to 2001 QR_{322}'s orbit. Despite the improved precision with which the orbit of 2001 QR_{322} is known, we find that the best-fit solution remains balanced on a knife-edge, lying between the same regions of stability and instability noted in our earlier work. In the future, we intend to carry out new observations that should hopefully refine the orbit to an extent that its true nature can finally be disentangled.

Keywords: Neptune Trojans, Solar system formation, Solar system evolution, Centaurs, Comets, 2001 QR322, Dynamical Methods

Introduction

In 2001, astronomers carrying out the Deep Ecliptic Survey ([36][37]) announced the discovery of five new trans-Neptunian objects, including one given the designation 2001 QR_{322}. In the discovery circular [1], the proposed orbit for that object would have made it a Plutino (e.g. [2][3]), trapped in Neptune's 2:3 mean-motion resonance. Indeed, the circular states: "*The assumed perihelic Neptune 2:3-resonance orbit for 2001 QR322 keeps the object more than 16 AU from Neptune over a 14 000-year period*".

As a Plutino, 2001 QR_{322} would not have been particularly remarkable – well over a hundred have been found to date. However, it was soon realised that 2001 QR_{322} was significantly more interesting. Follow-up observations in November and December 2002 led to major revisions in the best solution for the objects orbit, and in January 2003, it was announced that 2001 QR_{322} was, in fact, a Neptune Trojan – the first to be discovered [4]. In that circular, it was noted that, "*[a]ccording to the above orbit, the 1:1 Neptune librator remains more than*

20 AU from Neptune over a 14 000-year period. E. Chiang has confirmed the object's status as the first known "Neptune Trojan" by integrating the orbit over 10^9 years".

Following up on the discovery, two independent studies examined the orbital stability of the newly detected Neptunian Trojan. [5] employed a Frequency Map Analysis to produce maps of the diffusion rate of hypothetical Uranian and Neptunian Trojans. They noted that 2001 QR_{322} lay close to the border of a stable region for low inclination Neptune Trojans, but found its orbit to be highly stable. They performed numerical integrations of a population of test particles based on the best-fit orbit of 2001 QR_{322}, and found that only 10% escaped from the Trojan cloud over the lifetime of the Solar system, inferring that the object must be primordial, rather than a recent capture.

This result was strongly supported by the work of [6], who found that whilst the orbital evolution of 2001 QR_{322} within the Neptunian Trojan cloud was chaotic, perturbed by the ν_{18} secular resonance, this was insufficient to cause the object to escape from the Trojan cloud. In their simulations, the authors found that "*[t]he probability of escape to a non-Trojan orbit in our simulations was low, and only occurred for orbits starting near the low-probability edge of the orbital element distribution (largest values of initial semimajor axis and small eccentricity)*". The stable nature of 2001 QR_{322}, it seemed, was confirmed, and was thereafter assumed by studies considering the formation and evolution of the Neptunian Trojan population (e.g. [7][8]).

In 2009, we began a project to examine whether it was possible to use the distribution of the Neptune Trojan population to constrain the nature of the giant planet's outward migration. It was clear from the orbits of the Plutinos that Neptune must have migrated over a considerable distance (e.g. [9][10]), but the newly discovered Neptune Trojans offered the opportunity to test the models of planetary migration to see which, if any, could reproduce the observed distribution, and predict the range of orbits over which future Trojans would be found (e.g. [11][12][13][14]).

In the course of that work, we noticed that the best-fit orbital solution for 2001 QR_{322} had changed significantly over the years since the work of [5] and [6], as a result of new observations. With a longer observational arc available, the orbit of 2001 QR_{322} had become better constrained, with orbital elements that had shifted significantly from the original studies. We decided to see whether the new orbit remained dynamically stable.

To do this, we carried out detailed *n*-body dynamical simulations of the new orbit ([15]), and found that the new solution was balanced precariously between regions of dynamical stability and instability. In our simulations, test particles located at a semi-major axis greater than 30.30 au were found to be significantly less stable than those at smaller semi-major axes. The nominal best-fit solution for the semi-major axis of 2001 QR_{322} at the time of that work lay at 30.3023 au, right at the very inner edge of the unstable region.

In our simulations, half of the test particles considered were removed from the Solar system within just 590 Myr – a period far shorter than the system's age, but not so short that it did not remain feasible that 2001 QR_{322} had formed in the Neptune Trojan cloud, or had been captured during that planet's migration, in the Solar system's youth. Given the sharp delineation between regions with greatly differing stability, our results highlighted the critical importance of further follow-up observations of 2001 QR_{322}, to better constrain the objects orbit and to help resolve on which side of the dynamical divide it actually lies.

In this work we present the preliminary results of a fresh study of 2001 QR_{322}'s dynamical stability, based on an updated orbital solution published on the Asteroids Dynamics Site (AstDyS; [16]) website in January 2014. In the next section we describe the set-up of our new simulations, before presenting our preliminary results. We then conclude with a discussion of those results, and of the future work we plan to undertake.

The Simulations

In order to study the stability of the orbit of 2001 QR_{322}, we took the best-fit orbital solution from the Asteroids Dynamic Site, AstDyS ([16]) on 24th January 2014. The full solution, with uncertainties, is given in Table 1. For comparison, we also present the orbital elements used in our previous work, given in red italicised text, as obtained on 26th January 2009 from the same website. Whilst the uncertainty on the semi-major axis, a, has increased slightly, the uncertainties of the other elements have dropped by a factor of ~2. We note, also, that the value of some elements has changed by significantly more than their original uncertainties[1]. Taken in concert, this highlights the critical importance of follow-up observations for Solar system objects – by extending the observational arc over which an object has been followed, its orbit can be greatly refined.

Element	Value	1-σ uncertainty[2]
***a* (au)**	30.2848	0.009292
	30.3023	*0.008813*
e	0.027298	0.0001605
	0.031121	*0.0003059*
***i* (°)**	1.322	0.0005654
	1.323	*0.0009417*
Ω (°)	151.599	0.01484
	151.628	*0.02328*
ω (°)	163.415	0.4789
	160.73	*0.8316*
***M* (°)**	66.336	0.4753
	57.883	*0.7818*
Epoch (JD)	2456600	
	2454800	

Table 1: The best-fit orbital elements, and their associated 1-σ uncertainties, for 2001 QR_{322}. The values given in black are those used in the current work, and were obtained from [16] on 24th January 2014. The values given in red italics are those used in our previous work ([15]), obtained from [16] on 26th January 2009, and are included here to show how the best-fit solution has changed as a result of new observations being made. Here, a is the semi-major axis, e the eccentricity, i the inclination, Ω the longitude of the ascending node, ω the

[1] The value of the semi-major axis, for example, has changed by 0.0175 au, a shift of twice the stated uncertainty in the 2009 values. The changes in M and ω are even more striking – with their values shifting my many times the stated 2009 uncertainties.

[2] We note, here, that the values presented in this table, and used in our work, are the precise values as taken from the AstDyS system. It is readily apparent that the uncertainties in a given value (column 3) stretch to significantly more significant figures than given for the 'best fit' value (column 2). Whilst this is not ideal, we felt it best to exactly reproduce the data as taken from the AstDyS website, to ensure reproducibility of our results.

longitude of perihelion and M the mean anomaly of 2001 QR_{322} at the epoch given in the final row.

To study the long-term stability of the orbit of 2001 QR_{322}, we used the Hybrid integrator within the *n*-body dynamics package MERCURY ([17]) to follow the orbital evolution of an ensemble of massless test particles under the gravitational influence of the four giant planets for a period of four billion years. This technique (following the long term evolution of many objects using MERCURY) has proved highly successful in determining the dynamical stability of objects in our own Solar system (e.g. [15][18][19]). It has also been used to probe questions in astrobiology (e.g. [20][21][22][23]) and exoplanetary science (e.g. [24][25][26]). It allows the chaotic orbital evolution of the objects in question to be quantified in a probabilistic sense, as well as enabling the creation of stability maps that allow the behaviour as a function of initial orbital elements to be examined.

As in our earlier work, we created an ensemble of clones of 2001 QR_{322} for our integrations, centred on the nominal best-fit orbit. The clones were spread across the full ±3σ uncertainty range for each of the six orbital elements considered. In our earlier studies of both Solar system objects (e.g. [27][28]) and exoplanetary systems (e.g. [25][26]), we have found that the orbital semi-major axis and eccentricity of objects typically play by far the most important role in determining their long-term stability – a fact that was clearly demonstrated in our earlier studies of 2001 QR_{322} ([15]). For that reason we constructed our ensemble to maximise our resolution in these orbital elements. We tested a total of 51 unique values of semi-major axis, distributed evenly across the full ±3σ uncertainty range. At each of these semi-major axes, we tested 51 unique eccentricities, again evenly spread across the full ±3σ uncertainty range in that element. At each of these locations in *a-e* space, we tested five discrete values of inclination, and three unique values of the longitudes of perihelion and ascending node, and three mean anomalies, each spread evenly over the full ±3σ uncertainty range[3]. In total, this produced a test sample of 351,135 test particles (51 x 51 x 5 x 3 x 3 x 3).

The orbits of these test particles were then integrated forward in time under the gravitational influence of the four giant planets, Jupiter, Saturn, Uranus and Neptune, with an integration time-step of 120 days. Objects were removed from the simulations when they collided with one of the giant planets, fell into the central body, or were ejected to a barycentric distance of 1000 au, as in our previous studies of the Neptunian and Jovian Trojans ([15][18][27][28]). When objects were removed in this manner, the time at which the ejection or collision occurred was recorded.

Preliminary Results

Of the 351,135 clones of 2001 QR_{322} integrated in this work, 99,949 survived for the full four billion years of the integrations (a 28.46% survival rate). During the first few million years of the simulations, no ejections or collisions occurred – with the first test particle to be removed coming after 3.66 million years. After this slow start, the decay began to proceed apace, with fully half the test particles being removed in the first 600 million years. By recording the time at which each test particle was removed, we are able to create a dynamical map that illustrates how the stability of 2001 QR_{322} depends on its initial orbit, as can be seen in Figure 1, below.

[3] We therefore tested the best-fit inclination value along with four others, located -3σ, -1.5σ, +1.5σ and +3σ from that value. For longitude of perihelion, ascending node, and mean anomaly, we therefore tested the best-fit values along with those +3σ and -3σ away.

Equally, one can plot the decay of the number of test particles as a function of time, as can be seen in Figure 2.

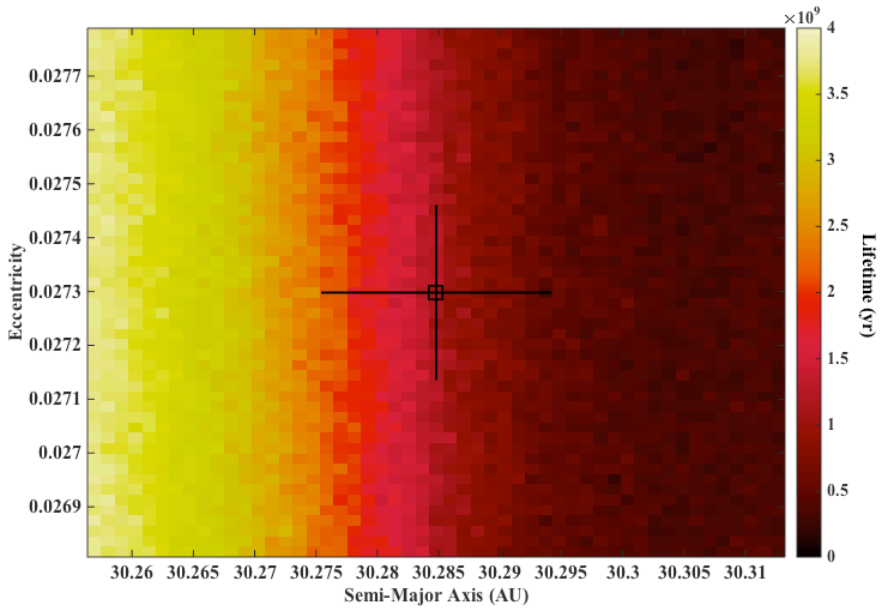

Figure 1: The mean dynamical lifetime of the orbit of 2001 QR_{322} as a function of its initial semi-major axis and eccentricity. The nominal best-fit orbit lies at the centre of the plot, within the small hollow box, and the horizontal and vertical lines that radiate from it represent the 1-σ uncertainties in semi-major axis and eccentricity. The lifetime plotted at each a-e location is the mean of 135 discrete simulations. It is clear that the best-fit orbital solution for 2001 QR_{322} falls right on the boundary between a region of high stability and one that is far more chaotic.

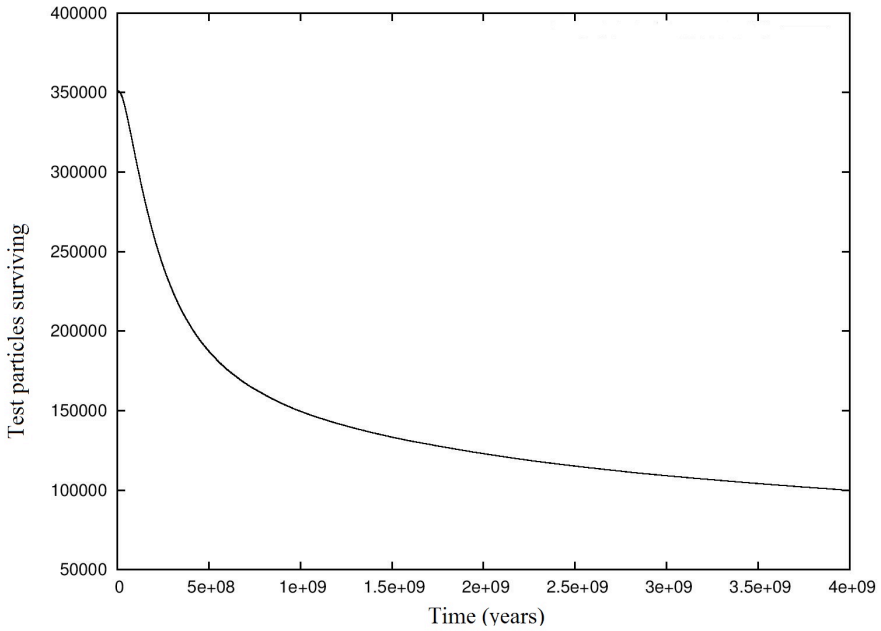

Figure 2: The number of test particles surviving as a function of the time elapsed in our simulations. After a short period of dynamical relaxation (the first particle removed survived for 3.66 Myr), the population decays in a broadly exponential manner, although the 'half-life'

of that exponential decay increases as time passes, as the objects from the least stable reaches of a-e space are removed.

Discussion and Conclusions

In our previous study of the stability of 2001 QR_{322} ([15]), we examined the evolution of an ensemble of 19,683 test particles, cloned in a six-dimensional swarm centred on the nominal best-fit orbit available at the time. That work revealed an object balanced on a dynamical precipice – right on the boundary between stable and unstable regions.

With a more refined orbit, based on a longer observational arc, we anticipated that new simulations could answer the question of 2001 QR_{322}'s stability. On one hand, the best-fit solution might have moved to a more stable region of orbital element space, and we could therefore conclude that 2001 QR_{322} was most likely captured as a Neptune Trojan in the final stages of planetary migration (e.g. [12]), or had formed with the planet and been carried along with it as the planet migrated to its current resting place (e.g. [11]). On the other, it was equally possible that the improved orbit for 2001 QR_{322} could place it firmly in an unstable region – suggesting that it might only recently have been captured as a Neptunian Trojan (as is thought to be the case for 2004 KV_{18}; [28]).

In this work we expand upon our previous study of 2001 QR_{322}, taking advantage of the greatly increased computational capacity available to us. We simulated a population of test particles more than an order of magnitude larger than in our previous work, and followed their evolution for a factor of four times longer (4 Gyr vs. 1 Gyr). This has allowed us to increase the resolution with which we can map the dynamical stability of 2001 QR_{322}'s orbit, as well as allowing us to probe cases where the instability occurs on timescales longer than those considered in our earlier work.

Whilst our detailed analysis of the results is still ongoing, it is immediately apparent from examination of Figure 1 that the stability of 2001 QR_{322} remains strongly dependent on the initial semi-major axis of its orbit. Despite the longer observational arc and generally smaller uncertainties in the best-fit orbit, that solution remains precariously balanced between regions of significant dynamical stability and instability. As in our earlier work, fully half of the test particles considered were removed from the Solar system within the first 600 Myr of our simulations. Indeed, despite the changes to the orbital solution, our results are remarkably similar to those we obtained in 2010.

Our simulations reveal that all *a-e* locations within the 1-σ uncertainties are unstable on timescales less than ~2 Gyr, which in turn suggests that the object is truly dynamically unstable. That said, it should be noted that instability on timescales of hundreds of millions of years, or several billion years, is not incompatible with the idea that 2001 QR_{322} has been trapped in the Neptunian Trojan cloud since the cessation of planetary migration (as discussed in [15]).

To illustrate this point, let us assume, for the sake of argument, that the initial population of the Neptunian Trojan cloud was large[4], and then assume that a non-negligible subset of that population moved on orbits similar to that of 2001 QR_{322}. In such a scenario, it is readily apparent that a significant population of such objects could survive to the current day. For a

[4] This seems a reasonable assumption, given that estimates of the *current* Neptunian Trojan population have ranged as high as 10^7 objects more than 1 km in diameter (e.g. [29]).

population decaying with a dynamical 'half-life' of 600 Myr, ~1% would be expected to survive for four billion years. Furthermore, as we argued in [30], such a scenario would allow the Neptunian Trojans to act as a continual source of fresh material to the Centaur population, and from there, to the inner Solar system[5].

Given that objects escaped from the Neptunian Trojan cloud at all locations plotted in Figure 1, it is clear that even the most stable orbital solutions for 2001 QR_{322} do not preclude its eventual escape to the Centaur population. We still require the orbit of 2001 QR_{322} to be further constrained before we can conclusively determine its true stability.

To that end we plan to obtain follow-up observations of 2001 QR_{322} in 2016, with the goal of further refining the best-fit solution to its orbit, and hopefully answering the question of its true dynamical stability, once and for all.

Acknowledgements

JH is supported by USQ's Strategic Research Fund: the STARWINDS project. The authors thank Richard Schwarz and an anonymous reviewer for their comments and feedback on our work during the review process, which helped us to improve the clarity and flow of our paper.

References

1. Wasserman, L. H., Chiang, E., Jordan, A. B., Ryan, E. L., Buie, M. W., Millis, R. L., Kern, S. D., Elliot, J. L., Washburn, K. E. and Marsden, B. G., " MPEC 2001-V11 : 2001 QQ322, 2001 QR322, 2001 RU143, 2001 RV143, 2001 RW143", *Minor Planet Center Electronic Circular 2001-V11*, 2001, available at http://www.minorplanetcenter.net/iau/mpec/K01/K01V11.html

2. Yu, Q. and Tremaine, S., "The Dynamics of Plutinos", *The Astronomical Journal*, 1999, 118, pp. 1873 – 1881

3. Chiang, E. I. and Jordan, A. B., "On the Plutinos and Twotinos of the Kuiper Belt", *The Astronomical Journal*, 2002, 124, pp. 3430 – 3444

4. Pittichova, J. A., Meech, K. J., Wasserman, L. H., Trilling, D. E., Millis, R. L., Buie, M. W., Kern, S. D., Clancy, K. B., Hutchison, L. E., Chiang, E. and Marsden, B. G., "MPEC 2003-A55 : 2001 QR322", *Minor Planet Center Electronic Circular 2003-A55,* 2003, available at http://www.minorplanetcenter.net/iau/mpec/K03/K03A55.html

5. Marzari, F., Tricarico, P. and Scholl, H., "The MATROS project: Stability of Uranus and Neptune Trojans. The case of 2001 QR322", *Astronomy and Astrophysics*, 2003, 410, pp. 725 – 734

[5] The Centaurs are the direct parent population to the short-period comets (e.g. [31][32]), and are likely themselves sourced from a variety of regions, including the Scattered Disk (e.g. [33]), the Oort Cloud (e.g. [34][35]), and the Jovian and Neptunian Trojan clouds (e.g. [30]).

6. Brasser, R., Mikkola, S., Huang, T.-Y., Wiegert, P., and Inanen, K., "Long-term evolution of the Neptune Trojan 2001 QR322", *Monthly Notices of the Royal Astronomical Society*, 2004, 347, pp. 833 – 836

7. Chiang, E. I. and Lithwick, Y., "Neptune Trojans as a Test Bed for Planet Formation", *The Astrophysical Journal*, 2005, 628, pp. 520 – 532

8. Nesvorný, D. and Vokrouhlický, D., "Chaotic Capture of Neptune Trojans", *The Astronomical Journal*, 2009, 137, pp. 5003 – 5011

9. Malhotra, R., "The origin of Pluto's peculiar orbit", *Nature*, 1993, 365, pp. 819-821

10. Hahn, J. M. and Malhotra, R., "Orbital Evolution of Planets Embedded in a Planetesimal Disk", *The Astronomical Journal*, 1999, 117, pp. 3041 – 3053

11. Lykawka, P. S., Horner, J., Jones, B. W. and Mukai, T., "Origin and dynamical evolution of Neptune Trojans – I. Formation and planetary migration", *Monthly Notices of the Royal Astronomical Society*, 2009, 398, pp. 1715 – 1729

12. Lykawka, P. S. and Horner, J., "The capture of Trojan asteroids by the giant planets during planetary migration", *Monthly Notices of the Royal Astronomical Society*, 2010, 405, pp. 1375 – 1383

13. Lykawka, P. S., Horner, J., Jones, B. W. and Mukai, T., "Formation and dynamical evolution of the Neptune Trojans – the influence of the initial Solar system architecture", *Monthly Notices of the Royal Astronomical Society*, 2010, 404, pp. 1272 - 1280

14. Lykawka, P. S., Horner, J., Jones, B. W. and Mukai, T., "Origin and dynamical evolution of Neptune Trojans – II. Long-term evolution", *Monthly Notices of the Royal Astronomical Society*, 2011, 412, pp. 537 - 550

15. Horner, J. and Lykawka, P. S., "2001 QR322: a dynamically unstable Neptune Trojan?", *Monthly Notices of the Royal Astronomical Society*, 2010, 405, pp. 49 - 56

16. The AstDyS website, http://hamilton.dm.unipi.it/astdys/ ; described in Knezevic, Z. and Milani, A., "Asteroids Dynamic Site – AstDyS", *IAU Joint Discussion 7: Space-Time Reference Systems for Future Research at IAU General Assembly - Beijing*, 2012

17. Chambers, J. E., "A hybrid symplectic integrator that permits close encounters between massive bodies", *Monthly Notices of the Royal Astronomical Society*, 1999, 304, pp. 793- 799.

18. Horner, J., Müller, T. G. and Lykawka, P. S., " (1173) Anchises – thermophysical and dynamical studies of a dynamically unstable Jovian Trojan", *Monthly Notices of the Royal Astronomical Society*, 2012, 423, 2587 - 2596

19. Kiss, Cs., Szabó, Gy., Horner, J., Conn, B. C., Müller, T. G., Vilenius, E., Sárneczky, K., Kiss, L. L., Bannister, M., Bayliss, D., Pál, A., Góbi, S., Verebélyi, E., Lellouch, E., Santos-Sanz, P., Ortiz, J. L., Duffard, R. and Morales, N., "A portrait of the extreme solar system object 2012 DR_{30}", *Astronomy and Astrophysics*, 2013, 555, article id. A3

20. Horner, J. and Jones, B. W., "Jupiter friend or foe? I: The asteroids", *International Journal of Astrobiology*, 2008, 7, pp. 251 - 261

21. Horner, J. and Jones, B. W., "Jupiter - friend or foe? II: the Centaurs", *International Journal of Astrobiology*, 2009, 8, pp. 75 - 80

22. Horner, J., Jones, B. W. and Chambers, J., "Jupiter - friend or foe? III: the Oort cloud comets", *International Journal of Astrobiology*, 2010, 9, pp. 1 - 10

23. Horner, J. and Jones, B. W., "Jupiter - friend or foe? IV: The influence of orbital eccentricity and inclination", *International Journal of Astrobiology*, 2012, 11, pp. 147 - 156

24. Marshall, J., Horner, J. and Carter, A., "Dynamical simulations of the HR8799 planetary system", *International Journal of Astrobiology*, 2010, 9, pp. 259 - 264

25. Robertson, P., Horner, J., Wittenmyer, R. A., Endl, M., Cochran, W. D., MacQueen, P. J., Brugamyer, E. J., Simon, A. E., Barnes, S. I. and Caldwell, C., "A Second Giant Planet in 3:2 Mean-motion Resonance in the HD 204313 System", *The Astrophysical Journal*, 2012, 754, article id. 50

26. Wittenmyer, R. A., Horner, J. and Marshall, J. P., "On the dynamical stability of the proposed planetary system orbiting NSVS 14256825", *Monthly Notices of the Royal Astronomical Society*, 2013, 431, pp. 2150 - 2154

27. Horner, J., Lykawka, P. S., Bannister, M. T. and Francis, P., "2008 LC18: a potentially unstable Neptune Trojan", *Monthly Notices of the Royal Astronomical Society*, 2012, 422, pp. 2145 - 2151

28. Horner, J. and Lykawka, P. S., "2004 KV_{18}: a visitor from the scattered disc to the Neptune Trojan population", *Monthly Notices of the Royal Astronomical Society*, 2012, 426, pp. 159 - 166

29. Sheppard, S. S. and Trujillo, C. A., "A Thick Cloud of Neptune Trojans and Their Colours", *Science*, 2006, 5786, pp. 511 – 514

30. Horner, J. and Lykawka, P. S., "Planetary Trojans – the main short of the short period comets?", *International Journal of Astrobiology*, 2010, 9, pp. 227 – 234

31. Levison, H. F. and Duncan, M. J., "From the Kuiper Belt to Jupiter-Family Comets: The Spatial Distribution of Ecliptic Comets", *Icarus*, 1997, 127, pp. 13 - 32

32. Horner, J., Evans, N. W. and Bailey, M. E., "Simulations of the population of Centaurs – I. The Bulk statistics", *Monthly Notices of the Royal Astronomical Society*, 2004, 354, pp. 798 – 810

33. Volk, K. and Malhotra, R., "The Scattered Disk as the Source of the Jupiter Family Comets", *The Astrophysical Journal*, 2008, 687, pp. 714 – 725

34. Brasser, R., Schwamb, M. E., Lykawka, P. S. and Gomes, R. S., "An Oort cloud origin for the high-inclination, high-perihelion Centaurs", *Monthly Notices of the Royal Astronomical Society*, 2012, 420, pp. 3396 - 3402

35. Emel'yanenko, V. V., Asher, D. J. and Bailey, M. E., "A Model for the Common Origin of Jupiter Family and Halley Type Comets", *Earth, Moon and Planets,* 2013, 110, pp. 105-130

36. Millis, R. L., Buie, M. W., Wasserman, L. H., Elliot, J. L., Kern, S. D. and Wagner, R. M., "The Deep Ecliptic Survey: A Search for Kuiper Belt Objects and Centaurs. I. Description of Methods and Initial Results", *The Astronomical Journal*, 2002, 123, pp. 2083 – 2109

37. Elliot, J. L., Kern, S. D., Clancy, K. B., Gulbis, A. A. S., Millis, R. L., Buie, M. W., Wasserman, L. H., Chiang, E. I., Jordan, A. B., Trilling, D. E. and Meech, K . J., "The Deep Ecliptic Survey: A Search for Kuiper Belt Objects and Centaurs. II. Dynamical Classification, the Kuiper Belt Plane, and the Core Population", *The Astronomical Journal*, 2005, 129, pp. 1117 - 1162

Astrobiology with Mars'Obot: Identifying Microbial Life Forms Using Ground-based Remote Sensing.

S.W. Hobbs [1], J. D. A. Clarke [2] and K.A. Campbell [3]

[1] *School of Physical, Environmental and Mathematical Sciences, University of New South Wales Canberra, Australian Defence Force Academy, Northcott Drive, Canberra, Australian Capital Territory 2600, Australia.*

[2] *MarsSociety Australia, P.O. Box 327, Clifton Hill, VIC 3068, Australia*

[3] *School of Environment, The University of Auckland, Private Bag 92019, Auckland 1142, New Zealand*

Summary: Geothermal spring environments are colonised by microbial organisms tolerant of environments otherwise hostile to life. Such environments are analogous to some of the earliest environments for terrestrial life. Hot springs are known to have existed on Mars in the past and they too may once have been home to Martian microbes. Studying these environments present a number of challenges, including researcher safety and protection of ecologically fragile environments. Field robots can potentially assist in managing both challenges. We describe the performance of a teleoperated rover developed by Mars Society Australia to investigate extreme forms of life at two geothermal study sites in New Zealand using a non-contact thermometer and multispectral camera. We found that single and multiple filtered imagery utilising visible and near infrared (NIR) was useful in detecting photosynthetic microbes, and that multiple filtered images provided the best results for life detection. Our study provides insights into the incorporation of robotic methods for astrobiological research.

Keywords: Astrobiology, robotics, remote sensing, Mars analogue research, hot springs, New Zealand.

Introduction

Various types of teleoperated and autonomous robots have been used extensively in underwater scientific research, often in conjunction with direct human presence, e.g. divers and/or crewed submersibles [1]. Both teleoperated and semi-autonomous vehicles have been utilised for surface exploration of the Moon and Mars [2, 3, 4]. However, use of robotics for terrestrial surface science has been limited, other than to test concepts for planetary exploration [5]. Nonetheless, robotic technology has outstanding potential for collecting data from sites where hazards, fragility, or contamination are potential issues. Geothermal areas combine all these factors, exposing researchers to boiling water and noxious fumes and often having delicate structures with unique biotas.

In this paper we investigate the capabilities and limitations of a low-cost (<$1000) teleoperated vehicle in characterising extreme life forms within hot spring environments in the Rotorua area, Taupo Volcanic Zone, New Zealand. The vehicle was developed by Mars Society Australia (MSA) as part of the Marsobot project, and utilises commercial

off-the-shelf hardware and open source software [6]. Field work was carried out during the joint New Zealand Astrobiology Initiative (NZAI) and NASA Spaceward Bound New Zealand expedition (http://astrobiology.kiwi/) in January 2015.

Small robots such as these also may have potential for future Mars missions, in that they may complement larger robots being deployed by astronauts to investigate specific sites deemed too hazardous or fragile for direct exploration, or to use in follow-ups of initial site surveys. Previous examples of microrovers evaluated for Mars missions include the Rocky series developed in conjunction with the Sojourner Mars rover [7], and the FIDO vehicle designed to trial concepts employed in MER [8]. Additionally, the Mars Astrobiology Research and Technology Experiment (MARTE), a Mars analogue mission, as conducted in Spain simulated robotic drilling mission to search for subsurface life [9].

Extreme Life Forms

The search for life beyond Earth has been an ongoing quest for humanity since ancient times, although no definitive proof has yet been found [10]. Mars has traditionally been considered as a likely extraterrestrial abode for life, given its similarity to Earth, historically and physically, in relation to the other planets and moons of the Solar System, and because of its location within the outer boundaries of the "habitable zone" [11]. The first direct experiments designed to search for life on Mars were performed during the Viking missions of the mid-1970's [12]. Two robotic landers used four experiments that searched for signs of metabolic activity, as well as the presence of organic compounds. The subsequent results from these experiments showed no evidence for life nor its chemical by-products, and provided important data on the limitations of robotic searches for extraterrestrial life [13]. However, since the Viking missions, life has been found in far more diverse and extreme environments than thought possible in the 1970's, from cold dry deserts to hydrothermal vents in the deep sea, to geysers around hot springs on land [10, 14, 15]. The characterisation of life in these extreme environments has widened the possible settings and physico-chemical conditions under which life could flourish and expanded the criteria for biosignal detection, such as within thermal hot springs [16, 17].

Thermal Springs

Terrestrial hot springs of volcanic terrains are environments characterised by water heated by a geothermal (magmatic) heat source. They are of particular interest in that some hyperthermophilic microbes inhabiting them represent the most primitive forms of life [18, 19]. Siliceous hot spring deposits (sinter), and the nature of their associated microbial life interacting with local mineralogy, play an important role in astrobiological hypotheses related to the search and discovery for life on other planets and moons, as well as in expanding our understanding of early life on Earth [15, 16, 20, 21, 22, 23]. Additionally, evidence of past thermal springs sites also has been observed on Mars, specifically at Gusev Crater as discovered by the *Spirit* rover [24, 25]. Thus characterisation and analysis of active terrestrial hot springs settings will provide further insight into investigations of similar relict environments on other worlds, and allow enhancement of remote sensing and scientific investigation techniques for the detection of past and present life.

Previous research has revealed variations in mineralising biosignatures within many hot springs environments as a function of distance from the thermal vent [22, 23, 26, 27, 28, 29, 30]. This process of deposition of sinter and occurrence of microorganisms form zonal systems, which can act as indicators for temperature and pH conditions [19, 22, 23, 31, 32, 33, 34]. These zones also can be used to infer the location of specific mineralogy or biology, and were used to guide the Mars'Obot rover operations conducted at the Rotorua hot springs sites. We analysed these zones using the Mars O'bot rover, and compared our results with published findings [23]. This was carried out in order to determine the applicability of using a microrover to search for life in an analogous, active extremophile environment, and to identify shortcomings and avenues for future refinement of remote sensing methods in the field of astrobiology.

Study Sites

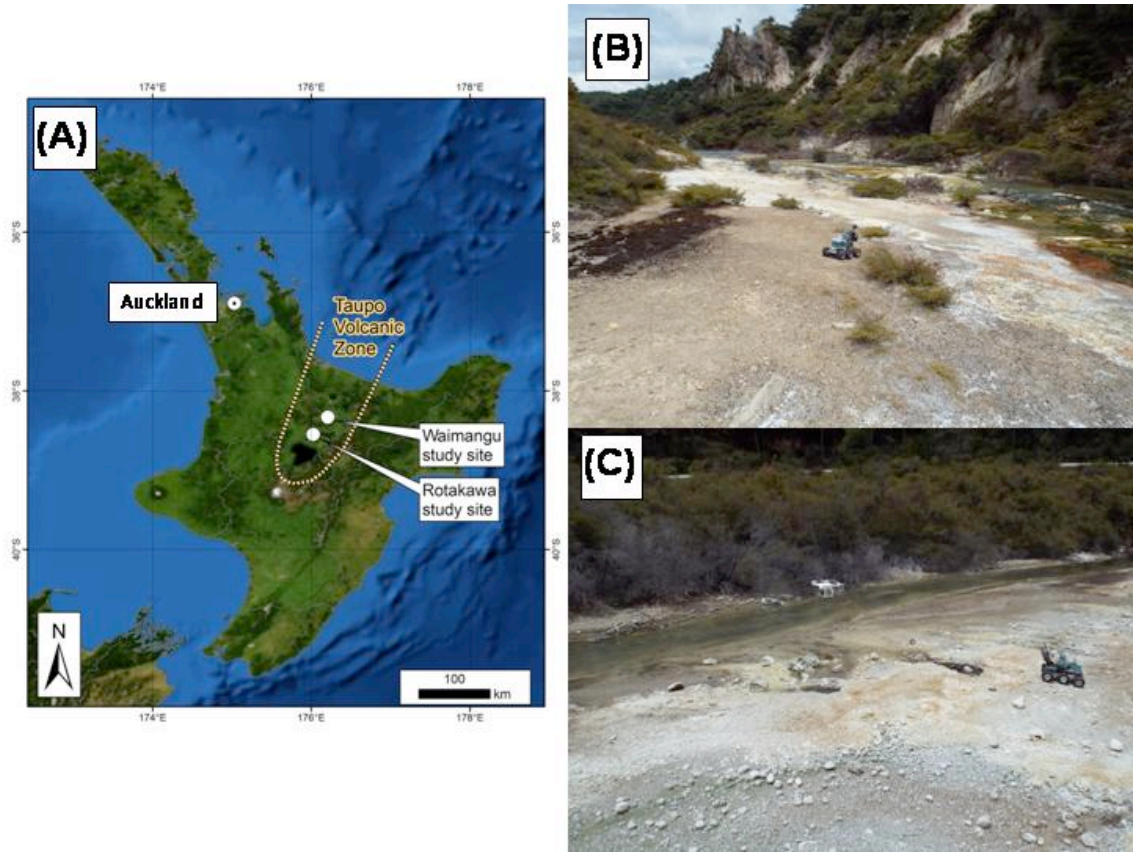

Fig. 1 (A) Overview of study locations in the Taupo Volcanic Zone, New Zealand. (B) Frying Pan Lake outflow stream location, Waimangu Geothermal Vally. (C) Pararíki Stream location, Rotokawa geothermal field.

MarsO'bot Junior underwent field trials at two hot spring sites in the Taupo Volcanic Zone, New Zealand, over the period 15-22 January, 2015 (Fig. 1A-C). Both field sites possess an abundance of microorganisms existing in a variety of temperature ranges.

The first field trial was conducted on the bank of the hot water creek and springs at the outlet of Frying Pan Lake, Waimangu Volcanic Valley (Fig. 1B) [35]. This

geothermal discharge area possesses water temperatures of approximately 50^{o} C with stream deposits forming sinters with trace elements of antimony, molybdenum, arsenic and tungsten [22]. The microbes in this stream were found [36] to be predominantly controlled by water acidity, as well as differing water temperature. The overflow stream from Frying Pan Lake supports multiple microbial life forms including cyanobacteria and algae as well as insect life [22].

The second site is located at the acid-sulphate-chloride springs debouching along the pumice-lined banks of Parariki Stream, Rotokawa Geothermal Field (Fig. 1C). These hot springs discharge acid-sulphate-chloride waters, generating acidic surface features [22, 37] and was the subject of a detailed sedimentary facies and biotic study [23]. Parariki Stream drains acidic Lake Rotorua into the Waikato River, with thermal springs appearing on the southern portion of the stream [23, 37, 38]. The Parariki Stream study area in the Rotokawa Geothermal Field covers approximately 130 m^2 and is located on the western floodplain, consisting of well sorted pumice alluvium. Water temperatures for the hot springs at this site were cited to be on the order of 40-91^{o} C, discharging clear acidic waters [23]. Four distinct types of stromatalitic sinter were identified, including ridge shaped, acid-etched sinter formations close to vents; 1 cm high spicular sinter rims growing on pumice clasts (>2 cm diameter) in somewhat cooler waters (30-85^{o} C); thin, parallel-laminated sinters forming under very shallow sheet flow areas; and thin, small cup-shaped sinter rims forming on small pumice clasts (<2 cm diameter) located on sandy material saturated with cooled thermal fluids [23]. All sites except for the sinters nearest the spring vents were generally found to be co-located with coccoidal green algal mats. These mats were found within a temperature range of 30–52.5^{o}C, being thickest at ~45^{o}C. The mats belong to the rhodophyte taxon Cyanidiophycease, thereby indicating that they are chlorophyll-based, using photosynthesis as part of its metabolic process [39].

Our aim was to use the instruments onboard our robot to remotely identify and characterise the occurrence of the extensively distributed green mats by exploiting the spectral response of photosynthetic biotic material in the visible and near infrared (NIR) wavelengths. Furthermore, we evaluated whether the microrover could identify the existence of sinter or other biota types at both sites.

Rover Design

Mars'Obot Junior, the rover used at the New Zealand hot springs, is designed around the Dagu Wild thumper six wheel drive chassis. This chassis features independent suspension for each wheel, as well as a 1:75 geared electric motor within each wheel hub. The vehicle is skid steered in a similar manner to the Soviet Marsokhod rover [40]. We chose skid steering owing to the ease at which it can be employed, and because it requires a minimum number of motors for its operation. We have based the control architecture of the rover on the Arduino 8 bit microcontroller. This controller is well supported and has been used in many robotics applications [41, 42]. The Arduino Uno consists of an Atmega 328 chip on a microcontroller development board. It is programmed using the open source Arduino environment that is based on C++. The Arduino Uno possesses 14 digital input/output pins and six analog input pins. We use these pins to operate the non-contact thermometer and operate the filter wheel of the multispectral camera.

In addition to the Arduino Uno we also have incorporated a second Arduino system into our design: The Wild Thumper controller. This controller is also based on the Atmega 368 and was designed specifically for the Dagu chassis we used for Mars'Obot [6]. The pre-installed controller software provides an interface between the 2.4GHZ remote control system and the rover. In addition the Wild Thumper controller provides battery monitoring and will automatically shut down current to the motors if battery voltage drops below a certain level.

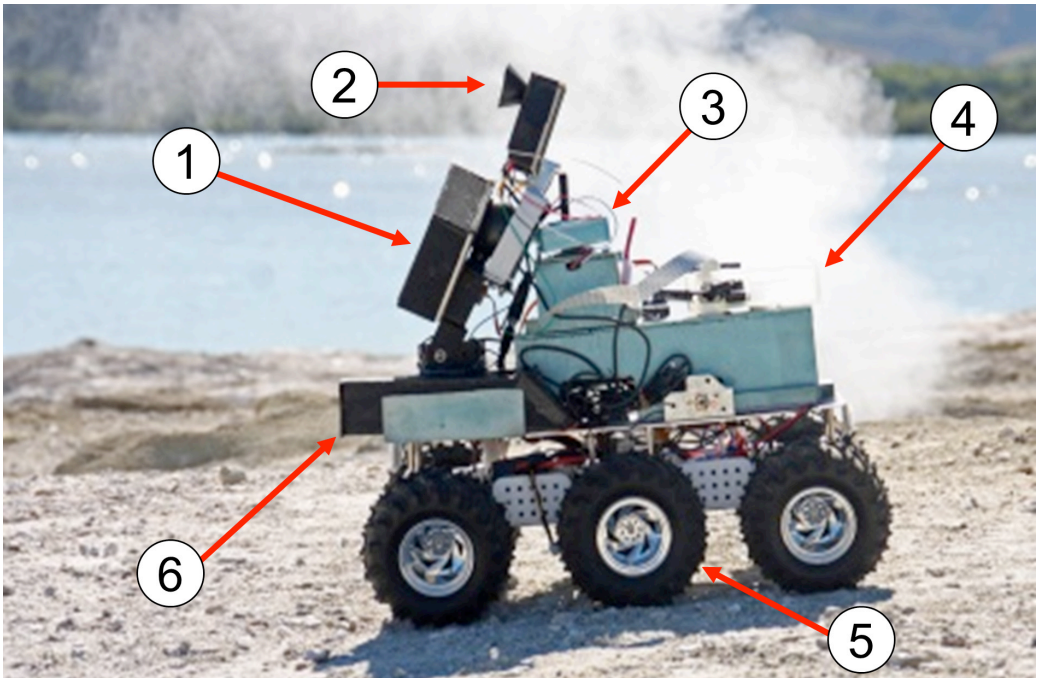

Fig 1. Overview of Junior rover with key components marked. (1) Multispectral imaging system. (2) Non-contact thermometer. (3) Serial modem. (4) Raspberry Pi and wifi link. (5) Electronics box and four wheel drive skid steer mobility. (6) Reflectance spectrometer.

Science Instruments

The instruments aboard Mars'Obot Junior were designed specifically to operate in the hot springs environment in New Zealand, to help characterise these environments and identify photosynthesising microbial life forms present. We aimed to detect the presence of chlorophyll-containing, photosynthesising microbial mats by photographing candidate sites through visible, red and NIR filters, and characterised their context through imaging, thermometry, and spectroscopy.

Multispectral camera

The primary instrument for this purpose is a Logitech Webcam modified to be NIR sensitive. A filter wheel containing an NIR cut filter allowing only visible wavelengths to pass, red (625 nm long bandpass for single-image photosynthesis detection) and 850 nm long bandpass NIR filter is fitted in front of the webcam to provide multispectral imaging in visible, red and NIR wavelengths. Similar filter arrangements have been used in

unmanned aerial vehicle (UAV) trials for monitoring vegetation such as crops and have proven useful for characterising vegetation type and health [26].

Table 1: Summary of scientific instruments carried on Junior

Instrument	Characteristics	Purpose
Multispectral camera	Logitech Webcam with visible, red and 850 nm NIR filter wheel.	Identify photosynthetic biota as well as provide visual record of environment.
Non-contact thermometer	Samples ambient plus sample temperature.	Sample temperature readings for hot spring vents
Visible light spectrometer	2592 x 1944 px Raspberry Pi camera with DVD diffraction grating and 1 mm slit.	Provide visible light spectra for photosynthetic biota.

We developed this camera in order to detect photosynthetic biota in the hot springs study sites. The multispectral methodology works by exploiting the high NIR reflectance of vegetation as compared to visible light wavelengths [27]. We thus were able to use the visible, and NIR images to create a false colour three band montage by adding the NIR channel and deleting the blue channel from the visible image. This process highlights the presence of vegetation and other NIR reflective elements within the scene which will display as a red colour in the resulting image. A similar process has been used to create false colour aerial and satellite imagery and serves to highlight photosynthetic biota within an area of interest [43; 44, 45].

We employed band mixing of the red and NIR channels in the false colour image developed as above to create Normalised Difference Vegetation Indices (NDVI). NDVI is a widely used method to quantify amount and vitality of vegetation in a scene by using the difference between the low reflectance of vegetation in red light wavelengths (~600 nm) and the higher reflectance in NIR wavelengths (850 nm) [46, 47]. The resulting index provides dimensionless values that allow inferences on the presence and health of photosynthetic biota in the study area [46, 48].

In addition to using two separate images to create an NDVI we tested the viability of using single-image processing in detecting photosynthetic biota in our study environment. We captured images through the 625 nm red filter and created NDVI from exploiting the blue and red channels of this image. This procedure relies on the theory that the blue channel of the camera contains more NIR than the red channel [45]. Previous application of this method has relied on a custom white balance setting to remove the red cast of the resultant image and to facilitate NDVI processing [45]. We achieved this post image capture by applying histogram equalisation across the red, green and blue bands to neutralise the red colour cast. We then compared the results of NDVI processing through the red filter with visible and NIR filters in order to determine the usefulness of single image capture through a single red filter versus multi image capture through visible and NIR filters. The success of this method would allow for single-image capture of a scene and significantly reduce the amount of time and bandwidth needed to sample a study site.

Spectrometer

Junior carried a visible light reflectance spectrometer based on a Raspberry Pi camera with a pixel resolution of 2592 x 1944, and a diffraction grating derived from a DVD. A version of this method of spectroscopy has been used in previous research, although predominantly for transmission [49]. Our instrument was intended to collect spectra from materials of interest in order to assist in identifying mineralogical or biological composition. Both the multispectral camera and spectrometer were controlled by a Raspberry Pi Model B on a 2.4 GHz wifi link.

Other instruments

Additional instruments carried on the rover included a 1.2 Ghz wireless camera for vehicle navigation and a Melexis non-contact thermometer. The thermometer output was read by the arduino and transmitted via serial link on command from the ground station. The thermometer was used to sample temperature readings around the hot springs in order to assist in assessing the type of environments inhabited by the extremophiles.

Rover control

In order to simplify the overall design and remain within budget we opted for a teleoperated mode of rover control. This mode has been used in previous space missions, such as the Lunakhod rovers sent to the Moon [40]. Teleoperation simulates the operation of the rover in conditions where live or near live communication is feasible, such as on the Moon or at a manned Mars base. Control of the Mars'Obot rover was achieved by a combination of a 2.4 Mhz four channel R/C system and an AP220 2.4 Ghz serial wireless modem. These were chosen for their simplicity, reliability and range, sufficient to control the rover within the specified operational radius of 30 m. The two channels of the R/C system control the forward/reverse motion of the rover and the steering.

Results

The surface of both hot spring sites consisted of loose material of sinter-derived and pumiceous pebbles ~ 1-3 cm in diameter overlying *in situ* sinter deposits (Fig. 2). Local slopes for both sites are less than 5^{o}, being predominantly creek bed. We found this terrain to be ideal for operating our skid steered rover and we encountered no mobility obstacles in operating in this terrain. The major geological and microbial components of both sites were imaged, spectra obtained and temperature readings collected. The rover traverse of the Waimangu Volcanic Valley site commenced approximately 6 m from the water edge and temperature readings ranged from 35^{o}C at the start of the traverse to 45^{o}C at the water's edge. Temperature readings of the water itself from the rover were ~20^{o} lower than those taken from a handheld unit, although readings of the stream bank correlated with those of a handheld device. The discrepancy was likely due to the inability of the rover servo to position the thermometer over the hottest source of the hot spring without risking damage to the rover. We have since designed an extension arm system for the non-contact thermometer to reach inaccessible sites.

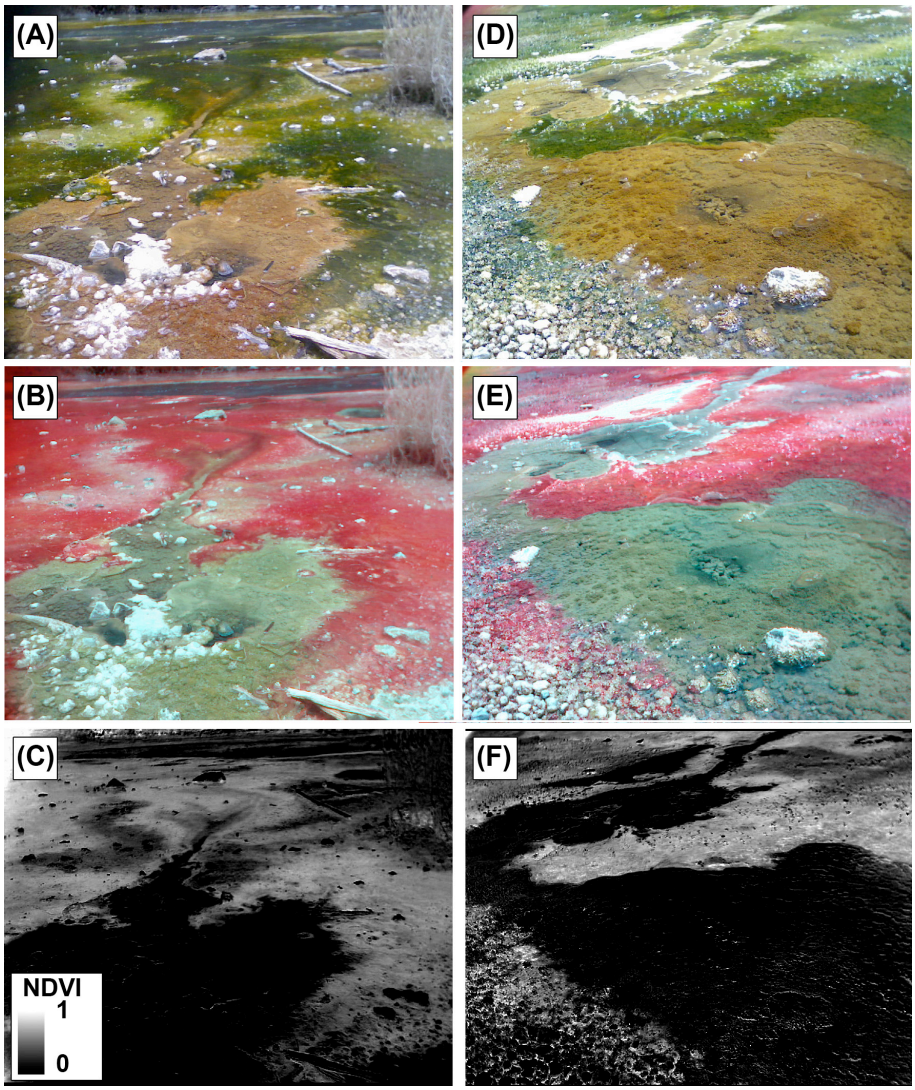

Fig 3. Visible, false colour and NDVI of sample sites derived from Junior's multispectral camera at Waimangu Volcanic Valley, New Zealand. (A) True colour (B) visible/NIR false colour and (C) NDVI images of an outflow vent. (D) True colour (E) visible/NIR false colour and (F) NDVI of microbial deposits.

Figure 3A-F shows multiband analysis as derived from visible and NIR filter photography of the Waimangu Volcanic Valley site as obtained from Junior's multispectral camera. Figure 3A-C were imaged from the site of an outflow vent near the stream shore. Cyanobacterial microbial life in the cooler waters surrounding the vent (30-35^{o}C) (green material, Fig. 3A) was very highly reflective in NIR and displayed as bright red in the false colour image (Fig. 3B). NDVI of this material was also approximating values of 0.5-0.6 (Fig. 2C). We found no evidence of photosynthetic life in the immediate vicinity of the vent itself, as revealed by NDVI values of 0 in this area (Fig. 3C). Temperature readings of the vent were 80-90^{o}C, generally being too high for cyanobacteria to survice. It is thus unlikely the brown material surrounding the vent is cyanobacteria. Additional imaging of sinters near the stream shoreline (Fig. 3D) revealed strong evidence for photosynthetic life forms bounding the cooler waters (30-35^{o}C) of the

outflow vent (Fig. 3E-F). We also observed the presence of microbial life at the base of the pebble-like sinter, illustrated in the bottom left of the false colour and NDVI analysis of Figs. 3E-F. This material was absent from the portions of sinter protruding from the stream flow.

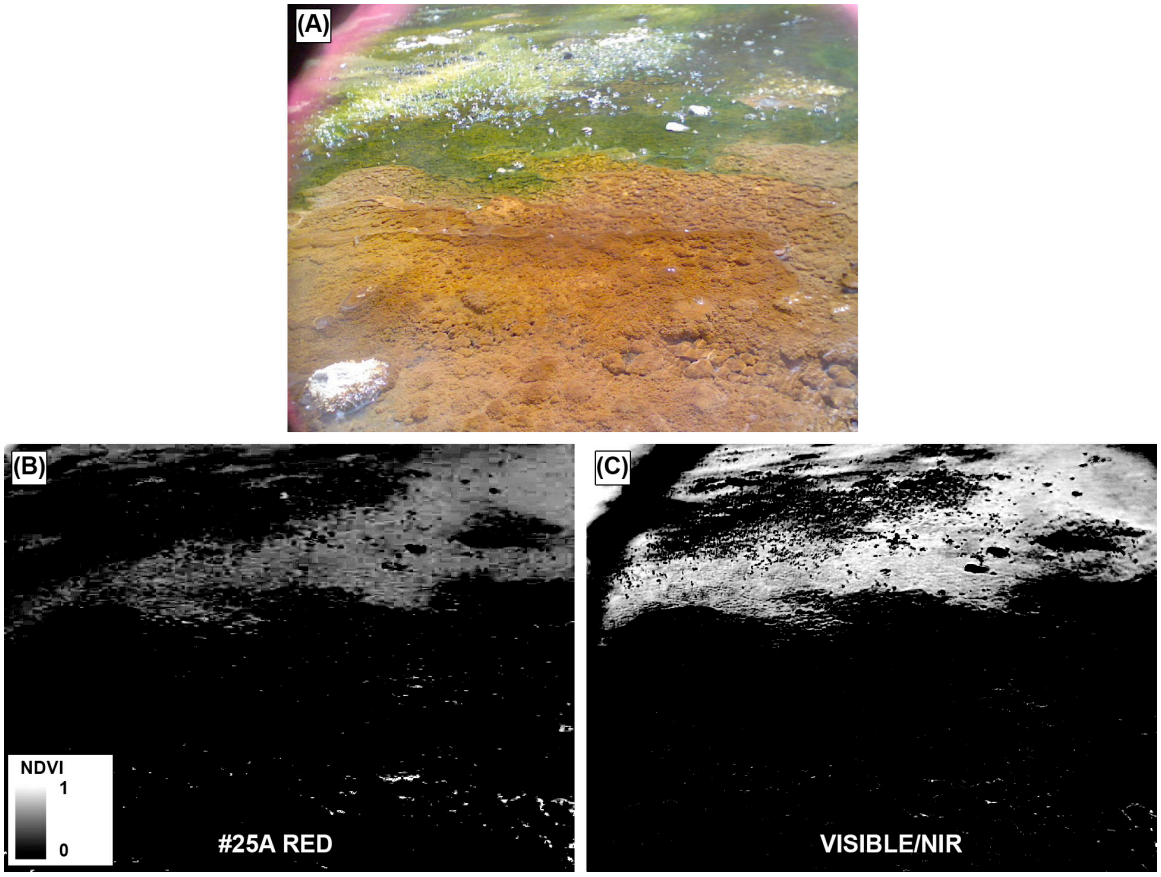

Fig 4. Visible and NDVI of comparison between visible/NIR and red filters from junior's multispectral camera at Waimangu Volcanic Valley. (A) True colour (B) NDVI derived from red filtered image and (C) NDVI derived from visible/NIR images.

We undertook comparative analysis of single filter NDVI and two filter imaging at Waimangu Volcanic Valley, although time constraints allowed us to only capture one image through the red filter at this site (Fig. 4). In order to achieve this we imaged a portion of stream shoreline partially containing algal microbial material (*Cyanidium,* [23]; Fig. 4A). NDVI analysis of the red filtered imagery revealed the presence of the algae (Fig. 4B), though the green algal material was more prominent in the NDVI analysis of the separate visible/NIR images.

We sampled temperatures of the Parariki Stream floodplain and vents at Rotokawa geothermal area using the non-contact thermometer on board Junior and compared them with readings from a hand-held device in a similar manner to the Waimangu site. Although readings of the floodplain for both instruments ranged from 30-40^{o}C, our samples from the actual vents were 52^{o}C, compared with 80^{o}C from the handheld device. Figure 5A-I shows multiband analysis as derived from visible and NIR filter photography

of Parariki Stream as obtained from Junior's multispectral camera.

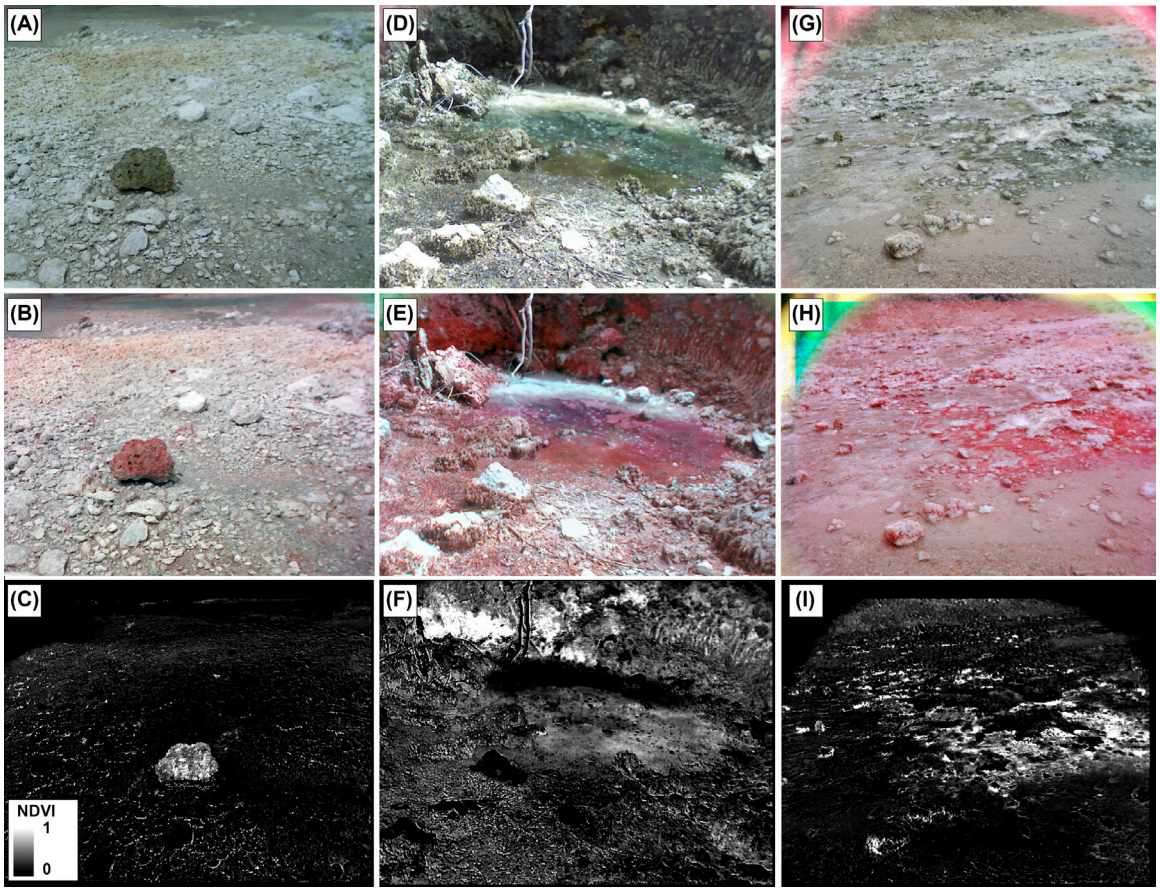

Fig 5. Visible, false colour and NDVI of sites around the Parariki stream from Junior's multispectral camera. (A, D, G) True colour (B, E, H) False colour derived from visible/NIR images. (C, F, I) NDVI derived from visible/NIR images.

We observed that sinters possessing green algal microbial material become prominent in false colour and NDVI analysis whereas other microbial types and mineralogy were not. Fig. 5A-C show analysis of a pumice clast containing algal material that was placed in a region of creek bed where algae was absent. We noted that the clast containing algal material was highly reflective in NIR whereas adjacent clasts embedded within the stream bed were not (Fig. 5B-C). We located a ~1 m diameter thermal pool with an abundance of algalmicrobial material growing around its rim (Fig. 5D). We were able to detect NIR from this pool, despite the green algal material being located underwater, which tends to absorb NIR radiation. We noted that the layer remained visible in false colour and NDVI analysis (Fig. 5E-F) although it was not as prominent as the background vegetation surrounding the pool. It is possible the water may have attenuated the transmission of NIR radiation from the submerged algal material. Fig. 5G-H shows the location of thin layered green algal deposits surrounding rockier material. As with the other sites, the green algae layer was prominent in the false colour and NDVI analysis (Fig. 5 G-H). NDVI values for this layer were high (0.8-1, Fig. 5I) in the densest portions of this green algal layer, which contrasted with lower values present in the imaged clast (0.5-0.8, Fig. 5C) and pool (0.3-0.4).We noted that the green algal layer was

absent from the top of the rocky material, probably due to the absence of water in this region. In addition to the algal material being present on the base of the rocky layer, it was also observed mixed within some of the pumice clasts, as evidenced by the high NDVI reading of the large clast in the foreground (Fig. 5H-I).

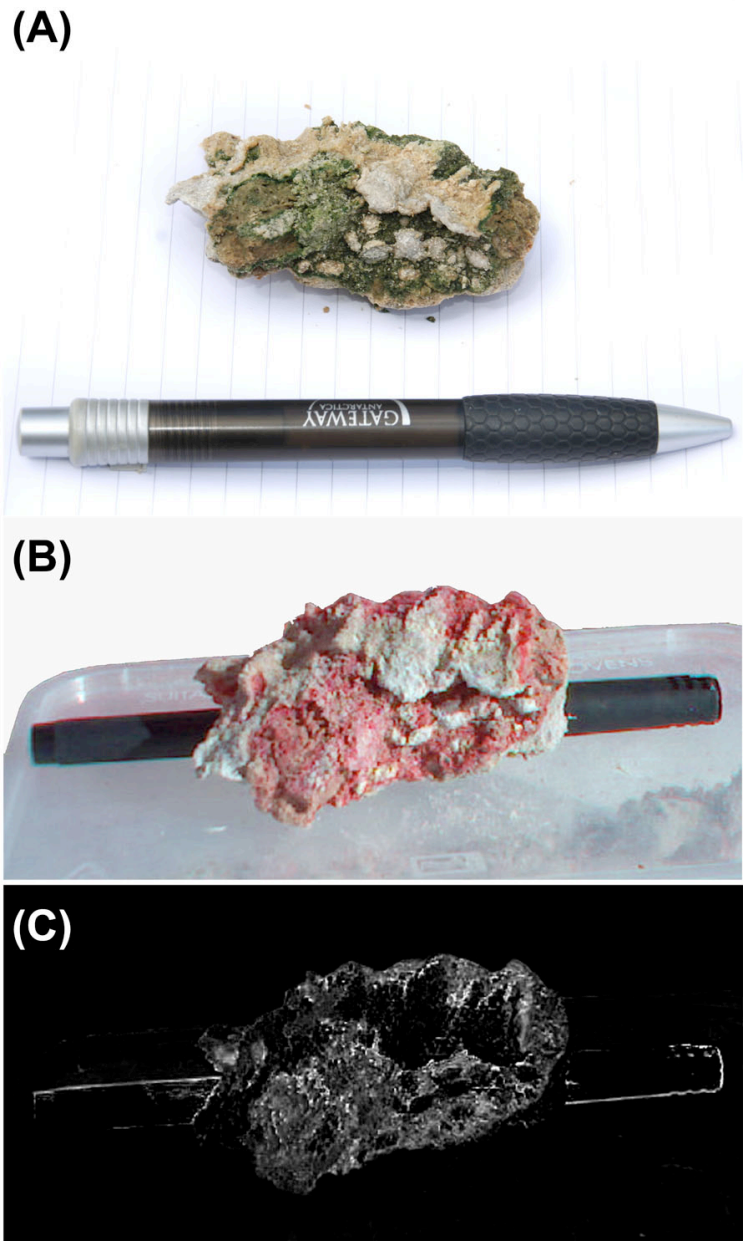

Fig 6. (A) Visible, (B) false colour and (C) NDVI of returned sinter sample taken from the Rotokawa stream containing endolithic green algae. The highlighted area around the scale pen is a product of band mixing the image.

We extracted a sample of sinter from the Rotokawa stream for analysis by Junior in a controlled environment (Fig. 6A-C). The sinter was a portion of a larger pumice clast located ~5 m upstream of the water edge. Unfortunately time constraints precluded context imaging of the sample in situ. Junior imaged the sample in direct sunlight at a

distance of 25 cm using the visible and NIR filters. The returned sample clast was impregnated with endolithic green algal material in a similar manner to that observed in the foreground clast in Fig. 5G-I. Visible imagery showed the algae to be green-brown in colour and present within 5 mm of the outer surface of the clast (Fig. 6A). False colour imagery was able to confirm the biological nature of the material, displaying as red in Fig. 6B. NDVI analysis revealed values of 0.3-0.6 (Fig. 6C). There was no discernable difference in NDVI values between the green and brown coloured algal deposits, indicating similar levels of chlorophyll-based photosynthesis for both types of biota. Similar coloured cyanobacteria were analysed by [30] in the outflow of Frying Pan Lake.

Discussion

We were able to successfully operate a small rover in a range of hot springs environments of the Taupo Volcanic Zone near Rotorua, and to return data in regards to some types of extremophiles at two study sites. The rover was able to negotiate the terrain at both sites, with the low slopes and sinter/pebble matrix of the traverse sites proving ideal for the skid-steered mobility of the rover. We found that rover operations were limited to 30 minutes, as constrained by battery life for the vehicle.

Although we were able to successfully obtain temperature readings at both study sites from the non-contact thermometer, we found that readings of the hottest areas in the hot spring vents were underrepresented by 20-30^{o}C. This is probably due to the inability to rotate the instrument platform more than 45^{o}, precluding unobstructed sampling of the vents. It is also possible the non-contact thermometer collection area was too large to obtain unmixed readings of the hottest regions of the study site.

Multispectral imagery of a hot spring site using robotic rovers showed that identification of photosynthetic biological material is possible by using modest budget, off-the-shelf technology. Additionally quantitative assessments on the abundance and health of this biotic material may also be achieved using NDVI analysis. The visible/NIR method was appropriate for this task; however, we were not able to confidently distinguish between other types of extremophiles or mineralogy using this method. Detailed analysis would require the use of narrow pass geologic filters, microscopy and high resolution spectroscopy. These will be included in a future Marsobot rover.

Additionally we found that NDVI on photosynthetic material may be calculated using single imagery collected through a #25A red filter. We note the values derived from this procedure were lower than those sampled through separate images collected through separate visible and NIR filters. It is likely the discrepancy may result from NIR leakage between the red and blue channels of the camera. Thus while this method would be appropriate for healthy vegetation exhibiting high NIR reflectance, it would be less appropriate for diseased or senescent vegetation with lower NIR reflectance.

Obtaining these results has provided useful information on the capabilities and limitations of using robotic sensors to search for extreme forms of life. The results show that it is possible to map the distribution of at least some types of microbial life using low-cost instruments that can be fitted to a small rover. However, these observations are preliminary only, and the rover does not substitute for more sophisticated studies involving sample return, microscopy and other laboratory methods [19, 20, 21], beyond the capabilities of small robots such as Junior. The application of such field robotics in

studying fragile and dangerous field sites would be to assist in prioritising the sites for direct sampling by field scientists. Also of importance is ensuring adequate power storage reserves to carry out missions of useful duration, either in the form of larger batteries or batteries that can be rapidly replaced with ones fully charged.

In relation to the robotic astrobiological exploration of Mars, the difficulty in obtaining conclusive evidence for biological, as opposed to mineralogical activity has been acknowledged [11, 20], particularly in the field of paleomicrobiology where return of samples, site revisits and sophisticated laboratory techniques are required to assist in distinguishing life from non-life or on ancient well-preserved hydrothermal sites such as the Warrawoona Group of the Pilbara Region [50]. So far the only specific search for life experiments performed by Viking highlighted the inherent problems of trying to obtain conclusive evidence for life within the limits of robotic methods [11]. Moreover, the size, power and weight constraints of planetary spacecraft limit the carriage of instrumentation to only a few, carefully chosen, experiments. Thus our testing of proposed instruments within a hot springs environment analogous to those extant on early Mars provide useful benchmarks for designing future robotic astrobiological missions targeting such features.

Conclusion

We conducted field trials of Marsobot Junior, a microrover class teleoperated vehicle, within the hot springs environment of Rotorua, New Zealand. We found that multispectral imagery using visible and NIR to be a useful tool in identifying photosynthetic microbial material from mineralogy in extreme environments. We were also able to characterise biological material within a pumice clast sampled from the Parariki Stream study site. Although single-filter multispectral imagery also provided useful data we suggest that radiation leakage between channels limit this technique to sampling healthy vegetation. Time constraints derived from rover energy requirements restricted the amount of data that could be gathered by the rover and highlights some of the difficulties in using robots for astrobiological research. Results and lessons learned from Junior's mission, especially with respect to instrument selection, design and on power reserves, will be used to further develop instrumentation for astrobiological and extremophile research.

Acknowledgements

The authors would like to gratefully acknowledge the assistance of Mars Society Australia, Haritina Mogadishu and the Kiwispace team, and the Faculty of Science at the University of Auckland for their assistance in Spaceward Bound.

References

1 Yoerger D., Bradley, A.M., Jakuba, M., German, C.R., Shank. T., and Tivery, M. Autonomous and remotely operated vehicle technology for hyrothermal vent discovery, exploration, and sampling. *Oceanography* 20(1), p152-161, 2007

2 Karachevtseva, I, Oberst, J., Scholten, F., Konopikhin, A., Shingareva, K., et al.

Cartography of the Lunokhod-1 landing site and traverse from LRO image and stereo-topographic data. *Planet. Space Sci* 85, p175-187, 2014.

3 Zhang, J., Yang, W., Hu, S., Lin, Y., Fang, G. et al. Volcanic history of the Imbrium basin: A close-up view from the lunar rover Yutu. *Proc. Nat. Acc. Sci* 112(17), p5342–5347 2015.

4 Grotzinger J.P., Crisp, J., Vasavada, A.R., Anderson, R.C. Baker, C.R. et al. "Mars Science Laboratory mission and science investigation". *Space Sci Rev*. 170, p5–56 (2012).

5 Gingras, D., Allard, D., Lamarche, T., Rocheleau, S.G., Gemme, S. et al, Lunar Rover Remote Driving using Monocameras under Multi-Second Latency and Low-bandwidth: Field Tests and Lessons Learned. *Proceedings of i-SAIRAS2014*. Accessed online on 15/5/05 http://robotics.estec.esa.int/i-SAIRAS/isairas2014/Data/Session%205a/ISAIRAS_FinalPaper_0048.pdf

6 Hobbs, S.W., Clarke, J.D.A., Mann, G.A. "Field testing Marsobot: a Mars Society Australia robotics project". *Proceedings of the 13th ASSC Conference*, 2014.

7 Hayati, S., Volpe, R., Backes, P., Balaram, J., Welch, R., et al., "The Rocky 7 Rover: a Mars sciencecraft prototype". *Proceedings of the 1997 IEEE International Conference on Robotics and Automation*, 2458-2464, 1997.

8 Anderson, R.C., Haldermann, A.F.C., Dohm, J. Huntsberger, T., "A Dress Rehersal for the 2003 Mars Exploration Rovers", In Clarke, J.D.A. (ed.) *Mars Analog Research*, America Astronautical Society Science and Technology Series 111, p117-128. Univelt, San Diego, California, 2006.

9. Stoker, C.R., Cannon, H.N., Dunagan, S.E., et al. "The 2005 MARTE robotic drilling experiment in Rio Tinto, Spain: objectives, approach, and results of a simulated mission to search for life in the Martian subsurface." *Astrobiology* 8, 921-945, 2008.

10 Jheeta, S., "Final frontiers: the hunt for life elsewhere in the Universe." *Astrophys. Space Sci.* 348, 2013.

11 Barlow, N.G., *Mars: An Introduction to its Interior, Surface and Atmosphere*, Cambridge University Press, Cambridge, 264 pp, 2008.

12 Snyder, C.W., The missions of the Viking Orbiters. *J. Geophys. Res* 82, 3971-3983, (1977).

13 Kelly, R.M., "Going to extremes: observations from the biology/engineering interface". *College of Engineering*, North Carolina State University, 2003.

14. Van Dover, C.L., 2000. *The Ecology of Deep-Sea Hydrothermal Vents*. Princeton University Press, Princeton, New Jersey, pp. 1 – 424, 2000.

15. Campbell, K.A., Guido, D.M., Gautret, P., Foucher, F., Ramboz, C. and Westall, F. in press. Geyserite in hot-spring siliceous sinter: Window on Earth's hottest terrestrial paleoenvironment and its extreme life. *Earth-Science Reviews*,doi:10.1016/j.earscirev.2015.05.009, 2015.

16. Barns, S.M., Delwiche, C.F.D., Palmer, J.D., Dawson, S.C., Hershberger, K.L., Pace, N.R., Phylogenic perspective on microbial life in hydrothermal ecosystems, past and present, In Bock, G.R., Goode, J.A., (Eds), *Evolution of Hydrothermal Ecosystems on Earth (and Mars?),* Ciba Foundation Symposium 202, John Wiley and Sons, Chichester, 1996.

17. Capece, M.C., Clark, E., Saleh, J.K., Halford, D., Heinl, N., Hoskins, S., Rothschild, L.J. Polyextremophiles and the constraints for terrestrial habitability. J. Seckbach et al. (eds.), *Polyextremophiles: Life Under Multiple Forms of Stress*. Cellular Origin, Life in Extreme Habitats and Astrobiology 27, 3–59, DOI 10.1007/978-94-007-6488-0_1, 2013

18 Henley, R.W. Chemical and physical context for life in terrestrial hydrothermal systems: chemical reactors for early development of life and hydrothermal ecosystems, In Bock, G.R., Goode, J.A., (Eds), *Evolution of Hydrothermal Ecosystems on Earth (and Mars?),* Ciba Foundation Symposium 202, John Wiley and Sons, Chichester, 1996.

19 Jones, B., Renaut, R.W., Rosen, M.R., "Stromatolites forming in acidic hot-spring waters, North Island, New Zealand". *Palaios*, 15, 450-475, 2000.

20 Farmer, J.D., Des Marais, D.J., Exploring for a record of ancient Martian life. *J. Geophys. Res.* 104, 26977-26995, 1999.

21. Walter, Malcolm R., The quest for a second origin of life. *Elements*, 11, 14-15, 2015.

22. Reysenbach, A.-L., Voyteck, M., Mancinelli, R., *Thermophiles: Biodiversity, Ecology, and Evolution*. Kluwer Academic-Plenum Publishers, New York, 205 pp, 2001.

23. Schinteie, R., Campbell, K.A., Browne, P.R.L., Microfacies of stromatolitic sinter from acid-sulfate-chloride springs at Parariki Stream, Rotokawa Geothermal Field, New Zealand. *Paleontologia Electronica* 10, 1-33, 2007.

24. Ruff, S.W., Farmer, J.D., Calvin, W.M., Herkenhoff, K.E., Johnson, J.R., Morris, R.V., Rice, M.S., Arvidson, R.E., Bell III, J.F., Christensen, P.R., Squyres, S.W., Characteristics, distribution, origin and significance of opaline silica observed by Spirit rover in Gusev Crater, Mars. *J. Geophys. Res.* 116, E00F23, 2011.

25. Yen, A.S., et al., Hydrothermal processes at Gusev Crater: an evaluation of Paso Robles class soils. *J. Geophys. Res.* 113: E06S10.

26. Walter, M.R., 1976b. Hot-spring sediments in Yellowstone National Park. In: Walter, M.R. (Ed.), *Stromatolites*: Elsevier, Amsterdam, 489–498.

27. Cady, S.L., Farmer, J.D., *Fossilization processes in siliceous thermal springs: trends in preservation along thermal gradients*. In: Bock, G.R., Goode, G.A. (Eds.), 150–173, 1996.

28. Handley, K.M., Campbell, K.A., Character, analysis and preservation of biogenicity in terrestrial siliceous stromatolites from geothermal settings. V.C. Tewari and J. Seckbach (eds.), *STROMATOLITES: Interaction of Microbes with Sediments*, Cellular Origin, Life in Extreme Habitats and Astrobiology 18, 359–381. DOI 10.1007/978-94-007-0397-1_16, 2011.

29. Havig, J.R., Raymond, J., Meyer-Dombard, D.R., Zolotova, N., Shock, E.L., Merging isotopes and community genomics in a siliceous sinter-depositing hot spring. *J. Geophys. Res*. 116, G01005, doi:10.129/2010JG001415, 2011.

30. Jones, B., Renaut, R.W., Rosen, M.R., Microbial biofacies in hot-spring sinters: a model based on Ohaaki Pool, North Island, New Zealand. *Journal of Sedimentary Research* 68, 413–434, 1998.

31. Jones, B., Renaut, R.W., Rosen, M.E., Vertical zonation of biota in microstromatolites associated with hot springs, North Island, New Zealand. *Society for Sedimentary Geology*, 220-236, 2004.

32. Guido, D.M., Campbell, K.A., Jurassic hot spring deposits of the Deseado Massif (Patagonia, Argentina): characteristics and controls on regional distribution. *Journal of Volcanology and Geothermal Research* 203, 35–47, 2011.

33. Lynne, B.Y., Mapping vent to distal-apron hot spring paleo-flow pathways using siliceous sinter architecture. *Geothermics* 43, 3–24, 2012.

34. Lowe, D.R., Anderson, K.S., Braunstein, D., The zonation and structuring of siliceous sinter around hot springs, Yellowstone National Park, and the role of thermophilic bacteria in its deposition. In: Reysenbach, A.M., Voytech, M., Mancinelli, R. (Eds.), *Thermophiles: Biodiversity, Ecology and Evolution*: Kluwer Academic/Plenum Publishers, New York, 143–166, 2001.

35. Jones, B., Renaut, R.W., Konhauser, K.O., Genesis of large siliceous stromatolites at Frying Pan Lake, Waimangu geothermal field, North Island, New Zealand. *Sedimentology* 52, 1229–1252, 2005.

36. Brock, T.D., Brock., M.L., The algae of Waimangu cauldron, New Zealand, distribution in relation to pH. *Journal of Phycology*, 6, 371-375, 1970.

37. Teece, C.I.A., Sinters deposited from acid-sulfate chloride waters at the Rotakawa geothermal field (Taupo Volcanic Zone, New Zealand). *Unpublished Msc Thesis*, University of Aukland, Aukland, 2000.

38. Grange, L.I., The geology of the Rotorua-Taupo subdivision. *Department of Scientific and Industrial Research, Geological Survey Bulletin*, 37, Wellington, 1937.

39. Schinteie, R., Siliceous sinter facies and microbial mats from acid-sulfate-chloride springs, Parariki Stream, Rotakawa Geothermal Field, Taupo Volcanic Zone, New Zealand. *Unpublished Msc Thesis*, University of Aukland, Aukland, 2005.

40. NASA National Space Science Data Center. *Luna 17/lunokhod,*. Accessed online on 15/5/05 http://nssdc.gsfc.nasa.gov/database/MasterCatalog?sc=1973-001A, 2005.

41. Shue, S., Hargrove, C., Conrad, J., Low Cost Semi-Autonomous Sentry Robot. *IEEE Proceedings*, 2012.

42. Gonullu, M.K., Development of a Mobile Robot Platform to be used in Mobile Robot Research, *Masters thesis*, Middle East technical University, 2013.

43. Shaw, J.A., et al., Multispectral imaging systems on tethered balloons for optical remote sensing education and research. *J. Appl. Remote Sens.* 61, doi:10.1117/1.JRS.6.063613, 2012.

44. Sugiura, R., Noguchi, N., Ishii, K., "Remote-sensing technology for Vegetation Monitoring using an Unmanned Helicopter". *Biosystems Engineering* 90, pp369-379, 2005.

45. Horning, N. *Red vs. blue filter for NDVI*, Accessed online on 15/5/05 http://publiclab.org/notes/nedhorning/10-30-2013/red-vs-blue-filters-for-ndvi, website accessed 11 May 2015.

46. Tucker, C.J., Red and photographic infrared linear combinations for monitoring vegetation. *Remote Sensing of the Environment* 8, 127-150, 1979.

47. Zha, Y., Gao, J., Ni, S., Use of normalized difference built-up index in automatically mapping urban areas from TM imagery. *International Journal of Remote Sensing* 24, 583-594, 2003.

48. Jackson, T.J., Chen, D., Cosh, M., Li, F., Anderson, M., Walthall, C., Doriaswarmy, P., Ray Hunt, E., Vegetation water content mapping using Landsat data derived normalized difference water index for corn and soybeans. *Remote Sensing of Environment* 92, 475-482, 2004.

49. Wang, S.X., Zhou, X.J., "Spectroscopic Sensor on Mobile Phone", Patent 7,420,663 (US, 2008).

50. Brown, A.J., Walter, M.R., Cudahy, T.J., Hyperspectral imaging spectroscopy of a Mars analog environment at the north pole dome, Pilbara Craton, Western Australia. *Australian Journal of Earth Sciences* 52, 353-364, 2005.

A4 Rover Proposal: A Small Planetary Science Rover for Geologic and Astrobiology Investigations for Mars Surface Exploration

Steven Hobbs [1, 2], Connor Coleman-Jennings [2], Jonathan Clarke [2], Siddharth Pandey [2], and David Willson [3]

[1] *School of Physical, Environmental and Mathematical Sciences, University of New South Wales Canberra, Australian Defence Force Academy, ACT, Australia*

[2] *MarsSociety Australia, P.O. Box 327, Clifton Hill, VIC 3068, Australia*

[3] *NASA Ames Research Center, Pasadena, CA.*

Summary: No minirover (2 kg) class vehicle has ever landed on the Red Planet. The small size of a minirover would make it an ideal secondary payload with its own independent mission in a similar manner to Cubesat missions. This proposal outlines designs for the "A4 rover" that will trial mobility and scientific data collection in Mars analogue environments in Australia, the USA and India. These results will be used to refine designs for the A4 Rover and contribute to the design of a space qualified vehicle. The project is a collaboration of UNSW Canberra, NASA Ames Research Center, and the NASA Spaceward Bound program. A series of research test criteria was created to test the efficiency and performance of the rover under a variety of environmental conditions. Physical outcrops are defined and characterized for rover trials in Canberra (Australia), Mars Desert Research Station (MDRS) in Utah (USA), and Ladakh (India). The planned tests will answer specific questions regarding how a minirover will perform in a Martian environment and meet agreed upon research criteria.

Introduction

Mobile robots sent to Mars have been between the range of 10-900 kg in weight, with power generated by solar – 20W Sojourner, 140W Mars Exploration Rover (MER) – and nuclear sources (125W electrical energy, Curiosity). Volume, mass and power constraints limit the type and volume of data that can be returned from these vehicles and their mobility. The larger rovers, such as Mars Exploration Rovers (MER) and Curiosity, were extremely expensive to build and operate [1, 2, 3, 4]. Curiosity costed billions of dollars, and its launch date was delayed for two years due to cost and design issues [1, 5]. Curiosity's relatively large size allowed for the inclusion of many scientific experiments, but its bulk limited it to the exploration of just one specific Martian landing area [2]. Although the two robots of the MER mission were less expensive (~700 million), only two landing sites could be explored [2], owing to the limited manoeuvrability and autonomy of large rovers. The construction and deployment of smaller, cheaper rovers, would allow a larger number of vehicles to be built, consequently enabling the exploration of a greater area of the Martian surface, while being relatively unaffected by possible budget cuts to the missions [5]. These advantages prompt investigations into the design, construction and testing of small rovers for scientific research potential. We present in this paper our proposal to investigate what astrobiological/geological research objectives could be achieved by our minirover proposal, designed to fit onto an A4 sheet of paper and named the A4 Rover (Fig. 1).

The A4 Rover is an extension of the Marsobot program which is intended to develop small scale rovers to investigate applications of robotic surface platforms in Planetary Science. Previous Marsobot rovers were taken to the Arkaroola region, a semi-arid site analogous to Mars, to undertake engineering field trials as part of the Arkaroola Mars Robot Challenge Expedition [6]. Two rovers were trialled in this environment against engineering criteria developed by the US National Institute of Standards and Technology (DHS-NIST-ASTM for response robots [6, 7, 8]) during MSA's Arkaroola Robot Challenge in July 2014. An additional rover was included in the New Zealand Spaceward Bound trip to the hot springs in Rotorua, New Zealand [9]. This rover tested a multispectral camera and non-contact thermometer in identifying and characterising extreme forms of life within acid and alkaline hot spring areas thought to be analogous to early Mars environments [10]. In this present work we will describe the mechanical and electronic design of the A4 Rover, research collaboration and test objectives, including proposed testing sites in Australia and overseas.

Background

Recent advances in microtechnology and mobile robotics make it possible to build small autonomous or remotely controlled space vehicles that have the potential to save on payload weight, launch and landing costs for planetary missions. One successful example of mini-rovers is the MUSES-CN Minirover proposed and developed in the late 1990's for the JAXA Hayabusa Asteroid mission [9]. MUSES-CN was a lightweight but extremely mobile vehicle that opened new application frontiers [11]. The minirover was developed for a Japanese asteroid mission designed to rendezvous with the asteroid 1989ML [11]. Despite weighing 1 kg and generate a maximum of 2.3 W of power, the minirover was able to carry a geology camera with a nine position filter wheel, an IR spectrometer, wheel encoders, and a laser rangefinding diode [11].

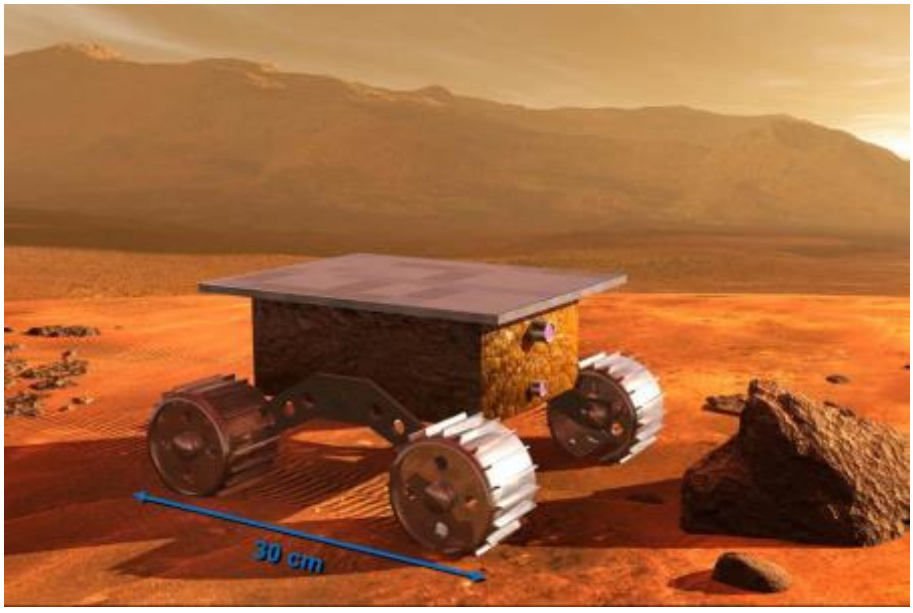

Fig. 1: Artist's impression of the proposed A4 minirover on the surface of Mars.

A minirover 30 cm size long, such as what we propose for the A4 Rover (Fig. 2) could be carried as an alternate payload for a primary space mission, thus saving on costs and maximizing the mission scientific output. No vehicle of this class has ever been sent to Mars, and as such operation of a vehicle this size, as well as the distinctive science that can be gathered is largely unknown. The aim of this proposal is to outline a small, 2 kg class minirover built to explore sites of astrobiological significance on the surface of Mars. The physical architecture and proposed scientific instruments to be tested will now be discussed.

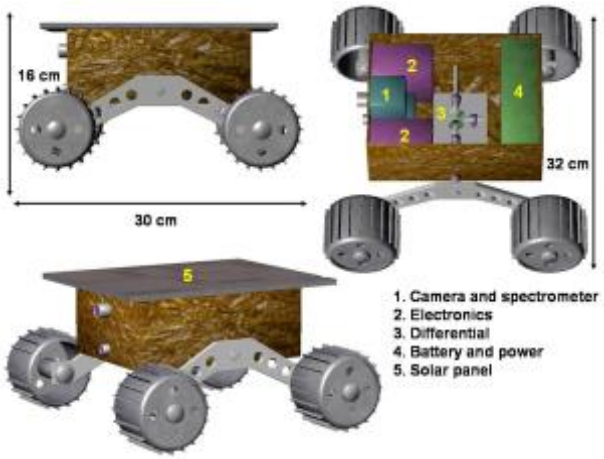

Fig. 2: Schematics of the proposed A4 minirover.

Physical Architecture

The proposed physical architecture for the A4 rover is shown in simplified form in Fig. 2. A warm electronics box (WEB) will house the camera and spectrometer (1), support electronics (2), the suspension differential (3) and battery (4). The solar panel will be fitted on top of the WEB (5). The relative size and position of the bogie arms and wheels are also shown. Holes will be drilled into the bogie arms to save weight. This has been standard practice for the Sojourner, Spirit and Opportunity rovers. A block diagram of the proposed A4 Rover software architecture is shown in Fig. 3. The power subsystem is interfaced with a watchdog circuit in order to render the rover safe in case of undervoltage or microprocessor latchup. Mobility of the vehicle is controlled by user command via the communications link for the terrestrial version and semi-autonomously for the space qualified version. Wheel encoders, IMU and obstacle avoidance sensors all interact to achieve safe and productive rover mobility.

The science sensors interact with the communications system via the microprocessor and may be tele-commanded, or controlled automatically in semi-autonomous operations. All data readings returned from the sensors will be transmitted to Earth via a primary payload or relay orbiter via the A4 Rover communication system.

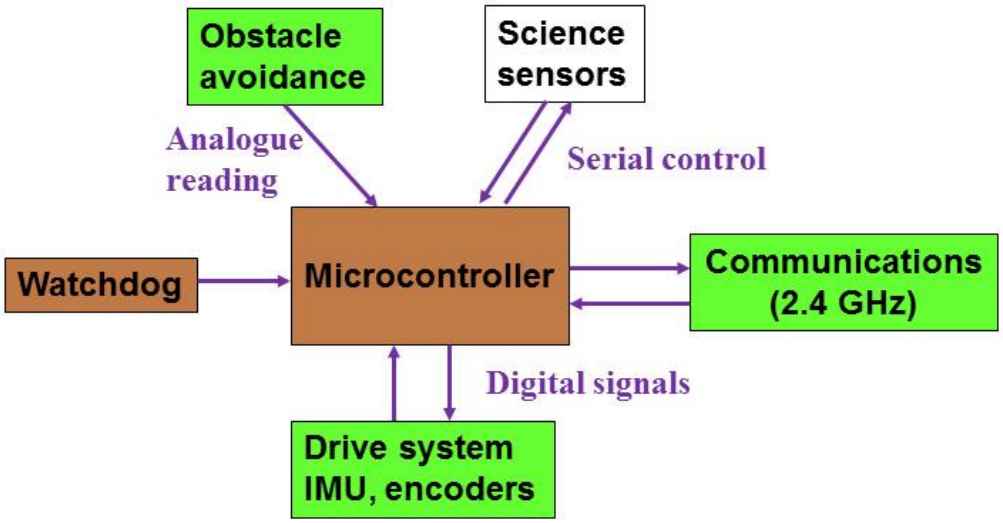

Fig. 3: Proposed A4 Rover software architecture.

Scientific Instruments

The proposed instruments on board the A4 Rover are intended to yield useful data in diverse landing sites, such as at Gale Crater [12] or at more homogenous sites similar to the Viking 1 landing site [13]. Four scientific instruments are proposed to be carried aboard the A4 rover. These include a filtered multispectral camera, a visible/NIR spectrometer, a non-contact thermal imaging system and a weather instrument. Multispectral cameras have been included in a variety of Mars missions, including Viking, Pathfinder, MER and Curiosity [12, 13, 14, 15]. Filters for this camera will permit sensitivities in the visible and NIR bands in order to characterise mineralogy and possible biology of the rover's study site (e.g., [16]). The prime focus for the camera will be set to 30 cm in order to enable macro style imagery to be collected from smaller materials, such as coarse grains of sand. Microscopic analysis has also been an established process for investigating existing or relict life forms [12, 17, 18] and provides a level of detail not available to mast-mounted imaging systems, such as those aboard MER [19]. Past microscopic imagers carried aboard FIDO, MER and Curiosity rovers were designed to simulate a geologist's hand lens and were capable of resolutions of ~30um/pixel [12, 19]. Data returned from these instruments have provided critical information on fine scale geology. We will take advantage of the A4 Rover's close proximity to the ground to provide extreme close-up imagery of feature of interest. Similarly the spectrometer proposed will provide mineralogical context of features of interest. Spectra will be sampled by the rover driving up to a feature of interest and be transmitted to a ground station.

Non-Contact thermometer.

Thermal imaging will enable characterisation of the local geology, providing ground truth for thermal inertia estimations of classes of regolith previously performed by TES and THEMIS [20, 21]. Different surface temperatures of different rocks and soils at the same time of day will yield useful information on the thermal properties and thus help inform thermal inertia mapping from orbit. We have used the Melexis MLX90614 Non-contact sensor in our New Zealand Marsobot field excursion [22]. The sensor is capable of sensing temperatures from -70 to +380^{o}C and has a field of view of 90 degrees [22]. We propose using a version of this sensor for undertaking calibrated thermal measurements of regolith during the Martian sol for research into Martian geological thermal inertia properties.

Environment sensors

Weather sensors have been carried on board previous Mars missions and have been useful in obtaining weather data (e.g., [22]). We propose to include a temperature and pressure sensor onboard the A4 rover. We trialed the use of the BMP085 temperature and pressure sensor [23] and DHT-22 temperature sensor [24] during robotic trials in Arkaroola in 2014 [6,7, 8]. The weather station will enable sampling of local temperatures and pressures at the landing site. Additionally the weather station has the potential to provide calibration temperatures for the thermal imaging system.

Camera

Cameras carried on board previous mars missions have returned an abundance of information about the surface of the red Planet (eg. [13, 14, 25]). Filter wheels have been popular in enabling multispectral images to be taken at different wavelengths of light in order to assist in characterizing minerals of interest [14]. The MER Pancam used filters ranging from 400-1100 nm to provide true colour images and also to assess the degree of crystallinity of iron bearing silicates as well as secondary weathered iron oxides prevalent on Mars [14]. The CCD camera aboard the A4 rover will provide context and environmental imagery of the A4 Rover study site. Owing to the small size of the rover and limited power and thus bandwidth capability, a low resolution camera type is favoured. The CCD camera will be sensitive to wavelengths between 400-1000 nm and a series of filters will be used to allow imagery capture through bands that would facilitate mineralogical and biota detection. Such filters would include 450 nm near-UV, 625 nm red, 750, 850 and 1000 nm NIR, as well as using the camera's bayer filter to provide additional red, green and blue channels. These filters correlate with those carried onboard MER Pancam [14], and will allow characterisation of iron oxide products described above. We are considering using a serial camera such as the Linksprite 2M camera [26]. This camera has the ability to interface with our chosen Arduino microprocessor, operate via serial commands and is able to take images up to two megapixel resolution [26]. Removal of the IR cut filter within this camera will enable it to be sensitive to NIR wavelengths.

Rover Power and Electronics

Power

Power for the rover is to be supplied by a pair of 3.7 V 5Ah Sony 18650 Li-ion cells. These commercially available cells are mature products, manufactured to high standards and have been routinely used in satellite applications [27]. These cells were also used in the Beagle 2 lander that arrived at Mars in conjunction with the Mars Express mission in 2003 [27]. The bettery pack will be recharged through 6 watts of solar cells mounted on the rover top. A voltage regulator and watchdog circuit will deliver appropriate voltage to the battery array, prevent overcharging and preclude discharge back through the solar panel at night.

Drive

Mobility for the A4 robot will be provided by four Maxon RE16 motors with precious metal brushes combined with Maxon 157:1 planetary reduction gears. These motors were used in the 1996 Sojourner Rover that worked on Mars as part of the Mars Pathfinder mission. Additionally larger versions of the Maxon motors, the RE22, have been used in the Mars Exploration Rovers Spirit and Opportunity [28]. The A4 Rover is intended to last one Martian week and be able to drive up to 20 m radius from its deployment site. These objectives provide a balance between mission cost and the return of useful science. We note that the Sojourner rover exceeded its design time of one Martian week [29] and would use additional time the A4 Rover survives on the Marian surface for extended exploration.

Suspension

Suspension for the A4 rover will be achieved by two rocker bogie arms linked by differential within the rover body. Rocker bogies have so far successfully been used in a number of planetary rover missions, including Sojourner, Spirit and Opportunity [30]. Field performance of the Sojourner Rover revealed that the six wheeled, rocker bogie configuration proved to be greater than that required for the available terrain [30, 31]. This indicates a smaller rover would be less likely to require six wheels while still retaining a significant degree of mobility. Additionally the four wheeled rocker bogie system was employed in the skid-steered “Solar Rover” developed by malin Space Science Systems in 2005 [30]. The A4 Rover will also be skid-steered, using differential drive to turn. This method of steering minimises the number of motors required to four vice the 11 motors carried in the Sojourner Rover [19], reducing weight and power requirements.

Skid steering is a proven method of mobility, and was the preferred mobility method for the Soviet Lunakhod and Marsokhod rovers [32, 33]. We have also successfully trialled this form of locomotion in National Institute of Standards and Technology (NIST) testing in Arkaroola, South Australia, in 2014 [8]. Disadvantages to this system are its complexity and the space that the differential drive will occupy in the rover body. Additionally, motors will have to be housed in order to protect them from dust and dirt ingress.

Wheels

Additionally wheel traction and design is one of the major considerations influencing the design of planetary rovers. Wheel traction is generally dependent on vehicle type and loading conditions, surface properties and the shape of the terrain [34, 35, 36]. The 13 cm diameter 7 cm wide wheels of the Sojourner Mars rover, with dimensions comparable to the A4 Rover, were machined from a single piece of aluminium possessing metal spikes for greater grip [37]. Loading on each of these wheels was approximately 2.5 kg, and enabled Sojourner to travel 104 m on the Martian surface, and negotiate rocks, sand and dust found at the Ares Vallis landing site [31, 38]. Additionally encoders in Sojourner were used to measure actual wheel traverse with revolutions undertaken by the rover motors to estimate wheel slippage and infer composition of the terrain [29, 31, 38].

We propose to machine our rover wheels from aluminium with cleated tread. Wheels of this type have been used on all of the flown Mars rovers, including Sojourner, MER and Curiosity [38]. Width and diameters for the A4 Rover wheels will be 5 cm and 8 cm respectively, comparable to the 13 cm diameter 7 cm wide wheels of the Sojourner Mars rover [31, 32, 37, 38]. These dimensions will accommodate most of the motor inside the wheel hub, as well as provide greater traction and hence mobility. We also aim to use encoders to assist in rover navigation but also infer surface traction via wheel slippage estimate wheel slippage and infer composition of the terrain [29, 31, 32].

Command and Control

The terrestrial version of the A4 Rover is intended to be teleoperated in order to make use of limited field times in India. Additionally teleoperation will maximise science and mobility data return by allowing real-time testing of the rover. Control for the rover is intended to be via a serial modem interface that will transmit commands between the rover and a ground station. A simple command line interface will facilitate mobility and science instrument operations commands. Serial telemetary modems used for UAVs have been successfully trialled in our ground robotic testing at Arkaroola out to a range of at least 200 m [6, 7, 8]. Additionally 2.4 Ghz remote control has proven to be very robust with similar ranges. These ranges are also comparable with a communications scenario between the A4 rover and a primary lander mission, allowing for operation within the 20 m radius as proposed above. We propose that science data be operated via a serial link while direct rover mobility will be controlled via a 2.4Ghz R/C control system.

We have considered autonomous operations for the design of the A4 rover, considered necessary for operation on Mars where signal trip times vary between 4–20 minutes [39, 40]. Traditional navigation aids such as GPS or compass are useless on Mars and other methods have included use of inertia measurements, obstacle avoidance sensors and wheel odometers to track distance [41]. Simultaneous Localisation and Mapping (SLAM) is considered the most effective means of autonomous navigation [41, 42, 43], using a combination of odometry, obstacle avoidance sensors, inertial navigation units, as well as camera imagery. We aim to use three Sharp IR sensors to provide awareness of obstacles in front of the robot, while wheel encoders on the two rear wheels will be used to measure distance travelled. An IMU, such as the MPU-6050 [43] will be used to measure turn and acceleration, providing additional information on determining the rover's location and movements. We will also trial Structure from Motion (SfM) from the A4 rover camera, to

determine the effectiveness of generating 3D elevation models that could be used for obstacle avoidance [41].

Processor

The Arduino series of microcontrollers host open source architecture, easy to use programming in C++ and an abundance of online documentation. Additionally Arduinos consume low amounts of power, have been used in robotics, and have flown in space as part of the Ardusat project. The Arduino would interface with our proposed camera and spectrometer, and motor controller system. A disadvantage of these types of microcontrollers is the limited memory available for programming and data storage (~32k), requiring science data to be transmitted to a ground station rather than stored. The use of an Arduino Mega would allow for greater memory storage (64k+), and external memory storage options, such as the use of an SD card are possible with the Arduino. This could be used for storing science data that can be retrieved at a later time. We aim to use an SD card along with an Arduino Mega to for vehicle control, where imagery and scientific date are stored. The data is then read off the card via the Arduino and transmitted via serial modem to a ground station. Our NIST trials of these modems have shown a range of ~200 m line of site [8]. Initial trials of this method performed at the beginning of 2016 have also proved successful and data logging will also be useful for the engineering test criteria outlined in Table 1.

Proposed A4 minirover research team

This technology development and capability demonstration project is based upon possible astrobiological/geological research objectives for Mars surface studies. Jonathan Clarke (Mars Society Australia) will formulate the investigation scientific objectives. David Willson (NASA Ames) will assist with the space qualified component selection, while Steve Hobbs and Siddharth Pandey shall design and build the rover and carry out the testing at designated outcrop locations chosen on the basis of the scientific objectives. Continued testing will also be conducted during the NASA Spaceward Bound program due to commence in Arkaroola in July 2016 and India in August 2016.

Rover Deployment Considerations

The A4 rover will be designed around CubeSat-like features. The popularity of CubeSats is largely owed to independent operations [44], and the utilisation of spring loaded boxes (Poly Picosatellite Orbital Deployers, or P-PODs), which keep the CubeSats quarantined from the main payload before flinging them into space. CubeSats can thus be launched from any rocket with thrust to spare. The A4 rover will conceptually be designed to be deployed from the carrier lander without interaction with the carrier, or intervention from mission control. It must be fail safe, so that even if the rover fails to deploy or deploys incorrectly it will have no impact on carrier operations. Designing the deployment system will not be possible until the specifications of the carrier are known. The mass of the deployment system must be included in the impact of the A4 project on a primary payload carrier system, which will have tighter mass constraints than a CubeSat launcher [45]. CubeSats have been designed to operate independently of the carrier, even at Mars distances [46] for space missions. This may be

possible for the A4 Rover, and is a topic for future research. If we are unable to design a cost-effective system that could communicate direct with Earth, then a shorter range communication system (as with Sojourner, see [21]) link to a primary payload or relay satellite may be necessary. Data and command transmissions would then be batched as a low priority so as not to interfere with the primary payload's other operations. As the A4 rover is low power we propose to trial proven low power 2.4 GHz serial modem technology with the ability to communicate over extended line of sight distances to a simulated relay station.

Planetary protection

As shown in Table 1 the A4 rover and its deployment mechanism will be a category IV mission for planetary protection purposes.

Table 1. The place of the A4 rover within established COSPAR planetary projection categories [21, 47].

Planetary Targets/Locations	Mission Type	Mission Category	Comment
Undifferentiated, metamorphosed asteroids; Io.	Flyby, Orbiter, Lander	I	N/A
Venus; Earth's Moon; Comets; non-Category I Asteroids; Jupiter; other Jovian Satellites (except Europa); Saturn; Saturnian Satellites (except Titan and Enceladus); Uranus; Uranian Satellites; Neptune; Neptunian Satellites (except Triton); Kuiper-Belt Objects (< 1/2 the size of Pluto)	Flyby, Orbiter, Lander	II	N/A
Icy satellites, where there is a remote potential for contamination of the liquid-water environments, such as Ganymede (Jupiter); Titan (Saturn); Triton, Pluto and Charon (Neptune)	Flyby, Orbiter, Lander	II*	N/A
Mars; Europa; Enceladus.	Flyby, Orbiter	III	N/A
Lander systems not carrying instruments for the investigations of extant Mars Life.	**Lander, Probe**	**IVa**	**A4 rover**
Lander systems designed to investigate extant Martian Life.	Lander, Probe	IVb	N/A
Missions investigating Martian Special Regions, even if they do not include life detection experiments. Martian Special Regions include those within which terrestrial organisms are likely to replicate and those potentially harboring extant Martian Life.	Lander, Probe	IVc	N/A
Venus; Moon	unrestricted Earth-Return	V (unrestricted)	N/A
Mars; Europa; Enceladus;	restricted Earth-Return	V (restricted)	N/A

Astrobiological and Astrogeological Science Objectives

The A4 rover is intended to test and characterise mobility and collection of science data for a minirover class vehicle in three Mars analogue environments in Australia and India. The A4 rover will trial a skid-steer, rocker bogie suspension system on environments expected to be observed on Mars such as ice-rich sediment, sands and loose stones. Results from these experiments will provide valuable data for rovers in this class. These results will be used to refine mobility and locomotion designs for the A4 Rover and contribute to the design of a space qualified rover.

Terrestrial site selection

The sites for A4 testing are listed below, individually.

The Arkaroola quarry site (Fig. 3A) was extensively used during the Arkaroola Mars rover challenge expedition in 2014 [7] to test different rovers. There are a wide range of surfaces and materials present, including re-sedimented fined-grained soil on the quarry floor, steep regolith slopes, steep slopes of loose quarried regolith, and rough to-very rough rocky outcrops of shallowly dipping siltstones with large iron oxide concretions (Fig. 3B). At this site the A4 can be tested for: trafficability on flat surfaces, steep and rocky slopes; imagery, and spectroscopy of surfaces and specific outcrops (both shallowly dipping slates with large concretions).

The outcrops near the MDRS habitat in Utah (Fig. 3C) show a wide range of surfaces, including fine grained and pebble covered flat surfaces, low angle slows and rocky outcrops of sandstone, siltstone, and shale. These later show a wide range of trace fossils and sedimentary structures including ripples, burrows and root impression. Potential tests at this side include: trafficability on flat surfaces, steep and rocky slopes; imagery, and spectroscopy of surfaces and specific outcrops.

Preliminary qualitative studies of Ladakh indicate many different environments suitable for testing the A4 rover. These include sand dunes, alluvium, permafrost, and steep, rocky surfaces, to be available within a short time frame during the planned Spaceward Bound expedition to the area in July 2016.

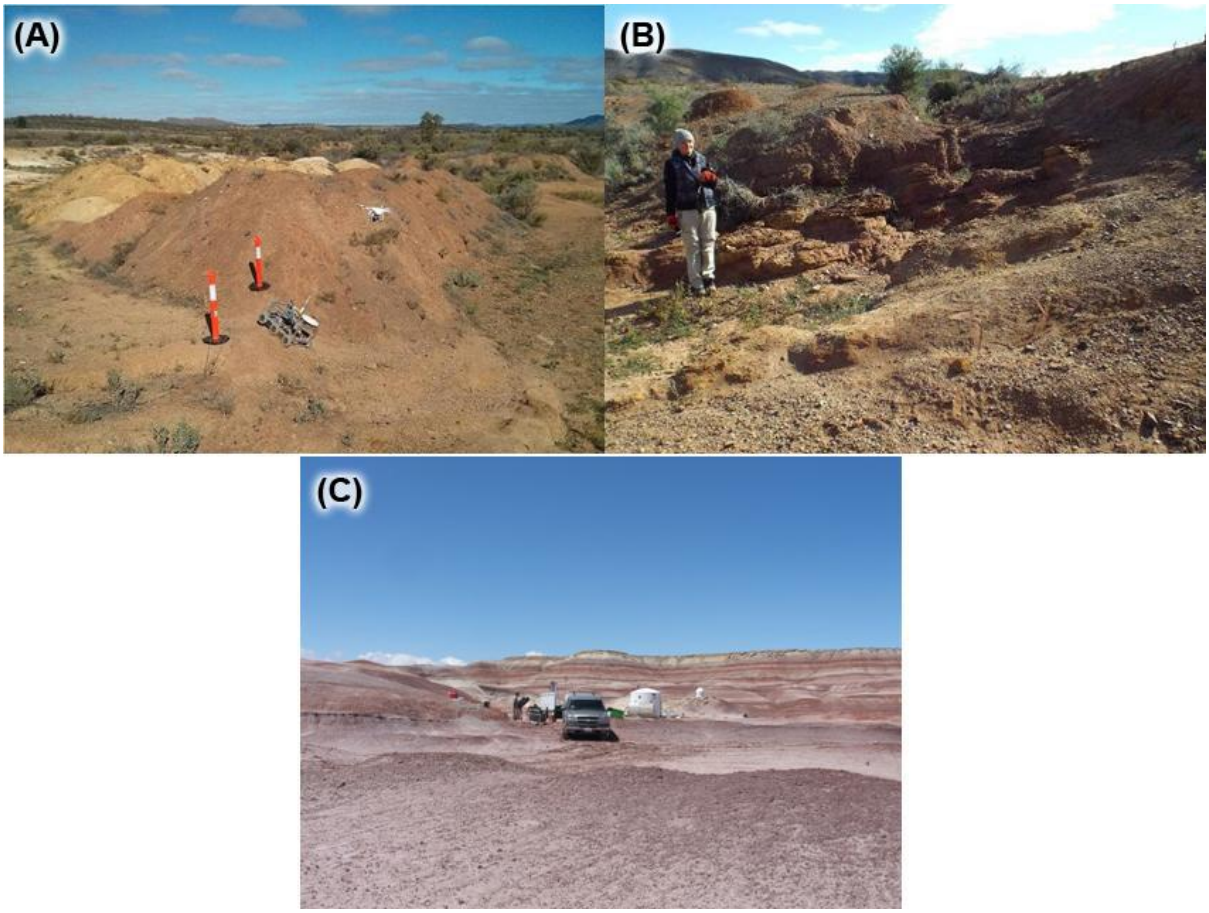

Fig. 4: (A) Slopes and spoil heaps in Arkaroola quarry, test rover for scale. (B) Outcropping siltstones and iron oxide concretions in gully on quarry side. Nicky Wheaton for scale. (C) View across the low rise of the MDRS site back towards the hab. Vehicles are parked on an outcrop during a drilling test.

Research Test Criteria

We chose a series of research test criteria (Table 2) related to our standardised engineering trials performed at Arkaroola [6, 7, 8]. These criteria are designed to ground-test the performance of the A4 rover under outdoor terrain conditions reasonably representative of those on Mars [29, 48]. Results from these tests will be analyzed and presented in future research. The vacuum test, vacuum freeze test and dust tolerance test are designed to more closely simulate the arid, near-vacuum, dusty conditions found on Mars [40]. As they carry greater risk to the vehicle they are planned to be conducted following completion of the previous tests.

Table 2. Research test criteria.

Test Type	Primary criteria/performance indicator	Secondary citeria
Range test	Complete 30 m traverse from starting point (Complete/not complete)	Sandy, rocky, loose pebbles
Endurance test	Complete 30 m traverse from starting point (Complete/not complete)	Monitor energy consumption, CPU resets.
Mobility test	Drive rover successfully over diverse terrain (Successful traverse/slippage/bogging)	Test trafficability on slopes, sandy, rocky and loose pebble surface.
Scientific data return	Acquire data from full payload for each test site (Qualitative and quantitative assessment of data)	Camera: image sample, spectrometer, take reading, thermometer, sample temperature.
Scientific data return II	Characterise immediate environment using rover full payload (Complete/human interaction required)/	Sample min 20 m^2 of target area using full sensor suite.
Vacuum test	Operate rover successfully within 7 mbar atmospheric environment for 1 hour (Complete/not complete)	Monitor controller, scientific instruments and motor performance.
Vacuum/freeze test	Operate rover successfully within refrigerated (-20^{o}c), 7 mbar atmospheric environment for 1 hour (Complete/not complete)	Monitor batteries, controller, scientific instruments and motor performance.
Dust tolerance test	Operate rover in sealed environment contaminated with iron oxide dust for 1 hour (Complete/not complete)	Characterize wear on moving parts, as well as degradation of electronics.

Conclusion

The A4 Rover project is designed to develop and field test a 2 kg minirover in Mars-like conditions in order to develop a space qualified vehiclefor planetary science. In order to remain flexible, the A4 Rover will be developed to be carried as a secondary payload to a larger primary mission, either in a similar manner to that of Cubesats or a more integrated approach. while also able to operate as a primary payload with communication assistance from an external relay system. The A4 rover is intended to test and characterise mobility and collection of science data for a minirover class vehicle in three Mars analogue environments in Australia and India. Results from these experiments will provide valuable data for rovers in this class. These data will be used to refine mobility and locomotion designs for the A4 Rover and contribute to the design of a space qualified rover. Additionally environmental, spectroscopy and imaging science sensors will be trialled in analogous environments in order to obtain data from environments that may be useful in an astrobiological context.

References

1. Seitzen, F., 2009. Mars laboratory lands on red ink. *Aerospace America*, 2009.

3. Stern, A., The low-cost ticket to space. *Scientific American* 308, 68-73, 2013.

4. McCurdy, H.E., Learning from history: Low-cost innovation in National Aeronautics and Space Administration, International Journal of Project Management 31, 705-711, 2013.

5. Bhattacharjee, Y., Scientists decry cuts that would doom ExoMars missions, *Science* 335, www.sciencemag.org, last accessed 20 February 2016.

6. Mann, G. A., Small, N., Clarke, J. D. A. and Sheh, R. "Standardized Engineering Assessment of Field Robots in a Mars-like Environment", International Journal of field robotics. Submitted.

7. Clarke, J.D.A., Held, J.M., Dahl, A.,. Field robotics, astrobiology and Mars analogue research on the Arkaroola Mars Robot Challenge Expedition. *Proceedings from the 14th Australian Space Research Conference*, 2014.

8. Hobbs, S.W., Clarke, J.D.A., Mann, G.M. Field Testing Marsobot, A Mars Society Australia Robotics Project. *Proceedings of the 14th Australian Space research Conference*, 2014.

9. Hobbs, S.W., Campbell, K.A., Clarke, J.D.A., Astrobiology with Mars'Obot: identifying microbial life forms using ground based remote sensing. *Proceedings of the 15th Australian Space research Conference (this volume)*, 2015.

10. Barns, S.M., Delwiche, C.F.D., Palmer, J.D., Dawson, S.C., Hershberger, K.L., Pace, N.R., Phylogenic perspective on microbial life in hydrothermal ecosystems, past and present, In Bock, G.R., Goode, J.A., (Eds), *Evolution of Hydrothermal Ecosystems on Earth (and Mars?),* Ciba Foundation Symposium 202, John Wiley and Sons, Chichester, 1996.

11. Wilcox, B.H., Jones, R.M., The Muses-CN minirover and related technology. *IEEE Proceedings*, 0-7803-5846, 2000.

12. Grotzinger, S J., and 25 colleagues, "Mars Science Laboratory mission and science investigation". *Space Sci. Rev*. 170, 2012.

13. Soffen, G.A.,The Viking Project. *J, Geophys. Res.* 82, 3959-3970, 1977.

14. Bell III, J.F., and 24 colleagues, "Mars Exploration Rover Athena Panoramic Camera (Pancam) Investigation", *Journal of Geophysical Research*, 2003.

15. Soderblom, L.A., Bell III, J.F., Exploration of the Martian surface 1992-2007, in: The Martian Surface: Composition, Mineralogy and Physical Properties, ed. J.F. Bell III, *Cambridge University Press*, New York, 2008.

16. Westalla, F., and 13 colleagues, "An ESA study for the search for life on Mars", *Planetary and Space Science* 48, 181-202, 2000.

17. McKay, C.P., "The Search for Life on Mars". In: Whitter, D.C.B. (Ed). *Planetary and Interstellar Processes Relevant to the Origins of Life*, Springer Netherlands, 289pp, 1997.

18. Schinteie, R., Campbell, K.A., Browne, P.R.L., "Microfacies of stromatalitic sinter from acid-sulphate-chloride springs at Pararaki Stream, Rotorua Geothermal Field, New Zealand." *Palaeontologia Electronigia* 10, 2007.

19. Herkhenhoff, K.E., and 22 colleagues, "Textures of the soils and rocks at Gusev Crater from Spirit's microscopic imager. *Science* 305, 2004.

20. Christensen, P.R., and 10 colleagues, The Thermal Emission Imaging System (THEMIS) for the Mars 2001 Odyssey mission. Space Science Reviews, 110(1-2), 85-130, 2004.

21. Christensen, P.R., 2006. Mars Global Surveyor Thermal Emission Spectrometer Data processing user's guide V 1.6. Available from http://tes.asu.edu/mgst/document/process.pdf (last accessed 9 April 2012).

22. Adafruit, using Melexis MLX90614 Non-Contact sensors. Adafruit Learning System, *http://learn.adafruit.com/using-melexis-mlx90614-non-contact-sensors.com,* website accessed 19 may 2015.

23. Bosch Sensortec, "BMP085 digital pressure sensor datasheet", Accessed January 2015 (Online) http://dlnmh9ip6v2uc.cloudfront.net/datasheets/Sensors/Pressure/BST-BMP085-DS000-06.pdf.

24. Nguyen, T., Slonaker, J., Kadous, M., "Semi-autonomous wireless controlled robot." Capstone Senior Design Project, Indiana University, 2012.

25. Mutch, T.A., Jones, K. L., *The Martian Landscape*", NASA SP-425, 160pp, 1978.

26. Linksprite, http://store.linksprite.com/jpeg-color-camera-serial-uart-interface-ttl-custom-features, website accessed 19 December 2015.

27. Pearson, C., Thwaite, C., Russel, N., The use of small cell lithium-ion batteries for small satellite applications. *18th Annual AIAA/USU Conference on Small Satellites*, SSC04-V-3, 2004.

28. Phillips, R., Palladino, M., Courtois, C, Development of brushed and brushless DC motors for use in the Exomars drilling and sampling mechanism. *Proceedings of the 41st Aerospace Mechanisms Symposium, Jet Propulsion Laboratory*, 2012.

29. Golombek, M. P., Bridges, N. T., Moore, H. J., Murchie, S. L., Murphy, J. R., Parker, T. J., Rieder, R., Rivellini, T. P., Schofield, J. T., Seiff, A., Singer, R. B., Smith, P. H., Soderblom, L. A., Spencer, D. A., Stoker, C. R., Sullivan, R., Thomas, N., Thurman, S. W., Tomasko, M. G., Vaughan, R. M., Wänke, H., Ward, A. W., and Wilson, G. R., Overview of the Mars Pathfinder Mission: Launch through landing, surface operations, data sets, and science results. *Journal of Geophysical Research* 104(E4), 8523-8554. 1999

30. Roman, M.J., Design and analysis of a four wheeled planetary rover. *Msc Thesis,* University of Oklahoma, 2005.

31. Mishkin, A., Sojourner: an insider's view of the mars Pathfinder Mission. Berkley Books, 2003.

32. Newsom, H. E., Bishop, J., Cockell, C., Roush, T.L., Johnson, J.R., "Search for life on Mars in surface samples: Lessons from the 1999 Marsokhod rover field experiment." Journal of Geophysical Research 106, pp 7713-7720, 2001.

33. NASA National Space Science Data Center. Luna 17/lunokhod, 2005. URL http://nssdc.gsfc.nasa.gov/database/MasterCatalog?sc=1973-001A.

34. Bekker, M.G., Theory of land locomotion. *University of Michigan Press*, 1956.

35. Bekker, M.G., Introduction to terrain-vehicle systems. *University of Michigan Press,* 1969.

36. Yong, J.Y., Terramechanics and off-road vehicle engineering: terrain behaviour, off-road vehicle performance and design, 2nd edition. *Elsevier Ltd,* 2010.

37. Young, A., Lunar and planetary rovers: the wheels of Apollo and the quest for Mars. Praxis Publishing Ltd, 2007.

38. Baker, B., Reconfigurable wheels: re-inventing the wheel for the next generation of planetary rovers. *Msc Thesis,* Massachusetts Institute of Technology, 2012.

39. Squyres, S.W., Roving Mars, Scribe Publications, Victoria, 422 pp, 2005.

40. Barlow, N.G., Mars: An Introduction to its Interior, Surface and Atmosphere, *Cambridge University Press*, Cambridge, 264 pp, 2008.

41. Post, M.A., Planetary micro-rovers with Bayesian autonomy, *PhD Thesis*, York University, Toronto, 2014.

42. Baily, T., Durrant-Whyte, H., Simultaneous localization and mapping (SLAM): part II, *Robotics Automation Magazine*, IEEE 13, 108-117, 2006.

43. Arduino, http://playground.arduino.cc/main/mpu-6050#intro, website accessed 15 October 2015.

44. Hand, E. Thinking inside the box. *Science* 348, 176-177, 2015.

45. Heidt, H., Puig-Suari, J., Moore, A.S., Nakasuka, S., Twiggs, R.J., Cubesat: A new generation of Picosatellite for education and industry low-cost space experimentation, *14th Annual/USU Conference on Small Satellites,* 2000.

46. Segret, B., Vannitsen, J., Agnan, M., Porquet, A., Sleimi, O., Deleflie, F., Miau, J.J., Juang, J.-C., and Wang, K. BIRDY: an interplanetary CubeSat to collect radiation data on the way to Mars and back to prepare the future manned missions. *Proceedings SPIE 9150, Modeling, Systems Engineering, and Project Management for Astronomy VI*, 91501N (August 4, 2014); doi:10.1117/12.2056114.

47. Cospar 2005. Cospar Planetary Protection Policy. Address when accessed 6/6/15 http://w.astro.berkeley.edu/~kalas/ethics/documents/environment/COSPAR%20Planetary%20Protection%20Policy.pdf.

48. Anderson, R.C., Haldermann, A.F.C., Dohm, J. and Huntsberger, T., "A Dress Rehersal for the 2003 Mars Exploration Rovers", *Mars Analog Research*, San Diego, California, 2006.

Analysis of Multiple Processes in Martian Gullies.

S.W. Hobbs [1], D.J. Paull[1], J.D.A. Clarke [2]

[1] *School of Physical, Environmental and Mathematical Sciences, University of New South Wales, Australian Defence Force Academy, Northcott Drive, Canberra, Australian Capital Territory 2600, Australia*

[2] *Mars Society Australia. P.O. Box 327, Clifton Hill, VIC 3068, Australia.*

Summary: Similarities of Martian gullies to terrestrial counterparts, and their superposition on young features, have been interpreted as evidence that liquid water has acted as an erosive process in Mars' recent past. We used a GIS to examine and analyse multiple datasets to study gullies in Noachis Terra. Previous comparison to terrestrial gullies indicated that although liquid water had a major influence in gully erosion, other significant processes were also instrumental in their evolution. Here we present the results of our ongoing research of Noachis Terra gullies, aimed at quantifying the extent and chronology of different processes operating on these features. We found evidence for wet-based processes subsequently modified by non-fluvial processes. Erosion at many studied sites appeared to be periodic and varied with magnitude. Our study indicates that global assumptions may not work at the local scale and that local environmental conditions must be taken into account before any meaningful analysis of gullies can be carried out.

Keywords: Mars, fluvial, gully, erosion, Noachis Terra.

Introduction

The discovery of young features on Mars resembling terrestrial, water carved, hillside gullies carries profound implications on the presence of liquid water in recent times [1]. Since their discovery, many hypotheses for Martian gully formation and evolution have been proposed. These have included non-fluvial processes such as dry mass wasting [2], pressurised CO_2 based flows [3, 4, 5] or frosted granular flow [6]. Fluvial hypotheses were aquifer-based groundwater seepage [1], geothermal heating [7], melting of snowpacks [8, 9], near-surface ground ice [10], or degradation of ice-rich material, such as the Latitude Dependent Mantle (LDM) [11, 12, 13].

Recent work [5, 14] on contemporary gully activity in conditions that appeared unfeasible for liquid water erosion in current Martian climatic conditions, indicated a CO_2 frost-based mechanism for gully erosion, with CO_2 frost thought to have lowered the angle of repose for gully slopes. This would enable mass flow and subsequent erosion at slope angles below the angles required for dry mass wasting, which had previously been cited as evidence for liquid water [15]. Observations of seasonal accumulation of CO_2 frost in favourable temperature ranges also seemed to support this hypothesis [5, 14], negating the need to invoke fluvial mechanisms for gully erosion. There is however a growing body of evidence indicating liquid water exists on Mars today [16, 17]. Moreover Martian gully morphology, such as V-shaped channels [11], incision depths of tens of metres [18], concave long profiles [19, 20] and sinuosity [21] are consistent with formation through fluvial processes [11, 13, 15, 19, 20, 22, 23 and 24]. Additionally, temperature and obliquity modelling indicate historic planetary obliquity excursions allowed for deposition of ice-rich material in regions

equatorward of the poles, such as the mid-latitudes, where gullies are found [9, 10, 11, 12]. Subsequent melting of this ice rich material in the Martian mid-latitudes would have provided favourable conditions for liquid water erosion that may no longer operate during lower obliquity periods, such as present day Mars [9, 10, 11, 12, 13, 25]. This raises the possibility of multiple processes operating on Martian gullies in different periods of time. In this work we explore the possibility of multiple processes by investigating small-scale changes on a Noachis Terra gully site using high resolution HiRISE imagery and a digital elevation model (DEM).

Our study area (hereafter termed "the primary site") is a ~13 km diameter fresh looking crater centred at 40° 21' 20" S and 20° 05' 30" E, in the Martian southern hemisphere (Fig. 1A). Gullies are located on the pole facing rim of the crater (Fig. 1B). We previously investigated four of these gullies and compared them with terrestrial analogues on the escarpment of Lake George, New South Wales [26]. Additionally, we placed our findings in a wider context by conducting analysis on semi-arid and sub-humid gullies in Island Lagoon, South Australia and Pasture Hill, New Zealand, respectively [18]. Our previous results showed that the equator-facing rim of this crater possesses features we assessed to have been formed by flows of volatile poor material, and we classified these as dry ravines due to their similar morphology to terrestrial dry talus flows. We conducted slope and hydrologic analysis on the gullies at this crater, using Manning and Darcy-Weisbach equations in order to infer flow velocities and discharge rates, and compared them with a similar analysis performed at semi-arid and temperate gully settings [27]. We found that our studied Martian gullies shared similar characteristics to terrestrial gullies and concluded that their sinuous, V-shaped channels and smooth, concave-up profiles indicate that water was the primary erosive agent. However, we also found evidence of additional different types of erosive processes. We thus concluded [18, 22-23] that:

- Our Martian gullies were consistently located in or near ice related features;
- Gully morphology appears dependent on presence and thickness of erodable slope material – an observation supported by the fact that none of our gully channels had eroded to bedrock;
- Although liquid water appeared as the dominant erosive agent, we found also evidence of other types of erosive processes;
- The Martian gullies we studied may have evolved and been eroded via complex interaction of multiple water, ice and dry processes as separate episodes over time;
- Gully slopes on Mars and Earth appeared inherited to some degree from the host environment. This may have implications for dry/water based slope angle inferences (e.g., angle of repose, static *vs*. kinetic friction)
- Gully shape appears dependent on the local geology, climate and environment, requiring gully models and inferences to be placed in the context of the environment of the study site.

In this work we build from our earlier findings, and attempt to further characterise the types of erosive processes that have acted on the primary site. We also refine the chronological sequence of these processes.

Methods

We used the orthorectified HiRISE imagery and digital elevation model (DEM) from [26] to analyse 24 gullies on the pole-facing wall of the primary site. The 1 m resolution DEM was derived from a HiRISE stereo pair (ESP_011817_1395 and ESP_011672_1395) created using NASA Ames Stereo Pipeline [28, 29] using the NASA Ames Stereo Pipeline (ASP) method by [30]. The ASP methodology uses automated geodesy and stereogrammetry tools requiring limited human input to generate high quality 3D surface models useful for scientific research [30]. We validated our ASP-created DEM for accuracy by comparing spot heights between the HiRISE DEM and a ready-made areoid-referenced HRSC DEM (H2639_0000_DA4). Although height measurements from the DEMs were comparable within the limits of the resolution provided by the HRSC DEM, shadowed regions of the HiRISE DEM produced frequency noise and spurious artefacts. These were mitigated by applying a 3 X 3 low pass filter to reduce frequency noise [22], and by avoiding artefact prone regions of the DEM produced from the HiRISE stereo pair. Surficial analysis of the gullies was conducted using a HiRISE image at a resolution of 50 cm/pixel, orthorectified from our HiRISE DEM.

The appearance of polygonal imprinting of Martian terrains has been interpreted to infer the presence of ice-rich material in Martian mid-latitude areas [11, 12, 13, 28, 29]. Observations of similar polygonal terrain within terrestrial cold-based environments has been used to support this hypothesis [13, 28], with much of the ice-rich material existing on Mars as "latitude dependent mantle" (LDM) [13, 30]. In our analysis we use the presence and degradation of polygonal terrain coexisting with features diagnostic of dry mass wasting (spur and gully morphology, homogenous talus flows, 31, 32), previously observed at our study site, to determine the chronology of erosion. We also infer the type of erosive processes acting on the gullies at the primary site by classifying our gully channels and depositional aprons according to the criteria listed in Table 1 (illustrated in Fig. 2 and 3).

Table 1: Classification of gullies at the primary site.

Feature	Type	Definition	Example:
Channel	1	Channel embedded within crater wall; imprinted with polygons	Fig. 2A
Channel	2	Channel embedded within crater wall; polygons partially collapsed	Fig. 2A
Channel	3	Channel embedded within crater wall; little or no polygon imprinting	Fig. 2B
Channel	4	Superposed channel; little or no polygon imprinting	Fig. 2C
Apron	A	Degraded depositional apron imprinted with polygons (inactive, wet-based origin)	Fig. 3B, C
Apron	B	Depositional apron displaying small scale channelling or braiding (likely wet-based)	Fig. 3A, B
Apron	C	Homogenous depositional apron with no polygonal imprinting, channelling or braiding (likely dry-based flow)	Fig. 3A, B

Type 1-3 channels are defined by the main gully channel incised within the crater wall, with the degree of polygonal imprinting used to separate the channel type (Fig. 2A-B). Type 4 channels are classified based on features contained within a Type 1-3 channel, with no polygonal imprinting (Fig. 2C). Fig. 2D-F shows a transitional Type-2 channel exhibiting partially collapsed polygons in its upper portions (Type 2), and lack of these features downslope (Type 3).

We were able to identify three distinct types of depositional aprons at our study site, classified as Type A-C. Type A aprons are the most heavily degraded, entirely imprinted with

polygons (Fig. 3B, C). Type B aprons are fresher (Fig. 3A, B), and exhibit some form of small scale channel incision or braiding that may indicate fluvial processes [1, 23]. Type C aprons showed the simplest morphology, with no polygonal overprinting, incision or braiding (Fig. 3A, B).

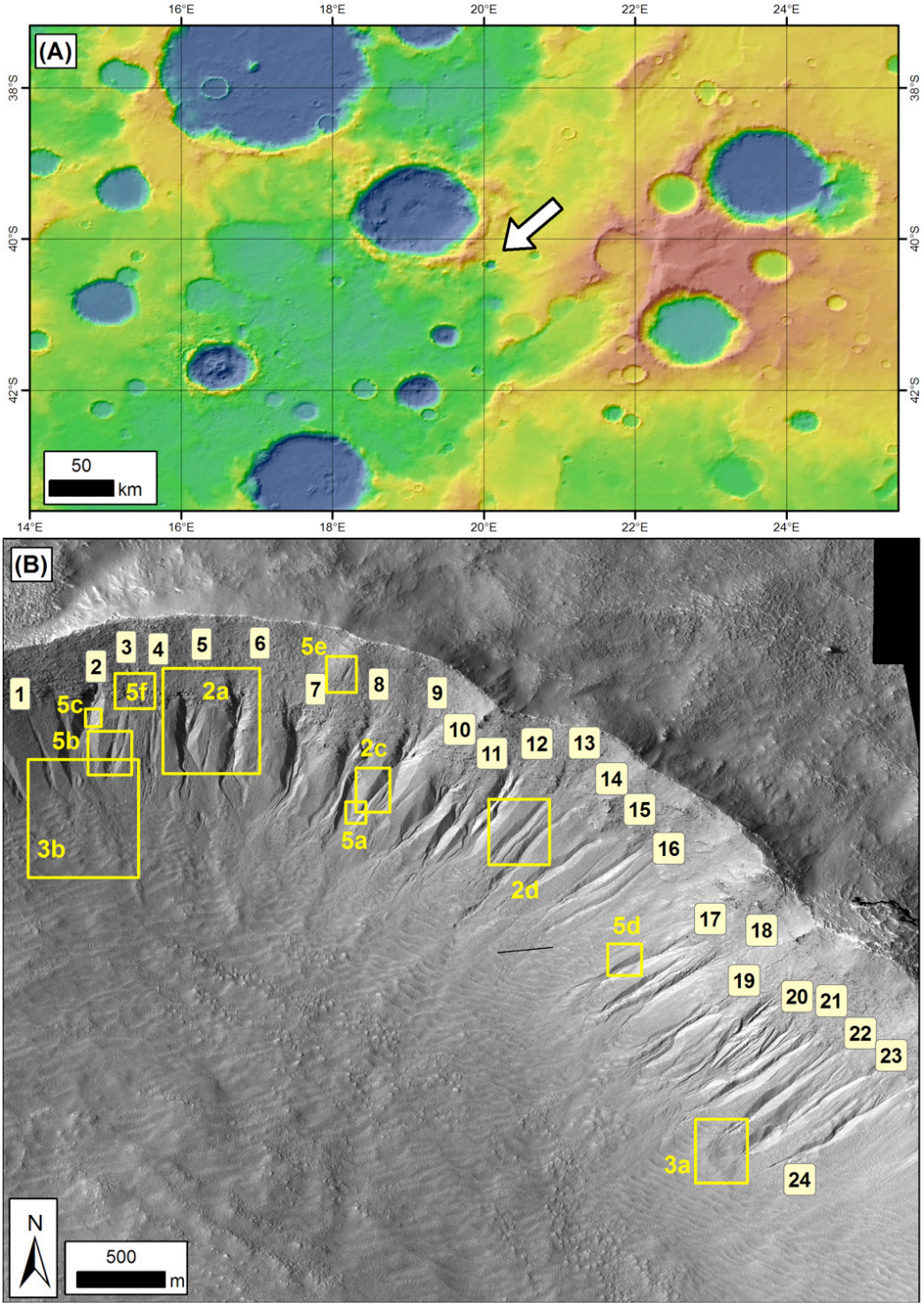

Fig 1. (A) Overview of gully study site in Noachis Terra. (B) View of 24 studied pole-facing gullies (numbered). Extents of Figs. 2,3 and 5 are shown as rectangular frames.

Results and Interpretation

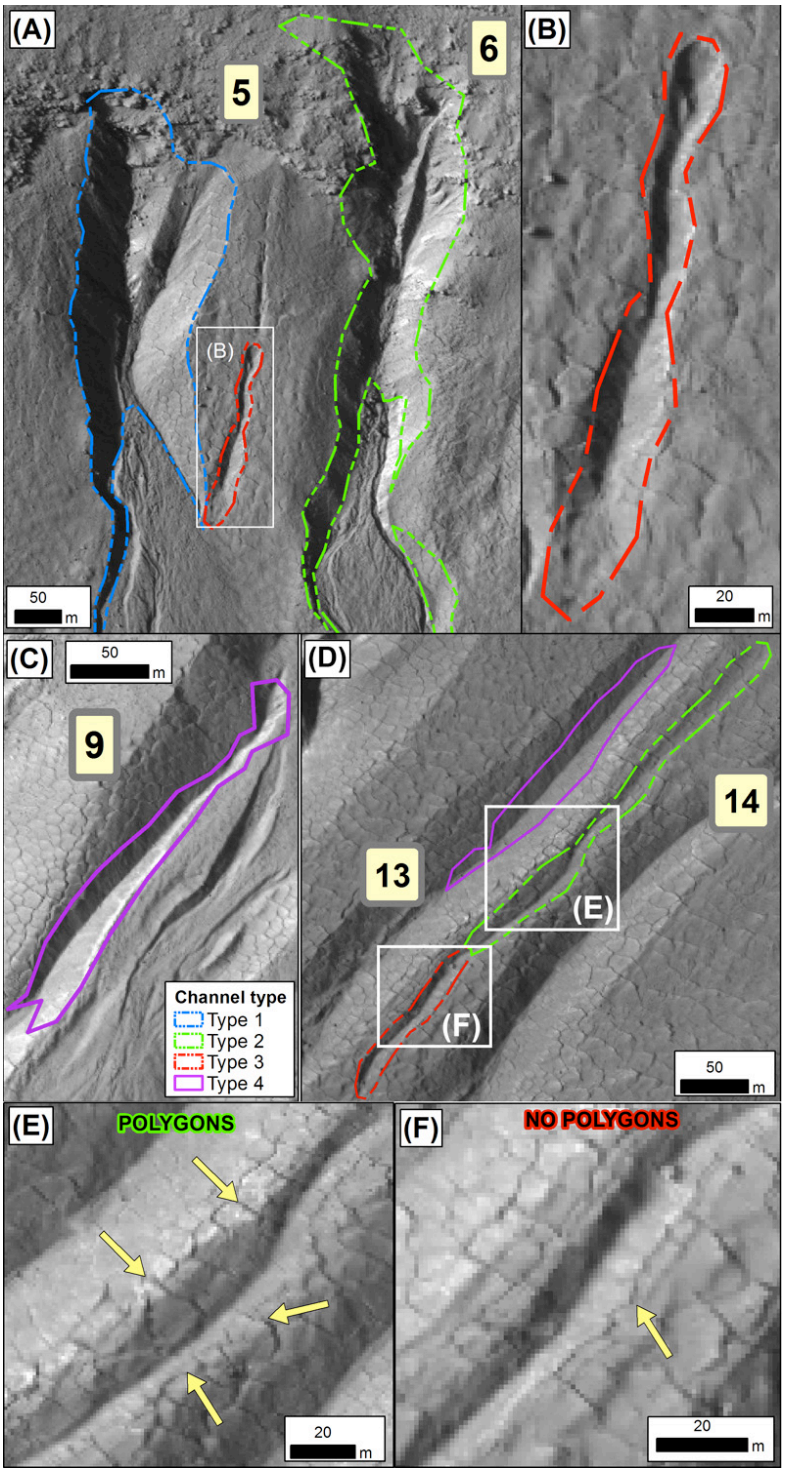

Fig 2. Classification of gully channels. (A) Type 1 (dashed blue). Type 2 (dashed green). Type 3 (dashed red). (B) Close-up view of channel of Type 3. (C) Type 4 channel superposed within the larger Type 1 channel of gully 9. (D) View of a ~15 m wide channel with diverse morphology. Extents of parts E and F are shown as rectangular frames. (E) Upper portion of the channel shown in part D with yellow arrows highlighting polygonal imprinting (Type 2). (F) Lower portion of the channel shown in part D highlighted by a yellow arrow and showing an absence of polygons.

Figs. 4-5 show the results of our gully channel and apron classification. Our observations suggest gully evolution through multiple erosive episodes. The main gully channels were

predominantly Type 1 or Type 2; we were only able to identify one Type 3 channel, located east of Gully 5 (Fig. 2A-B). There are more (14) Type 1 gullies than Type 2 gullies (10) and we were unable to identify a trend in Type 1-2 channels with regards to gully orientation. We identified eight Type A aprons at our study site. These aprons extended further downslope than the Type B and C aprons and resided on slopes ranging from 6-21^{o}, below the angle of kinetic friction [15]. The Type A apron below Gully 1 was the only feature that directly deposited below a gully channel (Fig. 4). The remaining Type A aprons were superposed by Type B and/or Type C aprons. The degradation, polygonal overprinting (Fig. 3B, detail Fig. 3C) and superposition of Type A aprons by fresher deposits indicate these represent an early period of gully evolution. The size and extent of these aprons suggest the gully erosion required to form them may have been more extensive than subsequent episodes of gully erosion. Episodic erosion is also supported by the presence and superposition of Type B and C aprons. Type C aprons appeared to represent the most recent episode of gully erosion as suggested by their superposition on other gully apron types (Fig. 6A). In most cases Type C aprons are associated with the small, superposed Type 4 channels with little polygonal overprinting (Gully 3, 9, 11, 23 and 24, Figs. 4-5A, B, Fig. 6A) though we found additional Type-C aprons associated with Type 1 (Gully 4 and 14, Fig. 4A) or Type 2 channels (Gullies 2, 18, Fig. 4A and 19, Fig. 4B). We also note the presence of Type B aprons associated with Type 4 channels (Gully 10 and 11, Fig. 4A-B) as well as Type C aprons at the base of Type B aprons (Gullies 6 and 10, Fig. 4A-B, 17 and 21, Fig. 5A-B). Additionally, Gullies 22-23 (Fig. 3A) and 18-19 (Fig. 5B), possess adjacent type B and C aprons.

Detailed analysis of two Type 4 channels within Gully 3 show an additional Type C apron (lower red arrow, Fig. 6B) associated with a ~30 m long scale mass wasting feature (upper left red arrow Fig. 5B) below a Type C apron at the base of the channels. This feature suggests erosion at tens of metres scale has taken place at our study site. Type B aprons were found throughout the study site. These aprons are predominantly associated with gully channel types 1-3 (Fig. 4-5A, B), though were also located at the base of five Type 4 channels (Gullies 5, 13, 15, 18 and 22). Of these, Gully 18 also possesses a Type C apron adjacent to the Type B apron (Fig. 3A, 6A).

Fig. 6 C-F shows tens of metres scale features found at our study site. Fig. 6C shows a ~20 m wide patch of polygonal terrain within Type 2 Gully 2. This patch represents a relict polygonal surface that likely formerly covered the entire gully channel and is currently being removed through subsequent mass wasting processes. Slope angles for the channel wall in this area (25-32^{o}) approach those we previously postulated to support dry mass wasting [27]. High slope values (30-35^{o}) may also explain the region of collapsed channel wall within Type 2 Gully 17 (Fig. 6D). Polygonal terrain is more extensive here than at Gully 2, suggesting mass wasting rates for this gully may have been lower. We identified a ~20 m wide gully located within rocky material above the heads of Gullies 7 and 8 (Fig. 6E).

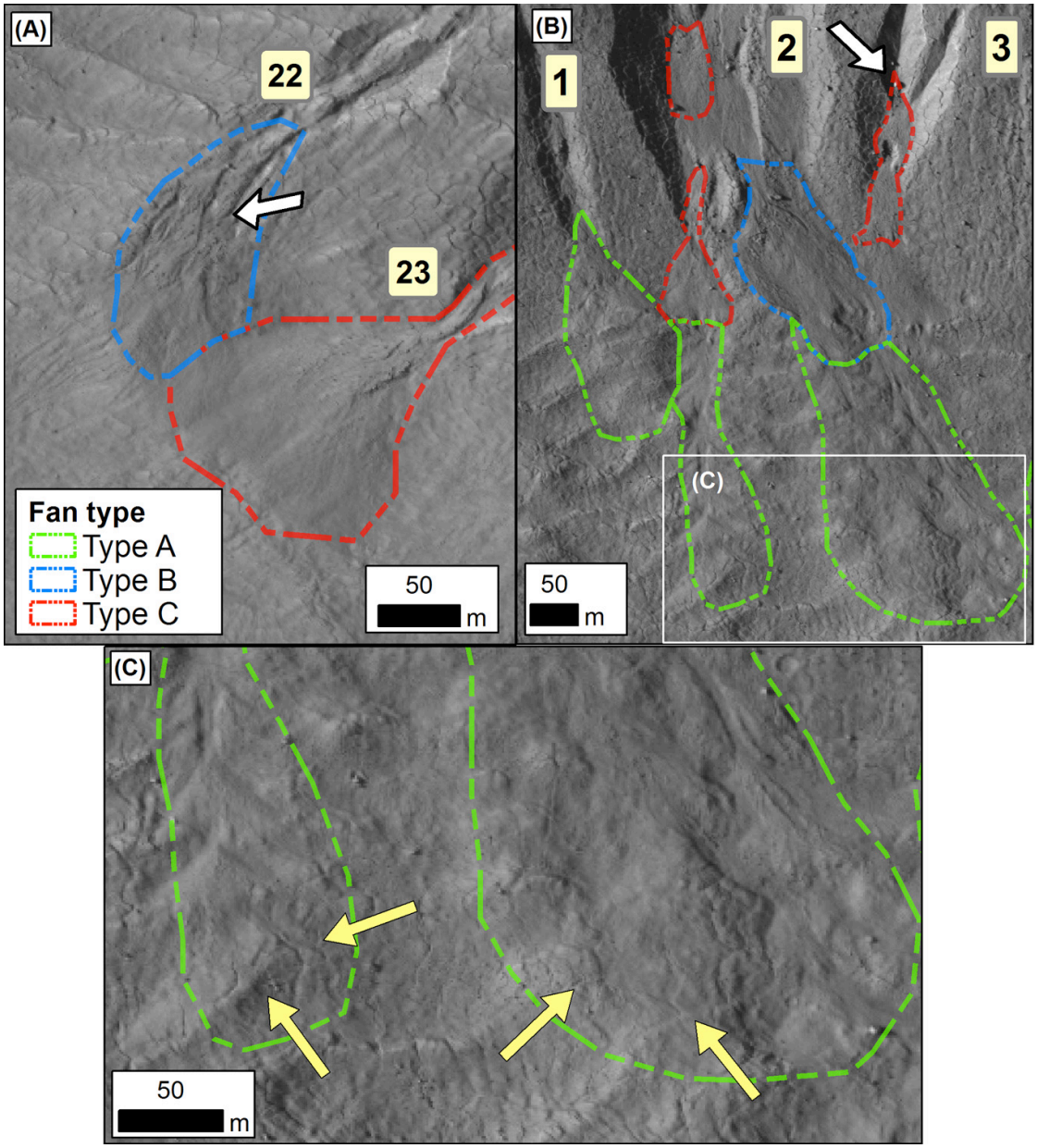

Fig 3. Classified gully aprons at our study site. (A) Type A (dashed blue apron with braiding marked by a white arrow), Type B (dashed red) (B) Type A, B, and C (dashed green) aprons located near Gullies 1-3.

The morphology of this feature changes from a 50 m long alcove (White arrow) to ~ 3 m wide channels (black arrow). This change in morphology coincides with a change in texture of the underlying regolith. We observed a dependence of gully morphology on underlying regolith in our previous research [18, 26] and such morphological changes have also been observed elsewhere on Mars [24].

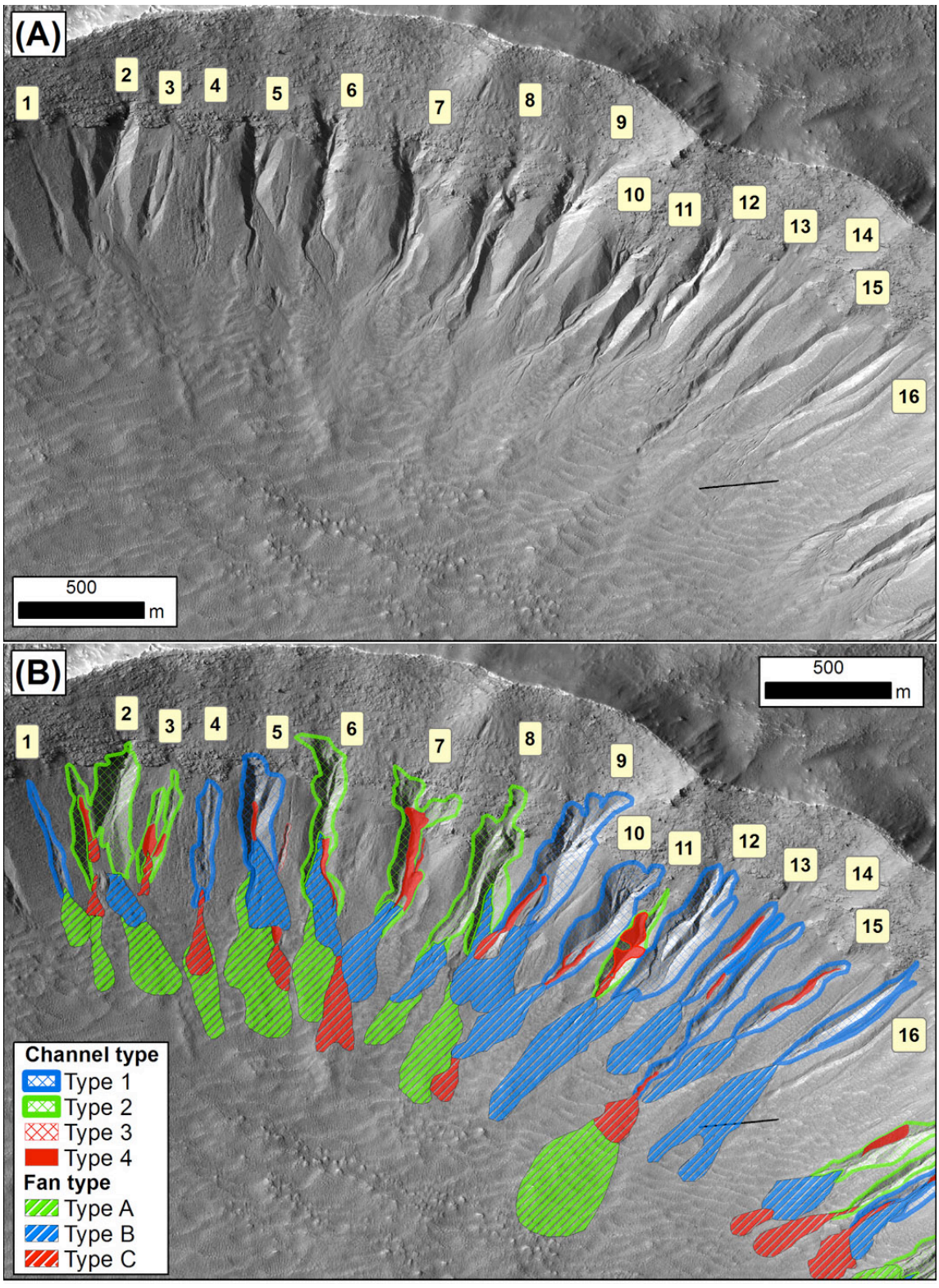

Fig 4. Classified gully channels and aprons at our study site. (A) Detailed view of Gullies 1-16. (B) Classification for Gullies 1-16.

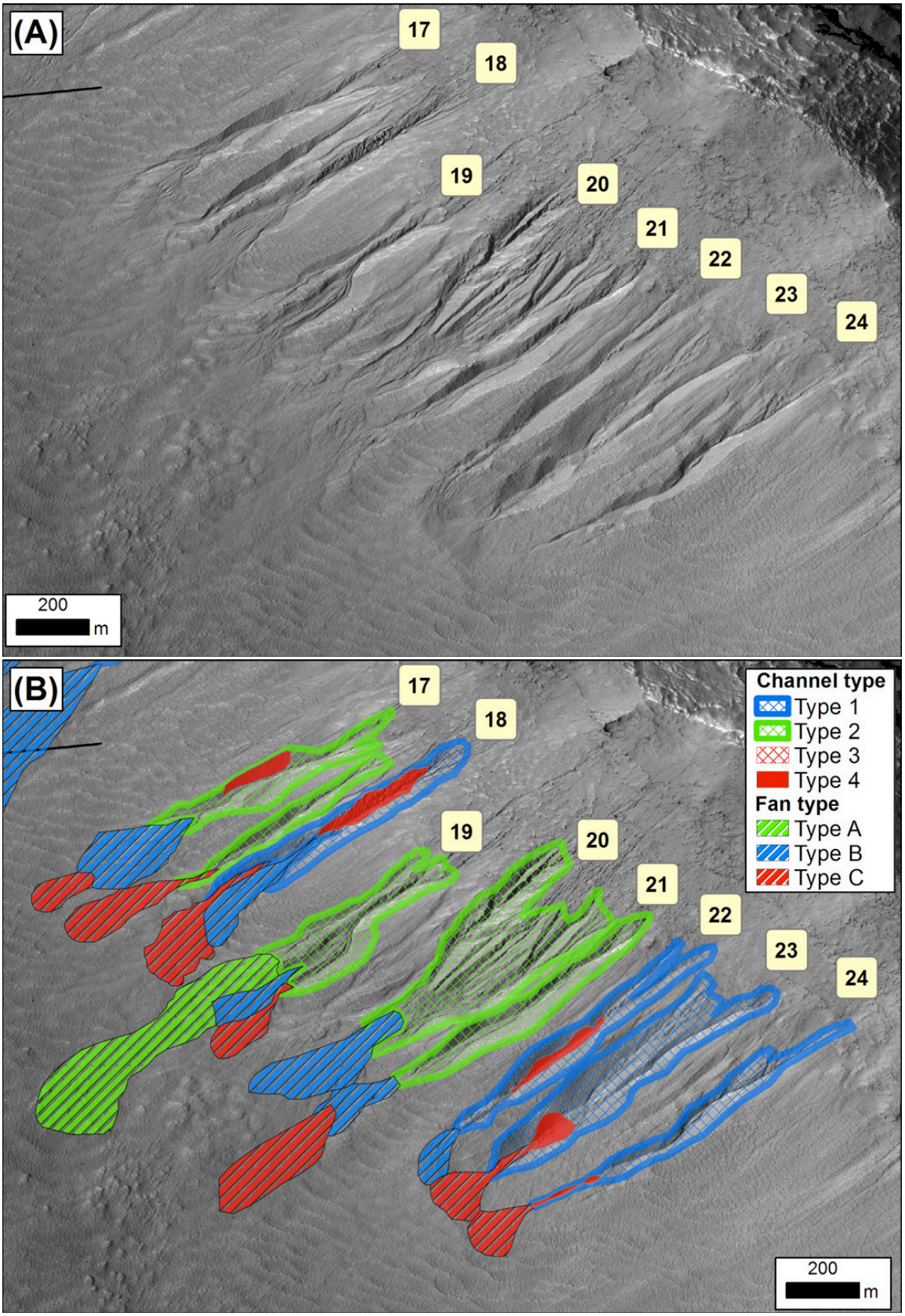

Fig 5. (A) Detailed view of Gullies 17-24. (B) Classification of Gullies 17-24.

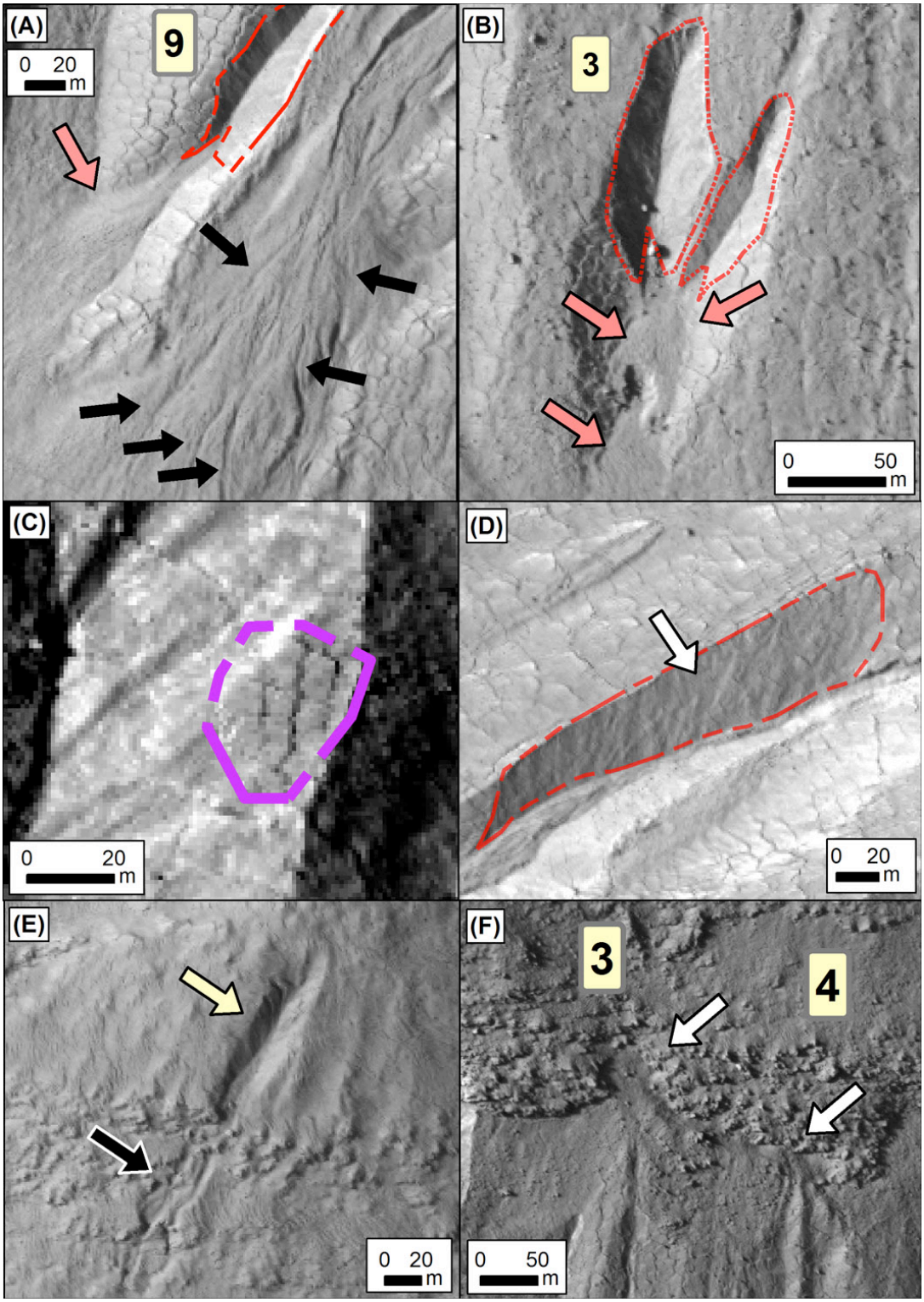

Fig 6. Sub-100 m-scale features at our study site. (A) Superposition of Type C apron over older material (red arrow) from a Type 4 channel in Gully 9. Black arrows denote the braiding within a nearby Type B apron. (B) Detail of Type 4 channels within Gully 3. Upper right red arrow marks the location of a Type C apron at the base of these channels. An additional Type C apron resides downslope (lower red arrow) below a ~10 m wide mass wasting feature (upper left red arrow). (C) A ~20 m wide patch of polygonal terrain within Type 2 Gully 2. (D) Collapsed channel wall within Type 2 Gully 17. (E) A 50 m long gully alcove residing within rocky material. The morphology of this feature changes from a 50 m long alcove (white arrow) to ~ 3 m wide channels (black arrow). (F) Cross drainage feature (white arrows) at the heads of Gullies 3 and 4.

We suggest the morphology of this gully has been affected by changes in underlying material. We also noted the sinuous channels of this gully drain into the alcove of Gully 7 (Fig. 1B), suggesting fluvial erosion with liquid water as a major component, as opposed to CO_2 frost or dry mass wasting origin. Additional evidence for fluvial activity was observed at the heads of Gullies 3 and 4 (Fig. 6F). A cross drainage feature (white arrows) was identified at the heads of these gullies and appeared to track directly beneath a rocky layer and feed into the channels of Gullies 3 and 4. It is likely liquid water has followed a local topographic low in this area that has facilitated cross drainage into two gullies.

It has been suggested that initial slope collapse over debris-covered ice at our primary site would lead to exposure and subsequent melting [29]. This would provide a feedback loop, exposing more ice that would melt and lead to further slope failure until the store of volatiles was exhausted. The conclusion of this process was postulated to leave lag-deposits behind, as well as deposit material at the channel base [29]. Although plausible in some cases, we found this hypothesis fails to account for the sub-metre drainage channels within our classified Type B aprons (Fig. 3A), the presence of a small gully we observed embedded within rocky material above our studied gullies (Fig. 6E), and the cross drainage occurring above Gullies 3 and 4 (Fig. 6F). These features instead suggest that meltwater may have also originated from this rocky layer. We also note that our studied gullies originate from below this unit, further suggesting a relationship between the rocky layer and the gullies. Our observations of differing morphology between gully channels, such as smooth walled Type 4 channels embedded within overprinted Type 1 channels (Figs. 4-5A, B) suggest a more complex regime of erosion at our study site.

Our analysis of the relationship between polygonal terrain and the morphology of our gullies revealed trends in gully erosion at our study site. Type 1 and 2 channels were embedded within the crater wall and we infer these to be predominantly water-based. This is due to evidence of polygon imprinting as well as V-shaped morphology, and presence of smaller sub-channels draining onto many of the gully heads. We suggest Type 1 and to a lesser extent, Type 2 valleys to have formed during a period of high obliquity of the planetary rotation axis. Degradation of ice-rich material in this environment would have provided liquid water for gully erosion, as postulated by previous research [9, 10, 11, 12, 13, 25]. Observed evidence for superposition of aprons at the base of the Type 1 and 2 channels indicate that they were carved by multiple erosive episodes occurring over a period of time. We also suggested multiple erosive events is in our previous hydrological analysis of this site [27]. We note that the Type A aprons extended further downslope than any of the identified Type B or Type C aprons, possibly suggesting greater erosive power that has facilitated a larger amount of deposition.

We noted the presence of Type 4 channels and subsequent depositional aprons superposing Type 2 channels (illustrated in Fig. 6A). The Type 4 channels were typically associated with Type C aprons, suggesting that these channels may be associated with, or modified by, dry mass wasting processes. It is possible the fluvial processes, possibly as suggested by [32] gave way to mass wasting of lag deposits once the supply of volatiles was exhausted. We considered whether post-fluvial CO_2 activity may have operated on these channels. The lack of polygonal imprinting and homogenous Type-C aprons is similar in appearance to dry mass wasting deposits [31], although it is also possible these aprons may have been formed by deposition of lag material as suggested by [29]. This also may account for Type C aprons depositing at the base of gully channels thought to be carved by liquid water (Type 1 Gullies 3 and 13, Fig. 4A, B). Thus Type C aprons may be consistent with fluvial erosion of ice-rich material that left behind lag deposits. During our investigation of the terrestrial gully sites [18, 26, 27], we observed evidence of subsequent channel modification that occurred after their formation by liquid water [18, 22]. We also observed

abundant evidence of complex erosion involving more than one process, such as frost shattering and dry mass wasting [18, 22]. Consistent with recent literature [19, 29, 33, 34], our study suggests that Martian gully formation is not necessarily restricted to just one process.

Conclusion

We analysed 24 gullies on the northern wall of a fresh looking crater in Noachis Terra. Our analysis involved classifying the channels and depositional aprons with features diagnostic of the past presence of liquid water, such as presence and degradation of polygonal terrain or braiding within depositional aprons, and existence of features diagnostic of dry mass wasting (spur and gully morphology, homogenous talus flows). We found a diverse morphology at our study site, and evidence for multiple episodes of gully activity. Early rates of gully activity were likely to be higher than subsequent events, but we were unable to conclusively identify a transition from "wet-based" erosion to dry mass wasting. We suggest that gullies at our study site have evolved through a complex interaction of a number of water, ice or dry processes.

Acknowledgements

We gratefully acknowledge the HiRISE team for providing the data used in this work, and Monica Pondrelli for earlier processing of the HiRISE-derived DEM. Critical reviews of this manuscript by Monica Pondrelli, Miguel de Pablo Hernandez and Graziella Caprarelli helped to improve the presentation of this paper.

References

1. Malin, M.C. & Edgett, K.S., Evidence for recent groundwater seepage and surface runoff on Mars, *Science*, 288(5475), 2330-2335, doi: 10.1126/science.288.5475.2330, 2000.

2. Treiman, A.H., Geologic settings of Martian gullies: Implications for their origins. *J. Geophys. Res. [Planets]* 108(E4), 8031, doi: 8010.1029/2002je001900, 2003.

3. Hoffman, N., White Mars: A new model for Mars' surface and atmosphere based on CO2. *Icarus* 146(2), 326-342, 2000.

4. Musselwhite, D.S., Swindle, T.D. & Lunine, J.I., Liquid CO_2 breakout and the formation of recent small gullies on Mars, *Geophysical Research Letters*, 28(7), 1283-1285, doi: 10.1029/2000gl012496, 2001.

5. Dundas, C.M., Diniega, S., Hansen, C.J., Byrne, S., & McEwen, A.S., Seasonal activity and morphological changes in Martian gullies. *Icarus* 220, 124-143, 2012.

6. Hugenholtz, C., Frosted granular flow: A new hypothesis for mass wasting in Martian gullies. *Icarus* 197(1), 65-72, 2008.

7. Hartmann, W.K., Thorsteinsson, T., Sigurdsson, F., & Martian hillslide gullies and Icelandic analogues. *Icarus* 162(2), 259-277, 2003.

8. Christensen, P.R., Formation of recent Martian gullies through extensive melting of water-rich deposits. *Nature* 422(6927), 45-48, 2003.

9. Williams, K.E., Toon, O.B., Heldmann, J.L., Mckay, C., & Mellon, M.T., Stability of mid-latitude snowpacks on Mars, *Icarus*, 196(2), 565-577, doi: 10.1016/j.icarus.2008.03.017, 2008.

10. Costard, F., Forget, F., Mangold, N., & Peulvast, J.P., Formation of recent Martian debris flows by melting of near-surface ground ice at high obliquity. *Science* 295(5552), 110-113, 2002.

11. Dickson, J.L., & Head, J.W., The formation and evolution of youthful gullies on Mars: Gullies as the late-stage phase of Mars' most recent ice age. *Icarus* 204(1), 63-86, 2009.

12. Schon, S.C., Head, J.W., & Keys to gully formation processes on Mars: Relation to climate cycles and sources of melt-water. *Icarus* 213(1), 428-432, 2011.

13. Schon, S.C., & Head, J.W., Gasa impact crater, Mars: Very young gullies formed from impact into latitude-dependant mantle and debris-covered glacier deposits? *Icarus* 218, 459-477, 2012.

14. Raak, J., Reiss, D., Appere, T., Vincendon, M., Ruesch, O. & Hiesinger, H., Present-day seasonal gully activity in a south polar pit (Sisyphi Cavi) on Mars. *Icarus*, in press, doi: 10.1016/j.icarus.2014.03.040, 2014.

15. Lanza, N.L., Meyer, G.A., Okubo, C.H., Newsom, H.E. & Wiens, R.C., Evidence for debris flow gully formation initiated by shallow subsurface water on Mars, *Icarus*, 205(1), 103-112, 2010.

16. McEwen, A.S., Ojha, L., Dundas, C.M., Mattson, S.S., Byrne, S., Wray, J.J., Cull, S.C., Murchie, S.L., Thomas, N. & Gulick, V.C., Seasonal flows on warm Martian slopes, *Science*, 333(6043), 740-743, doi: 10.1126/science.1204816, 2011.

17. Martin-Torres, F.J., et al., Transient liquid water and water activity at Gale Crater on Mars. *Nature Geoscience Letters,* 8, 357-360, 2015.

18. Hobbs, S.W., Paull, D.J. & Clarke, J.D.A., A comparison of semi-arid and sub-humid terrestrial gullies with gullies on Mars: Implications for Martian gully erosion, *Geomorphology*, 204, 344-365, doi: 10.1016/j.geomorph.2013.08.018, 2014a.

19. Yue, Z., Hu, W., Liu, B., Liu, Y., Sun, X., Zhao, Q., & Di, K., Quantitative analysis of the morphology of Martian gullies and insights into their formation. *Icarus,* 243, 208-2014, 2014.

20. Conway, S.J., Balme, M.R., Kreslavsky, M.A., Murray, J.B., & Towner, M.C., The comparison of topographic long profiles of gullies on Earth to gullies on Mars: a signal for water on Mars. *Icarus,* 253, 189-204, 2015.

21. Mangold, N., Mangeney, A., Migeon, V., Ansan, V., Lucas, A., Baratoux, D. & Bouchut, F., Sinuous gullies on Mars: Frequency, distribution, and implications for flow properties, *Journal of Geophysical Research-Planets*, 115, Artn E11001, doi: 10.1029/2009je003540, 2010.

22. Kolb, K.J., McEwen, A.S. & Pelletier, J.D., Investigating gully flow emplacement mechanisms using apex slopes, *Icarus*, 208(1), 132-142, 2010.

23. Johnsson, A., Reiss, D., Hauber, E., Hiesinger, H. & Zanetti, M., Evidence for very recent melt-water and debris flow activity in gullies in a young mid-latitude crater on Mars, *Icarus*, 235, 37-54, 2014.

24. Harrison, T.N., Osinski, G.R., Tornabene, L.L., & Jones, E., Global documentation of gullies with the Mars Reconnaissance Orbiter Contect Camera and implications for their formation. *Icarus,* 252, 236-254, 2015.

25. Dickson, J.L., Fassett, C.I., Head, J.W., Forget, F., & Madeleine, J-B., Formation of gullies on mars by water at high obliquity: quantitative integration of global climate models and gully distribution. *Proceedings of the 46th Annual Lunar and Planetary Science Conference*, The Woodlands, Texas. Lunar and Planetary Institute, Houston, TX, abst 1035, 2015.

26. Hobbs, S.W., Paull, D.J., & Clarke, J.D.A., The influence of slope morphology on gullies: Terrestrial gullies in Lake George as analogues for Mars. *Plan. Space Sci.*, 81, http://dx.doi.org/10.1016/j.pss. 2012.10.009, 2013.

27. Hobbs, S.W., Paull, D.J., & Clarke, J.D.A., A hydrological analysis of terrestrial and Martian gullies: Implications for liquid water on Mars, *Geomorphology*, 226, 261-277, 2014b.

28. Broxton, M.J. & Edwards, L.J., The Ames Stereo Pipeline: Automated 3D surface reconstruction from orbital imagery. *Proceedings of the 39th Lunar and Planetary Science Conference*, March 10-14 2008, League City, TX, abst 2419,2008.

29. Moratto, Z.M., Broxton, M.J., Beyer, R.A., Lundy, M. & Husmann, K., Ames stereo pipeline, NASA's open source automated stereogrammetry software., *Proceedings of the 41st Annual Lunar and Planetary Science Conference, Lunar and Planetary Institute*, abst 2364, Houston, TX., 2010.

30. Broxton, M.J., Beyer, R.A., Moratto, Z., Lundy, M. & Husmann, K., The Ames Stereo Pipeline: NASA's Open Source Automated Stereogrammetry Software, A part of NASA NeoGeography Toolkit, Version 2.00, *Intelligent Robotics Group*, NASA Ames Research Centre, 88 pp, 2011.

31. Mustard, J.F., Cooper, C.D. & Rifkin, M.K., Evidence for recent climate change on Mars from the identification of youthful near-surface ground ice, *Nature,* 412(6845), 411-414, 2001.

32. Conway, S.J., & Balme, M.R., Decameter thick remnant glacial ice deposits on Mars. *Geophys. Res. Lett*., 41, doi: 10.1002/2014GL060314, 2014.

33. Kreslavsky, M.A. & Head, J.W., Mars: Nature and evolution of young latitude-dependent water-ice-rich mantle, *Geophys. Res. Lett*., 29(15), Artn 1719, 2002.

34. Hungr, O., et al., A review of the classification of landslides of the flow type. *Environ. Eng. Geosci.* VII(3), 221-328, 2001.

35. McEwen, A.S., and 32 colleagues, A closer look at water-related geologic activity on Mars, *Science*, 317(5845), 1706-1709, 2007.

Evaluating the Performance of Field Science in an Analogue EVA suit: Stromatolite Identification by Geologists and Non-Geologists

Jonathan D. A. Clarke[1], Maureen Cooper[2], Simon George[3], Steve Hobbs[2], Sarah Houlahan[3], Guy M. Murphy[2], Ken Silburn[2], Doug Sprigg[4], Marg Sprigg[4], and James Waldie[2, 5]

[1] *Mars Society Australia, 43 Michell St, Monash, ACT 2904, Australia*
[2] *Mars Society Australia, P.O. Box P.O. Box 327 Clifton Hill, VIC 3068, Australia*
[3] *Department of Earth and Planetary Sciences, Macquarie University, Sydney, NSW 2109, Australia*
[4] *Arkaroola Wilderness Sanctuary, Private Bag 106, Port Augusta, SA 5700, Australia*
[5] *School of Aerospace, Mechanical & Manufacturing Engineering, RMIT University, GPO Box 2476, Melbourne VIC 3001, Australia*

Summary: Understanding the constraints of field work while in a space suit is critical when considering crewed exploration on the surface of the Moon, Mars and other accessible Solar System bodies. Mars Society Australia studied the effect of simulated space suits on field work during the Arkaroola Mars Robot Challenge Expedition in 2014. A simulated EVA suit from the Victorian Space Science Education Centre was used. The study attempted to assess the validity of predictions made from earlier trials in the Pilbara region with a different suit. The trial showed, as predicted, that the performance of geologists was greater than non-geologists, as determined by accuracy of observations. However we also observed, contra predictions, the analogue EVA suit did not degrade observational performance, but enhanced it. Further trials are recommended to test these observations. Perhaps most importantly, the experiment confirmed that suited geologists and appropriately briefed non-geologists would have no difficulty in correctly identifying stromatolite-like features on Mars.

Keywords: Mars analogue research, EVA suits, geology, astrobiology, human factors research, stromatolites, Arkaroola.

Introduction

Detailed, complex, and sophisticated field science investigations will be a key part of future crewed missions to the Moon and Mars (Refs. 1, 2, 3). Quantifying the capabilities of scientists and non-scientists to do such investigations while wearing EVA suits is important for designing mission goals, setting expectations, refining suit and field tools or instrument design, and mission architecture.

A prior example of this was the development of procedures, systems, and technology for Apollo EVAs on the Moon. These were based on extensive trials of varying levels of fidelity at many sites including Hawaii, New Mexico, and Arizona (Ref. 4). Trials included full and partial simulations with actual and simulated EVA suits or parts of suits (e.g. gloves, backpacks, helmets, etc.) As a result of these trials the need for suit cooling was indentified, along with the need for specialised tools to overcome postural limitations of the gas-pressure suits and the safety of using standard geological tools such as rock hammers while wearing EVA helmets.

This paper describes a small, low-cost trial that examines one particular aspect of the performance of science tasks, the recognition of stromatolites by geologists and non-geologists under analogue EVA conditions and the suitability of one analogue EVA suit to such studies. It builds on previous research (Ref. 5) and is intended to more complex and sophisticated studies at a later date.

Aim

The aim of the trial was to assess the suitability of the Victorian Space Science Education Centre (VSSEC) analogue EVA suits to test the ability of geologists and non-geologists to recognise specific scientific features. Stromatolite outcrops were chosen as typifying a class of readily recognised feature of great scientific interest if found on Mars, that occurred in the field area, and had been used for other trials (e.g. Ref. 5).

This was done by testing a set of pre-trial predictions, based on experience given by Ref. 5) which were:

1) Useful field science and operational research can be performed while wearing analogue EVA suits.

2) The suits measurably reduce observational abilities compared to an unsuited baseline (termed "ground truth" in Ref. 5).

3) (a) That geologists would make fewer observations than non-geologists but
(b) would out-perform them in the accuracy of their observations; and

4) The performance of geologists would be less impeded than that of non-geologists.

Of these predictions, 1), 2), 3(b), and 4), consistent with common sense expectations of the limitations of working in an EVA suit. Prediction 3(b) however, is not, as we would have expected geologists to make more observations. This unexpected result may be due to the greater degree of metal processing by the experienced and trained observer resulting in greater caution before voicing their observations as a statement.

For this experiment we note that, while the VSSEC suits overall are a poor gas-suit analogue (although better as a mechanical counter-pressure suit analogue, e.g. Ref. 6, the study was an observation trial, and therefore the helmet is most significant in contributing to the success or otherwise of tasks performed in the suit. The helmet of the chosen suit is a good analogue for a real space suit (Ref 6).

Experiment Context

The experiment was carried out during the Mars Society Australia (MSA) Arkaroola Mars Rover Challenge Expedition (Ref. 7), which took place in the northern Flinders Ranges, South Australia, in

July 2014 . This expedition conducted research across several fields relevant to Mars exploration, including palaeobiology, operations research, field robotics, as well as suit trials, in a Mars analogue environment side by side with educational and public engagement programs. The Arkaroola region had been previously selected by MSA as an ideal location for such multidisciplinary analogue research programs (Ref. 8).

Scenario

The scenario used in the study was the investigation of a potentially fossiliferous carbonate outcrop on Mars identified by satellite imagery and hyperspectral data and accessed by a sortie from a landing site several tens of km distant. Geologically-briefed engineers and specialized geologists would spend a limited amount of time assessing whether or not the outcrop contained mesoscopic signs of life in the form of stromatolites. These are typically columnar or hemispherical structures formed by the growth of generally shallow water and usually photosynthetic microbial communities (see benchmark compendium in Ref. 9). As the oldest macroscopic structures constructed by life (Refs. 10, 11) stromatolites and other microbial structures are targets to be looked for in the astrobiological exploration of Mars (Refs. 12, 13). Indeed possible microbial structures have already been observed on Mars (Refs. 14, 15), although their validity remains to be tested.

The limited time for assessment per location is also analogous to the Apollo-like traverses where a number of locations were visited on an EVA (see Ref. 16 for examples from Apollo 14). Each location was allocated an investigation time duration on the EVA schedule. Thus the Apollo astronauts undertook investigations within scheduled time limits to, assess, take samples and document geological locations. If the investigation showed that more time at the location would provide better science return then a decision was made to change the schedule for the remaining EVA.

Study site

The site was required to have moderate (10-20%) outcrop and reasonable number (i.e., enough to be easily found in the allocated time) of stromatolites. The site also should not be too rocky or have excess vegetation for safety reasons and needed to be accessible by vehicle, which could be driven to within about 50 m of the base.

Fig. 1: The Google Earth image of the test site south of Arkaroola. The scale bar is 57 m.

The selected site (Figures 1, 2) was at 30°26'29.47"S and 139°19'45.42"E with an elevation of 204 m above sea level at the foot of slope. It is 14.3 km in a direct line south of Arkaroola, and 18.1 km by road. The outcrop begins 55 m east of the Arkaroola road.

The outcrop is west dipping at 25-35°, northeast-southwest trending strike ridge composed of stromatolitic grey limestone with stratabound orange-brown to yellow dolomitisation and cross-cutting dolomite and calcite veins. The best exposures were found on the lower part of the ridge. The outcrop is a low strike ridge 400 m long, 40 m wide and about 5 m high, and is visible in Google Earth imagery (Fig. 1). The Google Earth aerial photography resolution is about ~30 cm, which is equivalent to the HiRISE camera on the Mars Reconnaissance Orbiter (MRO) and to ASTER (Advanced Spaceborne Thermal Emission and Reflection Radiometer) hyperspectral data, which has a resolution of 15 m (Ref. 17), roughly equivalent to the CRISM (Compact Reconnaissance Imaging Spectrometer for Mars) instrument on the MRO, as per Ref. 18). The ridge is visible as a FeOH and MgOH feature in the visible to near infrared ASTER data and has having low silica in thermal infrared ASTER, this suggests the presence of ferroan dolomite.

The outcrop is approached from the east across a lightly gullied parna-mantled pediment with minor alluvial reworking of siltstone fragments. Because of the approach direction and the topography the outcrop mostly represents the bedding plane, although cross sections are exposed on the sides of some blocks. Vegetation consists of forbs and small Acacias. Areas of denser vegetation, mostly on the ridge, were avoided during the course of the experiment to avoid entanglement. The area used in the trial was ~70 m x ~20 m.

Fig. 2: The low ridge of Trezona Formation selected for the experiment.

The outcrop was mapped as Trezona Formation (Ref. 19). This Neoproterozoic formation (Ref. 20) is composed of grey to pink, fine-grained, oolitic, intraclastic and stromatolitic limestone with variable dolomite interbedded with shale and siltstone. The ooids and complex intraclasts are often stained red by haematite and were term "hieroglyphic limestone" by Mawson (Ref. 21). Stromatolites are of two types: broad elongated hemispheres with cuspate ridges and pseudo-columnar forms. The Trezona Formation has been subsequently assigned to the Cryogenian (Ref. 22).

The stromatolites at the outcrop are simple columns, typically 5-10 cm high and 2-5 cm across. They are exposed largely as circular impressions on the upper surfaces of bedding planes on massive to slabby outcrop (Figure 3). The outcrop is grey, with stromatolites partly enhanced by patchy dolomitisation and silicification. Side views are difficult to obtain as because of the massive to slabby nature of the outcrop, however side views can be obtained on loose blocks, generally small enough to be picked up by hand. Where pervasively dolomitised, however, the stromatolitic textures are obliterated by the buff to red-coloured secondary carbonate.

Methods

Analogue EVA Suits

The analogue EVA suits (Figure 4) worn on the expedition were originally developed as a collaboration between Strathmore Secondary College and MSA in 2004 for VSSEC. As they would be used daily by groups of students exploring a simulation Mars landing site, the key requirements were safety, robustness, comfort, low cost, easy donning/doffing, high maintainability, and the provision of a memorable EVA suit-like experience and appearance for the wearer. As such, the suits were developed as a basic mimicry of a future gas-pressurised planetary exploration suit. Accurate generation of the high joint torques of true gas-pressurised suits was not pursued as this would compromise almost every design priority; however bulky gloves and boots were specified to provide some inhibition to mobility and hand dexterity. Cotton drill coveralls were provided by Yakka in a wide range of sizes to form a replica gas-pressurised garment.

Fig. 3: Bedding plain exposures of small hemispherical stromatolites at test site. A pocket knife (10 cm) provides scale.

MSA developed a pseudo life-support system consisting of a helmet, backpack and ventilation system based on previous analogue suit designs and experience from the MarsSkin program. The helmet configuration was based on two half sphere domes: a clear upper dome and solid base dome with a large entry port and neck ring. The clear dome can be attached in various alignments so that the inevitable scratches produced from closely inspecting objects can be rotated away from the line of vision, while also reducing the frequency and cost of replacement domes. Strathmore Secondary College requested that the helmets be easily removable, so they rest lightly on the shoulders of the wearer.

Life support is contained within a Boblbee hard-shell backpack. High ventilation sufficient to meet safety requirements is met by two fans that are installed inside a simulated oxygen canister on the backpack and plumbed to each side of the helmet. This ventilation air is directed forwards against the faceplate to reduce fogging and prevent cold spots on the head by small deflectors internal to the helmet, improving appearance and covering any sharp edges of attachment plumbing. A 7Ah 12V lead-acid battery provides approximately 5 hours of ventilation, and gives appropriate weight to the life-support system. For long duration EVAs, water packs can be stored in the backpack and connected to a bite valve mounted inside the helmet. UHF radios can also be incorporated, for example by the use of a simple 'snoopy cap', headphones, microphone and VOX operation. Normally at VSSEC the communications are carried out through a WiFi system operated by a laptop computer, also carried in the backpack.

Participants

The seven participants of the study comprised three with geological training and four without. "Geologists" were those with some degree of formal geological training. "Non-geologists" had a range of qualifications, including general science, paramedical, education, and heritage. All had been briefed on what to look for verbally and with illustrations, and had seen similar stromatolites in the

field previously, both at Arkaroola and elsewhere. The participants were four males and three females, with both genders represented in each skill-set. Ages varied from 20s to 60s. Only one participant had previous experience in testing analogue EVA suits, being part of the team in Ref. 5.

Fig. 4: VSSEC analogue EVA suits of the type worn for this experiment.

Experimental Method

Each experiment lasted 20 minutes and was supervised by the experiment controller. Participants were directed to leave the starting point and walk to the northern end of the target area. When they reached the first limestone outcrop the start of the timed experiment commenced. The participants performed the observations at their own pace.

The participants were required to point out any stromatolites and describe them as probable or possible. Probable stromatolites were features identified as stromatolites with a high degree of confidence. Possible stromatolites were features identified as possibly stromatolitic but with lower confidence. False positives (sites identified as probable or possible stromatolites that were judged as non stromatolitic by the experiment controller) and false negatives (sites rejected as stromatolites that were considered stromatolitic by the controller), were also noted. Communications were transmitted via a UHF radio on VOX setting for the suit and manual setting for the controller.

Assessment of each observation was by the controller, who had previously scouted the site and has thirty years experience in field geology, including extensive field experience with stromatolites of Holocene (West Australia, South Australia), Pleistocene (South Australia), Ordovician (Tasmania), Cambrian (South Australia), Neoproterozoic (South Australia), Mesoproterozoic (Queensland, Northern Territory) and Archean (West Australia) age. Additional comments on the impact of the equipment on operations by the wearer were also recorded by the controller.

After the suited trials were completed the same participants were asked to repeat the exercise but without wearing the suit. The same observations were made and these were assessed in the same manner as the previous suited trial.

Ethical review was not necessary as it was suit performance that was being assessed rather than the human wearers.

All results from the tests were tallied and entered in an Excel spreadsheet.

Results

Suited Results

The results of the suited results are shown in Table 1. Overall 89.2% of the observations were judged correct. As expected, geologists were more accurate than non-geologists in their identifications, with 97.0% accuracy compared to 84.2%. Overall, observers were more likely to make a false positive identification (7.8%) than a false negative (3%), however the likelihood of a geologist making a false positive or negative observation was the same (1.5%). Non-geologists were eight times more likely to make a false positive observation than geologists and 2.6 times more likely to make a false negative.

Table 1: Results of the trial: Accuracy while suited

SKILL	PROBABLE	POSSIBLE	FALSE POSITIVE	FALSE NEGATIVE	TOTAL	TOTAL VALID	TOTAL ERRORS
GEOLOGISTS	36	28	1	1	66	64	2
%	54.5	42.4	1.5	1.5	99.9	97.0	3
NON-GEOLOGISTS	49	36	12	4	101	85	16
%	48.5	35.6	11.9	3.9	99.9	84.2	15.8
TOTAL	85	64	13	5	167	149	18
%	50.9	38.3	7.8	3	100	89.2	10.8

Unsuited Results

Results of the unsuited trials are shown in Table 2. Overall 87.4% of the observations by geologists and non-geologist were correct. Geologists were more accurate than non-geologists in their identifications, 94.9% as against 80.9%. A false positive identification was less likely (5.5%) than a false negative (7.1%). Unsuited, geologists made a false positive identification 3.4% of the time and a false negative 1.7% of the time). Non-geologists made false negative identifications 11.8% of the time compared with false positives 7.4% of the time. Thus non-geologists were almost seven times more likely to make a false negative observation than geologists and were just over 1.3 times more likely to make a false positive.

Table 2: Results of the trial: Accuracy while unsuited

SKILL	PROBABLE	POSSIBLE	FALSE POSITIVE	FALSE NEGATIVE	TOTAL	TOTAL VALID	TOTAL ERRORS
GEOLOGISTS	24	32	2	1	59	56	3
%	40.7	54.2	3.4	1.7	100	94.9	5.1
NON-GEOLOGISTS	27	28	5	8	68	55	13

%	39.7	41.2	7.4	11.8	99.5	80.9	19.1
TOTAL	51	60	7	9	127	111	16
%	40.2	47.2	5.5	7.1	100	87.4	12.6

Table 3: Results of the trial: Number of observations

SKILL	SUITED	# OBSERVATIONS	# OBSERVERS	MEAN
GEOLOGIST	YES	66	3	22
NON-GEOLOGIST	YES	101	4	25.3
TOTAL	YES	167	7	23.9
GEOLOGIST	NO	59	3	19.7
NON-GEOLOGIST	NO	68	4	17
TOTAL	NO	127	7	18.1

Qualitative comments by participants

All participants commented on experiencing several difficulties when wearing the suits. There was difficulty in seeing out of the helmets when looking up-sun, because of glare associated with light scattering from scratches and dust on the helmets. Rock colour was more difficult to assess in the helmets, possibly from slightly reduced contrast and the previously mentioned light scattering. There was uncertain footing because of the large boots worn and the associated increase in care needed while moving, especially with respect to foot placement. Participants only occasionally crouched or knelt to make observations. Sometimes loose specimens were picked up, however most exposures were on large slabs, precluding handling.

Discussion

Caveats

The sample size of this study is small and therefore conclusions drawn from the above statistics are both tentative and provisional. It is the researcher's aim to expand on these results with future trials.

Success of predictions

Prediction 1), that useful field science can be performed while wearing analogue EVA suits, was confirmed. This is as expected from the success of Apollo astronauts on the Moon.

Prediction 2), that the suit would impede performance was not borne out (Tables 1 and 2). Overall the suited and unsuited participants scored 89.2% and 87.4% correct results respectively. Geologists correctly identified stromatolites better when suited compared to non-suited (97.0% versus 94.9%), as did non-geologists (84.2% versus 80.9%).

Prediction 3(a), that geologists would make fewer observations than non-geologists, was only partly borne out (Table 3). The prediction was correct while the participants were suited, with an average of 22 observation per geologist as opposed to 25.3 for the non geologists. When unsuited, geologists made more observations per observer (19.7) than non-geologists (17) on an observer basis.

Prediction 3(b), that geologists would out-perform non-geologists in the accuracy of their observations was validated (Table 3). Geologists achieving 12.8% greater accuracy in identifications while suited and by 14% while unsuited, compared with non geologists.

Prediction 4), that geologists would be less impeded by the suits than non-geologists, was shown to be incorrect (Tables 1 and 2). While neither group were noticeably impeded by the suit, the performance gap between the geologists and non-geologists narrowed from 3.3% without a suit to 2.1% while wearing a suit, and geologists made more observation while not wearing the suit than non-geologists.

Possible explanations

The apparent increase in performance whilst wearing a suit is a surprise. Ref. 5 reported that while using the University of North Dakota's NDX-1 pressurised suit participants made 25% fewer observations than when unsuited and made three times as many incorrect observations. This was not repeated. There are several explanations for this discrepancy:

1. These analogue suits do give not an accurate representation of the difficulties of doing field science in a gas-pressurised EVA suit, in particular the greater flexibility of the VSSEC suits (Figure 5).

2. Because the unsuited trials were carried out subsequently to the suited trails, the participants may have been more fatigued and less capable of observations than when they were wearing the suits. A priori this appears unlikely as the tests lasted only 20 minutes and the participants were all in good health and of reasonable fitness.

3. It is possible that the actual wearing of the suit may have led to increased observational focus and thought in the participants whilst carrying out the test.

4. It may also be possible that the participants did not take the unsuited test as seriously and so were less diligent in their observations.

5. The participants in the NDX suit trials in the Pilbara had no previous experience in wearing or working with the suit. The suit was not individually fitted and some wearers experienced significant discomfort from the poor fit. It is possible that greater training and familiarity might eliminate the difference in suited and unsuited performance while wearing the NDX suit.

6. Furthermore the Pilbara trials were carried out over rougher terrain than at Arkaroola. This would have resulted in the participants directing more attention to operating the suit and less to observations.

7. During the Pilbara trials the weather was very warm, and all participants experienced over-heating leading to fogging and misting to greater or lesser degrees, which significantly hampered the ability to make geological observations. Similar issues were not experienced with the VSSEC suit, due to cooler weather and the different suit design.

Fig. 5: The high flexibility of the VSSEC suits enables the wearing to easily crouch down while inspecting rocks on the ground.

Further Work

Further work with the VSSEC suit will be needed to test the seven possibilities above, and assess the validity and implications of the trials. We recommend that several further trials should be carried out to test these hypotheses.

1) As a minimum more unsuited trials in the same area with a similar mix of skill sets should be carried out to establish a baseline.

2) If the VSSEC or similar suits are available, the trials should be repeated, but this time with the suited test last. This would allow the possibility of fatigue to be explored and determine whether similar patterns are observed. Together these would test hypotheses 1-4 proposed above to explain the data.

3) A repeat of the NDX test with experienced wearers who more closely match the size requirements of the suit should be carried out to test hypothesis 5 above; and

4) Trials at a different, more rugged stromatolite site at Arkaroola with the VSSEC suits (or similar) and a less difficult stromatolite (or equivalent) site with the NDX-1 suit would assess whether rougher terrain impacts significantly on performance.

We are currently planning on carrying out trials 1) and 2) in a further expedition to Arkaroola in July 2016.

Applications to Mars

Any Mars mission will consist of a small team, perhaps numbering six, of cross-trained astronauts, some with more specialised training in field science than others (Ref. 1). This regard they will not be dissimilar to Apollo astronauts, who were mostly from test-pilot backgrounds with formal training in engineering with some cross-training in geology, and only one geologist (Ref. 4). As with Apollo, astronauts will be under time constraints forced by EVA logistics, to a degree rare on Earth (Ref. 23). Unlike Apollo, astronauts on Mars will have the ability to revisit sites of interest during their 500-600 day surface mission (Ref. 1). The superior performance of the geologists in the trial underlies the importance of having trained field expertise on Mars, however it is neither possible nor desirable to have a crew made up entirely of such people. However the fact that motivated and informed, if not with formal training, could also make useful observations highlights the importance of cross-training of astronauts of other specialisations. The success of that cross-training will be partly dependent on the breath and realism of that training, for example it is unlikely that any of our non-geologists would have recognised stromatolites without the briefing they previous received and exposure to examples elsewhere in the Arkaroola region.

Conclusions

This study showed that, as expected, VSSEC (and similar) analogue suits allow useful trials of crewed exploration of planetary surfaces within the limitations of their abilities to represent actual EVA suit performance. In particular they show that wearers, both geologists and non- geologists, are able to make the required observations despite wearing a helmet.

As per the predictions based on Ref. 5 and recommendations of Ref. 2, performance of geologists was measurably greater than non-geologists, as determined by accuracy of observations. This was irrespective of whether or not the VSSEC suit was worn, however the performance differential between the two increased when suits were worn.

However, contra predictions in Ref. 5, the VSSEC analogue EVA suit did not appear to degrade observational performance, but enhance it.

Multiple hypotheses were generated as possible explanations of these differences between what was predicted and was measured. Further trials are recommended to test these using VSSEC (or similar suits) and, if possible the NDX-1 suit.

Finally, and perhaps most importantly, as per the Mars scenario that framed the experiment, suited geologists and appropriately briefed and trained non-geologists appear to have no difficulty in correctly identifying stromatolite-like features on Mars, should they be encountered.

Acknowledgements

We thank the Victorian Space Science Education Centre for the loan of their suits. Funding for the expedition was provided by CSIRO, the Australia-India Council, and Australian Geographic, and Saber Astronautics. In-kind support was provided by Saber Astronautics, UNSW, Macquarie University, Murdoch University and the Arkaroola Resort. David Willson of NASA Ames Research Center also provided much useful commentary on the paper.

References

1. Hoffman, S. J. (ed.) *The Mars Surface Reference Mission: A Description of Human and Robotic Surface Activities*. NASA/TP—2001–209371, 2001.

2. Schmitt, H.H., Snoke, A.W., Helper, M.A., Hurtado, J.M., Hodges, K.V., and Rice Jr., J.W. Motives methods and essential preparation for planetary field geology on the Moon and Mars. *Geological Society of America Special Pap*er 483, 2011, 1-15.

3. Beaty, D. Niles. P., Hays, L., Bass, D., Bell,M. S., Bleacher, J., Cabrol, N. A., Conrad, P., Eppler, D., Hamilton, V., Head, J., Kahre, M., Levy, J., Lyons, T., Rafkin, S., Rice, J., and Rice, M. *Scientific Objectives for the Human Exploration of Mars*. MEPAG Science Analysis Group. Web address when accessed 10/9/15 http://mepag.nasa.gov/reports/HSO%20summary%20presentation%20FINAL.pdf, 2015

4. Wilhelms, D. E. *To a Rocky Moon*. University of Arizona Press, Tucson, 477p, 1993.

5. Willson, D., Rask, J. C., George S.C., deLeon, P., Bonaccorsi, R., Blank, J., Slocombe, J., Silburn, K., Steele, H., Gargarno, M., and McKay, C. P. The performance of field scientists undertaking observations of early life fossils while in simulated spacesuit. *Acta Astronautica* 93, 2014, 193–206.

6. Waldie, J., Wisely, D., Ischia, D., and Harvey, B. MarsSkin: a mechanical counter pressure Mars analogue space suit. *Proceedings of the second Australian Mars Exploration Conference*, 2002. Web address when accessed on 20/9/15 http://old.marssociety.org.au/amec2002/proceedings/18-James_Waldie_MarsSkin_full_paper.htm

7. Clarke, J. D. A., Held, J. M., Dahl, A., Wheaton, N., and the Arkaroola Mars Robot Challenge Expeditioners. Field Robotics, Astrobiology and Mars Analogue Research on the Arkaroola Mars Robot Challenge Expedition. *Proceedings of the 2014 Australian Space Research Conference* p237-250, 2014. Web address when accessed on 20/9/15 http://www.nssa.com.au/web-resources/downloads.html

8. Mann, G. A., Clarke, J. D. A., Gostin, V. A. Surveying for Mars Analogue Research Sites in the Central Australian Deserts, *Australian Geographical Studies*, 30(1), 2004 116-124.

9. Walter, M. R. 1976 (ed.). *Stromatolites*. Elsevier, Amesterdam, 790p.

10. Allwood A.C., Walter M. R., Kamber B.S., Marshall C.P. and Burch I.W. Stromatolite reef from the Early Archaean era of Australia. *Nature* 441, 2006, 714-718.

11. Clarke, J. D. A. and Stoker, S. R. Searching for stromatolites: the 3.4 Ga Strelley Pool Formation (Pilbara, Western Australia) as a Mars analogue. *Icarus* 224, 2013, 413-423.

12. Walter, M.R. and Des Marais, D.J. Preservation of biological information in thermal-spring deposits—developing a strategy for the search for fossil life on Mars. *Icarus* 101, 1993,129–143.

13. McKay, C. P. and Stoker, C. R. The early environment and its evolution on Mars: implications for Mars. *Reviews of Geophysics* 27, 1989, 189-214.

14. Noffke, N. Ancient Sedimentary Structures in the < 3.7 Ga Gillespie Lake Member, Mars, that compare in macroscopic morphology, spatial associations, and temporal succession with terrestrial microbialites. *Astrobiology* 15(2), 2015, 1-24.

15. Ruff, S. W. New observations reveal a former hot spring environment with high habitability and preservation potential in Gusev Crater, Mars. *Abstracts of 46th Lunar and Planetary Science Conference*, Abstract 1613, 2015

16. Marquez, J. J. Assessment of Scheduling and Plan Execution of Apollo 14 Lunar Surface Operations. *Proceedings of the 40th International Conference on Control Systems,* AIAA 2010-6104, 10p, 2010

17. Brown, A. J., Cudahy,T. J., and. Walter, M. R. Hydrothermal alteration at the Panorama Formation, North Pole Dome, Pilbara Craton, Western Australia. *Precambrian Research* 151, 2006, 211–223

18. Brown, A. J., Hook, S. J., Baldridge, A. M., Crowley, J. K., Bridges, N. T., Thomson , B. J., Marion, G. M., de Souza Filho, C. R. and Bishop, J. L. Hydrothermal formation of Clay-Carbonate alteration assemblages in the Nili Fossae. region of Mars. *Earth and Planetary Science Letters* 297, 2010, 174–182.

19. Coats, R. P. *COPLEY, South Australia, sheet SH54-9.* South Australian Geological Survey 1:250,000 series, 1973.

20. Preiss, W. V. (compiler). *The Adelaide Geosyncline –Late Proterozoic stratigraphy, sedimentation, paleontology, and tectonics*. South Australia Geological Survey Bulletin 53, 1987.

21. Mawson, D. Cambrian and Sub-Cambrian formations at Parachilna Gorge. *Transactions of the Royal Society of South Australia* 62, 1938, 255-262.

22. Maloof, A.C., Rose, C. V., Beach, R., Samuels, B. M., Calmet, C. C., Erwin, D. H.,. Poirier, G. R., Yao, N. and Simons, F. J. Possible animal-body fossils in pre-Marinoan limestones from South Australia. *Nature Geoscience* 3, 2010, 653 – 659.

23. Chaikin, A. *A man on the Moon*. Penguin Books, New York, 670p, 1998.

Chemical Complementarity between the Gas Phase of the Interstellar Medium and the Rocky Material of Our Planetary System

Haiyang Wang and Charles H. Lineweaver

Planetary Science Institute, Research School of Astronomy and Astrophysics, Research School of Earth Sciences, The Australian National University, Canberra, ACT, 2611, Australia.

Summary: We compare the elemental depletions in the gas phase of the interstellar medium (ISM) with the elemental depletions in the rocky material of our Solar System. Our analysis finds a high degree of chemical complementarity: elements depleted in the gas phase of the ISM are enriched in the rocky material of our Solar System, and vice versa. This chemical complementarity reveals the generic connections between interstellar dust and rocky planetary material. We use an inheritance model to explain the formation of primordial grains in the solar nebula. The primary dust grains inherited from the ISM, in combination with the secondary ones condensed from the solar nebula, constitute the primordial rocky material of our planetary system, through the effects of the progressive accretion and sublimation. Added to the partial condensation from the solar nebula, terrestrial planets are formed from these primarily inherited and secondarily condensed dust grains, by sublimation in our planetary system. The semi-major-axis-dependence of the chemical composition of rocky planetary material is also observed by comparing elemental depletions in the Earth, CI chondrites and other types of carbonaceous chondrites.

Keywords*:* Elemental depletion; Interstellar medium; Protoplanetary disk; Primitive meteorites; Terrestrial planets

Introduction

Investigations of UV spectra of stars since the 1970s have revealed interstellar absorption features produced by atoms in their favoured ionization stages in the interstellar medium (ISM) [1]. Atomic abundances of heavy elements relative to that of hydrogen are below the reference cosmic abundances that implicitly refer to solar abundances. The reduction of heavy elements represents the missing atoms in the ISM gas phases. This feature is reinforced by the correlation of the increase of elemental depletions of the ISM gas phases with increasing condensation temperature, which is a proxy for how refractory an element is. In a study of abundances along 243 different sight lines from more than 100 papers, Jenkins (2009) [1] characterized the systematic patterns for the depletions of 17 different elements (C, N, O, Mg, Si, P, S, Cl, Ti, Cr, Mn, Fe, Ni, Cu, Zn, Ge, and Kr), from which he constructed a unified quantitative scheme that could lead to a better estimate of dust compositions.

The rocky material of our Solar System may be representative of rocky material in other planetary systems. The depletion of volatile elements relative to the solar abundance is a characteristic signature in primitive meteorites [2][3][4] and terrestrial planets [5][6][7][8]. The search for ‘mysteries’ (volatile-rich component) [9] continues with the search for "lost planets" [10], a scenario that is similar to the search for "missing atoms" in the ISM gas phase from Field (1974) [11] to Jenkins (2013) [12]. Lewis et al. (1987) [13] reported the discovery of presolar grains in carbonaceous chondrites. The major types of presolar grains like

diamond, silicon carbide, and graphite found in meteorites are good noble gas carriers. Their abundances are quite diagnostic of nebular and parent-body thermal events, since these different presolar grains are destroyed at different temperatures [4]. Extensive investigations of carbonaceous chondrites [14][15] have shown a correlation between presolar grain abundances and bulk meteorite elemental abundance patterns. Based on the examination of interstellar gas and dust composition and comparison with meteoritic data, Yin (2005) [16] revealed that the depletion patterns of moderately volatile elements have a potential connection between the interstellar dust and the meteorites. The potential connection, or chemical complementarity, will be discussed further in this paper.

Elemental Depletions in the ISM Gas Phase

Elements can be classified into three categories based on the range of the elemental condensation temperature (T_C): highly volatiles (T_C <~500 K), moderately volatiles (~500 K< T_C < ~1400 K), and refractories (T_C >~1400 K), as shown in Fig. 1 for the simulated elemental depletions in the ISM gas phase. The x-axis is the 50% condensation temperature from Lodders (2003) [17] that indicates the volatility of an element. The y-axis is the logarithmic depletion factor (or the abundance ratio) of an element in the ISM gas phase relative to the cosmic reference abundances that are taken to be solar abundances. The abundance ratios of highly volatiles are approximately identical to the reference values while those of moderately volatiles are comparably lower than the reference values. The refractories are depleted considerably. The profound reductions of refractories and moderately volatiles inevitably prompt us to ask "where are these missing atoms?".

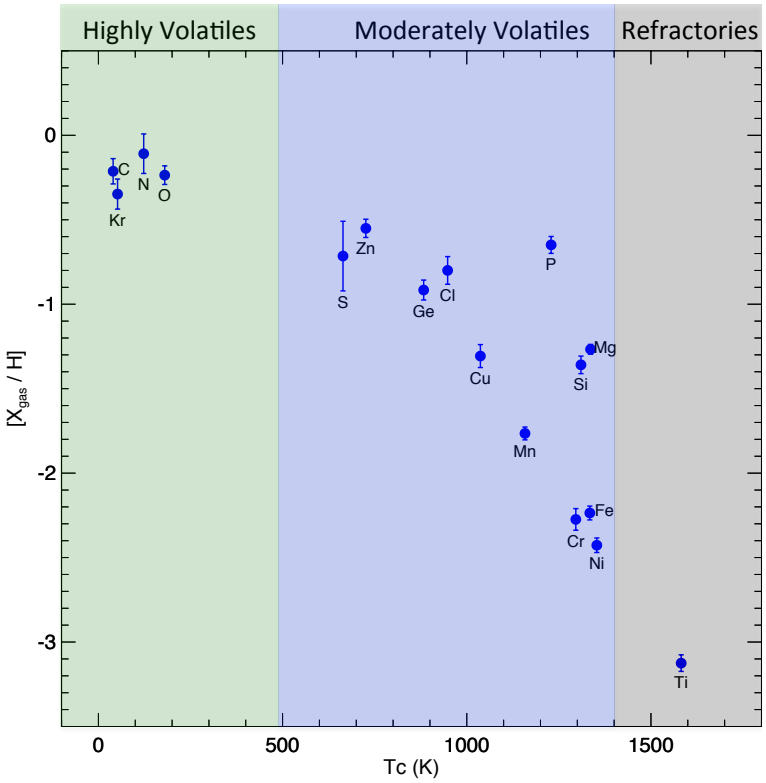

Fig. 1: The logarithmic depletion factors of elements in the ISM gas phase as a function of the elemental condensation temperature (T_C) [17]. Elements are classified into three categories based on the range of T_C: highly volatiles (T_C <~500 K), moderately volatiles (~500 K< T_C < ~1400 K), and refractories (T_C >~1400 K).

The theoretical foundation for the above simulation is a unified quantitative scheme, developed by Jenkins (2009, 2013) [1][12], which relates the logarithmic depletion factor [X_{gas}/H] for an element X to the sight-line parameter F_* as shown in Eqn. 1. Fig. 2 illustrates the manner of parameterizing the depletion trends for different elements. The zero point z_X for F_* is chosen to make the covariance of the errors in the other two parameters, A_X (slope) and B_X (vertical offset) be zero.

$$[X_{gas}/\mathrm{H}] = B_X + A_X(F_* - z_X) \tag{1}$$

The above unified form for elemental depletion in the gas phase is derived from a more straightforward parametric form Eqn. 2 that defines the logarithmic depletion of an element X in terms of its depletion factor below the logarithm reference cosmic abundances ($\log(X/\mathrm{H})_{\mathrm{ref}}$)

$$[X_{gas}/\mathrm{H}] = \log[N(X)/N(\mathrm{H})]_{\mathrm{obs}} - \log(X/\mathrm{H})_{\mathrm{ref}} \tag{2}$$

where $N(X)$ is the column density of element X, and $N(\mathrm{H})$ represents the column density of hydrogen in both atomic and molecular form.

It is followed by the quantitative answer to the question "where are these missing atoms?". The missing atoms are presumably locked up in the form of dust grains, the complementary composition of which can be estimated from the above logarithmic depletion factor by

$$(X_{\mathrm{dust}}/\mathrm{H}) = (1\text{-}10^{[X/\mathrm{H}]_{\mathrm{gas}}})\bullet(X/\mathrm{H})_{\mathrm{ref}} \tag{3}$$

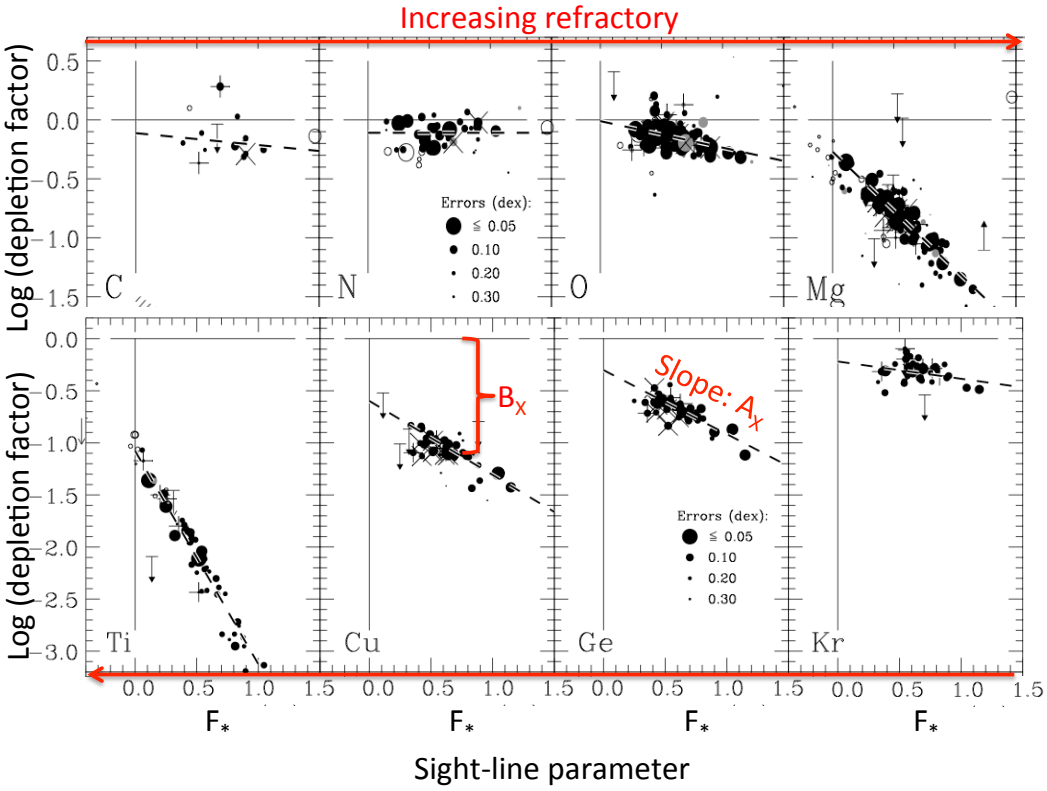

Fig. 2: Examples for 8 different elements that illustrate the manner of parameterizing the depletion trends in the ISM gas phase, adapted from [1][12]). The red arrows indicate the increasing refractory of elements in the upper and lower panels.

Elemental Depletions in Rocky Material of Our Planetary System

Primitive meteorites and the Earth are the representatives of rocky material in our planetary system. Elemental abundances in CI chondrites, one of most primitive meteorites, are regarded as the best proxy for the solar abundances, with exceptions of the highly volatile elements H, C, N, O and the noble gases He, Ne, Ar, Kr, Xe [17][18]. Relative to CI chondrites, all other groups of meteorites, as well as the Earth, are considerably depleted in moderately volatile elements (see Fig. 3 and Fig. 4).

Fig. 3 is probably the most comprehensive comparison of elemental abundance patterns of different types of meteorites relative to CI chondrites plotted as a function of the condensation temperature, completed by Davis (2006) [4]. He described well the differences of abundance patterns of carbonaceous chondrites, ordinary chondrites and enstatite chondrites. Here, we would like to, nevertheless, emphasize their global similarities: (1) Moderately volatile elements are depleted, more or less, in all non-CI chondrites; (2) Refractory elements are approximately identical or slightly enriched compared to CI chondritic abundances, complementary to the depletion of their counterparts in the ISM gas phase as shown in Fig. 1; (3) The not-shown but well-accepted large depletion of highly volatiles in all chondrites compared with the proto-solar abundance is complementary as well to their ISM counterparts (Fig.1) that are approximately equal to the cosmic reference abundance.

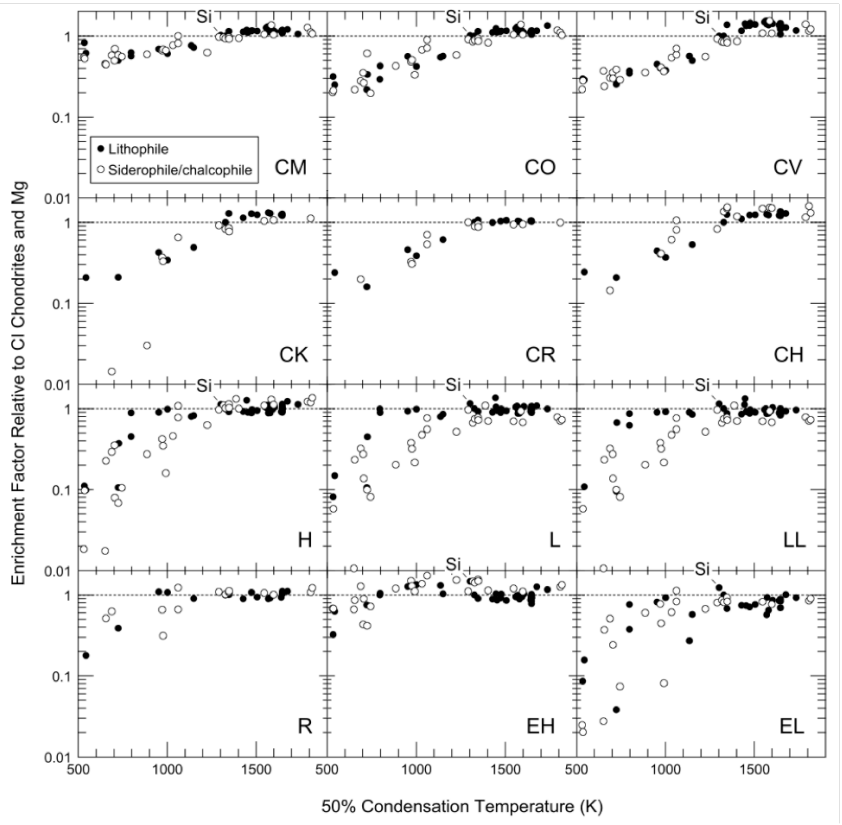

Fig. 3: The comprehensive comparison of CI-normalized elemental abundance patterns of various primitive meteorites, inclusive of carbonaceous chondrites (CM, CO, CV, CK, CR, CH), ordinary chondrites (H, L, LL, R), and enstatite chondrites (EH, EL), plotted as a function of 50% condensation temperature [17]. The normalization-reference element is magnesium. The figure is from [4].

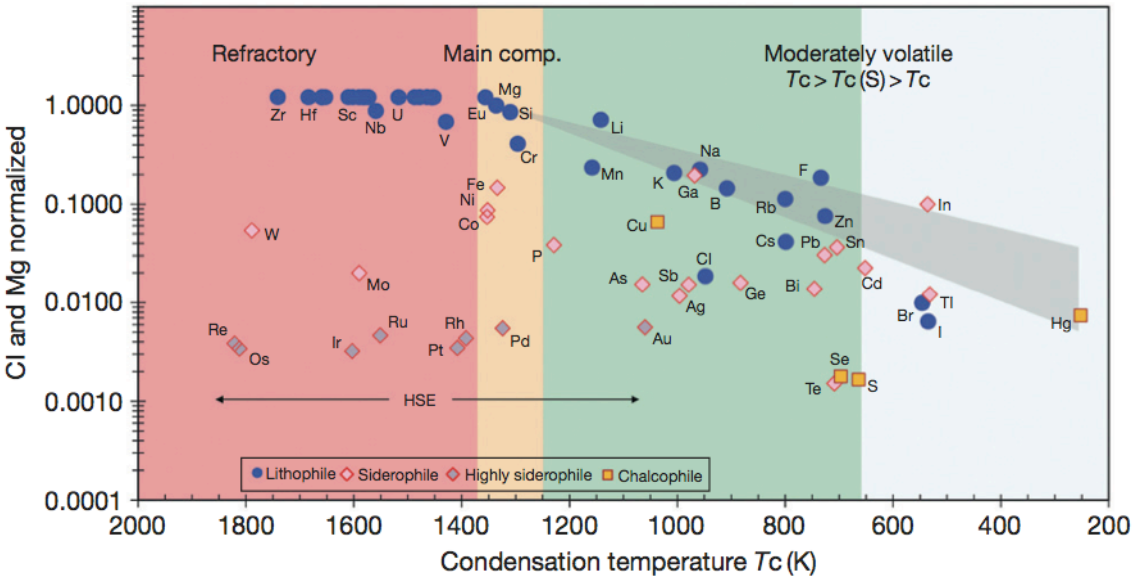

Fig. 4: The comparison of CI-normalized abundances of geochemically classified elements in bulk silicate Earth plotted against the 50% condensation temperature [17]. The normalization-reference element is magnesium. The interesting elements for this cosmochemical analysis here are only lithophiles (indicated by blue dots). The figure is from [7].

Fig. 4 shows the CI-normalized abundances of geochemically classified elements in the bulk silicate Earth (the bulk Earth excluding the core), plotted as a function of elemental condensation temperatures by Palme and O'Neil (2014) [7]. Here, we only care about lithophile elements (blue dots in Fig. 4), which are the dominant elements in bulk silicate Earth. It is clear that the abundance of refractory lithophiles (with condensation temperature greater than ~ 1400 K) are approximately identical to that of CI chondrites, against the feature of the depletion of their counterparts in the ISM gas phase as shown in Fig. 1. The considerable depletion of moderately volatile elements is subject to further processes (e.g. evaporation) of the terrestrial building-blocks, consisting of the inherited pre-solar grains from the interstellar dust and the newly condensed solids from the solar nebula. The detailed interpretations are presented in the Discussion.

Chemical Complementarity

From the above separate descriptions of elemental depletions in the ISM gas phase and in the inner Solar System rocky bodies, we see some potential complementary features between them. Yin (2005) [16] particularly discussed this topic from the comparison of dust composition and meteoritic data.

Three examples of interstellar data are plotted against the 50% condensation temperatures, as shown in Fig. 5a from [16]. As investigated in Fig. 1, refractory elements are highly depleted, and moderately volatile elements are progressively less depleted in the gas phase, indicating that these depleted elements are locked up in the dust. When compared to meteoritic data in Fig. 5b, the most intuitive and striking feature is that the abundances of interstellar gas phases are *complement*ary to the meteoritic data.

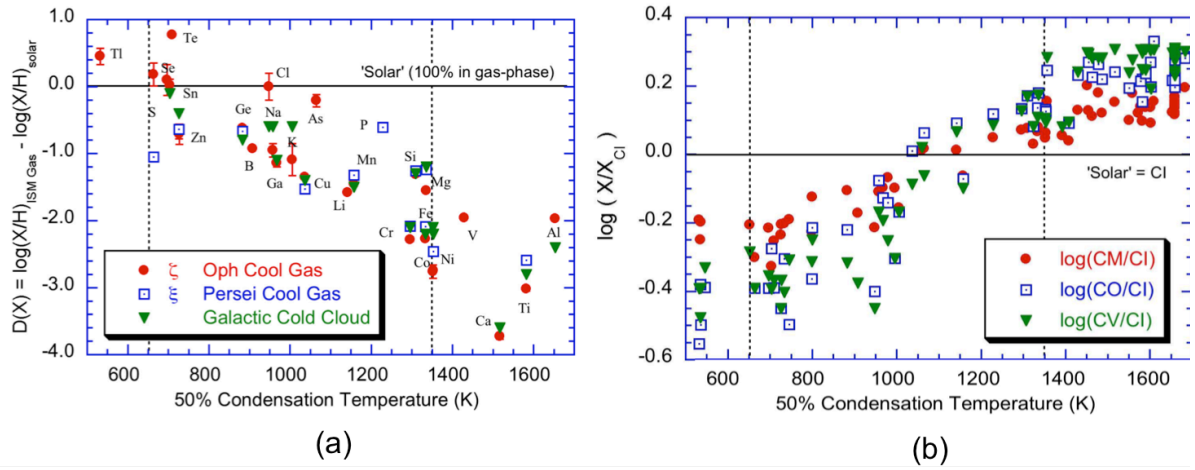

Fig. 5: (a) Interstellar gas phase abundance of three examples relative to solar and (b) Primitive meteoritic abundance relative to CI, as a function of 50% condensation temperature [17]. For moderately volatile elements, interstellar gas phase data is 'mirror-imaged' by the meteoritic data. The figures are adapted from [16]

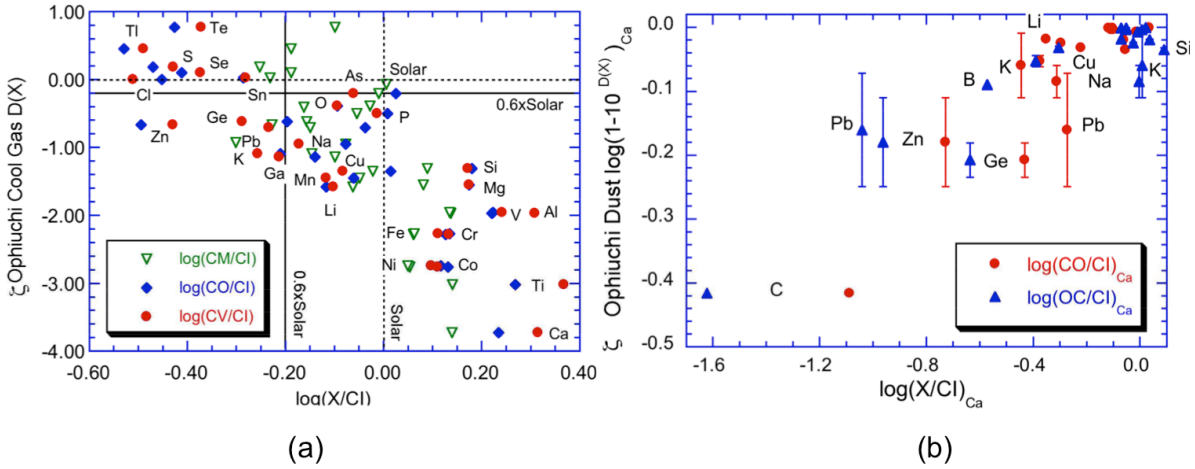

Fig. 6: (a) The relative abundance of moderately volatile elements in the primitive meteorites is anti-correlated with that in interstellar gas. (b) The calculated ISM dust composition is positively correlated with that of primitive meteorites for moderately volatile elements. The figures are adapted from [16].

Whereas, the depletion scales in the ISM gas phases and meteoritic data are apparently different by comparing the y-axes of Fig. 5a and 5b. Namely, this complementarity is not equivalent quantitatively. It is understandable. For interstellar dust, it is a long journey to form a 'primitive meteorite' after experiencing countless processes including shock-wave compression, condensation, sublimation, accretion, fractionation, burning (when passing through the Earth's atmosphere), and weathering (on the surface of the Earth). During these processes, its properties have been modified extensively. The majority of raw features in interstellar dust, therefore, are destroyed, and only a few tiny features are luckily reserved in forms of primitive meteorites that we can directly measure today. Among the few weakly reserved features, *chemical complementarity* between the ISM gas phases and the meteorites is the most striking one, whereas, the comparable scale between them is not expected.

Plotting the y-axis of Fig. 5a and Fig. 5b together as shown in Fig. 6a, it is clear that the interstellar gas is anti-correlated with the primitive meteoritic composition, underscoring that the provenance of the primitive meteorites is essentially the interstellar dust. In place of y-axis of Fig. 6a to the calculated dust composition from Eq. (3) as shown in Fig. 6b, the dust composition shows positive correlation with meteoritic composition for moderately volatile elements, further reinforcing the connections between primitive meteorites and the interstellar dust.

Based on the above comparisons, Yin (2005) [16] proposed an 'Inheritance Model' to explain the chemical connections between the interstellar dust and the material in the early active solar nebula. We schematically draw the mechanism in Fig. 7 to connect the diffuse interstellar medium to the protoplanetary disk, which corresponds to Yin (2005) [16]'s descriptions for these processes: (1) In the diffuse interstellar medium where elemental depletions are observed, the volatile elements are in the hot ionized gas phase, and the refractory elements are locked in the dust grains; (2) In the cold and dense molecular cloud stage, the gas phase consists of H and He only. Organic-rich icy mantles condense with all the volatile elements on to the refractory cores. Grain growth may have already occurred at this stage; (3) Collapse happens in the densest molecular cloud core with the continuous increase of surrounding gas pressure, leading to the rapid formation of the solar nebula with rotating gas and dust surrounding the central proto-star (namely the protoplanetary disk). The condensed layer of volatiles on most grain surfaces could easily be vaporized or sublimated when the grain is subjected to a reheating event, such as adiabatic compression or passage through shock waves prevalent during the collapse phase and in the early active solar nebula.

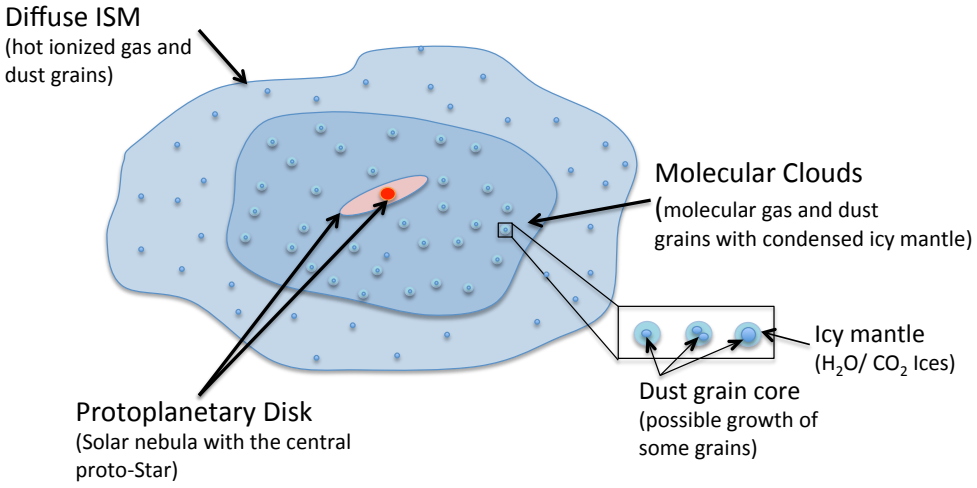

Fig. 7: Schematic processes of dust grains inherited from the ISM to protoplanetary disk

Discussion

In addition to the chemical complementarity drawn from the comparison of elemental depletions between the ISM and the rocky planetary material, the other striking feature is the semi-major-axis dependency if investigating the elemental depletions in the inner solar system material specifically.

Fig. 8 is a comprehensive comparison of elemental depletion patterns among the bulk Earth, CI chondrites, and other non-CI carbonaceous chondrites (CCs) normalized to the proto-Sun

by using the highly refractory aluminium as the normalization-reference element. Firstly, we can compare the normalized abundance of refractory (black dots), moderately volatile elements (green dots) in the non-CI CCs. From this comparison we can draw a similar conclusion as drawn from Fig. 3, namely the approximate equality of refractory elements and the increasing depletions of moderately elements, versus the decrease of the elemental condensation temperature, in the non-CI CCs relative to the Sun. Secondly and also more importantly, Fig. 8 additionally incorporates the elemental depletion pattern of the Earth ('blue' band in this figure) and that of CI chondrites ('red' band), from which we can clearly see their different elemental depletion trends. Contrary to the depletion trends in the ISM gas phases, the elemental depletion magnitudes in the rocky material of our planetary system are anti-correlated with the elemental condensation temperature. Meanwhile, considering the semi-major-axis of Earth (1 AU), CI (beyond 3 AU), and other CCs (within 2-3 AU), the depletion magnitude for the same element decreases with increasing distance to the Sun. The depletion slope and the depletion-transitional elements also vary correspondingly. Analysis of these patterns, various comparisons and implications will be investigated in detail in Wang et al. (2016) [8]. But a critical conclusion that we can learn from this comparison is that the elemental depletion in the rocky material of our planetary system is semi-major-axis dependent and dominated by the effect of evaporation or sublimation.

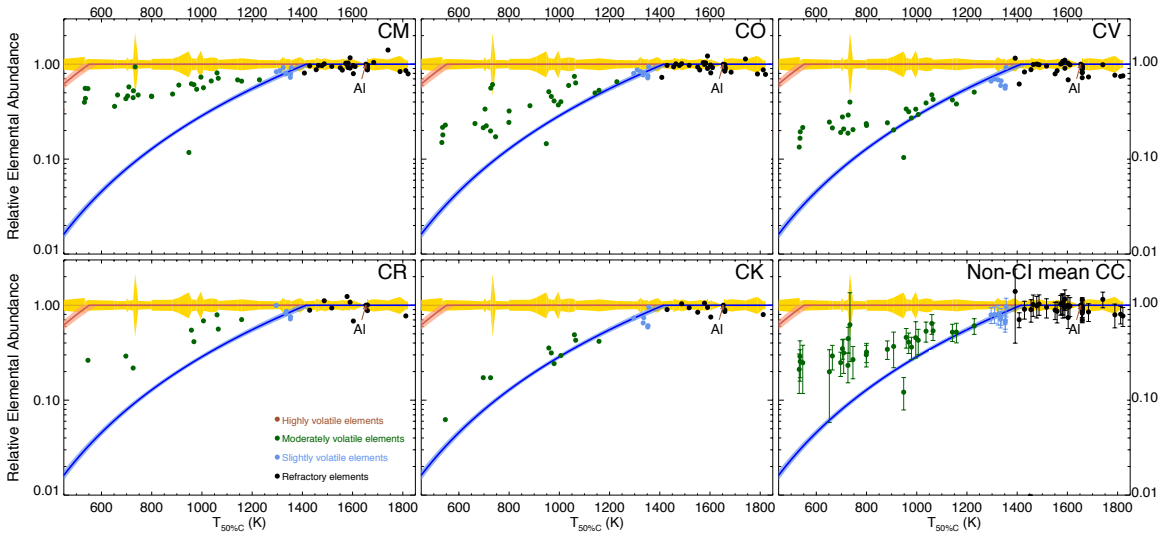

Fig. 8: The comprehensive comparison of the elemental depletion patterns of the bulk Earth ('blue' band), CI chondrites ('red' band), and five types of non-CI carbonaceous chondrites along with their mean, relative to the proto-Sun. The normalization-reference element is aluminium. The feature of semi-major-axis-dependency of elemental depletions in the inner Solar System rocky material can be drawn from this comparison, analogous to the feature of chemical complementarity drawn from the comparison between the ISM and the inner Solar System rocky material.

In addition, somebody may suspect whether this evaporation also works for giant gas planets like Jupiter. It deserves to be emphasized that evaporation or sublimation works through the Solar System, but it only has a significant influence on the rocky planets in the inner part of our system. Beyond the snowline, the effect of evaporation is considerably decreased, and enormous quantities of volatiles are able to survive and finally build up on those gas planets including Jupiter.

Conclusions

Several conclusions can be derived from the analysis of elemental depletion in the gas phase of the ISM and that in the rocky material of the Solar System, in terms of the chemical evolution processes between them:

1. In the gas phase of the interstellar medium, refractory and moderately volatile elements are depleted. The missing atoms are locked in the interstellar dust or large molecules and are inherited by the material that forms a planetary system.
2. In the (terrestrial) planetary disk, depletions of moderately volatile elements show complementarity with the depletions in the ISM gas phase. The progressive processing of pre-solar grains inherited from the interstellar dust, along with newly formed solids in planetary disk, lead to planetesimals that form terrestrial planets.
3. The semi-major-axis-dependent elemental depletions in rocky planetary material are mainly subject to the effect of evaporation or sublimation, other than condensation that may govern the interstellar gas phase elemental depletion.

Acknowledgment

We acknowledge that the idea of this work was inspired by Yin (2005), and relied on Davis (2006), Jenkins (2009, 2013), Palme and O'Neil (2014), and Wang et al. (2016). We also thank Michael Dopita and Ralph Sutherland for helpful comments.

References

1. Jenkins, E.B., "A Unified Representation of Gas-Phase Element Depletions in the Interstellar Medium", *ApJ*, Vol. 700, 2009, pp. 1299-1348.
2. Alexander, C.M. O'D, Boss, A.P., and Carson R.W., "The Early Evolution of the Inner Solar System: A Meteoritic Perspective", *Science*, Vol. 293, 2001, pp. 64-68.
3. Krot, A.N., Keil, K., Goodrich, C.A., et al., "Classification of Meteorites", *Treatise on Geochemistry*, Holland, H. and Turekian, K., Ed.,, 2003, Vol.1, pp. 83-128.
4. Davis, A.M., "Volatile Evolution and Loss", *Meteorites and the Early Solar System II*, Lauretta, D.S. and McSween, H.Y., Jr., Ed., 2006, Part IV, pp. 295-307.
5. Kargel, J.S. and Lewis, J.S., "Composition and Early Evolution of Earth", *Icarus*, Vol. 105, 1993, pp. 1-25.
6. McDonough, W.F., "Compositional Model for the Earth's Core", *Treatise on Geochemistry*, Holland, H. and Turekian, K., Ed., 2003, Vol. 2, pp. 547-568
7. Palme, H. and O'Neil, HStC., "Cosmochemical Estimates of Mantle Composition", *Treatise on Geochemistry,* 2nd Edition, Holland, H. and Turekian, K., Ed., 2014, Vol. 3, pp. 1-39
8. Wang, H., Lineweaver C.H., and Robles, J., "Elemental Devolatilization Patterns of Material in the Solar System", *Icarus*, in prep, 2016
9. Higuchi, H., Ganapathy, R., Morgan, J.W., et al., "Mysterite: A Late Condensate from the Solar Nebula", *Geochim. Cosmochim. Acta*, Vol. 41, 1977, pp. 843-852.
10. Halliday, A. N., and Porcelli, D., "In Search of Lost Planets – The Paleocosmochemistry of the Inner Solar System", *Earth Planet. Sci. Lett.,* Vol. 192, 2001, pp. 545-559.
11. Field, G. B., "Interstellar Abundances: Gas and Dust", *ApJ*, Vol. 187, 1974, pp. 453-459.

12. Jenkins, E.B., “Depletions of Elements from the Gas Phase: A Guide on Dust Compositions”, *The Life Cycle of Dust in the Universe: Observations, Theory, and Laboratory Experiments,* Taipei, Taiwan, 18-22 November, 2013, Proceedings of Science, URL: http://pos.sissa.it/archive/conferences/207/005/LCDU2013_005.pdf.
13. Lewis, R. S., Ming, T., Wacker, J. F., et al, “Interstellar Diamonds in Meteorites”, *Nature*, Vol.326, 1987, pp. 160-162.
14. Huss, G. R., Meshik, A. P., Smith, J. B., et al. “Presolar Diamond, Silicon Carbide, and Graphite in Carbonaceous Chondrites: Implications for Thermal Processing in the Solar Nebula”, *Geochim. Cosmochim. Acta,* Vol. 67, no. 24, 2003, pp. 4823-4848.
15. Huss, G. R., “Implications of Isotopic Anomalies and Presolar Grains for the Formation of the Solar System”, *Antarct. Meteorite Res.,* Vol. 17, 2004, pp. 133-153.
16. Yin, Q.-Z., “From Dust to Planets: The Tale Told by Moderately Volatile Elements”, Chonrites and the Protoplanetary Disk, ASP Conference Series, Krot, A.N., et al., Ed., 2005, Vol. 341, pp. 632-644
17. Lodders, K., “Solar System Abundances and Condensation Temperatures of the Elements”, *ApJ*, Vol. 591, 2003, pp. 1220-1247.
18. Anders, E. and Grevesse, N., “Abundances of the Elements: Meteoritic and Solar”, *Geochim. Cosmochim. Acta*, Vol. 53, 1989, pp. 197-214.

On Power Measured and Predicted for Oblique HF Propagation

David J. Netherway* and Robert S. Gardiner-Garden†

* *Defence Science and Technology Group, PO Box 1500, Edinburgh, SA, Australia, 5111*
† *Defence Science and Technology Group, 13 Garden St., Eveleigh, NSW, Australia, 2015*

Summary: The power received by oblique incidence sounders and the power estimated using parameterised models of the ionosphere have been compared. Statistical accumulations of sporadic E (Es) observations verified that antenna gain models and receiver chain gains had been well determined with root-mean-square differences of up to approximately 3dB. The expected received power for a 3 day period was modelled using analytic ray-tracing through an ionosphere specified by multiple quasi-parabolic parameters determined for the E, F1 and F2 layers and the parameters height and critical frequency determined for the sporadic E layer(s). The differences between measurement and model had means of 1-2dB with standard deviations around 6dB for each of the E and F regions. To achieve a good match for the Es observations, the ratio of blanketting to critical frequency was set to 20% in the Es model suggesting a method for measuring this ratio using oblique propagation.

Keywords: Ionosphere, HF propagation, oblique incidence, multiple quasi-parabolic, analytic ray-tracing.

Introduction

A component of the frequency management and track registration systems of the Australian Defence Force's Jindalee Operational Radar Network (JORN) of over-the-horizon radars (OTHR) is a network of oblique incidence sounders (OIS). These are used to characterize the ionosphere over Australia as an adjunct to other sensors such as vertical incidence (VIS) and backscatter (BSS) sounders. Experimental systems have extended this network over the last few years and, in particular, the last few months for the ELOISE experiment reported in more detail by others elsewhere in these proceedings [1], [2].

Robust automatic scaling of ionograms from the network of OISs has enabled determination of multiple quasi-parabolic (MQP) parameters [3], [4] characterising the 3 primary layers of the ionosphere (E, F1 and F2), the critical frequency (foEs) and height (hEs) for up to two sporadic E layers [5] and their variability [6]–[8].

This paper presents comparisons between measurements of the power received by OISs and the power estimated by analytical ray tracing (ART) [4], [9] through these parameterised models of the ionosphere.

Received Power Model

Once the propagation path has been determined, the power received for a one-way path can be calculated using

$$P_R = P_T(\lambda/4\pi)^2 \frac{G_T(\beta_T)G_R(\beta_R)}{Ld_e^2} \tag{1}$$

where, assuming spherical geometry, the effective distance is given by, see for example [10], [11],

$$d_e^2 = r_e \sin(D/r_e) \frac{\sin(\beta_R)}{\cos(\beta_T)} \left| \frac{dD}{d\beta} \right| \tag{2}$$

and the symbols are defined as follows:

P_R	received power
P_T	transmitted power
λ	wavelength
β_T	elevation at transmit antenna
β_R	elevation at receive antenna
G_T	transmit antenna gain (dependent on frequency and elevation)
G_R	receive antenna gain (dependent on frequency and elevation)
L	path loss
d_e	effective distance
r_e	radius of the Earth
D	ground range of receiver from transmitter.

The path loss, L, includes ionospheric absorption (non-deviative and deviative absorption) and the receive antenna polarisation mismatch (3dB on average).

System check using statistical accumulation of received Es power

In order to assess the accuracy with which we can understand propagation losses and the power measured in high frequency (HF) electromagnetic wave propagation over an ionospheric path we wish first to understand how well we can model the equipment, antenna gain patterns and sensitivity as a function of frequency and elevation. To this end we use a methodology based on statistical accumulation of E region power reported previously [12], but developed further here.

Antenna Gain

The gains of our OIS receive and transmit antennas have been modelled using Numerical Electromagnetics Code (NEC) [13]. The gain pattern of a receive antenna, the “low angle omni-directional (LAO) monopole”, is shown in Fig. 1. The gain pattern of a transmit antenna, a wide-band biconical monopole designed to cover 2-45MHz (WM245), is shown in Fig. 2. Antennas lengths are such that to cover the required HF band there are significant nulls and gain variations across frequency and elevation.

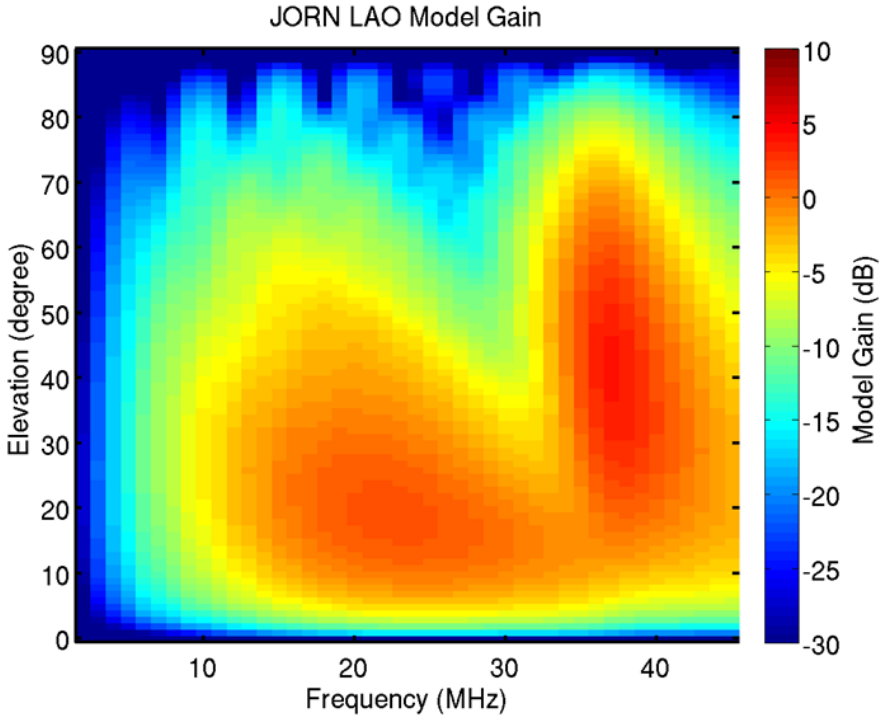

Fig. 1: NEC model of LAO OIS receive antenna gain

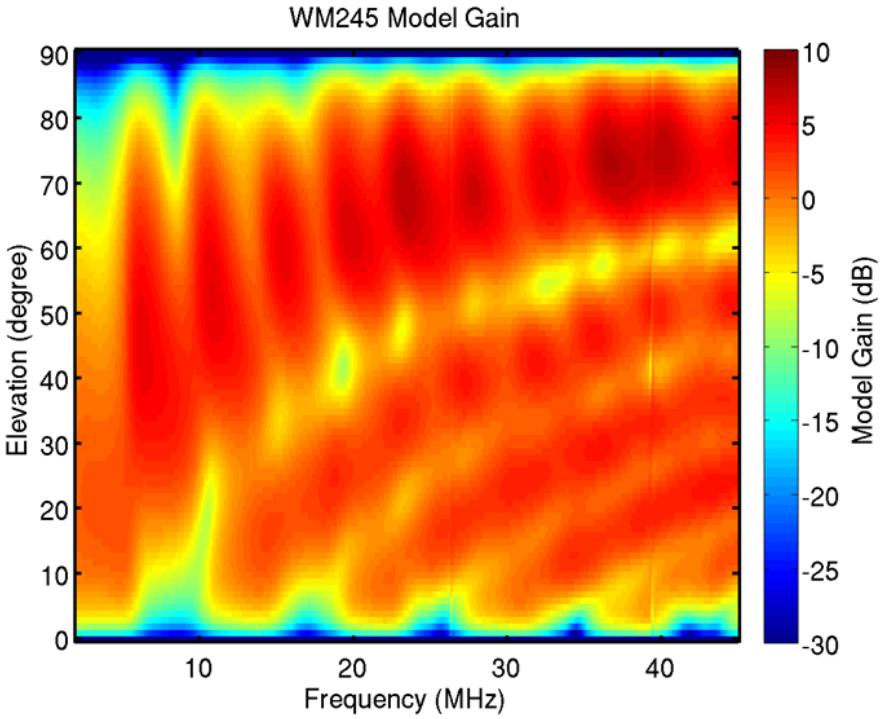

Fig. 2: NEC model of WM245 OIS transmit antenna gain

Receive Chain Gain Calibration

The gain/loss between receive antenna and receiver measurement was calibrated by injecting a swept frequency signal into the receive path at the base of the antenna and simultaneously

measuring the injected signal with a separate OIS receiver at the base of the antenna and with the receiver at the end of the receive chain. The two receivers were identical within the measurement error. The receive chain includes amplifiers and splitters for other users of the antenna. There was found to be a variation of up to 8 dB over the various receive sites and with frequency. This calibration has been included in subsequent model power calculations.

E Region Power Measurement

Received OIS power on short and medium length paths can be readily partitioned into that received via 1 hop propagation from the E and Es layers and via propagation with longer delays such as via F layer or multiple hops. This is achieved by partitioning the received power by delay less than or greater than from a 1 hop path reflected from a height of 160km. The peak power in the E region for a given path can be accumulated over time and an example is shown for two paths in Fig. 3 for a 3 day period with strong Es. The power variations appear consistent with antenna gain pattern nulls (e.g. 10 MHz for the Lynd River-Longreach path, designated R1R <– LYN) and a diurnal and frequency dependent pattern of absorption (lower received power at low frequencies during the day when D layer absorption is strong).

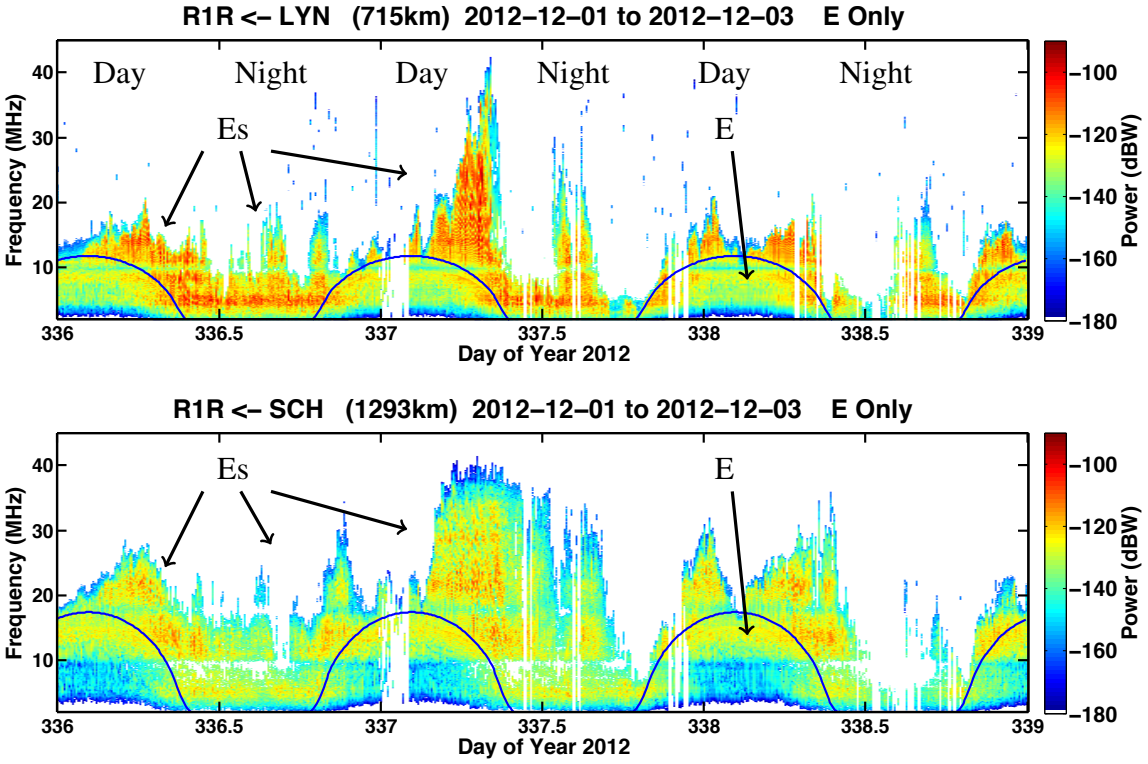

Fig. 3: E region power for 3 days (1-3/12/2012) and 2 paths. The blue lines show the maximum observable frequency of normal diurnal E propagation (MOF_E). The power at higher frequencies than the MOF_E is from sporadic E propagation.

Paths of different lengths (varying between 300 and 2000km) and different heights produce returns with a narrow range of effective elevations and hence a discrete set of effective elevations of samples.

The received power can be statistically accumulated so that we can construct the percentiles of received power over a month of data for each path. Choosing the 95th percentile selects power near the maximum but reduces the impact of outliers. The 95th percentile of received power minimizes variations from all propagation effects on power and leaves only the frequency and elevation variations due to the antenna gain patterns. An additional filter (designated "foEs filter" in the title of Fig. 4) was applied to the data before accumulation. This excluded data at frequencies greater than 80% of the determined maximum observable frequency for Es propagation (MOF_Es) in order to provide the additional outlier rejection associated with MOF_Es determination so that included power measurements were more likely from a strongly reflective layer.

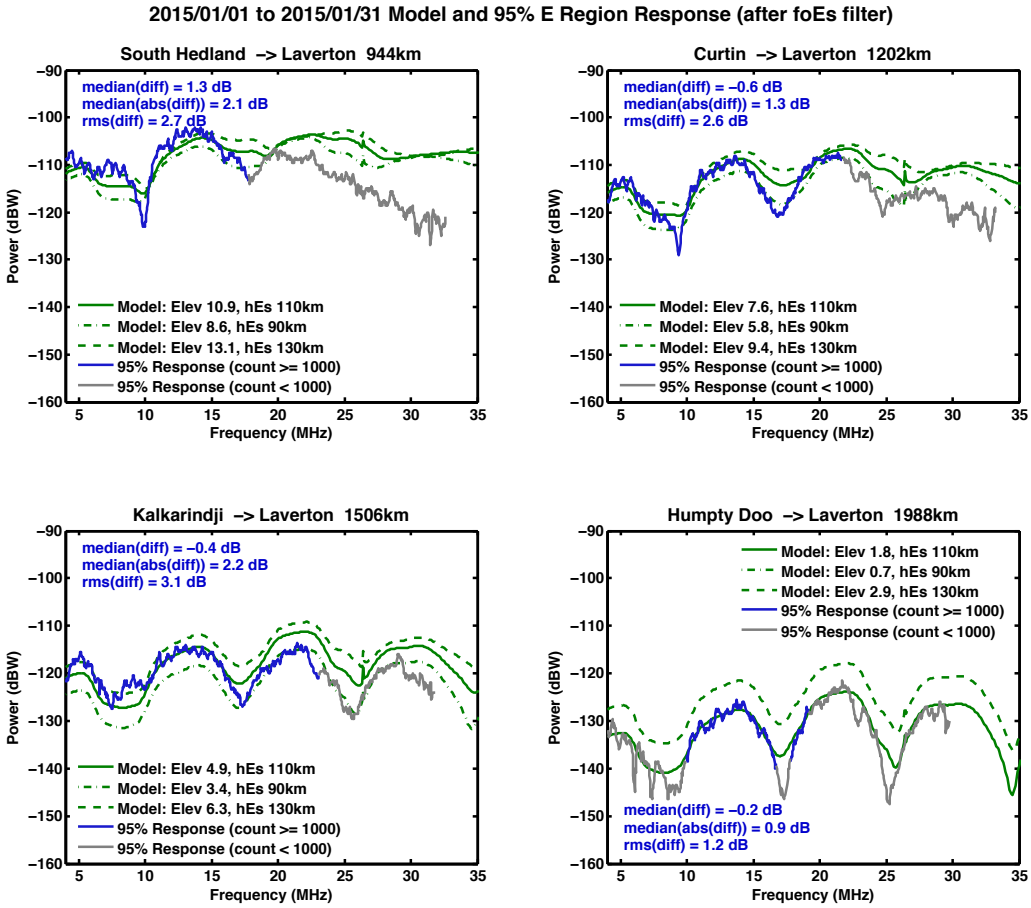

Fig. 4: Comparison of measurement and model. The blue and grey lines show the measured power (response) with the number of contributing points above and below 1000 respectively; the continuous green lines show the modelled power for hEs = 110km; the dashed green lines show the modelled power for hEs = 90 and 130km. The figure legends show the corresponding elevations for these Es heights, for each OIS path, and some statistics of differences between measurement and the hEs = 110km model for frequencies corresponding to the blue curve.

This statistical estimate of near maximum power propagated via the E region was then compared with the power obtained using the simple geometric model of oblique propagation associated with a mirror reflector as given by (1) and (2).

The assumptions being made here are:

1) Es power is from a tightly grouped set of heights and hence elevations,
2) reflection is from a spherically symmetric non-tilted layer,
3) low reflection loss can be associated with the 95th percentile of samples and
4) absorption is a secondary effect when night-time data is included.

The results of comparisons of measurement and model for OIS paths to Laverton, Western Australia are shown in Fig. 4. The blue lines give the 95th percentile measurement curves where the number of points contributing to the statistics is greater than 1000, the grey curves following on at higher frequencies indicate the result when there are less than 1000 contributing points. The green curves give the model power for Es heights (hEs) of 90, 110 and 130km. These correspond to different elevations for the different ground ranges of the different OIS paths and these are shown in the legends of Fig. 4. The measurement data is for all heights in the E region 80-160km but the Es heights are predominantly in the range 90-130km. The missing 90km curve for the Humpty Doo to Laverton path is a consequence of the one hop associated propagation being below the horizon. The data could be broken down to smaller height, and hence elevation, ranges to more finely sample the elevation patterns but this has been left as future work. Where the number of sample points was greater than 1000 the root-mean-square differences between measurement and the model with virtual height 110km were up to approximately 3dB for the four paths in Fig. 4.

This is an excellent result for validation of model HF antenna gain patterns because they are difficult to measure directly and reliably in the field. Further, the establishment of this methodology has provided an alternative assessment of the status of remote equipment (e.g. detection of degradation due to weather conditions), often difficult due to the variability of ionospheric propagation.

Propagation via all layers

The power received for a path of ground range 1506 km (Kalkarinji to Laverton designated R2R<-KAL) is shown in Fig. 5a for 3-5 August, 2014. The black trace shows the measured MOF_F2 (maximum observable frequency for the F2 layer) for the oblique path. At higher frequencies, power from Es propagation is occasionally visible. As discussed above, the power received via E region propagation can be displayed separately by considering returns in the specified delay window, as shown in Fig. 5b. Now the diurnal variation of normal E is visible, along with weaker Es returns otherwise masked by the stronger 1 hop F2 propagation.

Multiple quasi-parabolic ionospheric model

The use of multiple quasi-parabolic (MQP) layers to model the vertical distribution of the electron concentration [3], [9] allows oblique analytic ray-tracing if the Earth's magnetic field is neglected. Effects of the Earth's magnetic field can subsequently be well approximated [4]. The 10 parameters of the MQP model characterising the 3 primary layers of the ionosphere (E, F1 and F2) are routinely determined [5]–[8] from OIS ionograms. These parameters are taken to represent the vertical distribution of the electron concentration in the ionosphere at the mid-point of the OIS path. The multiple sounders, including VIS, can be used to make a spatial model of the ionosphere [7]. But here, comparisons will be made between measurement

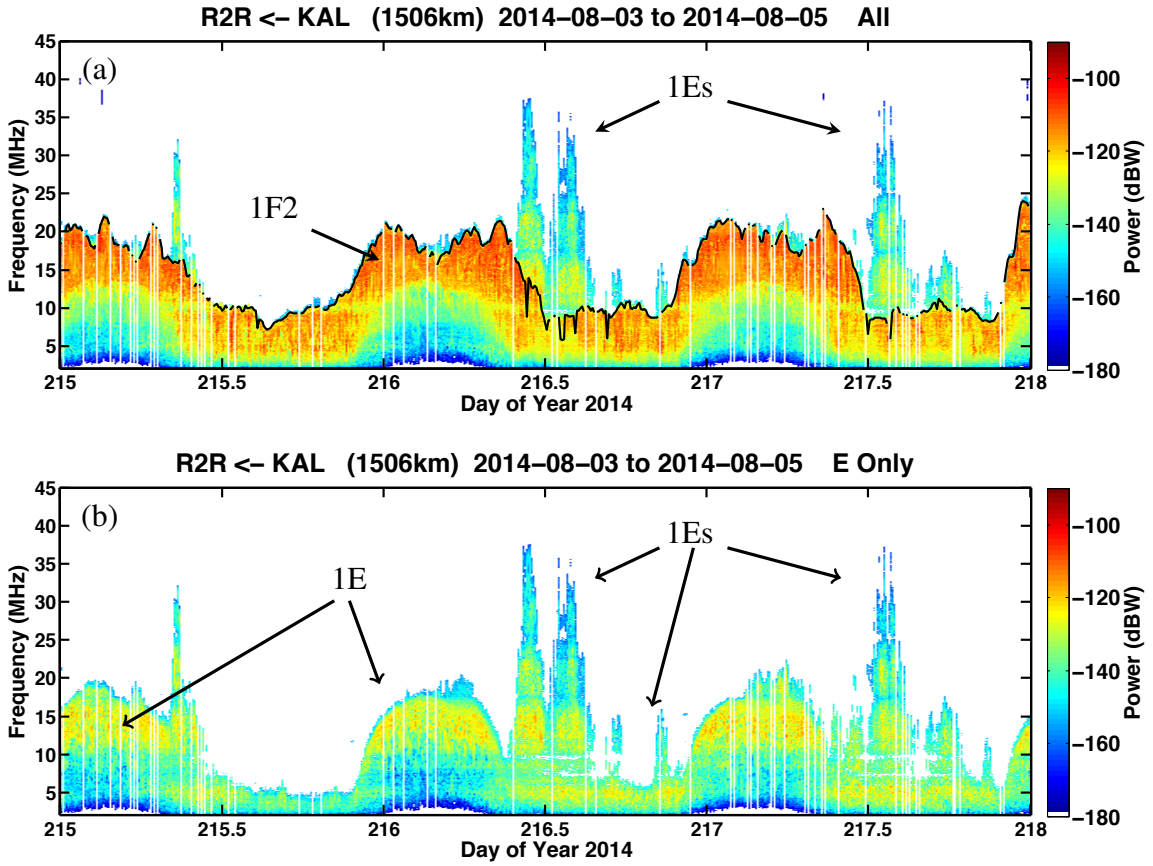

Fig. 5: Received power at Laverton from the transmitter at Kalkarinji (1506km) for (a) all delays and (b) delays corresponding to propagation via the E region. Examples of 1 hop F2 (1F2), normal E (1E) and sporadic E (1Es) are marked. The black line indicates the automatically determined MOF_F2.

and model for a specific sounder with the ionosphere modelled as geocentric and spherically symmetric to provide a baseline for future work (e.g. models that include spatial variation, filtering over time and various ray-tracing models).

Absorption

In the preceding section where statistical accumulations of Es data were used, and the night time data was included with its low absorption, it was found unnecessary to include absorption in the model. Here, it is necessary to include an absorption model and the George-Bradley [11], [14] model has been used.

Partial reflection from, and transmission through, Es layers

A simple but effective model of partial transmission and partial reflection from sporadic E layers is to use frequencies foEs and fbEs to characterise an Es layer. For vertical incidence, foEs is the highest frequency reflected from the layer and corresponds to the plasma frequency

of the highest electron density within the illumination area. The blanketting frequency, fbEs, is the frequency below which all frequencies are strongly reflected and this corresponds to the plasma frequency of the minimum electron density within the illumination area. Sinno et al. [15] provide empirical formulae for the reflection and transmission losses of an Es layer as a function of foEs, fbEs and the angle of incidence, ϕ, on the layer. For instance, the expression for the reflection loss, R, is given for a frequency, f, as

$$R(dB) = 20log_{10}(1 + 10p^n) \tag{3}$$

where

$$n = 2.077/log_{10}(foEs/fbEs) \tag{4}$$

and

$$p = f\cos(\phi)/foEs. \tag{5}$$

Ray tracing through the non-Es layers provides the angle of incidence on the Es layer at the specified or measured height.

Results

The modelled received power for the Kalkarinji to Laverton OIS is shown in Fig. 6 where it is clear that it captures the main features visible in the measurement data shown in Fig. 5.

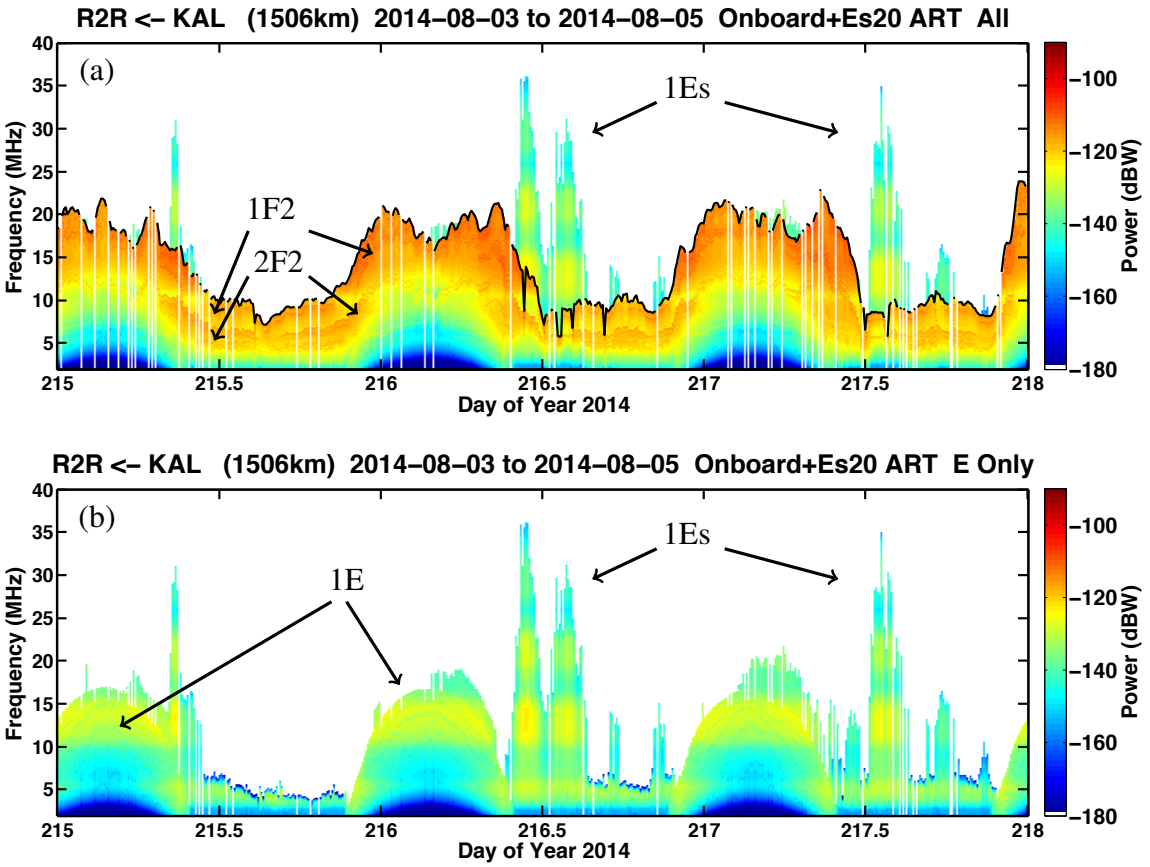

Fig. 6: Modelled received power corresponding to the measured power shown in Fig. 5 for (a) all delays and (b) E region propagation only.

Also visible in Fig. 6a is the second hop F2 (2F2) leading edge with O-X splitting (e.g. at day 215.5 the F2 leading edge is around 10 MHz and the 2F2 leading edge is around 7.5MHz). In the measurement data this is not clear, possibly indicating that our forward scattering model over-estimates the power. Or it may simply be that the ionosphere differs slightly at the 2 hop reflection regions and smears out the received power. Investigation of this has been left for future work.

Differences in power between measurement and model were then determined at each time-frequency point when both model and measurement have power levels greater than -150dBW. This is to exclude potentially large differences in dBW at very low power levels.

The power differences (Figs. 7 and 8) have medians within 1dB of zero and standard deviations around 6dB. This indicates that there are no major systematic errors and that our models of the ionosphere and propagation capture a significant portion of the power variation. While unmodelled focussing and defocussing would contribute to the variance, residual structure in Figs. 7 and 9 indicates that there is scope for model improvement.

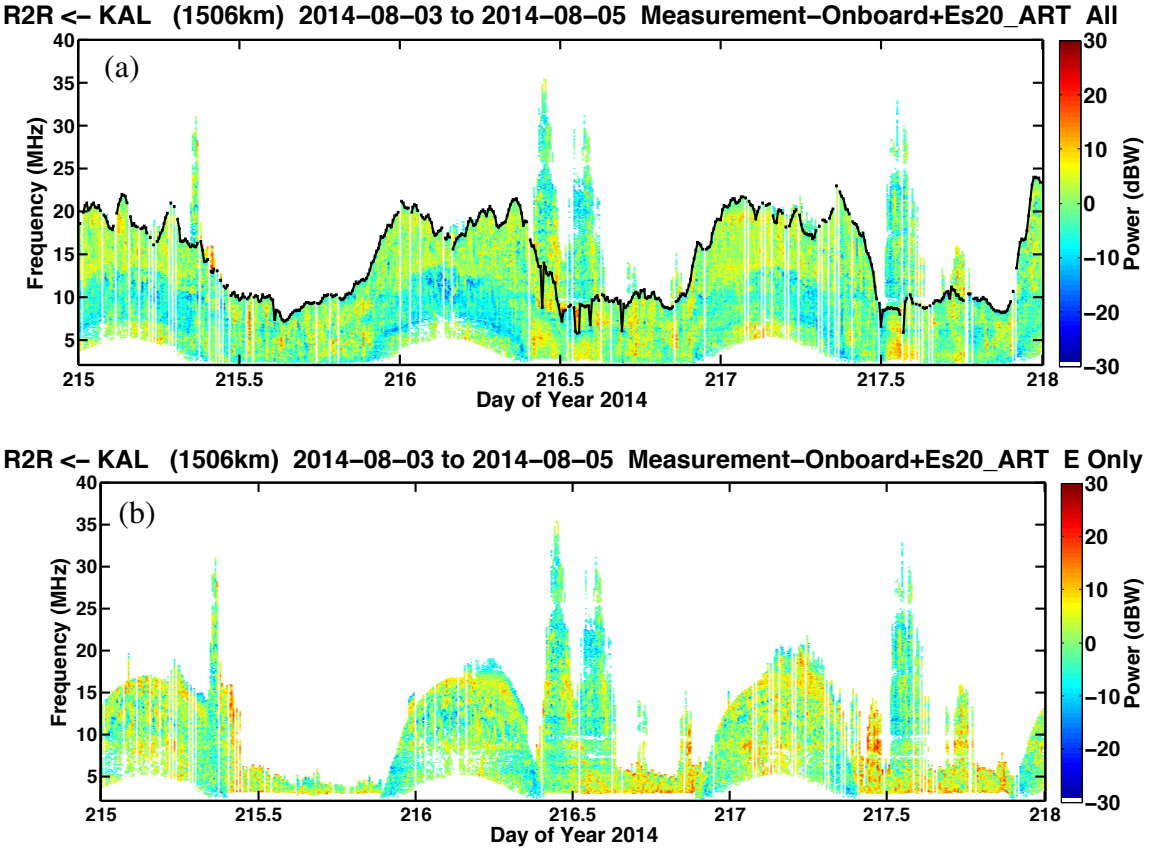

Fig. 7: Power differences between measurement, Fig. 5, and model, Fig. 6, for (a) all delays and (b) E region propagation only. The power differences have medians within 1dB of zero and standard deviations around 6dB.

In Figs. 8a and 9a propagation via the "F plus1" region refers to propagation having delay greater than would occur for one hop propagation with equivalent virtual height 160km. That is, delays longer than those for one hop E region propagation. Therefore this partition of the received power includes one hop propagation via F1 and F2 regions and multiple hop

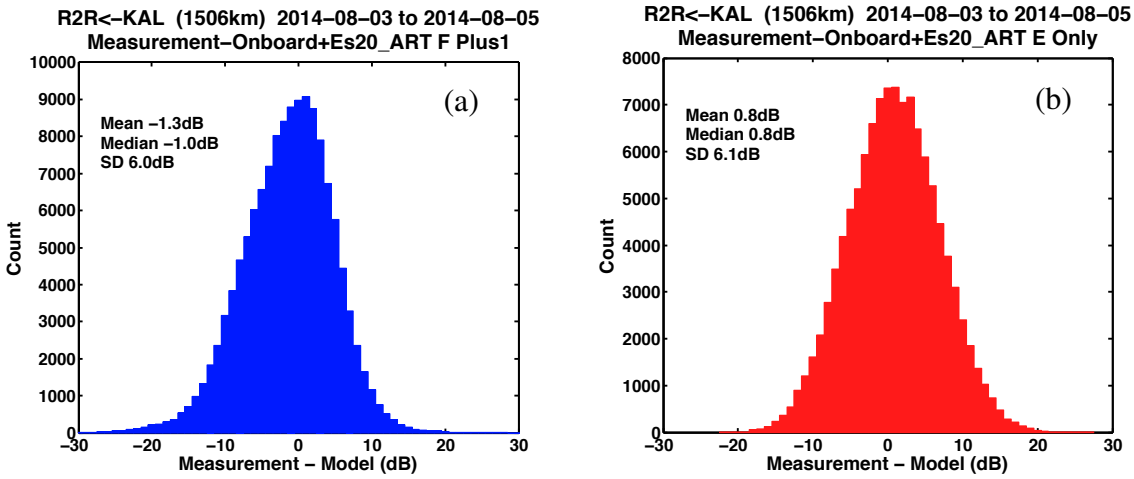

Fig. 8: Histograms of power differences between measurement and model for propagation delays corresponding to virtual heights (a) greater than, and (b) less than, 160km.

propagation from all layers. Other designations such as "F plus2" refer to other methods for partitioning the power but are beyond the scope of this paper. The term "Onboard" used in Figs. 6-9 indicates that the MQP and Es parameters used were from the on-board real-time processing occurring in the OIS receiver rather than from other processing of the archived ionograms. The term "+Es20" indicates that Es was included in the model with the ratio fbEs/foEs set to 20%, as discussed below. The term "ART" refers to ray tracing using ART rather than other ray tracing methods. These terms in the image titles distinguish the various processing options available to us.

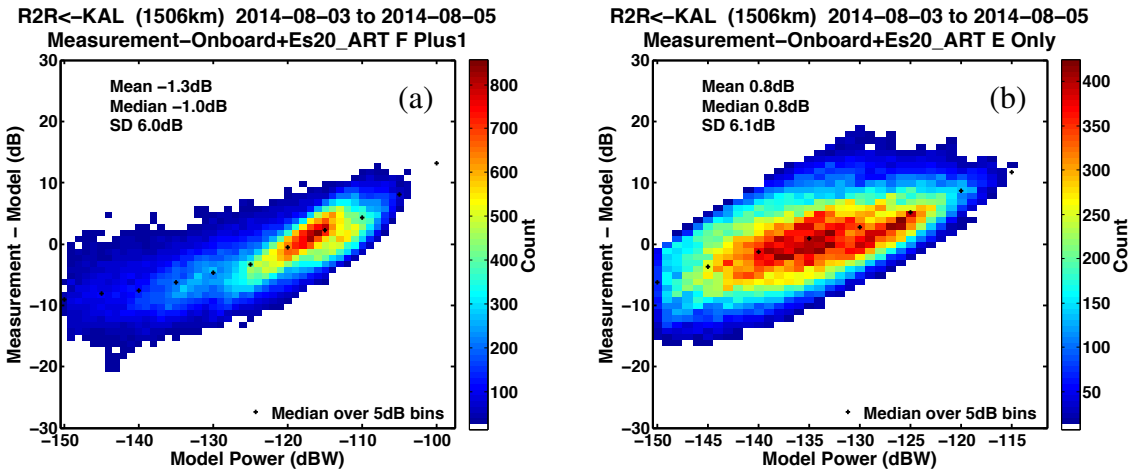

Fig. 9: Power dependence of power differences between measurement and model for propagation delays corresponding to virtual heights (a) greater than, and (b) less than, 160km. The black dots indicate the median over 5dB wide power bins.

The ratio fbEs/foEs used in (4) was set to 20% here. This is lower than the range of values (50-100%) found by Sinno et al. [15] and may indicate greater sensitivity in our methodology. When a higher default value (80%) was initially used there were obvious (>10dB) differences

between measurement and model for propagation via Es. Such an improvement obtained by adjusting only one parameter indicates that it may be possible to estimate fbEs/foEs using oblique propagation by this method. It is often difficult to measure fbEs directly from vertical propagation because its frequency is often quite low.

Conclusions

For applications that use HF propagation in a manner where there are multiple paths of propagation, it is desirable to estimate the power of all possible modes that could be received. The work presented here represents a baseline of how well power can be estimated using simple models of the ionosphere and propagation.

For system validation, the whole transmitter to receiver system was assessed using statistical accumulations of oblique incidence sounder observations of propagation via sporadic E. The 95th percentile of power received via one hop propagation from the E region was taken as representative of propagation having low loss reflection from a spherical mirror at Es heights. The geometry under this assumption provided the elevation angles for evaluation of the antenna gain patterns. Excellent agreement was found between measurements over a one month period with root-mean-square differences with respect to this model of up to approximately 3dB (with the Es height set to a typical value of 110km) providing confidence that the system was sufficiently well calibrated. Conversely, this method provides a method for measuring antenna gain patterns and this is particularly useful at low elevations where the gain decreases rapidly with decreasing elevation.

Next the expected received power for a 3 day period was modelled using analytic ray-tracing through an ionosphere specified by multiple quasi-parabolic parameters determined for the E, F1 and F2 layers and the parameters height and critical frequency determined for the sporadic E layer(s). Initial work showed a good match for propagation via the E, F1 and F2 layers but showed significant differences for propagation via the Es layer(s). Subsequently it was found that good power matching between model and measurement was achieved by adjusting the ratio of sporadic E blanketting frequency to critical frequency (fbEs/foEs). When this ratio was set to 20% for the 3 day period, the differences between measurement and model had a median of approximately 1dB and standard deviations around 6dB for propagation via each of the E and F regions. This excellent match immediately suggested a method for measuring the fbEs/foEs ratio using oblique propagation.

Acknowledgments

The authors would like to thank Andrew Heitmann for providing the MQP and Es parameters through his OIS processing algorithms, Adrian Quinn for calibration of the OIS receiver chain and Charlie Williams for providing the antenna gain patterns.

References

[1] Heitmann, A., Gardiner-Garden, R., MacKinnon, A., Reid, I. and Ward, B., “Preliminary observations of ionospheric disturbances using 2D angle-of-arrival estimation on oblique

incidence soundings", *Presentation published with Proceedings of the 15th Australian Space Science Conference*, Short, W. and Cairns, I., Eds., National Space Society of Australia, Canberra, 2016.
[2] Ward, B., Gardiner-Garden, R. and Heitmann, A., "ELOISE - Towards an enhanced understanding of ionospheric variability and its impact on radio wave propagation", *Presentation published with Proceedings of the 15th Australian Space Science Conference*, Short, W. and Cairns, I., Eds., National Space Society of Australia, Canberra, 2016.
[3] Dyson, P.L., and Bennett, J.A., "A model of the vertical distribution of the electron concentration in the ionosphere and its application to oblique propagation studies", *Journal of Atmospheric and Terrestrial Physics*, Vol. 50, No. 3, 1988, pp. 251-262.
[4] Bennett, J.A., Chen, J. and Dyson, P.L., "Analytic Ray Tracing for the Study of HF Magneto-iononc Radio Propagation in the Ionosphere" *Applied Computational Electromagnetics Society Journal* Vol. 6, 1991, pp. 192-210.
[5] Gardiner-Garden, R., Ayliffe, J., Durbridge, L.J., Frazer, G.J., Heitmann, A., Praschifka, J., Scarman, G. and Turley, M.D.E., "A new high-fidelity oblique HF receiving system", *Proceedings of the 12th Ionospheric Effects Symposium (IES)*, Alexandria, Virginia, USA, May 2008.
[6] Gardiner-Garden, R., Heitmann, A., Northey, B. and Turley, M., "Modelling uncertainty in a real-time model (nowcast) of the ionosphere", *Proceedings of the 12th Ionospheric Effects Symposium (IES)*, Alexandria, Virginia, USA, May 2008, pp. 482-491.
[7] Gardiner-Garden, R., Heitmann, A. and Fraser, G., "Variability Observed in a High Fidelity Model of the Ionosphere based on a Dense network of Vertical and Oblique Incidence Sounders", *Proceedings of the 13th Ionospheric Effects Symposium (IES)*, Alexandria, Virginia, May 2011.
[8] Heitmann, A. and Gardiner-Garden, R.S., "Ionospheric Modelling with a Dense Network of Oblique Incidence Sounders", *Presentation published with Proceedings of the 12th Australian Space Science Conference*, Short, W. and Cairns, I., Eds., National Space Society of Australia, Melbourne, 2012.
[9] Croft, T.A. and Hoogasian, H., "Exact ray calculations in a quasi-parabolic ionosphere with no magnetic field" *Radio Science*, Vol. 3, 1968, pp. 69-74.
[10] Coleman, C.J., "On the simulation of backscatter ionograms", *Journal of Atmospheric and Terrestrial Physics*, Vol. 59, No. 16, 1997, pp. 2089-2099.
[11] Davies, K., *Ionospheric Radio*, Peter Peregrinus Ltd., London, United Kingdom, 1975.
[12] Netherway, D.J., Gardiner-Garden, R.S., Heitmann, A. and Williams, C., "HF Antenna Model Gain Validation", *Presentation published with Proceedings of the 14th Australian Space Research Conference*, Short, W. and Cairns, I., Eds., National Space Society of Australia, Adelaide, 2015.
[13] Burke, G.J. and Poggio, A.J., "Numerical Electromagnetics Code (NEC) User's Guide", Lawrence Livermore Laboratory, CA, 1981.
[14] George, P.L. and Bradley, P.A., "Relationship between h.f. absorption at vertical and oblique incidence" *Proceedings of the Institute of Electrical Engineers* Vol. 120, No. 11, 1973, pp.1355-1361.
[15] Sinno, K., Kan, M. and Hirukawa, Y., "On the reflection and transmission losses for ionospheric radio wave propagation via sporadic E", *Journal of the Radio research Laboratories*, Vol. 23, No. 110, 1976, pp. 65-84.

Improving Differential Interferometry using Global Atmospheric Models

Zheyuan Du, Linlin Ge and Alex Hay-Man Ng

Geoscience and Earth Observing System Group (GEOS), School of Civil and Environmental Engineering, UNSW Australia, Sydney, Australia

Summary: Earth surface displacement can lead to ground hazards, namely changes of river flow path and collapses of private and public infrastructures. In the last two decades, Differential Synthetic Aperture Radar Interferometry was widely applied to monitor such events with great success. However, its result can be significantly degraded due to atmospheric phase screen (APS). Two Global Atmospheric Models (GAMs) were exploited to predict the APS for different interferograms generated from both C-band ENVISAT Advanced Synthetic Aperture Radar (ASAR) and L-band ALOS Phased Array type L-band Synthetic Aperture Radar (PALSAR) dataset over three test sites with differential topographic conditions, North China Plain, Qinghai Mountains and Ordos Basin, China, respectively. The result proves that such method can be applied to predict the APS reasonably well when the topographic change is significant over study region.

Keywords: Differential Interferometry, Global Atmospheric Model, Atmospheric Phase Screen.

I. Introduction

Earth surface deformation can lead to changes of river flow paths, increased flooding extent, as well as collapses of private and public infrastructure (Ge et al., 2014).These ground hazards can not only threaten individuals' daily life and properties, but also cause major impacts on national economy. In the 2015 Nepal earthquake, at least 8,600 people were killed. Some parts of the city was destroyed all of a sudden and the economic loss totaled to more than US$5 billion (Ge et al., 2015). In addition, during the processing of hard rock and underground coal mining, thousands of miners died every year all over the world as a direct result of the long-term accumulated subsidence (Zhao and Jiang, 2015). Therefore, having the ability to measure the earth surface deformation in near real time could let us have a better understanding of nature hazards, and eventually minimize the impacts and help the local government or associated councils to make better decisions.

Differential Synthetic Aperture Radar Interferometry (hereafter called DInSAR) was widely applied to monitor such events with great success over the last two decades in events such as volcanic eruption, earthquake deformations and coastline erosion. The traditional DInSAR process was carried out by utilizing an externally provided DEM to remove the topographic information from the interferogram and capture the surface changes. The concept of DInSAR was first mentioned by Gabriel (Gabriel et al., 1989). However, it took a further four years before Massonnet demonstrated the first DInSAR result for the 1992 earthquake in Landers, California using the two-pass DInSAR technique. The accuracy was proved to be at centimeter-level, which was extremely competitive to conventional field survey techniques (Massonnet et al., 1993, Massonnet et al., 1994, Zebker et al., 1994). Zebker then proposed

the three-pass DInSAR technique in 1994; the main idea was to calculate the topographic phase signal by using an extra InSAR pair with very short temporal baseline (Zebker et al., 1994). Since then, DInSAR has been applied to many applications with great successes, namely, glacial motion monitoring (Gray et al., 1998), observation of volcanic swelling (Massonnet et al., 1996, Lanari et al., 1998, Hu et al., 2009), earthquake deformations measurement (Massonnet et al., 1993, Massonnet et al., 1994, Zebker et al., 1994, Suga et al., 2001, Ge et al., 2008, Hensley et al., 2009), underground mining detection (Ge et al., 2001, Ge et al., 2007, Hu et al., 2013), and underground water extraction monitoring (Chang et al., 2004, Ge et al., 2014). The DInSAR technique can measure topographic surface displacement with a greater likelihood of high accuracies when the time gap between two image acquisitions is relatively small. Therefore, temporal baseline is reduced and a dense grid of pixels can be applied. However, there are certainly some limitations which constrain DInSAR performance (Ferretti et al., 2001), especially when monitoring low-velocity subsidence within a long time period; the differential interferograms are focused to have large temporal and spatial baseline with the consequence of degrading the interferogram phase and hence only large coherent areas can be used to extract useful information. In addition, atmospheric phase screen (APS) could also degrade the quality of deformation estimation.

Experiments have been conducted over the past two decades by many researchers to better understand and mitigate the APS. Li et al. (2007) used both the Jarque-Bera and the Hinich methods to test the atmospheric signal in four SAR interfergrams over Shanghai, and found that the atmospheric signals in all interferograms are non-Gaussian distribution. Onn and Zebker (2006) exploited Taylor's "frozen-flow" hypothesis to correct the atmospheric bias, and they proved that additional improvement can be obtained when GPS measurements prior and after each SAR acquisition is available. Ferretti et al. (2001) exploited the spectral characteristics in designing filters to model and remove atmospheric artifacts from nonlinear deformation. Many other researches use external data, namely, meteorological model, GPS, MODIS to mitigate these effects; Li et al. (2006) used the concept of power law nature of the atmospheric effects to remove the atmospheric spectrum with meteorological and GPS data. Mathew et al. (2014) proposed a method to correct both troposphere and ionosphere components using MODIS and Total Electron Content (TEC) data and the final result agrees well with GPS measurement. These methods based on external data are proposed to mitigate the effect and most of them can reduce the atmospheric effect by about 20-40 percentages. Besides, these methods often rely on the atmospheric conditions (Cloud condition) and external data available. Others are based on simple data analysis or numerical weather prediction model.

APS is generally caused by the heterogeneity of the troposphere and ionosphere, of which troposphere mainly consists of atmospheric turbulence and atmospheric stratification, the later one has a major impact on the changes in vertical direction (atmospheric turbulence phase delay can be eliminated by using time-series analysis, such as PSI (Ferretti et al., 2001) and SBAS (Berardino et al., 2002) while ionospheric phase delay can be estimated using a dense GPS network equipped with 2-frequency GPS receivers. However, both of them are beyond the scope of this paper). The atmospheric stratification component is similar to orbital ramps and DEM errors, which are hard to distinguish from linear orbit error especially for longer wavelengths SAR (Agram and Simons, 2015). Recently, many researchers have tried to use Global Atmospheric Models (GAMs) to predict the tropospheric stratification phase delays at the SAR image acquisition time (Jolivet et al., 2011, Jolivet et al., 2014, Li et al., 2009). Doin et al. (2009) quantitatively validated the potential of GAMs (ERA-Interim (European Center for Medium-Range Weather Forecasts (ECMWF)), the North American Regional Reanalysis

(hereafter NARR), and NASA's Modern Era-Retrospective Analysis for Research and Applications (MERRA)) by comparing with empirical corrections. In this paper, we chose to use ERA-Interim and MERRA to estimate the APSs for both C-band ENVISAT ASAR and L-band ALOS PALSAR datasets.

II. Technology

DInSAR interferometry is characterized by single pass or repeat pass interferometry according to the number of platform passes over the same scene. Typically, repeat pass interferometry is operated to capture the same area twice at different times using only one antenna, the time difference is called the revisit time. The basic geometry of the SAR system is illustrated in Fig.1, where the first acquisition is called master image and the following one is slave image.

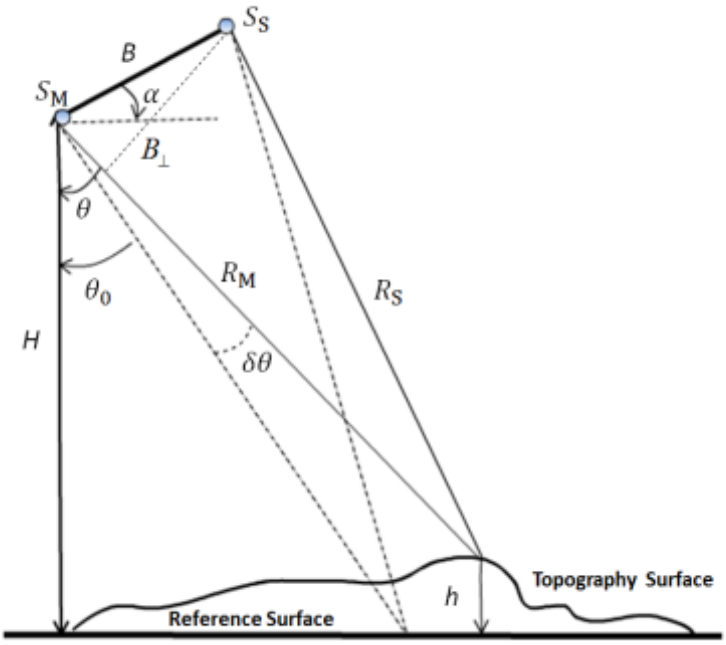

Fig. 1: Geometry of SAR system

Based on the geometric structure showing in Fig. 1, an interferometric phase $\emptyset$ (.) can be obtained based on complex images (Single Look Complex) from master and slave acquisitions. The master and slave SLC images are co-registered precisely at first for the convenience of calculating interferometric phases accurately (Touzi et al., 1999).This phase component is closely related to the range difference according to the geometry(Zebker and Goldstein, 1986, Ge et al., 2007, Ng et al., 2009):

Where λ is the carrier wavelength of radar pulses, θ is the look angle to the image pixel on the topographic surface, R_M and R_S are the range distances between antenna positions and topography target, α is the angle between the baseline and horizontal direction, D is the displacement of the image pixel along LOS direction, B is the length of baseline, $\emptyset$ (.) refers to the raw interferogram (Rosen et al., 1996).

$$\emptyset(.) = \frac{4\pi}{\lambda}(R_M - R_S) \quad (1)$$

$\emptyset$ (.) can also be written as equation (2) when assuming there is no ground displacement between two acquisition time.

$$\emptyset(.) \approx \frac{4\pi}{\lambda} B \sin(\theta - \alpha) \quad (2)$$

Then the earth ellipsoid phase need to be simulated based on orbit parameters so that they can be eliminated from raw interferograms. It is also known as the extension of ground surface along range direction (Fig. 1), which is called flat earth effect. The flat earth phase can denote as the following equation when assuming that the topography is absent from the reference surface:

$$\emptyset_{\text{flat}} = \frac{4\pi}{\lambda} B \sin(\theta_0 - \alpha) \quad (3)$$

Where $\emptyset_{\text{flat}}$ is referred to flat earth phase, by removing the phase component from $\emptyset$ (.), the result "flattened" phase is given:

$$\emptyset_{\text{flattened}} = \emptyset(.) - \emptyset_{\text{flat}} = \frac{4\pi}{\lambda} B \cos(\theta_0 - \alpha)\, \delta\theta \quad (4)$$

The relationship between $\delta\theta$ and height of the target h is given by (Rosen et al., 1996):

$$\delta\theta \approx \frac{h}{R_{\text{M}} \sin\theta_0} \quad (5)$$

Where θ_0 the local incidence angle, h is the topography target height refers to the reference surface, $\delta\theta$ is the difference between θ and θ_0.

It is worth nothing that the above equation is a purely based on geometric structure. In reality, the ground deformation, orbital error, atmosphere disturbance and noise information should be considered as well, therefore, the new equation is become:

$$\emptyset_{\text{flattened\_corr}} = \emptyset_{\text{topo}} + \emptyset_{\text{defo}} + \emptyset_{\text{orbital}} + \emptyset_{\text{atmos}} + \emptyset_{\text{noise}} \quad (6)$$

Here, these five components denote phases contributed by underground feature deformation, topography, orbital, atmosphere artefacts, and noise. Among which, topographic phases $\emptyset_{\text{topo}}$ is normally removed by importing an external data contains terrain information. As a result, such component can be simulated based on this external data, in this paper, a three arc-second (approx. 90m resolution) Digital Elevation Model was generated by the version 2 Shuttle Radar Topography Mission (SRTM) to remove the surface information from the interferogram. However, due to the inaccuracy of the DEM, there will remain some noise contributed by topography residual phase, such noise can be eliminate with high quality DEM, and we assume this part is included inside of $\emptyset_{\text{noise}}$.

The phase component $\emptyset_{\text{orbital}}$ is made up of linear-component dominant phase and nonlinear phase, the linear component can be eliminated by using ground control points. An alternative way to do this is by applying a FFT to transfer the interferometric signals into the frequency domain and measure the frequency of the signal with maximum power, which is called residual phase changing rate (Zhang et al., 2009, Ng et al., 2012). However, residual nonlinear topographic residual phases caused by orbital errors, are difficult to remove and therefore are considered to be included in $\emptyset_{\text{noise}}$.

The phase component $\emptyset_{atmos}$ in this paper is refers to as atmospheric stratification component. A python based atmospheric correction tool – PyAPS was exploited to estimate the stratified troposphere delay from GAMs (Jolivet et al., 2014), and removed from the differential interferogram. The detailed equation can be found in Du et al. (2016). A 5 x 5 low pass adaptive filter was then exploited to eliminate the component $\emptyset_{noise}$.

At last, a differential interferogram mainly composed of deformation phases can be obtained. Because interferograms are based on relative phases (-π to π), the conversion processes to obtain absolute values are necessary so that the relationships between phases and displacement values can be built, which is also known as phase unwrapping. The relationship between deformation phase and displacement value D is presented in equation (7) (Fornaro et al., 2009). The processing flowchart of DInSAR technique can be found in Figure 2.

$$\emptyset_{defo} = -\frac{4\pi}{\lambda} D \tag{7}$$

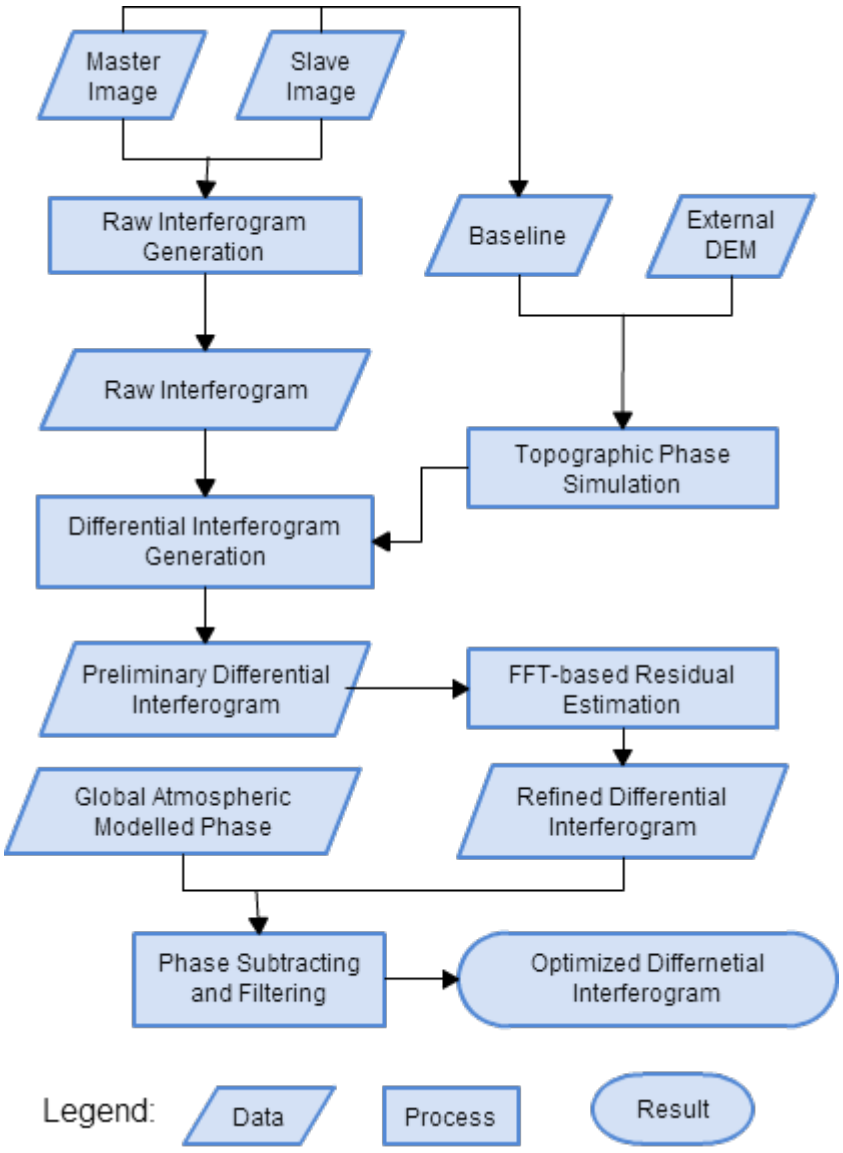

Fig. 2: Processing flowchart of DInSAR technique

III. Result and Discussion

ERA-Interim is a global reanalysis of ECMWF, which can provide a global 0.7° grid's estimation of water vapor partial pressure, temperature and geopotential elevation along 37 pressure levels every 6 hours daily (Start at 0:00 UTC). MERRA is also a global atmospheric reanalysis, which can be utilized to estimate the same variables during the same period of time. The difference is that MERRA is along 42 pressure levels on a global grid (0.5° x 0.75° along longitude and latitude, respectively). The detailed description of ERA-Interim and MERRA can be found in Dee et al. (2011) and Rienecker et al. (2011), respectively.

Table 1 Images for Interferometric Pairs Used

Location	Satellite	Orbit	Interferometric Pair Date (dd/mm/yyyy)	Incidence Angle	Line/Pixel Spacing	Perpendicular Baseline (m)
Qinghai	ALOS-1	Ascending (Track 477 Frame 714)	13/06/2009-29/07/2009	38.7°	18.7 m/ 19.1 m	112.5
North China Plain	ALOS-1	Ascending (Track 447 Frame 750, 760,770)	25/01/2010-12/03/2010	38.7°	18.7 m/ 19.1 m	602.89
Ordos	ENVISAT	Descending (Track 176 Frame 2805)	04/12/2011-02/02/2012	23°	15.6 m/ 25.5 m	110.7

In this paper, the experiments were conducted over Qinghai Mountains, North China Plain and Ordos Basin, China, respectively with 3 pairs of SAR images acquired from L-band ALOS-1 PALSAR and C-band ENVISAT ASAR (Table 1). Since the acquisition time for ALOS and ENVISAT were 2:00 pm UTC and 3:00 am UTC, respectively, the APS (derived from both GAMs) for ALOS were estimated at 12:00 pm UTC while the APS for ENVISAT were estimated at 6:00 am UTC.

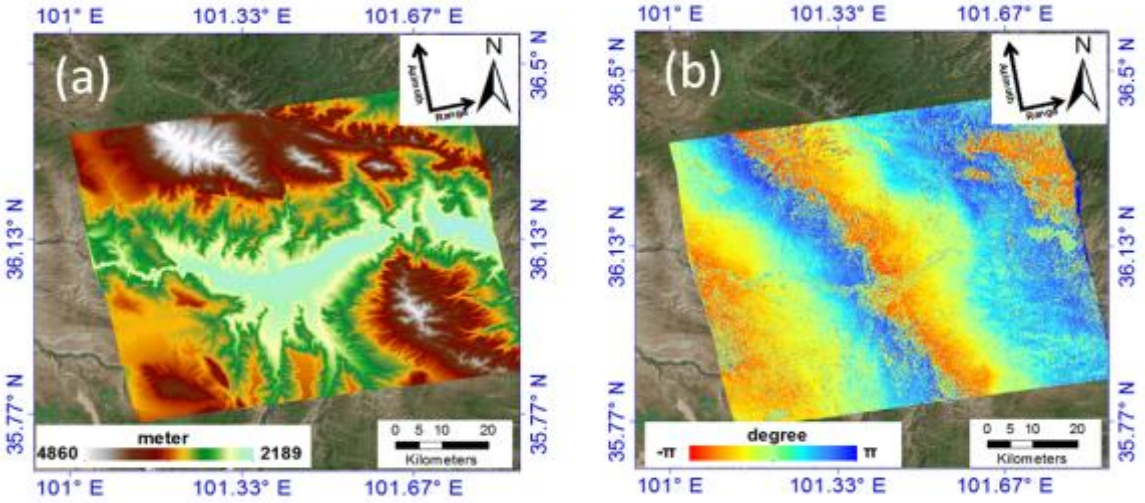

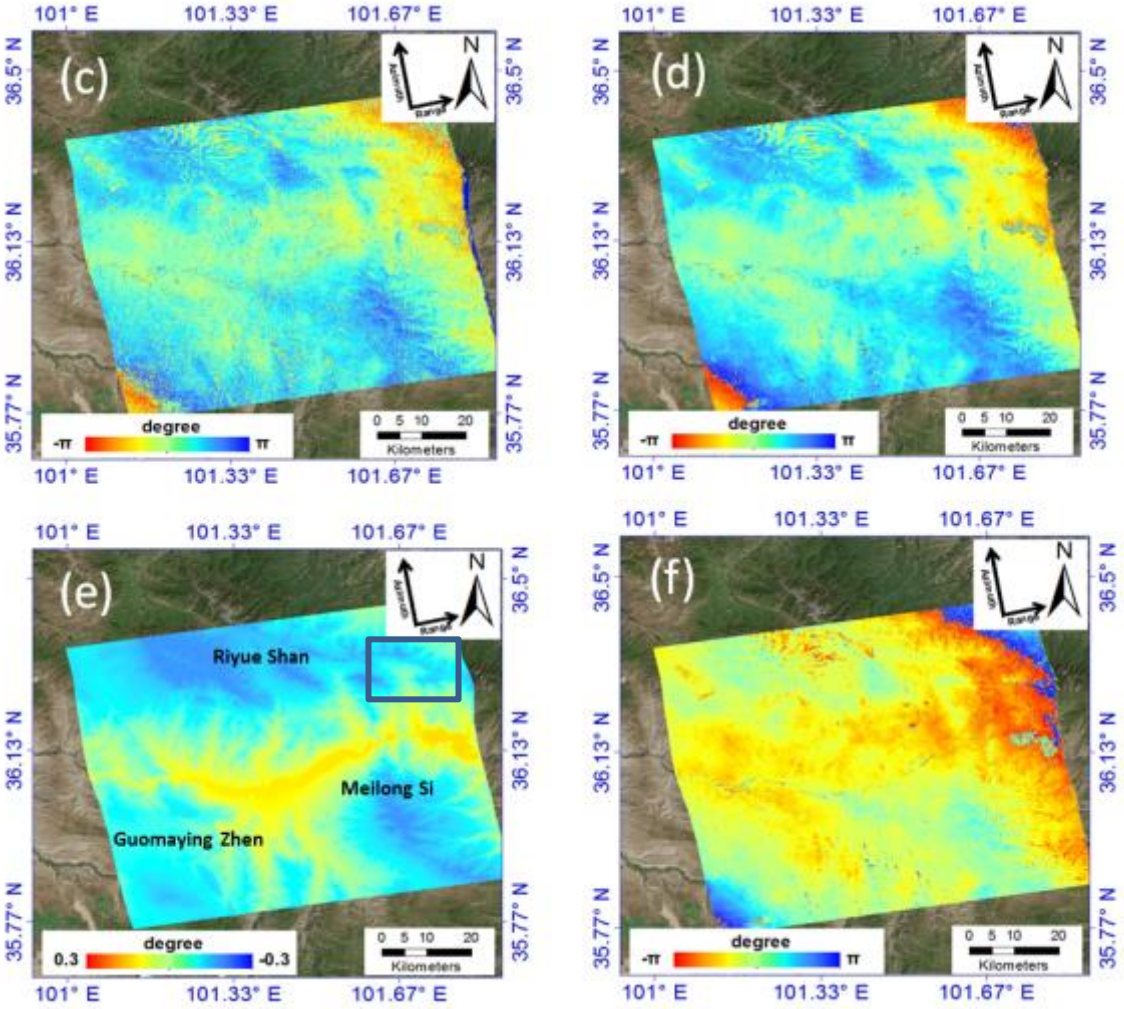

Fig. 3: (a)DEM over Qinghai Mount (b) The primary differential interferogram (c)The de-ramped differential interferogram without denoising (d)The de-ramped differential interferogram (e)APS derived from MERRA (f) Differential interferogram after APS correction. The de-ramped interferogram is generated from ALOS-1 PALSAR pairs of June 13, 2009 and July 29, 2009.

Figure 3 shows a 46 day interferogram covering an area in Qinghai Mountains, extending from Guoyaming Zhen in the southwest to the Riyue Shan in the north. The elevation change is from 2189 meter to 4860 meter. The spatial perpendicular baseline $B_{\perp}$ is 112.5 m. Due to the relatively short temporal baseline, we consider the deformation signals are negligible. An example of linear oribt error overpriting of the APS signal is shown in Figure (b) and (c). The APS prediction derived from MERRA (Figure 3 (e)), reproduces the refined de-ramped differential interferogram reasonably well (after low adaptive filter) (Figure 3 (d)). It is clear that most blue fringes near Riyue Shan, Guomaying Zhen and Meilong Si are correlated with elevation, which are referred to the atmospheric stratification phase delay. However, some of the predicted patterns are not seen in Figure 3 (d), e.g. the northeastern phase delay marked with red rectangular box. Figure 3 (f) is the differential interferogram after the APS correction. At this stage, most elevation related atmospheric fringes have been removed. Phase unwrapping process then can be applied to Figure 3 (f).

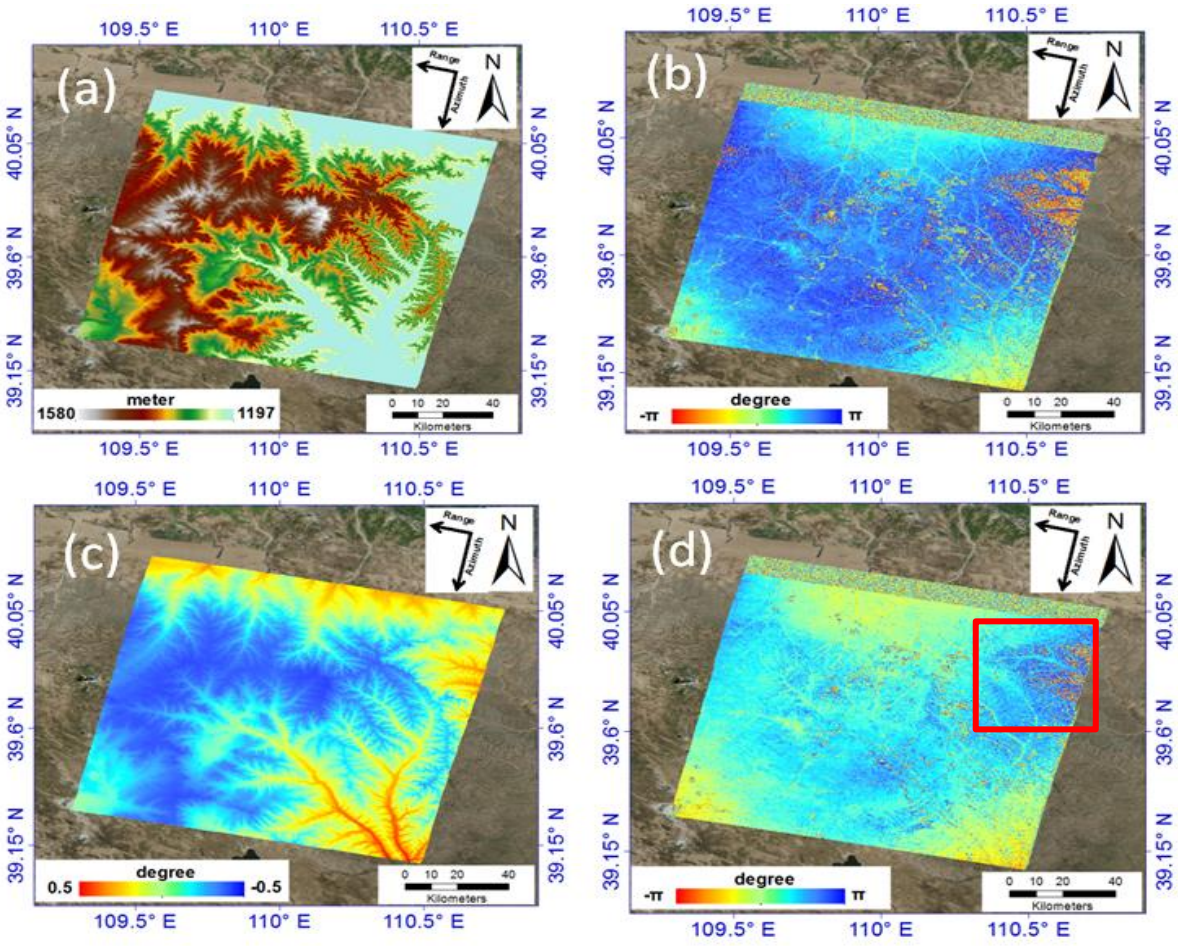

Fig. 4: (a) DEM over Ordos Basin (b) The de-ramped differential interferogram (c)APS derived from MERRA (d) Differential interferogram after APS correction. The de-ramped interferogram is generated from ENVISAT ASAR pairs of December 04, 2011 and February 02, 2012.

Figure 4 demonstrates a 60 day interferogram over Ordos Basin, the elevation change is ranging from 1197 m to 1580 m, which is not significant (Figure 4 (a)). The spatial perpendicular baseline $B_{\perp}$ is 110.7 m, and we also assume there is no deformation during this relative short period of time. Figure 4 (b) is the de-ramped interferogram generated from ENVISAT ASAR pairs of December 04, 2011 and February 02, 2012. The blue fringes of the interferogram from the west to the middle part, which are correlated with elevation to some extent, has been removed from Figure 4 (d). However, no clear correlation is visible in the northeast parts marked with red rectangular box. Apart from that, the APS predicted from the outputs of MERRA (Figure 4 (c)), reproduces the observed phase in the de-ramped differential interferogram quite well with a reduction of standard devation of 31.5% in Figure 4 (d). It is worth noting that some atmospheric stratified signals not well modelled, especially over the northeast parts, are in low-elevation terrains. In this case, MERRA produce poor relationship between phase and elevation on low-elveation terrains.

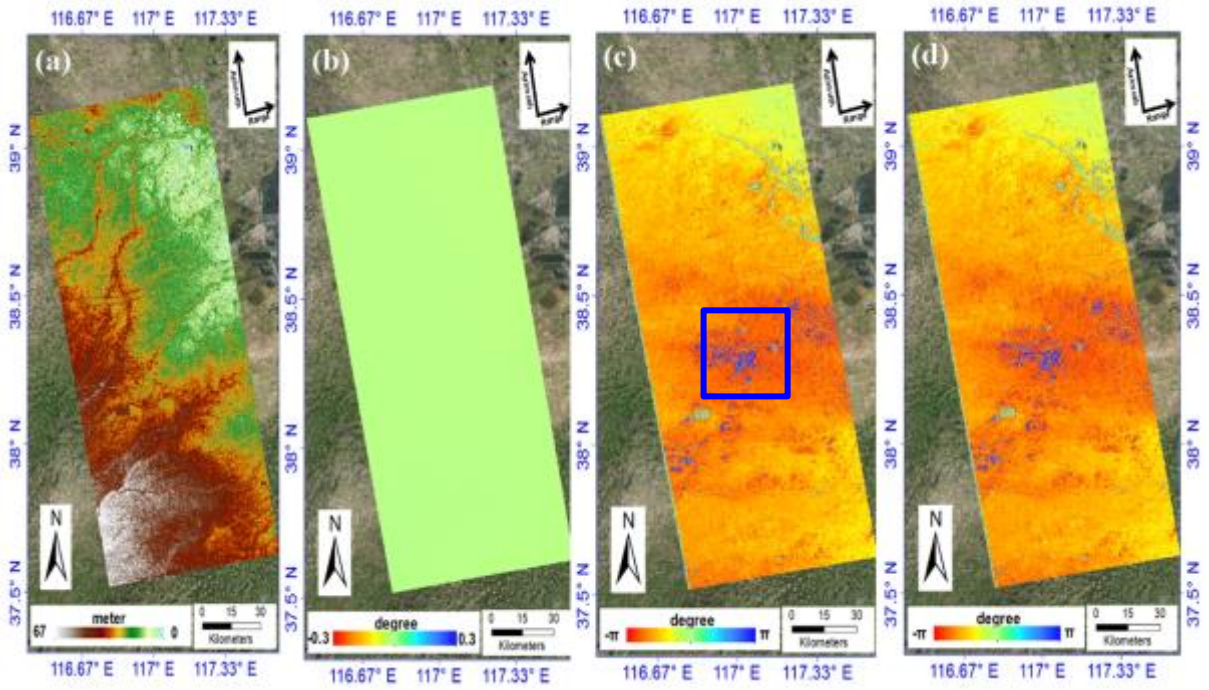

Fig. 5: (a) DEM over North China Plain (b) The de-ramped differential interferogram (c)APS derived from ERA-Interim (d) Differential interferogram after APS correction. The de-ramped interferogram is generated from ALOS-1 PALSAR pair of August 09, 2009 and February 09, 2010.

Figure 5 (a) shows the DEM information over North China Plain, the range of the elevation is from 0 m to 67 m. Figure 5 (b) is the de-ramped differential interferogram generated from ALOS-1 PALSAR pairs of January 25, 2010 and March 12, 2010, the image contains some noise because of the large perpendular baseline of 602.89 m. Figure 3 (c) is the predicted APS from ERA-Interim reanalysis, while Figure 4 (d) is the refined differential interferogram after the APS correction. It is clear that ERA-Interim fail to predict the atmospheric phase delay. A possible explaination is that the study region is within low-elevation terrains with the elevation change of 67 m, which is not significant. Therefore, atmospheric turbulence phase delay should be the dominant factor. Besides, some anthropogenic activities marked by blue rectangular box could also cause phase difference.

Conclusion and Future work

In this paper, we initially gave a brief description of a new DInSAR approach and SAR images acquired from two satellite radar sensors: ALOS-1 PALSAR and ENVISAT ASAR were utilized to generate the differential interferograms over three test sites with different topographic conditions, North China Plain, Ordos Basin and Qinghai Mountains. Two GAMs (MERRA and ERA-Interim) were then exploited to estimate the atmospheric stratification phase delay. Both of them can provide reasonable results, e.g. a reduction of standard deviation account for 31.5% was estimated in Ordos Basin. However, there are still some residual atmospheric phases not being well modelled by these two GAMs. Three possible reasons might be: 1) some anthropogenic activities over these regions. 2) parts of the study region are within low-elevation terrains, where the range of topographic change is small. 3) The estimation time for atmospheric stratified phase delay is slightly different from SAR image acquisition time. For the future work, we would like to model the APS for X-band

satellites, for example, TerraSAR-X and COSMO-SkyMed, and further evaluate the effectiveness of this method.

Acknowledgement

This research was supported under Australian Research Council's Discovery funding scheme (project number DP130101694). The author would like to thank the European Space Agency (ESA) and the Earth Remote Sensing Data Analysis Centre (ERSDAC) for providing the ENVISAT ASAR and ALOS PALSAR data, respectively.

References

AGRAM, P. & SIMONS, M. 2015. A noise model for InSAR time series. *Journal of Geophysical Research: Solid Earth*.

BERARDINO, P., FORNARO, G., LANARI, R. & SANSOSTI, E. 2002. A new algorithm for surface deformation monitoring based on small baseline differential SAR interferograms. *Geoscience and Remote Sensing, IEEE Transactions on,* 40**,** 2375-2383.

CHANG, C., CHANG, T., WANG, C., KUO, C. & CHEN, K. 2004. Land-surface deformation corresponding to seasonal ground-water fluctuation, determining by SAR interferometry in the SW Taiwan. *Mathematics and Computers in Simulation,* 67**,** 351-359.

DEE, D., UPPALA, S., SIMMONS, A., BERRISFORD, P., POLI, P., KOBAYASHI, S., ANDRAE, U., BALMASEDA, M., BALSAMO, G. & BAUER, P. 2011. The ERA ‐ Interim reanalysis: Configuration and performance of the data assimilation system. *Quarterly Journal of the Royal Meteorological Society,* 137**,** 553-597.

DOIN, M.-P., LASSERRE, C., PELTZER, G., CAVALIÉ, O. & DOUBRE, C. 2009. Corrections of stratified tropospheric delays in SAR interferometry: Validation with global atmospheric models. *Journal of Applied Geophysics,* 69**,** 35-50.

DU, Z., GE, L., LI, X. & NG, A. H.-M. 2016. Subsidence monitoring in the Ordos basin using integrated SAR differential and time-series interferometry techniques. *Remote Sensing Letters,* 7**,** 180-189.

FERRETTI, A., PRATI, C. & ROCCA, F. 2001. Permanent scatterers in SAR interferometry. *Geoscience and Remote Sensing, IEEE Transactions on,* 39**,** 8-20.

FORNARO, G., PAUCIULLO, A. & SERAFINO, F. 2009. Deformation monitoring over large areas with multipass differential SAR interferometry: a new approach based on the use of spatial differences. *International Journal of Remote Sensing,* 30**,** 1455-1478.

GABRIEL, A. K., GOLDSTEIN, R. M. & ZEBKER, H. A. 1989. Mapping small elevation changes over large areas: differential radar interferometry. *Journal of Geophysical Research: Solid Earth (1978–2012),* 94**,** 9183-9191.

GE, L., CHANG, H.-C. & RIZOS, C. 2007. Mine subsidence monitoring using multi-source satellite SAR images. *Photogrammetric Engineering & Remote Sensing,* 73**,** 259-266.

GE, L., NG, A. H.-M., LI, X., ABIDIN, H. Z. & GUMILAR, I. 2014. Land subsidence characteristics of Bandung Basin as revealed by ENVISAT ASAR and ALOS PALSAR interferometry. *Remote Sensing of Environment,* 154**,** 46-60.

GE, L., NG, A. H.-M., LI, X., LIU, Y., DU, Z. & LIU, Q. 2015. Near real-time satellite mapping of the 2015 Gorkha earthquake, Nepal. *Annals of GIS,* 21**,** 175-190.

GE, L., RIZOS, C., HAN, S. & ZEBKER, H. Mining subsidence monitoring using the combined InSAR and GPS approach. Proceedings of the 10th International Symposium on Deformation Measurements, 2001. 1-10.

GE, L., ZHANG, K., NG, A., DONG, Y., CHANG, H.-C. & RIZOS, C. 2008. Preliminary Results of Satellite Radar Differential Interferometry for the Co-seismic Deformation of the 12 May 2008 Ms8.0 Wenchuan Earthquake. *Geographic Information Sciences,* 14**,** 12-19.

GRAY, A., MATTAR, K., VACHON, P., BINDSCHADLER, R., JEZEK, K., FORSTER, R. & CRAWFORD, J. InSAR results from the RADARSAT Antarctic Mapping Mission data: estimation of glacier motion using a simple registration procedure. Geoscience and Remote Sensing Symposium Proceedings, 1998. IGARSS'98. 1998 IEEE International, 1998. IEEE, 1638-1640.

HENSLEY, S., ZEBKER, H., JONES, C., MICHEL, T., MUELLERSCHOEN, R. & CHAPMAN, B. First deformation results using the NASA/JPL UAVSAR instrument. Synthetic Aperture Radar, 2009. APSAR 2009. 2nd Asian-Pacific Conference on, 26-30 Oct. 2009 2009. 1051-1055.

HU, Z., GE, L., LI, X., ZHANG, K., NG, A. H.-M. & RIZOS, C. 2009. Alos Palsar Observation of Kilauea Volcano activities from 2006 to 2009. *in International Conference on Geo-spatial Solutions for Emergency*
Management & 50th Anniversary of the Founding of the Chinese Academy of Surveying & Mapping. Beijing, China.
HU, Z., GE, L., LI, X., ZHANG, K. & ZHANG, L. 2013. An Underground-Mining Detection System Based on DInSAR. *Geoscience and Remote Sensing, IEEE Transactions on,* 51**,** 615-625.
JOLIVET, R., AGRAM, P. S., LIN, N. Y., SIMONS, M., DOIN, M. P., PELTZER, G. & LI, Z. 2014. Improving InSAR geodesy using global atmospheric models. *Journal of Geophysical Research: Solid Earth,* 119**,** 2324-2341.
JOLIVET, R., GRANDIN, R., LASSERRE, C., DOIN, M. P. & PELTZER, G. 2011. Systematic InSAR tropospheric phase delay corrections from global meteorological reanalysis data. *Geophysical Research Letters,* 38.
LANARI, R., LUNDGREN, P. & SANSOSTI, E. 1998. Dynamic deformation of Etna volcano observed by satellite radar interferometry. *Geophysical Research Letters,* 25**,** 1541-1544.
LI, Z., DING, X., HUANG, C., WADGE, G. & ZHENG, D. 2006. Modeling of atmospheric effects on InSAR measurements by incorporating terrain elevation information. *Journal of Atmospheric and Solar-Terrestrial Physics,* 68**,** 1189-1194.
LI, Z., DING, X., HUANG, C., ZOU, Z. & CHEN, Y. 2007. Atmospheric effects on repeat-pass InSAR measurements over Shanghai region. *Journal of atmospheric and solar-terrestrial physics,* 69**,** 1344-1356.
LI, Z., FIELDING, E. J. & CROSS, P. 2009. Integration of InSAR time-series analysis and water-vapor correction for mapping postseismic motion after the 2003 Bam (Iran) earthquake. *Geoscience and Remote Sensing, IEEE Transactions on,* 47**,** 3220-3230.
MASSONNET, D., FEIGL, K., ROSSI, M. & ADRAGNA, F. 1994. Radar interferometric mapping of deformation in the year after the Landers earthquake. *Nature,* 369**,** 227-230.
MASSONNET, D., ROSSI, M., CARMONA, C., ADRAGNA, F., PELTZER, G., FEIGL, K. & RABAUTE, T. 1993. The displacement field of the Landers earthquake mapped by radar interferometry. *Nature,* 364**,** 138-142.
MASSONNET, D., THATCHER, W. & VADON, H. 1996. Detection of postseismic fault-zone collapse following the Landers earthquake. Nature**,** 612-616.
MATHEW, J., MAJUMDAR, R. & VINOD KUMAR, K. 2014. Estimating the atmospheric phase delay for quantifying co-seismic deformation using repeat pass Differential SAR Interferometry: Observations from 20th April 2013 Lushan (China) Earthquake. *ISPRS-International Archives of the Photogrammetry, Remote Sensing and Spatial Information Sciences,* 1**,** 57-64.
NG, A. H.-M., CHANG, H.-C., GE, L., RIZOS, C. & OMURA, M. 2009. Assessment of radar interferometry performance for ground subsidence monitoring due to underground mining. *Earth, planets and space,* 61**,** 733-745.
NG, A. H.-M., GE, L., LI, X. & ZHANG, K. 2012. Monitoring ground deformation in Beijing, China with persistent scatterer SAR interferometry. *Journal of Geodesy,* 86**,** 375-392.
ONN, F. & ZEBKER, H. 2006. Correction for interferometric synthetic aperture radar atmospheric phase artifacts using time series of zenith wet delay observations from a GPS network. *Journal of Geophysical Research: Solid Earth (1978–2012),* 111.
RIENECKER, M. M., SUAREZ, M. J., GELARO, R., TODLING, R., BACMEISTER, J., LIU, E., BOSILOVICH, M. G., SCHUBERT, S. D., TAKACS, L. & KIM, G.-K. 2011. MERRA: NASA's modern-era retrospective analysis for research and applications. *Journal of Climate,* 24**,** 3624-3648.
ROSEN, P. A., HENSLEY, S., ZEBKER, H. A., WEBB, F. H. & FIELDING, E. J. 1996. Surface deformation and coherence measurements of Kilauea Volcano, Hawaii, from SIR‐C radar interferometry. *Journal of Geophysical Research: Planets,* 101**,** 23109-23125.
SUGA, Y., TAKEUCHI, S., OGURO, Y., CHEN, A., OGAWA, M., KONISHI, T. & YONEZAWA, C. 2001. Application of ERS-2/SAR data for the 1999 Taiwan earthquake. *Advances in Space Research,* 28**,** 155-163.
TOUZI, R., LOPES, A., BRUNIQUEL, J. & VACHON, P. W. 1999. Coherence estimation for SAR imagery. *IEEE Transactions on Geoscience and Remote Sensing,* 37**,** 135-149.
ZEBKER, H. A. & GOLDSTEIN, R. M. 1986. Topographic mapping from interferometric synthetic aperture radar observations. *Journal of Geophysical Research: Solid Earth (1978–2012),* 91**,** 4993-4999.
ZEBKER, H. A., ROSEN, P. A., GOLDSTEIN, R. M., GABRIEL, A. & WERNER, C. L. 1994. On the derivation of coseismic displacement fields using differential radar interferometry: The Landers earthquake. *Journal of Geophysical Research: Solid Earth (1978–2012),* 99**,** 19617-19634.
ZHANG, K., NG, A.-M., LI, X., CHANG, H.-C., GE, L. & RIZOS, C. A new approach to improve the accuracy of baseline estimation for spaceborne radar interferometry. Geoscience and Remote Sensing Symposium, 2009 IEEE International, IGARSS 2009, 2009. IEEE, V-162-V-165.

ZHAO, X. & JIANG, X. 2015.
Coal mining: Most deadly job in China [Online]. Available: http://www.chinadaily.com.cn/english/doc/2004-11/13/content_391242.htm [Accessed June 3 2015].

Study of Sporadic E using Daytime GHz Scintillation Observations in the Equatorial Region

Aramesh Seif[1], Kefei Zhang[1], Roland T. Tsunoda[2], Brett Carter[1], and Robert Norman[1]

[1]*SPACE Research Centre, RMIT University, Melbourne, Victoria, Australia*
[2]*Center for Geospace Studies, SRI International, Menlo Park, California, USA.*

Summary: The occurrences of 1.5 GHz daytime scintillations were recorded simultaneously at the Universiti Kebangsaan Malaysia (UKM) and a station at Langkawi during November and December 2010. The characteristics of daytime GHz scintillation and their relationship with E-region irregularities in the equatorial region were investigated. Ground-based measurements of scintillation were analyzed together with those of amplitude scintillation from Global Navigation and Satellite System (GNSS) radio occultation (RO) observations. Ground-based scintillation observations showed that strong amplitude scintillation with the S4 index exceeding 0.6 was frequently observed at UKM, but not at Langkawi, which is located closer to the magnetic dip equator. The results obtained from GNSS RO measurements revealed that daytime GHz scintillations observed at the two equatorial stations, UKM and Langkawi, were likely associated with blanketing sporadic (E_{sb}).

Keywords: Ionospheric Scintillation; Blanketing Sporadic E; Radio Occultation, GNSS

Introduction

Interactions of several atmospheric and ionospheric parameters occasionally generate thin-sheet layers of enhanced electron density in the altitude range between 90 and 110 km, with thickness of 0.5 – 5 km and a horizontal extent of 10-1000 km [1]. These thin sheets are called sporadic E (*Es*) layers because of their apparent intermittent appearances in time and space. The understanding of the *Es* formation process in mid-latitudes is explained via the wind shear theory proposed by Whitehead [1]; however, this theory fails to operate at dip equator, where inclination angles are very small [2]. Therefore, a better understanding of formation of this phenomenon at equatorial region is required.

Ionospheric scintillations at gigahertz (GHz) frequencies have been observed during both daytime and nighttime [3, 4, 5]; these studies have suggested that nighttime GHz scintillations arise from electron-density irregularities in the F region, while daytime GHz scintillation appear to be associated with blanketing sporadic E (E_{sb}). Most of the studies of E_{sb} related scintillation have focused on occurrences in the mid-latitude and low-latitude regions, where E_{sb} can form from the presence of wind shear. Hence, the question arises, what happens in the equatorial region, where the inclination angle is very small. Our discussion, above, shows that little is known about both the nature of E_{sb} and daytime GHz scintillations near and in the equatorial region. Given that we have a database of scintillations that was compiled from GPS measurements made from two stations in the equatorial region we elected to investigate the occurrences of E_{sb} in association with daytime GHz scintillations. In this paper, we present results from an analysis of daytime GHz scintillation data recorded by GPS ground-based stations, UKM and Langkawi, in the equatorial region. To identify the occurrence of E_{sb} over these two stations, we have used GPS-COSMIC radio occultation data.

Data and Methodology

The results presented herein were all derived from observations at two stations UKM, and Langkawi recorded by a dual-frequency GPS receiver, GSV4004 in November and December 2010. Details of the stations locations are shown in Table 1. We analysed only those data on which observations at both stations are available.

Table1. Information on stations

Station	Geographic Latitude	Geographic Longitude	Dip Latitude
UKM	2.55° N	101.46° E	5.78°S
Langkawi	6.19° N	99.51° E	1.90°S

The GSV4004 receiver is specifically designed to measure amplitude scintillation at the L1 (1.575 GHz) frequency for each GPS satellite. The intensity of amplitude scintillation is quantified with the S4 index, which is derived from the detrended signal intensity (SI) [6]. The GPS receiver provides the S4 index every 60 s [6]. This study is based on the analysis of the S4 index database. The amplitude scintillation recorded by the GSV4004B receiver has two parameters, total S4 (S_{4t}) and S_{4cor}. The total S4 (S_{4t}) is computed over a 60-second interval in real-time but includes the effect of ambient noise. In this work the corrected S4 was calculated by removing the ambient noise using the following Eq. (1)

$$S4 = \sqrt{S_{4t}^2 - S_{4cor}^2} \qquad (1)$$

To investigate daytime ionospheric scintillation activity, the S4 index has been analysed during 0600-1800h LT (2200-1000h UT). In addition an elevation angle of greater than 15º was adopted to reduce the multipath effects in this analysis, which is similar to the analyses by other researchers [7, 8]. The daytime scintillation events were classified into three levels: strong $S4 \geq 0.4$, moderate $0.3 \leq S4 \leq 0.4$ and weak $0.2 \leq S4 \leq 0.3$.

To be considered daytime scintillation the following threshold conditions of $S4 > 0.2$ for more than 4 min were implemented. Following Seif et al, 2015, three criteria were used to minimize the effects of multipath in our observations; they are as follows: (1) Set a threshold value where only the satellite signals that arrive at the receiver with an elevation angle of greater than 15° were used, (2) Consider times of lock greater than 240 s. In fact, the 'lock time' of the satellite signal is a useful parameter to allow the lock time of the receiver to be observed for each satellite pass. In other words, if the receiver loses lock, or does not maintain lock long enough (i.e. < 240 s), then the data can be disregarded, and (3) Use a multipath elimination technique to distinguish whether the S4 measurements were caused by scintillation or multipath [6].

The COSMIC Data Analysis and Archive Centre (CDAAC) provide the "scnLv1" data, which is the time series of amplitude scintillation (S4 index) for each RO event. The 1-Hz S4 index is used to represent the occurrence of the ionospheric irregularities in the E region. Specifically, we use the occurrence rate of S4 larger than the threshold of 0.3, which implies moderate to strong scintillation. Please note that we use the maximum S4 index from each RO profile rather than the whole profile to make the statistical analysis of the irregularity occurrence. There are two main reasons why the GPS RO S4 is different from the ground-based measurements: (1) the geometry with respect to the plasma irregularities is substantially different, and (2) the on-board GPS receivers measure the root-mean-square of the intensity

fluctuations over a 1 s interval, which is not strictly an S4 index, but rather an approximation [9]. As demonstrated by Wu et al. [10], Arras et al. [11], and Chu et al. [12], the 50-Hz signal-to-noise ratio (SNR) from the occultation antenna could also be used to identify E_{sb} occurrence and it might have a higher percentage than 1-Hz S4 used here if the vertical scale of *Es* is less than ~2 km (roughly corresponds to ~1 Hz sampling). Therefore, in this study, the E_{sb} occurrence is represented by the occurrence rate of the S4 index larger than 0.3 in the altitude range of 90 to120 km.

RESULTS

Occurrence of Daytime Scintillation Observed at Two Equatorial Stations

Fig.1 shows the percentage occurrence of daytime scintillation events observed from November to December 2010 at UKM and Langkawi stations. The comparison of daytime GHz scintillation is interesting because of the location of the stations, which enables us to study E_{sb} in accordance with daytime GHz scintillation occurred at two equatorial stations, where Langkawi represents measurements very close to the magnetic dip equator and UKM denotes a station far away from the magnetic dip equator. It is clear from Fig.1 that the percentage occurrence of daytime scintillations events observed at UKM station is much higher than at Langkawi. The implication is that scintillation is less frequent at the dip equator and more intense away from the magnetic dip equator. This also suggests that daytime scintillation varies with latitude. This is consistent with the result obtained from Oyinloye [13] who showed the occurrence of E_{sb} at dip equator is very low and becomes enhanced with increasing the latitude. Hence, this shows scintillations are most likely to be associated with E_{sb}.

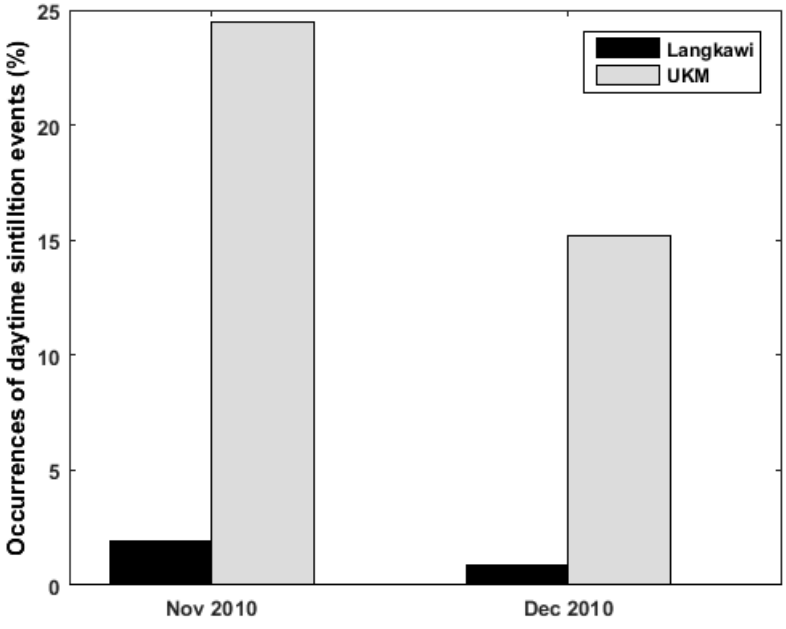

Fig 1. Percentage occurrences of daytime GHz scintillations observed at two GPS stations UKM (dip latitude = 5.78°S) and Langkawi (dip latitude = 1.90°S) in November and December 2010.

Daytime GHz Scintillation and its Relationship with E_{sb}

Further analyses were conducted to verify the relationship between daytime scintillation and E_{sb}. In order to explain daytime scintillation associated with thin layer E_{sb}, we present a model of a horizontal E_{sb} layer, which displays the variation of the propagation path length as a function of elevation angle through the E_{sb} layer. This model allows us to compare S4 values measured at one elevation angle with those measured at another elevation angle. In fact, we use the distribution of S4 index as the distribution of irregularity strength.

We are interpreting this observation in terms of changes in the propagation path length through an E_{sb} layer; that is, horizontally stratified and uniformly filled with scintillation-producing irregularities. That is, the E_{sb} layer should be at a fixed altitude above the surface of the Earth, and the thickness of the layer will be measured in the direction from the center of the Earth upward through the location of interest. Using this geometry, we draw a curve that represents the propagation path length as a function of elevation angle. Then, we assumed all increases in S4 are produced only by the propagation path length, we can then draw a curve to fit that shape.

For this purpose, we assume that the E_{sb} layer is a horizontal slab of some thickness and contains some irregularities in plasma density. If we look vertically through that slab, the propagation path length would be the thickness of the E_{sb} layer. We then assume that the irregularities, integrated through the thickness of the E_{sb} slab, produce scintillation. This should be the minimum value for S4 for this example, where scintillation occurred at 90º elevation angle. As the elevation angle decreases from 90º, the propagation path through the E_{sb} slab becomes oblique. This oblique path length should be longer than the path length in the vertical direction. For this horizontal slab and a flat earth, the oblique path length should equal to the vertical path length (the thickness of E_{sb} layer) divided by the sine of the elevation angle. We then apply this equation in order to draw a curve in Figures 2 and 3 to show whether the plasma-density fluctuations are approximately the same strength over the two stations UKM and Langkawi.

Fig. 2 shows scintillation (S4 index, black region) as a function of elevation angles at UKM in November 2010. The red curve displays the variation of the propagation path length as a function of elevation angle through the E_{sb} layer. It shows that the scintillation tends to occur at low elevation angles. Thus, this finding suggests that the propagation path length may be important. However, it can be seen clearly that bursts of enhanced scintillation (S4 index) occur, which are not necessarily confined to low elevation angles. This result is consistent with the earlier findings that GHz scintillations from E_{sb} at low latitudes are relatively rare. The bursts of S4 index enhancement at UKM seem consistent with the latitudinal distribution of E_{sb}.

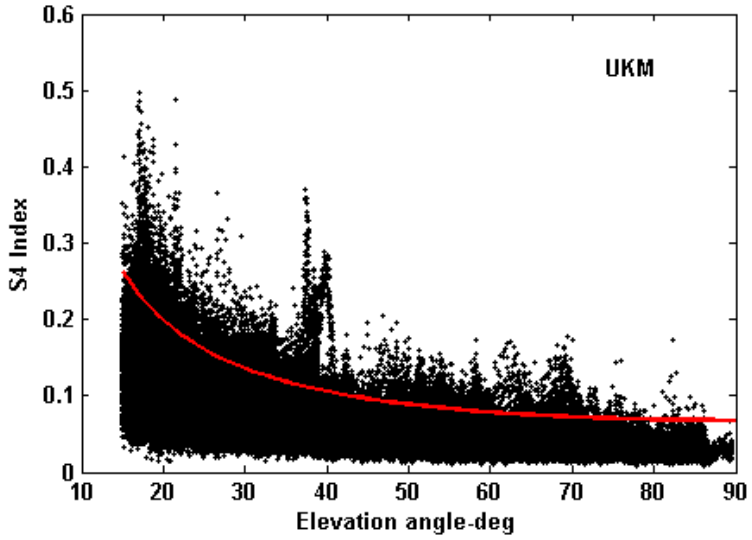

Fig 2. Distribution of scintillations (S4 index) as a function of elevation angle observed at UKM in November 2010.

Fig. 3 shows scintillation (S4 index, black region) as a function of elevation angle at the Langkawi station in November 2011. In other words, we assumed that the irregularities in the E_{sb} layer have some fixed intensity. Thus, the scintillation strength becomes proportional to the irregularity strength multiplied by the oblique propagation path length. This should mean that the S4 index value at 90º elevation angle is proportional to the irregularity intensity. Then, if all increases in the S4 index value are produced only by the propagation path length, we draw a red curve to fit that shape. In our plot of all the S4 values versus elevation angle, the top value seems to follow a curve that may resemble this kind of curve. All points above the red curve are associated with scintillation events when the irregularity strength increased substantially.

The finding that the top of the black region of the UKM plot is not as smoothly varying as the Langkawi curve suggests that the irregularities are not uniformly distributed in the layer. The higher S4 in the near-vertical direction over UKM compared with Langkawi is suggestive of a latitudinal dependence. The variability of the top of the black region of the UKM curve may also have latitudinal dependence, which is most likely to be associated with the magnetic-dip latitude. In fact, the irregular variation in the upper boundary of the black region suggests that E_{sb} is patchy, not only in latitude but also in longitude. This behavior is consistent with the expected behavior of E_{sb} [14].

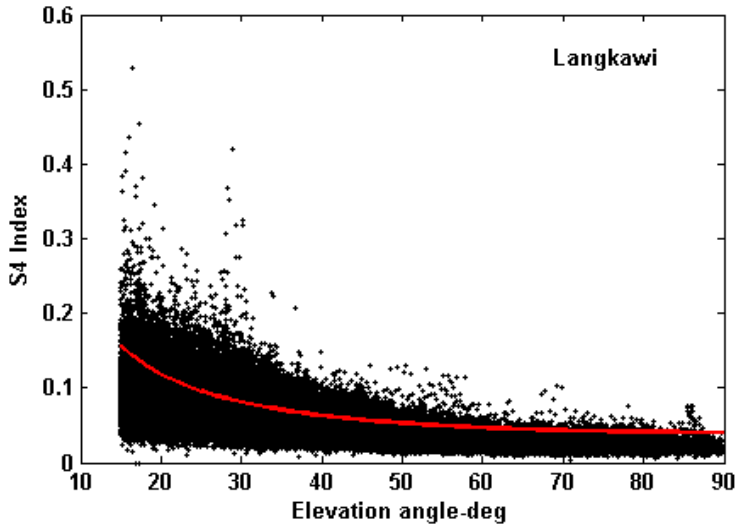

Fig 3. Distribution of GHz scintillations (S4 index) as a function of elevation angle observed at Langkawi.

Geographic Location of Scintillation Events

To determine where daytime scintillation occurs at two equatorial stations UKM and Langkawi, the geographic distribution of daytime scintillation is presented in Fig. 4.

Fig. 4 shows the geographical location of scintillations for three ranges of S4 indices. The locations correspond to their ionospheric pierce point (IPPs) for an altitude of 110 km. Two sets of colors are used: cool set (blue, magenta, and dark red) for Langkawi and warm set (green, yellow, and red) for UKM. The curved, light blue and green bands indicate the IPPs tracks from various GPS satellites, where S4 is negligible. The locations of the two stations are shown by triangles.

As can be seen from the Fig. 4 daytime GHz scintillation events occur frequently over UKM and Langkawi, where satellite elevation angles are low. This finding is consistent with the idea that scintillation-producing irregularities are embedded in a relatively thin layer, and longer path lengths through irregularities are necessary to produce significant scintillations (as our model shows in previous section). This need for low elevation angles is also consistent with the idea that E_{sb} layers are involved. This is also consistent with results obtained by Zeng and Sokolovskiy [15] who used GPS RO, and concluded that the scintillations resulting from E_{sb} were a result of wave interference caused by defocusing of the GPS signal within the E_{sb} layer. This mechanism works for low elevation angles.

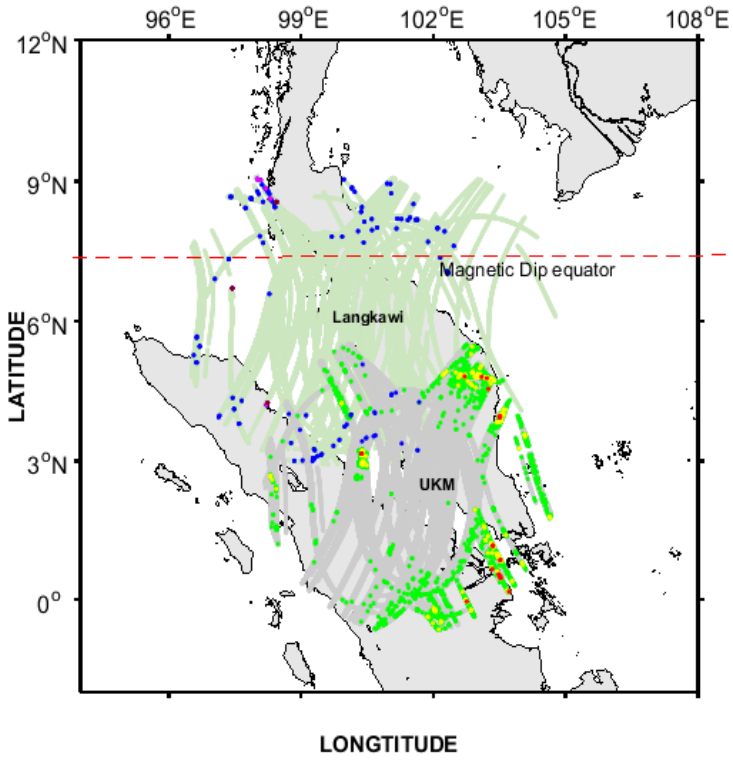

Fig.4. Geographic distribution of daytime scintillation events (S4 index) at different levels measured at all GPS satellites observed at UKM and Langkawi in November and December 2011 over Malaysia. The levels of scintillation intensity at UKM are coded for S4 ≥ 0.2 (green), S4 ≥ 0.3 (yellow), and S4 ≥ 0.4 (red), while those at Langkawi are coded as S4 ≥ 0.2 (blue), S4 ≥ 0.3 (magenta), and S4 ≥ 0.4 (dark red). The red dashed line shows the location of the magnetic-dip equator.

Radio Occultation Comparison

In this paper, the COSMIC RO observations during November and December 2010 were used to study the relationship between E_{sb} and daytime GHz scintillation occurrence. Specifically, the 1-Hz S4 index from COSMIC POD antennas are used to identify the daytime ionospheric irregularity occurrences in the E region such as E_{sb}.

The percentage occurrence of scintillations at UKM and Langkawi in association with E_{sb} using RO data in November and December 2010 is presented in Fig. 5. The statistical results indicate association of scintillation and E_{sb} during daytime at UKM and Langkawi stations in Malaysia. Note that the statistical results obtain from this study should be different from ground based GPS receivers because of different observational geometry. The ground based GPS receiver should be less sensitive to the E_{sb}.

To investigate occurrence of E_{sb} using RO during this period, we measured RO events in the E region (altitude between 90 to 120 km), which are attributed to presence of E_{sb} [14]. The tangent point locations for each RO event used in this study only limited to the daytime (0600-1800 LT), longitude (93ºE-106ºE) and latitude (3ºS-10ºN) in the time of S4 was measured.

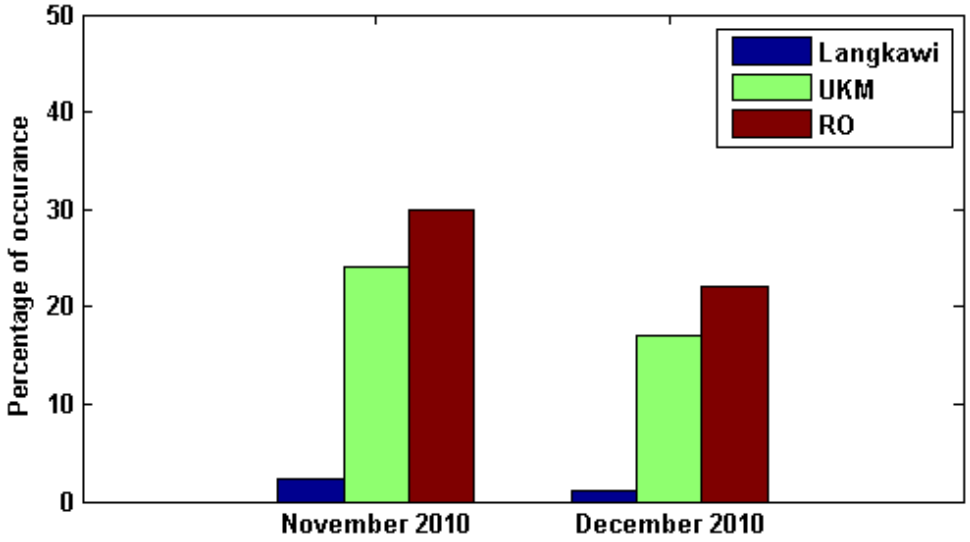

Fig. 5: The percentage occurrence of daytime GHz scintillation events in association with E_{sb}. Occurrence of E_{sb} with COSMIC radio occultation observations were measured from longitude (93°E-106°E) and latitude (3°S-10°N) in November and December 2010.

Conclusion and Summary

This paper concentrated on study of E_{sb} using daytime GHz scintillation in the equatorial region in Malaysia, where little or no previous information existed. Characteristics of the daytime GHz scintillation using GPS ground based stations show daytime GHz scintillation is weak, where is very close to the magnetic dip equator and is intense and more frequent away from the magnetic dip equator. A preliminary comparison has been done in the present paper between the E_{sb} measurements of L1 C/A code at 50-Hz sampling rate obtained from GPS-COSMIC radio occultation and the simultaneous observations of ground-based scintillation indicate that E_{sb} is associated with daytime GHz scintillation. Further analysis has been conducted to support this idea; that is, elevation angle-dependence of daytime GHz scintillation also shows irregularities consistent with thin layer E_{sb} and support interpretation that thin layer E_{sb} responsible for producing daytime scintillation.

Acknowledgements

This research was supported by a 2015 Endeavour Australian Fellowship awarded to A.Seif who gratefully acknowledges as well as financial support of the RMIT University through the ARC (LP130100243) and Space Research Environment (SERC) Research Program 2 projects that led by Prof K. Zhang. This research was also supported by the Victorian Postdoctoral Research Fellowship awarded to B. A. Carter. R. T. Tsunoda was supported by the National Science Foundation under grant ATM-1242815, and the Air Force Office of Scientific Research under Contract FA9550-15-C-0018. The COSMIC RO data was retrieved from the CDAAC website (http://cdaac-www.cosmic.ucar.edu/cdaac/). A. Seif gratefully acknowledges the GPS data that provided by Mardina Abdullah from National University of Malaysia as well as and the Langkawi National Observatory for providing the Langkawi station's data. The paper results were presented as an oral at 15th ASRC conferences.

References

1. Whitehead, J., The formation of the sporadic-E layer in the temperate zones, *Journal of Atmospheric and Terrestrial Physics,* Vol, 20, 1961, pp. 49–58.

2. Chandra, H. and Rastogi R. G. "Blanketing sporadic E layer near the magnetic equator", *Journal of Geophysical Research,* 80, 1975, pp.149, doi:10.1029/JA080i001p00149

3. Cervera M. A. and Thomas R. M., "Latitudinal and temporal variation of equatorial ionospheric irregularities determined from GPS scintillation observations" *Ann. Geophys.*, 24, 2006, pp. 3329–3341.

4. Zou, Y. H. "Ionospheric scintillations at Guilin detected by GPS ground-based and radio occultation observations". *Advances in Space Research*. 47(6), 2011, PP 945–965.

5. Seif, A. Abdullah, M., Hasbi, A.M. and Zou, Y. "Investigation of Ionospheric scintillation at UKM station Malaysia during low solar activity" *Acta Astronautica Journal*, Vol 81, 2012, pp. 92–101.

6. Van Dierendonck, A. J., Klobuchar, J. and Hua, Q. "Ionospheric scintillation monitoring using commercial single frequency C/A code receivers" in *Proceedings of ION GPS-93,* Salt Lake City, Utah. 1993.

7. Cervera M. A., Thomas, R.M, Groves K.M., Ramli, A.G. and Effendy " Validation of WBMOD in the Southeast Asian region", *Radio Science*, Vol 36, No. 6, PP. 1559-1572.

8. Seif, A., Tsunoda R.T., Abdullah, M. Hasbi A.M., "Daytime Gigahertz Scintillations Near Magnetic Equator: Relationship to Blanketing Sporadic *E* and Gradient-Drift Instability, Earth, Planets and Space Journal, DOI: 10.1186/s40623-015-0348-2.67:177. PP.1-13. http://www.earth-planets-space.com/content/67/1/177.

9. Ko, C. P., and H. C. Yeh, "COSMIC/FORMOSAT-3 observations of equatorial F region irregularities in the SAA longitude sector", *Journal Geophysical. Research*, 115, 2010, A11309, doi:10.1029/2010JA015618.

10. Wu, D. L., Ao, C. O., Hajj, G. A., M. de la Torre Juarez, and Mannucci A. J., "Sporadic E morphology from GPS-CHAMP radio occultation", *Journal Geophysics Research.,* 110, 2005. A01306, doi:10.1029/2004JA010701.

11. Arras, C., Wickert J., Beyerle G., Heise S., Schmidt T., and Jacobi C., "A global climatology of ionospheric irregularities derived from GPS radio occultation", *Geophysical Research Letter.,* 35, 2008, L14809, doi:10.1029/2008GL034158.

12. Chu, Y. H., Wang C. Y., Wu K. H., Chen K. T., Tzeng K. J., Su C. L., Feng W., and Plane J. M. C., "Morphology of sporadic E layer retrieved from COSMIC GPS radio occultation measurements: Wind shear theory examination", *Journal Geophysics Research.,* 119, 2014, pp. 2117–2136, doi:10.1002/2013JA019437.

13. Oyinloye, J . O., "A study of sporadic E in the equatorial region", *Planet Space Science*, Vol. 19, 1971, pp. 1131–1139. doi:10.1016/0032-0633(71) 90109-7.

14. Tsunoda, R. T., "On blanketing sporadic E and polarization effects near the equatorial electrojet", *Journal of Geophysical Research,* Vol. 113, A09304, doi:10.1029/2008JA013158, 2008, pp. 1-10.

15. Zeng, Z., and S. Sokolovskiy, "Effect of sporadic E clouds on GPS radio occultation signals". *Geophysical. Research. Letter*, 37, 2010, L18817, doi:10.1029/2010GL044561.

Observations of a Travelling Ionospheric Disturbance over Adelaide, Australia

Anne. M. Unewisse, Manuel. A. Cervera, Trevor. J. Harris and Andrew. D. Cool

Defence Science and Technology Group, PO Box 1500 Edinburgh SA, 5111, Australia

Summary:

A Travelling Ionospheric Disturbance (TID) passing over Adelaide, Australia was observed simultaneously in 630.0 nm airglow images and high time resolution 2 – 22 MHz ionospheric sounder data by the Defence Science and Technology Group (DST group) on the 27th of January 2014 from approximately 10 UT to 20 UT. A comparison between the two observations shows a strong inverse correlation between the night-time ionospheric virtual height measurement, h'F, and airglow intensity in both large and small scale features. This event was unusual in two ways: a) it occurred at solar maximum and b) part of the TID split into a smaller TID before reforming. TID wavelength, velocity and period parameters calculated from both airglow and high-frequency (HF) radio measurements and are found to be in agreement.

Keywords: Airglow imaging, ionospheric studies, thermospheric banding, TIDs

Introduction

Travelling Ionospheric Disturbances (TIDs) are quasi-periodic waves commonly seen in the ionosphere during geomagnetically quiet times. They are divided into small, medium and large scale classes by velocity, period and/or wavelength but accepted definitions vary widely [1-4]. Large scale TIDs (LSTIDS) have periods ranging from 45 minutes to several hours, horizontal speeds of 200-1000 m/s and wavelengths ~1000 km [5]. They are thought to result from geomagnetic storms in auroral zones and travel westward and equatorward [3].

Medium Scale TIDs (MSTIDS) have periods ranging from 30-90 minutes, horizontal speeds of 50-100 m/s and wavelengths of 100-300 km [6]. They arise from a variety of sources including tropospheric jet streams, atmospheric gravity waves, cold fronts and passage of the solar terminator [5]. Night time MSTIDs tend to travel equatorward and westward in the southern hemisphere and are associated with electro dynamical forces [4]. Their daily and seasonal variation is thought to be due to field-aligned irregularities embedded in the Sporadic E (Es) layer [7]. Long term (7 – 10 years) studies over Brazil [1, 8] and Indonesia [2] suggest that MSTIDs occur almost exclusively at solar minimum with the rate of observed MSTIDs decreasing with decreasing solar activity.

Small-scale TIDs are less well understood but may be associated with local convective activity, lightning strikes and cold fronts propagating into the ionosphere [3]. They have periods of less than 30 minutes and wavelengths of less than ~100 km [5].

When TIDs are present at F-layer altitudes they cause a characteristic periodic rise and fall in bottom side F-layer measurements recorded by High Frequency (HF) radio sounders [1, 9, 10], Incoherent Scatter Radars (ISR) [11-13] and GPS-TEC ground and space based instruments [4, 14]. Increasingly, F-layer TIDs are imaged using all-sky airglow imagers [15-18] due to their low cost / good sky coverage benefit. A single airglow imager can cover a 180 degree field of sky much more cheaply than an array of GPS sensors or a satellite based sensor.

F-layer 630nm red airglow is a result of the three step chemiluminescent reaction [2, 13]:

$$O^+ + O_2 \rightarrow O_2^+ + O \quad (1)$$
$$O_2^+ + e^- \rightarrow O\left(^1D\right) + O \quad (2)$$
$$O\left(^1D\right) \rightarrow O\left(^3P\right) + hv_{630.0nm} \quad (3)$$

so that airglow production is dependent on both electron and O^+ density which are approximately equal at F-layer altitudes making it a sensitive indicator of F-layer height [19]. Daytime airglow intensity is dominated by solar ionization with a small contribution from re-combination whereas night-time airglow is fuelled by recombination alone. The change in airglow intensity from day to night can take 2-3 hours to stabilize after sunset [20].

As airglow brightness is dependent on species density, the passage of a TID through the F-layer is indicated by a series of parallel dark and light bands in 630 nm airglow images travelling in a direction perpendicular to their alignment [6, 13, 17, 20]. Due to the Earth's magnetic field and direction of rotation, airglow bands tend to align northwest to southeast in the Northern hemisphere travelling southwest [20] whereas in the southern hemisphere, they align northeast to southwest and travel northwest [5, 19, 21].

Studies of airglow correlation with HF [1], incoherent scatter radar [11, 13] and TEC measurements [14] have found that dark airglow bands are associated with increasing F-layer heights and the bright airglow bands with decreasing F-layer heights. This brightness/F layer height relationship is also seen in 'brightness waves' [12] and plasma bubbles [16, 22].

This paper examines TIDs observed near solar maximum in January 2014 using all-sky 630 nm airglow images and HF sounder ionogram data over one night of experimental opportunity. Wavelengths of various components of TIDs are calculated using HF and airglow data and the results compared.

Equipment

Airglow imager

The Defence Science and Technology (DST) Group's Thermospheric Radar Airglow Correlation Experiment (TRACE) imager has operated from Edinburgh, SA (34.7S, 138.62 E) since January 2012 in support of atmospheric studies at altitudes of interest to High Frequency (HF) Over-The-Horizon Radar (OTHR). It images airglow originating from altitudes of around 96 km (E layer) and 250 km (F layer).

TRACE consists of a Keo Sentry camera with 180 degree field of view (FOV), 24mm / F4.0, achromatic fisheye lens and a 16 bit back illuminated 1024 x 1024 CCD with a pixel size of 13.3μm x 13.3μm [23]. The imager's FOV corresponds to image diameters of ~1000 km at an altitude of 250 km at F-layer heights [24].

The TRACE imager has five available 2 nm bandwidth filters designed to isolate airglow lines originating from altitudes in the E and F ionospheric regions. They are centred on: 557.7 nm O(1S) oxygen emission primarily from an altitude of 96 km, 630.0 nm O(1D) oxygen emission (250 km), 777.4 nm O(5P) oxygen emission (350 km), 589.3 nm sodium doublet emission (92 km) and 572.4 nm used to measure local non-airglow background conditions (the control image). Images are obtained in a continuous cycle through selected filters with typical exposure times of 2 minutes. F-layer airglow reported in this paper is imaged at 630 nm with 2 minutes exposures taken approximately 8 minutes apart.

HF Sounders

DST Group's HF Vertical Incidence Sounder (VIS) [5, 25] is located at Woodside Army Barracks, South Australia and consists of a cross-delta antenna with 24 m mast and 21 m arms for transmission and a crossed magnetic loop antenna for reception. A second temporary receiving antenna is occasionally located 40 km away at the St Kilda receiving station forming a Quasi-Vertical Incidence Sounder (QVIS) with an ionospheric probe point half way between the two sites. The transmitted waveform is a continuous-wave (CW) signal swept linearly in frequency from 2 – 22 MHz (a chirp) via a solid-state digital waveform generator fed into a 100 W power amplifier (although transmitted power was nominally 50 W). The receivers use a digital sweeping oscillator feeding into a wide-band A/D, and a GPS to maintain time synchronisation. An ionogram of both Ordinary (O) and Extraordinary (X) polarisation mode data was produced approximately once a minute in both the VIS and QVIS systems.

Experimental overview

From December 9, 2013 to February 16, 2014, HF Radar Branch of DST Group, South Australia, conducted an HF radio wavelength sounding experiment as part of the JORN VIS replacement project [25] using the Woodside VIS and St Kilda receive Rx in the vicinity of TRACE, located at Edinburgh. The locations of TRACE, the Woodside VIS, the St Kilda Rx and the two ionospheric probe points are shown in Figure 1a. The two sounders lay within TRACE's 1000 km field of view (see Figure 1b) which presented an ideal opportunity to explore airglow / HF sounder correlations. The results presented here were obtained on the 27th of January, 2014 during a geomagnetically quiet (Kp = 1) period.

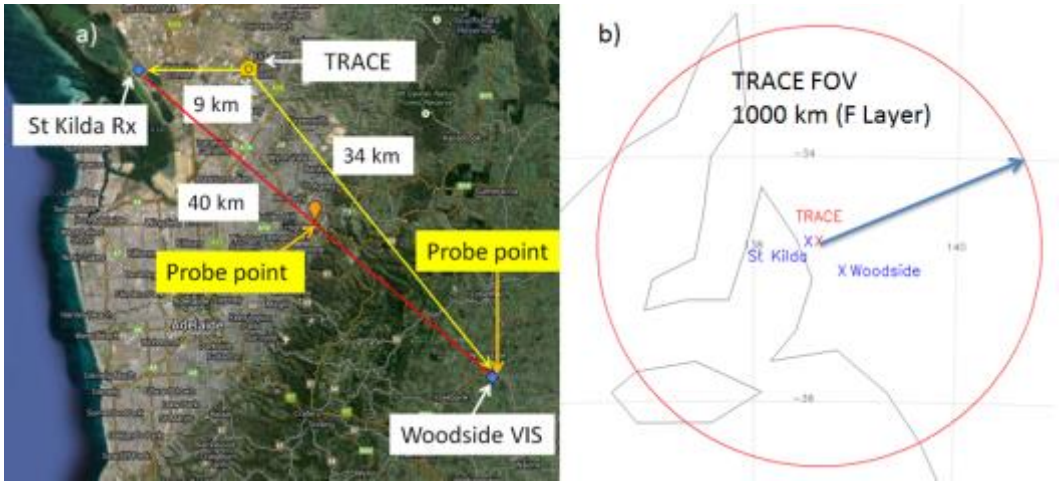

Figure 1a) The layout for HF sounder testing and TRACE and b) the TRACE FOV showing the position of the ionospheric Woodside and ST Kilda sounders relative to TRACE. The probes are the ionospheric sampling points of the Woodside-St Kilda QVIS path and Woodside VIS.

HF Observations and Analysis

Figure 2 shows four example ionograms recorded by the VIS (top row) and QVIS (bottom row) during the night of the 27th January 2014. The O mode is plotted in red and the X mode in blue. Both splitting of the F-layer trace and spread F is seen at 16:10 UT and 18:19 UT. Multi-hop Sporadic E (E_S) is also evident.

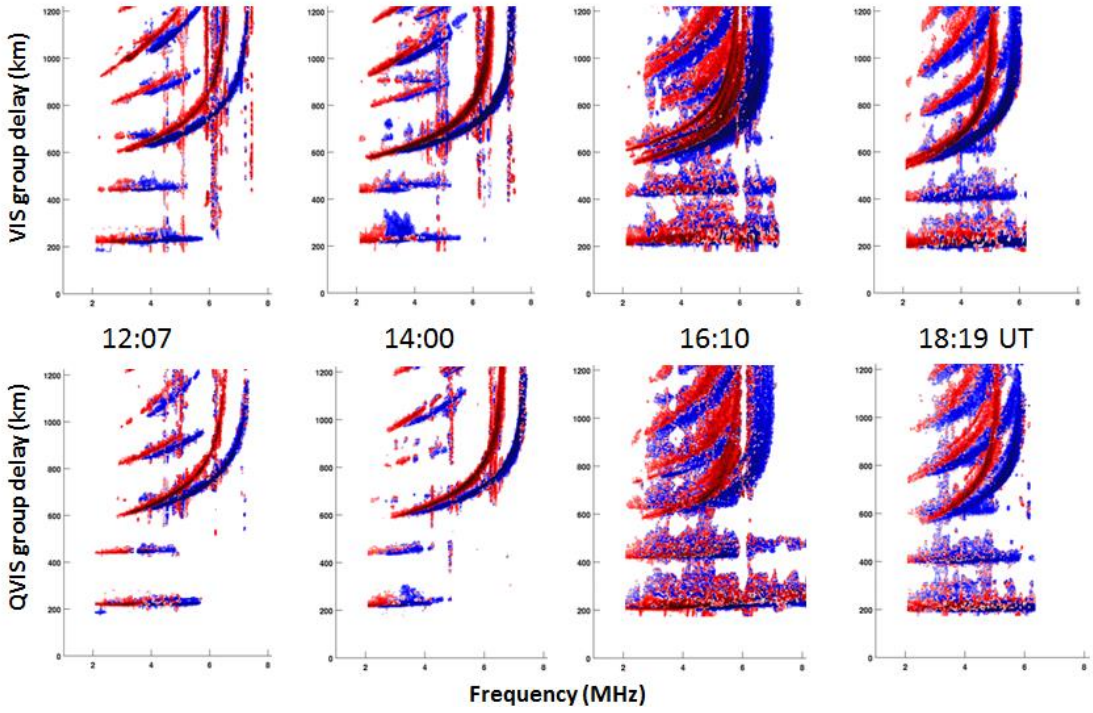

Figure 2 Woodside VIS (top) and Woodside-St Kilda QVIS (bottom) ionograms obtained on the night of the 27th January, 2014Group delay vs Frequency for two hourly intervals (UT).

The O and X mode ionograms are processed separately using the automatic method outlined in Harris et al. [25] to determine the bottom side ionospheric layer heights. An example of the virtual height analysis of two O mode ionograms at 12:07 UT and 16:10 UT from the Woodside VIS is shown in Figure 3. The thin green and thin orange lines are both the F2 trace and purple and the thick green lines are both the true height estimate. The true height estimates are produced from the ionospheric inversion process. It can be seen that the F2 layer height has risen by approximately 20 km from 12:07 UT to 16:10 UT as the ionogram becomes more disturbed. X mode data (not shown) exhibits a similar trend.

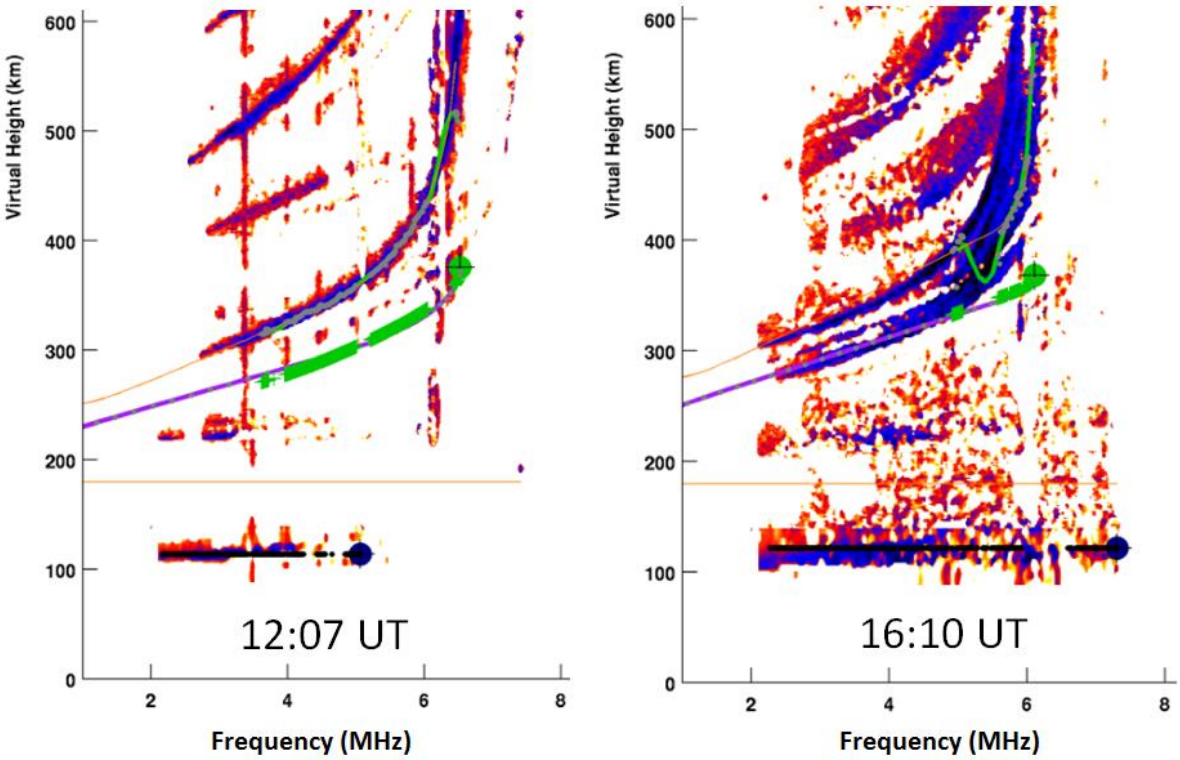

Figure 3 Virtual height estimates from two O mode ionograms from Woodside VIS taken at 12:07 UT and 16:10 UT on 27th January, 2014.

Figure 4 shows the minimum virtual height detected for the various ionospheric layers over time derived from a) Woodside-St Kilda QVIS and b) Woodside VIS data. The time resolution is approximately 1 minute. The identified layers are indicated; green: day-time F2 (h'F2) which become the night-time F (h'F), purple: E (h'E) and blue: sporadic E (h'Es). Significant spread F was seen throughout the night. Wave-like variation in night time h'F from ~12 UT – 20 UT indicates the presence of a large-scale TID in the F-layer [5, 9]. Sunset was at approximately 10 UT and sunrise, 20 UT.

The peaks in Figure 4 occur when the electron density is low; allowing the transmitted HF radio signal to travel further through the ionosphere before it is reflected. Conversely, a higher density of electrons means the transmitted signal is reflected from lower altitudes (hence smaller h'F) which correspond to the troughs in Figure 4.

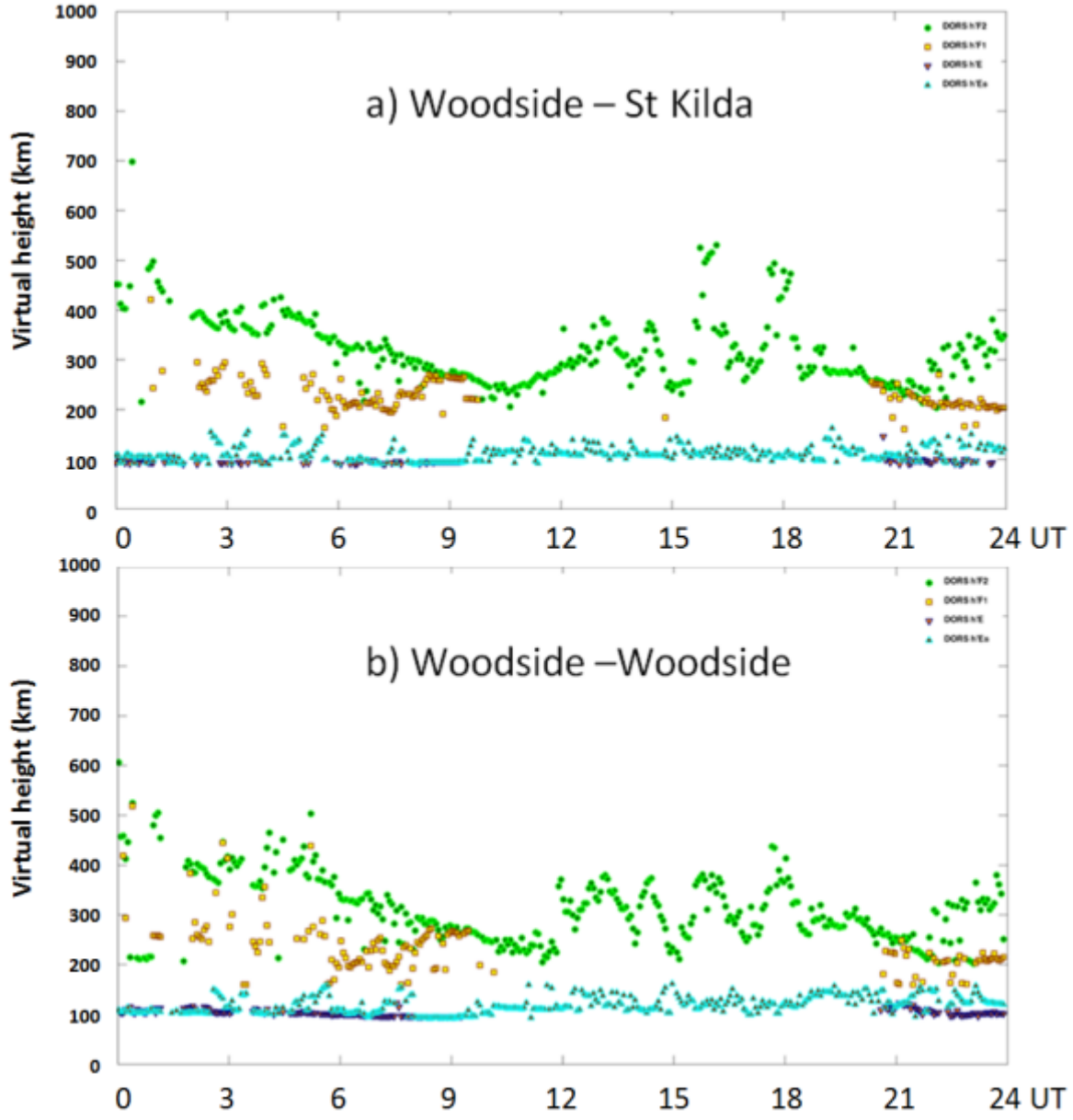

Figure 4 27th of January 2014 virtual height vs time measurements for a) Woodside to St Kilda Quasi-Vertical Incidence Sounder and b) Woodside Vertical Incidence Sounder.

The four main h'F peaks observed by both sounders occur at approximately 13:05, 14:25, 16:05 and 18:00 UT and the troughs lie at approximately 12:30, 13:55, 15:05 and 17:05 UT. The wavelength between peaks increases as the night progresses and correspond to periods of: 73 minutes, 101 minutes and 117 minutes (±4 minutes). Smaller scale structure is evident after 15 UT.

Airglow Observations and Analysis

Airglow contrast is insufficient to exhibit significant airglow features until around 14 UT – four hours after sunset. Figure 5 shows a series of 630 nm airglow images from 15 UT to 17 UT encompassing the last two peaks in Figure 4. Airglow images have exposure times of 2 minutes and are presented, by convention, with North at the top and East to the left. Each image spans 1000 km x 1000 km. Contrast has been enhanced by removing the temporally

closest 572.5 nm background image. All images have dark frames subtracted; are corrected for line-of-sight and van Rhijn effects [26]; and undergo star mimimization; before being converted from pixels to km [27].

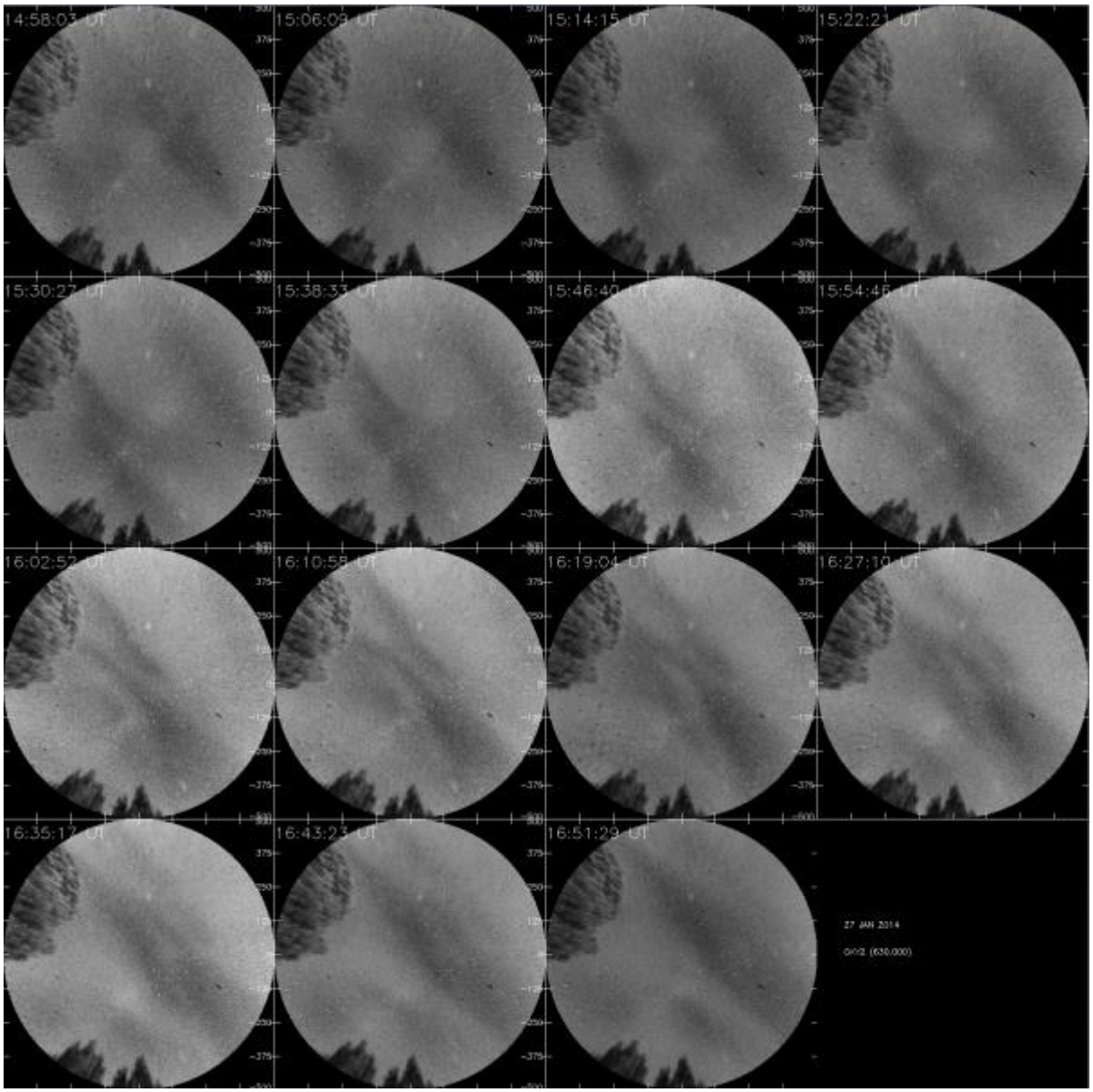

Figure 5 Airglow 630 nm images from 15 UT to 17 UT. North is top, East is to the left.

Bright regions in Figure 5 indicate airglow enhancement and dark regions, airglow depletions. Note each image is auto-scaled to promote higher contrast for publication purposes and, as such, the scale of each image can not be related directly to other images. Changing depletion patterns are evident with the SE depletion splitting into two and then three parts from 15:30 – 16:30 UT before reforming. This event is reflected in small scale variations in Figure 4.

Median airglow over a 10x10 pixel region centred on the zenith was calculated for the 630.0 nm airglow emission and background (control) and plotted in Figure 6. The background measurements indicate variations in non-airglow light levels. The approximate times of the h'F parameter troughs (solid line) and peaks (dashed line) in Figure 4 are marked on Figure 6. The airglow measurements follow a typical pattern: a drop off in intensity in the hours after

sunset (10 UT) due to the loss of the strong solar ionization source of electrons; followed by a post-midnight (13:30 UT) rise [20], a pattern which is not seen in the control data. The airglow rise reaches its first peak at 14:30 UT at which point, typical airglow TID oscillations become apparent [28].

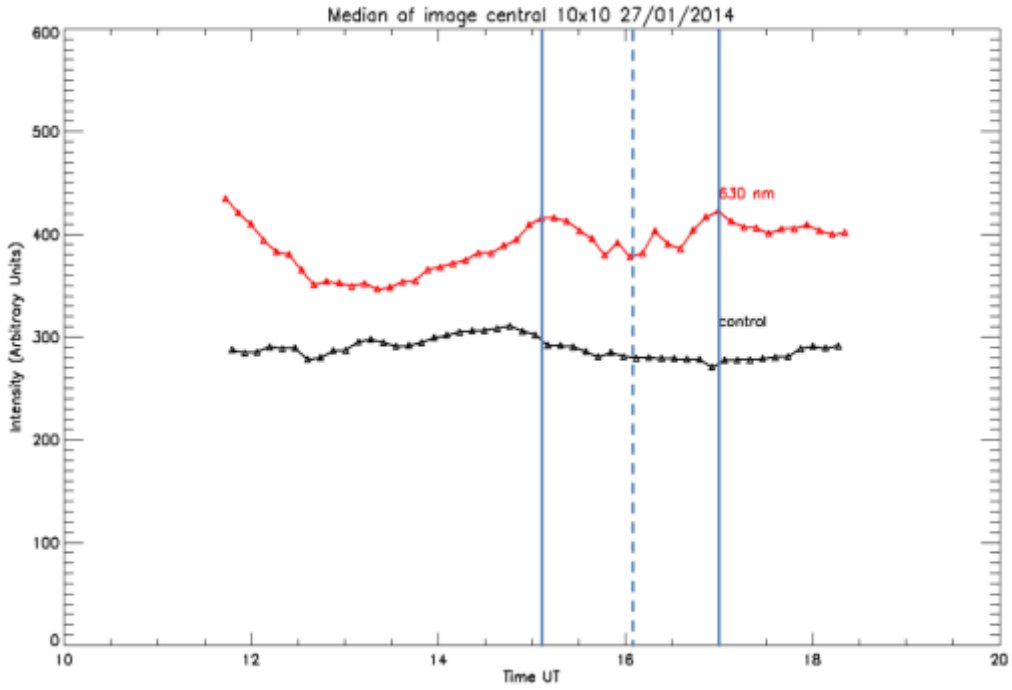

Figure 6: Median airglow over a 10x10 pixel square at zenith for 630.0 nm (red) airglow and 572.5 nm (black) background or control emissions. Solid blue lines mark the approximate times when the ionospheric h'F parameter is at a minimum and the dashed blue line indicates the approximate time when the ionospheric h'F parameter is at a maximum.

Major airglow intensity peaks are seen at 15:10 UT and 17:00 UT, in agreement with the position of the h'F troughs in Figure 4 at 15:05 UT and 17:00 UT. The major airglow trough falls at 16.1 UT, the same location as the h'F peak. Smaller airglow intensity peaks, seen at 15:55 UT and 16:20 UT, correspond to smaller peaks and troughs seen in the h'F data. This strong inverse relationship between h'F virtual height and zenith airglow intensity for the two peaks and one trough agrees with previous lower time resolution HF radio sounder results for single airglow peaks [1, 10] and is a direct result of local electron density. Raised electron densities correspond to brighter airglow but also reflect transmitted HF radio waves at lower altitudes leading to low values of h'F. Conversely, lower electron density leads to fainter airglow and higher h'F measurements.

TID wavelengths were calculated by taking a slice through the airglow images perpendicular to the direction of motion at an angle fitted by eye. A band of 30 pixels was averaged and smoothed to form an average 'slice profile' which is used to derive the TID wavelengths, periods and velocities. An example of the method for the large and small spatial TIDs is shown in Figure 7.

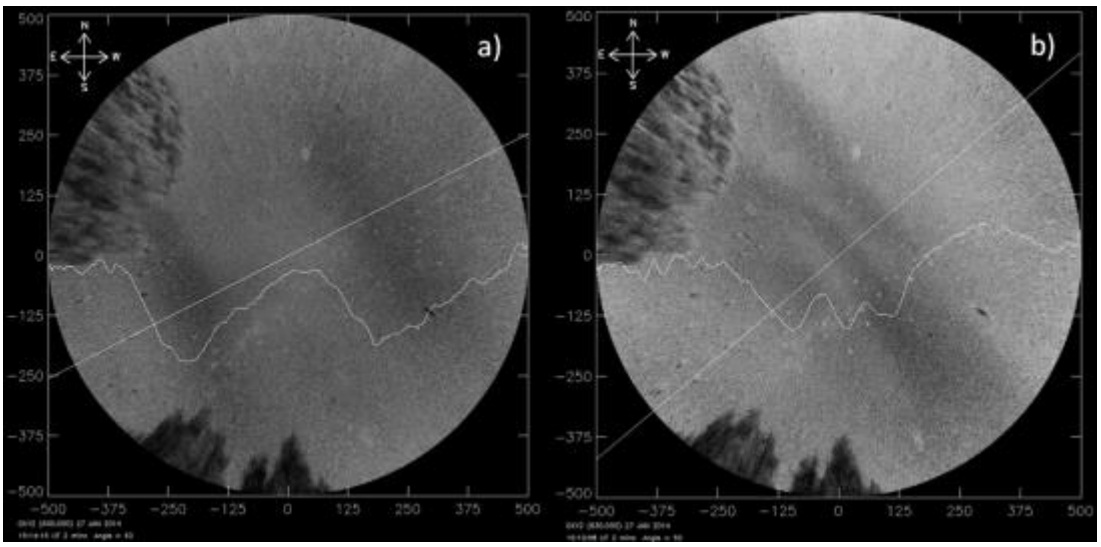

Figure 7 Airglow images with corresponding slices and the resulting slice profile: a) 15:14:15 UT with a slice angle of 297 degrees as measured from North through East and b) 16:10:58 UT with a slice angle of 310 degrees.

From 15 UT to 15:30 UT, there are two widely spaced bands traveling at a bearing of 297^{o} with wavelength of around 456 km; the NE depletion band has velocity ~68 m/s. This corresponds to a period of 114 minutes, in agreement with the 117 ± 4 minute period seen in the h'F variation. The average wavelength of the three band system seen from 15:54 to 16:27 UT is 101 km and the average velocity is 76 m/s leading to a period of approximately 22 minutes. This splitting correlates with the fine structures seen in the h'F variation of Figure 4 at this time but the data is not well resolved enough to estimate a wavelength.

Discussion

A comparison between the VIS and QVIS h'F vs time measurements of Figure 4 and the airglow images of Figure 5 shows that large scale wave-like disturbances (456 km wavelength) appear as correspondingly motions in the HF data and banded structures in airglow images. Furthermore, electron density enhancements are indicated by bright airglow regions and h'F troughs, and depletions as dark airglow regions and peaks in h'F.

The unusual transient splitting of one of the depletions into three smaller depletions with wavelengths of around 101 km seen in Figure 5 from 15:30 UT to 17 UT is probably due to local ionospheric instabilities as the direction of motion remained constant and the original depletion reformed after a short time. The high time resolution of the HF sounder measurements allowed these smaller scale wave-like disturbances to be detected as small-scale scattered regions in the h'F vs time plots. More detail could be gained with higher sampling rates. Future work on estimating wavelengths in both the airglow and HF data using Fourier analysis may provide more information. No loop or orbital cusp features were seen in individual ionograms when smaller scale wave-like features were present as have been observed in other similar experiments [5, 9].

As expected from previous studies, these TIDs were seen when the night was geomagnetically quiet (Kp = 1) thus it is unlikely that the cause of the TIDs were anything other than an ionospheric disturbance.

Previous long term studies of airglow and HF data over Brazil [1, 8] found medium scale TIDs occur almost exclusively at solar minimum with none observed during solar maximum. Similarly, a study of TIDs in Indonesia in airglow found the rate of observed MSTIDs decreased with decreasing solar activity [2]. Interestingly, the TID reported here occurred at solar maximum, albeit a low sunspot number maximum. TRACE is currently performing a survey of E and F-layer airglow data which should reveal a better estimate of solar maximum TID occurrence in South Australia.

The summer TIDs presented in this paper and those seen on the subsequent night, travelled in a North-Westerly direction, consistent with other southern hemisphere summer F-layer TID directions reported in Japan and Indonesia [19].

Conclusion

A solar maximum Travelling Ionospheric Disturbance (TID) seen over Adelaide, Australia on the 27th of January 2014 from approximately 10 UT to 20 UT was imaged simultaneously by the Defence Science and Technology Group at 630.0 nm using the Thermospheric Radar Airglow Correlation Experiment (TRACE) and two high sample rate 2 – 20 MHz High Frequency (HF) radio sounders within the TRACE 1000 km field of view.

The h'F vs time plots constructed from both Vertical Incidence Sounder data and Quasi-Vertical Incidence Sounder data displayed a characteristic TID wave-like pattern with an increasing period from 73 minutes from 12 UT to 117 minutes by 18 UT.

Airglow images confirmed a complex pattern of NE-SW aligned depletion bands moving with velocity ~68 m/s in a North-Westerly direction corresponding to medium to large scale TIDs with similar periods to those seen in the HF data. One of the depletions split into three short-lived small-scale depletions with average wavelength ~101 km. This splitting is probably due to local ionospheric instabilities and was detected in the high time resolution h'F measurements.

A comparison of median airglow density and HF radio h'F measurements found a strong inverse relation between airglow brightness and h'F values for TIDS, consistent with previous work. Both measurements were found to be good indications of F-layer electron density variation.

References

1. D. C. M. Amorim, *et al.*, "Long-term study of medium-scale traveling ionospheric disturbances using O I 630 nm all-sky imaging and ionosonde over Brazilian low latitudes," *Journal of Geophysical Research: Space Physics,* vol. 116, p. A06312, 2011, doi:10.1029/2010JA016090.
2. D. Fukushima, *et al.*, "Observation of equatorial nighttime medium-scale traveling ionospheric disturbances in 630-nm airglow images over 7 years," *J. Geophys. Res.,* vol. 117, p. A10324, 2012, doi:10.1029/2012ja017758.
3. R. D. Hunsucker, "Atmospheric gravity waves generated in the high-latitude ionosphere: A review," *Reviews of Geophysics,* vol. 20, pp. 293-315, 1982, doi:10.1029/RG020i002p00293.
4. Y. Otsuka, *et al.*, "GPS observations of medium-scale traveling ionospheric disturbances over Europe," *Ann. Geophys.,* vol. 31, pp. 163-172, 2013, doi:10.5194/angeo-31-163-2013.
5. T. J. Harris, M. A. Cervera, and D. H. Meehan, "SpICE: A program to study small-scale disturbances in the ionosphere," *Journal of Geophysical Research: Space Physics,* vol. 117, p. A06321, 2012, doi:10.1029/2011JA017438.
6. K. Shiokawa, *et al.*, "Statistical study of nighttime medium-scale traveling ionospheric disturbances using midlatitude airglow images," *Journal of Geophysical Research: Space Physics,* vol. 108, p. 1052, 2003, doi:10.1029/2002JA009491.
7. S. Saito, *et al.*, "Observational evidence of coupling between quasi-periodic echoes and medium scale traveling ionospheric disturbances," *Ann. Geophys.,* vol. 25, pp. 2185-2194, 2007, doi:10.5194/angeo-25-2185-2007.
8. C. M. N. Candido, *et al.*, "Statistical analysis of the occurrence of medium-scale traveling ionospheric disturbances over Brazilian low latitudes using OI 630.0 nm emission all-sky images," *Geophysical Research Letters,* vol. 35, 2008, doi:10.1029/2008GL035043.
9. M. A. Cervera and T. J. Harris, "Modeling ionospheric disturbance features in quasi-vertically incident ionograms using 3-D magnetoionic ray tracing and atmospheric gravity waves," *J. Geophys. Res.,* vol. 119, pp. 431-440, 2014, doi:10.1002/2013JA019247.
10. M. Kubota, H. Fukunishi, and S. Okano, "Characteristics of medium and large-scale TIDs over Japan derived from OI 630-nm nightglow observation," *Earth Planets Space,* vol. 53, pp. 741-751, 2001.
11. I. Seker, D. J. Livneh, and J. D. Mathews, "A 3-D empirical model of F region Medium-Scale Traveling Ionospheric Disturbance bands using incoherent scatter radar and all-sky imaging at Arecibo," *Journal of Geophysical Research: Space Physics,* vol. 114, p. A06302, 2009, doi:10.1029/2008JA014019.
12. Y. Otsuka, *et al.*, "Optical and radio measurements of a 630-nm airglow enhancement over Japan on 9 September 1999," *Journal of Geophysical Research: Space Physics,* vol. 108, p. 1252, 2003, doi:10.1029/2002JA009594.
13. J. H. Klenzing, *et al.*, "Multi-instrument observations of an MSTID over Arecibo Observatory," in *General Assembly and Scientific Symposium, 2011 XXXth URSI*, 2011, pp. 1-4.
14. H. Takahashi, *et al.*, "Plasma bubble monitoring by TEC map and 630 nm airglow image," *Journal of Atmospheric and Solar-Terrestrial Physics,* vol. 130–131, pp. 151-158, 2015, doi:10.1016/j.jastp.2015.06.003.

15. T. Ogawa, *et al.*, "Observations and modeling of 630 nm airglow and total electron content associated with traveling ionospheric disturbances over Shigaraki, Japan," *Earth, Planets and Space,* vol. 54, pp. 45-56, 2002/01/01 2002, doi:10.1186/BF03352420.
16. A. A. Pimenta, *et al.*, "Ionospheric plasma blobs observed by OI 630 nm all-sky imaging in the Brazilian tropical sector during the major geomagnetic storm of April 6–7, 2000," *Geophysical Research Letters,* vol. 34, p. L02820, 2007, doi:10.1029/2006GL028529.
17. K. Shiokawa, *et al.*, "Observation of nighttime medium-scale travelling ionospheric disturbances by two 630-nm airglow imagers near the auroral zone," *Journal of Atmospheric and Solar-Terrestrial Physics,* vol. 103, pp. 184-194, 2013, doi:10.1016/j.jastp.2013.03.024.
18. A. Taori and A. Sindhya, "Measurements of equatorial plasma depletion velocity using 630 nm airglow imaging over a low-latitude Indian station," *Journal of Geophysical Research: Space Physics,* vol. 119, p. 2013JA019465, 2014, doi:10.1002/2013JA019465.
19. K. Shiokawa, Y. Otsuka, and T. Ogawa, "Propagation characteristics of nighttime mesospheric and thermospheric waves observed by optical mesosphere thermosphere imagers at middle and low latitudes," *Earth Planets Space,* vol. 61, pp. 479-491, 2009.
20. F. J. Garcia, *et al.*, "Airglow observations of mesoscale low-velocity traveling ionospheric disturbances at midlatitudes," *Journal of Geophysical Research: Space Physics,* vol. 105, pp. 18407-18415, 2000, doi:10.1029/1999JA000305.
21. A. A. Pimenta, *et al.*, "Thermospheric dark band structures observed in all-sky OI 630 nm emission images over the Brazilian low-latitude sector," *Journal of Geophysical Research: Space Physics,* vol. 113, p. A01307, 2008, doi:10.1029/2007JA012444.
22. K. J. W. Lynn, Y. Otsuka, and K. Shiokawa, "Simultaneous observations at Darwin of equatorial bubbles by ionosonde-based range/time displays and airglow imaging," *Geophys. Res. Lett.,* vol. 38, p. L23101, 2011, doi:10.1029/2011gl049856.
23. A. Unewisse, *et al.*, "TRACE: A New Relocatable Airglow Imager," presented at the Proceedings of the 13th Australian Space Science Conference Sydney., 2014.
24. T. Ogawa, *et al.*, "Simultaneous ground- and satellite-based airglow observations of geomagnetic conjugate plasma bubbles in the equatorial anomaly," *Earth Planets Space,* vol. 57, pp. 385-392, 2005.
25. T. J. Harris and A. D. Quinn, "The DSTO Ionospheric Sounder Repacement for JORN (03B1)," presented at the Proceedings of the 14th International Ionospheric Effects Symposium, Virginia, USA, 2015.
26. P. J. Van Rhijn, "On the brightness of the sky at night and the total amount of starlight," *Astrophys. J.,* vol. 50, 12/1919 1919, doi:10.1086/142513.
27. A. Unewisse, A. Cool, and M. Cervera, "Observations of a Mesospheric bore over Edinburgh, Adelaide," presented at the Proceedings of the 14th Australian Space Science Conference, Adelaide, 2015.
28. F. J. Garcia, *et al.*, "Mesoscale structure of the midlatitude ionosphere during high geomagnetic activity: Airglow and GPS observations," *Journal of Geophysical Research: Space Physics,* vol. 105, pp. 18417-18427, 2000, doi:10.1029/1999JA000306.

The Australian Space Eye: low surface brightness imaging from space

Anthony Horton*, Lee Spitler*†, Naomi Mathers‡, Roger Franzen‡, Mike Petkovic‡, Sam Reisenfeld† and Jon Lawrence*

* *Australian Astronomical Observatory, Australia*
† *Macquarie University, Australia*
‡ *Australian National University Advanced Instrumentation and Technology Centre, Australia*

Summary: The Australian Space Eye is a proposed astronomical space telescope based on a 6U CubeSat platform. The aims of the project are to demonstrate Australian capability to execute CubeSat missions, develop the specific capabilities required for astronomical research with CubeSats, demonstrate the low surface brightness imaging performance of a small space telescope and exploit that performance to undertake measurements of the extra-galactic background light anisotropies and image low surface brightness structures around nearby galaxies. A 90 mm aperture refracting telescope will enable deep broadband imaging in the astronomical i' and z' bands (approximately 700 to $1000\,\mathrm{nm}$) with a field of view of $1.67^\circ \times 1.25^\circ$ and spatial sampling of $3''$ per pixel. The main technical challenge for astronomical imaging from CubeSats is achieving the instrument pointing stability required to enable long exposures. We plan to combine micro-thruster attitude control with precision star tracking in the telescope focal plane.

Keywords: CubeSat, nanosatellite, astronomical imaging, low surface brightness, extra-galactic background light, pointing stability, micro-thruster

Introduction

In December 2014 the Research School of Astronomy and Astrophysics (RSAA) at the Australian National University (ANU) hosted the AstroSats 2014 workshop. The purpose of the workshop was to "bring together the astronomical research and satellite engineering communities to explore science cases and astronomical instrumentation concepts suitable for small satellites" with a goal to "identify well-justified and viable missions taking advantage of the facilities and capabilities at Australian institutions... that could be funded within existing grant schemes." In this context 'well-justified' referred to a requirement that the missions could be justified on the basis of the astronomical results they would be expected to produce, not just by the development of technology and accumulation of expertise (valuable as those outcomes would be). When combined with an additional constraint that proposed spacecraft should be no larger than a 6U CubeSat and the cost constraints imposed by existing grant schemes this is a very challenging requirement, essentially it requires identifying a compelling science programme that is within the capabilties of a very small instrument in low earth orbit but which could not be done by ground based instruments of comparable cost (which would in general be much larger).

In response to this call for proposals we developed the Australian Space Eye concept, an extension to space of recent developments in the use of small ground-based telescopes for low surface brightness astronomical imaging. 10 proposals were selected for presentation at the workshop and from these a peer review process indentified three as suitable for development for funding opportunities in 2015, Space Eye being one of them. Consequently we have further refined the concept and sought funding via an ARC LIEF grant. In this paper we describe the motivation and aims of the Australian Space Eye concept, and provide a summary overiew of the technical aspects.

The description in this paper reflects the state of the Australian Space Eye concept at the date of initial submission (16th November 2015). At this time Space Eye was a proposal still under development. For a more up to date and complete description readers are referred to Horton et al 2016[1] or subsequent publications.

Motivation

As discussed in the introduction the scientific competitiveness of the Australian Space Eye depends on identifying aspects of astronomy particularly well suited to a small telescope situated in space. We will discuss each of these aspects in turn.

Small telescopes & systematic errors

While large astronomical telescopes are able to detect extremely faint compact or point-like objects their sensitivity to diffuse emission is limited by systematic errors from a number of sources. A significant contribution to these systematic errors is contaminination with light from brighter objects within/near the instrument's field of view, caused by a combination of diffraction, scattered light and internal reflections. The difficulties caused by these effects have been discussed by, for example, Sandin [2, 3] and by Duc et al [4], who noted that the simpler optics of small telescopes suffer less from internal reflections. In addition small telescopes can more readily be constructed with unobscured apertures to minimise diffraction, and simpler optics also make them less prone to internal scattering of light. The resulting competitiveness of optimised small telescopes in the context of 'low surface brightness' (LSB) imaging has been demonstrated by the Dragonfly Telephoto Array, an astronomical imaging system based on an array of telephoto camera lenses [5]. This instrument exhibits less diffraction/scattering/internal reflections than other telescopes for which comparable data are available [5, 2] and the system has produced impressive results, including the discovery of a new class of 'ultra-diffuse galaxies' (UDGs) [6]. Two of this paper's authors (AJH & LS) are currently assembling an instrument based on the same principles, the Huntsman Telephoto Array. A single imaging unit prototype can be seen in Fig. 1.

The case for space

The effects of atmospheric absorption and turbulence on ground based astronomy in terms of accessible wavelengths and spatial resolution are well known, the former in particular has been the primary motivation for many space telescopes. Due to essentially complete absorption

Fig. 1: The Huntsman Eye, a prototype imaging unit of the Huntsman Telephoto Array, during on-sky testing in September 2014

by the atmosphere gamma-ray, X-ray, ultraviolet and far infrared astronomy are only possible with space-based instruments. Neither of these two effects are important for the Australian Space Eye, however. We rule out the specialised optics and image sensors required for gamma ray, X-ray and infrared observations due to the cost, volume/mass and thermal limitations of a CubeSat mission and concentrate on wavelength regions accessible with silicon based image sensors and conventional optics, i.e. $\sim$ 200–1000 nm. At these wavelengths there is little to no spatial resolution advantage from situating the telescope above the atmosphere because a telescope small enough to be a CubeSat payload would be limited by the fundamental diffraction limit in either case.

There are however two other effects of the atmosphere which are relevant to Space Eye: atmospheric scattering and emission. Atmospheric scattering spreads the light from astronomical objects in a similar way to scattering from the instrument's optics however the impact is compounded by the fact that the distribution of aerosols in the atmosphere is spatially and temporally variable, the amount of scattered light surrounding a given source can vary by several percent of the source brightness even in good 'photometric' conditions, on timescales of minutes to months. The variability in the scattering makes it difficult to accurately characterise and subtract [7], thereby introducing problematic systematic errors. Similar issues arise from atmospheric emission, particularly at longer wavelengths ($>$ 700 nm). Here the atmosphere glows increasingly brightly, primarily due to line emission from OH^* molecules in

the mesophere, reducing the sensitivity of ground based telescopes. This emission is sensitive to dynamic processes in the upper atmosphere (e.g. gravity waves) and consequenty it is also spatially and temporally variable on timescales of minutes and longer [8] which makes accurate subtraction difficult. As a result of these effects locating a telescope in space not only helpfully reduces both scattered light and sky background levels but crucially makes both far more stable. Above the atmosphere the only sources of scattered light are associated with the instrument itself and the dominant source of sky background is the zodiacal light [9] which, while it does exhibit large scale spatial and seasonal variations, is much less variable, more uniform and more predicatble than atmospheric emission.

We conclude that a CubeSat based astronomical telescope may be scientifically competitive, especially an optimised telescope performing measurements that are typically limited by systematic errors. We identify the 700–$1000\,\mathrm{nm}$ wavelength region as particularly promising as it is accessible to instrumentation compatible with the constraints of a CubeSat mission while ground based instruments would be hampered by bright atmospheric emission, in terms of both reduced sensitivity and increased systematic errors. We have based the Australian Space Eye proposal on two science goals which would be well served by a telescope operating in this regime, the measurement of extragalactic background light anisotropies and imaging of low surface brightness structures around nearby galaxies. These are discussed in more detail in the next section.

Aims

The aims of the Australian Space Eye project, starting with the most general, are as follows:

- Demonstrate Australian capability to execute a CubeSat mission, from start to finish.
- Develop the specific capabilties required for astronomical research from CubeSats, for example high instrument pointing stability to enable long exposures
- Characterise the on-orbit performance of a small astronomical telescope, in particular with respect to instrument stability, calibration, systematic error levels and low surface brightness imaging sensitivity
- Use the Space Eye telescope to make measurements of extra-galactic background light anisotropies in the i' and z' bands
- Use the Space Eye telescope to image low surface brightness structure around nearby galaxies.

Extra-galactic background light anisotropy

The epoch of reionisation marks the period $\sim$ 12.5-13 billion years ago where most of the Universes hydrogen became ionised. Exactly how reionisation progressed sets the initial conditions for the subsequent evolution of baryonic matter in the Universe. For this reason major international astronomical facilities are now being designed to directly observe this important epoch, such as the $51 million Murchison Widefield Array in Western Australia. We know the Universe finished reionisation 12 billion years ago [10] but the observed sources of ionising UV radiation at this period cannot do it alone. Astronomers therefore infer the existence of a so far undetected population of faint galaxies that collectively can ionise the

Universes hydrogen [11]. The primary science goal of the Space Eye mission is detecting this faint galaxy population by measuring its impact on the power spectrum of spatial anisotropies in the extragalactic background light (EBL). This is a powerful measurement technique to observe astronomical objects that are too faint to be detected individually.

Extragalactic background light observations have been reported [12, 13, 14, 15] however interpreting the EBL signal is difficult because observations have only been conducted at infrared wavelengths. Indeed, Zemcov et al. conclude: "...measurements extending into the optical will help discriminate the Epoch of Reionisation background component using the redshifted Lyman cutoff." [15] Optical EBL observations at $< 1.0\,\mu\mathrm{m}$ is the main objective of a planned sounding rocket optical telescope (CIBER-2) [16]. However the faint galaxy population signal will be at or even below the systematic uncertainties of CIBER2 (assuming the same limits as CIBER [15]), primarily because CIBER2 makes use of a reflecting telescope design which is not optimal with respect to diffraction and scattering of light.

This shortcoming is what the Space Eye mission is designed to overcome: it will consist of a refracting telescope optimised for faint EBL signals in the i' and z' bands. To securely detect the faint signal the Space Eye will significantly reduce the two dominant sources of systematic uncertainties: flatfielding errors and contribution from pointspread function wings [15]. Furthermore by collecting data over many months (versus a few hours with CIBER2) we can obtain a more secure measurement of the EBL signal and determine its origin. With observations of the faint EBL at 0.7-$1.0\,\mu\mathrm{m}$ with i' and z' band filters we will be able to detect restframe UV light from the population of faint ionising galaxies [16]. The Space Eye EBL constraints will be combined with infrared measurements from the literature to constrain the properties of the faint galaxy population. The Space Eye data will better discrimate between the EBL signal and diffuse starlight from the outer parts of galaxies [14, 16].

Signatures of galaxy growth

As a secondary astronomy mission we plan to target several nearby galaxies in order to obtain images at the lowest possible surface brightness levels in order to detect extremely faint structures in their outskirts. When the Space Eye i' and z' band imaging is combined with optical (g' and r' band) imaging from ground based low surface brightness imaging instruments (e.g. Dragonfly and Huntsman) we can better constrain the stellar age and chemical content of these faint structures. Detecting these structures and measuring their composition will help us understand their origin: are they younger and/or metalpoor compared to the rest of the galaxy? Were they built from the accretion of satellites? Early and latetype galaxies will be targeted, including some galaxies located within galaxy groups and clusters. These observations will also provide a local constraint on the intra-halo stellar population, which is needed for isolating the reionization signal in the EBL observations.

This facility will enable the detection of previously inaccessible signatures of galaxy formation and evolution. Such faint structures could only be seen around our Milky Way Galaxy and other nearby galaxies at the Space Eye imaging wavelengths by using Hubble Space Telescope imaging of resolved stars [17]. With its limited field of view Hubble cannot map entire galaxies. The Space Eye will allow us to do this for moderately distant galaxies and allow us to detect stellar structures and measure their stellar ages and chemical compositions. By characterising these ancient signs of galaxy growth we can validate theoretical models

of galaxy formation, which underpin theory and interpretation of observations in the field of astrophysics.

Space Eye Concept

The desire to make Space Eye fundable within existing grant schemes means that we restricted ideas for the concept to those compatible with standard nano-satellite form factors and no larger than a 6U CubeSat. In developing the concept we aimed to identify the miminal mission that would still meet our aims.

Optical payload

The top priority in the design of the Space Eye telescope is that the point spread function (PSF) should be as clean as possible, i.e. we should minimise diffraction, scattering and internal reflections. This suggests a telescope with an unobstructed circular aperture, all transmissive optics, high performance anti-reflection coatings and minimised surface count. The maximum telescope aperture is strongly constrained by the $100\,\mathrm{mm}$ cube based CubeSat form factor standard and the decision to limit the maximum size of the spacecraft to 6U. The largest circular aperture that could be accommodated on the end/side faces of a $3 \times 2 \times 1$U CubeSat is approximately $90\,\mathrm{mm}$ so this is what we specified. The scientific aims of the Space Eye call for $\sim 3''\,\mathrm{pixel}^{-1}$ spatial sampling and an instantaneous field of view of $> 1°$.

While for ground based astronomy at these wavelengths CCD image sensors are used amost exclusively for Space Eye we favour a CMOS image sensor (CIS). CMOS image sensors have higher radiation hardness, lower power consumption and, in general, smaller pixels than CCDs of comparable performance, all of which make them appealing for space applications. Small pixels are particularly desirable for Space Eye as they allow a shorter focal length telescope for a given pixel scale, which makes it easier to fit the optics within the available space. We have selected the CIS115 from e2v, a CMOS image sensor with 2000×1504 $7\,\mu\mathrm{m}$ pixels which has been developed specifically for space use (e.g. ESA JUICE mission) [18, 19]. To maximise sensitivity the image sensor should be operated at $-40\,°\mathrm{C}$, which we plan to achieve using a passive cooling radiator system. A photograph of a prototype CIS115 is shown in Fig. 2.

With the CIS115 the desired $\sim 3''\,\mathrm{pixel}^{-1}$ spatial sampling results in a $481\,\mathrm{mm}$ telescope focal length and a field of view of $1.67° \times 1.25°$. We have produced a baseline optical design which meets our requirements using 5 elements in 5 groups, this design is shown inside a 3U volume within Space Eye in Fig. 3. Also shown in Fig. 3 is a pop-out baffle to prevent stray Earth/Moon light entering the instrument.

Spacecraft platform

The Space Eye will be based on the Endeavour platform from Tyvac Nano-Satellite Systems Inc. This highly integrated, high performance platform incorporates almost all the functionality required for a functional 3-6U Cubesat, including C & DH (core system board, application

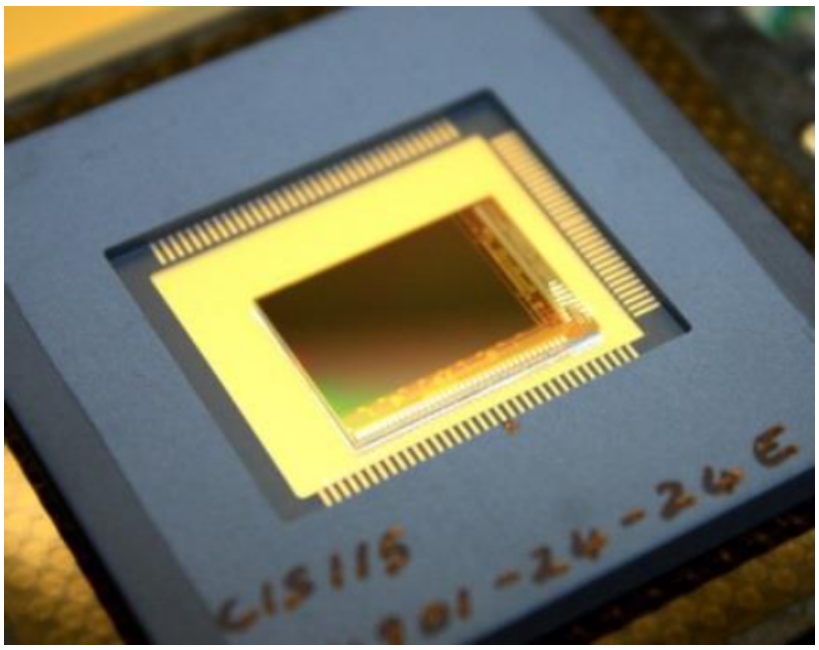

Fig. 2: Prototpe e2v CIS115 image sensor.

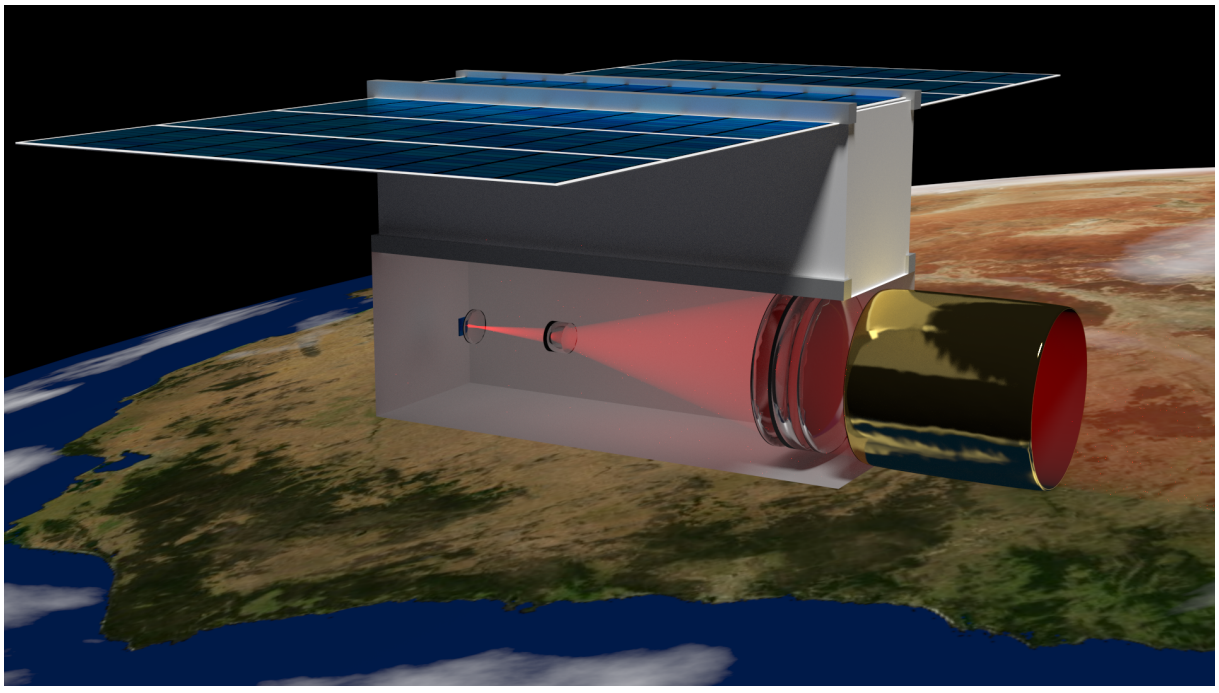

Fig. 3: Artist's impression of the Australian Space Eye in orbit over the Tasman Sea. In this cutaway diagram the lenses, beam path and image sensor of the baseline optical design are shown.

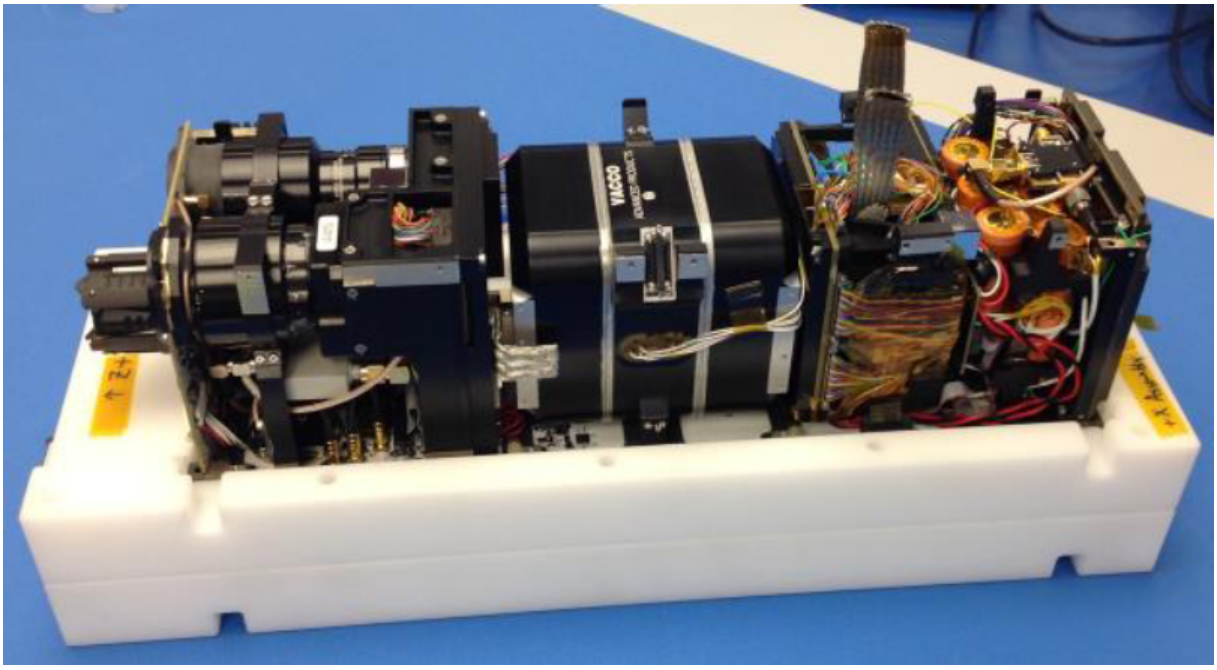

Fig. 4: CPOD CubeSat with panels removed, reproduced from paper [20]. The 1U on the left is occupied by the CPOD mission payload, the 1U in the centre contains a VACCO Industries cold gas propulsion system and the 1U on the right contains the Tyvak Endeavour avionics and battery pack.

specific daughter boards), EPS & Thermal management (PMAD controller, battery modules, solar/multi-function panels), ADCNS (control system, star trackers, inertial reference module, reaction wheel assembly) and structural & mechanical parts (structural frame, hold down & release mechanisms, enclosures & mounting hardware). In a typical configuration the avionics package (C & DH, EPS, ADCNS), including battery modules, occupies approximately 1U of volume, and example is shown in Fig. 4. As can be seen in Fig. 3 the Space Eye telescope will occupy a 3U volume leaving a final $\sim$ 2U of volume for mission specific hardware, e.g. the image sensor control board, communication equipment, additional battery modules.

Attitude determination & control

The main technical challenge for astronomical imaging from CubeSats is instrument pointing stability. Long exposures are required to prevent image sensor noise overwhelming the faint signals from the sky and the instrument must be kept stable to within less than 1 pixel for the duration of the exposures to avoid blurring. For Space Eye the required exposure times are 300s and 1 pixel corresponds to $3''$, these requirements are well beyond the capabilties of any current commerically available CubeSat ADCS system. Improvements are required in both the attitude determination and attitude control aspects.

This challenge has already been confronted by another astronomical CubeSat mission, ExoplanetSat [21, 22], which requires a pointing stability of $1''$. Their approach was to improve the accuracy of attitude determination by adding fine star tracker image sensors in the focal plane of the main optics, alongside the science image sensor. To overcome the limitations of their reaction wheel based attitude control system (jitter, etc.) they plan to use ‘sensor shift

image stabilisation', an approach similar that used by some consumer cameras, i.e. mounting the focal plane assembly on an x-y piezo stage to compensate for small high frequency (~ 4–$12\,\mathrm{Hz}$) pointing errors. A hardware-in-the-loop testbed demonstrated $< 2.7''$ (3σ) stability while simulations suggested $< 1.4''$ should be possible [23].

Like ExoplanetSat Space Eye will use fine star tracking in the telescope focal plane to provide the precision attitude information required. Dedicated sensors adjacent to the main image sensor could be used however the CIS115 image sensor and its control electronics are capable of continuously reading out sub-regions of the image sensor for fine star tracking while the remainder of the sensor is simultaneously doing for a long science exposure. A fraction of the science image is lost in this way however avoiding a dedicated set of fine star tracking sensors and associated control electronics reduces complexity considerably.

For attitude control Space Eye plans to use micro-thrusters, thereby avoiding the jitter associated with reaction wheels. The details are still to be determined however potentially suitable cold gas microthrusters systmes are already available, e.g. the VACCO Industries propulsion system used in the CubeSat Proximity Operations Demonstration (CPOD) mission [20] (see Fig. 4) which could be reconfigured for attitude control. Electric propulsion micro-thrusters designed to provide propulsion and attitude control for CubeSat are coming to market (e.g. Accion Systems Inc. ion electrospray thrusters) and the high specific impulse could offer longer mission life and/or lower mass/volume.

Operations concept

The Space Eye science goals require making repeated observations of a small number of target fields in order to achieve the maximum sensitivity possible. The fields will be chosen to be close to the ecliptic poles in order to minimise the background due to zodiacal light and also far from the Galactic plane to minimise absorption by Galactic dust. Fig. 5 shows results from a performance model of the Space Eye in which the relative sensitivity was calculated for $45^\circ \times 45^\circ$ boxes around both North and South ecliptic poles in March, June, September and December. The sensitivity values are relative to the value that would be obtained at the North ecliptic pole in the absence of dust. The signal to noise calculations used the Zodical light model described in Giavalisco, Saba & Bohlin[24], dust extinction calculated from the Planck reddening maps[25], filter transmission profiles from DECam (http://svo2.cab.inta-csic.es/theory/fps/index.php?&mode=browse&gname=CTIO&gname2=DECam), CIS-115 QE values from Soman et al.[19], and CIS-115 dark current and read noise values from Wang et al.[18]. After a total of 1 month of exposure time ($2.6 \times 10^6\,\mathrm{s}$) a relative sensitivity of 1 would correspond to 1σ per pixel sensitivity limits of $2 \times 10^{-20}\,\mathrm{W\,m^{-2}\,arcsecond^{-2}\,\mu m^{-1}}$ in i'band and $3 \times 10^{-20}\,\mathrm{W\,m^{-2}\,arcsecond^{-2}\,\mu m^{-1}}$ in z' (30 and $29\,\mathrm{AB\ mag/arcsecond^2}$ respectively).

The Space Eye will be designed to continue to operate for at least a year in orbit in order to ensure each field can get a suitable amount of observing time. To make this possible we will require a relatively high altitude orbit for a CubeSat, $800\,\mathrm{km}$ Sun-synchronous orbit would meet our requirements and is serviced by frequent launches.

We anticipate being able to take data for approximately half of each orbit which, given our typical exposure time, image sensor resolution, 16 bit per pixel depth and an assumed compression ratio of approximately 2 means $400\,\mathrm{MB}$ of science data per day. Downlinking

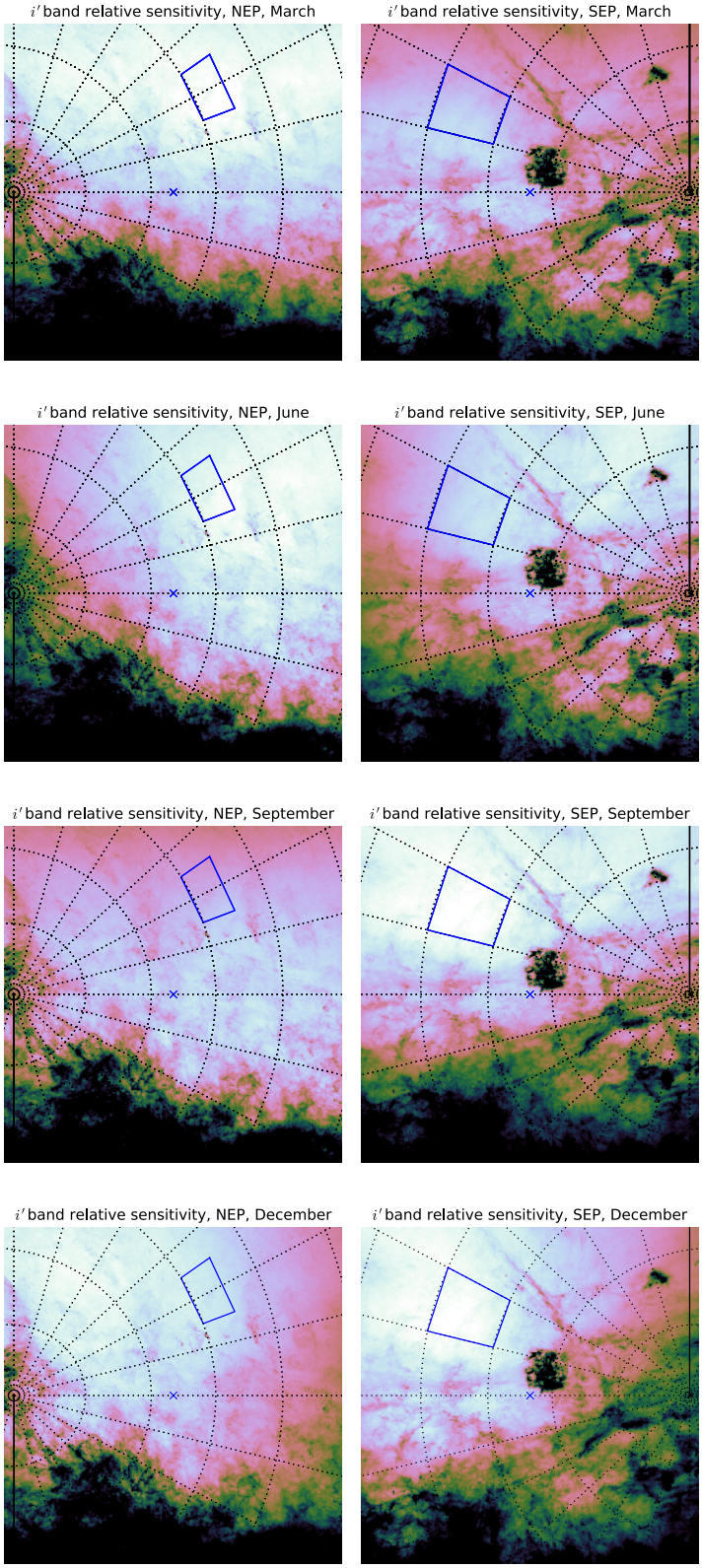

Fig. 5: Predicted i' band sensitivity relative to the ecliptic pole, zero extinction case. The maps show $45° \times 45°$ gnomonic projections centred on the north and south ecliptic poles in March, June, September and December, with a colourmap running from halved sensitivity (black) to full sensitivity (white). Equatorial coordinate grids are also shown, with 1 hour spacing in RA and $10°$ in dec, as well as the outlines of the designated target regions.

this volume of data from a CubeSat would be a challenge, but is achievable. Space Eye communications were discussed by one of the authors (SR) in this conference, and also in [26]. The processed data will be analysed following the procedure documented in detail by Zemcov et al [15].

Project status

An application for ARC LIEF grant funding for Space Eye was submitted in April 2015. The LIEF proposal included 15 named investigators and was supported by 8 Australian universities, the Australian Astronomical University, California Polytechnic State University (San Luis Obispo) and Tyvak Nano-Satellite Systems Inc. Despite positive assesor feedback the Space Eye was unfortunately not amongst the successful proposals announced in November 2015. A grant proposal for the 2016 round is currently being planned.

Conclusion

By minimising instrumental systematic errors and avoiding entirely those associated with atmospheric effects it is possible for a small, CubeSat based astronomical space telescope to be scientifically competitive with larger ground based facilities, at least for certain types of measurements. We have developed the Australian Space Eye concept, a 6U CubeSat based space telescope intended to measure extra-galactic background light anisotropies and image low surface brightness structures around nearby galaxies in the i and z bands (700–$1000\,\mathrm{nm}$). Instrument pointing stability of $< 3''$ over $\geq 300\,\mathrm{s}$ is required to enable the long exposures needed to mitigate the effects of image sensor noise. This requirement is challenging but by combining fine star tracking in the telescope focal plane with micro-thruster attitude control it is achievable.

Acknowledgments

The authors wish to thank everyone who has contributed to the Australian Space Eye concept and grant proposal.

References

[1] A. Horton et al., "The Australian Space Eye: studying the history of galaxy formation with a CubeSat," *Proc. SPIE*, vol. 9904, p. 9904-56, 2016

[2] C. Sandin, "The influence of diffuse scattered light. I. The PSF and its role in observations of the edge-on galaxy NGC 5907," *Astron. Astrophys.*, vol. 567, p. A97, 2014

[3] C. Sandin, "The influence of diffuse scattered light. II. Observations of galaxy haloes and thick discs and hosts of blue compact galaxies," *Astron. Astrophys.*, vol. 577, p. A106, may 2015. [Online]. Available: http://adsabs.harvard.edu/abs/2015A{%}26A...577A.106S

[4] P.-A. Duc et al., "The ATLAS 3D project XXIX. The new look of early-type galaxies and surrounding fields disclosed by extremely deep optical images," *MNRAS*, vol. 446, pp. 120–143, 2015

[5] R. G. Abraham and P. G. van Dokkum, "UltraLow Surface Brightness Imaging with the Dragonfly Telephoto Array," *Publ. Astron. Soc. Pacific*, vol. 126, no. 935, pp. 55–69, 2014

[6] P. G. van Dokkum et al., "Forty-Seven Milky Way-Sized, Extremely Diffuse Galaxies in the Coma Cluster," *Astrophys. J.*, vol. 798, no. 2, p. L45, 2015

[7] J. T. McGraw et al., “Ground-based observatory operations optimized and enhanced by direct atmospheric measurements,” *Proc. SPIE*, vol. 7739, p. 7739-29, 2010
[8] G. Moreels et al., “Near-infrared sky background fluctuations at mid- and low latitudes,” *Exp. Astron.*, vol. 22, no. 1-2, pp. 87–107, 2008
[9] C. Leinert et al., “The 1997 reference of diffuse night sky brightness,” *Astron. Astrophys. Suppl. Ser.*, vol. 127, no. 1, pp. 1–99, 1998
[10] G. D. Becker et al., “Evidence of patchy hydrogen reionization from an extreme Ly$alpha$ trough below redshift six,” *MNRAS*, vol. 447, no. 4, p. 3402, 2015
[11] B. E. Robertson et al., “New Constraints on Cosmic Reionization From the 2012 Hubble Ultra Deep Field Campaign,” *Astrophys. J.*, vol. 768, no. 1, p. 71, 2013
[12] A. Kashlinsky et al., “Tracing the first stars with fluctuations of the cosmic infrared background.” *Nature*, vol. 438, no. 7064, pp. 45–50, 2005
[13] M. Ackermann et al., “The Imprint of the Extragalactic Background Light in the Gamma-Ray Spectra of Blazars,” *Science (80-.).*, vol. 338, no. 6111, pp. 1190–1192, 2012
[14] A. Cooray et al.“Near-infrared background anisotropies from diffuse intrahalo light of galaxies.” *Nature*, vol. 490, no. 7421, pp. 514–6, 2012
[15] M. Zemcov et al., “On the origin of near-infrared extragalactic background light anisotropy,” *Science (80-.).*, vol. 346, no. 6210, pp. 732–735, 2014
[16] A. Lanz et al., “Studying extragalactic background fluctuations with the Cosmic Infrared Background ExpeRiment 2 (CIBER-2),” *Proc. SPIE*, vol. 9143, p. 9143-3N, 2014
[17] M. B. Peacock et al., “Detection of a Distinct Metal-Poor Stellar Halo in the Early-Type Galaxy NGC 3115,” *Astrophys. J.*, vol. 800, no. 1, p. 13, 2015
[18] S.-Y. Wang et al., “Characteristic of e2v CMOS sensors for astronomical applications,” *Proc. SPIE*, vol. 9154, p.9154-2I, 2014
[19] M. Soman et al., “Design and characterisation of the new CIS115 sensor for JANUS, the high resolution camera on JUICE,” *Proc. SPIE*, vol. 9154, p. 9154-07, 2014
[20] J. Bowen, M. Villa, and A. Williams, “CubeSat based Rendezvous, Proximity Operations, and Docking in the CPOD Mission,” in *Proc. 29th AIAA/USU Small Satellite Conf.*, p. SSC15-III-5, 2015
[21] M. W. Smith et al., “ExoplanetSat: detecting transiting exoplanets using a low-cost CubeSat platform,” *Proc. SPIE*, vol. 7731, p. 7731-27, 2010
[22] M. Smith et al., “The ExoplanetSat Mission to Detect Transiting Exoplanets with a CubeSat Space Telescope,” in *Proc. 25th AIAA/USU Small Satellite Conf.*, p. SC11-XII-4, 2011
[23] C. M. Pong et al., “One-arcsecond line-of-sight pointing control on exoplanetsat, a three-unit CubeSat,” *Advancements in the Astronautical Sciences*, vol. 141, pp. 147–166, 2011
[24] M. Giavalisco, K. Sahu, and R. Bohlin, “New estimates of the sky background for the HST exposure time calculator,” *STScI Instrument Science Tech. Rep.*, 2002
[25] A. Abergel et al., “Planck 2013 results. XI. All-sky model of thermal dust emission,” *Astron. Astrophys.*, vol. 571, p. A11, 2014
[26] S. Reisenfeld, L. Spitler, and A. Horton, “The Australian Space Eye: Ultra-faint astronomy imaging from Space,” in *33rd AIAA Int. Commun. Satell. Syst. Conf. Exhib.*, p. AIAA 2015-4337, 2015

Experience gained from Satellite Design Projects

Li Qiao[1], Andrew G Dempster[2] , Wayne L Hargreaves[1]

[1]*Capability System Centre, School of Engineering and Information Technology, University of New South Wales, Canberra, 2610, ACT, Australia*
[2]*Australian Centre for Space Engineering Research, University of New South Wales, 2052, NSW, Australia*

Summary: UNSW ACSER has undertaken two space mission design projects since 2010. The Synthetic Aperture Radar (SAR) formation satellite mission, also known as Garada project, (phase 0/1), was initiated at the end of 2010 and the QB50 CubeSat mission is ongoing since 2011. This paper presents key management lessons gained and identified by the staff and students involved in the aforementioned two projects. First this paper provides an introduction to the two space projects, including the management challenges confronted because the unique characteristics of a university-run space project. The experiences gained are presented from three perspectives: team, task and quality control and the corresponding discussion focuses on the control of cost, schedule and scope. The lessons learned from the projects as well as some recommendations are offered for future projects.

Keywords: System engineering, satellite mission, CubeSat, Experience management

1. Introduction

Since late 2010, two satellite projects have been pursued in University of New South Wales. The first mission was to design an earth observation Synthetic Aperture Radar (SAR) satellite known as "Garada", for Australian soil moisture and other applications using several satellites flying in formation.

The Garada project was funded under the Australian government's Australian Space Research Program (ASRP), with the feasibility study and conceptual design completed mid-2013. Funding did not continue. This work was the mission analysis phase study (Phase 0), investigating potential earth observation applications and designing SAR satellites at system level, which can be up to 2000kg. On the contrary, the second space mission conducted is a cube satellite project which is only 2kg in weight. Part of the global QB50 mission, our satellite, called "UNSW EC0", is mainly funded by the university due its educational purposes. The CubeSat mission has been through its mission analysis phase (Phase 0), feasibility and preliminary definition phase (Phase A and B), and detailed definition phase (Phase C).

Those thousand-kilogram satellites require national levels of support to operate, while a cube satellite can be run by a university. There are several reasons why the tiny satellites are not

just simple and meaningless toys anymore. Frist, several microsatellite missions have demonstrated that these satellites become accepted tools for doing space missions for science and defence. Cube satellites are particularly suitable as a focus for education and training by providing a means for providing direct, hands-on experience of all stages and aspects of a real satellite mission—from design, construction, test and launch through to orbital operation [1]. Second, its implementation requires less complexity and management compared to those national-level missions. Small missions like CubeSat is affordable and do not require large, sophisticated development and test facilities[2]. The engineering and management of a CubeSat changes significantly, as the complexity is reduced. Thus it can be developed in a normal laboratory environment in a university and can still be reliable on orbit.

Spacecraft ranges from a few grams to thousands of kilograms [2], and the two projects happens to span the two ends. No matter the size and mass, like every satellite mission implementation, developing a satellite is multi-disciplined and complicated; thus it requires the application of system engineering practices. In reality, systematic design planning is performed in many space projects [1] and standards have been drafted regarding the experience gained in space projects [3]. However, this systems engineering is not always delivered effectively, which can be seen from the recent U.S Government Accountability Office and NASA studies of space systems documents and the MIT-based Lean Advancement Initiative studies[4].Space agencies, such as NASA and ESA, have accumulated management experience from running projects, especially failed projects [5][6].The success of a given space project is often jeopardized by problems that had happened before [7].A simple fact is the success of the project is not only a technical issue.

Considering the experiences from the two projects may be helpful for feasible solutions to the problem of the future systems, this paper presents some management issues confronted and the recommended solutions for running space projects within the context of a university environment. The structure of the paper is as follows. Section 2 provides a brief background on space project management and introduces the challenges we met in an Australian university when we conducted the research and development of a space project, and the requirement to have a distinct management method from previous projects. Sections 3, 4, 5 discuss the details of the issues and experiences taken from the previous projects from three aspects, which are team, process, and components. Section 6 draws the conclusion.

2. Challenges

The methods for managing university-run space projects vary radically from industry. For example, using conventional experience and methods to manage the CubeSate in university has the possibility to cause a failure. Those who have experience in managing major, expensive and large systems should not apply the same methods to the CubeSat. From time to time, the leader feels it is difficult to impose the previous experiences and methods in managing projects on the new CubeSat project.

An incomplete list on Wikipedia shows that, since 2003, only 100 cube satellites have successfully reached orbit; numerous others have been developed and lost to launch failures or never launched [8].Cube satellites are reported to be built in rapid time-scales, typically 12-18 months, however it is very conditional. For instance, if the local team has a lack of experience of space mission development, the result is a longer timeline. Australia tends not to have a lot of experience of space mission projects. In addition, the environments for space education and industry are so different here compared to other countries with space industries. In this situation, the chance of work turning out to be more complex than anticipated is much more than usual.

The final goal is to deliver a cube satellite product with scarce available resources using scarce available resources of time, people and budget. In fact, the time and budget are kinds of observations to indicate how well the project is managed.

The available budget for the program is limited and easy to exceed; even if a large part of the required funds are available before the project starts. Like most educational cube satellite missions, only limited funds exist at most universities for such educational projects and it is easier to find small amounts of money than a large [9].The team at a university is strictly limited, the project has deadlines, therefore it is vexing to let the limited team deal with the limited time, cost and non-limited complexity and risk. Apparently, the project complexity and risk should be well controlled.

3. Team control

Does a small team mean flexibility and high efficiency? Not necessarily. At times, can be hard to maintain focus, thus team control is vital.

3.1. Characteristic of the team

In universty, all the workers are assigned by the team leader, such as a professor. The group has much fewer members than those in a typical R&D group in space industries. For instance, the CubeSat development team is normally small in size, e.g. 6 to 10 people. Fewer group members do not mean that the management is easy. It is suggested that, according to the requirement of the project, the candidate is more an engineer rather than a scientist when picking members, if the process is strongly focussed on engineering practice.

In the university, the group involved several research fellows (post-docs) and some academic staff, e.g. professor, A/professor, Senior lecturers, lecturers. It should be noticed that their time is not fully dedicated to the project. In addition, students may assist on the edge of the core. They step in at different time. For these roles, it is difficult to ensure that all the different people can support the project through difficult times.

Recruiting a lot of experienced veterans to the project is impossible most of time. In fact, there are not many candidates available, especially in Australian. Most of the group members are relatively young research associates. The desired situation is that the same team can be maintained during the whole project lifecycle. Thus the same team will confront all the issues from concept design to development, to the final assembly and testing.

Normally one team member is assumed to look after one work package/subsystem in the project. One team member typically only knows the dependency relations between the components or subsystems they design and directly use, thus they are not able to track whole system-wide dependencies [10]. The question is who looks after system-wide dependency relations in the group? In this circumstance, if a system engineer (SE) position is located in the team, the role of this position is to keep a cool overview and pay close attention to the interfaces where two or more systems or system elements work together, and establish an interaction network with stakeholders and other organisational units of the organisation. Also, the role of this position is to manage the budget and enhance communications in the project team.

However, sometimes, we still pay more attention to techniques in a specific domain rather than the whole integrated system. For instance, many projects cannot afford a specific position for system engineer due to, e.g. the budget. If there is no such system engineer position set up, the work of the system engineer should be assigned to a specific member, e.g. chief engineer or project manager or the leader of the project. The system engineer's job is more than looking after the budget but is also the one to make decisions within the group.

3.2. Team Structure

Assume node 1 represents the manager, nodes 2 to 7 represent the 6 research associates/assistants (RAs) working on the project. Management stucture 1 in Figure 1 is easy to understand. The edge between node 1 and the other nodes is in the form of meetings and reports. However, this hierarchical-like system can not help increase working effieiency in a small space mission, as the success of the mission relies highly on the links within nodes 2 to 7, represented in the star-style structure 2 illustrated shown in Figure 2.

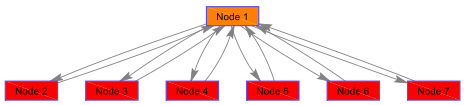

Figure 1 Management structure 1

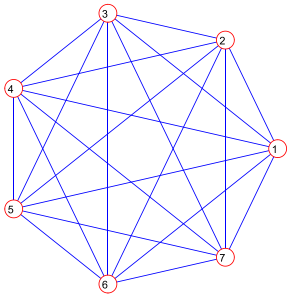

Figure 2 Management structure 2

Even if Node 1 represents the manager or professor in most cases, it does not mean the manager has more weight when making technical decisions. All the individuls have an equal chance to demerit the product and everybody is responsible for the overall outcome. Stucture 2 emphasises that any problems popping up from one member require the entire team's focus for resolution.

The linkages added in structure 2 compared to structure 1 cannot be naturally groomed. On the contrary, these links requires special protection. For instance, everyone likes to simplify their own work. Consciously or unconsciously, reducing sharing and communication is an option to control the work load. Sometimes, communication is avoided artificially and intentionally as the links may bring more work.

As we discussed, we expect the whole team will be present during the whole lifecycle, but sometimes a member resigns and is replaced. As the size of the team is small, a member resigning will cause a considerable effect on the whole project. besides, the newcomer needs time to become familiar and productive, and other group members may feel exhausted.

3.3. Communication enhancement

One way to hold the whole team together is to enhance communication and tightly control interface specifications. It is very useful to allocate the disciplines with the most frequent interaction or other affinities close to each other [11].

The manager should consider watching the inter-communication activity as ongoing work. Sometimes, the manager has to force the members to keep them updateed, i.e. catch-up meetings are the daily job so that all changes should be noticed in the group. There is not much ability to tolerate problems. Clearing up issues weekly is necessary in the form of unformal meeting taking more time.

The actual work may take much more time than planned. Staff working in a university can readily overwork in their own desire for promotion and publication. These may cause distractions and extra working pressure. Eventually, it may bring low working efficiency and potential mistakes. If the team is overwhelmed, not only will quality will suffer, but also the time cannot be ensured. For a small team, a member who cannot be open and active must be removed from the team. One is working on a certain package and there is no specific peak in the structure. Working alone and perfectly is not always possible in a small team.

In any case, the people playing the manager role should keep an eye on the balance between workload and pressure and pay attention to overload and exhaustion in the group.

4. Time (Schedule) control

Time is a key observation by management system. Any form of waste happening inside the project, such as unstable requirements, poor coordination, quality problems and management frustration, can eventually result in waste of time, leading to the project failure. Therefore, when making any decision, the very first question to ask is the necessity to spend the time on it.

4.1 Balance with research and education

Normal spacecraft projects do not facilitate substantial involvement of students or junior employees. Neither Garada nor EC0 is defined as a student-led operation; however both are operated within the context of a university environment; the two must achieve science, engineering and educational objectives. Furthermore, from the fun perspective, the Cube satellite EC0 is partly supported from teaching (as opposed to research) funds. Thus, the involvement of students is considered as a key educational outcome.

The project will achieve its education goal mostly via recruitment of students. Their involvement is essential and it has been observed that the students are able to make significant contributions to the project from our experiences. The students are assigned to a team member, and then carry out part of a task. More or less, the team member has been assigned a workload. Therefore, the time and energy assumption of the corresponding staff should be watched and guided at the same time.

The balance definition starts the recruitment of each RA position. For instance, the position is recruited for the mission only, or has other commitments, such as assistant in teaching and writing proposal, reports and papers. Knowing these requirements/constraints of the project better can help avoid being potentially overwhelmed. Again due to small team, the performance and capacity of the team can easily affect the project progress.

4.2 Requirement & Complexity Control

However, it may not always be obvious why requirements are necessary, particularly since much of our decision making in our personal and business lives is not conducted using formal methodologies. But the idea is at least to understand the importance of the requirements, try to control the complexity and keep the requirement simple and clear [12].

For university-run projects, there may not be specific clients as clearly as in industry. Part of the reason for developing the CubeSat is to lead the discipline and enhance the university reputation. Therefore, at the beginning, the requirement may simply be something like “we want to build a cube satellite”, then look for requirements that can be finished in the time line. Therefore, it is acceptable for small educational missions to begin with non-fixed

requirements. The best design requirements for the cube satellite are sufficient to support the mission goal and are simple in complexity.

We expect all the team members share a commitment to achieve mission success by minimising unnecessary requirements and complexity, as well as schedule. Sometimes it is not easy to do this. Innovation is encouraged in univerisities, and academics are excited to set more fancy and smart goals which might, in fact, be impossible to achieve. The manager needs courage to say NO to the new ideas. It is suggested that each member has a single local object, and only keep stable and clear fundamental requirement so that the whole team will not lose its focus.

4.3 Schedule Timeline

Once the requirements are determined, the manager has to find ways to save time and finish the project in the time frame. Bad scheduling could slowly grow to the point of triggering the program's failure or cancellation. Nobody likes hurrying. It is good if possible to accelerate progress ahead of schedule as the future is always unpredictable.

When assign the takes, most of the work should emphasise building/testing rather than designing. Once the design is done, take caution to unnecessary changes as it will waste time on meeting, discussion and re-work. It is smart to build quickly once the design is completed, then switch toward to the test phase. Test should starts as early as possible, as testing inevitably costs time and money. Take the thousand hour test for instance; it will take much more than thousand hour to demonstrate it.

The reason we emphasise time is that the intense work and frustration is always inevitably underestimated by all the team members [2], from engineers to managers, who want to save time and money.

5. Quality/Risk control

Getting the whole system working is the goal, thus the quality/risk management is crucially important. The question arises whether the entire reliability could still meet space requirements. This section addresses the quality/Risk control from aspects of components selection, ordering and testing.

5.1 Components selection and Ordering

Differently from other satellites, the CubeSat is factorised. It has customized size and the components can be ordered from some existing markets such as "CubeSat Shop" [13]. These suppliers makes selection and choice of components very convenient and can help to eliminate time spent on the purchasing process In fact, it is seen as one of the advantages is the adoption of commercial-off-the-shelf (COTS) microelectronic technologies developed for

terrestrial use and adapted to space [1].It is acceptable to use COTS components as a CubeSat does not have as many as components as big satellites, and is not expected to have longer mission lifetime. In addition, it helps eliminating unnecessary time on selection and ordering.

The quality of this CubeSat is controlled by several aspects related to each component, such as who orders, who tests and assembles the components. It is suggested to pay attention to the hidden risk of the choice. Attention must be paid to failures of components, and weak links. Especially in the case that a component will affect more than one work packages, i.e. more than one team member is involved, trade-offs should be performed. Any components in the mission should be approved by the entire team, as least the majority part of the team, so all are confident in terms of risk and reliability.

5.1 Testing

Testing is the only solution to answer if the commercial components are qualified. That is the reason why we suggest that entering testing phase as early as possible to allocate sufficient time for it.

Again due to small team, one work package is normally assigned with one person. This means there is insufficient control of the quality of the work that person does. This brings risk that if this work's complexity increases based on the limitations of this person, and there is no way other staff can help out. In order to understand the real performance of the purchased components as early as possible, it is better to code, debug and test the real hardware. It is not suggested to spend much more time on simulation. The testing must be conducted thoroughly, as it is impossible to fix problems on board a launched satellite. The responsibility for receiving the parts and acceptance testing is with the engineer who ordered them[2].

Conventional testing requires a set of testing facilities, such as clean room, vacuum chamber, shacking table, air bearing platform, rotating platform, Helmholtz Coil System, and illuminating source modelling sun, earth etc. However in our case, it is hard to find all the facilities on the campus. Therefore, we need to look for a simplified testing method, which is affordable and viable. It is be acceptable not to test every subsystem of the cube satellite. It is acceptable to test the entire satellite directly. Furthermore, it is acceptable to use qualitative testing rather than quantitative testing. For instance, a simple way to test sun sensors is to inspect the sign of the output value with different incident directions of illumination.

6. Conclusion

This paper presents the management experience gained from the two space projects operated at ACSER at UNSW. Small team, short project period and low budget are common constraints to steer the projects. Though small satellites are reportedly built in rapid time-scales, it is very conditional on the limited team and facilities. Success relies on the balance

of team, time, and quality control. The following lessons learned can be summed up for future university-run space projects.

- The mission focus should be tight, small and clear. Pay attention to unnecessary change of requirments.
- Limit the amount of work of the small team. More work may bring more credit, however it will dilute the focus one the fundamental programs.
- Enhance the communication of team, especially weak links. Avoid the task and pressure so the small team is not overwhelmed. Pay attention to member resigns and new comes.
- Accelerate progress ahead of schedule. Emphasise building/testing rather than designing.
- The quality and risk is the results testing realistically, especially for the go-to-space mission.
- It is prefer that the engineer who tests the components is the one who ordered them. For CubeSat, it is acceptance to use simplified testing approaches if lacking for. testing facilities

7. Acknowledgements

The Garada project was funded by the Australian Space Research Program "SAR Formation Flying". The UNSW EC0 is part of the educational Space Engineering programme supported by UNSW. The authors acknowledge the support of the Australian Centre for Space Engineering Research.

References

1. Sweeting, M. N. and Underwood, C. I. *Small Satellite Engineering and Applications, in Spacecraft Systems Engineering*, Fourth Edition (eds P. Fortescue, G. Swinerd and J. Stark), John Wiley & Sons, Ltd, Chichester, UK., 2011.
2. Spagnulo, M.,Fleeter, R.,Balduccini, M.,Nasini, F., *Space Program Management: Methods and Tools*. Springer Science & Business Media.2012
3. ISO Standards(16192:2010): Space systems – Experience gained in space projects (Lesson learned)—Principles and guidelines. June 15, 2010
4. Systems Engineering Handbook. INCOSE (International Council on Systems Engineering) v.3.2.2. San Diego,CA. October 2011
5. Stamatelators, M., Dezfuli, H. Probabilistic Risk Assessment Procedures Guide for NASA Managers and Practitioners. NASA/SP-2011-3421 Second Edition, December 2011.
6. ECSS (European cooperation for space standardization) Requirements and Standards Division. *Space Project Management*. Report number ECSS-M-30A.Netherlands. 19 April 1996.
7. Garon, S. "Space project management lessons learned: a powerful tool for success." *Journal of Knowledge Management*, Vol. 10, No. 2, 2006, pp. 103-112.

8. Straub J.,Korvald C., Nervold A., et al. OpenOrbiter: "A Low-Cost, Educational Prototype CubeSat Mission Architecture". Journal of *Machines*, Vol 1, 2013, pp. 1-32.
9. Alminde, L.; Bisgaard, M.; Bhanderi, D.; Nielsen, J.D., "Experience and methodology gained from 4 years of student satellite projects," in. *Proceedings of 2nd International Conference on Recent Advances in Space Technologies, 2005(RAST 2005),* Vol. 9 , No. 11, 2005, pp.94-99.
10. Ding, H.; Arber, L.; Lui, S.; Caccamo, M., "The dependency management framework: a case study of the ION CubeSat,". *Proceedings of 18th Euromicro Conference on Real-Time Systems, 2006*, pp. 1-10
11. Bandecchi, M., Melton, B. and Ongaro, F., "Concurrent Engineering Applied to Space Mission Assessment and Design". *ESA bulletin*. September 1999.
12. Faulconbridge, R. I. and M. J. Ryan. *Managing Complex Technical Projects: A Systems Engineering Approach*, Artech House.2003
13. CubeSatShop. http://www.cubesatshop.com/

Systems Engineering Essentials for Small Satellite Missions

Sana U. Qaisar, Sean L. Tuttle and Mike J. Ryan

University of New South Wales
Canberra, ACT, 2601, Australia

Summary: The availability of miniaturized, commercial-off-the-shelf (COTS), low-cost satellite components has encouraged the design and development of small satellites by relatively inexperienced organizations and individuals seeking low-cost and fast-delivery missions with "good enough" reliability requirements, through non-traditional risk-taking approaches. Currently, there are no standard systems engineering practices or guidelines for building such plug-and-play satellites. As a result, the accepted satellite design trade-off between the available limited resources and the reliability compromise is likely to be sub-optimal. In this paper, we focus on selection of the physical architecture of the satellite to highlight the concern. We propose dynamic exploration of multiple architecture designs, derived from relevant COTS databases, to determine an architecture that improves the system reliability under the given constraints. The proposed approach is demonstrated through the presentation of a commercial Cube Satellite example based on real data. The outcomes of this paper can potentially contribute to small satellite standardization efforts.

Keywords: small satellites, reliability, architecture design, tradespace exploration, optimization, off-the-shelf solutions, cube satellites, standardization.

Introduction

The number of small satellites being launched, particularly of decreasing mass (Table 1), has increased significantly over the past few years with 160 launches of less than 50kg mass recorded in 2014 alone (SpaceWorks, 2015). The main reasons for this growth include miniaturization of once-bulky satellite components, their off-the-shelf availability and low cost, which combine to make building, launching and operation of small satellite constellations increasingly feasible.

Category	Satellite Mass (kg)
Large	1000
Medium	500 to 1000
Mini	100-500
Micro	10-100
Nano	1-10
Pico	0.1-1
Femto	<0.1

Table 1. Classification of small satellites by mass (NASA, 2014)

Some examples of recent small satellite endeavours being carried out by professional organizations include:

- 1 Billion Dollars investment in SpaceX by Google and Fidelity Investments for developing space based internet capability.
- Global internet service to be provided by OneWeb Ltd on a network of 648 lightweight LEO satellites.
- Cyclone Global Navigation Satellite System (CyGNSS) by NASA for weather predictions.
- The U.S. Army Space and Missile Defense Command/Army Forces Strategic Command's Nanosatellite Program (SNaP) for enhanced communication using existing UHF tactical radios.

These examples illustrate that the current focus on investments in the small satellite sector remains in the areas of high-resolution Earth imaging at near-real-time rate for asset monitoring etc., scientific experiments such as atmospheric modelling and measurements, space-based internet for global connectivity, and coverage for improved military communications.

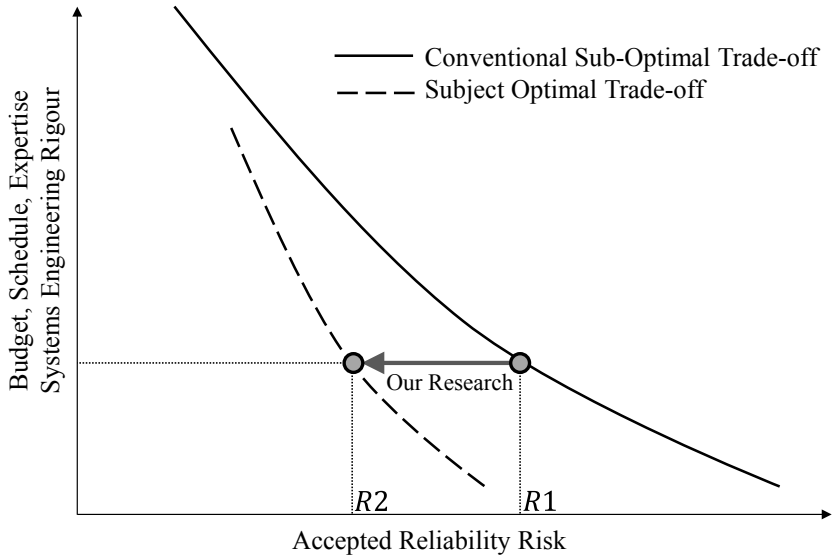

Figure 1. The trade-off between application of resources and reliability risk

At the same time, the evolution of small satellites has encouraged relatively inexperienced organizations and individuals, seeking low-cost and fast-delivery missions with "good enough" reliability requirements, to design and build satellites through non-traditional risk-taking approaches—for example, university satellite projects conducted by students (Meijers, 2004). For the rest of the discussion, in this paper, by 'small satellite', we refer to this class of satellites, distinguished by the risk approach and design philosophy, rather than physical size. As illustrated in Figure 1, as a general principle, a drop in the level of project resources including budget, schedule, workforce, etc. results in an increase in the risk to system reliability. For satellite design endeavours constrained by relatively limited resources and low reliability requirements, application of formal Systems Engineering (SE) rigour is neither affordable nor embraced by the non-traditional workforce involved (Naveen, 2006). Although design can achieve a target level of reliability risk, the accepted risk is based on one-off expert judgement and is not optimized with respect to the available resources (Riddle, 1998). This may prohibit some conceivable mission potential, resulting in a sub-optimized capability which fails to meet the full operational potential available in the design space (Bonyan, 2010).

Hence, it is important that SE be applied, particularly at the initial stages of the program, in order to provide a basis for developing mission strategies, managing requirements, conducting risk assessments, performing cost estimation and design trades etc. (Ross et al., 2010). On the other hand, the design and development of small satellite missions does not entail all aspects traditionally associated with large spaceflight projects, such as the financial and risk consequences. This calls for a shift in the SE philosophy towards a "lean thinking" approach so the missions can benefit from formal SE rigour by appropriately adapting them to the needs of the small mission environment without excessive overhead (Robertson, 2004; Hunyadi et al., 2005).

The broader scope of our research is to investigate and develop novel approaches for preserving the SE advantage across the system life-cycle without upsetting the relaxed attitude towards building small satellites. Some of the potential investigation areas that address this objective are listed as follows.

- Developing frameworks for system verification by analytical-data and simulations instead of physical prototyping.
- Planning the verification process in the context of the satellite program, rather than individual satellites, i.e. verification by similarity.
- Understanding the testing trade-offs between launch requirements and the operational risk.
- Developing SE procedures that account for the un-traditional, sometimes geographically-dispersed and limited human resource.

In this paper, however, as illustrated in Figure 1, we focus on selection of the physical architecture of the satellite, during the system design phase, for optimizing the trade-off between the available limited resources and the system reliability. That is, to determine architecture designs that reduce the conventionally accepted reliability risk for the same level of resources (improving the system reliability from $R1$ to $R2$ in Figure 1). The same approach can also be used to reduce the required resources to achieve the same desired level of reliability.

The architecture design for small satellites is driven by the available low-cost, sometimes non-space-qualified and untested off-the-shelf components and technologies. Unfortunately, there is no systematic framework nor guidelines in place to assist the designers of such satellites to make informed and optimal decisions to prevent unnecessary risks and expensive design iterations.

Some efforts, within the small-satellite community, have been recently initiated to address these concerns. The following activities, carried out by the Space Systems and Operations Sub-Committee at the International Standardization Organization (ISO TC20/SC14) and the Study Group 4.18 at the International Academy of Astronautics are in progress to develop the definitions and standards for such satellites (Cho and Graziani, 2015).

- Draft under preparation for definition and requirements of small satellites seeking low-cost and fast-delivery.
- ISO/19683: Standard under development for design qualification and acceptance tests for the low-cost and fast-delivery satellites.

The majority of member countries in sub-committee ISO TC20/SC14 have, so far, agreed on use of the term "Lean" for this class of satellites to reflect the design philosophy rather than size or mass of the satellite.

Physical Architecture Design

The physical architecture of a system is composed of a number of physical elements (or components) connected together in a specific way (i.e. through the interfaces), to perform the desired functions (Simon, 1969). Candidate physical architectural designs (or simply designs) are created by considering alternatives of one or more system components (SEBoK, 2015). As mentioned earlier, since the subject small satellite is largely built through COTS components, the architecture design is essentially determined by the availability and compatibility of COTS alternatives of each physical element in the architecture. The key challenge for system architect, in this case, is therefore the *selection of the best COTS alternative for each physical element* in support of an overall architecture that meets the system requirements and constraints.

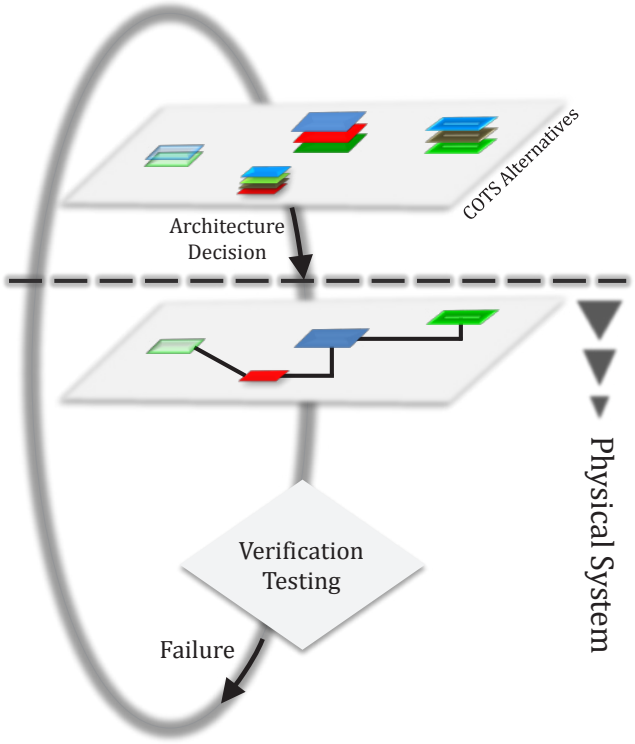

Figure 2. Conventional approach to small satellite architecture design

In the existing practices of designing small satellites, the decision of architecture design is influenced by expert judgement and historical data from a project with similar specifications. As illustrated in Figure 2, even though few back-of-the-envelope candidate architectures are naturally considered, the exploration is usually stopped as soon as the requirements are met, and the design is deemed as 'satisfactory' (Riddle, 1998). Moreover, to meet the design objective (e.g. minimizing cost), the designer may be inclined towards optimising the individual system elements rather than the overall system architecture, as explained with an example, later in the paper. Also, the design decisions tend to be made at the beginning of the design process and the designer commits to a physical architecture to compatibility and feasibility verifications. The testing for verification is performed on the physical system and any failures encountered provide feedback to modify the architecture design, requiring expensive iterations both in terms of the cost and the schedule; neither of which is affordable in lean satellite programs. This design paradigm can be described as a 'decide-build-test' sequence where design decisions are followed by testing a physical system.

Proposed Approach for Architecture Selection

As illustrated in Figure 3, in the proposed approach, a tradespace is derived from the COTS databases of standardized components (providing relevant data for several alternatives of each system element). This allows the designer to explore a multitude of solutions, in an interactive and recursive manner, until an optimal solution is agreed. The design decisions are thus delayed until the feasibility and optimality are proven. This design approach can be described as an 'explore-test-decide' sequence. The input is accepted from the designer, in terms of specifications of the physical elements of system architecture, trade parameters, their relative importance and constraints such as the budget and schedule. The input can then be processed by software applications and tools which consult the relevant COTS databases and produce the tradespace.

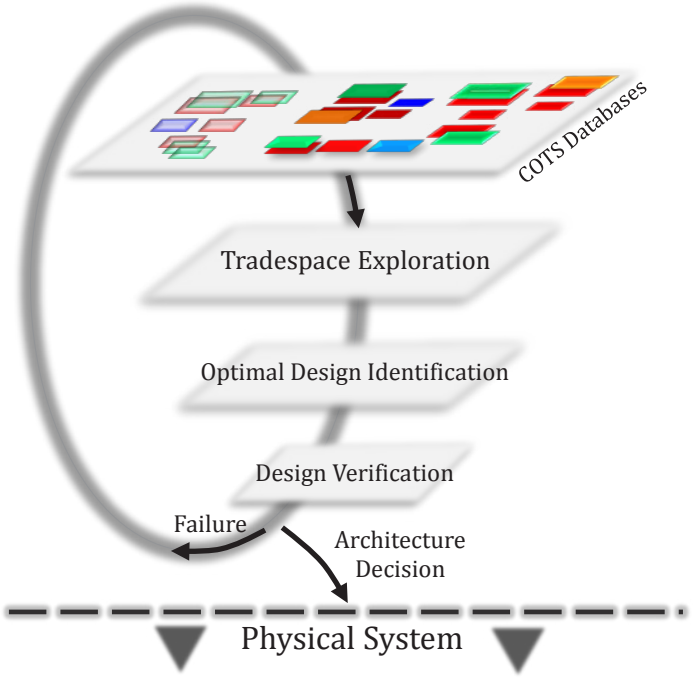

Figure 3. Proposed approach for architecture selection of small satellites

The tradespace exploration for architecture design and other contexts has been previously applied, for example, in the design of aerospace and embedded systems (Gries, 2004; Ross and Hastings, 2005; Palermo et al., 2015; Valerie et al., 2015). However, those systems are largely developmental and the tradespace is complicated by a number of uncertainties throughout the design process. The COTS-based systems, in this context, are relatively simple and well understood, making the tradespace evaluations and exploration more feasible.
The proposed approach is demonstrated through a cube satellite example based on real data, as described in the following section.

Example CubeSat System

The example CubeSat system, considered for demonstrating the proposed approach, comprises six COTS components, herein referred as subsystems, including Communication, Power, Attitude Control, Solar Panels, Command & Data Handling, and Antenna. The number and specifications of COTS alternatives for each subsystem are listed in Table 2. The data is acquired from the CubeSat web-shop which offers relevant information for standardized off-the-shelf CubeSat components from a number of manufacturers (CubeSat

Web-Shop, 2015). The trade parameters, considered in the example include mass, volume and cost. The constraints are defined in terms of maximum acceptable system mass, system volume and system cost as 900g, $7.5\times10^5 mm^3$ and 40000€ respectively. The relative importance of trade parameters is represented by a utility function (curve) passing through the tradespace, implying, generally, a higher value (acceptable cost) for designs with relatively smaller mass and volume. The COTS databases in the proposed framework are represented by the data provided in Table 2.

Subsystem	Alternative	Reference	Mass (g)	Volume $\times10^3(mm)^3$	Cost k€
Communication	1	ISIS VHF/UHF	85	129.6	8.5
	2	ISIS UHF/VHF	75	129.6	8.5
	3	ISIS TXS	62	129.6	8.5
	4	NanoCom U482C	75	154.8	8

Subsystem	Alternative	Reference	Mass (g)	Volume $\times10^3(mm)^3$	Cost k€
Power	1	NanoPower P31U	200	138.24	3.8
	2	NanoPower P31US	240	198.72	2.45
	3	NanoPower PBX	370	316.48	5.5
	4	Crystalspace P1U	80	112.32	5.4

Subsystem	Alternative	Reference	Mass (g)	Volume $\times10^3(mm)^3$	Cost k€
Solar Panels	1	ISIS	50	16.17	2.5
	2	NanoPower 110	59	17.383	2
	3	NanoPower 110U	59	16.979	2.75

Subsystem	Alternative	Reference	Mass (g)	Volume $\times10^3(mm)^3$	Cost k€
Attitude Control	1	ISIS VHF/VHF	196	146.89	8
	2	Nano-SSOC-D60	6.5	3.55	3.6
	3	CubeControl	112	87.36	4.2
	4	Nano-SSOC-A60	4	2.263	2.8

Subsystem	Alternative	Reference	Mass (g)	Volume $\times10^3(mm)^3$	Cost k€
Command Data-Handling	1	NanoMind A712D	55	86.4	47.5
	2	ISIS	94	107.136	43
	3	Cube Computer	60	86.4	45
	4	Q6 Processor	23	56.316	18.75

Subsystem	Alternative	Reference	Mass (g)	Volume $\times10^3(mm)^3$	Cost k€
Antenna	1	UHF/VHF	100	67.228	4.5
	2	HICPICO	110	8	4.6

Table 2. Specifications of example CubeSat system

The tradespace is initially constructed by assessing all possible combinations of one COTS alternative, at a time, from each subsystem. The trade parameters of resulting system design are computed through addition of constituent subsystem alternatives as follow:

$$M_{S,d} = \sum_{i=1}^{6} m_{i,k} \qquad 1 \leq k \leq 4 \tag{1}$$

$$V_{S,d} = \sum_{i=1}^{6} v_{i,k} \qquad 1 \leq k \leq 4 \tag{2}$$

$$C_{S,d} = \sum_{i=1}^{6} c_{i,k} \qquad 1 \leq k \leq 4 \tag{3}$$

Where $M_{S,d}$, $V_{S,d}$ and $C_{S,d}$ respectively denote system mass, system volume and system cost, with subscript d representing the size of tradespace, i.e. the number of designs presented in the tradespace, while $m_{i,k}$, $v_{i,k}$ and $c_{i,k}$ signify the mass, volume and costs of kth alternative of subsystem i, respectively.

Tradespace of CubeSat System

Figure 4 shows the tradespace of example system with the edges of the 3-dimensional container representing the system constraints described above. As shown in Figure 4, the tradespace presents a multitude of solutions within the constraint-boundaries as well as a few solutions falling outside it due to incompatibilities or other factors such as long lead time.

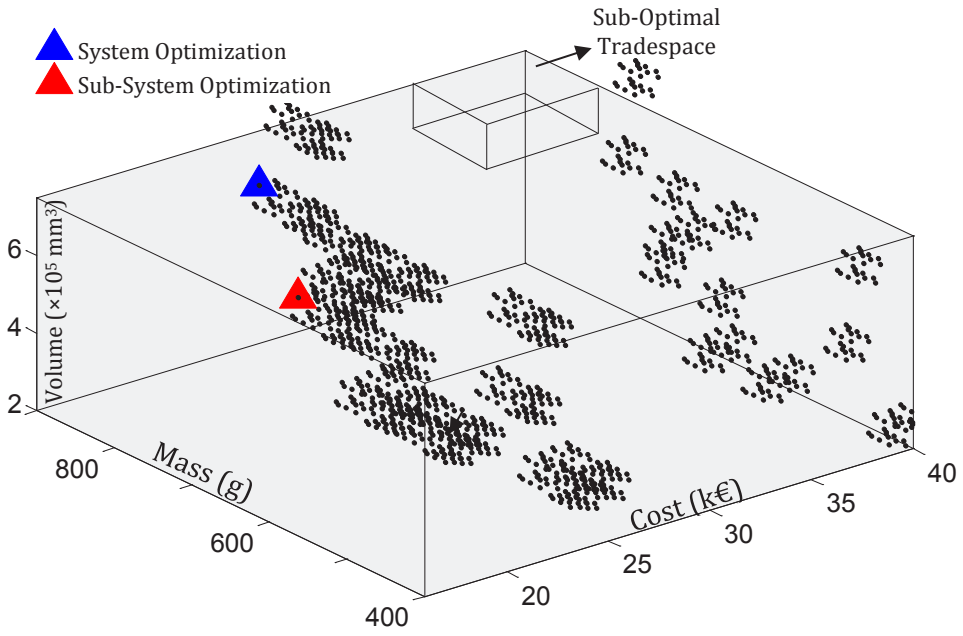

Figure 4. Volume-mass-cost tradespace for the example CubeSat system

From Figure 4, it can be inferred that design decisions made without a systematic exploration of the full tradespace are likely to result in a sub-optimal trade-off, as discussed below.

The tradespace exploration may be stopped as soon as the constraints are met, which may be based on a sub-optimal or possibly the worst section of the full tradespace, as indicated in Figure 4. Consequently, the potential higher-value opportunities present in the full tradespace (e.g. lower cost and volume solutions) will not be identified.

The design decisions may be focused on optimizing subsystems as a simple strategy for achieving a system design that is within the tradespace—that is, choose the best subsystem in each case that has the optimal volume-mass-cost trade. However, optimization of subsystems invariably comes at the cost of sub-optimizing the system (Faulconbridge and Ryan, 2014). For example, if the design objective is to minimize the system cost per unit volume, the designer may select, for each subsystem, the COTS alternative with lowest cost-to-volume ratio, resulting in the design marked as blue triangle in the tradespace in Figure 4. On the other hand, the full tradespace exploration at system level discloses the optimal value design (having the lowest cost-to-volume ratio) marked as red triangle in Figure 4. The numerical values of cost-to-volume ration, for the two (sub-optimal and optimal) designs, are listed in Table 3. As highlighted in Table 3, a sub-optimal power sub-system (with a larger cost/volume value) leads to an optimal system design, whereas selection of an optimal power supply leads to a suboptimal design (given the cost-to-volume utility function). This simple case emphasises the value of tradespace exploration, in that the contributions of the given sub-optimal power sub-system to system volume is relatively high such that the overall system cost-to-volume ratio is smaller than achieved with the optimal power sub-system.

Design	Sub-Systems						System
	Communication	Power	Solar Panels	Attitude Control	Command & Data Handling	Antenna	
Sub Optimal	0.0516	0.0123	0.1150	0.0480	0.0401	0.0669	0.0402
Optimal	0.0516	0.0173	0.1150	0.0480	0.0401	0.0669	0.0379

Table 3. Cost/volume data for the example sub-optimized and optimized system designs

Whilst all feasible solutions in the tradespace represent technically acceptable architecture designs, they are discriminated by the utility function (curve) which represents their value assessed by the stakeholders. In other words, the utility curve represents understanding of the trade parameters, in terms of their relative importance, by the stakeholders. The example utility curves in Figure 5 show that solutions with relatively smaller mass and/or volume are accepted at higher cost. All solutions falling on the curve represent an acceptable trade-off with same value, while those located above the curve imply a sub-optimal trade. Having two curves in the example tradespace in Figure 5 captures the fourth trade dimension, i.e. the system reliability, so that for competitive systems with higher reliability, a higher cost is acceptable. This also motivates the designers to create solutions which access the higher reliability curve.

In the example tradespace, this aspect is illustrated by adding an identical redundant power sub-system to a design (shown as red triangle in Figure 5). The redundant parallel subsystem improves the subsystem reliability as:

$$\ddot{R} = 1 - \left(1 - \dot{R}\right)\left(1 - \dot{R}\right) \tag{4}$$

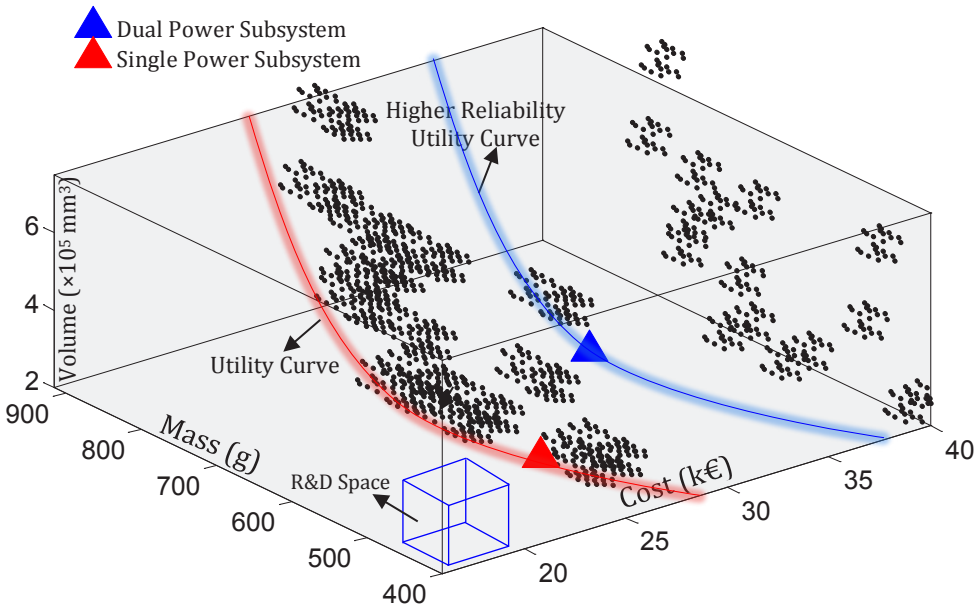

Figure 5. Volume-mass-cost tradespace for the example CubeSat system with utility function

where $\ddot{R}$ and $\dot{R}$ denote the reliability of power subsystem with and without the redundancy, respectively. This, in turn, improves the overall system reliability, and the new design (shown as a blue triangle in Figure 5) settles on the higher-reliability utility curve. The reference to specifications of the above design is provided in Table 4. Hence, by the proposed systematic exploration, the reliability of system is improved, while complying with the given cost, mass and volume constraints. This illustrates the principal point of this paper. That is, a tradespace-based design approach can improve system reliability (or reduce risks) for a given level of resources. The utility curve may or may not agree with the conventional Pareto frontier solution of such design optimization problems. This is because Pareto frontier provides optimal solution to single or multiple objectives problem formulated in terms of (purely technical) tradespace parameters. The utility curve brings additional information, typically extracted from business plan of the organization, to the tradespace, connecting technical aspects of the designs to business outcomes. The tradespace exploration also indicates research and development (R&D) opportunities of interest to stakeholders, for example, for improving a design by replacing or modifying individual system components, beyond the conventional Pareto frontier, as indicated by the R&D space in Figure 5.

Sub System	Communication	Power	Solar Panels	Attitude Control	Command & Data Handling	Antenna
Alternative	1	4	2	4	2	2

Table 4. Reference to specifications of improved-reliability architecture design

Conclusions

In this paper, we highlight the importance of developing novel approaches to the application of SE to small satellite missions constrained by limited budget, schedule and expertise. The discussion is focused around selection of physical architecture for COTS-built satellites in such missions. A tradespace-exploration based approach is proposed to identify architecture designs which optimize the trade-off between the available resources and the system

reliability. The proposed approach allows the designer to explore a multitude of solutions derived from relevant COTS databases of available system elements, during the system design phase, before committing to a physical architecture.
The proposed approach is demonstrated with a real cube satellite example. By adding redundancy to one of the subsystems, an architecture design of higher reliability was conceived, demonstrating the otherwise missed opportunities of optimizing the trade-off for given constraints. Even though we have considered four trade parameters (mass, volume, cost and reliability) for purposes of the illustration, the proposed approach provides a foundation for incorporating additional dimensions in the tradespace, such as sechedue, power consumption, heat dissipation and test profile.
The research work presented in this paper can potentially contribute to Lean satellite standardization efforts, being carried out at ISO.

References

1. Bonyan, H., "Looking into Future Systems Engineering of Microsatellites", Aerospace Technologies Advancements, ISBN 978-953-7619-96-1, INTECH, 2010, Croatia.
2. Cho, M. and F. Graziani, "International Standardization on Lean Satellites; Definition and Requirements", 6th Nanosatellites Conference, July 4-10, 2015, Kobe, Japan.
3. CubeSat Web-Shop. 2015. http://www.cubesatshop.com/
4. Dove, R., and L. Ralph, "Fundamentals of Agile Systems Engineering – Part1", INCOSE, 2014, Las Vegas, NV.
5. Faulconbridge, R., and M.J. Ryan, "Systems Engineering Practice." Argos Press, 2014, Canberra.
6. Gries, M., "Methods for Evaluating and Covering the Design Space during Early Design Development", Integration, the VLSI Journal, 38, 2004, 131–83.
7. Hunyadi, G., et al., "The AFRL/STP Nanosat-2 Mission on Delta IV Heavy: A Demonstration of Current Responsive Space Capabilities", IEEE Aerospace Conference March (Paper #1169), 2005, Big Sky, MT.
8. Meijers, M.A., et al. 2004. "Applying Systems Engineering to University Satellite Projects." INCOSE, 1921–1829.
9. Mission Design Division Staff Ames Research Center, "Small Spacecraft Technology State of the Art", Moffett Field, California, 2014, NASA/TP–2014–216648/REV1.
10. Naveen M., "A Systems Engineering Approach to Small Satellite Mission Formalization", Master Thesis, Mississippi State University, August 2006.
11. Palermo, G., A. Golkar, and P. Gaudenzi, "Earth Orbiting Support Systems for Commercial Low Earth Orbit Data Relay: Assessing Architectures through Tradespace Exploration", ACTA Astronautica, 2015, 111, 48–60.
12. Robertson, B., D. Radcliffe, and S. Russell, "Systems Engineering on Small Satellite Projects", 4S Symposium: Small Satellites, Systems and Services (ESA SP-571), 20–24 September, 2004, La Rochelle, France.
13. Riddle E., "Use of Optimization Methods in Small Satellite Systems Analysis", Proceedings of 12th AIAA/USU Conference on Small Satellites, Logan, UT, 1998.
14. Ross, A. M., and D. E. Hastings, "The Tradespace Exploration Paradigm", INCOSE International Symposium, 2005, Rochester, New York.
15. SEBoK, "Guide to the Systems Engineering Body of Knowledge", 2015, 1.4 http://sebokwiki.org/wiki/Guide_to_the_Systems_Engineering_Body_of_Knowledge_(SEBoK)
16. Simon, H.A, "The Sciences of the Artificial", 3rd Edition, MIT Press, 1969, Cambridge.
17. Space Works, "Small Satellite Market Observations", 2015. http://www.spaceworksforecast.com/docs/SpaceWorks_Small_Satellite_Market_Observations_2015.pdf
18. Valerie, B., et al., "Guiding Tradespace Exploration within an Engineered Resilient Systems Context", Conference on Systems Engineering Research, 2015, 44, 649–658.

Preliminary Design of an Asteroid Flyby Mission using CubeSat Technology

Noor T. Huq, Dr Nathan Kinkaid

School of Mechanical and Manufacturing Engineering, UNSW Australia, University of New South Wales, Sydney, New South Wales, 2052, Australia

Summary: The first step involved in asteroid mining is to prospect target asteroids to determine their composition and *in situ* value. This paper examines the preliminary design of a low cost asteroid prospecting mission constructed as a 6U CubeSat. This probe will piggyback onto a satellite launched into Geostationary Earth Orbit. From there, it will utilise a low thrust Electrospray thruster to boost itself into a High Earth Orbit with apogee intersecting the trajectory of the target asteroid. This will allow the spacecraft to conduct a flyby of an asteroid passing through the Earth-Moon system. During the flyby, the probe will make observations of the asteroid using optical instruments and beam back data afterwards. The asteroids 2014 US7, 2015 EG and 2013 ED68 are chosen as potential targets that will pass through the Earth's sphere of influence between the years 2018-2022. Aspects of the probe's design are examined, with emphasis at this stage placed on payload design and choice of propulsion. Other aspects of this spacecraft's design are considered in brief. This mission will act as an intermediate challenge to bridge the gap between current use of CubeSats in Low Earth Orbit and their future use for interplanetary space exploration.

Keywords: CubeSat, asteroid mining, asteroid prospecting, asteroid flyby

Introduction

As ambitious governmental and commercial activities in space begin to commence, it will become increasingly feasible to mine resources from space to avoid launching large volumes of material aboard expensive rockets. Governmental drivers for asteroid mining include ambitious projects to explore the Moon and Mars, and commercial drivers include construction of more advanced space based infrastructure.[1] Cutting edge technologies, such as renewable energy technologies and electronics, nowadays use significant amounts of trace elements that are in short supply. These include rare earth elements that find use in high-strength magnets, lighting phosphors, polishing compounds and ceramics. [2] Other trace elements that may run into supply shortfalls include gold, cobalt, nickel, osmium, manganese, palladium, and platinum. [3] Growth in space infrastructure will require such elements for present day and future space technologies.

As with an Earth based asteroid mining program, targets for mining must first be prospected to determine what materials can be gained. Promoters of asteroid mining, such as Planetary Resources and Deep Space Industries typically suggest small prospector missions that can piggyback on a larger mission to reduce launch costs. This is seen in the design of Planetary

The profile of this prospective mission is as follows:

- The probe will hitch a ride aboard a rocket launching into Geostationary Earth Orbit (GEO);
- The probe will use its own engines to boost into an elliptical High Earth Orbit (HEO) with its apogee intersecting the trajectory of the passing asteroid;
- A flyby with the target asteroid will be conducted;
- The asteroid will be observed with optical instruments to determine its shape and composition; and
- The probe will beam back information after the flyby is complete.

Mission Goals

The goals of this mission are to:

- Perform a flyby of an asteroid passing through Earth's sphere of influence;
- Investigate the appearance and composition of the target asteroid using optical instruments;
- Minimise costs by using the CubeSat architecture and hitching a ride to GEO; and
- Act as a testing ground for technologies that may be used aboard interplanetary CubeSats.

Target Selection and Preliminary Orbital Analysis

Target asteroids for this mission were identified using the NASA Jet Propulsion Laboratory's Near Earth Object (NEO) Close-Approach Tables[8]. Any asteroids that pass through the plane of the Earth's equator within the Earth's Hill Sphere (sphere of influence) are considered as potential targets. Earth's Hill Sphere has a radius approximately equal to 1.5 million km or 3.90 times the semi-major axis of the Moon's orbit. This target selection criterion is selected instead of simply choosing asteroids that pass through Earth's Hill Sphere, despite forming a much smaller subset of asteroids. Only three asteroids fulfil this criterion out of the nine that pass through Earth's Hill Sphere between the years 2018-2022. Due to the nature of the target selection criterion, there is no guarantee that these three asteroids will be suitable targets the next time they encounter the Earth. This criterion is selected as the six asteroids that do not pass through the plane of Earth's equator inside Earth's Hill Sphere would require extremely high inclination orbits for a flyby to be attempted. Such orbits would require plane change manoeuvres from the initial geostationary parking orbit that are prohibitively expensive in terms of required delta-v and fuel. Data on asteroids that fulfil this criterion between the years 2018-22 is provided in Table 1. This range of dates is selected to allow time to develop this spacecraft and negotiate a piggyback arrangement with a geostationary launcher.

The profile of this prospective mission is as follows:

- The probe will hitch a ride aboard a rocket launching into Geostationary Earth Orbit (GEO);
- The probe will use its own engines to boost into an elliptical High Earth Orbit (HEO) with its apogee intersecting the trajectory of the passing asteroid;
- A flyby with the target asteroid will be conducted;
- The asteroid will be observed with optical instruments to determine its shape and composition; and
- The probe will beam back information after the flyby is complete.

Mission Goals

The goals of this mission are to:

- Perform a flyby of an asteroid passing through Earth's sphere of influence;
- Investigate the appearance and composition of the target asteroid using optical instruments;
- Minimise costs by using the CubeSat architecture and hitching a ride to GEO; and
- Act as a testing ground for technologies that may be used aboard interplanetary CubeSats.

Target Selection and Preliminary Orbital Analysis

Target asteroids for this mission were identified using the NASA Jet Propulsion Laboratory's Near Earth Object (NEO) Close-Approach Tables[8]. Any asteroids that pass through the plane of the Earth's equator within the Earth's Hill Sphere (sphere of influence) are considered as potential targets. Earth's Hill Sphere has a radius approximately equal to 1.5 million km or 3.90 times the semi-major axis of the Moon's orbit. This target selection criterion is selected instead of simply choosing asteroids that pass through Earth's Hill Sphere, despite forming a much smaller subset of asteroids. Only three asteroids fulfil this criterion out of the nine that pass through Earth's Hill Sphere between the years 2018-2022. Due to the nature of the target selection criterion, there is no guarantee that these three asteroids will be suitable targets the next time they encounter the Earth. This criterion is selected as the six asteroids that do not pass through the plane of Earth's equator inside Earth's Hill Sphere would require extremely high inclination orbits for a flyby to be attempted. Such orbits would require plane change manoeuvres from the initial geostationary parking orbit that are prohibitively expensive in terms of required delta-v and fuel. Data on asteroids that fulfil this criterion between the years 2018-22 is provided in Table 1. This range of dates is selected to allow time to develop this spacecraft and negotiate a piggyback arrangement with a geostationary launcher.

Table 1: Close approach data on asteroids 2014 US7, 2015 EG and 2013 ED68 from JPL's NEO Close-Approach Tables [8]

Asteroid name	Optimal Flyby Date	Approximate size (m)	Distance (km)	Distance (lunar radii)	Delta-v required to reach (km/s)
2014 US7	18/10/2018	13 – 30	1.42×10^6	3.70	1.21
2015 EG	6/3/2019	17 – 37	1.13×10^6	2.95	1.19
2013 ED68	15/3/2022	7 – 15	0.718×10^6	1.87	1.15

The optimal flyby date is the day that each asteroid will pass through the plane of Earth's equator within the Earth's Hill Sphere. Approximate size was determined from absolute magnitude provided in the CA Tables corroborated with JPL's absolute magnitude to approximate radius conversion table. [9] Distance shown is the approximate expected distance of the asteroid from the Earth when the asteroid passes through the Earth's equatorial plane. Delta-v to reach each asteroid was estimated using the 2 body approximation and assuming impulsive manoeuvres, with the probe starting in GEO, then transferring into an elliptical orbit with an apogee equal to the asteroid distance.

While CubeSats are generally launched into LEO, a GEO parking orbit was chosen to reduce the delta-v required. A CubeSat starting from GEO would require 1.21km/s of delta-v to reach a flyby orbit with asteroid 2014 US7, much less than a CubeSat in LEO, which would require 3.20km/s. An inordinate amount of fuel would be required aboard the CubeSat to perform such a manoeuvre from LEO. While it may, however, be more difficult to negotiate volume aboard a spacecraft being launched into GEO, a parking orbit in GEO remains far superior to one in LEO.

An alternative option would have been to remain in geostationary transfer orbit (GTO) with a perigee at LEO altitude and an apogee at GEO altitude. By thrusting from perigee in such an orbit, even less fuel would be used. However, the issue with this orbit type is that it is unlikely that the argument of perigee of such an orbit would be as desired. This would require using significant amounts of fuel to adjust argument of perigee, nullifying the advantage of such an orbit. This leaves a parking orbit in GEO as the best option for this mission.

It is clear from Table 1 that similar amounts of energy (between 1.15-1.21km/s) will be required to visit each of these asteroids despite the great variation in their distance from the Earth. This makes all three viable targets for flyby. Approximately 1.25km/s of delta-v can, for now, be allocated for entering the desired flyby orbit with the 2 body impulsive Hohmann transfer assumption. This value will change when these assumptions are refined as a method of propulsion is chosen and more detailed simulations including the gravity of the Moon and Sun are run. Additional delta-v will also be needed for adjusting true anomaly and for station keeping during the transfer ellipse.

Current Design

At this stage, only a few aspects of the design of this spacecraft have been considered in detail – the payload and propulsion. Other aspects of the design have been examined to a lesser degree of detail. These are the attitude determination and control system and power supply. While a few subsystems have not yet been examined, such as the telecommunications, command and data handling and thermal protection, a basic configuration can be drafted from this. This configuration is shown in Figure 2. In this basic configuration, a volume within the spacecraft not filled by other subsystems was allocated for the remaining subsystems. This volume has dimensions of 126×90×90mm. In addition, a gap of 5mm is allocated between all subsystems and the outer wall of the CubeSat structure to either allow a considerable thickness for the outer walls, or allow for insertion of special materials to act as radiation or thermal shielding.

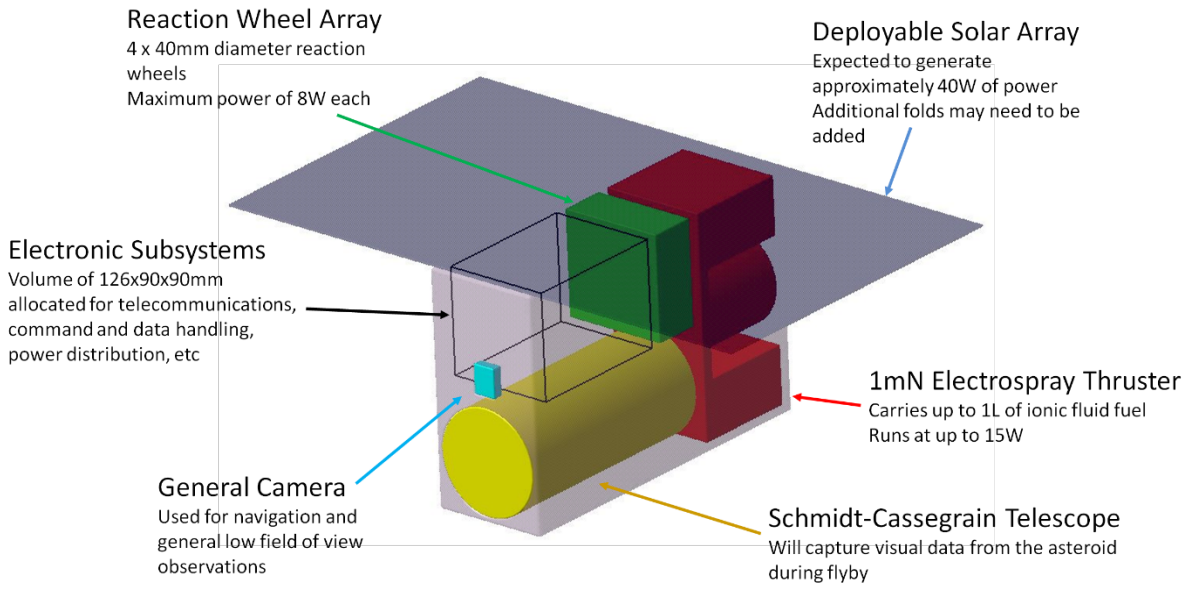

Figure 2: Basic configuration of the asteroid flyby CubeSat, including some general information on subsystems

Some general specifications for this spacecraft are provided in Table 2. As the final mass of components is not known, an expected mass and expected dry mass are given based on the assumption that this spacecraft will, as a 6U CubeSat, weigh 6 times heavier than a normal 1.4kg CubeSat. The dry mass is based on the expected mass minus the weight of fuel for the electrospray thruster. The given launch dimensions reflect this spacecraft's identity as a 6U CubeSat. The spacecraft's deployed dimensions reflect the deployment of the spacecraft's solar panels, as shown in Figure 2. These solar panels are expected to provide up to 40W of power in orbit. As already stated, the spacecraft's starting parking orbit will be geostationary and will finish in a highly elliptical HEO.

Table 2: General specifications for asteroid flyby CubeSat

Expected Mass (kg)	8.4
Expected Dry Mass (kg)	6.7
Launch Dimensions (mm)	100 × 200 × 300
Deployed Dimensions (mm)	500 × 200 × 300
Planned Mission Duration	Up to 2 years
Power (W)	40
Parking Orbit	Geostationary
Final Orbit	Elliptical High Earth

Up to 2 years is allocated for this mission. This is necessary for two reasons. As launches into GEO are fairly infrequent, it is unlikely that this spacecraft will be launched shortly before the passage of the target asteroid, and will have to languish for months in parking orbit. In addition, this spacecraft's Electrospray thruster is similar to an ion thruster, in that it has very low thrust but high efficiency. Approximately 4 months of continuous acceleration will be required by this thruster to reach the required 1.25km/s of delta-v. As this engine will be firing close to the perigee of the spacecraft's orbit, these 4 months of thrust will need to be spread out over the course of a year or more. Considering the fact that CubeSats are generally failure prone[6] and the long lifespan proposed for this spacecraft, it may be necessary to launch more than one of these spacecraft for each target asteroid.

The following sections will examine the design choices and analyses made so far in further detail. These include the decisions that lead to the use of a Schmidt-Cassegrain telescope for the main payload of this mission, as well as the choice of the Electrospray thruster.

Payload

The payload for this mission consists of two cameras – a small Raspberry Pi camera module, and one attached to a 85mm aperture diameter Schmidt-Cassegrain telescope (SCT). The small camera is to be used for attitude determination and navigation in general, as well as low field of view observations. The telescope is to be used for capturing visual information from the asteroid during flyby. A telescope is needed for this purpose as it is assumed that the spacecraft will not pass close enough to the asteroid for the small camera to be able to capture images of it. The telescope may also see another use as an astronomical instrument and capture images and measurements of planets and stars before and after the flyby.

The Raspberry Pi camera module was chosen as a commercial off-the-shelf (COTS) part for this purpose due to the excellent documentation regarding the module's usage as well as its low cost. The camera module is shown in Figure 3. This camera is also very small and light, with dimensions of 25×20×9mm and a mass of 3g. The choice of camera is, however, not finalised

at this stage. Further investigation into the Raspberry Pi camera module and other cameras will need to take place to determine whether it is suited to launch and orbital conditions.

Figure 3: Raspberry Pi camera module[10]

In the course of this research, it is mainly the optical portion of the asteroid telescope that has been examined. The camera attached to the telescope may be based on either a CCD (charge-coupled device) or a CMOS (complementary metal-oxide-semiconductor). A COTS part is unlikely to be found for this specific application, and as such, this part may have to be constructed specifically for this mission. The optical portion (mirrors, lenses and housing) of the telescope payload cannot be a COTS part and will need to be built specially. This is because there is currently a lack of COTS telescopes built for use aboard a CubeSat, and ground based telescopes used by hobbyists are generally too large and bulky. The optical portion of this telescope will be a SCT. The SCT layout is well known for providing a long focal length despite its compactness. This is done with two mirrors, as shown in Figure 4. This layout of convex and concave mirrors allows most SCTs have a focal length 10 times the diameter of their primary mirror.[11] This makes this layout perfect for a volume restricted CubeSat mission.

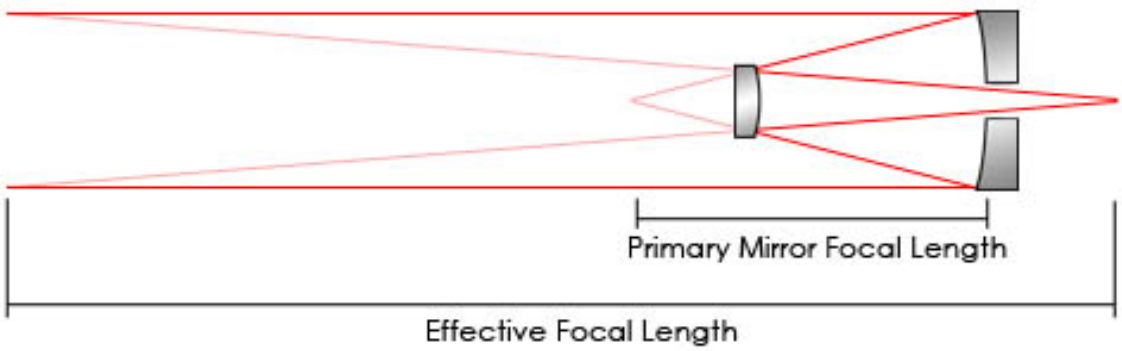

Figure 4: How a SCT achieves such a long focal length.[11]

The dimensions of a CubeSat restrict the aperture of the primary mirror to approximately 85mm. Angular resolution can be calculated with:[12]

$$Angular\ Resolution\ (radians) = 1.22 \times \frac{Wavelength}{Aperture}$$

An aperture of 85mm and a wavelength between 390-750nm is assumed for angular resolution calculations. This gives an angular resolution between 1.15 to 2.22. 1.15 arc seconds is thus the smallest possible pixel size that will be needed for the image sensor. Even if the spacecraft misses its target by a significant margin and conducts its flyby at 1000km from the target asteroid, the three target asteroids will be visible at an angular diameter of between 2 to 6 arc seconds depending on actual size of the three asteroids. The telescope will still be able to see the asteroid as a point of light at such a distance, allowing it to make barely any measurements under this worst case assumption. As this will likely produce little information, a close flyby with the target asteroid is needed. The minimum pixel size for this telescope at various flyby distances is shown in Table 3.

Table 3: Minimum pixel size at various distances

Distance to CubeSat (km)	2	5	10	20	50	100	200	500
Pixel size (m)	0.011	0.028	0.056	0.112	0.280	0.560	1.120	2.799

Bus

Not all subsystems of the spacecraft bus could be examined over the course of this research. Choice of propulsion has been examined in detail, with the Busek 1mN Electrospray Thruster, a COTS part, chosen for this spacecraft. In addition, approximately 1L of fuel is to be included on the spacecraft, coming to a total mass of approximately 1.7kg. The thruster is shown in Figure 5. The design of this spacecraft's attitude determination and control system and power supply has also been examined to a lesser degree.

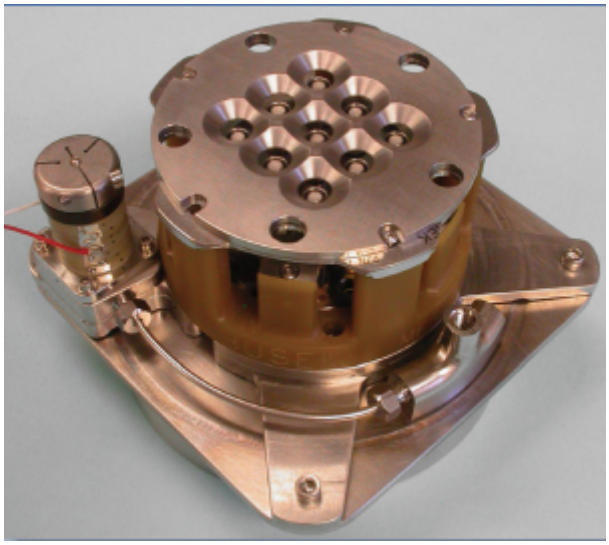

Figure 5: Busek 1mN Electrospray Thruster[13]

The Busek 1mN Electrospray Thruster was chosen for this spacecraft as it has an ideal compromise between efficiency and thrust. Other thrusters either provide better thrust but require more fuel than could fit aboard a 6U CubeSat, or are extremely efficient but would require years of continuous thrusting to reach the target flyby orbit. The 1mN Electrospray Thruster provides 1mN of thrust, which would require approximately 4 months of continuous thrusting to reach the target flyby orbit. And with a specific impulse (I_{sp}) of 800 seconds, it only requires approximately 1.15kg of fuel to achieve 1250m/s of delta-v. The thruster itself weighs 1.15kg.[13] And as per the current configuration, the thruster and fuel are afforded 2Us of space, allowing for approximately 1.7kg of fuel and 1770m/s of delta-v. This extra 520m/s can be used to account for deficiencies in the 2 body impulsive Hohmann transfer assumption. This extra fuel can also assist with adjustments of true anomaly in the parking orbit phase and reduce asteroid flyby distance.

This spacecraft's attitude determination and control subsystem will likely consist of Sun and Earth sensors for attitude determination and reaction wheels for control. The Sun and Earth sensors will likely consist of COTS visual sensors, but they have not been chosen yet. The small Raspberry Pi camera payload may also be repurposed as a Sun and Earth sensor if needed during the course of the mission. Attitude control is achieved using a system of 4 reaction wheels positioned to allow for redundancy if one reaction wheel fails. Reaction wheels are chosen instead of a control moment gyro as they are more efficient for spacecraft the size of a 6U CubeSat.[14] At this moment, Blue Canyon Tech's RWP050 reaction wheels are to be used aboard the spacecraft.[15] Once further simulations are conducted to determine the pointing accuracy and turn rate required by this spacecraft's telecommunications and payload, a final choice of reaction wheel mode can be made.

This spacecraft will be powered by deployable solar panels that will remain fixed once in orbit. These solar panels are expected to provide approximately 40W of power under the assumption of 20% efficiency. The solar cells will be COTS parts that may offer higher efficiencies than the 20% assumption. The solar panels will likely not be equipped with the ability to point towards the Sun to save weight and reduce complexity. Depending on power and pointing requirements, this capability may need to be added in the future, along with additional folds.

Challenges Posed by Other Subsystems

A fairly small volume (126×90×90mm) remains on the current configuration for the remaining key subsystems that will be needed on this spacecraft – telecommunications and tracking, command and data handling, and power storage and distribution. The telecommunications and tracking subsystem will likely carry the largest burden of these systems. It will need to continuously relay system health metrics on a low bandwidth antenna to allow the ground station to analyse the performance of the spacecraft whenever it is in range of the ground station. A high bandwidth antenna may be necessary to send payload data from general observations or from the target asteroid itself. A tracking system will be needed to determine the position of the spacecraft with a significant degree of accuracy, so as to help the spacecraft hone into a close flyby with the target asteroid. The command and data handling system (and other electronic subsystems) will likely need redundancy as well as significant rad-hardening to ensure the

spacecraft's fairly long life span doesn't take a toll on its performance. The design of the power storage and distribution will be problematic in that a significant volume of power storage may be necessary to provide a necessary buffer for the high power subsystems aboard this spacecraft. Such subsystems include the Electrospray thruster and the telecommunications. All of these electronic subsystems will likely be constructed from COTS parts.

Beyond these subsystems, there are also the structure and mechanisms, thermal control and radiation mitigation subsystems. The structure of this spacecraft can either be constructed from frames or 3D printed. While a frame structure will likely be cheaper and can be put together in a modular fashion, a 3D printed structure can be printed as 1 piece, removing joints and thus reducing complexity. Mechanisms are not currently considered, but may become necessary for the solar panels. Simulations will need to be undertaken to determine whether the thermal control and radiation mitigation subsystems will be necessary. Radiation will be a particular challenge as CubeSats are generally designed to take into account single event upsets and to ignore radiation damage over time due to their short mission spans.[6]

Conclusion

This research has examined the preliminary design of a low cost, asteroid prospecting mission designed as a 6U CubeSat. This mission will piggyback aboard a launch into GEO. From there, it will employ low thrust, high efficiency Electrospray thrusters to conduct a flyby of the target asteroid. During the flyby, it will use its main telescope payload to take optical measurements of the target asteroid, which it will then beam back to Earth. These readings will allow for determination of the asteroid's size, shape and composition, allowing the spacecraft to fulfil the role of a prospecting mission. As further strides are made into space, such missions will become increasingly necessary to characterise the physical characteristics of Near-Earth Asteroids. While all aspects of this mission have not yet been designed, the remaining subsystems have been considered to some degree, and challenges in their design identified. This mission will thus be able to act as an intermediate challenge to bridge the gap between current use of CubeSats in LEO and future use of CubeSats for interplanetary space exploration.

Future Work

There is a significant amount of future work that can be undertaken from this research before the spacecraft proposed can even be considered for launch. Most of the future work will be to further examine the aspects of the spacecraft's design. Some examples are listed as follows:

- An analysis of the feasibility of using the Moon's gravity to slingshot the spacecraft into an encounter with the target asteroid;
- Further design and constructing a prototype of the SCT payload, which may also be marketable as a CubeSat space telescope for other missions; and
- Simulation of the effects of long periods of space radiation exposure versus the effects of single event upsets on electronic components regularly used on CubeSats.

References

[1] M. Sonter, "The Technical and Economic Feasibility of Mining the Near-Earth Asteroids," in *49th IAF Congress*, Melbourne, 1998.

[2] N. Nassar, X. Du and T. Graedel, "Criticality of the Rare Earth Elements," *Journal of Industrial Ecology,* vol. 0, no. 00, pp. 1-11, 2015.

[3] D. Andrews, K. Bonner, A. Butterworth, H. Calvert, B. Dagang, K. Dimond, L. Eckenroth, J. Erickson, B. Gilberston, N. Gompertz, O. Igbinosun, T. Ip, B. Khan, S. Marquez, N. Neilson, C. Parker, E. Ransom, B. Reeve and T. Robinson, "Defining a successful commercial asteroid mining program," *Acta Astronautica,* vol. 108, no. 2015, pp. 106-118, 2014.

[4] Planetary Resources, "Arkyd Headquarters," 2015. [Online]. Available: http://www.planetaryresources.com/arkyd/. [Accessed 7 August 2015].

[5] Deep Space Industries, "Prospecting," 2015. [Online]. Available: https://deepspaceindustries.com/prospecting/. [Accessed 7 August 2015].

[6] S. Antunes, DIY Satellite Platforms, Sebastopol, CA: O'Reilly Media, 2012.

[7] D. Selva and D. Krejci, "A survey and assessment of the capabilities of Cubesats for Earth Observation," *Acta Astronautica,* vol. 74, no. 1, pp. 50-68, 2012.

[8] National Aeronautics and Space Administration - Near Earth Object Program, "NEO Earth Close-Approaches," 24 August 2015. [Online]. Available: http://neo.jpl.nasa.gov/cgi-bin/neo_ca?type=NEO&hmax=all&sort=date&sdir=ASC&tlim=future&dmax=5LD&max_rows=100&action=Display+Table&show=1. [Accessed 25 August 2015].

[9] National Aeronautics and Space Administration - Near Earth Object Program, "Absolute Magnitude (H)," 25 August 2015. [Online]. Available: http://neo.jpl.nasa.gov/glossary/h.html. [Accessed 25 August 2015].

[10] Pi Australia, "Camera Module," 2015. [Online]. Available: http://raspberry.piaustralia.com.au/products/camera-module. [Accessed 27 October 2015].

[11] Starizona, "Telescopes: Schmidt-Cassegrains," 2014. [Online]. Available: http://starizona.com/acb/basics/equip_telescopes_scts.aspx. [Accessed 27 October 2015].

[12] T. Huard and M. Loewenstein, "Angular Resolution," 2010. [Online]. Available: https://www.astro.umd.edu/~thuard/astr288c/lecture6-notes.pdf. [Accessed 27 October 2015].

[13] Busek Space Propulsion Systems, "Busek Electrospray Thrusters," 2015. [Online]. Available: http://www.busek.com/index_htm_files/70008500G.pdf. [Accessed 28 October 2015].

[14] R. Votel and D. Sinclair, "Comparison of Control Moment Gyros and Reaction Wheels for Small Earth-Observing Satellites," in *26th Annual AIAA/USU Conference on Small Satellites*, Logan, Utah, 2012.

[15] Blue Canyon Tech, "Reaction Wheels," 2015. [Online]. Available: http://bluecanyontech.com/portfolio-posts/reaction-wheels/. [Accessed 28 October 2015].

Strategy for flybys of numerous Earth passing asteroids

W. Crowe[1,2], N. Kinkaid[1,2], J. Olsen[1], J. Page[1]

[1]*School of Mechanical and Manufacturing Engineering, University of New South Wales Australia, Sydney, 2052, NSW, Australia*

[2]*Australian Centre for Space Engineering Research, University of New South Wales Australia, Sydney, 2052, NSW, Australia*

Summary: Many Potentially Hazardous Asteroids (PHAs) will fly through the Earth-Moon system several times before possible impact. Furthermore, asteroids that pass through the Earth-Moon system are likely to be discovered only a few weeks before flyby. Recent development of small spacecraft, especially CubeSats, shows promise in their use for a number of space missions. Without leaving Earth orbit, opportunistic near-intercepts of PHAs using small spacecraft may provide improved and more regular characterisation of these asteroids than observations from Earth-based facilities alone. Such missions could also be launched at short notice when a new PHA is detected. A mission is proposed where a mothership releases several CubeSat-sized spacecraft to intercept PHAs as they fly closely past the Earth. This research investigates the technology that is in development and already available that could be used for such missions, as well as the establishment of design considerations for the missions. It is found that missions like this could be used to characterize all closely flying asteroids with iterative improvements in CubeSat technology thus improving the number and quality of asteroid investigation.

Keywords: PHA, NEA, orbital mechanics, asteroid prospecting

Introduction

Potentially hazardous asteroids often make multiple flybys past the Earth before they impact with it. For example, the asteroid Apophis, is predicted to make eleven flybys before a possible impact with the Earth in 2060 [1]. Such close approaches present an opportunity to investigate asteroids in detail. Although, these asteroids are in the vicinity of the Earth for only short periods of time, a significant amount of information can be gleaned during these periods through *in-situ* exploration by spacecraft. When asteroids are discovered shortly before they make their first flyby, planning a mission becomes difficult.

In this research, a mission is proposed to investigate and characterise potentially hazardous asteroids that fly by the Earth. The mission will have the capacity to:

- visit a large number of asteroids over the mission's lifetime
- initiate a flyby at short notice
- characterise the asteroids *in-situ* during flybys

The current space mission approach of using a single, monolithic spacecraft is not appropriate in this instance, as a visit to more than one asteroid would result in the use of a prohibitively large quantity of fuel.

Small spacecraft have recently become more robust and versatile in mission capabilities. The recent explosion in small spacecraft missions has generated further development of their

systems and capabilities [2, 3]. Using small spacecraft reduces the amount of fuel required for each intercept and as their cost is very low there is a possibility that each spacecraft can be single-use.

The resulting mission architecture calls for a "mothership" spacecraft which contains many small "interceptor" spacecraft. To enable planar access to the entire Earth-Moon system with a low delta-V, the mothership is to maintain a near-circular, high-altitude orbit of Earth. The mothership then manages communications, orbital station-keeping and radiation mitigation for an open-ended period of up to several years. When an asteroid intercept opportunity is determined, one or more interceptors are deployed, using their own engines to intercept the asteroid, before relaying the characterisation data back to the Earth.

Near intercepts of asteroids have been used on many space missions to provide data on the target asteroid without the need to use much of the delta-V budget of the mission[4]. The drawback of this strategy is that the data is incomplete when compared with that from rendezvous missions. Generally, spectral images of only one side of the asteroid can be taken depending on its spin rate and the spacecraft trajectory. Some mass estimates of the asteroid can also be made. A recent example of this type of mission is the Rosetta mission, which flew by 21 Lutetia in 2010 at a distance of approximately 3170km and at relative velocity of 15km/s [5]. This asteroid is larger than most that fly through the Earth-Moon system, but the results of the mission indicate the type of data that could be produced by a simple flyby. For example, Fig. 1 shows an actual image captured of 21 Lutetia during flyby alongside the very best computer generated image estimated from Earth-based light-curve studies.

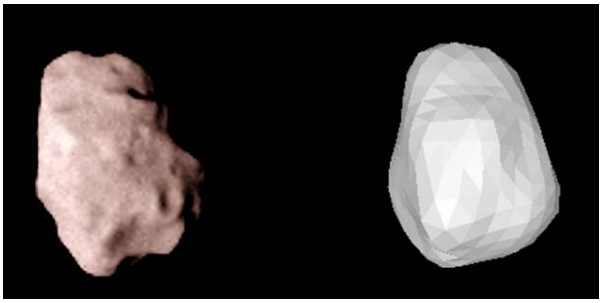

Fig. 1: Comparison of 21 Lutetia from the Rosetta Spacecraft camera (left) and shape light-curve estimates (right). Credit: European Space Agency

Many missions have been designed to rendezvous with asteroids outside of the Earth-Moon system [6, 7]. The benefit to this strategy is that any asteroid can be rigorously investigated *in-situ*, due to the spacecraft's long stay-time. The negatives include the requirement for greater delta-V, the need for long travel and lead times, the pressure on communications to span vast distances, slow data transfer and the need for the single spacecraft to have high reliability and redundancy in its systems.

Near-Earth Asteroids

Near-Earth Asteroids (NEAs) are those asteroids that are in orbits with a semimajor axis of less than 1.3 Astronomical Units (*AU*) [1]. A small, but non-negligible percentage of these have a chance of impacting with the Earth. Some of the potential impactors are large enough

to cause significant damage, so are known as Potentially Hazardous Asteroids (PHAs). A total of 12,775 NEAs have been discovered as of July 1, 2015, with 1,603 of these PHAs. More are being discovered all of the time, with 1,554 NEAs discovered in the year to July 1, 2015.

Another interesting group of NEAs are those that fly within 3.1 Lunar Distances (*LD*), or 1.19×10^6km of the Earth. This distance is just outside the region where the Earth's gravity plays a major part in orbital dynamics. In the year to July 27, 2015, 102 asteroids were detected passing within this distance from the Earth. This subset, which will be described as the *indicative subset* henceforward has been used to make predictions about the number of asteroids passing close to the Earth in future years as well as some of their attributes. At present, the indicative subset gives a picture of the number (and size) of asteroids that we can detect using both professional and amateur sky surveys. There are likely more asteroids passing the Earth, especially of smaller size, which have not yet been detected. Fig. 2 presents a picture of the ranges of distances at which the detected asteroids in the indicative subset passed the Earth.

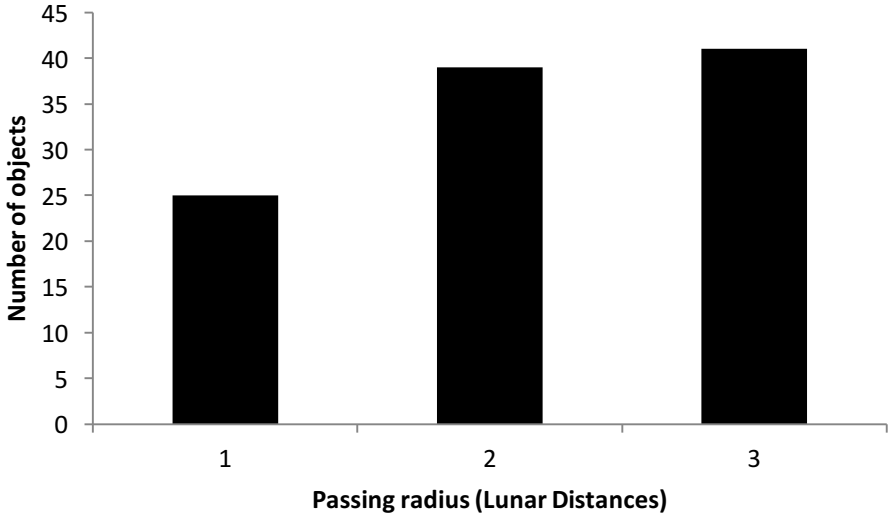

Fig. 2: Number of asteroids of the indicative subset passing close to the Earth in different radius bins

The approximate diameter of an asteroid in the indicative subset can be estimated from that asteroid's absolute magnitude (brightness) if we assume it is spherical in shape and that it has an average albedo. In this study we have used Eqn 1, taken from the European Space Agency (ESA) [8], which uses the absolute magnitude, *H*, to find the assumed spherical diameter, D_S. After removing one outlier from the indicative subset, the average size of the asteroids detected is approximately 20 metres in diameter. The assumed spherical diameters D_S of the asteroids from the indicative subset are displayed in Fig. 3.

$$D_s = \frac{1329}{\sqrt{0.1}} \times 10^{-0.2H} \quad (1)$$

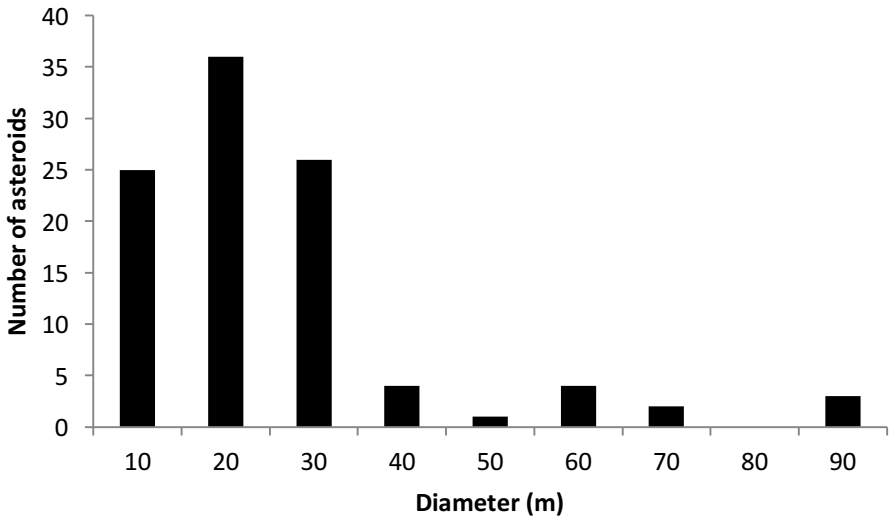

Fig. 3: The sizes of asteroids in the indicative subset predicted by Eqn 1

In the indicative subset, the time between detection of an asteroid and its closest approach of the Earth was generally less than a month. This provides impetus to have spacecraft ready for deployment at short notice. Fig. 4 shows the approximate time between discovery and flyby for the indicative subset.

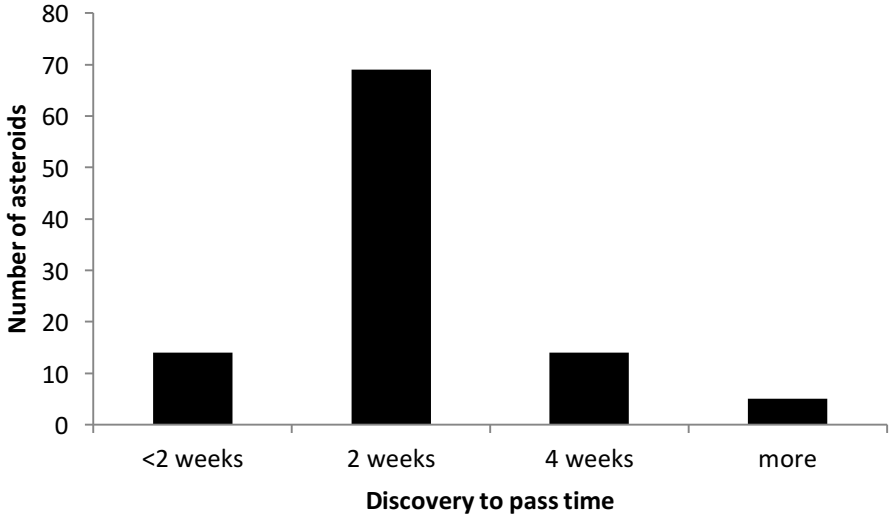

Fig. 4: Time between discovery and flyby of asteroids in the indicative subset

Some of the asteroids from the indicative subset will pass close to the Earth repeatedly. As an example, asteroid 2015 HQ171 passed Earth in 2015, within a month of its discovery. It is predicted to pass Earth again in 2048 within 3 Lunar Distances (*LD*) of the Earth. Asteroids such as this pose some risk to the Earth in the future, and if any asteroid intersects the orbit of the Earth then its orbit has the potential for repeated close approaches.

For an asteroid to be a PHA, it must make threatening close flybys of the Earth and have an absolute magnitude of 22 or less. The asteroid 357439 (2004 BL86) was the only asteroid to

pass close to Earth of this type in the last year, although it is unlikely to make another close approach for many hundreds of years. Another PHA, 2010 MA113, will flyby close to Earth (at less than $0.1LD$) in 2036, followed by a probable impact in 2061 [1], although its orbit is yet to be fully characterised and receive a final designation.

Orbital Analysis

Analysis for this proposed mission was performed using the two-body approximation with the Earth and a relevant spacecraft. The analysis assumes three possible major maneuvers to be taken by an interceptor spacecraft after release from a mothership. The first is an initial burn to intercept the asteroid as it passes through the orbital plane of the mothership. The second is a possible lowering of the intercepting orbit perigee, so that the interceptor may be in a better position to communicate with ground stations. The last maneuver serves to lower the perigee again to intercept the Earth's atmosphere and burn up.

The two-body approximation allows for some useful assumptions about the behaviour of the orbits as time goes to infinity. The influence of the Moon is unlikely to affect the orbital trajectory and so its gravitational field was neglected. The sphere of influence is the radius beyond which perturbations due to the Sun is larger than those due to the Earth. It is a useful limit to the two body approximation that is used in patched conics and was taken as a soft limit to the effective use of the orbits calculated within. It was taken to be:

$$r_{SOI} = a_E \left(\frac{m_E}{m_S}\right)^{\frac{2}{5}} = 9.29\times10^5 km, \quad (2)$$

Where r_{SOI} refers to the radius of the sphere of influence in kilometres, a_E is the semimajor axis of the Earth's orbit around the Sun in kilometres, m_E is the mass of the Earth and m_S the mass of the Sun.

Staging Orbit

The interceptor spacecraft has to be launched from a staging orbit. This is a circular orbit that is positioned high above the Earth to reduce the fuel required to reach passing asteroids. Geocentric Earth Orbit (GEO, an orbit of 4.2e4kmfrom the centre of the Earth) and a High Earth Orbit (HEO, in this case an orbit of 1e5km from the centre of the Earth) were chosen as reference staging orbits in this study, with analysis shown in Fig. 5,6,7 and 8.

When in orbit, orbital plane-change maneuvers are fuel-intensive. With this in mind, interceptor spacecraft have been limited to the orbital plane of the staging orbit so that they can have a greater range for a given amount of fuel. This means that a passing asteroid needs to fly through the plane of the staging orbit in order to be intercepted.

It is possible for an asteroid to pass close to the Earth and not fly through the projection on the plane covered by a single staging orbit. To mitigate this issue, having three mothership spacecraft, occupying three orthogonal planes, allows for asteroids with all flyby configurations to be intercepted.

If this approach is taken, and a conservative estimate is made that there is no perturbation on the asteroid from the Earth, then no asteroid could pass closer than the minimum distance (r_{min}), without passing within the intercept range of one of the three orthogonal planes. The

minimum distance, r_{min}, is equal to r_{plane} over the square root 2, where r_{plane} is the maximum distance on the plane that the interceptor spacecraft can travel away from the Earth.

Interception

Interceptor spacecraft could be directed into an elliptical orbit to intercept asteroids. The staging orbit acts as the intercept orbit perigee for a perfectly phased interception, where the asteroid plane intersection acts as minimum apogee. When out of phase, intercepting ellipses can be created by solving Lambert's problem over a range of times. A baseline delta-V estimate for this first maneuver, using analytic approximations for Hohmann transfers [9], is shown in Fig. 5.

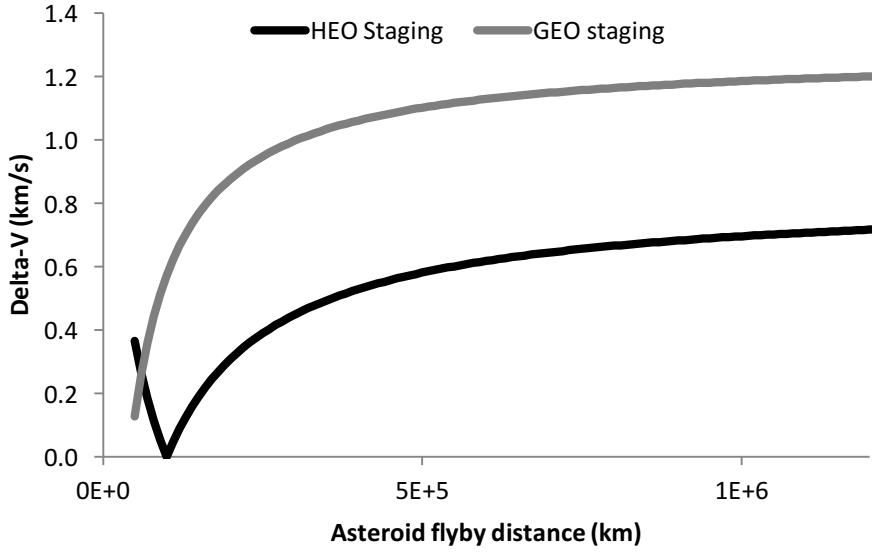

Fig. 5: Delta-V calculation for maneuver to intercept asteroids with asteroids intersecting the staging plane at various distances (assuming perfect phasing and single-impulse transfers)

A lower holding orbit increases the initial thrust required for the intercept, but also reduces the period of the mothership about the Earth. This makes phasing of efficient orbits easier to achieve.

Fig. 6 shows the amount of time required to access asteroids passing at different radii from Earth. The time to intercept, when using Hohmann transfers, increases above fourteen days as the intercept distance passes $1.5LD$. This means that some asteroids will not be accessible when there is a short time between discovery and flyby, as well as a distant intersection radius.

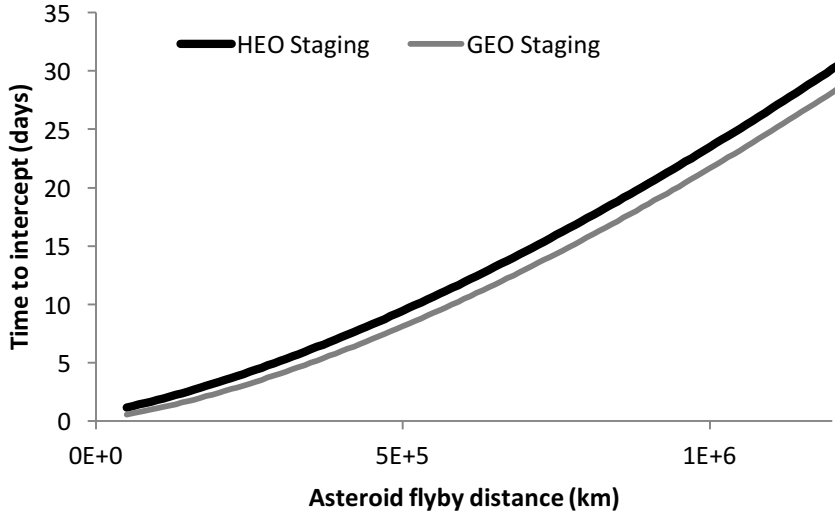

Fig. 6: Time taken in days from interceptor launch to intercept (assuming perfect phasing and single-impulse transfers)

Communications Pass

After intercepting the asteroid, the elliptical orbit of the interceptor spacecraft will carry it back towards Earth. If a Hohmann maneuver was used, the spacecraft will have a perigee at the altitude of the staging orbit. The staging orbit altitudes investigated here are well above those currently used by small spacecraft to transmit data and so a special orbit may be required.

A thruster burn at apogee is the most efficient way to reduce the perigee to the desired altitude. At high apogees, the fidelity required to achieve a given perigee is greater, so a maneuver must be chosen that is in no threat of impacting with the Earth.

End-of-Life

The high orbits that the interceptors will take are currently sparsely-populated, but have the potential for wide use. To ensure deorbit, the interceptor spacecraft could thrust to lower its perigee to within the Earth's radius. This produces an atmospheric burn, an end-of-life common to Low Earth Orbit (LEO) spacecraft. Again, the most efficient place for this maneuver to take place is at the orbital apogee. The delta-V required for a range of intercept orbital configurations is shown in Fig. 7. If both the communication pass and end-of-life maneuvers are separately made at apogee, then they will require the same amount of energy as if only a single burn were employed. This maneuver has the potential to cause the interceptor spacecraft to cross highly populated orbits of other spacecraft, so the danger should be evaluated before the maneuver is performed.

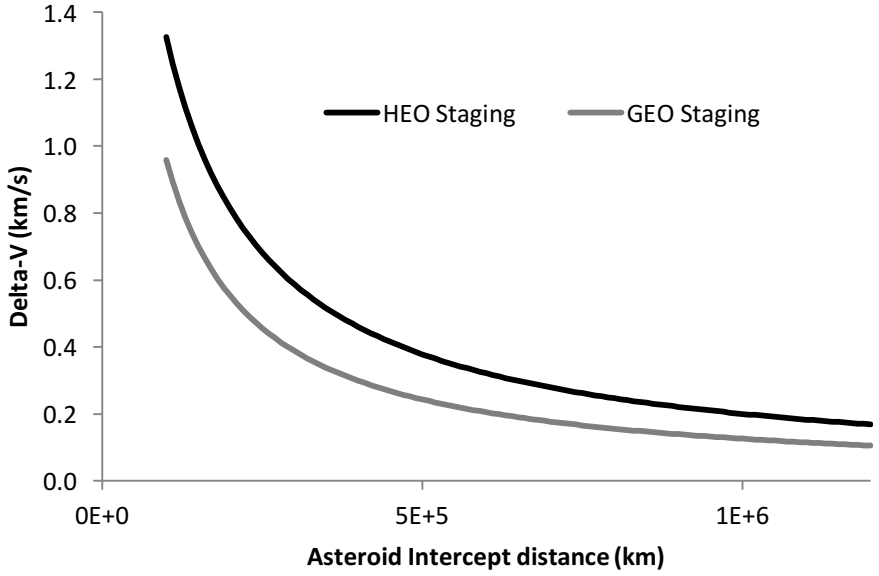

Fig. 7: Delta-V calculation for maneuver at end-of-life, assuming Hohmann transfer and using different staging orbits (single-impulse, minimum transfer energy, from the elliptic intercept orbit to an elliptic Earth-intercept)

The total delta-V from launch out of the mothership to end-of-life has been estimated and shown in Fig. 8. The combination of maneuvers effectively composes a bi-elliptic transfer, the efficiency of which increases as the apogee becomes large.

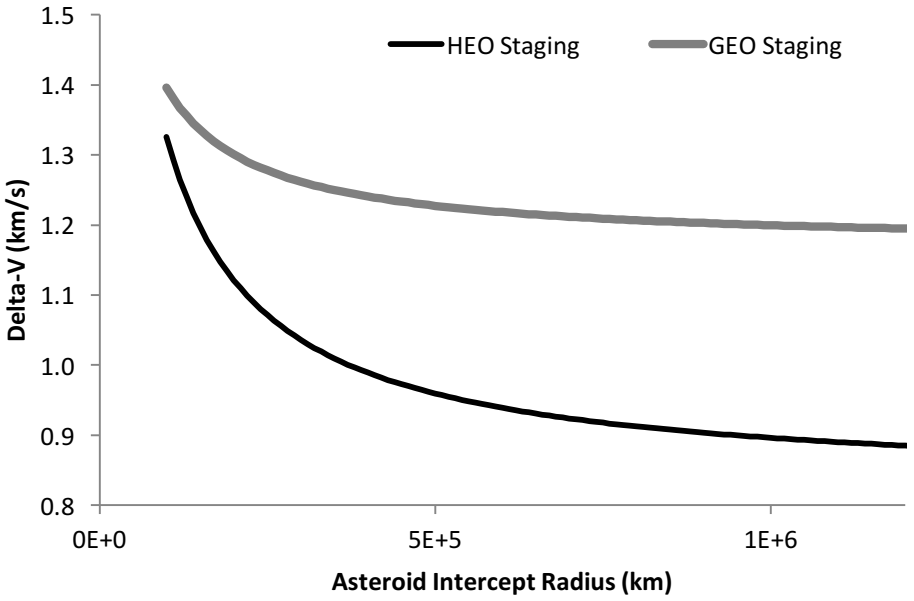

Fig. 8: Total delta-V calculation (combining the data from Fig. 5 and 7)

Quality of Intercept

The asteroid will pass with both a temporal and spatial error, although the certainty of an asteroid's orbit is likely to be refined in the lead-up to a flyby event, as it becomes easier to observe. Both asteroid and spacecraft will have errors associated with their orbits, making it difficult to know if the intercept will result in a crash or they will pass one another.

The flyby velocity of the asteroid will likely dominate the relative velocity of the spacecraft intercept. This is because the spacecraft will be close to apogee, and so have a low geocentric velocity at the time of intercept. The flyby velocities of the asteroids of the indicative subset vary between 1 and 30 km/s, with an average of 11.6 km/s. These compare to the relative velocities during asteroid flyby of deep space missions [10-12].

An additional trajectory design consideration for an individual asteroid is the angle between spacecraft, asteroid and the Sun during approach and intercept. It is possible to trade an increase in delta-V for a longer stay-time on a sunlit portion of the asteroid if cameras and other passive sensors are used on the interceptor spacecraft.

Spacecraft

This mission will require two different types of spacecraft. The first type is a mothership, which serves as a stable for the second type, which is an interceptor spacecraft. The mothership requires good communication to the Earth, enabling command over the interceptors. It would be responsible for the station-keeping of the staging orbit and hold the launch mechanism and storage for many interceptor spacecraft, as well as some protection from high energy particles from the Sun and elsewhere. Most of these components have been tried and well tested on other large spacecraft.

A launch system for small spacecraft has also been developed and tested, viz: the NanoRacks CubeSat Deployer [13]. Up to six units of CubeSats can be launched by each deployer. Although the entire contents of a deployer must be released at once, this could allow for a small swarm to be used to intercept each asteroid. The launchers deploy at velocities of 0.5 to 1.5 m/s, which could allow for safe clearance between the mothership and interceptors before launch to the asteroid.

Interceptors

The interceptor spacecraft must be single-use, due to the difficulty of recovery. With recent developments in CubeSat capabilities, this platform is ideal for the design of interceptors. There are many benefits to be gained from using a spacecraft of this nature, in that commercial-off-the-shelf bus and components drive costs and design time down. Due to likely further development of CubeSats, there should be many more useful features built for them in the near future.

Reliable CubeSat thrusters are currently in development to enable CubeSats to change orbit after release from their launcher. Although still in development, chemical thrusters for CubeSats have the ability to provide the delta-V required, in the time-frame required, to intercept asteroids flying-by the Earth. A chemical thruster in the late stages of testing that would partially fulfil the requirements set for this mission is the Aerojet Rocketdyne MPS-120XL, which could provide a delta-V of 539m/s to a 4kg, 3 Unit (3U) CubeSat [14]. Due to the emerging large market for CubeSats, it is likely that more powerful and smaller thrusters will exist in the near future as commercial-off-the-shelf components.

The interceptor spacecraft will be designed to capture important asteroid data such as size, shape, albedo and a subset of surface features. Use of a multi-spectral camera may allow estimation of the dominant surface mineralogy of the asteroid. These data could be captured for all asteroids that are intercepted, albeit only the Sun-facing portion of the asteroid will be visible during the flyby. The ESA has made plans to develop a hyperspectral camera that will

fit inside a CubeSat [15]. Any sensors that are incorporated into the interceptor will have to fit with engine/propellant (currently 2U for required delta-V) and Attitude Determination and Control System (ADCS), (currently 0.5U). There are now commercial-off-the-shelf ADCS solutions for CubeSats that incorporate star-trackers, communications, reaction wheels and momentum control [16-18].

Estimating the mass of asteroids during spacecraft flybys is also possible and is currently performed through detecting changes in the movement of spacecraft as they are perturbed by the gravity of these relatively heavy bodies. The change in movement is determined through a change in radio frequency detected through a Doppler shift. For this type of measurement to be possible, there will need to be communication between the spacecraft and a ground station. The spacecraft will also need to be perturbed sufficiently by the asteroid, meaning that the asteroid will have to be of sufficient mass, with a sufficient flyby velocity at a sufficiently low minimum distance. The final condition normally required is knowledge of the spacecraft's distance from the asteroid during flyby. This will unlikely be possible, although Takahashi and Scheeres [19] have shown that this is unnecessary if a delta-V maneuver is made during the flyby.

Communications

The CubeSat-sized interceptor spacecraft will spend most of their trajectory far from Earth. This will make communications difficult, as current solutions for deep space spacecraft are heavy and require a large volume. Lowering the orbital perigee after asteroid flyby will provide periodic opportunities to communicate at a closer range.

The interceptors will also have to communicate with the mothership prior to and just after deployment. The mothership can act as the main conduit of control from Earth to interceptors before launch to targets.

Discussion

This research points to the possibility of characterising many asteroids as part of a single mission. All of the asteroids that can be characterised using this method will be NEAs, with a subset of these being PHAs. The proposed mission will be capable of acquiring data for those asteroids discovered a short time before flyby. To make the intercepts robust, several spacecraft could perform each characterization, with each spacecraft lost after a single flyby. This mission architecture allows characterization of asteroids that are discovered only weeks before closest approach.

The asteroids that can be characterised using this method are all of value for the purposes of asteroid science, hazardous asteroid mitigation and asteroid prospecting. The data gathered from so many close observations can be used to better infer the characteristics of asteroids in less accessible regions of the Solar System.

From synthesis of the orbital analysis with the current development of CubeSats, this mission is feasible. The mission would have to make concessions on the targets that could be reached however, with many missed through phasing or unreachable with the current thrusters. Delta-V could be increased slightly with good design, cutting the mass of the interceptor spacecraft, although, this would extend the range only slightly.

There are iterative improvements on the way for most CubeSat components and it is likely that major improvements in propulsion and savings in component mass will occur within the

next few years to meet new market demand. This technological progress should increase the feasibility of the mission presented here and allow for a significant increase in the number of asteroids that can be visited by spacecraft.

References

1. NASA/JPL. *Near Earth Object Program*. [cited 2015 07-27-2015]; Available from: http://neo.jpl.nasa.gov/.
2. Toorian, A., K. Diaz, and S. Lee. *The cubesat approach to space access*. in *Aerospace Conference, 2008 IEEE*. 2008. IEEE.
3. Klesh, A.T., et al., *INSPIRE: Interplanetary NanoSpacecraft Pathfinder in Relevant Environment.* American Institute of Aeronautics and Astronautics, 2013.
4. Schoenmaekers, J. and R. Bauske. *Re-design of the Rosetta mission for launch in 2004*. in *18th International Symposium on Space Flight Dynamics*. 2004.
5. ESA. *Rosetta: Asteroid (21) Lutetia*. [cited 2015 06-29-2015]; Available from: http://sci.esa.int/rosetta/47389-21-lutetia/.
6. Veverka, J., et al., *The landing of the NEAR-Shoemaker spacecraft on asteroid 433 Eros.* Nature, 2001. **413**(6854): p. 390-393.
7. Glassmeier, K.-H., et al., *The Rosetta Mission: Flying Towards the Origin of the Solar System.* Space Science Reviews, 2007. **128**(1-4): p. 1-21.
8. ESA. *Space Situational Awareness – NEO*. [cited 2015 07-27-2015]; Available from: http://neo.ssa.esa.int/web/guest/home.
9. Curtis, H., *Orbital mechanics for engineering students*. 2013: Butterworth-Heinemann.
10. Pätzold, M., et al., *Asteroid 21 Lutetia: low mass, high density.* Science, 2011. **334**(6055): p. 491-492.
11. Yeomans, D., et al., *Estimating the mass of asteroid 433 Eros during the NEAR spacecraft flyby.* Science, 1999. **285**(5427): p. 560-561.
12. Yeomans, D., et al., *Estimating the mass of asteroid 253 Mathilde from tracking data during the NEAR flyby.* Science, 1997. **278**(5346): p. 2106-2109.
13. NanoRacks. *Smallsat Deployment*. [cited 2015 06-29-2015]; Available from: http://nanoracks.com/products/smallsat-deployment/.
14. Rocketdyne, A. *CubeSat*. [cited 2015 07-27-2015]; Available from: https://www.rocket.com/cubesat.
15. ESA. *Space Engineering and Technology: Hyperspectral Imaging by Cubesat on the Way*. 2014 [cited 2015 06-29-2015]; Available from: http://www.esa.int/Our_Activities/Space_Engineering_Technology/Hyperspectral_imaging_by_CubeSat_on_the_way.
16. CubeSatShop.com. [cited 2015 07-27-2015].
17. Space, C. *CubeSat Attitude Determination and Control Systems*. 2015 [cited 2015 07-27-2015].
18. Technologies, B.C. *Attitude Control Systems*. [cited 2015 07-27-2015].
19. Takahashi, Y. and D.J. Scheeres, *Small-Body Postrendezvous Characterization via Slow Hyperbolic Flybys.* Journal of Guidance, Control, and Dynamics, 2011. **34**(6): p. 1815-1827.

Design of a Photovoltaic Power System for a Mars Analogue Research Station

Keira Doherty [1], Yao Xiong Loo [1], Nicole Blinco [1] and Jonathan Clarke [2]

[1] *Research School of Engineering, Australian National University, Canberra, Australia*
[2] *Mars Society of Australia, P.O. Box 327, Clifton Hill, VIC 3068, Australia*

Summary: The Australian Mars Analogue Research Station (Mars-Oz) developed by the Mars Society of Australia is a prototype habitat on Earth that provides research crews the opportunity to live and conduct research under constraints similar to what they would find on Mars. Mars-Oz will be deployed in Arkaroola, South Australia, and will require a stand-alone power system to sustain its operations. A solar-based power system was found to be the most suitable due to the abundance of sunlight and suitable weather conditions at the Mars-Oz site. Systems engineering and design-based approaches were adopted to develop a conceptual design of the power system based on the design requirements. The power system was divided into three subsystems: power generation; energy storage; and electricity supply. Suitable solar panels, mounting structures, storage batteries and power conditioning equipment such as inverters and charge controllers were selected by comparing different commercial products using engineering requirements that were developed from the design requirements.

Keywords: Photovoltaic power system, Systems engineering, Mars Analogue Research Station, Mars-Oz

Introduction

The Mars Society is an international not-for-profit organisation that has been an advocate for Mars research, exploration and settlement since 1998 [1]. One of the important roles of the Mars Society is the development and management of Mars Analogue Research Stations. These are prototype habitats on earth that provide research crews an opportunity to live and conduct research under constraints similar to what they would find on Mars [1].

One such station, Mars-Oz, is currently planned to be deployed on a private nature reserve in Arkaroola, South Australia [1]. Shown in Fig. 1, Arkaroola is a Crown land lease that is run as a private conservation park and eco-tourist resort. It is located in the northern Flinders Ranges 700km north of Adelaide, the capital city of South Australia.

Two building modules are planned for Mars-Oz. The habitat module will consist of living quarters, a laboratory, and a kitchen to accommodate the research crew, while the cargo module will include a separable garage section and a nose section for storage. The overall architecture of Mars-Oz is based on that of real Mars missions [2].

One of the key characteristics of a habitat that simulates life on Mars is that it should be, as far as possible, self-sustaining. For this reason, Mars-Oz requires a stand-alone power system that can reliably generate electricity throughout the day and night to avert reliance on the electrical grid and fuel-powered generators, which are used by majority of Arkaroola residents. A power system that utilises the solar resource was selected due to its cheaper operation cost relative to

other resources and favourable climate offered at Arkaroola: sunny with approximately 181 days per year without cloud cover, and dry with a relatively low annual rainfall of 258.5 mm [3]. Electricity generated from the power system will be used to power appliances and equipment in the habitat module.

The use of photovoltaics (PV) to generate electricity for Mars-Oz differs to other analogue stations such as HI-SEAS (Hawai'i Space Exploration Analog and Simulation) and MDRS (Mars Desert Research Station), which use propane generators [4, 5]. One of the reasons why solar was chosen as the energy source for Mars-Oz was to ensure that the power system would be self-sustaining, that is, not reliant on the crew to ensure that there will be sufficient fuel.

Fig. 1: Location of Arkaroola in South Australia where Mars-Oz is planned to be constructed

Design requirements of the solar power system were as follows:

- The power system should generate electricity from a solar resource;
- The power system must be able to deliver an average daily output of 52 kWh throughout the operational period of Mars-Oz when it is occupied during winter;
- The system should be designed to be within the budget of AUD$100,700;
- The system must be designed to be suitable for the operational environment;
- Strategies for minimising risks associated with safety of personnel, system failure and changes in operational conditions should be identified and proposed; and
- The system must be designed to meet all applicable industry and government standards and regulations.

Operation of a solar resource-based power system can take two forms: PV or concentrated solar thermal technologies. Preliminary investigation revealed that amongst the two, PV was the most suitable choice due to its lower cost and smaller scale of operations.

Methodology

Two methodologies were utilised concurrently in this project: the systems engineering approach, and various design-based processes.
Fig. ***2*** illustrates the systems engineering methodology that was applied. The translation of design requirements into system requirements, along with the development of corresponding verification procedures, helped ensure that the final system concept complied with the design

requirements.Twelve system requirements were established from the six design requirements listed above. These were ranked using a pairwise analysis for prioritisation purposes, and the final results are shown in Table 1.

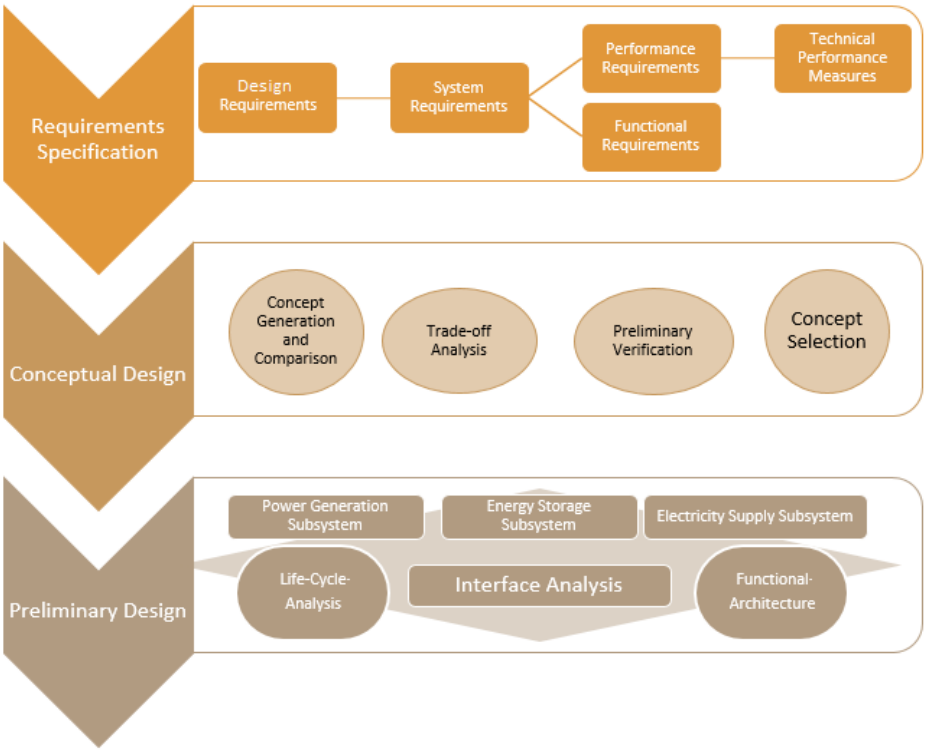

Fig. 2: Systems engineering approach utilised for the design of the Mars-Oz power system

Table 1: Ranking of system requirements for the power system

Rank	System Requirement
1	The system shall provide a daily average of 52 kWh of electrical energy to Mars-Oz during winter
2	The system shall generate electrical power using solar radiation as its energy source
3	The storage system shall be compatible with the power system
4	Energy stored in the storage system shall be able to supply the Mars-Oz with electricity whenever the solar resource is insufficient
5	The system shall comply with all applicable national, state and local regulatory codes and standards
6	The system should cost less than or equal to AUD$100,700
7	The system should be capable of operating in an environment with atmospheric temperatures ranging from -6°C to 46°C
8	The storage system and power conversion equipment should be able to be installed in available space within Mars-Oz
9	The system should be designed such that the need for and difficulty of ongoing maintenance is minimised
10	The system's environmental impact should be minimised
11	The power system should not be installed on the Mars-Oz structure
12	The system should be designed such that the ease of installation is maximised

The system requirements from Table 1 were then translated into engineering requirements, and categorised into either functional or performance requirements, so that they could be more easily incorporated into the design process. The engineering requirements were further decomposed into technical attributes, which provide detailed information such as metrics and target values on how to achieve each requirement. Table 2 shows one of the performance requirements and associated technical attributes for the first system requirement in Table 1.

The direction of improvement (D.O.I) describes the "direction" of optimisation the attribute should be designed in. All of the attributes for performance requirement R1.1 (solar collection area) have positive D.O.Is, which means that they should be maximised. While not shown in Table 2, the relationships between attributes of different performance requirements were also mapped so that potential trade-offs that would influence the system design could be identified.

Table 2: List of technical attributes associated with performance requirement R1

R.I.D.	Performance Requirement	Metric	D.O.I.
R1	The system shall provide a daily average of 52 kWh of electrical energy to Mars-Oz during winter		
R1.1	Solar collection area	Area (m^2)	+
R1.1.1	Number of solar panels	Integer	+
R1.1.2	Effective area of individual solar panel (excludes frame and electrical contacts)	Area (m^2)	+

System requirement Engineering requirement Technical attribute

Each of the technical attributes were then assigned a verification strategy to ensure that the system design would meet the design requirements. Technical attribute R1.1.1 (number of solar panels) for example, would be verified by simply counting the number of solar panels that are delivered to the installation site, and ensuring that they are the correct product. Given the large number of technical attributes and verification strategies involved in this project, they have not been included in this paper.

The design of the power system was split into three subsystems: the power generation; energy storage; and electricity supply subsystems, whose functions were to collect and generate energy from solar radiation, store that energy for back-up use, and to supply it to the Mars-Oz, respectively. Table 3 outlines the processes that were employed to design each subsystem.

Table 3: Summary of processes employed to design the Mars-Oz power system

Design methodology	Description
Power generation subsystem	
Comparison and selection of photovoltaic panel	Evaluation matrices were used to determine that Tindo Karra 260W DC polycrystalline silicon solar panels would be the most suitable because of their lower levelised cost of electricity. They are also an Australian brand that is manufactured in Adelaide.
Worst-case solar radiation analysis	The size (in kW) of the PV system was estimated using solar radiation data from Arkaroola for the "worst" month of June (i.e. the month that sees the lowest irradiation).

Design methodology	Description
Comparison and selection of panel mounting structure	Evaluation matrices were used to determine that the fixed (non-tracking) PV-ezRack SolarTerrace III mounting system would be most suitable for securing the panels.
Calculation of optimal panel inclination angle	Maximum irradiation in Arkaroola occurs on a surface tilted at 50° from the horizontal. Due to limitations with the mounting system however, the panel inclination angle was optimised to be 45°.
Configuration of mounted panels with respect to Mars-Oz	The mounted solar panels were configured such that transmission losses and shading from the Mars-Oz would be minimised, whilst still being close to the cargo module where the power conditioning equipment would be stored.
Wind loading analysis	ANSYS was used to simulate the stress and strain that the mounting structure would experience under typical Arkaroola wind speeds. The results were found to comply with AS/NZS 1170.2 *Structural design actions – Wind actions*.
Comparison and selection of charge controller model	Evaluation matrices were used to determine that the EP Solar Tracer-1215RN charge controller would be most suitable for regulating the amount of charge going into the batteries from the PV panels.
Energy storage subsystem	
Cloudy day analysis	The maximum number of consecutive cloudy days in winter in Arkaroola of 4 days meant that approximately 2 days of energy storage would be required. Due to budget constraints however, this was revised to 1 day of storage.
Comparison and selection of battery model	Evaluation matrices were used to determine that Victron Energy lead acid batteries (BAT412201100) would be most suitable for the Mars-Oz power system.
Selection of battery controller and monitor models	A battery controller and monitor from Victron Energy were recommended because they are the same brand as the batteries and so will be directly compatible. Battery controllers record operational parameters of the battery, while battery monitors display properties logged by the battery controller.
Electricity supply subsystem	
Comparison and selection of inverter model	Evaluation matrices were used to determine that Victron Energy Phoenix 24/5000 inverters would be the most suitable for converting DC power into AC for use in Mars-Oz.
Identification of need for backup generator and power logging system	A diesel backup generator and PV power logging system were recommended to be installed, but were not examined in detail in this project due to time and scope constraints.
Selection and configuration of transmission cables, cable protection and surge protection	The transmission cabling was designed to provide the most efficient arrangement from the PV array, much of which will be exposed to the environment and so requires cable protection. Breakers were used for surge protection to protect electrical components from the effects of electricity surges in the circuitry.

Design methodology	Description
Selection and configuration of earthing equipment	Earthing was incorporated into the system to ground any excess electrical charge and to protect conductive components of the system in the event of a lightning strike or a fault in the live wire insulation.
Configuration of equipment inside the Mars-Oz cargo module	The batteries, battery controller and monitor, inverters and charge controllers were configured inside the nose section of the Mars-Oz cargo module where they could safely operate under optimal ventilation conditions.

Mars-Oz Power System Design

Power Generation Subsystem

Photovoltaic Panels

Various solar panel brands were investigated to determine which would be the most suitable for the Mars-Oz power generation subsystem. Panel specifications such as their rate of degradation and cost were obtained from data sheets and compared using evaluation matrices.

The Tindo Karra 260W panel was found to be the most suitable as it was calculated to have the lowest levelised cost of electricity at $0.045/kWh, which was 9% lower than the second-best option. Being an Australian brand with an Adelaide branch presents an additional advantage of using these panels because transportation costs to Arkaroola can be minimised.

The required size of the PV system was estimated to be 29.2 kW_p (kilowatt peak) based on results from the worst month analysis[1] conducted with a system performance ratio of 65%. This meant that 128 solar panels were required. A fixed inclination angle of 45° will be used for the panels to ensure that their electrical output is winter-biased, thus allowing more energy to be generated in winter when Mars-Oz is habited.

Charge Controllers

Charge controllers provide the following functions:

- Reduction of voltage generated by the PV panels (150 V) to that required to power other components in the power system (24 V);
- Regulation of the amount of charge going into the batteries from the PV panels to prevent overcharging; and
- Prevention of overnight current discharge from the batteries to the PV panels.

An evaluation matrix applied to the two charge controller technologies available in the market indicated that Maximum Power Point Tracking would be more suitable than Pulse Width Modulation due to their lower cost and relative abundance. The three most suitable models of this type were then compared using another evaluation matrix, with the EP Solar Tracer-1215RN deemed to be the most suitable.

[1] The worst month analysis is based on the assumption that if the PV panels can provide sufficient electricity for Mars-Oz during the month with the lowest solar radiation in Arkaroola, it should be able to provide sufficient electricity for all other months in the year.

Mounting Structure

Three different PV panel mounting structures were considered: fixed (non-tracking), single-axis tracking, and double-axis tracking. It was found that the small increase in electricity generated by panels mounted on single-axis or double-axis systems in comparison to fixed mounting systems is not justifiable due to the higher costs and maintenance required.

Application of an evaluation matrix on the three most suitable fixed mounting systems found that the PV-ezRack SolarTerrace III would be best because it is the most cost-effective and easy to install. Its inclination angle is also adjustable and would be able to support the PV panels at the required angle of 45°; a feature that the other designs lack.

Energy Storage Subsystem

Battery Size Calculation

Storage batteries were deemed the most appropriate energy storage system due to their market abundance and commercial maturity. Battery capacity required for the power system was determined from the cloudy day analysis[2], in which it was found that the maximum number of consecutive cloudy days over a typical year in Arkaroola is four [3]. The required battery capacity was therefore calculated to be 173 kWh with a maximum depth of discharge of 60%. However, budget and space constraints limited this to 24 hours' worth of storage, which equates to a storage capacity of 87 kWh. A backup generator is expected to be used up to five times during winter to compensate for this smaller battery storage capacity.

Battery Selection

Two different types of battery technologies were considered: lead acid and lithium ion. Various models were evaluated against the relevant system requirements and technical attributes, and it was found that Victron Energy (BAT412201100) lead acid batteries would be the most suitable. This was primarily because lead acid batteries are less expensive than lithium ion batteries, and the Victron Energy batteries can be sourced from Adelaide.

Based on the properties of the selected battery system, they were recommended to be configured as shown in Fig. 3. Two units of batteries should be connected in series to build up to the required system voltage of 24 V, with seventeen rows of batteries connected in parallel to build up to the required capacity of 87 kWh.

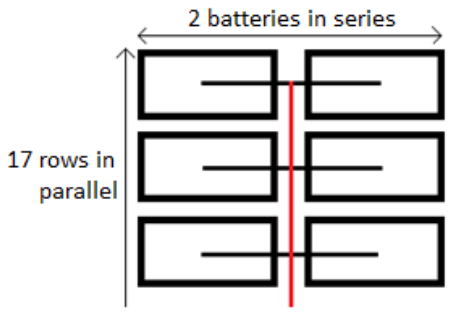

Fig. 3: Recommended configuration of the storage batteries

[2] The last 15 years of weather data in Arkaroola was examined in the cloudy day analysis to determine the maximum number of consecutive cloudy days that occur in a typical year. This is an important parameter for determining the total required battery capacity.

Battery Controller and Monitor

Battery systems typically include a battery controller and monitor. These were sourced from the same manufacturer as the inverter and batteries to ensure compatibility of the system. The battery controller (VE.Net) records operational parameters of the battery such as voltage and temperature to calculate the actual state of charge of the batteries [6], while the battery monitor (Victron Blue Power Panel PX) displays properties logged by the battery controller.

Electricity Supply Subsystem

Inverter Selection

An inverter converts direct current (DC) power from the PV panels and batteries into alternating current (AC) for use by electrical appliances in Mars-Oz. Three types of inverters exist in the market: grid-tied, modified sine wave and pure sine wave. The pure sine wave inverter was found to be most suitable because it has the highest efficiency of the three technologies and is therefore preferable for stand-alone power systems.

Three pure sine wave models were compared based on daily peak load requirements of Mars-Oz, which was calculated to be 15 kW from a compiled list of electrical appliances and equipment that are expected to be used each day. The Victron Energy Phoenix 24/5000 inverter was found to be the most suitable because of its comparatively low upfront cost and small number of required units. It also has a high rated efficiency of 94%.

Backup Generator

It is recommended that a backup generator be installed as part of the Mars-Oz power system. Despite there being an energy storage system, it is likely that there will be a shortage of electricity provided to Mars-Oz in the event of continuously cloudy weather. Output power of the backup generator will be in AC, which means that it can be directly used by electrical appliances and equipment without having to pass through the inverters or other power conditioning equipment. It is expected that this backup generator will use diesel fuels since these are commonly used in the Arkaroola Village.

Due to time and scope constraints, research on suitable backup diesel generators to adopt for the power system were not conducted. Nevertheless, it is recommended that a backup generator be included in the system to that ensure sufficient energy can be provided to the Mars-Oz regardless of the weather conditions.

Alternatively, power conservation measures could be put in place to reduce electricity consumption. These were not investigated during this study, but would involve minimising the use of some equipment such as the hot water taps and air conditioners.

Power Logging System

A power logging system is an important component of a PV system, particularly an off-grid one, so that performance of the system can be recorded to identify potential faults. The recommended Victron Energy inverter can be connected to free Victron Energy software called *VE Configure* which monitors the inverter output [7]. Unfortunately, this software only provides instantaneous feedback and does not log output over time.

The currently recommended system does not include logging capabilities for the system's power generation performance. Off-the-shelf logging systems that are currently available in the market either do not interface well with the recommended components or were deemed not applicable due to contraints, such as lack of internet connectivity at the Mars-Oz site. It is therefore recommended that the metering capabilities of the sytem be explored further beyond what has been discussed.

Wiring and Circuit Protection

Transmission Cables

Tinned copper solar cables must be used for the transmission of electricity from the power generation subsystem towards the storage and supply subsystems, and will also be used for the grounding of the panels for circuit protection. The cables are designed specifically for PV applications due to their durability and high current rating. External cabling should be installed with an additional protective layer of PVC conduit running through the ground for protection from water and the weather.

The recommended arrangement of the live and grounding cables is shown in Fig. 4. The grounding rod should be installed in the middle section of the array to reduce the amount of cabling required and therefore cabling costs. The configuration within the interior of the cargo module has not been detailed, and it is recommended that this be investigated in the future.

It was calculated that 987 m of live cabling and 98 m of ground cabling would be required. This length of cable is controlled by the configuration of the panels and their location with respect to Mars-Oz. The entire array was designed to be built on flat ground as close to Mars-Oz as possible, but where it will not be shaded by the Mars-Oz modules or surrounding landscape. The panels themselves were positioned to ensure that they would not shade each other and that transmission losses through the cables would be minimised.

Grounding

Grounding is required for the system in the event that excess electrical charge is present. In particular, grounding of the cables is required to prevent circuit overcharge. The DETA Earth Rod from Bunnings Warehouse was found to be the most suitable option for this purpose [8]. It is a standard copper rod that is used for grounding purposes, priced at $11.55 for 1.5 m. Two of these rods would be sufficient to ground the entirety of the system. A layout of the live and grounding cables of the system is shown in Fig. 4.

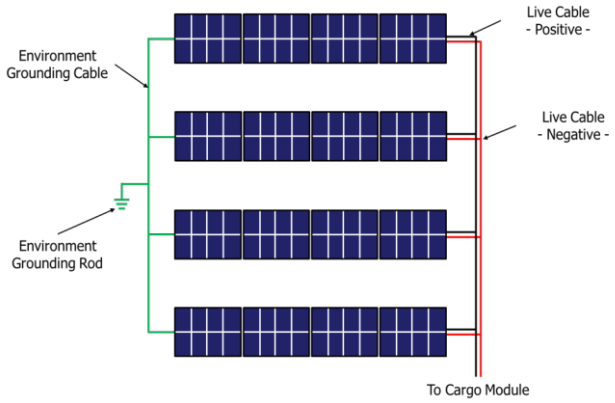

Fig. 4: Configuration of transmission cables from PV panels to the Mars-Oz cargo module

Cable Protection

Cable protection is required for the power system since a significant part of the cabling will be exposed to the environment. It is recommended that PVC piping be used to add an additional layer of insulation to the cables to provide protection from exposure to the elements.

It was assumed that the cables will be separate from all other components when leaving the PV panels so that they would then combine into a formation of 8 cables for each row of panels and 32 for the entire PV array. Due to the natural formation of how the wires would fit when bundled together, the diameter of the formations will be 3 and 7 cables-width respectively for the 8 and 32 configuration.

Surge Protection

Surge protection is required to protect an electrical system from the effects of electricity surges in the circuitry. Surge protection is achieved through the use of fuses or circuit breakers. Breakers were selected for the Mars-Oz power system because they are reusable, while fuses need to be replaced after a surge occurs. Sourcing replacement components for the remote site would be costly and time-consuming.

A wide range of circuit breaker technologies is available on the market. The most suitable breaker was found to be the residual current breaker with over-current protection (RCBO), which allows for the grounding of charge when an overcurrent occurs. This is beneficial because it prevents charge from building up within an overcharged panel. Additionally when an overcharge occurs further down the circuit, the RCBO would trip the circuit so that component damage is minimised.

As per AS/NZS 5033 Clause 3.3 [9], breakers should be located after all vital circuit components. As such, it was recommended that the RCBOs be placed in the following configuration:

- After each string of PV panels: 32 units operating at 55 A
- Before each battery and inverter: 38 units operating at 160 A
- Before the Mars-Oz module: x number of units operating at 65 A, where x is the number of circuits within the module.

Final Design

Power System

As outlined above, the Mars-Oz power system design will contain the following key elements:

- 128 Tindo Karra 260W polycrystalline photovoltaic solar panels;
- 16 Clenergy PV-ezRack SolarTerrace III non-tracking PV mounting arrays;
- 34 Victron Energy BAT412201100 lead acid batteries for 24 hours' storage; and
- 4 Victron Energy Phoenix 24/5000 inverters.

A simplified schematic of the Mars-Oz power system is shown in Fig. 5. The components in this diagram combine to form the power generation subsystem, energy storage subsystem, and electricity supply subsystem. Due to the large number of components in the system such as PV panels, batteries, and charge controllers, the schematic has depicted them as blocks.

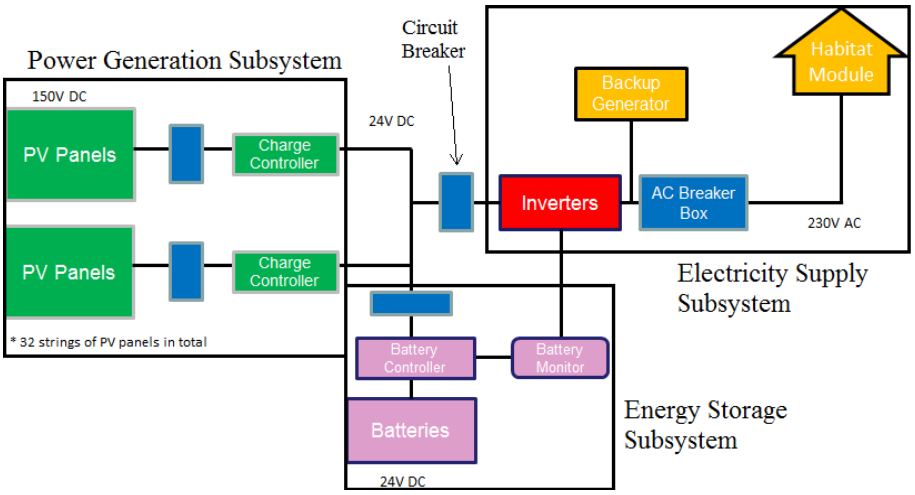

Fig. 5: Simplified schematic of the Mars-Oz power system

The power generation subsystem comprises 128 solar panels. Four panels are connected in series and each of these 32 strings are connected in parallel. The panels are mounted such that each mounting unit supports 8 panels. Four mounting arrays will be installed side-by-side in a 4 × 4 matrix, with the modules tilted at 45° from the horizontal and oriented to face True North for optimal performance in the winter. This configuration is shown in Fig. 6.

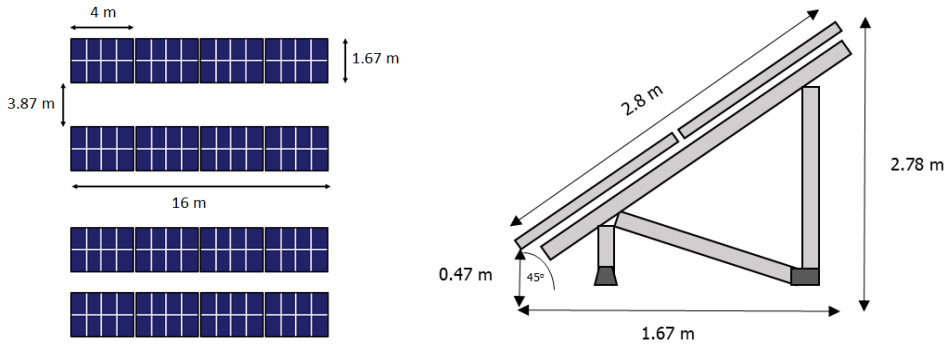

Fig. 6: (Left) Configuration of the PV panels; (right) tilt and sizing of the mounting units

Components Allocation

Fig. 7 shows the configuration of power conditioning equipment within the Mars-Oz cargo module, including batteries, inverters and charge controllers. The cargo module has been designed as a storage compartment, so placing the power conditioning equipment within the cargo module allows some of the safety concerns associated with their operation near people (e.g. flammability of batteries and the discharge of hydrogen gas) to be addressed.

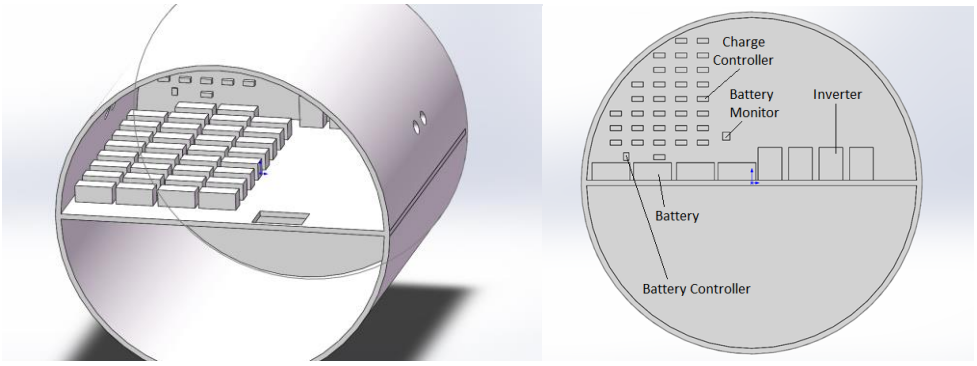

Fig. 7: Configuration of power conditioning equipment within the Mars-Oz cargo module

Ventilation must be incorporated into the cargo module to ensure that hydrogen from the lead acid batteries can be discharged into the atmosphere, preventing the built-up of hydrogen gas that would be hazardous to humans and become an explosion risk at critical concentrations. The ventilation pathways created by holes in the module walls will permit natural ventilation through the area. Calculations based on battery specifications and AS 4086.2 [10] informed that a total of four ventilation holes will be needed for the proposed power system design, each with a diameter of 200 mm and having the same size as windows in the habitat module.

Conclusion

Error! Reference source not found. presents the components of the recommended Mars-Oz power system design, including the manufacturer, model and present cost of each component. The total system cost is $106,371, which is $5,671 over the provided budget of $100,700. It is expected that when the system is installed however, the price of the solar panels and batteries will have decreased due to the rapid development of these technologies.

Table 4: Summary of the recommended components in the final design

Component	Manufacturer	Model	Number of units	Unit cost ($)	Total component cost ($)
PV panel	Tindo	Karra 260W DC	128	300.00	38,400
Mounting system	Clenergy	PV-ez Rack SolarTerrace III	16	750.00	12,000
Battery	Victron Energy	BAT412201100	34	724.14	24,621
Inverter	Victron Energy	Phoenix 24/5000	4	4,127.07	16,508
Charge controller	EP Solar	Tracer-1215RN	32	86.66	2,773
Logging system	Victron Energy	Blue Power Panel GX & VE.Net	1	694.00	694
Wiring and circuit protection					11,375
Transmission cables*	Altronics	Various	1,123 m total	Various	4,269
Earthing rod	DETA earth rod	6751B	2	11.55	23
Cable protection**	Various	Various	186 m total	Various	1,794
Surge protection***	Various	Various	Various	Various	5,289
				Total system cost $	**106,371**

*The transmission cables comprise live and ground cables as well as high current cables, which cost $3.50 and $11.95 per metre respectively [11].

**Cable protection consists of PVC piping of different diameters: 15mm and 20mm costs $9 per metre and 50mm costs $29 per metre [12].

***Surge protection comprises three different circuit breakers that will be located throughout the system.

References

1. Mars Society, 2015. *The Mars Society*. Available from: http://www.marssociety.org (Accessed 2 March 2015).

2. Willson, D. and Clarke, J., 2007. A Practical Architecture for Exploration-Focused Manned Mars Missions Using Chemical Propulsion, Solar Power Generation and In-Situ Resource Utilisation, *Proceedings of the 6th Australian Space Science Conference*.

3. Bureau of Meteorology, 2015. *Climate statistics for Australian locations*. Available from: http://www.bom.gov.au/climate/averages/tables/cw_017099.shtml (Accessed 5 March 2015).

4. Binsted, K. and Gifford, S., 2015. *Hawaii Space Exploration Anolog and Simulation*. Available from: http://hi-seas.org/wp-content/uploads/2016/01/HISEASMediaKit_01132016.pdf (Accessed 22th May 2016).

5. Generac, 2015. *Generac Supports the Mission to Mars*. Available from: http://gens.lccdn.com/GeneracCorporate/media/Library/Case%20Studies/0166580SBY-mars-trailer-LOW-RES.pdf (Accessed 22nd May 2016).

6. Victron Energy, 2015. *VE.Net Battery Controller Manual*. Available from: http://www.victronenergy.com/upload/documents/Manual-VBC-12-24-48-EN.pdf (Accessed 28 May 2015).

7. Victron Energy, 2015. *Support and Downloads*. Available from: http://www.victronenergy.com.au/support-and-downloads/software (Accessed 28 May 2015).

8. Bunnings Warehouse, 2015. *Deta Earth Rod*. Available from: http://www.bunnings.com.au/deta-earth-rod_p4430624 (Accessed 28 May 2015).

9. Standards Australia/Standards New Zealand, 2014. *AS/NZS 5033:2014 Installation and safety requirements for photovoltaic systems*, SAI Global, Sydney.

10. Standards Australia, 1997. *AS 4086.2:1997 Secondary batteries for use with stand-alone power systems, Part 1: Installation and maintenance*, SAI Global, Sydney.

11. Altronics, 2015. *W4208 Power Cable 160A 287/0.30, Solar Photovoltaic Cable*. Available from: http://www.altronics.com.au/ (Accessed 15 May 2015).

12. IP Supplies Group, 2015. *Pipe Supplies Australian Specification*. Available from: http://www.pipeonline.com.au/listProduct/PVC+PIPE/PRESSURE+PIPE (Accessed 23 May 2015).

Stereolithographic 3D Printed Nozzles for Cold Gas Propulsion Experiments

Courtney A. Bright, Sean L. Tuttle and Andrew J. Neely

School of Engineering and Information Technology, UNSW Canberra, ACT, Australia, 2600

Summary: High resolution stereolithographic 3D printed nozzles are under consideration for use in a thrust stand for cold gas propulsion experiments. 3D printed nozzles allow single-piece construction of small, complex internal geometries and fast, inexpensive geometry changes for parametric studies. However, investigation was required to determine the outgassing characteristics of the stereolithographic resin, the geometric accuracy of the prints, and the achievable surface finish for o-ring seal compatibility and smooth fluid flow. Outgassing tests demonstrated vacuum compatibility for the conditions expected during thrust stand operation: 0.01 mbar pressure and ambient temperature. The internal contour of the printed nozzle was measured with a high resolution profilometer and matched the expected geometry well, with a mean tolerance of ± 0.06 mm. A surface roughness of 0.1 μm was achieved by wet sanding and polishing the 3D prints, which was found to be sufficient for o-ring seal requirements and hydraulically smooth flow.

Keywords: Propulsion, 3D printing, fluidic thrust vectoring, thrust balance, outgassing, dimensional accuracy, surface finish, vacuum.

Introduction

A biaxial thrust stand is under development at UNSW Canberra for fluidic thrust vectoring (FTV) cold gas propulsion experiments. FTV involves asymmetric injection of a secondary fluid into a supersonic nozzle to deflect the thrust through an oblique shock wave and momentum of the secondary fluid, as illustrated in Fig. 1. The technique has the potential to improve propulsion system efficiency and precision by compensating for centre of mass excursions and thruster misalignment. The thrust stand has been designed for operation in the UNSW Canberra vacuum chamber, which has an internal volume of approximately 2.5 m^3 and currently maintains a vacuum level of 0.01 mbar. All testing will be run at ambient temperature. As the vectoring behaviour changes when the ambient pressure rises above the exit pressure of the nozzle [1], a small nozzle throat diameter (2 mm) is required to maximise the possible test time for a given nozzle area ratio.

The thrust stand consists of two parallel 1/2 inch stainless steel tubes to supply main and secondary high-pressure nitrogen gas to a 3D printed nozzle block with injectors and internal piping. Manufacture of the nozzle block by 3D printing allows the block to be constructed in one piece and permits fast and inexpensive geometry changes for parametric studies. The nozzle block is clamped between two aluminium plates, with the top plate threaded to connect to two Swagelok pipe fittings, each with an o-ring seal between the aluminium and 3D printed surfaces. The gas supply tubes are welded into rigid base plate and form an integral part of the

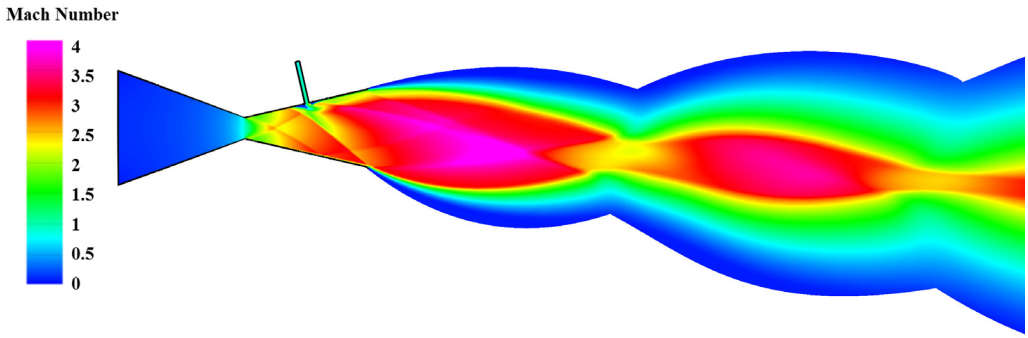

Fig. 1: Mach number contours of FTV with 5° vector angle.

thrust stand by acting as a cantilever when a force is applied to the nozzle, circumventing the issue of external forces from the piping when the system is pressurised. Axial and transverse thrust is inferred from strain and acceleration measurements at the cantilever base and end, respectively. The thrust stand design and a close-up view of the 3D printed nozzle block can be seen in Fig. 2.

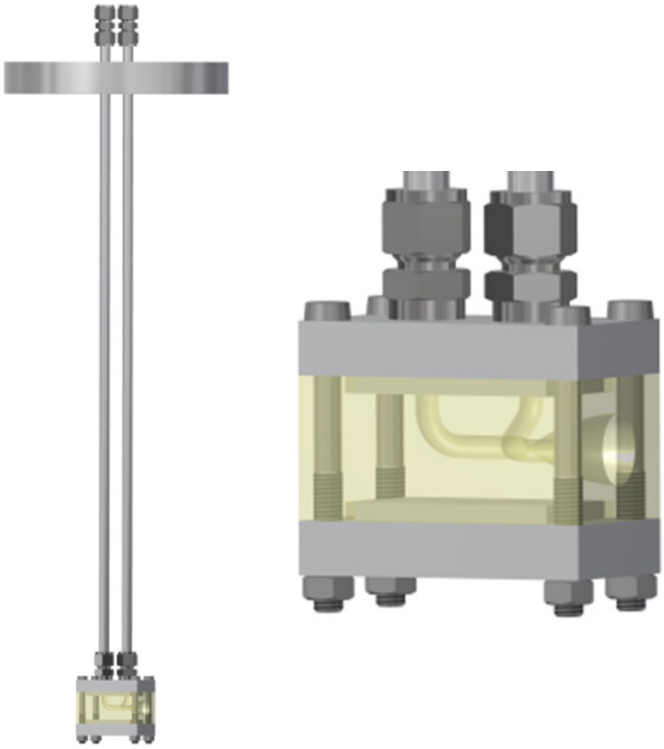

Fig. 2: Model of thrust stand (left) with close-up of 3D printed nozzle block (right).

The 3D printer chosen for manufacture of the nozzle blocks is a Form 1 high resolution desktop stereolithographic (SL) 3D printer, shown in Fig. 3. The high resolution printing provides a relatively smooth surface finish and allows the manufacture of very small injectors. The availability of clear resin also offers possibilities for internal flow visualisation. The printer works by directing a laser across a tray of liquid photo-reactive resin, causing successive thin layers to solidify. The layer thickness can be selected by the user: from 0.1 mm for rough prints up to 0.025 mm for high resolution prints. After each layer is formed, the printer

performs a peel process, where the newly solidified resin is peeled from the bottom of the resin tank. The layers are built up on a "build platform", which slowly pulls the model out of the liquid resin during printing, as shown in Fig. 4. The nozzle blocks take approximately 12 hours to print when the 0.025 mm layer thickness is selected.

Fig. 3: Formlabs Form 1 SL 3D printer.

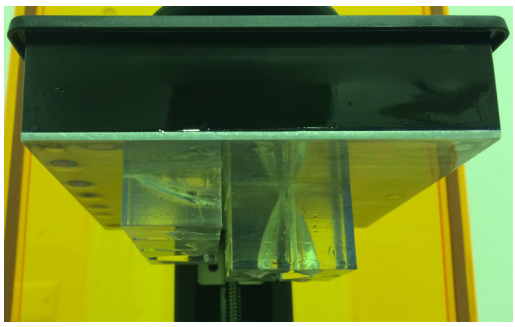

Fig. 4: Formlabs Form 1 SL 3D printer build platform with printed nozzles.

Before using the 3D printed nozzle blocks for the thrust stand, outgassing tests were required to determine the vacuum compatibility of the cured SL resin to avoid contamination of the vacuum chamber. The key criteria for vacuum compatibility is the total mass loss (TML) of a material when maintained at a specified pressure and temperature for a given length of time, expressed as a percentage of the original mass. A TML of less 1.00% over a 24 hour period is typically considered acceptable for space applications [2]. Investigation was also required to assess the geometric accuracy of the nozzles, particularly their symmetry about the nozzle axis. A significant asymmetry may produce side forces caused by the nozzle geometry rather than the secondary fluid injection. A smooth surface finish was also required for a sufficient o-ring seal between the 3D printed surface and the aluminium plate, and to avoid additional shock waves in the supersonic section of the nozzle. For static o-ring seals, a surface roughness of $Ra < 0.4$ μm is recommended for vacuum applications [3], where Ra is the arithmetic average of the absolute values of the profile height variations from the mean line, calculated over a specified cut-off length, which is typically around 1 mm. The

smoothness of the fluid flow inside the nozzle can be described by the extent that the wall roughness penetrates the viscous sublayer of the boundary layer, using a constant k^+:

$$k^+ = \frac{Ra\sqrt{\frac{\tau_w}{\rho_w}}}{\upsilon} \tag{1}$$

where τ_w is the boundary layer shear stress at the wall, ρ_w is the fluid density at the wall, and υ is kinematic viscosity. If the roughness profile falls within the viscous sublayer ($k^+ < 4$), the roughness has no effect on the flow and the wall is classified as hydraulically smooth. In the transitional roughness regime ($4 < k^+ < 60$), the roughness begins to have a noticeable effect on the flow velocity and weak shock waves may appear from the small ridges on the wall. When the flow is fully rough ($k^+ > 60$), the flow velocity is no longer effected by viscosity [4, 5]. The roughness values corresponding to each flow regime were calculated using flow conditions at the nozzle throat from computational fluid dynamics simulations, as follows:

- $Ra < 0.3$ μm: hydraulically smooth regime
- $0.3 < Ra < 4$ μm: transitional roughness regime
- $Ra > 4$ μm: fully rough regime

Method

Formlabs Clear Photoreactive Resin Version 02 was used for all prints, which is a mixture of methacrylated oligomers, methacrylated monomer, and photoinitiator [6]. When cured, the resin has a tensile strength of 61.5 MPa, Young's Modulus of 2.7 GPa, and a 5% weight loss temperature of 274°C [7]. When using an SL 3D printer, parts are typically oriented with flat surfaces at an angle of 10 to 20° to the build platform to prevent distortion by minimising the area subjected to the peel process in each new layer. A support structure is also often used to avoid print defects due to unsupported material during printing. Despite this, the nozzles were printed directly to the build platform with no orientation angle or supports to ensure that the layers were printed perpendicular to the nozzle axis. Printing the nozzles in this manner allows the inside of the nozzle to be left unsanded if necessary, as any shock waves forming on the small ridges inside the nozzle would be axisymmetric and thus have no contribution to the vectoring performance. The nozzles were printed in two halves to allow profilometer access to the internal contour. The print layout in the centre of the build platform can be seen in Fig. 5. The completed prints were rinsed in isopropyl alcohol (IPA) for approximately 30 minutes and left in natural light for a 24 hours to further cure. The nozzles have a throat diameter of 2 mm, exit diameter of 20 mm, and diverging length of 33 mm.

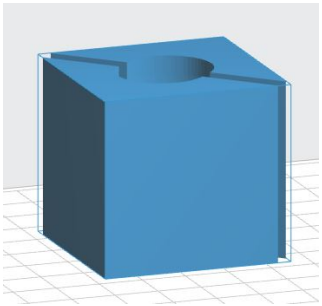

Fig. 5: Layout used for nozzle prints: directly to build platform with no supports.

Vacuum Compatibility

The American Society for Testing and Materials (ASTM) Standard E 595 - 93 [2] for total mass loss (TML) testing was followed to the extent possible with the available facilities. Ten 1 cm^3 cubes of approximately 1 g were printed, cleaned with lint-free cloth and IPA, and placed in a clean aluminium foil tray. A second piece of aluminium foil was also cleaned with IPA to provide a clean surface on the mass balance. The samples and aluminium foil were stored in a clean desiccator (a sealed vessel containing silica gel to remove moisture from the samples) when not in the vacuum chamber, as shown in Fig. 6. Nitrile gloves were worn during all handling procedures and care was taken to ensure the samples did not come into contact with anything that had not been thoroughly cleaned with IPA.

Fig. 6: Outgassing samples and aluminium foil stored in desiccator when not in vacuum chamber.

Immediately prior to vacuum exposure, each sample was weighed on a mass balance with a sensitivity of ± 10 μg, as shown in Fig. 7. The samples and aluminium foil tray were then placed inside the vacuum chamber with two thermocouples positioned immediately above the samples. The vacuum chamber set-up can be seen in Fig. 8. After the initial pump down, the vacuum chamber was maintained at a pressure of approximately 0.01 mbar and ambient temperature of approximately 20°C for 24 hours. The pressure and temperature were chosen to represent the FTV testing conditions as closely as possible. When the vacuum period was complete, the vent valve was opened and the chamber was backfilled with ambient air. The samples were then removed immediately and weighed for a second time. The total mass loss of each sample was then calculated as follows:

$$\%TML = \frac{mass_{initial} - mass_{final}}{mass_{initial}} \times 100 \quad (2)$$

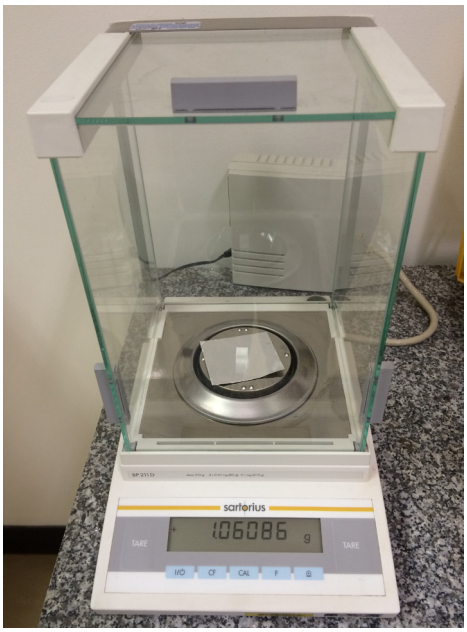

Fig. 7: Outgassing test sample on mass balance with ±10 μg sensitivity.

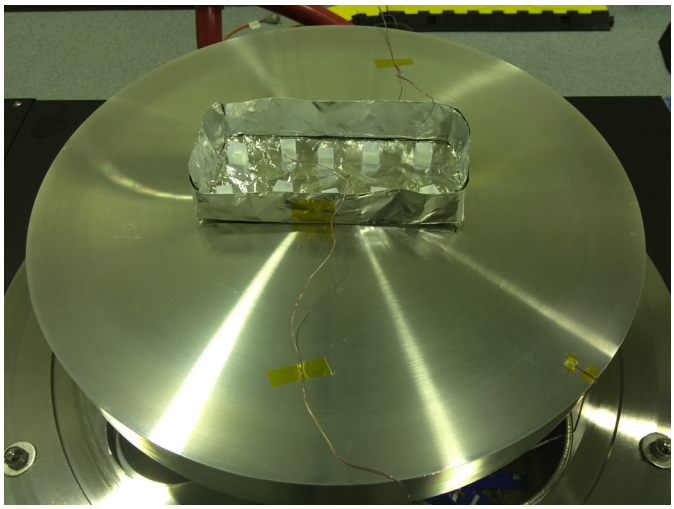

Fig. 8: Set-up of outgassing samples and thermocouples on thermally-controlled vacuum chamber base (chamber walls and lid removed at this point).

Geometric Accuracy

The printed nozzle contour was measured using a Nanovea PS50 optical profilometer for comparison with the computer aided design (CAD) model that was used as the printer input. The profilometer has a vertical range of 12 mm, which allowed the half-nozzles to be profiled in a single session. A 3D printed base was used to repeatably position the nozzle halves during profiling and maintain alignment with the profilometer axis. Measurements were taken with a horizontal resolution of 0.05 mm and vertical resolution of 133 nm.

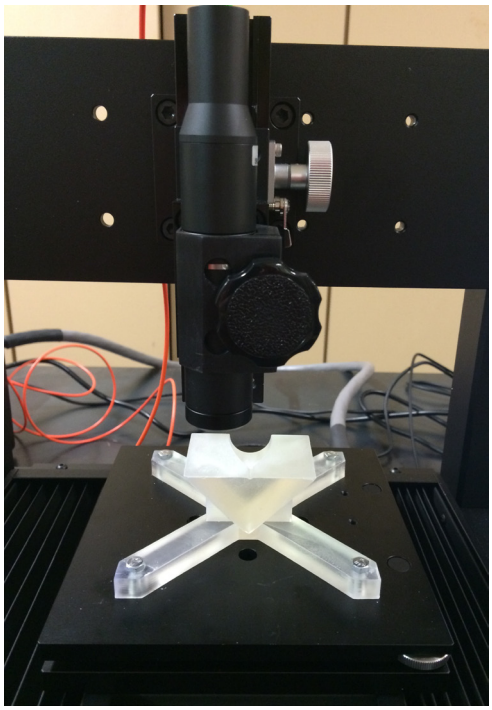

Fig. 9: Measuring the nozzle contour using the Nanovea profilometer with 3D printed nozzle holder.

Surface Roughness

Two flat, rectangular samples were prepared for surface roughness testing: a raw "as-printed" sample and a "sanded and polished" sample. The latter sample was prepared as follows:

1) Wet sand with 800 grit sand paper by hand for approximately 2 minutes
2) Wet sand with 1200 grit sand paper by hand for approximately 2 minutes
3) Polish with cork and Novus 3 Heavy Scratch Remover
4) Polish with cork and Novus 2 Fine Scratch Remover
5) Polish with microfibre cloth and Novus 1 Plastic Clean and Shine

The materials used for this process are shown in Fig. 10 with a polished nozzle block.

The Nanovea profilometer was again used for surface profile measurements, this time with a horizontal resolution of 0.01 μm and vertical resolution of 2.5 nm. With a profile length of 5 mm and cut-off length of 1 mm, the average roughness, Ra, was calculated as follows:

$$Ra = \frac{|Z_1| + |Z_2| + \ldots + |Z_N|}{N} \tag{3}$$

where Z is the vertical distance of the measurement point from the mean line and N is the number of data points within the cut-off length.

Fig. 10: Printed nozzle block with materials used to obtain surface finish.

Experimental Results

The total mass loss results for the 10 samples of cured SL resin are shown in Table 1. A mean TML of 0.007% was obtained for 24 hour exposure to the vacuum conditions expected for the FTV experiments (0.01 mbar pressure and ambient temperature of 20°C). This is well below the vacuum compatibility criterion of 1% total mass loss and is thus considered acceptable for use in the thrust stand. Further testing is required to determine the outgassing characteristics for ultra-high vacuum and elevated temperature applications.

Table 1: Outgassing test total mass loss results for 24 hour exposure to 0.01 mbar and 20°C

Sample	Initial Mass (g)	Final Mass (g)	TML (%)
A	1.08172	1.08161	0.010
B	1.10035	1.10026	0.008
C	1.06510	1.06502	0.008
D	1.09965	1.09955	0.009
E	1.12233	1.12220	0.012
F	1.09267	1.09263	0.004
G	1.08674	1.08668	0.006
H	1.11262	1.11257	0.004
I	1.07433	1.07425	0.007
J	1.05040	1.05037	0.003
Mean			0.007
Standard Deviation			0.003

The measured contour along the nozzle axis at the midpoint of the nozzle halves is shown in Fig. 11 against the input CAD geometry. For clarity, only every 20th point has been plotted.

The printed geometry can be seen to closely approximate the desired nozzle contour. Fig. 12 displays the printed nozzle circumference at the throat, midpoint of the diverging section, and exit. Again, the printed profile is a close match to the CAD geometry and no significant asymmetry is apparent. A small discrepancy from the circular profile can be seen at a radius of zero at the junction of the two nozzle halves, where the circular profile turns 90° to transition to a flat surface. Printing the nozzles in a single piece would eliminate this error, however, the vertical range of the available profilometer did not allow measurement of single-piece nozzles of this size. The mean tolerance of the 3D printed nozzle was found to be ± 0.06 mm, which is 3% of the nozzle throat diameter and 0.3% of the exit diameter. This tolerance was deemed acceptable for use in the thrust stand, with minor asymmetries to be accounted for with calibration.

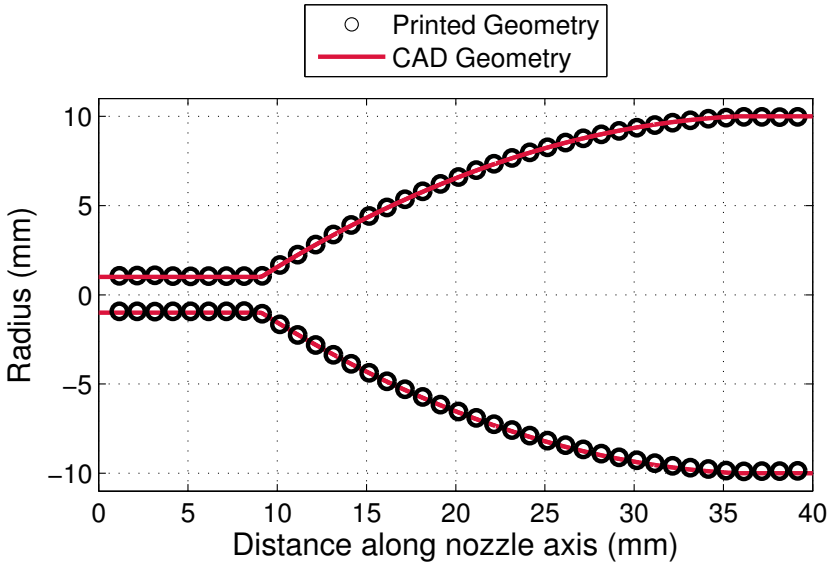

Fig. 11: Profilometer results for nozzle contour at midpoint of each nozzle half.

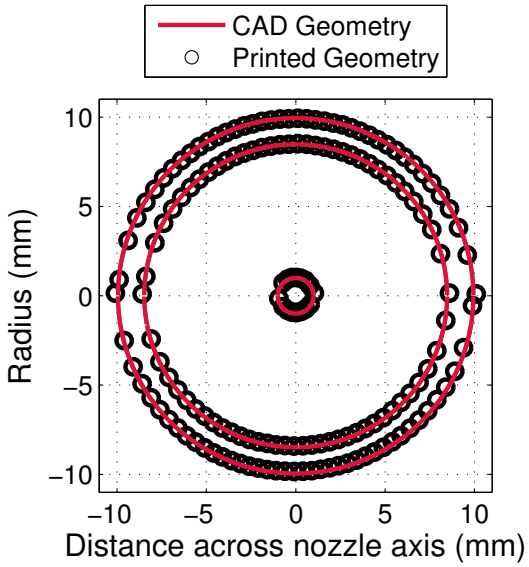

Fig. 12: Profilometer results for nozzle circumference at throat, midpoint, and exit.

The surface profiles of the raw and sanded and polished 3D prints are shown in Fig. 13. A waviness can be observed in the raw surface profile, which is thought to be due to minor distortions of the material from the peeling process during printing. With a cut-off length of 1 mm, the raw surface was found to have an average roughness of $Ra = 0.9$ μm $\pm$ 0.4 μm. The sanded and polished surface was substantially smoother, with an average roughness of $Ra = 0.1$ μm $\pm$ 0.08 μm, comparable to mirror-polished steel. The sanded and polished surface is smooth enough to provide an adequate o-ring seal against the aluminium plate of the thrust stand ($Ra < 0.04$ μm) and is well within the hydraulically smooth regime for the nozzle flow conditions. The raw surface is not smooth enough for the o-ring seal, therefore, the top and bottom surfaces of the nozzle block will need to be sanded and polished. The raw surface roughness falls within the low end of the transitional roughness regime ($4 < k^+ < 60$), therefore, weak shock waves are likely to be present if the nozzle interior is left unsanded. As sanding the nozzle interior is likely to alter the nozzle contour and symmetry, it is recommended that the nozzles are printed with the nozzle axis perpendicular to the build platform at an angle of 0° so that the roughness profile is axisymmetric with minimal impact on the vectoring performance.

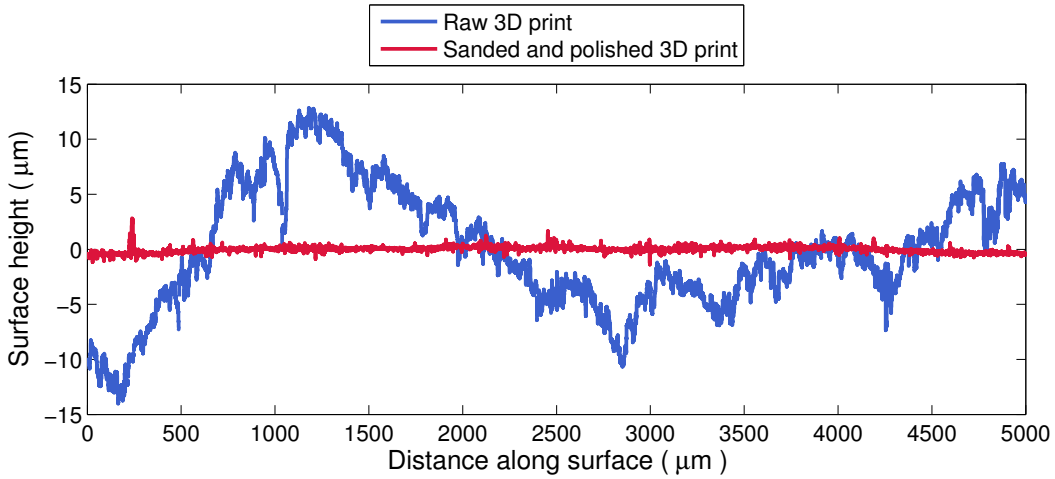

Fig. 13: Surface profile for "raw" and "sanded and polished" prints.

Conclusion

The suitability of stereolithographic (SL) 3D printed nozzle blocks for a fluidic thrust vectoring thrust stand has been investigated. A Form 1 high resolution desktop SL 3D printer was selected for printing the nozzles due to its high resolution and availability of clear resin. Formlabs Clear Photoreactive Resin Version 02 and a layer thickness of 0.025 mm was used for all prints. The outgassing characteristics of the cured SL resin were tested using the total mass loss (TML) method for the operating conditions expected for the thrust stand (0.01 mbar pressure and ambient temperature). A mean total mass loss of 0.007% was obtained for 24 hour exposure, which is well within the requirements for vacuum compatibility (TML $< 1\%$). Outgassing behaviour at ultra-high vacuum or elevated temperature has not yet been determined.

The geometric accuracy of the 3D prints was assessed by measuring the internal nozzle contour with a high resolution optical profilometer for comparison with the CAD model

geometry used as input for the printer. The printed geometry was found to closely match the required geometry, with a mean tolerance of ± 0.06 mm, which represents 3% of the nozzle throat diameter and 0.3 % of the exit diameter. No significant asymmetry was seen in the nozzle circumference and the results were deemed acceptable for use in the thrust stand. The roughness of two surface finishes was also analysed: a raw "as-printed" sample and a "sanded and polished" sample, which was wet sanded twice and subjected to three rounds of polishing. The raw surface was found to have an average roughness of 0.9 μm $\pm$ 0.4 μm, which was not sufficient for an o-ring seal and fell into the transitional roughness regime for the expected flow conditions. A surface roughness similar to mirror-polished steel was achieved with the sanded and polished sample, 0.1 μm $\pm$ 0.08 μm, which meets the criteria for o-ring seals for vacuum applications. The surface profile was in the hydraulically smooth regime and would thus have no impact on the supersonic fluid flow. Despite this, it was recommended that the nozzle interior be left raw to avoid altering the nozzle contour during sanding. Asymmetries due to the surface roughness can be eliminated by printing the nozzles directly to the build platform at an angle of 0°, minimising the impact of weak shock waves on vectoring performance.

Acknowledgments

The authors gratefully acknowledge Dr Philippe Lorrain and Laurent Le Page for assistance with running the outgassing tests and Dr Murat Tahtali for help with the 3D printing.

References

[1] Bright, C.A., Tuttle, S.L. and Neely, A.J., "The Effect of Vacuum on Shock Vector Control Performance", *Proceedings of the 19th Australasian Fluid Mechanics Conference*, Melbourne, Australia, December 8-11, 2014.

[2] American Society for Testing and Materials, *E 595-93: Standard Test Method for Total Mass Loss and Collected Volatile Condensable Materials from Outgassing in a Vacuum Environment*, ASTM Standards, Pennsylvania, 1993.

[3] Apple Rubber Produces Inc, *Seal Design Guide*, viewed 25 June 2015, http://www.applerubber.com/src/pdf/seal-design-guide.pdf.

[4] White, F.M., *Viscous Fluid Flow*, Second Edition, McGraw-Hill Inc, New York, 1991.

[5] Babinsky, H. and Inger, G.R., "Effect of Surface Roughness on Unseparated Shock-Wave Turbulent Boundary-Layer Interactions", *AIAA Journal*, Vol. 40, No. 8, 2002, pp. 1567-1573.

[6] Formlabs, *Formlabs Safety Datasheet - Clear: Photopolymer Resin for Form 1, Form 1+*, viewed 30 June 2015, http://formlabs.com/media/upload/Clear-SDS.pdf.

[7] Formlabs, *Formlabs Material Properties - Clear: Photopolymer Resin for Form 1+ and Form 1 3D Printers*, viewed 30 June 2015, http://formlabs.com/media/upload/Clear-DataSheet.pdf.

Effect of Self-shadowing and Attitude on Cubesat Solar Power Generation: A Case Study on UNSW EC0 QB50 Cubesat

Joon Wayn Cheong, Barnaby Osbourne, Jannick Habets

Australian Center for Space Engineering Research,
University of New South Wales

Summary: UNSW's QB50 [1] Cubesat harnesses solar power via three body-mounted and two deployable Photovoltaic panels. For a given mission, the amount of solar energy that can be generated can be optimised if non-mission-critical configurations such as the solar panel deployment angle and the satellite's attitude can be varied. Taking the orbit-averaged generated power as the function to maximise, a comprehensive set of 3D-based in-orbit simulations can then produce the optimal configuration for a mission. The simulation has been developed in Matlab^{TM} and incorporates 3D ray tracing algorithms to account for the shadowing effects of the deployed solar panels on the body-mounted solar panels. Taking into account the self-shadowing effect, a parametric study was then conducted to solve for the power output of the satellite at all orientations in 3D space.

Incorporating the various power efficiencies of the satellite load and Electrical Power Systems (EPS) module, the computed solar energy generated is then used to accurately predict the power margins of the system at a variety of operational modes and spacecraft attitudes. This analysis thus provides a useful guide to ensure that the design of our mission is operating within sufficient energy margins.

Taking the UNSW EC0 Cubesat mission as a case study, this analysis has shown that the effects of self-shadowing can reduce up to 30% of instantaneous output power, and thus is an important factor to be considered. By optimising the satellite roll and panel deployment angle, the satellite is able to maintain a positive power margin, as opposed to a negative power margin as observed in other non-optimised configurations.

System Overview

The electrical power subsystem (EPS) on UNSW-EC0 consists of the NanoPower P-series P31u V8.0 (GOMSpace) [2] and includes a 20Whr Li-ion battery. The EPS regulates and distributes the power to the loads. Furthermore, five solar panels from GOMSpace provide the input power. Three panels are body mounted and two solar panels are deployable.

The NanoPower P31u has 3 input channels with independent power-point settings giving an input power capacity of 30W. The NanoPower interfaces to triple junction solar cells and uses a boost-converter to condition the power output in order to charge the batteries. The input power and the energy stored in the batteries is used to feed two buck-converters supplying a 3.3V rated at 5A and a 5V rated at 4A output bus. NanoPower includes a microcontroller that provides maximum power-point tracking (MPPT), measures and logs voltages, currents etc. Commanding of the EPS is done using an I2C interface.

The 2400mAh lithium-ion battery is charged with all the available power from the solar cell inputs which is not used by the loads on the external power buses. The battery is protected against under-voltage and over-voltage and operates at a nominal voltage of 7.4V. A block diagram of the EPS can be seen in Figure 1. NanoPower has six latch-up protected and controllable outputs, two "always on" 3.3V and two "always on" 5V bus outputs and an always on direct battery voltage output.

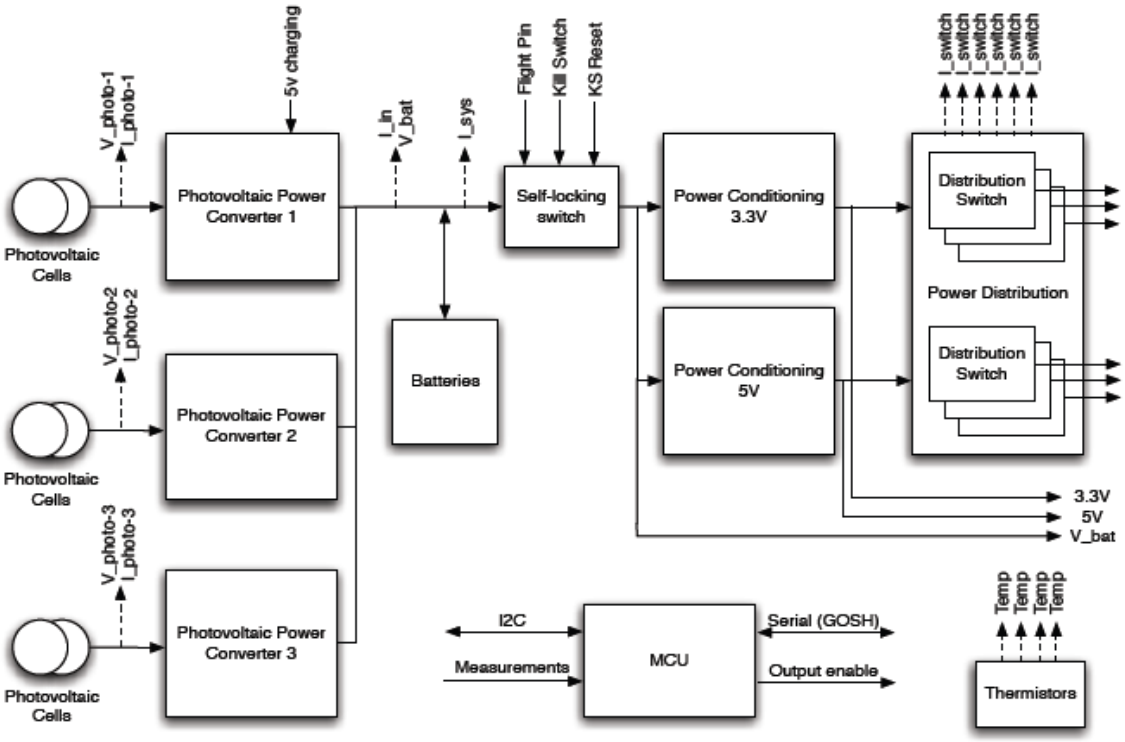

Figure 1 NanoPower Block Diagram

The solar panels consist of 4 triple-junction photo-voltaic cells each. The solar cells have an efficiency of 28.3% and an output power of 5.2W at 28 °C.

The satellite carries two deployable solar panels and three body mounted solar panels. The body mounted solar panels has four solar cells on each surface and are populated on the -X, +X and –Y surface of the satellite. The two deployable panels are hinged to the +Y and –Y surfaces. Both deployable panels has four solar cells each facing the -Y direction when deployed at 180°. This set-up has been chosen to increase the power output during nominal operations, i.e. velocity vector pointing.

Factors influencing power generation efficiency include spectral distribution, spatial distribution of power, temperature, and resistive load. For a satellite in space, only the spatial distribution of power, temperature and resistive load will vary. The resistive load can be varied until the peak or maximum power point (MPP) is achieved. MPP is achieved by the three Boost Voltage regulator on the EPS. The power at this point is recorded as Watt-peak (Wp). It is Watt-peak and the spatial distribution of power that is the focus of this paper. Temperature affects Watt-peak in the order of milli-watts, hence insignificant to our study. [3]

Simulation Methodology for Cubesat Power Generation

The purpose of this analysis is to provide a thorough understanding of the power input of the solar panels. In order to do this the orientation of the spacecraft with respect to a reference vector (i.e. the Sun) has been modelled. This fixes the orientation of the solar panels as well, resulting in an effective area that receives sunlight. Furthermore, the effect of self-shadowing on the solar panels has been taken into account to give an accurate representation of the problem. Self-shadowing is the effect of the shadow of the satellite's structure casting on its own solar panel, resulting in a lowered power generation capability.

Rotation Matrix Definition

First, the method to find the orientation of the satellite in a specified reference frame - in this case the inertial frame - is outlined. The sides of the spacecraft can be represented in the body frame (B-frame) as a set of vectors which serve as the vertices of the body [4]. The orientation of the body frame in a Local Vertical Local Horizontal (LVLH) can be described by three angles; roll, pitch and yaw (φ,θ,ψ). Any vector in the B-frame is transformed into the LVLH frame by a simple 3-2-1 axis rotation [5]:

$$\begin{bmatrix} x \\ y \\ z \end{bmatrix}_{LVLH} = T^{B\to LVLH} \begin{bmatrix} x \\ y \\ z \end{bmatrix}_{B}$$

$$T^{LVLH\to B} = T_1(\phi)T_2(\theta)T_3(\psi)$$
$$T^{B\to LVLH} = \left(T^{LVLH\to B}\right)^T$$

The vector can be further transformed into the orbital frame as:

$$T^{Orb\to LVLH} = T_1(-\pi/2)T_3(\pi/2)$$
$$T^{Orb\to LVLH} = \begin{bmatrix} 0 & 1 & 0 \\ 0 & 0 & -1 \\ -1 & 0 & 0 \end{bmatrix}$$
$$T^{LVLH\to Orb} = \left(T^{Orb\to LVLH}\right)^T$$

The rotation from the orbital frame to the inertial frame is done by rotating over the right ascension of the ascending node (Ω), inclination angle (i) and the true anomaly (u).

$$T^{I\to Orb} = T_3(u)T_1(i)T_3(\Omega)$$
$$T^{Orb\to I} = \left(T^{I\to Orb}\right)^T$$

The rotation matrix to convert from body frame to inertial frame is the product of the three individual rotations:

$$T^{B\to I} = T^{Orb\to I}T^{LVLH\to Orb}T^{B\to LVLH}$$

Solar Panel Power Generation

Secondly, a solar panel is modelled as a vector normal to its surface. By finding the incidence angle, β, between this vector and the reference vector, the projected area of the solar panel can be found [6]. The projection of the sun's ray unit vector onto the surface's normal vector is proportional to the power generated by the panels:

$$P_{in} = \cos\beta \cdot A \cdot P_{density}$$

where, $P_{density}$ is the power density in W/m^2 and A is the area of the solar panel in m^2. The angle β is found by using the scalar product:

$$\cos\beta = \frac{V_1 \cdot V_2}{|V_1||V_2|}$$

with V_1 the reference vector and V_2 the vector normal to the solar panel surface. The total power input to the EPS is equal to the power inputs from all the panels that are in sunlight added together.

Self-Shadowing based on Ray Tracing

This section details the computations for the illuminated area A of a solar panel by accounting for self-shadowing effects using ray tracing techniques [7]. In certain configurations the solar panels shadow parts of other solar panels or the complete panel. This reduces the power input of the solar panels. Preliminary analysis showed that this is a driving factor when determining the optimal roll and solar panel deployment angle. The method to find the shadowed area of a solar panel consists of three steps. Firstly, the vertices of the panel that shadow on the solar panel will be projected on a plane coinciding with the shadowed solar panel. Secondly, this vector will be expressed in a solar panel reference frame. Thirdly, the shadowed area will be calculated by evaluating which 2D case the configuration represents.

A simple shadow casting algorithm is used to map the vertices on the solar panel. Consider a vertex **A** which casts a shadow **Sa** on the solar panel as a result of a light source **L**. First, a vector **V** is constructed from the light source to the vertex:

$$\mathbf{V} = \mathbf{A} - \mathbf{L}$$

Next, this vector is lengthened so that it touches the plane of the solar panel:

$$\mathbf{V} = \mathbf{V} * \left(\frac{(\mathbf{y_1} + \mathbf{y_2})}{\mathbf{y_1}} \right)$$

with y_1+y_2 the distance from the light source to the plane and y_2 the distance from vertex A to the plane. The distances y_1+y_2 and y_2 are equal to:

$$y_1 + y_2 = \frac{\mathbf{N} \cdot \mathbf{L}}{|\mathbf{N}|}$$

$$y_2 = y_1 + y_2 - \frac{\mathbf{N} \cdot \mathbf{A}}{|\mathbf{N}|}$$

Lastly, the vector **V** is added to the position of the light source:

$$\mathbf{Sa} = \mathbf{L} + \mathbf{V}$$

The second step is to express this vector, which is expressed in the inertial frame, in the solar panel frame. The solar panel frame has two of its axis coinciding with the sides of the panel:

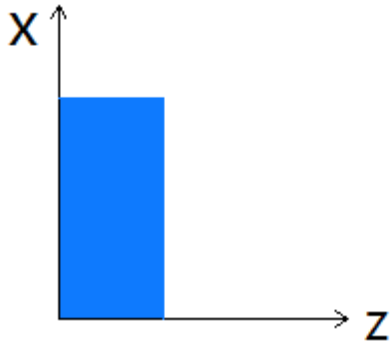

Figure 2 Example: a 2U solar panel viewed from the X-Z axis

The transpose of the rotation from the body frame to the inertial frame will express the shadow point in the body frame. Depending on which panel is shadowed the rotation matrix from the body frame to the solar panel frame can be determined, which is a function of the solar panel deployment angle.

The third step is to calculate the shadowed area. There are a number of cases possible depending on the geometry of the problem. For example, a vertex could lie outside of the filled area resulting in either a triangular shadow or an irregular polygonal shadow:

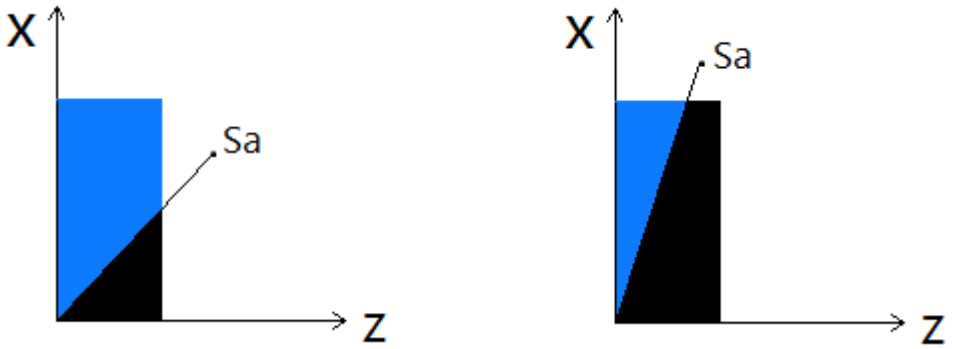

Figure 3 An example of geometry differences of the shadow projected on the solar panel. (Left) A triangle case. (Right) An irregular polygon shape.

Numerical Results for UNSW EC0 Cubesat

Time Variation of Generated Electrical Power

The method described above yields the power input to the system at any point in the orbit. For example, for an equatorial orbit ($i=0°$) at 320km altitude with solar panels deployed at 180° produces.

The 'No shadowing' power output is a simulation with transparent solar panels, i.e. even though a panel might be shadowed by another it still receives power in this simulation. As can be seen, the power output is smaller when self-shadowing effects are taken into account. The difference in the evaluation of instantaneous generated power can be up to 30%, which amounts to a significant 15% in difference in orbit averaged terms. The regions where the two cases overlap means no panels are in shadow. Between 1300s and 4000s, the spacecraft is in the earth's eclipse, resulting in zero power output.

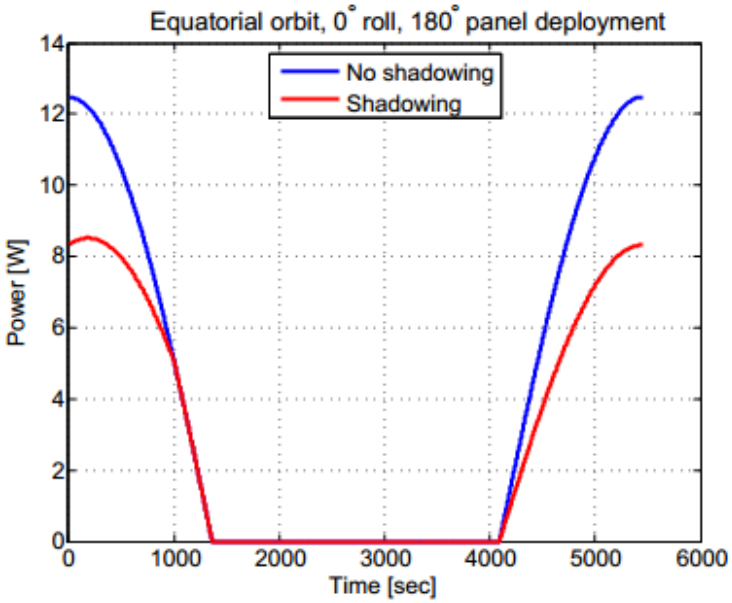

Figure 4 Typical power output profile

Analysis of Solar Panel Deployment Angle and Roll Angle

By computing the power input over an entire orbit the orbit average power can be determined. For this analysis, Orbit average power is computed for various deployment angle and satellite attitude roll angle to identify the optimal satellite configuration for power generation for a particular Sun Synchronous Orbit.

The simulation scenario assumes a circular orbit at 320 km altitude. The inclination is 98° and the right ascension of the ascending node (RAAN) is varied between 0° and 90° in steps of 15° corresponding to a local time of ascending node (LTAN) from 12 o'clock to 6 o'clock. For each LTAN (another representation of RAAN) the simulation is run for various combinations of solar panel deployment angle and roll angle. The power output expressed in this section is the orbit-averaged power.

The contour plots below depicts the power output as a function of roll angle and solar panel deployment angle. The roll angle is varied between -180° and 180° in steps of 3°. The solar panel deployment angle is varied between 90° and 180° in steps of 3° as well.

The first case in Figure 5 is an orbit with a LTAN of 12 o'clock at where the orbit intersects the equator directly at 0° longitude. In all LTAN configurations above, one particular deployment angle can be found to be best performing in most cases, yielding approximately 4W. However, this pales in comparison with the LTAN of 6 o'clock where the optimal power output is expected to be in excess of 11W (see Figure 7). In general terms, LTAN of 12 o'clock can be seen as the worst orbit in this analysis while LTAN of 6 o'clock is considered the best orbit.

Using the deployment angle of 160°,

Table 1 summarises the optimal roll angle for various LTAN. The table can be extrapolated for LTAN outside the range considered here as the result is analogous to the four quadrant system because the geometries remain the same.

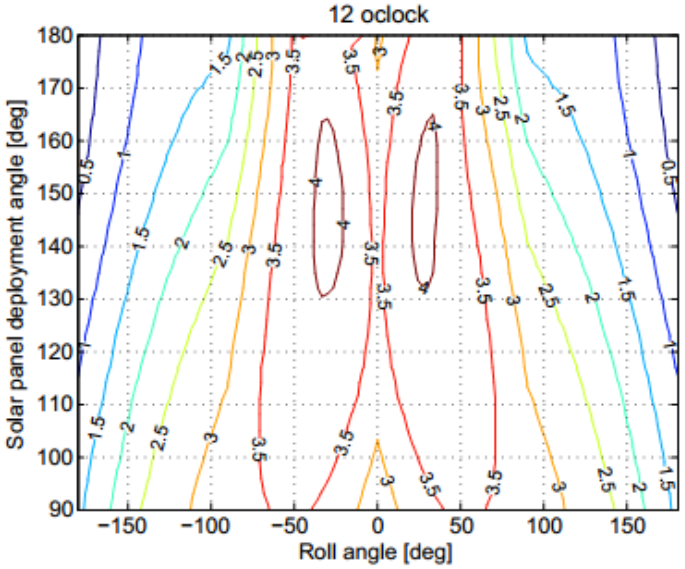

Figure 5 Power output at LTAN of 12 o'clock

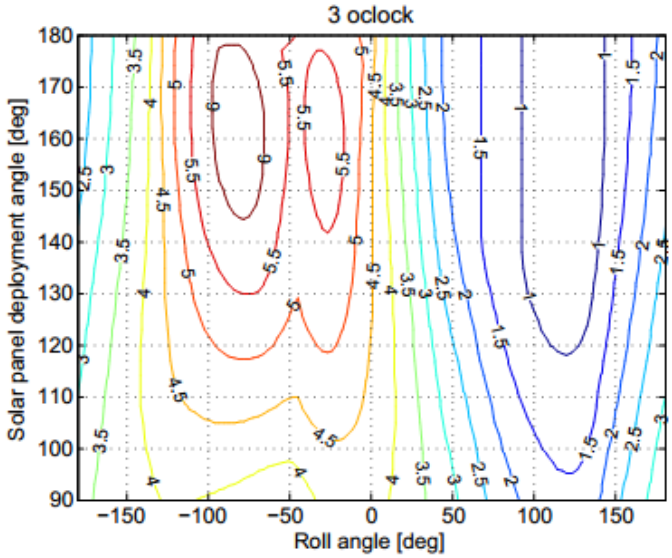

Figure 6 Power output at LTAN of 3 o'clock

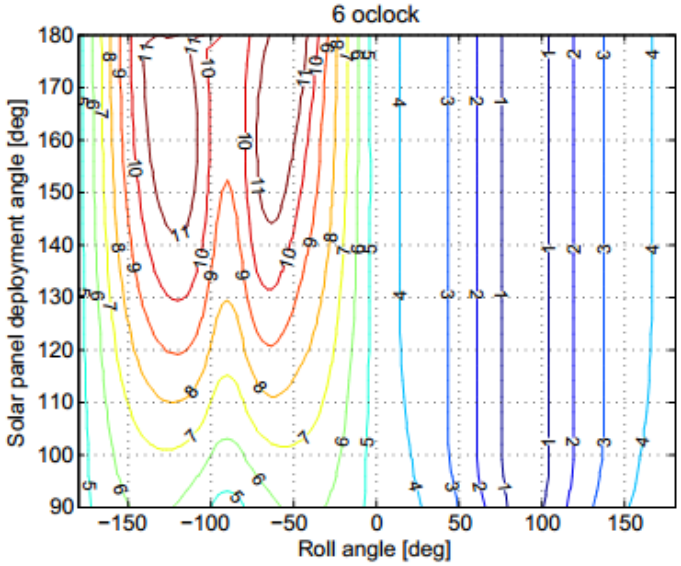

Figure 7 Power output at LTAN of 6 o'clock

Table 1 Summary of generated power and optimal roll angle for a given LTAN for solar panel deployment angle of 160°

LTAN	Orbit avg. power [W] 0° roll	Orbit avg. power [W] Optimal roll	Optimal roll angle [deg]
12 o'clock	3.22	4.05	30
1 o'clock	4.08	4.5	-51
2 o'clock	4.66	5.3	-66
3 o'clock	4.55	6.28	-81
4 o'clock	4.39	7.36	-96
5 o'clock	5.02	11.2	-123
6 o'clock	4.62	11.9	-123

Application to Electrical Power Margin Analysis

Efficiency of the EPS

The EPS contains two large power consumers, i.e. a boos-converter to convert the voltage from the solar cells up to the batteries and a buck converter to condition the power to the user. These two components determine the overall efficiency of the system. The NanoPower datasheet specifies the efficiency of both components. The boost converter's efficiency is a function of the input power (at a fixed battery and input voltage). Therefore, the overall efficiency of the system will depend on the input power as well. The buck converter's efficiency decreases with output current. The 3.3V converter and 5V converter have different efficiencies for a given output current. The overall efficiency of the system is determined by multiplying the efficiencies of both converters. As a result the efficiency depends on the power input and output current of the system. For each mode the efficiency has been determined accordingly.

Electrical Power Loads and Power Budget

The satellite's operation is simplified for this analysis such that it can only operate in one mode at any one time. Each mode will power up one mode or more. For any one particular mode, the

orbit averaged duty cycle of this load is used for calculation. The justification for orbit averaged duty cycles of each load and description of each mode will be discussed below.

Idle mode or Safe mode: in case the satellite switches to safe mode it is essential that the ground station can communicate with the satellite. Therefore, the UHF RX and UHF Beacon are on constantly. The other two vital components, i.e. the OBC and EPS are on as well. The attitude of the satellite is left uncontrolled.

ADCS Pointing mode: the OBC and EPS are turned on for 100% of the time as well as the components required to determine the attitude of the satellite, i.e. the CubeSense, course Sun sensors, magnetometer, gyroscope and Namuru GPS. The magnetorquers are in standby and have a duty cycle of 10% based on the power consumption in standby (i.e. 0.1W).

ADCS Detumbling mode: the ADCS system uses B-dot control to make sure the satellite is detumbled after it has left the launcher. The magnetometers and magnetorquers are at 100% duty cycle, as well as the gyroscope and course Sun sensors. CubeSense is in standby-mode hence the 28% duty cycle (0.1W standby / 0.36W).

Comms mode: for this mode, the UHF communications module is listening and transmitting data down to the ground. The attitude is maintained by using CubeSense, the gyroscopes and Namuru GPS receiver as sensors and the magnetorquers are on standby for control. The UHF transmitter requires 5W when transmitting thus increasing the power consumption of the satellite. The batteries are necessary to deliver extra power.

INMS mode: for the INMS mode it is crucial that the vehicle remains velocity-vector pointed. Hence the CubeSense, gyroscopes, course sun sensors and Namuru GPS receiver are on 100%. The magnetometers are 50% in standby mode and 50% active yielding a duty cycle of 70% considering the power input for the standby mode is lower (0.1W) than when active (0.96W).

Namuru mode: in this mode the radio occultation and radio reflectometry experiments are conducted. For the radio reflectometry experiment the satellite has to be pointed in the nadir direction. This requires attitude control, hence the sensors are turned on. The same as with the INMS mode the magnetorquers are expected to be active 50% of the time.

RUSH mode: the RUSH payload has no attitude control requirements hence the magnetorquers are put on standby to keep the satellite stable. Attitude sensors are turned on as well. At this point it is investigated whether RUSH can be running while the INMS is turned on. One of RUSH's tasks is to detects SEU's and the INMS data can be used to correlate between ion/neutron density and SEU's.

SeL4 mode: in order for seL4 payload to prove that it can perform mission critical task it has to perform the same ADCS tasks as the OBC. Hence, the same instruments as in the attitude determination mode are turned on as well as seL4 itself. The maximum power consumption of seL4 is 3W when it is performing an experiment. However, this will only run for 50% of the time. For the rest of the time a lower power level is required. Therefore, the duty cycle is set to 80%.

The UHF Communications mode, INMS mode, RUSH mode and seL4 mode do not have any roll angle requirements. Therefore, if all ADCS modules are fully operational, the roll angle can be commanded such that the power output is maximum. For a moderate case orbit of 3 o'clock LTAN with solar panel deployment angle of 135° at an optimal roll angle of around -90° (Figure 6). The orbit average power output is then expected to be at a higher level, at 5.5W. The generated power for nominal operation in Table 2 is based on this configuration and assumption.

The power budget spreadsheet is shown in Table 2. It demonstrates an overall positive power margin (36%) for operations when power profiles of the modes are considered in conjunction with the orbital average duty load.

Other Worst Case Considerations

A worst case has been considered; no solar panel deployment in an orbit with a LTAN of 12 o'clock. Thus, the satellite has only one solar panel facing the Sun. In this case, the orbit average power generated is expected to be 1.1W which allows it to still be marginally operational in idle mode (also known as the safe mode).

The detumbling mode is entered when the satellite is first deployed from its launcher or when the satellite is intermittently loses control of its attitude. When in Detumbling mode The orbit average power generation is 2.75W, given solar panel deployment angle of 135° has been chosen given a worst orbit at 12 o'clock LTAN. This is computed by taking a number of random orientations during one orbit. The power consumption of Detumbling mode is not shown in Table 2 for brevity but it is calculated to be within range of generated power.

Another scenario to consider is when the satellite can be stabilised to a default roll angle but unable to change its roll angle while in orbit. In practice, the default roll angle needs to be set to 0° so that it can satisfy all missions' requirements. However, this roll angle is not the best for solar power generation as can be seen in Figure 5-7. Given a worst case of LTAN of 12 o'clock and choosing the best possible solar panel deployment angle of 135°, the orbit averaged power generation in this case is found to be 3.5W (see Figure 5).

From the power margins calculated, it is clear that some modes require extra power from the batteries. However, it has to be noted that the power budget has been formed based on orbit average power generation. Some modes will only run for a couple of minutes which could mean the instantaneous power generation is sufficient even though the orbit average is insufficient. Currently, a mission scheduler is developed which takes into account instantaneous power generation and schedules the modes based on this.

Table 2 Orbit averaged power budget sheet for UNSW-EC0

			Power Budget by Average Operational Orbit					
		% Orbit time	0.167	0.032	0.600	0.002	0.150	0.050
Loads	**Power Consumption (W)**	**Units**	*Idle Mode*	*UHF Comms Mode*	*INMS Mode*	*Namuru Mode*	*RUSH Mode*	*seL4 Mode*
OBC	*0.29*	*1*	*100*	*100*	*100*	*100*	*100*	*100*
UHF RX	*0.2*	*1*	*5*	*100*	*0*	*0*	*0*	*0*
UHF TX	*5*	*1*	*5*	*100*	*0*	*0*	*0*	*0*
UHF TX (beacon)	*0.13*	*1*	*100*	*0*	*100*	*100*	*100*	*100*
Magnetorquer	*0.96*	*1*	*0*	*10*	*70*	*70*	*10*	*10*
CubeSense	*0.36*	*1*	*0*	*100*	*100*	*100*	*100*	*100*
Course Sun Sensors	*0.01*	*5*	*100*	*0*	*100*	*100*	*100*	*100*
Magnetometer	*0.05*	*1*	*100*	*0*	*0*	*0*	*0*	*100*
Gyroscope	*0.05*	*1*	*100*	*100*	*100*	*100*	*100*	*100*
EPS	*0.125*	*1*	*100*	*100*	*100*	*100*	*100*	*100*
Namuru GPS	*1.2*	*1*	*0*	*100*	*100*	*100*	*100*	*100*
RUSH: FPGA	*2*	*1*	*0*	*0*	*0*	*0*	*100*	*0*
seL4	*3*	*1*	*0*	*0*	*0*	*0*	*0*	*80*
INMS	*0.84*	*1*	*0*	*0*	*100*	*0*	*0*	*0*
Thermistors	*0.05*	*0*	*100*	*100*	*100*	*100*	*100*	*100*
Sum loads (W)			0.96	7.32	3.72	2.88	4.30	4.75
Efficiency			0.86	0.84	0.87	0.86	0.87	0.84
Power Consumed (W)			1.12	8.72	4.25	3.35	4.92	5.66
Power Generated (W)			5.5	5.5	5.5	4.5	5.5	5.5
Power Margin (%)			80	-59	23	26	10	-3

Total orbit averaged power margin

Power Consumed (W)	3.51	W/hr
Power Generated (W)	5.50	W/hr
Power Margin (%)	36	

Conclusion

A simplistic model for power analysis that ignores shadowing effects can lead to overoptimistic estimates for expected solar power generation. This paper showed that using simple vector calculations and transformation matrices, the average illumination of the solar panels due to its orientation, shadow and orbit can be accurately characterised for power budget analysis. It is shown via an example that the instantaneous power generated from solar panels can in reality be up to 30% lower (15% lower in orbit averages power generated) when actual self-shadowing effects are taken into account.

Using the UNSW EC0 Cubesat as a case study and accounting for self-shadowing effects, an optimum deployment angle for its deployable solar panels and an optimal satellite roll attitude can be found for a given LTAN (or RAAN) in a sun-synchronous orbit. This has been achieved with simple numerical vector calculations based on simple ray tracing techniques, without any assistance of any CAD software.

The computed solar power generation analysis is then applied into the case of UNSW EC0's power budget analysis. It is shown that the UNSW EC0 has a power margin of approximately

36%. In other words, this Cubesat mission can achieve – on average – 36% more power generation than the expected power consumption.

References

[1] Von Karman Institute. (2015). *QB50, an FP7 Project*. Available: https://www.qb50.eu

[2] GOMSpace. (2015). *Nanopower P31u*. Available: http://gomspace.com/?p=products-p31u

[3] (2016). *Effect of Temperature | PVEducation*. Available: http://www.pveducation.org/pvcdrom/solar-cell-operation/effect-of-temperature

[4] A. Noureldin, T. B. Karamat, and J. Georgy, "Basic Navigational Mathematics, Reference Frames and the Earth's Geometry," in *Fundamentals of Inertial Navigation, Satellite-based Positioning and their Integration*, ed: Springer, 2013, pp. 21-63.

[5] M. J. Sidi, *Spacecraft Dynamics and Control: A Practical Engineering Approach*: Cambridge University Press, 1997.

[6] W. De Soto, S. Klein, and W. Beckman, "Improvement and validation of a model for photovoltaic array performance," *Solar energy,* vol. 80, pp. 78-88, 2006.

[7] A. S. Glassner, *An introduction to ray tracing*: Morgan Kaufmann, 1989.

Attitude Determination and Control System Implementation for the EC0 (QB50 Project) at UNSW

James Bultitude, Ben Southwell, Tim Broadbent, Yiwei Han, Li Qiao,
Joon Wayn Cheong, Barnaby Osborne

Australian Center for Space Engineering Research (ACSER)
University of New South Wales, Sydney, Australia

Summary: An Attitude Determination and Control System (ADCS) is implemented to provide de-tumbling and pointing capabilities for the University of New South Wales EC0 Cubesat as part of the QB50 project. This ADCS implementation is based upon a MATLAB - STK simulation model developed at UNSW. The 2U Cubesat utilises a sun and an earth sensor, 3 axis gyroscope and 3 axis magnetometer to provide attitude determination through an extended Kalman filter. Based on the calculated attitude, the attitude control algorithm then actuates a set of varying pulse width modulated (PWM) outputs to the 3 axis Magnetorquer to manoeuvre the Cubesat. This paper details the software development and hardware integration and testing of the Detumbling controller of this system for a 2016 launch opportunity. The findings cover the functionality of the system, as well as a discussion of the low-cost testing methods selected for subsystem verification and validation.

Keywords: Attitude Determination and Control, Cubesat, Satellite, Magnetorquers, B-Dot, Magnetometers, Detumbling, QB50

Background

The QB50 Project at UNSW

The QB50 project is a planned network of 50 Cubesats which will be launched from the ISS in 2016 into a 'string-of-pearls' formation. These Cubesats will initially have the same altitude as the ISS and due to atmospheric drag, their orbit will decay over a mission lifetime period of three months or longer. As their orbit decays they will take readings of the largely unknown lower thermosphere and ionosphere. The measurements will be taken at many spatially and temporally separated points providing insight that traditional missions could not provide. The EC0's primary payload, which also is its primary objective, is the Ion Neutron Mass Spectrometer (INMS) which is used to characterise the content in the earth's atmosphere that the Cubesat is travelling in for scientific research. The UNSW QB50 will additionally carry the following experiments which dictate its secondary goals:

- Namuru Space GPS receiver: Developed entirely by UNSW to investigate the use of GPS reflected off the sea surface and refracted GPS signals over the ionosphere which can be used for sea state monitoring and weather prediction.
- seL4: A NICTA developed experiment to demonstrate the high-assurance seL4 Operating System in use in space environments to verify its fault tolerant capability.
- RUSH: A rapid recovery system from single event upsets, which should allow for rapid reconfiguration of hardware resources.

To achieve these objectives, the Cubesat will need to be capable of slowing its rotational speed from a tumbling state (a process called Detumbling) and manipulate its attitude such that the INMS payload will point in the direction of travel (a process called Pointing), This paper details the development and testing of the Detumbling subsystem for the Attitude Determination and Control System (ADCS) for this Cubesat. The best method for testing cube satellites ADCS which operates in rotational modes is determined to be an air bearing table system.

Air Bearing Test Beds

There are three main types of air bearing spacecraft simulators. Firstly, rotational tables allow for a body to be rotated in one, two or three degrees of freedom (DoF). They do not allow for any translational motion. Rotational simulators are good for investigating how well reaction wheels, magnetorquers and similar can actuate the spacecraft and oppose the influence of external torques. However they are limited in their applications; when translation is necessary, the simplest configuration is that of the planar test bed. They typically allow for motion in three degrees of freedom but some simple system only allow for two or possibly even one. It is also now possible to design a system that will allow complete simulation in all six degrees of freedom within set bounds [1].

Rotational or spherical systems are useful for testing orientation as they allow the relevant rotational DOFs. An ideal design would allow for complete freedom on all three axes of rotation, however typical spherical air bearing designs limits the pitch and roll. It provides a relatively external torque independent environment, with complete rotation freedom about the yaw axis, and constrained motion about the Pitch and Roll axes. This motion is constrained by the geometric constraints of the test system. A spherical air bearing was determined to be the appropriate test apparatus.

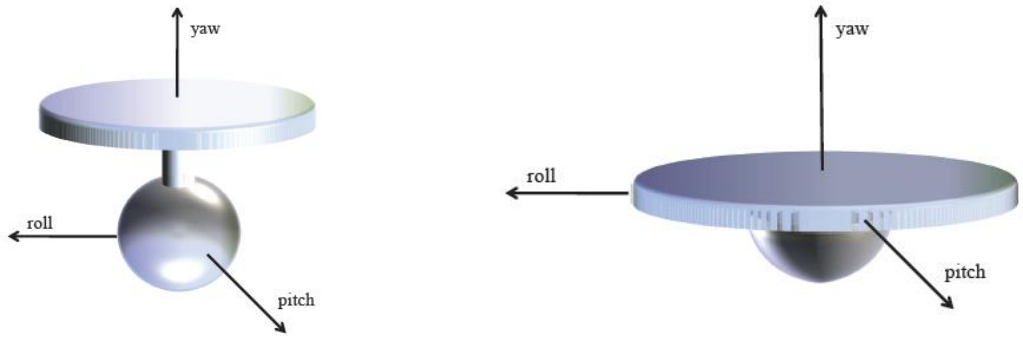

(a) *(b)*

***Figure 1**: Spherical Air Bearing Systems: (a) Umbrella Style and (b) Table Top[2]*

Two main types of spherical air bearing test systems exist; table top and umbrella style. Both configurations (see figure 1, above) allow for unconstrained 360 degree rotation about the 'z' or Yaw axis. Motion about the other two axes is constrained by the support structure for the air bearing. The umbrella style increases this freedom of motion, by moving the plate which contains the experiment away from the air bearings rotation region. The table top type is used in our ADCS testing.

The now popular cube sat under went ACS testing on a spherical air bearing test bed at York University. Because of the scale of the CubeSat, the entire satellite was able to be physically tested instead of a modelled copy. The test system included a manual balancing system, and platform electronics that include an on-board computer (OBC), wireless transceiver for

telemetry, reference inertial measurement unit (IMU), power distribution board, and batteries (Li et al., 2013) [5].

In this paper, the Table Top Spherical Air Bearing System is chosen for its simplicity in setting up. The Umbrella style requires the center of gravity (COG) to be accurately aligned with the center of rotation (COR) in all three dimensions whereas the equivalent alignment is required for only two dimensions for the Table Top style to function. For the case of the Umbrella style, a slight misalignment between COG and COR will result in an imbalance that can potentially damage the engineering model cubesat under testing. In configuring the Table Top style, the COG is positioned slightly lower than the COR to achieve a "bottom-heavy" configuration so that the balancing in the horizontal plane can be more easily achieved.

This paper focuses on the implementation and validation of the detumbling phase of ADCS. The cubesat's detumbling control system is imperative to ensure reliable communications and power systems at the most vulnerable phase of the cubesat's operation in space (i.e. post-deployment phase). Most published studies in ADCS has focussed on algorithms, and numerical simulations. There are no studies that describes the hardware test setup and specific parameter values used to verify the detumbling of an actual cubesat.

ADCS System

Sensors

The sensors on-board the EC0 consist of two three axis magnetometers, a three-axis MEMS Gyroscope, a three-axis accelerometer and a pair of earth/sun sensors. For Detumbling purposes, as detailed in this paper, only the magnetometer is utilised. The primary magnetometer is located on the on-board computer (OBC) PCB and is a HMC5843 manufactured by Honeywell. The secondary IMU sensor chip is integrated into the system for the purposes of redundancy and fast tracking debugging. This chip is the LSM303DLHC sensor manufactured by STMicroelectronics and is located on a custom board designed in house at UNSW. Both of the magnetometers are polled for data and are on separate I2C bus' providing some level of redundancy.

Actuator

The ISIS magnetorquer board – iMTQ – is a 3-axis magnetorquer system and was chosen for actuation of the Cubesat. This was due to the ease of integration as we were already sourcing components from ISIS as well as the simplicity and low mass, power and volume of magnetorquers in comparison to other attitude control actuators.

The magnetorquers produce torque via the interaction of a magnetic dipole moment created by the magnetorquer and the presence of an external magnetic field. The torque produced by the magnetorquers $\vec{T}$ is expressed as:

$$\vec{T} = \vec{m} \text{ x } \vec{B} \quad (1)$$

Where $\vec{m}$ is the magnetic dipole moment produced by the magnetorquers and $\vec{B}$ is the Earths magnetic field. It can be seen from equation 1 that the torque produced by the magnetorquers is not a function of the distance of them from the centre of rotation of the Cubesat easing constraints on placement of components in the Cubesat. It is also apparent from equation 1 that the control system is under actuated as the torque produced is always perpendicular to the Earth's magnetic field.

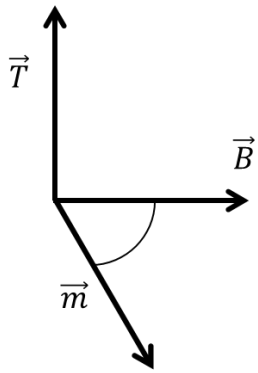

Figure 2: *The Torque produced from the interaction of the magnetic dipole moment and the Earth's magnetic field*

Detumbling Algorithm

The ADCS software is implemented in the GOMSpace NanoMind A712D OBC. The OBC integrates all of the sensors into a single runtime, directly controls the magnetorquers with embedded PWM controllers and hosts the Detumbling and the pointing task. Recalling that the purpose of Detumbling is to reduce the rotational rate of the Cubesat to a level which is an acceptable initial condition for the pointing controller; the Cubesat does not have to completely eliminate its angular velocity. Therefore, it is desirable to implement a robust controller in place of a better performing but more complex and less reliable controller for Detumbling.

The B-Dot controller is based on the measurement of the rate of change of body-fixed magnetometer signals of the Earth's magnetic field B in low Earth orbit (LEO) and applying a magnetic dipole moment along the direction of the rate of change of the Earth's magnetic field hence the name B-Dot [3]. The sign of the magnetic dipole moment along the B-Dot unit vector determines whether the resulting torque will be accelerating or decelerating the Cubesat.

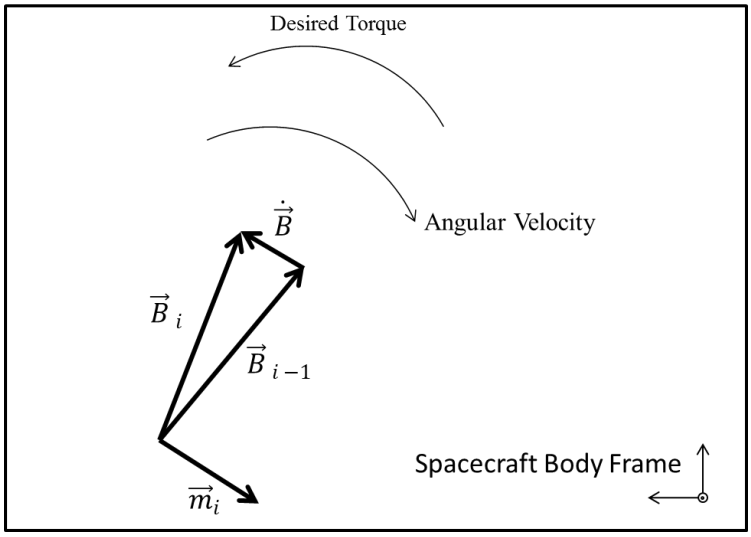

***Figure 3**: B-Dot in the spacecraft body frame*

Figure 3 illustrates that discrete sampling of $\vec{B}$ can be used to calculate $\dot{\vec{B}}$ through the backwards difference method.

For Detumbling, a gain is used to calculate the required magnetic dipole moment from $\dot{\vec{B}}$ which is expressed as:

the resultant torque is:

$$\vec{T} = \vec{m}_i \text{ x } \vec{B}_i \tag{2}$$

The torque can be seen to be in the opposite direction of the angular velocity of the spacecraft. The QB50 ADCS system requirements specify that the Cubesat must be able to detumble from a maximum of 10 degrees per second, therefore with a controller update rate of 1Hz the direction of $\dot{\vec{B}}$ from the difference between two subsequent measurements is sufficiently close to the true direction of $\dot{\vec{B}}$ for Detumbling purposes. Due to the simplicity and robustness of the B-Dot controller it was selected for our Detumbling algorithm.

Because the commanding of the magnetorquer is time-sensitive, extreme care must be taken in the RTOS task scheduling to ensure that either task execution jitter is not present or that the controller is implemented in such a way that it is jitter invariant. This was done by executing the ADCS task in its own thread and making use of queuing to reduce the jitter associated with calling functions and/or resources in other tasks or in hardware. This is not within the scope of this paper and is not discussed any further.

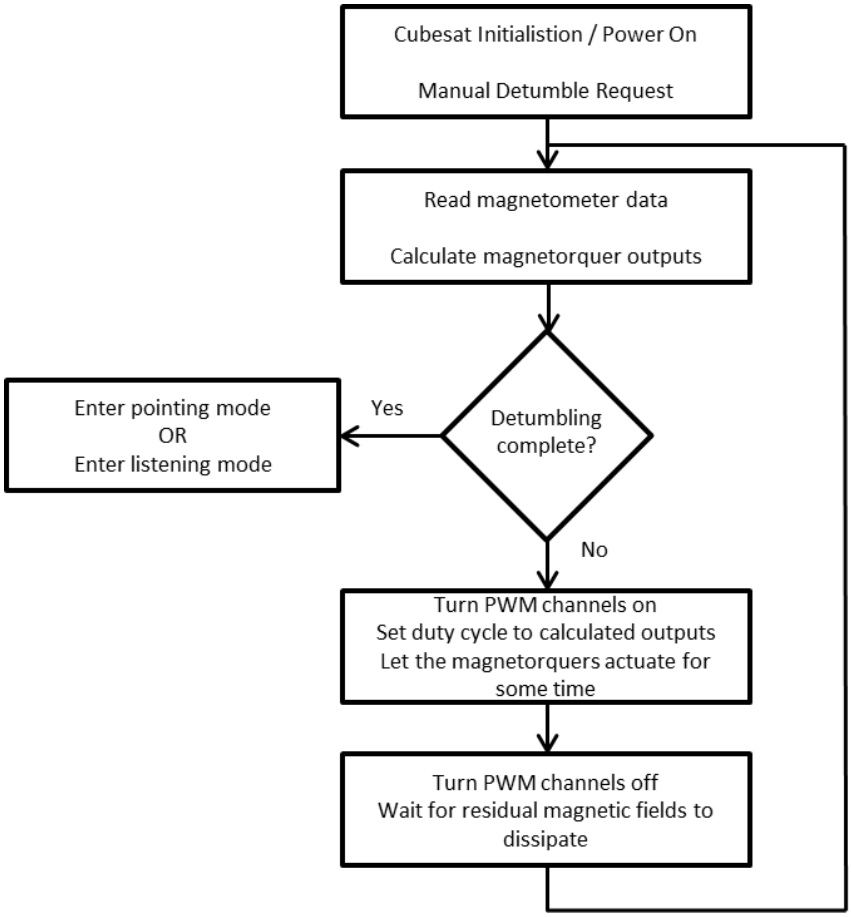

Figure 4: *State Transition Diagram of the Detumbling Task.*

A practical implementation of the B-Dot controller does not allow for the actuation of the magnetorquers permanently as they must be disabled to make magnetometer readings. The time that the PWM channels are disabled proportionally reduces the effective duty cycle of the magnetorquer and thus the average torque produced. Therefore, this time must be minimised. If T_{delay} is the time required for the residual magnetic field to dissipate and for the subsequent code to execute before re enabling the PWM channels then the maximum duty cycle achievable is $\left(T - T_{delay}\right)/T \times 100\%$.

In order to minimise T_{delay} we found that the stack configuration of the Cubesat was key. It was found that shields on some boards were retaining magnetic flux after the magnetorquers actuated leading to the next measurement being distorted. It was also found that empirical characterisation of the Cubesat was required before determining the required T_{delay}. Selecting the value of T_{delay} is the only compromise that is required to be made between robustness and performance when implementing the B-Dot controller.

ADCS Testing

The spherical air bearing test bed

In order to provide physical validation of the interface of hardware and software, a spherical air bearing was utilised for testing. The specifications of the spherical air bearing test setup are provided in Table 1.

Table 1 Specifications of apparatus used for testing the ADCS system

Blackridge BC120 Compressor	
Power	1875 Watts
Throughput	120 L/min
Capacity	40L tank
Nelson Air 3U Cubesat Spherical Air Bearing	
Maximum Pressure	90 psi (run at ~15 psi)
Flow Rate	<1 standard cubic feet per minute
Construction	Hard coat aluminium, stainless steel fasteners
Pitch & Roll Limits	±30 degrees in the ABB pitch and roll axis
Dimensions	250mm diameter bowl
Norgen Excelon B73G Filter and Regulator	
Input/output	3/8" Port
Filter	5 µm Element
Pressure relief	Relieving Diaphragm
Outlet pressure range	5 to 150 psi
RTi Oil Extractor	
Oil Extraction Method	Quad stage: stainless steel, cotton polyester, activated carbon, cotton polyester
Output	Polycarbonate tubing
Flow Rate	60 standard cubic feet per minute
Features	Automatic float drain

Figure 5: *The Filter and Regulator Assembly*

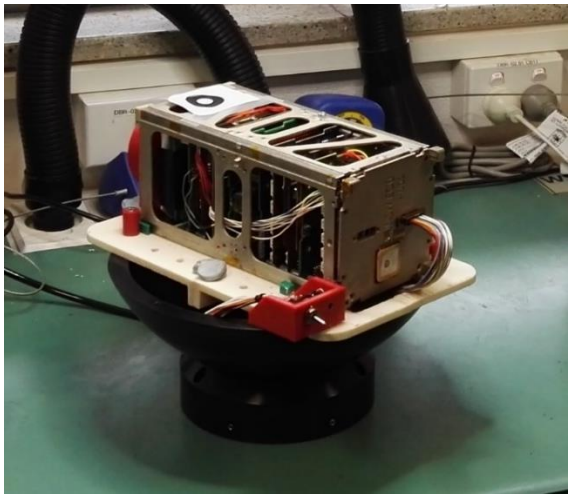

Figure 6: *The satellite located on top of its rapid prototyped 3d printed mount.*

Test Methodology

The satellite is mounted on a 3D printed supporting structure atop the air bearing. It is given an initial angular velocity slightly larger than the 10 DPS specified in the QB50 system requirements. An overhead camera is used to track the rate of angular motion in degrees per second by identifying and recording the position of a visual black and white 'target' marker.

An optical tracking system was implemented in OpenCV for tracking the angular velocity of the Cubesat as it is independent of the ADCS and therefore not susceptible to any software bugs that arise during development. It also provides real-time insights to the Detumbling experiment as well as a log file which is later imported into MatLab for analysis. Furthermore, a baseline test may be carried out easily; the baseline test is a characterisation of the satellite's the satellite in powered off state such that just the natural damping of the air bearing system and air friction within the rom causes the deceleration of the satellite. This can be captured and used as a reference when examining the Detumbling performance. It is important to do this because after the jets of the spherical air bearing apparatus are cleaned, after weight is added or remove from the Cubesat, or after the supply pressure is changed, the natural damping will change and any new experiments must be referenced against the new baseline.

Figure 7: *A typical view during a test, the colour image shows current position and confirms centring; the black and white demonstrates contrast and the number give a time stamp and angular rate in degrees per second*

Turbine Torque

The test setup does not provide an entirely external torque free environment. As air leaves the jets of the bearing cup face, it may not exit in a manner completely perpendicular to the bearing face. This may be due to the jets not being imperfectly aligned. The air may also have a very slight pressure of flow rate difference due to small differences in manufacturing, or the presence of external materials such as dust within the jets. The jets can be cleaned by removing the bearing cup and then wiped with isopropyl alcohol. If left uncleaned, air entering the jets may contain very small traces of dust that may cause clogging of the jets and exacerbate the turbine torque.

This uneven lift from the air jets creates an external torque on the system known as turbine torque. The magnitude and direction of this turbine torque must be re-characterised when the pressure and load weight for an experiment changes.

Balance and Inertial Properties
An ideal test system would place the centre of mass of the entire floated test unit about the centre of rotation of the same system. In this case, the lower steel bearing bowl is by far the heaviest part of the structure. Its centre of mass is located lower within the bowl than the centre of rotation of the system. The system has its centre of mass and rotation coincident in the other two axes.

An ideal system would have its centre of mass raised to this point. By locating the centre of mass below this point, this system is such that it will damp out motion particularly in the Air Bearing Body (ABB) X and Y axes and end up in a stable equilibrium. Raising the centre of mass too high will result in a highly unstable system on both roll and pitch axis. As a result, any imperfect balancing of weight along these two axes will easily result in a rapid acceleration along these axes and followed by an impact as it reaches the spherical air bearing's limits of these axes. This configuration raises the risk of damaging delicate components of the satellite. As such, our experimental setup was configured with a centre of mass below the centre of rotation. As the magnetorquers are not located at the centre of rotation not all of the torque produced by the magnetorquers is useful as a reaction torque from the support structure will be present to restrain the Cubesat.

Implementation Issues
Issues encountered during testing were the interfacing of the software algorithms with the hardware modules. These issues highlighted the importance of a complete system test with the engineering model hardware.

The ideal floating height of the Cubesat bearing is achieved when it is close enough to the air jets as it minimises turbine torque, but yet does not result in any friction with any other parts bottom platform of the air bearing. Thus, any change in the satellite bus and payload configuration will mean that achieving this ideal height requires the adjustment of set pressure of the air regulator.

Before full testing of the ADCS system, it is imperative to determine that the Magnetorquers are physically firing. This can be accomplished easily using a handheld compass and or magnetometer. This process was repeated whenever performing a baseline to remove potential for error.

Electro-magnetic Considerations
The environment that the satellite operates in inside the lab would ideally replicate the environment of the mission. Under typical operating conditions for the ADCS, the electromagnetic environment is of particular importance. The electromagnetic environment in the lab is far from uniform, unlike the expected mission environment. The presence of other lab equipment including computers, compressors, piping and cabling affects this environment. An ideal experimental setup would include a uniform magnetic field. This uniform environment could be accomplished through the use of a Helmholtz coil pair. A Helmholtz coil consists of a pair of loops on wire separated by their radii and both experiencing a similar current [4]. The centre of these coils should provide a fairly uniform magnetic field.

In order to further isolate the system from interference, a Helmholtz like coil pair was implemented. This air was not an idealised Helmholtz Pair, as the distance of separation of the coils was driven by the size of the satellite on its rotating air bearing platform.

The purpose of this Helmholtz like pair, was to allow the Cubesat to develop significantly more torque with the same magnetorquer actuation, as the torque developed is proportional to the magnitude of external magnetic field.

This will allow the Cubesat to overcome any bias torque such as the turbine torque in the air bearing setup, as no bias torques will act upon the Cubesat during spaceflight this test is valid in verifying the detumbling functionality.

The Helmholtz coil pair were fed in series with 28.5 V drawing 72mA. Satellite debugging outputs showed magnetometer readings of approximately 5 to 6 Gauss. This matches the expectations from calculations.

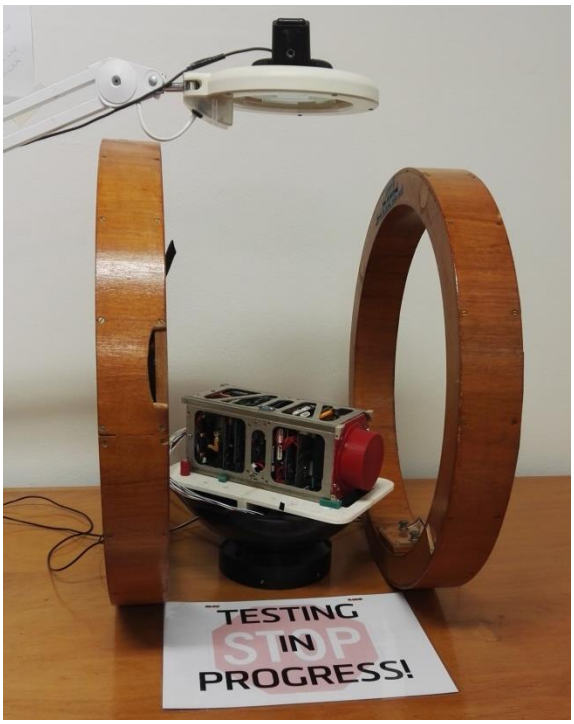

Figure 8: *The Final Test Configuration. The Helmholtz like pair is contained within the wooden boxes. The overhead camera is visible above.*

It is not just the magnetic field of the environment that is of concern. During testing, it was determined that the control system was not performing as expected. The satellite was disassembled and the magnetic properties of each component during operation were examined. It was found that the ferrous shields on the GPS board and Radio Communications board can be magnetised by the magnetorquers, thus were retaining a significant magnetic field.

The solution adopted is to reconfigure the board sequence in the stack to ensure sufficient separation between the magnetorquer and other ferrous materials. The magnetic characteristics of components are an important design consideration that is difficult to anticipate or simulate.

As such, careful testing and verification is necessary throughout all stages of the implementation.

Results

To verify the implementation of detumbling multiple tests were performed using an air bearing and HelmHoltz coil pair. In this section the results of these tests are presented and discussed. The tests were performed by placing the satellite on the air bearing such that the angular velocity would be about both the x and y axis of the satellites body frame. Testing detumbling about the z axis was not practical due to the instability of the set up required to spins the satellite about its z axis (high centre of mass) but the validation of detumbling about the x and y axis utilises the yz and xz magnetorquer coil pairs respectively confirming operation of all 3 magnetorquers with B-Dot control. The angular velocity of the satellite is tracked by a camera mounted above the air bearing and an application utilising openCV running on a PC. It can be seen that the angular velocity oscillates in the following plots; this is due to the misalignment of the camera with the rotational axis of the air bearing alongside minor rocking of the rocking of the bearing face due to slight mechanical imbalance.

Initial Tests without the Helmholtz Coil

Initially, the controller was tested without the use of the Helmholtz coil pair. As the functional requirements of the ADCS subsystem for the QB50 mission require detumbling capability from velocities up to 10 degrees per second (dps) all of the tests have initial velocities slightly higher than 10dps. The first test had an initial velocity of +11dps which corresponds to a negative angular velocity in the Y axis of the satellite body frame of 11 dps due to the way the satellite was mounted on the air bearing.

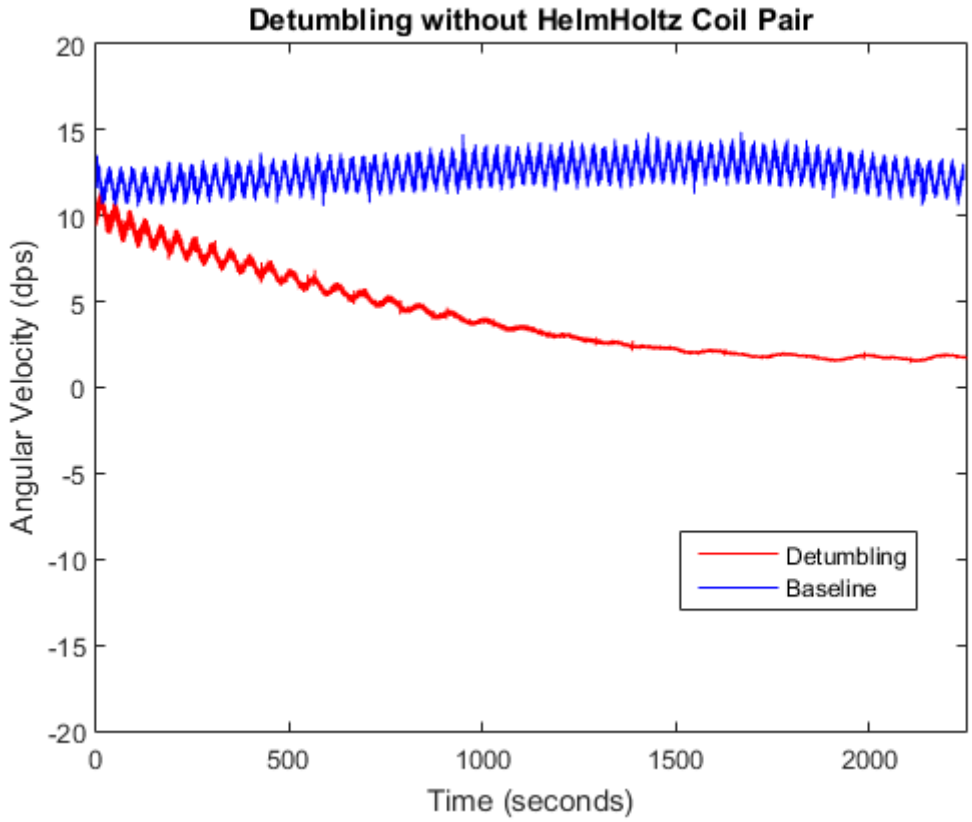

Figure 9: *Angular Velocity vs Time for the Baseline and Detumbling Tests without the HelmHoltz Coil Pair.*

In each of the tests a baseline is performed to act as a reference for the detumbling test. A baseline test consists of applying an initial angular velocity to the satellite and letting it run with the satellite turned off, whilst the detumble tests has the B-Dot algorithm running and magnetorquers actuating. The purpose of the baseline is to provide further insight into the test conditions that are not modelled and provide a reference to compare the detumble results against.

In Figure 9 above it can be seen that the detumbling curve is displaying the expected behaviour of decreasing its angular velocity although the detumble curve asymptotically approaches 1.5 dps (approx..). It can be seen by looking at the baseline curve that there is a considerable bias torque in the positive DPS direction. This error varies with respect the air pressure supplied to the system.

This initial test has verified that the B-Dot controller is operating as expected but for completeness (testing of the controller at angular velocities less than 1.5 dps) the HelmHoltz coil pair was utilised so that the torque developed by the satellite at low angular velocities was sufficient to overcome the turbine torque of the air bearing.

Testing with Helmholtz Coil Pair

The initial test using the HelmHoltz coil pair consisted of 2 baseline tests, one with the coils on and one with the coils off. The purpose of this was to investigate the effect of the strong

magnetic field on the material comprising the structure and components of the satellite. This was performed about the x axis of the spacecraft with a positive dps in the camera frame and negative angular velocity about the satellite x axis.

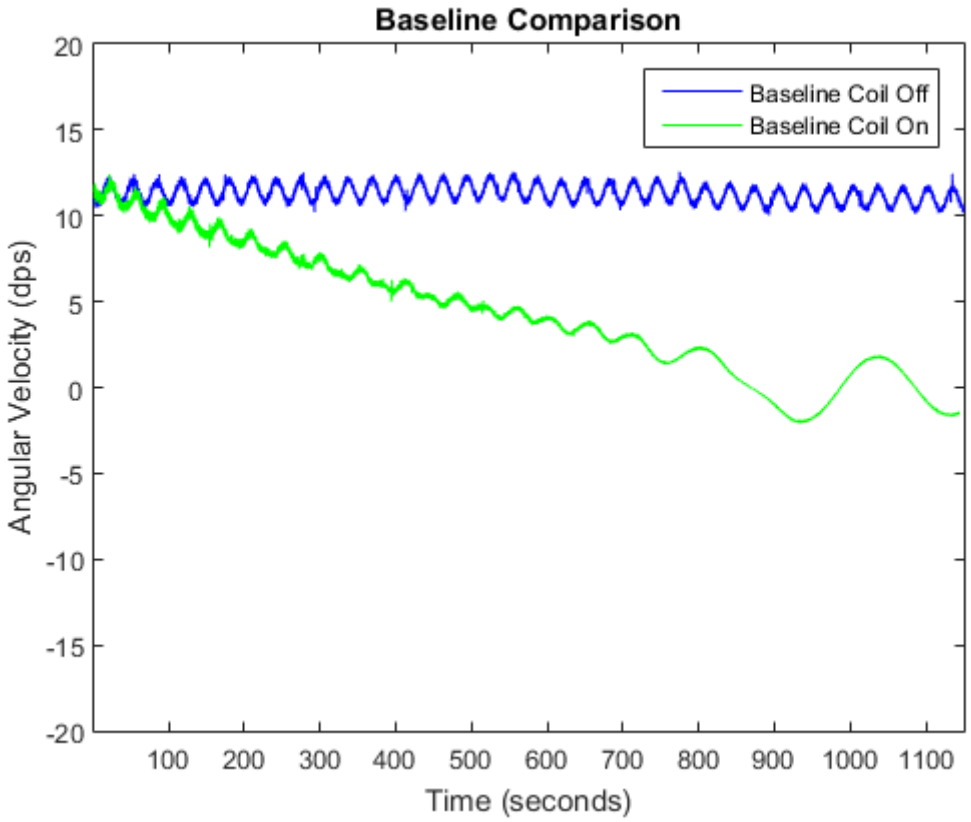

Figure 10: *Angular Velocity vs Time for the Two Baseline Runs with the HelmHoltz Coil On and Off*

In Figure 10 above it can be seen that the baseline test with the coil turned on has a significant damping torque as a result of the interaction of the strong magnetic field generated by the HelmHoltz coil and the material in the satellite alike cogging torque in a stepper motor. This torque is sufficient to overcome the bias torque at low angular velocities. For the remainder of this paper the baseline tests will be performed with the coil pair turned on to provide a suitable reference to compare the detumble tests that will be performed with the coil pair turned on.

Figure 11 depicts the results of two detumble tests about the x axis compared to the two baselines depicted in Figure 10, note the difference in time scale.

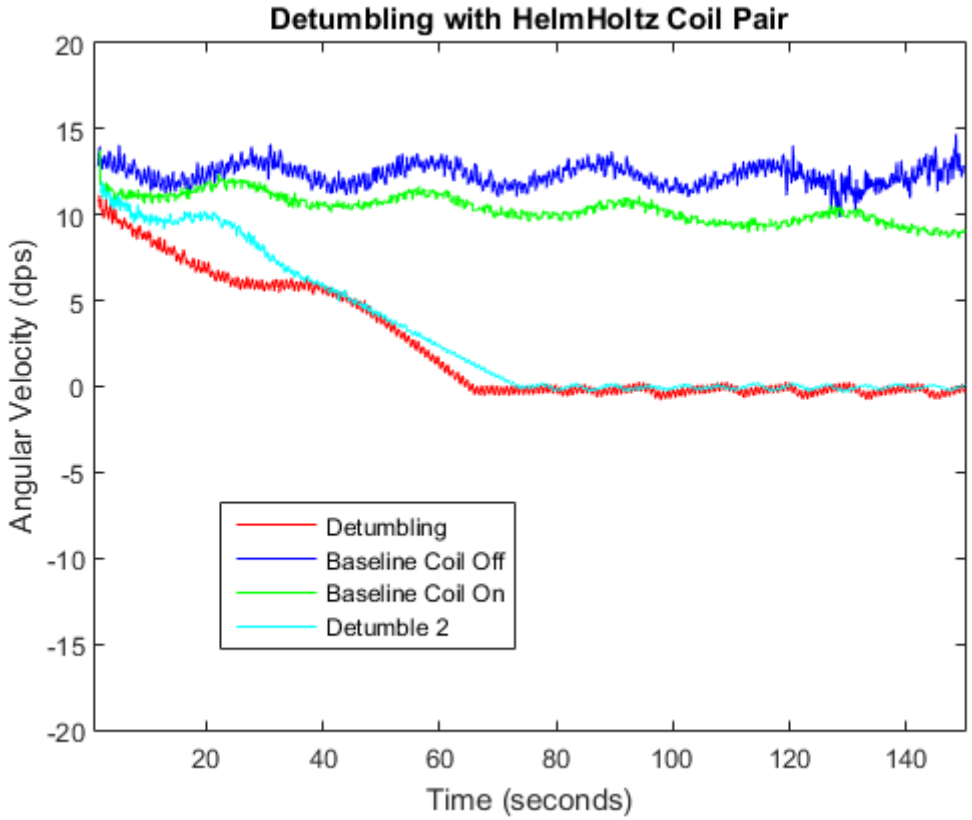

Figure 11: *Angular Velocity vs Time for the Two Baselines and Detumbling Tests Performed with the Helmholtz Coil*

The two detumble runs were performed before and after the baselines for completeness. With the HelmHoltz coil on, not only is the satellite able to develop enough torque to overcome the bias torque at low velocities but detumbling from greater than 10dps is achieved in less than 80 seconds.

Figure 12 depicts the detumbling and baseline results from both positive and negative initial velocities about the x axis whilst Figure 13 depicts the same tests about the y axis. These two figures demonstrate that the B-Dot detumbling algorithm has successfully been implemented on EC0.

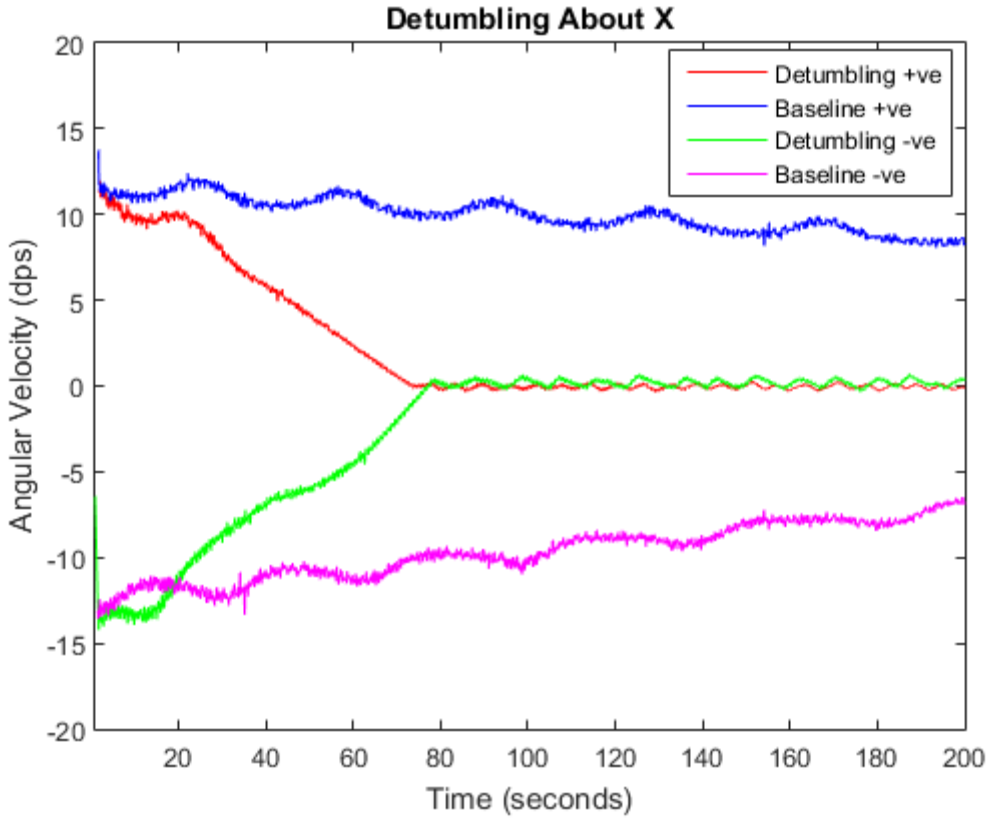

Figure 12: *Results of the Detumbling Tests About the X Axis.*

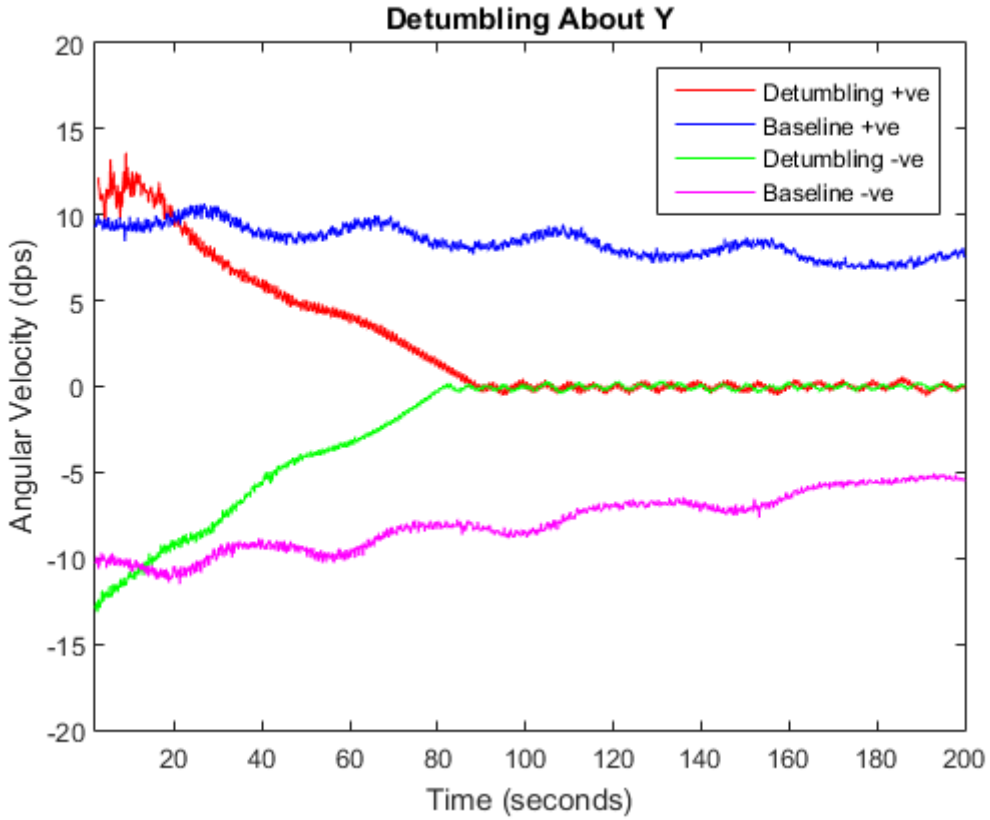

Figure 13*: Results of the Detumbling Tests About the Y Axis.*

It is of interest to investigate the effect of the bias torque further. In figure 12 and figure 13 there is no observable difference between detumbling from a positive or negative initial velocity. However, if we plot the 4 baselines obtained from the detumbling tests in Figure 12 and 13 over a longer period of time in Figure 14 it can be seen that the baselines with a negative initial velocity decelerate more rapidly than the baselines with a positive initial velocity. This agrees with the proposal of an observed bias torque in the positive direction of the camera frame.

The test was not repeated in the third axis, as it was deemed too dangerous to mount the satellite vertically, as a toppling of the rig could cause damage to flight hardware. Further, all axes of the magnetorquer had been tested, as two axes are utilised in each detumble test.

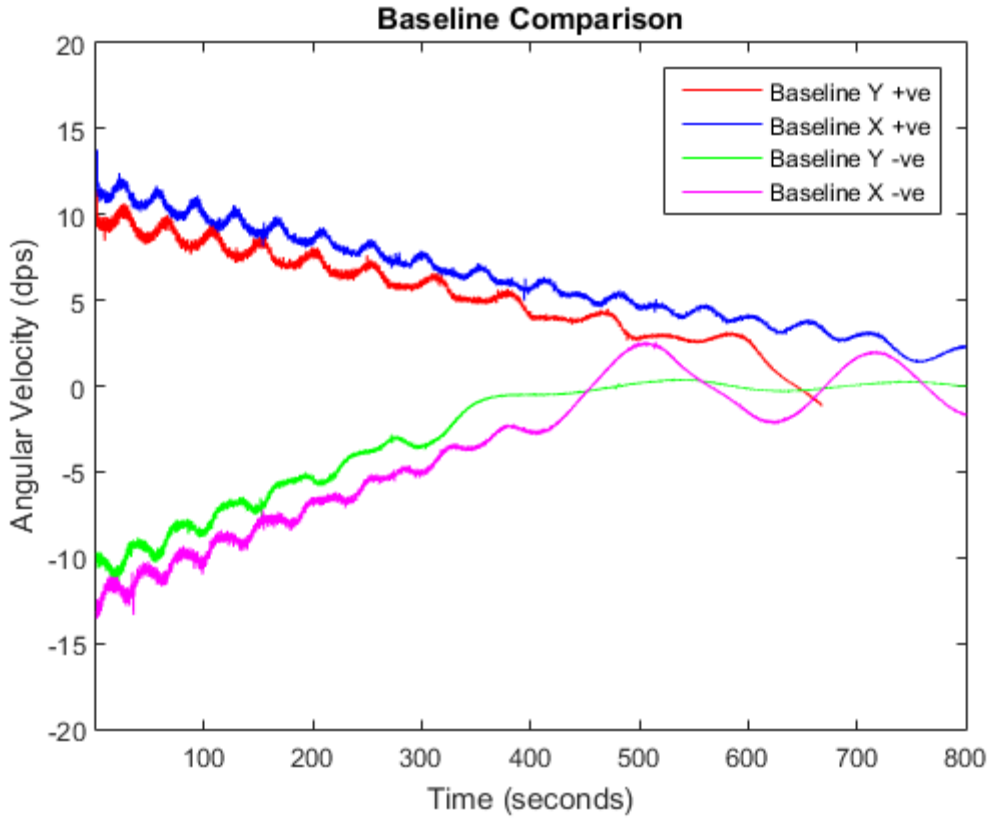

Figure 14: *Comparison of all of the Baseline Runs over a Longer Period of Time*

High Initial DPS Tests

The requirements of the ADCS subsystem for the QB50 mission state that the satellite must be able to detumble from an angular velocity of 10 dps. Whilst the previous results have demonstrated that EC0 meets these requirements it is interesting to investigate the performance of the B-Dot controller with a higher initial angular velocity. Figure 15 and Figure 16 depicts detumbling about the x and y axis similarly to Figure 12 and Figure 13 but with a much higher initial velocity of approximately 45 dps. It would be expected that the B-Dot controller is not as efficient at higher angular velocities as the angular displacement of the satellite between controller updates (at 1Hz) would result in suboptimal actuation. It can be seen in Figure 15 and Figure 16 that EC0 is able to detumble from an initial angular velocity greater than 4 times the expected mission limit.

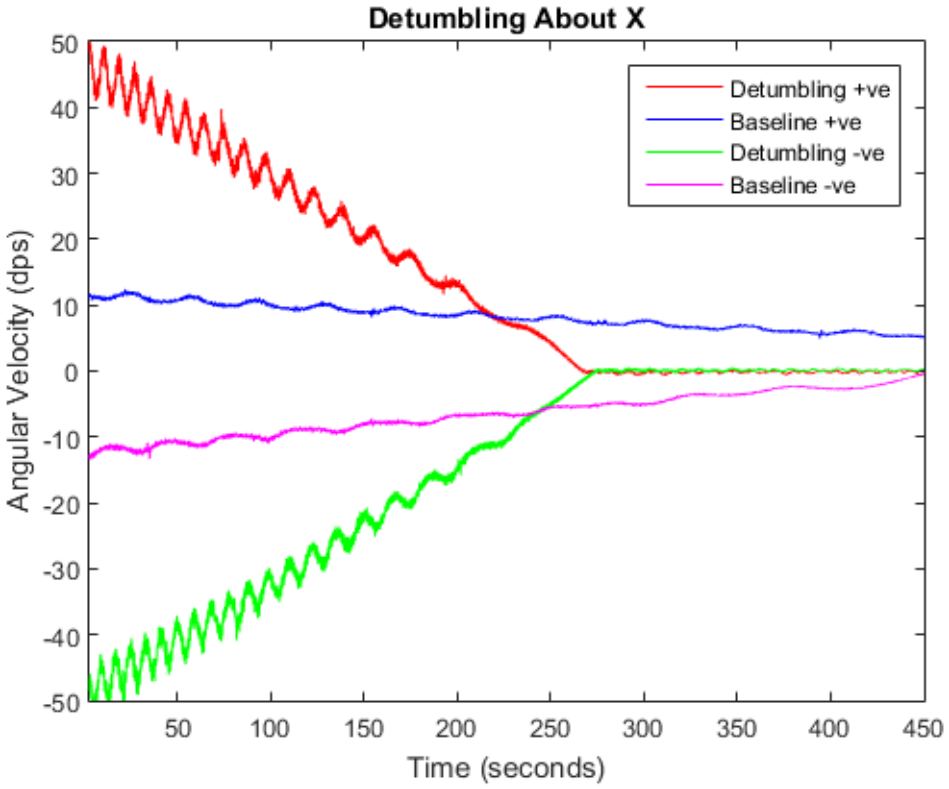

Figure 15: *Results of the High Initial Velocity Detumbling Tests About the X Axis.*

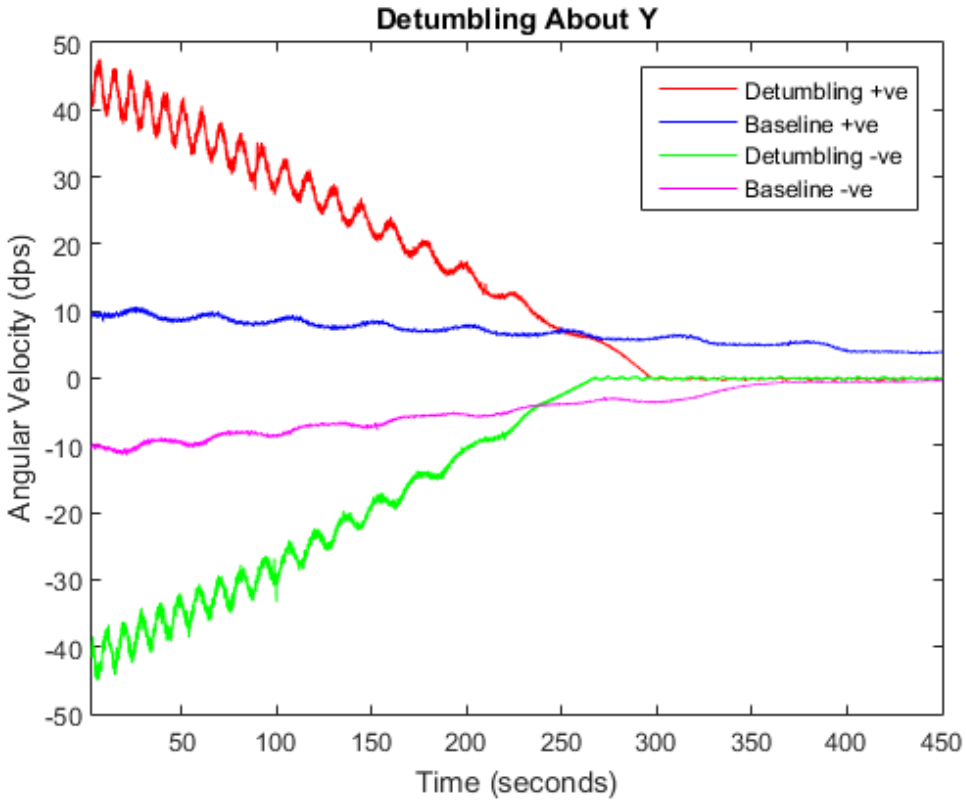

Figure 16: *Results of the High Initial Velocity Detumbling Tests About the Y Axis.*

Conclusion

Spherical air bearing testing is a valid and reliable method of testing a complete detumbling control loop for a cube satellite. When magnetometers and magnetorquers are the primary sensors and actuators in the system respectively, care must be taken to characterise how they interact not just with one another but with other components within the Cubesat.

Acknowledgments

The authors would like to acknowledge the work of the rest of the QB50 team and in particular our fellow ACSER team members.

References

[1] J. L. Schwartz, M. A. Peck, and C. D. Hall, "Historical review of air-bearing spacecraft simulators," *Journal of Guidance, Control, and Dynamics,* vol. 26, pp. 513-522, 2003.

[2] R. E. Snider, "Attitude Control of a Satellite Simulator Using Reaction Wheels and a PID Controller," DTIC Document2010.

[3] T. Flatley, W. Morgenstern, A. Reth, and F. Bauer, "A B-dot acquisition controller for the RADARSAT spacecraft," in *NASA Conference Publication*, 1997, pp. 79-90.

[4] D. J. DeTroye and R. J. Chase, "The Calculation and Measurement of Helmholtz Coil Fields," DTIC Document1994.

[5] LI, J., POST, M., WRIGHT, T. & LEE, R. 2013. Design of Attitude Control Systems for CubeSat-Class Nanosatellite. Journal of Control Science and Engineering, 2013, 15.

Optimal Path Planning for a SLAM Navigation System for the *Parrot AR Drone*

Nicholas Robinson

School of Aerospace, Mechanical & Mechatronic Engineering
University of Sydney, NSW, Australia, 2006
Email: nr@outlook.com.au

Summary: This paper discusses an optimal path planning method based on an improved form of the potential field path planning algorithm in literature for use on a quadcopter unmanned aerial vehicle (UAV) that is navigating in a Global Navigation Satellite Systems (GNSS) denied environment. This is useful for UAVs that must operate in built-up metropolitan areas and in urban canyons where the GNSS signal may be inaccurate or unreliable. Simultaneous Localisation and Mapping (SLAM) fuses inertial information and visual references (from cameras) to allow a robot to localise itself and build a map of its environment without any a priori knowledge, and can be used for navigation in these areas. An optimal path planning system is central to a SLAM system as it optimally decides which areas to visit in order to obtain a better position estimate and also to enlarge the map. The path planning system has been implemented in a 'proof-of-concept' test with dynamic replanning on a low-cost quadcopter UAV (*Parrot AR Drone*) to prove that the algorithm is robust. Future applications of the path planning algorithm could be for the large scale use of UAVs in metropolitan areas and path planning of the SPHERES on and around the ISS.

Keywords: unmanned aerial vehicles, optimal path planning, vision navigation systems, simultaneous localisation and mapping, quadcopters, collision avoidance, artificial intelligence, robotics

Introduction

The use of unmanned aerial vehicles (UAVs), particularly in urban and built-up environments, has increased rapidly over the past decade for personal and commercial uses. Traditionally, these UAVs have relied on Global Navigation Satellite Systems (GNSS) for navigation [1], although there are a number of issues with this in urban canyons where the GNSS result may become inaccurate, unreliable or imprecise due to the multi-path phenomenon [2]. One of the methods for solving this navigation problem is Simultaneous Localisation and Mapping (SLAM) [3], which couples images (from video cameras) to identify unique features with inertial measurements to build a map and localise in real time without any prior knowledge of the environment. As these features are repeatedly observed, the positional uncertainty reduces rapidly [3]. A collision-free trajectory from the current location to the goal must be repeatedly planned using an optimal path planning algorithm which takes into account the current knowledge of all obstacles. The requirement of computational efficiency of this algorithm is evident such that it does not interfere with the SLAM system which must operate at regular intervals.

There exist a number of methods of solving the path planning problem in the literature. Some of these methods include potential field methods [4]–[9], A*/D* graph theory methods

[10]–[12], rapidly-exploring random trees (RRT) [13], [14], admissible subspace trajectory optimisation (ASTRO) [15], [16] and neural networks [17]–[19]. Although most of these methods generate optimal paths, they are either very computationally slow (unsuitable for real time use) or too complicated for implementation on low-cost quadcopters such as the *Parrot AR Drone*. The method of potential field path planning, which was suggested in the early 1990s, has therefore been applied to this problem as it overcomes these issues. In former times, potential field path planning was a computationally expensive task, however on modern hardware it is very fast and relatively simple to implement. When the method was first suggested, there were a number of shortcomings including how local minima in the cost function were handled, as well as inefficient methods of generating the required elements of the cost function. This paper seeks to address these issues, and suggests a tested improved potential field path planning method that can be used in a range of areas in the aerospace industry. The path planning system has been implemented on the *Parrot AR Drone* within a SLAM navigation system (developed within the Advanced Flight Systems research group at the University of Sydney) to facilitate dynamic replanning in real time. Some applications of this research include the large scale use of UAVs in metropolitan areas and the path planning of the SPHERES on the ISS (research platform into satellite formation flying) [15], [16].

Potential Field Path Planning

To determine the optimal path through an environment, a potential energy function (weighted cost function) is defined as

$$\mathbf{U_{total}} = w_1\mathbf{U_{att}} + w_2\mathbf{U_{rep}} \tag{1}$$

where $\mathbf{U_{att}}$ is an attractive potential function that attracts the vehicle from the start to the goal (minimises path length) and $\mathbf{U_{rep}}$ is a repulsive potential function that repels the vehicle from obstacles and the environment boundaries to prevent collisions. The weights of the cost function are w_1 and w_2 and are subjectively based on the relative importance of path length minimisation and obstacle avoidance in the optimisation. The attractive and repulsive fields are weighted in order to achieve a path that meets some given optimality criteria. The trajectory that minimises the grad function of the total potential is then found to be the optimal path meeting the constraints of the optimisation. In developing the total potential function, there are a number of steps that need to be taken: generate the attractive potential function to attract the UAV to the goal, determine which points are traversable, generate the repulsive potential function and finally, combine the two potential functions together with weights to obtain the final total potential function.

Configuration Space

A configuration space is a region with a set of environment boundaries, current set of known obstacles, and a start and goal point to plan between such as that shown in Figure 1. The map of $\mathcal{C}$ is discretised into a square grid of points. The boundary of the configuration space is defined as the matrix extremities and the traversability property of each point is initialised as 1 (traversable). Each polygon obstacle is defined by its m number of vertices $v(1 \rightarrow m)$, and straight line edges are drawn between each of the vertices to form the shape of the obstacle.

Attractive Potential Function

There are a number of functions that can be used for the attractive potential field for potential energy field path planning, all with advantages and disadvantages. These include quadratic, conical and source/sink fields. Quadratic and conical potential functions are based on the distance from the goal, while source/sink fields (innovation in this research) are derived from classical aerodynamics potential flow theory and have the benefit that the gradient increases as the distance to the goal reduces, thus leading to faster convergence.

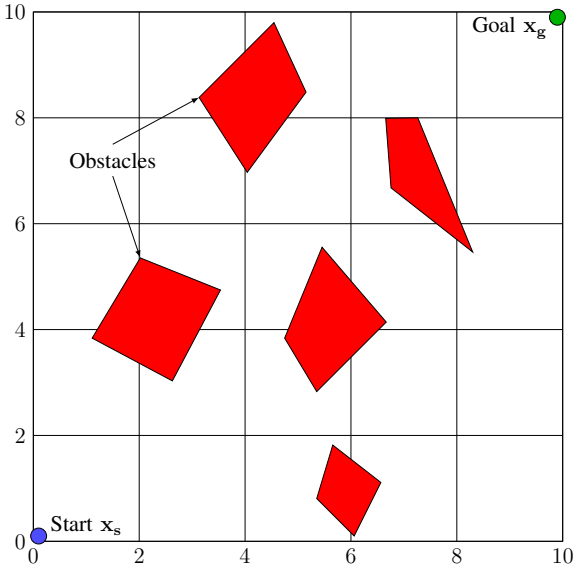

Fig. 1: A sample configuration space $\mathcal{C}$ with polygon obstacles

The preferred approach in this research is to take elements from potential flow theory used in classical aerodynamics [20] to develop the attractive function. A point where fluid flows out radially is called a 'source', and a point where fluid flows in radially is called a 'sink' [20]. These are shown in Figure 2 along with a free stream that flows from the start to the goal (on an angle θ_{SG}) and provides more flow potential between these points. The three elements can be combined to generate an attractive potential field function. The strength

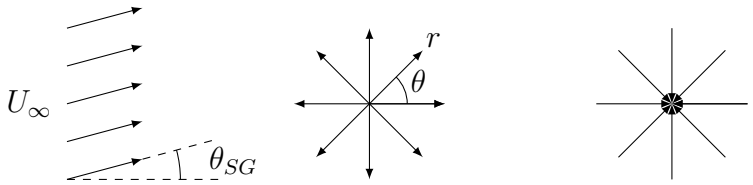

Fig. 2: Potential flow building blocks: free stream, source and sink

of the source/sink is $\pm\sigma$ (positive for a source and negative for a sink). It can be shown [20] that the potential function for a source or sink located at $x = x_0$ and $y = y_0$ is

$$\phi = \frac{\pm\sigma}{2\pi} \ln\left(\sqrt{(x - x_0)^2 + (y - y_0)^2}\right) \tag{2}$$

Placing a source at the start point, a sink at the goal point and a free stream in between, gives an attractive potential $U_{att_{ij}}$ at any point (x_{ij}, y_{ij}) in the field as,

$$U_{att_{ij}} = \overbrace{\frac{\sigma}{2\pi} \ln\left(\sqrt{(x_{ij} + x_s)^2 + (y_{ij} + y_s)^2}\right)}^{\text{Source}} - \overbrace{\frac{\sigma}{2\pi} \ln\left(\sqrt{(x_{ij} - x_g)^2 + (y_{ij} - y_g)^2}\right)}^{\text{Sink}}$$
$$+ \overbrace{Ux_{ij} \cos\theta_{SG} + Uy_{ij} \sin\theta_{SG}}^{\text{Free stream}} \tag{3}$$

$$\implies U_{att_{ij}} = \frac{\sigma}{4\pi} \ln\left(\frac{(x_{ij} + x_s)^2 + (y_{ij} + y_s)^2}{(x_{ij} - x_g)^2 + (y_{ij} - y_g)^2}\right) + Ux_{ij} \cos\theta_{SG} + Uy_{ij} \sin\theta_{SG} \tag{4}$$

The potential function is shown in Figure 3.

The benefit of this potential field is that it is continually and radially decreasing and has only one global/local minimum. This will help prevent the UAV from getting 'stuck' in points of local minima that can form around non-convex obstacles as found by Bortoff [4]. The attractive potential function based on sources and sinks is preferred over both the quadratic and conical functions due to their shortcomings in path suboptimality and convergence rate near the goal.

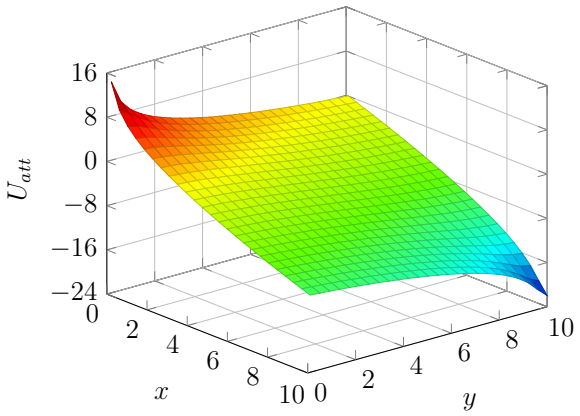

Fig. 3: Source/sink attractive potential field with the start point at $(0, 0)$ and the goal point at $(10, 10)$

Repulsive Potential Function

The obstacles are modelled as a repulsive potential field. A quadratic function is used to model the obstacles inside a *region of influence* denoted by D_i. Beyond a distance of D_i from the obstacle, there is no effect on the total potential field. This works as a safety margin to prevent the UAV from coming too close to the obstacle, accounting for the UAV size (0.5 $\times$ 0.5 m for the *Parrot AR Drone* [21]). The map bounds are also considered obstacles and are given a repulsive potential to push the UAV away from the extremities of the environment. Mathematically, the repulsive field is modelled as

$$U_{rep_{ij}} = \begin{cases} (|\mathbf{r_{ij}}| - D_i)^2, & |\mathbf{r_{ij}}| \leq D_i \\ 0, & |\mathbf{r_{ij}}| > D_i \end{cases} \quad (5)$$

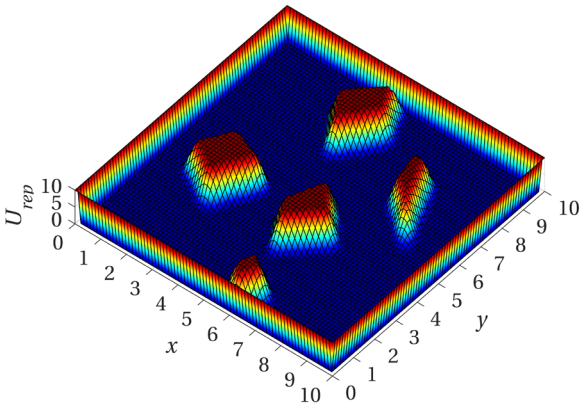

Fig. 4: Obstacles in configuration space $\mathcal{C}$ converted to a repulsive potential field

where $|\mathbf{r_{ij}}|$ is the distance to the nearest obstacle from (x_{ij}, y_{ij}). A significant issue in computational efficiency with this formulation is the calculation of $|\mathbf{r_{ij}}|$. Some of the methods that can be used that involve directly calculating this distance are the linear search algorithm and the $k$nn-search algorithm [22], however both these methods are computationally inefficient. A more efficient method proposed in this research approximates the parabolic shape of the function near obstacles using image morphological processing (where the traversability of nodes is used to form a binary image).

The repulsive potential field for the configuration space $\mathcal{C}$ (Figure 1), is shown in Figure 4.

Traversability of Points in Configuration Space

To generate the repulsive potential field, the obstacle locations and sizes must be defined. This is achieved by determining whether a particular point in the configuration space is traversable or not. For this purpose, a 'point-in-polygon' algorithm known as the Winding Number algorithm [23], [24] was used. The Winding Number algorithm counts how many

times (W) a closed curve C (comprised of edges E) wraps around a point P [23], [24]. Points with non-zero winding numbers are inside the polygon, while those with zero winding number are outside.

Image Morphological Processing

The points inside obstacles in the configuration space are determined using the Winding Number algorithm. This then produces a binary image of whether a point is traversable or not as shown in Figure 5.

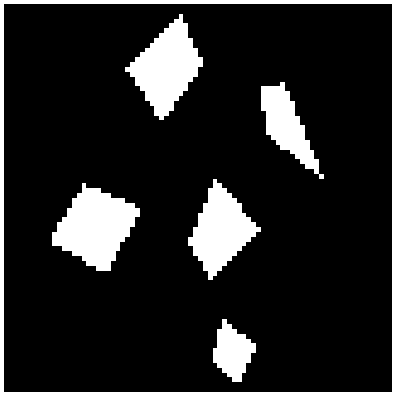

Fig. 5: Unprocessed binary image of point traversability

Image (or Mathematical) Morphological Processing [25] is the method whereby filtering is performed on images (typically binary images) to either erode or dilate the elements in the image. Convolution formulated as a matrix problem with a kernel matrix k of size $p \times q$ and an image matrix A of size $m \times n$, gives the convolved matrix B as

$$B_{ij} = \sum_{u=1}^{p} \sum_{v=1}^{q} A_{i-u+1,j-v+1} k_{uv} \tag{6}$$

This convolution can be thought of as the kernel matrix moving over the image matrix, and performing a dot product of the sub-matrices involved at each step.

In order to obtain the parabolic shape of the area within the region of influence D_i surrounding obstacles in the repulsive potential field (as an approximation to Equation 5), the kernel matrix is adapted to be a 2D parabolic function large enough to encompass the region of influence. The size of the kernel matrix is determined from the ratio between each discrete map node and the region of influence parameter D_i. The kernel matrix (normalised to 1) is then obtained as

$$k_{ij} = \frac{1}{\max(k)} \left[y_0 - \left(\left| j - \frac{q-1}{2} \right| (\Delta x)^2 + \left| i - \frac{p-1}{2} \right| (\Delta y)^2 \right)^2 \right] \tag{7}$$

shifted by y_0 to ensure the kernel matrix is zero at the extremities. As such, y_0 is given as

$$y_0 = \left(\frac{q-1}{2} \right) (\Delta x)^2 + \left(\frac{p-1}{2} \right) (\Delta y)^2 \tag{8}$$

k is symmetrical and although it is not expressly required that k be square, p and q must be odd. Convolving this parabolic kernel matrix with the image matrix gives the parabolic morphological transform. Applying this to the original image representation of the obstacles in the configuration space (see Figure 5) produces the new image shown in Figure 6.

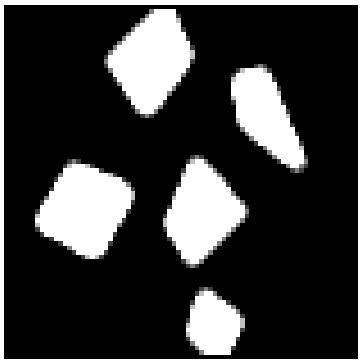

Fig. 6: Image morphologically processed obstacle map of configuration space $\mathcal{C}$

The morphological processing has dilated the obstacles by D_i, and the parabolic kernel has led to the smoothing of the edges. If this image is then represented as a surface plot (see Figure 4), the repulsive potential field is realised. Since this process only requires simple matrix operations, it is a computationally efficient method for obtaining the repulsive potential field and allows the path to be computed extremely rapidly.

The computation time for three possible methods used for calculating the repulsive potential function (other two methods considered are a linear distance based search as well as the $k$nn-search method [22]) are summarised in Table 1 that shows that the image morphological processing method is significantly faster than the other two algorithms. As such, Image Morphological Processing is used in this research to generate the repulsive potential function.

Table 1: Computation time (MATLAB) for the three methods of generating the repulsive potential field

	Computation Time (Seconds)		
Map Size (n)	**Linear Search**	***k*nn-search**	**Image Morphological Processing**
40	0.136	0.533	0.0076
80	1.64	2.11	0.0361
120	7.44	4.95	0.0989

Total Potential Function

The total potential field is the weighted cost function that the gradient is minimised on to obtain the optimal path. It is obtained by summing the normalise attractive and repulsive fields as a linear combination with weights w_1 and w_2 for the repulsive and attractive fields respectively. That is,

$$U_{tot} = \frac{w_1 U_{att}}{\max(U_{att})} + \frac{w_2 U_{rep}}{\max(U_{rep})} \tag{9}$$

The effect of the weight w_1 on path length is shown in Figure 7. The path length changes as w_1 changes, and there is a minimum between 7 and 8. Therefore, a value of 7.5 was selected for w_1. A value of 1 was selected for the second weight w_2 (for the repulsive component) since the region of influence parameter in the repulsive field ensures that obstacles are avoided provided w_1 is not too large with respect to w_2 (due to the upwards gradients around obstacles). Therefore, path length minimisation is effectively weighted as being 7.5 times more important than obstacle avoidance.

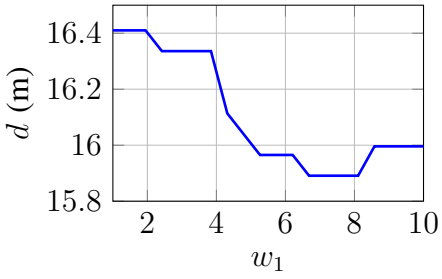

Fig. 7: Effect of w_1 on path length d

The resulting total potential field for configuration space $\mathcal{C}$ is shown in Figure 8.

Calculation of Optimal Path

The optimal path is determined by finding the path that has the largest magnitude continually decreasing gradient on the total potential function. Computationally, this is performed using the gradient descent method [26]. This ensures that the obstacles will not be traversed (as they start with very rapidly increasing gradients) and that the optimal path with respect to path length is obtained. The optimal path is the one that satisfies

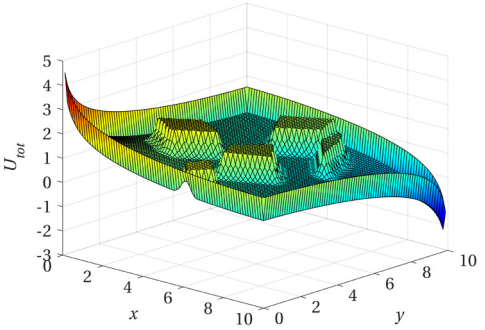

Fig. 8: Total potential field for configuration space $\mathcal{C}$ with $w_1 = 7.5$, $w_2 = 1$, $D_i = 0.5$

$$-\min(\nabla U) = -\min\left(\frac{\partial U_{tot}}{\partial x} + \frac{\partial U_{tot}}{\partial y}\right) = \min(\mathbf{F}) \tag{10}$$

Since $\mathbf{F} = -\nabla U$, the force required to move the UAV from the start to the goal is minimised by finding the minimum value of the total potential function for all 8 nodes surrounding the given point (3×3 matrix around the current point). The minimum total potential value must be smaller than any values already in the vector of potential values for the optimal path up to that point. This gives the UAV a strategy to leave a point of a local minimum that may be formed around non-convex obstacles by 'back-tracking'. The algorithm used to calculate the optimal path is given in Algorithm 1.

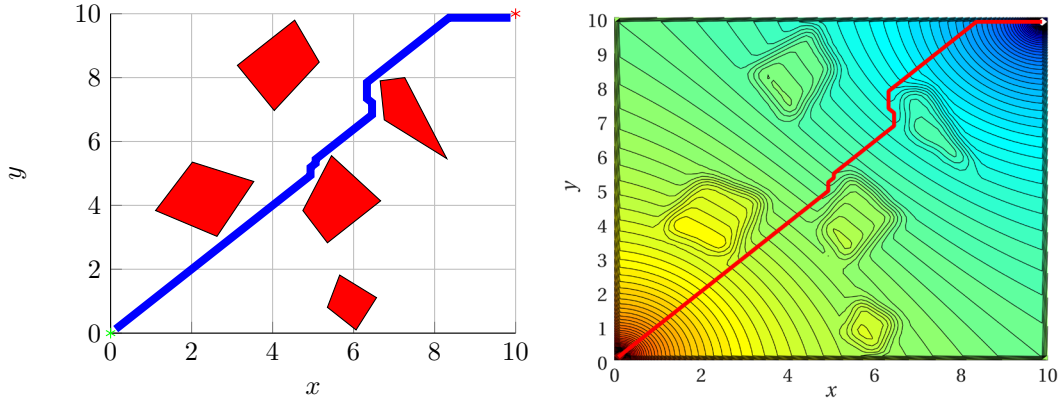

(a) Path

(b) Path with contours of U_{tot}

Fig. 9: Planned optimal path generated by source/sink attractive potential field

Using the source/sink attractive field, the optimal path through the configuration space $\mathcal{C}$ was calculated and is shown in Figure 9. There is some sub-optimality in the path, particularly in the approach to the goal and the 'zig-zagging' as the path traverses the discretised grid. In addition, there are 90 waypoints along the path which is far too complex a set of instructions for the drone to handle. Thus, a waypoint reduction algorithm is developed to overcome the sub-optimality and reduce the total number of waypoints.

Waypoint Reduction & Further Optimisation of Path

The waypoint reduction algorithm (similar approaches taken by [13], [27]) is posed as follows. Consider a straight line that extends from the first waypoint to each successive waypoint. Until this line intersects an obstacle, the straight line is continually increased in length. Once an obstacle is intersected, then the next waypoint in the reduced path becomes the previously traversed point. This new waypoint then becomes the point that straight lines are extended from. This process is repeated until the goal is reached. The path after undergoing waypoint reduction is shown in Figure 10 with the new waypoints shown as crosses. The waypoint reduction algorithm functions as required and further optimises the original path (with 90 waypoints), reducing the number of waypoints to 7. This result is similar to the outcome of the algorithm used by Yang et al. [13], which reduced a path with 45 waypoints down to 1.

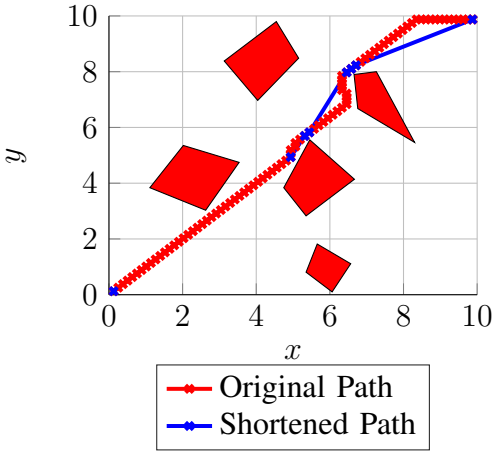

Fig. 10: Fully optimised path with number of waypoints reduced from 90 to 7

Algorithm 1 Calculation of the optimal path

Starting point $\rightarrow [X, Y]$
Row and column index of starting point $\rightarrow [r, c]$
Goal point $\rightarrow [X_g, Y_g]$
Row and column index of goal point $\rightarrow [r_g, c_g]$
Initialise path $\rightarrow Path(1) = [X, Y]$
$i = 2$ ▷ Counter for indexing vector
while X is not X_g AND Y is not Y_g **do**
    $U_{neighbour}$ = 3 × 3 matrix of U_{tot} surrounding current point $[X, Y]$
    min$(U_{neighbour}) \rightarrow U_{min}$
    index of U_{min} in $U_{neighbour} \rightarrow [r, c]$
    while $U_{min} > U_{min}$ from prev. step **do** ▷ Find way out if caught in local minimum
        $U_{neighbour}(r, c) = \infty$
        min$(U_{neighbour}) \rightarrow U_{min}$
        index of U_{min} in $U_{neighbour} \rightarrow [r, c]$
    end while
    $r_{new} = r_{old} - 1 + r$
    $c_{new} = c_{old} - 1 + c$
    $Path(i) = [X(r_{new}, c_{new}), Y(r_{new}, c_{new})]$ ▷ Add point to path
    $i = i + 1$ ▷ Advance counter
end while
Goal reached! $\rightarrow$ End of routine

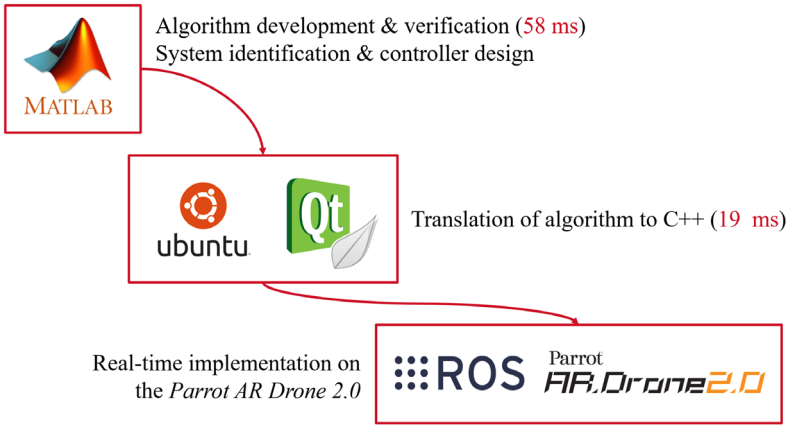

Fig. 11: Research testing work flow. There was a reduction in computation time after converting the algorithm to C/C++ from 58 ms to 19 ms.

Test Platform

The test platform used in this research was the *Parrot AR Drone 2.0* from *Parrot SA* [28]. Cheema et al. have developed an interface (in C/C++) to communicate with the drone for the purposes of engineering research in vision-based navigation and SLAM [29]. The Robot Operating System (ROS) is used rather than the Software Development Kit (SDK) from *Parrot SA*. ROS handles the low-level communication (bit stream) with the drone, making it more suitable to rapid prototyping and evaluation of code since more intuitive commands can be used [29]. The work flow in this research is shown in Figure 11.

Implementation of Path Planning with Known Set of Obstacles

In order to test the path planning algorithm and control strategies, a simple configuration space was designed inside the laboratory at *the University of Sydney*. This configuration space consisted of three cardboard boxes as obstacles, and start $(0.47, 2.80)$ and goal $(3.89, 2.86)$ points at either side as shown in Figure 12.

Real time position feedback in the simulated GNSS denied environment in the abscence of the SLAM navigation system was achieved using dead reckoning of the velocity (provided by the optical flow sensor on the UAV [30], [31]) and attitude measurements (provided by the magnetometer and MEMS rate gyroscope on the UAV).

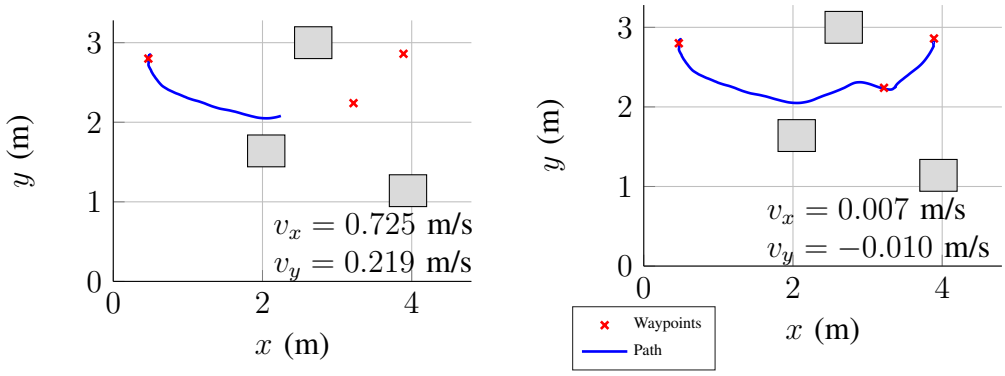

(a) $t = 10$ seconds (b) $t = 20$ seconds

Fig. 12: Results of implementation of path planning on the *Parrot AR Drone*

The optimal path was planned in 19 ms, and produced one waypoint between the start and goal points as shown in Figure 12. After take off, when the drone had stabilised into a steady hover, the autonomous position control was initiated to start flying the planned path. The results of the flight test are shown in Figure 12, which shows that the drone flew almost directly through all waypoints indicating the path planning system is working as expected.

Software Interaction & Implementation

For the implementation of dynamic path replanning, a number of software prerequisites were required. This software was developed by others in the research group [32], [33], and included a feature detection algorithm and a SLAM (Simultaneous Localisation and Mapping) navigation system. The interaction of all these software components is shown in Figure 13. The feature detection and SLAM systems operate at 30 Hz. This rate must be continuously maintained in order to minimise the build up of error in the state estimation. Therefore, the path replanning only occurs every three seconds with an up-to-date environment configuration space. This was viewed as an

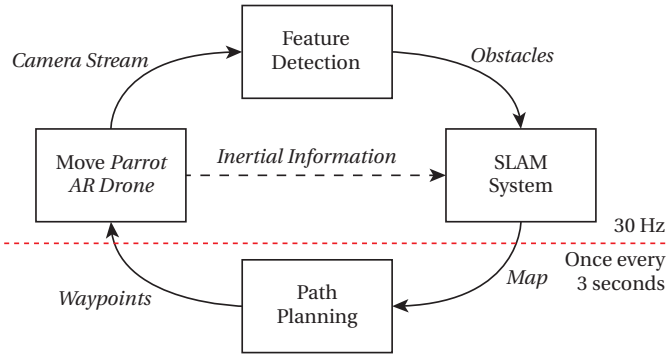

Fig. 13: Interaction of all software required in the implementation of dynamic path replanning for the *Parrot AR Drone*

appropriate amount of time given the speed that the UAV was commanded to move at (to ensure the quality of the results of the feature detection and SLAM systems).

The purpose of the feature detection algorithm [33] is to take an image stream from the front-facing camera of the *Parrot AR Drone* in real-time and identify unique features in the image. These unique features are obstacles that must be avoided by the drone, and therefore this information is required by the path planning system. The purpose of the SLAM system [32] is to fuse the feature detection with the inertial information (using an Extended Kalman Filter (EKF) [34]) coming from the *Parrot AR Drone*, to allow localisation and building of the environment map in real time. The SLAM system uses Inverse Depth Parameterisation (IDP) [35] to determine the distance to obstacles [32].

Simulation of Dynamic Path Replanning

The path planning algorithm, system identification and controller design were combined in a dynamic MATLAB simulation to verify the validity of dynamic path replanning. In this simulation, the true field of view (FOV) [33] of the camera was replicated such that only obstacles inside this region would be considered as 'detected' obstacles. The dynamic model identified and controllers designed were embedded into the simulation using state space methods to replicate the dynamic behaviour of the *Parrot AR Drone* as it moves through the environment.

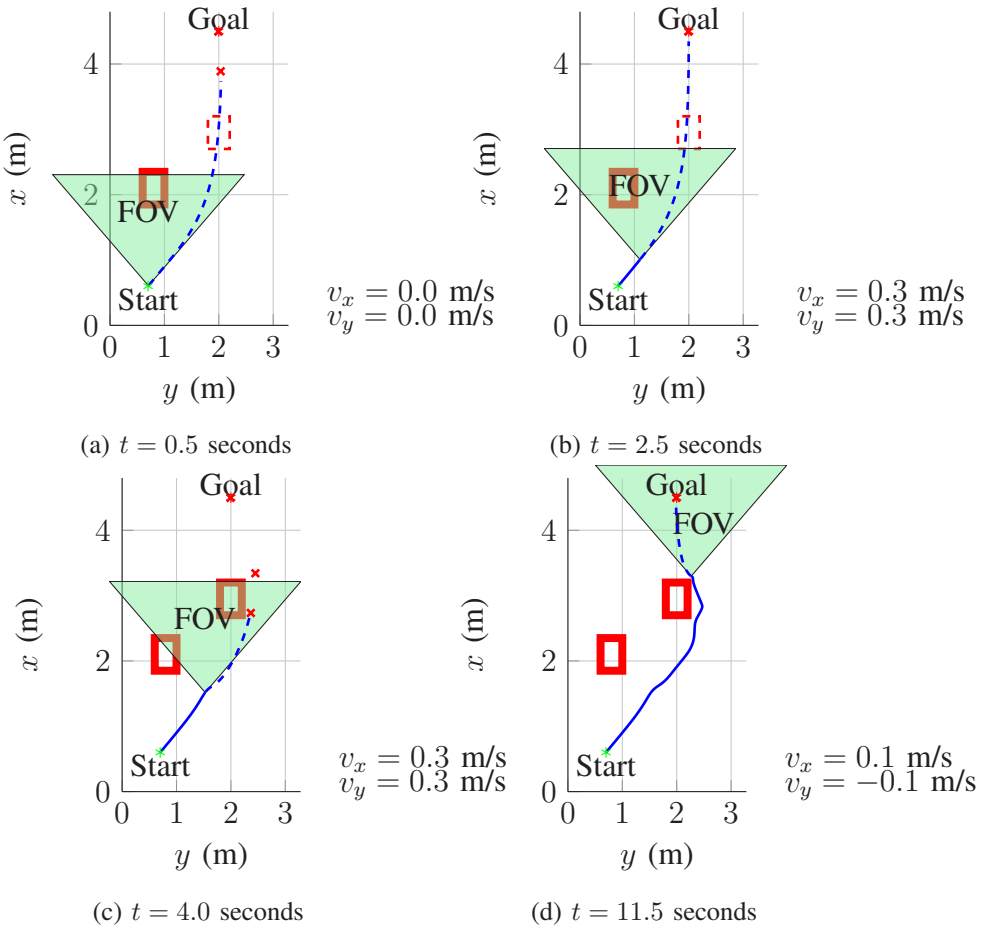

(a) $t = 0.5$ seconds

(b) $t = 2.5$ seconds

(c) $t = 4.0$ seconds

(d) $t = 11.5$ seconds

Fig. 14: Dynamic path replanning simulation results

The results of the simulation are shown in Figure 14, with replanning being done every 0.5 seconds. The red rectangles indicate the obstacles (dotted line indicates obstacles that are currently not known), the red crosses indicate the planned waypoints, the blue line indicates the path the UAV travelled, and the blue dotted line indicates the projection of where the UAV would travel if dynamic replanning were not functioning. Initially, obstacle is within the field of view of the drone as shown in Figure 14a. Therefore, a path is planned towards the goal, which intersects the second obstacle that the UAV does not know exists yet. The UAV begins to move (Figure 14b), and eventually the second obstacle comes in to the field of view of the UAV (Figure 14c). At this point, the path is replanned around this obstacle and the UAV continues towards the goal as shown in Figure 14d. Throughout the simulation, as would be the case in the real situation, any detected features are saved so they are still part of the map even when they are out of the field of view of the camera. This allows the SLAM system to reduce positional uncertainty in the case that the obstacle comes back into the field of view [32], [33]. The results demonstrate that the dynamic path replanning with an unknown map has been successfully validated, and that the system can be implemented on the *Parrot AR Drone* within the feature detection and SLAM systems. This approach to dynamic path replanning, where more and more of the map is observed over time, and the path planner continually plans paths to the goal, was also successfully implemented on a ground based vehicle by Stentz et al. [11].

Implementation of Dynamic Path Replanning on the *Parrot AR Drone* with Feature Detection and SLAM

The dynamic path replanning system was implemented on the *Parrot AR Drone* within the feature detection and SLAM systems. In this case, it was initially attempted to have full autonomous control (as was the case in the implementation with a known map and in the simulation), however due to the large uncertainties in positions of obstacles and the UAV from the SLAM system, this was not possible. Therefore, the drone was hand-flown (from the controlling computer) towards the planned waypoints that were generated from the dynamic path replanning algorithm. Autonomous control could be implemented in further work, by either expanding the testing area in size (such that uncertainties have less of an effect), or by redesigning the control to be model predictive control (MPC) [36].

The results of the dynamic path replanning are shown in Figure 15. In the map visualisation in the bottom left corner, the red dots indicate detected obstacles, the blue dots indicate the planned waypoints, the blue line indicates the SLAM position solution, and the green line indicates the dead reckoning position solution. Figure 15a shows that the first obstacle (triangle) is detected and a path is planned towards the goal at $x = 3.5$ m, $y = 2.5$ m (one waypoint generated). The UAV is then flown in the direction of this waypoint, and eventually the second obstacle (rectangle) is detected (Figure 15b). At this point, it is clear that a continuation of the original path would have gone straight through the second obstacle, and thus the path needs to be replanned. A second waypoint is generated to the right of the second obstacle towards which the UAV was flown (Figure 15c). From here, the optimal path is then to travel directly to the goal and this can be seen in Figure 15d. The build up of error in position between the dead reckoning and SLAM solutions can be seen as the two lines increasingly deviate from one another as the experiment progresses. The dead reckoning solution is clearly not as accurate as the SLAM solution as it passes more widely around obstacle 2. The SLAM performed better than the dead reckoning solution as it repeatedly observes the same obstacles to minimise position error unlike dead reckoning. This demonstrates a proof-of-concept of

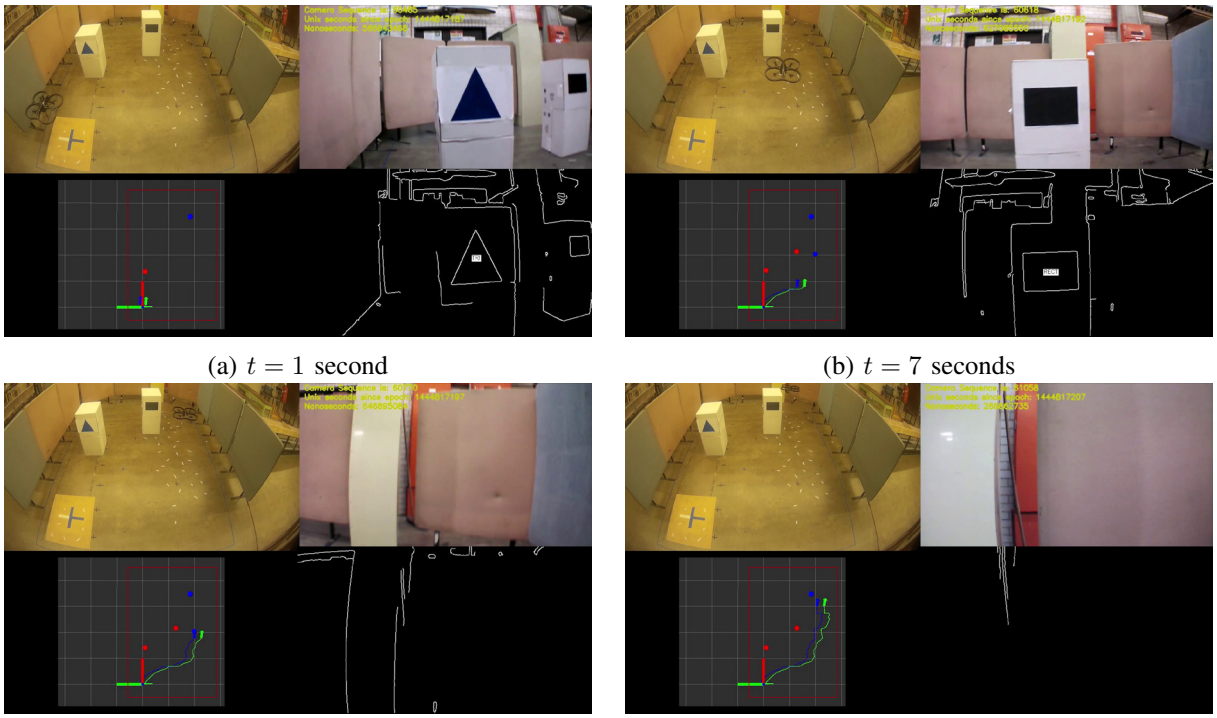

(a) $t = 1$ second

(b) $t = 7$ seconds

(c) $t = 11$ seconds

(d) $t = 22$ seconds

Fig. 15: Results of implementation of dynamic path replanning within feature detection and SLAM systems on the *Parrot AR Drone*. The red dots indicate detected features, blue dots indicate planned waypoints, and the blue and green lines are the SLAM and dead reckoning solutions respectively.

the dynamic path replanning working within the SLAM navigation system, which meets the original objectives of the research.

Conclusion

This research has developed an improved potential field path planning algorithm and successfully implemented the algorithm on a small UAV namely the *Parrot AR Drone* working within a SLAM navigation system. Although the scenarios tested are simple 'proof-of-concept' style problems, they have demonstrated the applicability and potential for the algorithm to be used in a wide variety of scenarios where collision-free paths in unknown GNSS-denied environments are required. The algorithm is already performing faster and more reliably than some others in the literature [5]. With further improvement of the algorithm to operate in three dimensions, handle more general obstacles and model the gust behaviour of the drone, the path planning system would become more robust. With these improvements, the algorithm developed in this research can be applied in the integration of unmanned aerial vehicles into civilian airspace, particularly in complex built-up environments and could also be applied to space vehicles such as the SPHERES on the ISS.

Acknowledgments

The author would like to thank A/Prof. Peter W. Gibbens (University of Sydney) for his supervision and guidance in this project. The author would also like to thank Trevor Wang, Jacob Hacker, Andy Ho and Simon Luo who contributed to the other elements of this project. Finally, the author would like to thank Wayne Short and the National Space Society of Australia for giving them the chance to present this paper at the 15th Australian Space Research Conference in Canberra, where it was awarded the best undergraduate student oral presentation.

Videos of the results of this research can be seen at the following links:

- Path planning and control with known map of obstacles: https://www.youtube.com/watch?v=PJENEHqLZFM
- Simulation of dynamic path replanning on the *Parrot AR Drone*: https://www.youtube.com/watch?v=hfOFqGWBIvo
- Results of dynamic path replanning integrated into SLAM and feature detection systems: https://www.youtube.com/watch?v=_GTO3of3U_s

For more information on the work conducted in this research, please contact the author at nr@outlook.com.au.

References

[1] T. K. Lau et al., "A Robust State Estimation Method Against GNSS Outage for Unmanned Miniature Helicopters," in *2010 IEEE International Conference on Robotics and Automation (ICRA)*. IEEE, 2010, pp. 1116–1122.

[2] P. D. Groves, "Shadow Matching: A New GNSS Positioning Technique for Urban Canyons," *Journal of Navigation*, vol. 64, no. 03, pp. 417–430, 2011.

[3] H. Durrant-Whyte et al., "Simultaneous Localization and Mapping: Part I," *Robotics & Automation Magazine, IEEE*, vol. 13, no. 2, pp. 99–110, 2006.

[4] S. A. Bortoff, "Path Planning for UAVs," in *Proceedings of American Control Conference, Chicago, Illinois, June 2000*, American Automatic Control Council, Ed. American Automatic Control Council, 2000.

[5] C. I. Connolly et al., "Path planning using Laplace's Equation," in *1990 IEEE International Conference on Robotics and Automation, 1990. Proceedings.* IEEE, 1990, pp. 2102–2106.

[6] J. Barraquand et al., "Numerical Potential Field Techniques for Robot Path Planning," *IEEE Transactions on Systems, Man and Cybernetics*, vol. 22, no. 2, pp. 224–241, 1992.

[7] Y. K. Hwang et al, "A Potential Field Approach to Path Planning," *IEEE Transactions on Robotics and Automation*, vol. 8, no. 1, pp. 23–32, 1992.

[8] S. S. Ge et al., "New Potential Functions for Mobile Robot Path Planning," *IEEE Transactions on Robotics and Automation*, vol. 16, no. 5, pp. 615–620, 2000.

[9] Y. Wang, "A New Potential Field Method for Robot Path Planning," in *Robotics and Automation, 2000. Proceedings. ICRA'00. IEEE International Conference on*, vol. 2. IEEE, 2000, pp. 977–982.

[10] Z. Qi et al., "An Improved Heuristic Algorithm for UAV Path Planning in 3D Environments," in *2010 2nd International Conference on Intelligent Human-Machine Systems and Cybernetics (IHMSC)*, vol. 2. IEEE, 2010, pp. 258–261.

[11] A. Stentz et al., "A Complete Navigation System for Goal Acquisition in Unknown Environments," *Autonomous Robots*, vol. 2, no. 2, pp. 127–145, 1995.

[12] S. Hrabar, "3D Path Planning and Stereo-based Obstacle Avoidance for Rotorcraft UAVs," in *2008 IEEE/RSJ International Conference on Intelligent Robots and Systems*. CSIRO ICT Centre, 2008.

[13] K. Yang et al., "3D Smooth Path Planning for a UAV in Cluttered Natural Environments," in *2008 IEEE/RSJ International Conference on Intelligent Robots and Systems*. Australian Centre for Field Robotics, 2008.

[14] M. Kothari et al., "A Probabilistically Robust Path Planning Algorithm for UAVs Using Rapidly-Exploring Random Trees," *Journal of Intelligent & Robotic Systems*, vol. 71, no. 2, pp. 231–253, 2013.

[15] B. J. Morrell et al., "Application of a Trajectory Optimisation Algorithm for Dynamic Obstacle Avoidance and Multiple Vehicle Coordination," *Fourth Australasian Unmanned Systems Conference*, vol. 1, 2014.

[16] G. E. Chamitoff et al., "Real-Time Maneuver Optimization of Space-Based Robots in a Dynamic Environment: Theory and On-Orbit Experiments," *AIAA Journal of Guidance, Navigation and Control*, 2014.

[17] F. Muñiz et al., *Neural Controller for a Mobile Robot in a Nonstationary Environment*. Citeseer, 1995.
[18] Y. Arai et al., "Adaptive Behavior Acquisition of Collision Avoidance Among Multiple Autonomous Mobile Robots," in *Proceedings of the 1997 IEEE/RSJ International Conference on Intelligent Robots and Systems, 1997. IROS'97.*, vol. 3. IEEE, 1997, pp. 1762–1767.
[19] S. X. Yang et al., "An Efficient Neural Network Approach to Dynamic Robot Motion Planning," *Neural Networks*, vol. 13, no. 2, pp. 143–148, 2000.
[20] A. Techet, "2.016 Hydrodynamics (13.012), Fall 2005," *Massachusetts Institute of Technology: MIT OpenCourseWare*, 2005.
[21] Parrot SA, "AR.Drone 2.0 Specifications," 2013. [Online]. Available: http://ardrone2.parrot.com/ardrone-2/specifications/
[22] K. Schwarz, "KDTree," *Stanford University*, 2014.
[23] C. Huang et al., "On The Complexity of Point-In-Polygon Algorithms," *Computers & Geosciences*, vol. 23, no. 1, pp. 109–118, 1997.
[24] D. G. Alciatore, "A Winding Number and Point-In-Polygon Algorithm," *Department of Mechanical Engineering Colorado State University, Fort Collins, CO*, 1995.
[25] E. R. Dougherty et al., *Hands-on Morphological Image Processing*. SPIE Press Bellingham, 2003, vol. 71.
[26] R. Fletcher et al., "A Rapidly Convergent Descent Method for Minimization," *Computer Journal*, vol. 6, no. 2, pp. 163–168, 1963.
[27] Z. Aljarboua, "Geometric Path Planning for General Robot Manipulators," in *World Congress on Engineering and Computer Science*, vol. 2, 2009, pp. 20–22.
[28] Parrot SA, "Parrot AR Drone 2.0," 2013.
[29] P. Cheema et al., *Development of a Multi-Threaded and Multi-Processed Control and Vision Navigation GUI for AR Drone 2.0*, ser. Engineering Project, 2014.
[30] S. Piskorski et al., "AR. Drone Developer Guide," *Parrot SDK*, vol. 1, 2012.
[31] S. S. Beauchemin et al., "The Computation of Optical Flow," *ACM Computing Surveys (CSUR)*, vol. 27, no. 3, pp. 433–466, 1995.
[32] T. S. Wang, *Monocular Simultaneous Localisation and Mapping for Autonomous Visual Navigation with the Parrot AR Drone*, ser. Engineering Undergraduate Honours Thesis, 2015.
[33] A. Ho, *Real Time Feature Detection for Feature Assisted Visual Navigation for the Parrot AR Drone*, ser. Engineering Undergraduate Honours Thesis, 2015.
[34] S. Haykin, *Kalman Filtering and Neural Networks*. John Wiley & Sons, 2004, vol. 47.
[35] J. Civera et al., "Inverse Depth Parametrization for Monocular SLAM," *IEEE Transactions on Robotics*, vol. 24, no. 5, pp. 932–945, 2008.
[36] C. E. Garcia et al., "Model Predictive Control: Theory and Practice – a Survey," *Automatica*, vol. 25, no. 3, pp. 335–348, 1989.

Investigation of the Izmit Earthquake with Interferometric SAR (InSAR), Global Navigation Satellite System (GNSS) Positioning and Coulomb Stress Modelling

Ruken Alac Barut, John Trinder, Chris Rizos

School of Civil & Environmental Engineering, University of New South Wales, Sydney, NSW, 2052, Australia

Summary: In 1999, the Izmit Earthquake struck Istanbul and its surroundings in northwest Turkey. It was one of the most devastating earthquakes of the twentieth century, significantly impacting on 20 million inhabitants and nearly half of the country's industry. The earthquake's epicentre was located on the North Anatolian Fault (NAF) in the Marmara region. The NAF is one of the best-known dextral strike-slip faults in the world because of its exceptional seismic activity and due to its important influence on the tectonics of the Marmara region. In order to analyse the Izmit earthquake the authors combined Interferometric Synthetic Aperture Radar (InSAR), Global Navigation Satellite System (GNSS) and Coulomb Stress Modelling. The InSAR and GNSS techniques are complementary, and can produce high spatial and temporal resolution information of surface deformation if data collection conditions are favourable. On the other hand, Coulomb Stress Change Modelling plays a role in understanding static stress transfer across an area as suggested by earthquake models. The resulting InSAR deformation map agrees with GNSS measurements and Coulomb stress modelling, demonstrating that the northern region of the NAF was deformed downwards. In addition, the GNSS results and horizontal displacement modelling were consistent with the NAF characterisations.

Keywords: InSAR, GNSS, Coulomb stress modelling, North Anatolian Fault (NAF), Izmit earthquake, deformation, co-seismic

Introduction

For more than two thousand years the Marmara region has been at the crossroads between East and West. It has been a continuously populated region of socio-economic importance, with the location of Istanbul as the capitals of both the Eastern Roman and Ottoman empires. The tectonics of the Marmara region in north-west Turkey are dominated by the right-lateral NAF. The NAF consists of several fault segments with lengths totalling 1200 km which started widening on the western side approximately 13 to 11 million years ago [1]. According to [2], there have been several significant seismic activities on the NAF due to this westerly widening. Therefore, critical assessments are needed to investigate the conditions of the most recent earthquake in the region, which is referred to as the Izmit Earthquake of 17th August 1999, located to the north-west of the NAF near the city of Istanbul. Figure 1 shows the tectonic characteristics of the Marmara area and NAF.

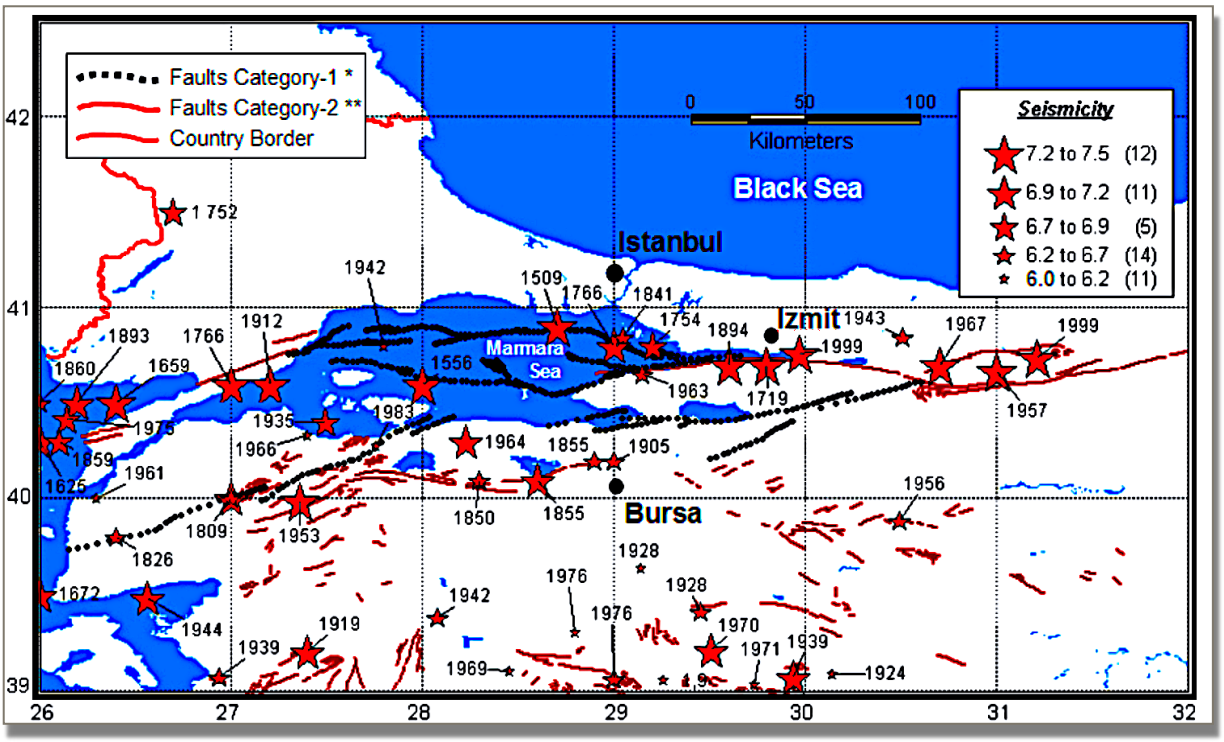

Fig. 1: The North Anatolian Fault (NAF) Zone in north-west Turkey. Red stars indicate hypocentres of major earthquakes with M ≥ 6.0 (A.D. 1509-1999). Black dotted lines are Category-1 faults which were visualised using bathymetric images and seismic reflection survey. Dark red lines are Category-2 faults (modified from [3]).

The Izmit earthquake occurred on the northern segment of the NAF with a moment 7.4 (Mw=7.4) and an X (MSK) maximum intensity [4]. The earthquake started at 00:01:39 UTC (3:02 a.m. local time), lasted 37 seconds and impacted a 100-150 km long section of the NAF. According to [5], the earthquake caused 17,479 deaths and 43,953 injuries. Future earthquakes are estimated to have the potential to cause a death toll of 70,000, 120,000 severe injuries and 60,000 heavily damaged buildings. In addition to this, the Izmit earthquake seriously impacted Turkey's industry, as one third of its gross domestic product (GDP) is derived from the Marmara region. In view of the intense interest in this earthquake, the authors sought to complement, rather than repeat previous work done on the data derived from this earthquake e.g. [6], [7], [8]. Following the Izmit earthquake there was 2 m rapid after-slip effect at 12-24 km below the epicentral area within a month after the earthquake, while close to the hypocentral area (the point within the Earth where the earthquake rupture starts), the slip distribution of the fault was 1 m [9]. [10] estimated a more than 2 m/yr after-slip rate immediately after the Izmit earthquake, and a 1.2 m/yr after-slip rate before the Duzce earthquake which occurred three months after the Izmit earthquake.

From a joint analysis of InSAR, GNSS and Coulomb stress change modelling techniques, the authors have determined the co-seismic and post-seismic deformation of the 17 August 1999 Izmit earthquake in terms of stress progression and displacement. One pair of SAR images from the European Remote Sensing (ERS-2) satellites was used, acquired before and after the earthquake. In addition, data from two continuously operating GNSS stations (DUMT and TUBI) have been utilised for the determination of displacements due to the seismic activity. Both of these GNSS stations belong to the MAGNET network (Marmara Continuous GNSS Reference Network) in the Marmara area, which were operating during the Izmit earthquake within the co-seismic rupture zone. Coulomb stress changes caused by the main shock are determined by the International Seismological Centre (ISC) catalogue, which is one of the

oldest and most detailed seismicity catalogues for global earthquake activities. The use of all three techniques show that the Izmit earthquake caused the northern part of the NAF to move in an easterly direction and the southern part to move in a westerly direction. This partially confirms that the fault extended westerly, underneath of the Gulf of Izmit. In addition this westerly movement changed the stress distribution and increased the deformation around the fault zone. The conclusion can be drawn that combination of these three techniques can provide additional knowledge of the distribution of co-seismic deformations and associated stress changes to improve the future estimates of seismic hazards on neighbouring faults.

Methodology

InSAR

InSAR is a remote sensing technique that calculates ground displacements using the difference in phases between two synthetic aperture radar images over the same area. It can be used to determine the surface displacement, measured in the satellite's line-of-sight (LOS) direction, with good spatial coverage and an accuracy ranging from a few mm to a few cm. The large footprint of these images can provide deformation information over wide areas, which is useful for understanding large area displacements even if only small displacements occur [11], [12]. Provided the coherence of the two images is suitable for determining their correlation, which is dependent primarily on the base length, the computed unwrapped phase differences appear as spatial fringes. Each fringe represents a difference of one cycle of the two-way travel time between the satellite and the target on the ground, e.g. [13], [14]. Interpreted in units of distance, each fringe represents half the wavelength of the satellite's radar propagation. Furthermore, SAR interferometry can be generated by one antenna recording images at two different times, for two distinct satellite orbits, and this technique is known as repeat-pass (2-pass) InSAR. Alternatively two antennas on a single platform and orthogonal in the flight direction can be used, for a technique known as single-pass (single-track) InSAR. Generating elevation data is the most common InSAR application using repeat-pass or single-pass interferometry. Figure 2a shows two antennas at different locations A_1 and A_2, while Figure 2b illustrates the repeat-pass interferometry principle in which the radar device located at A_1 is used to determine the surface differences between times of acquisition t_1 and t_2.

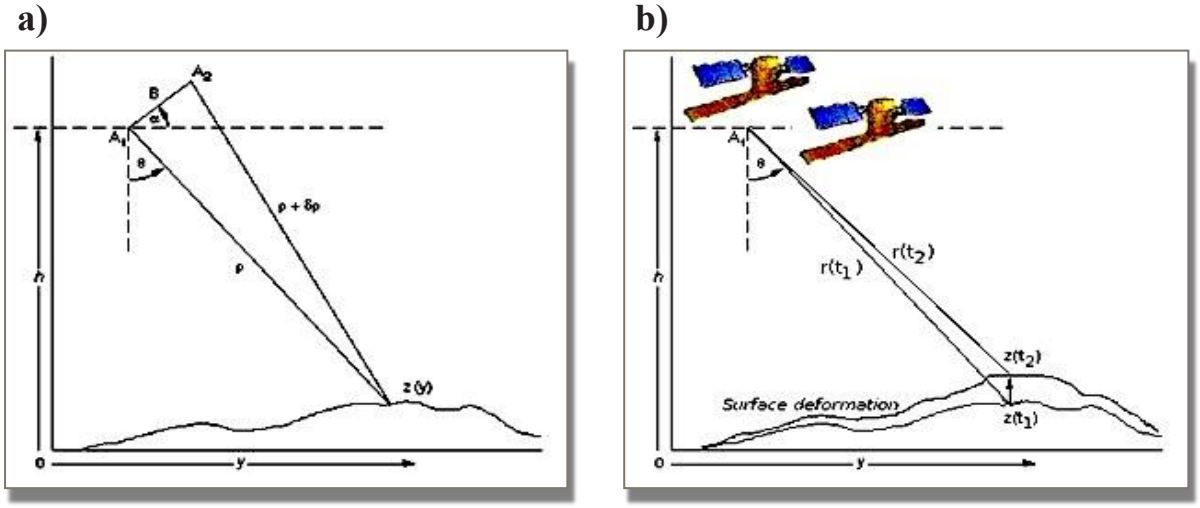

Fig. 2: Principle of InSAR measurement; a) Single-pass, b) Repeat-pass (modified from [15]).

GNSS

GNSS (Global Navigation Satellite Systems) are satellite systems which provide accuracy positioning and timing data using multiple signals received from a network of satellites. GPS (USA), GLONASS (Russia), Galileo (European Union) and Beidou (China) are well-known GNSS systems. The GNSS technology provides high accuracy positioning on the Earth's surface with global coverage, anywhere and at anytime. Range-like measurements are used to calculate 3-D position, velocity, and time (PVT) information of any point with cm level (or even higher) positioning accuracy. In the standard single point positioning mode four simultaneously tracked GNSS satellites are needed so that the four measurements can be used to compute the 3-D position of the GNSS receiver's antenna and the time correction to the receiver's clock. However, the augmented, high-precision GNSS techniques can be used for many geodetic and geoscience applications, including for monitoring ground motion due to a variety of geophysical phenomena. For example, during an earthquake, the position of GNSS receivers change and can be measured using high-precision GNSS techniques, including in real-time. In addition, GNSS techniques can play a significant role in elucidating seismic deformations [16], [17], even when the primary fault rupture does not reach the Earth's surface, by examining the stations' positions before and after the earthquake. Figure 3 indicates the geometric principle of single point positioning.

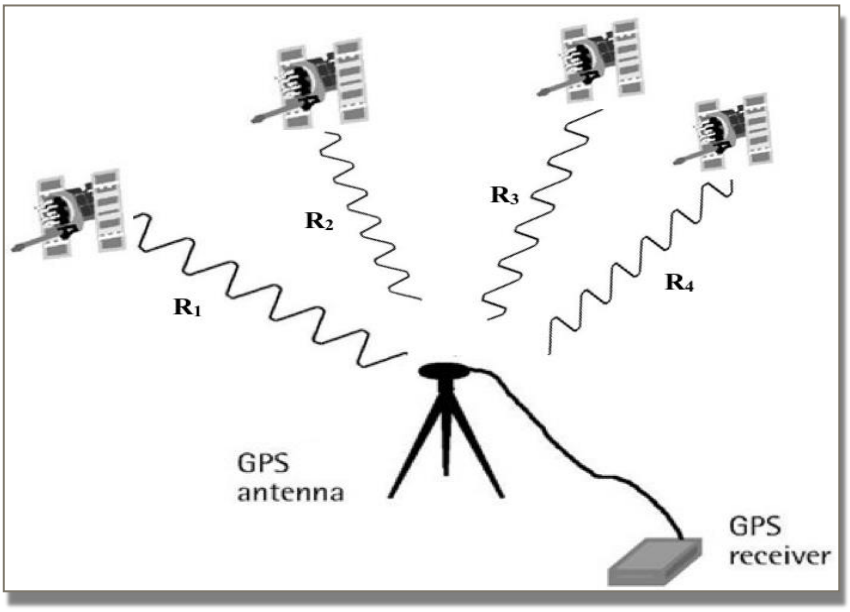

Fig. 3: A GPS receiver is used to measure position based on signals received from satellites and based on calculated distances R_1, R_2, R_3, R_4. Measurements signals from at least four satellites are used to estimate four parameters: position in 3 dimensions (x, y, z) and GPS time (t) (modified from [18]).

Coulomb Stress Change Modelling

Coulomb Stress Change Modelling provides an additional methodology with which to monitor and characterise both direct and indirect subsurface seismic activities over different scales. It describes the behaviour of an earthquake occurring at or near the faults. When an earthquake occurs it releases the stresses accumulated on the fault, and changes the stress field in the surrounding area [19], [20]. Coulomb Stress Change Modelling evaluates sources of seismic activity and the possibility of generating ground motion using focal mechanism data based on measurements of the earthquake, which are converted into 2D and 3D Earth

models, which are used to explore fault properties [21]. The focal mechanism datasets are based on the direction of arrival of the first waves (P-wave) from an earthquake at a seismograph, which reveal the direction of movement on a fault. The strike, dip, rake, slip, moment magnitude and source of depth information, allow the geometry and mechanism of the fault to be determined, as shown in Figure 4. The Coulomb Stress Changes depend on the fault mechanism of the earthquakes for assessing the static stress transfer and fault interactions. For this reason, in order to produce satisfactory results, information on the focal mechanism of the fault must be accurate. Even small changes in fault geometry can generate large differences in the results of Coulomb failure stress models.

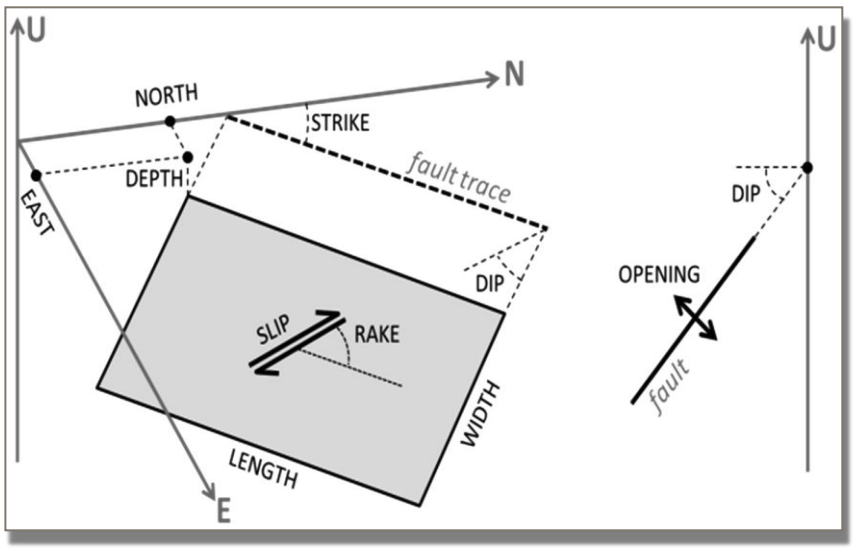

Fig. 4: Source parameters of faults: east and north position, depth, length, width, strike angle, dip angle, slip, (dislocation), rake (dislocation angle) and opening [22].

Data and Results

InSAR

The authors used data from the ERS-2 satellites to generate a mosaic of unwrapped interferograms for the Izmit earthquake. The available co-seismic imagery were acquired on the 13th August and 17th September 1999. The 25 m resolution Stripmap images were recorded with a mean incidence angle 23 degrees and a swath of 102.5 km (telemetered). The C-Band sensors on ERS-2 operate with a wavelength of 56 mm and repeat cycle of 35 days. As seen in Table 1, both co-seismic images were obtained from ascending orbits, and the resulting interferogram is displayed in Figure 5. The images were acquired four days before and 31 days after the Izmit earthquake, and processed using the ROI-PAC 3.0.1 software, which is mainly used for analysing topography and surface change. It is able to perform a range of tasks from raw data input to geocoded interferogram, based on the interferometric baseline, and uses the digital elevation model (DEM) and (optional) deformation model(s) as a reference to estimate surface displacement with millimetre level of precision.

Table 1: SAR satellite data used for co-seismic deformation.

Satellite	Date	Orbit	Orbit Track
ERS-2	13-08-1999	22556	Ascending
ERS-2	17-09-1999	23057	Ascending

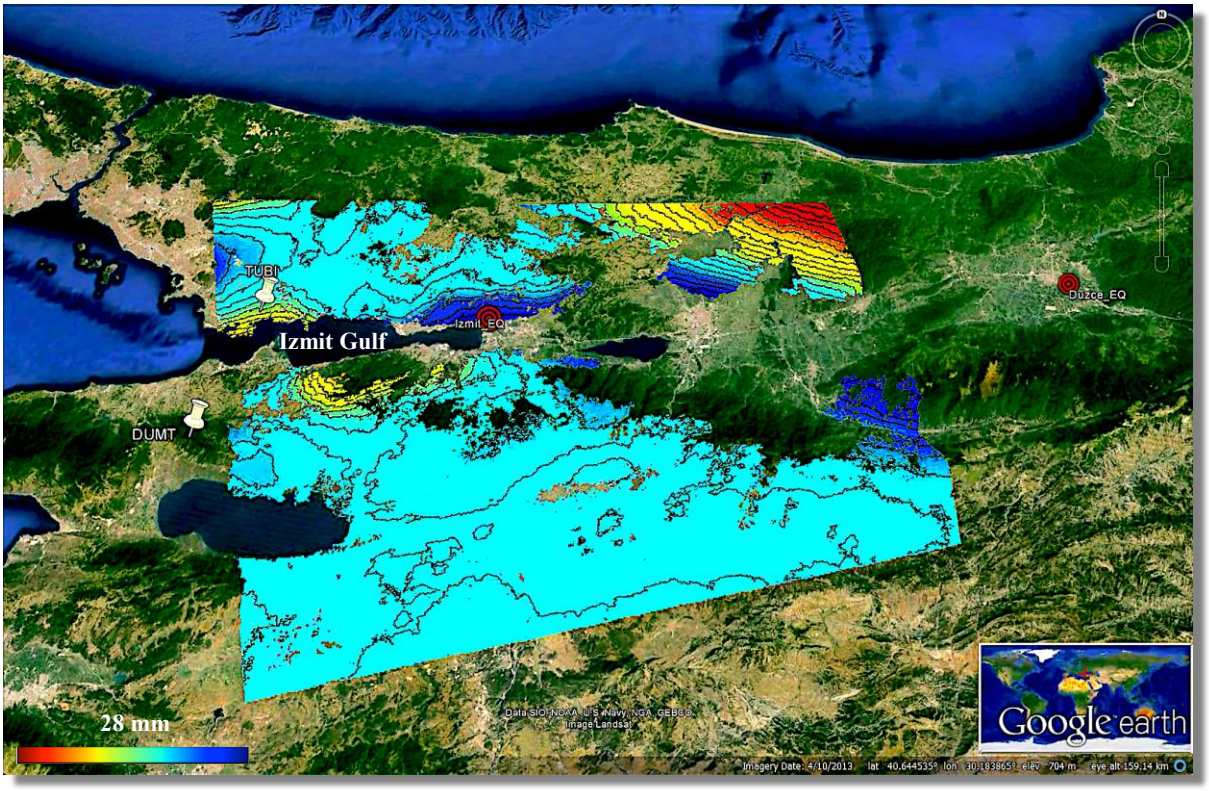

Fig. 5: Mosaic unwrapped phases derived from ERS-2 data displayed over a Google Earth image. The data were derived from ascending orbits on 13 August, 4 days before the earthquake and 17 September, 31 days after the earthquake . The colour code indicates the phase differences depending on surface changes.

Figure 5 shows high deformation areas in the interferogram, the highest value being 432 mm in the north-east section which is close to Duzce earthquake epicentre. The estimated accuracy of the InSAR deformation measurements according to [23], [24] is 10-20 mm. This ERS-2 SAR interferogram covers a long period of 31 days following the main shock, and includes significant post-seismic deformations. In this image the region of the epicentre and surrounding areas show large deformations, which are in good agreement with GNSS and Coulomb stress changes observations. There are also some blank areas where phase coherence, due to decorrelation, is lost and data cannot be obtained within the interferogram. The areas which have a high level of deformation, dense vegetation and water areas cause low coherence during SAR interferometry processing.

GNSS

Only two continuously operating GPS stations of MAGNET (DUMT, TUBI) were available and provided by the Scientific and Technological Research Council of Turkey (TUBITAK). As seen from Figure 6, DUMT is located south of the NAF, while TUBI is located north of the NAF. Each station is equipped with a Trimble 4000 SSE receiver with choke-ring antenna. Continuous GPS (CGPS) measurements were recorded with 30 s data sampling rate, and the elevation mask was 10 degrees. DUMT and TUBI datasets were processed using the AUSPOS web service to generate daily solutions, as shown in Table 2 for 17th August 1999. Additionally, the RTKLIB 2.4.2 software was used for data processing with 30 s kinematic epochs. Figures 7 shows the 30 s solutions for the DUMT and TUBI stations, for 17th August 1999.

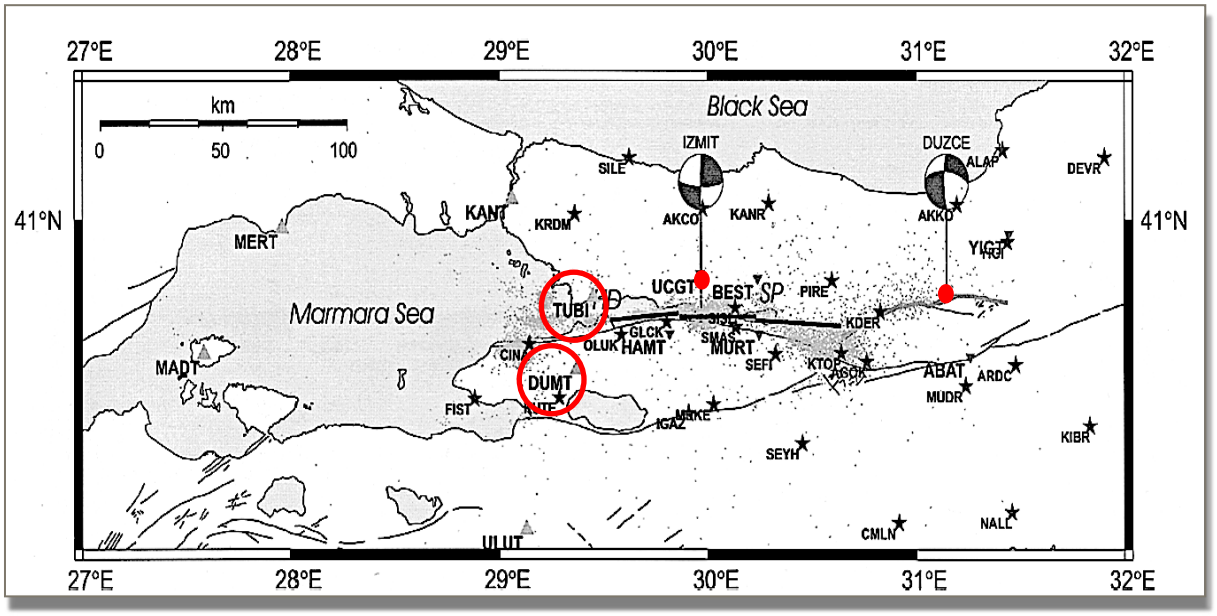

Fig. 6: Location of the MAGNET stations (▲), semi-continuous GPS stations (▼), and campaign sites (✶) in Marmara region. DUMT and TUBI have been identified with red circles. Beach balls and red dots indicate two major ruptures in 1999: Izmit and Duzce earthquakes. Black lines show the active faults [25].

The results from AUSPOS processing show that there was significant movement on the 17th August 1999 at both stations (Table 2). The DUMT station moved -305 mm north, -330 mm east and 30 mm upwards, while the TUBI station moved -331 mm north, 530 mm east and -64 mm downwards. The estimated accuracy of GNSS precise positioning is 3 to 5 mm for the horizontal components and 10 to 20 mm for the vertical components [26]. Therefore, as a result of the earthquake the DUMT movement was south-westerly whereas the TUBI station movement was south-easterly. Hence the movements in the northern part of the NAF were south easterly and in the southern part they were south westerly, indicating that this earthquake caused right-lateral movement.

Table 2: DUMT and TUBI station results processed using AUSPOS.

Station Name	17th August 1999		
	North (mm)	East (mm)	Height (mm)
DUMT	-305	-333	30
TUBI	-331	530	-64

The systematic differences between the patterns of co-seismic deformations have been identified by processing with the RTKLIB software as seen in Figure 7. The 30 s epoch solutions for the DUMT and TUBI stations indicate that there were displacements on the 17th August 1999. Although these results are questionable, due to the age of the dataset, for the co-seismic results there is still some consistency between DUMT and TUBI stations as the earthquake occurred at 01:39 (UTC).

a) DUMT **b) TUBI**

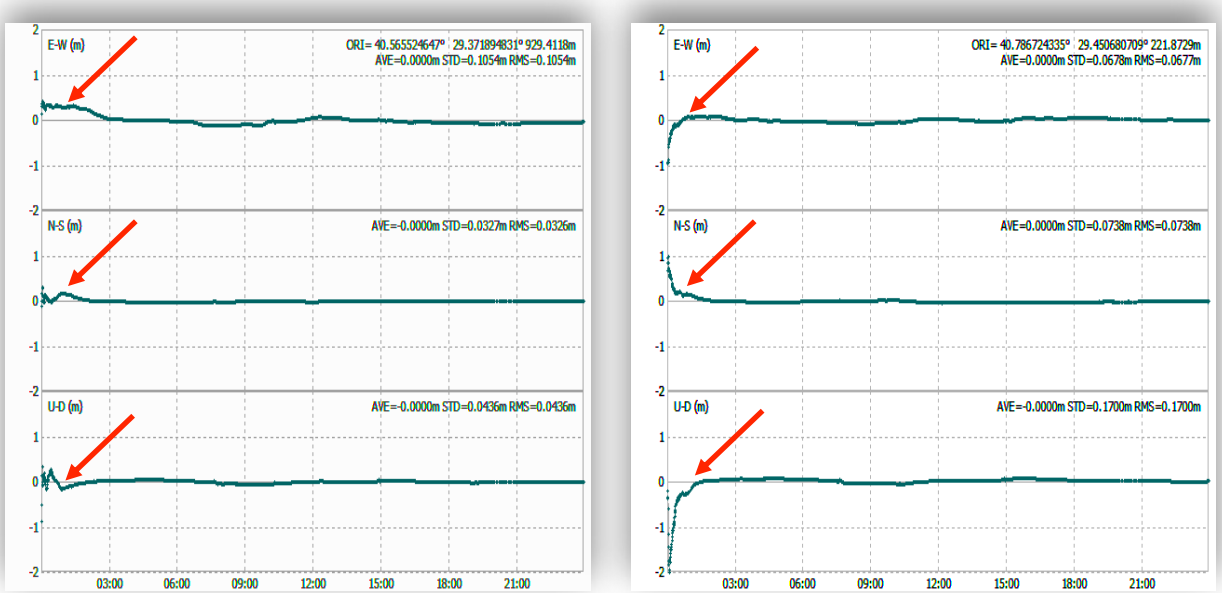

Fig. 7: On 17th August 1999, 30s epoch solutions; (a) DUMT GPS station and (b) TUBI GPS station. Data is from five days before the earthquake. The position varies over 24 hours in the north-south (N-S), east-west (E-W) and vertical (U-D) directions. Red arrows indicate the starting point of the earthquake.

In addition, the deformations of the TUBI continuous GPS station were calculated, and the InSAR and GPS deformation results were compared, as seen Table 3. At the TUBI station the difference in deformation estimates is 81 mm. The calculated deformations by InSAR are lower than the GNSS deformations because GNSS has the immediate data (co-seismic) whereas the InSAR data has 35 day differences between two SAR images. In that case the first image (13th August 1999) taken before the earthquake includes inter-seismic deformation and the second image taken after the earthquake (17th August 1999) includes co-seismic and post-seismic deformation. After the main shock (co-seismic) the seismic activity still continues but is less powerful than the main shock and can reverse the movement due to the

elastic behaviour in the mantle or lower crust. Since the DUMT GPS station is not within the area of the interferogram it was excluded from comparisons between GNSS and InSAR (Figure 5).

Table 3: Comparison between LOS from InSAR and GPS^{LOS} results at DUMT and TUBI.

Station Name	InSAR (mm)	GPS^{LOS} (mm)	InSAR and GPS^{LOS} Differences (mm)
DUMT	no data	-79	N/A
TUBI	82	163	81

Coulomb Stress Change Modelling

In addition to calculating the stress changes caused by the Izmit earthquake on 17th August 1999, the seismic focal mechanism data from the ISC were used in order to model this earthquake. In this model the best rupture parameters (strike, dip, rake and depth values of the faulting) have been chosen, and using Coulomb 3.3 software were used to generate the model of the Coulomb stress changes at depth. The coefficient of friction in all the calculations was assumed to be 0.4, which minimises the calculation error [27]. Figure 8 shows the calculated stress changes of the Izmit earthquake. Figure 9 shows the horizontal displacement, while Figure 10 indicates the vertical displacement.

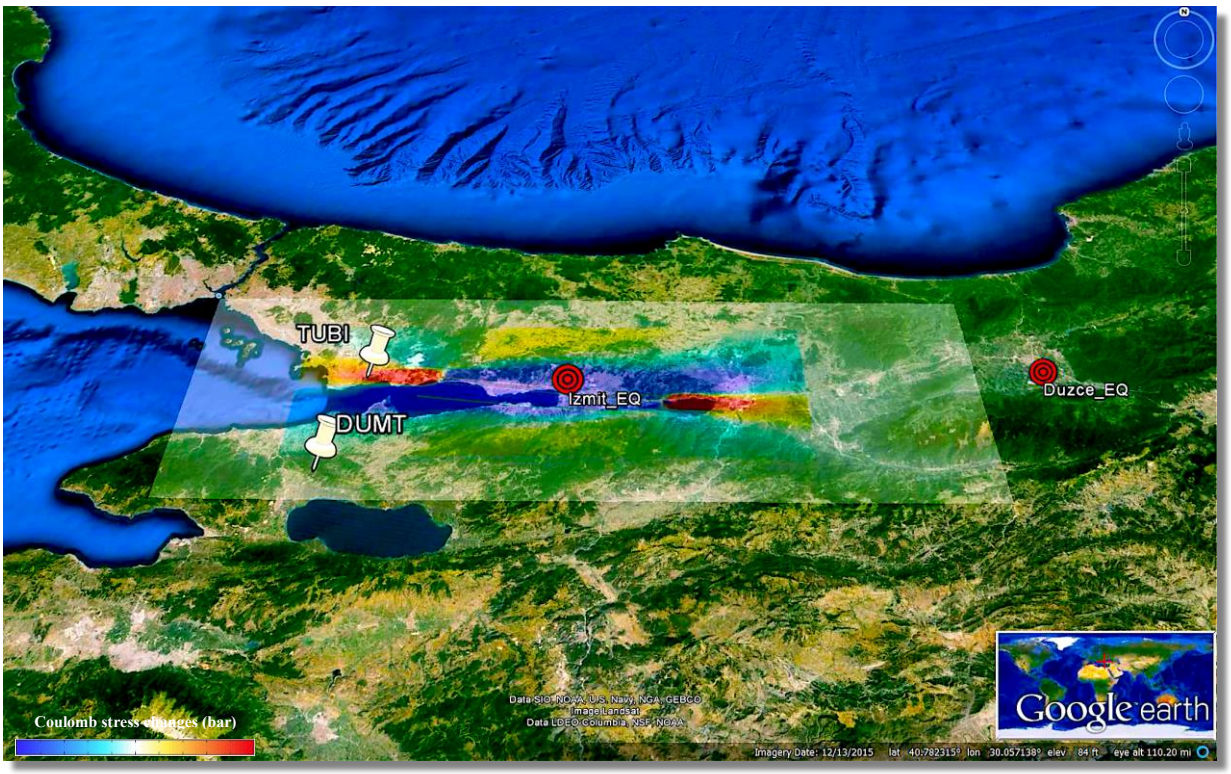

Fig. 8: Map of Coulomb stress changes, displayed on a Google Earth image for 17th August 1999. Model parameters: M_w =7.4, Strike = 271°, Dip = 78°, Rake = -168°, Depth =17 km, Time = 01:39 (UTC) and friction coefficient = 0.4. Epicentre of the earthquake and locations of the DUMT and TUBI stations are marked on the map. Colour code indicates the Coulomb stress changes; dark blue and red are high stress values.

As can be seen from Figure 8, the Izmit earthquake had a significant impact on the stress within the Marmara region. The accumulated Coulomb stress change increases by 5 bars, which confirms that this earthquake had increased the stresses around the fault. In addition the model shows that the area around the TUBI station was subject to greater stress than the area around the DUMT station. These observations, as well as the InSAR result in Figure 5 and the GNSS result in Table 2, suggest that the TUBI region was exposed to greater deformation than the DUMT region. Moreover, the stress changes over the fault beyond the rupture of the Izmit earthquake indicate that the main shock rupture bolstered stress over both the eastern and western continuation of the NAF which provides conditions for the occurrence of the after-shocks. The calculated horizontal displacement model shows right lateral movement, which is the characteristic feature of the NAF, as seen in Figure 9. Therefore there is clear evidence that the results of this model are consistent with geological data. Furthermore, inspection of Figure 10 indicates that the northern part of the Marmara region moved downwards while the southern part moved upwards, which corresponds to the calculated co-seismic Coulomb stress changes.

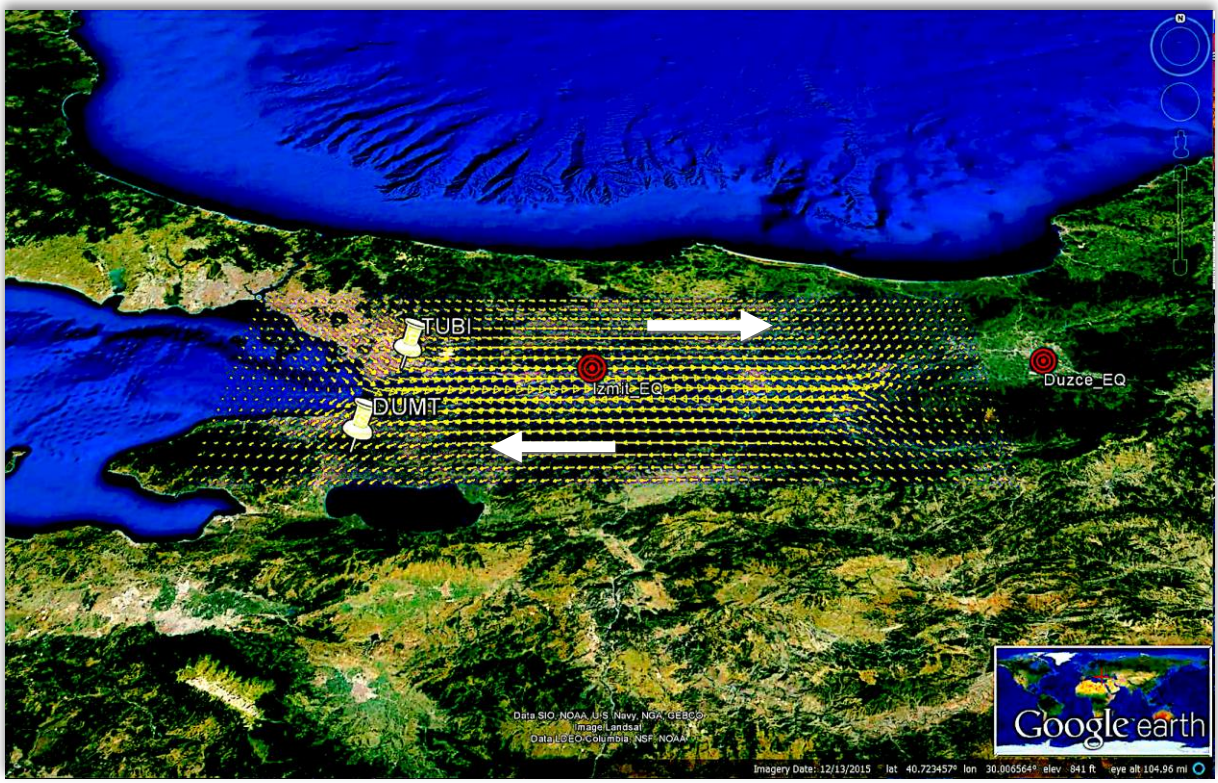

Fig. 9: The horizontal displacement model with layer displayed on a Google Earth image for 17th August 1999. Aftershock focal mechanisms: M_w= 7.4, strike = 271°, dip = 78°, rake = -168°, depth 17 km, time = 01:39 (UT). Red arrows show the direction of vectors due to earthquake.

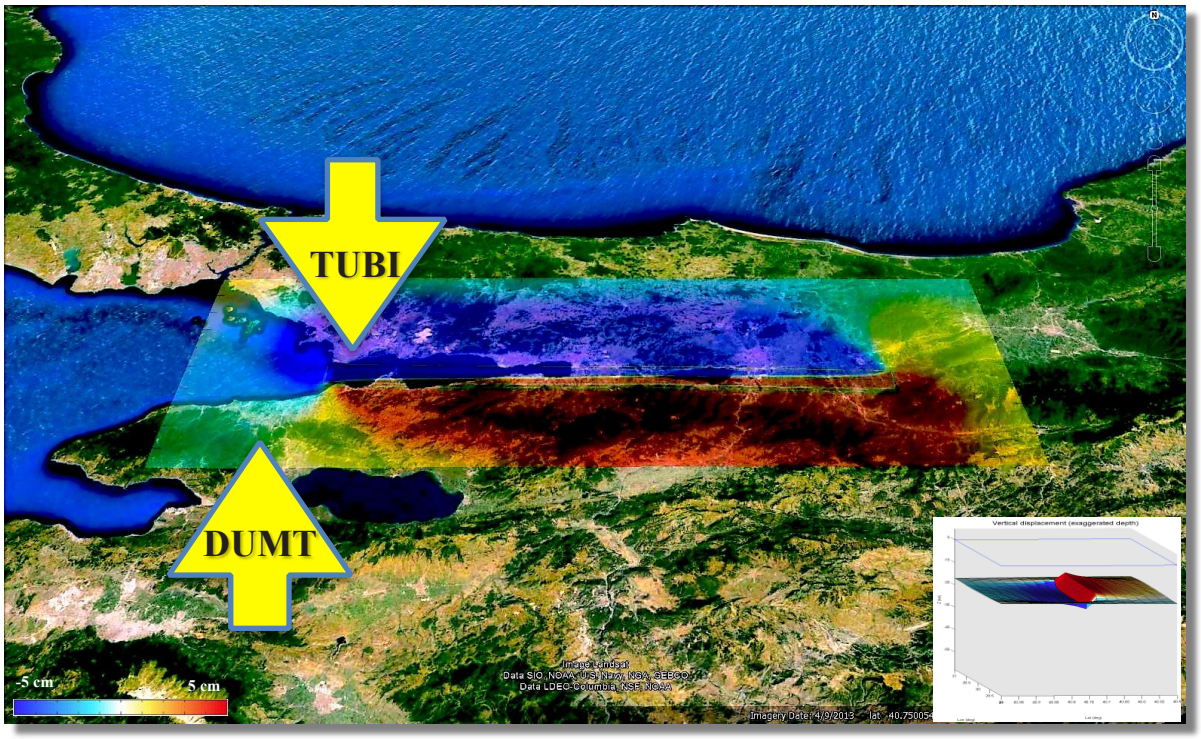

Fig. 10: The vertical displacement model overlaid on a Google Earth image, 17th August 1999. Aftershock focal mechanisms: M_w= 7.4, strike = 271°, dip = 78°, rake = -168°, depth 17 km, time = 01:39 (UT). Yellow arrows show the direction of movement of continuous GPS stations caused by the earthquake. Colour code indicates the vertical displacement; dark blue where the ground moving downward and red where the ground moving upward.

Conclusion

In order to determine the Izmit earthquake effects, InSAR and GNSS measurements, and Coulomb Stress Change Modelling were used in this paper. InSAR produces high spatial resolution information, whereas GNSS and focal mechanism data provide high temporal resolution. Together they can provide important information for measurement of earthquake deformation and analysis of earthquake hazards. The InSAR data indicates that the highest deformation is approximately 432 mm in the north-east of the interferogram, occurring 70 km north-east of the Izmit epicentre, as shown in Figure 5. This area is close to the Duzce earthquake epicentre, which occurred three months after the Izmit earthquake. In addition, the GNSS results show that the Izmit earthquake caused the northern part of the NAF to move in a south easterly direction and the southern part to move in a south westerly direction. This partially explains why the fault extended westwards of the surface faults, underneath of the Gulf of Izmit. Furthermore this westerly movement has changed the stress distribution and increased the deformation around the fault zone, which may be the reason for low coherence between the images. The calculated TUBI station LOS deformation was compared to the InSAR LOS deformation from Figure 5, and a 81 mm difference between the results was noted. This discrepancy could be because InSAR data includes 31 days post-seismic deformation. The Coulomb Stress Change Modelling (Figure 8) indicates that the stress changes caused by the Izmit earthquake are greater around the fault zone and epicentre, where the TUBI and DUMT stations are also located. Moreover, inspection of Figure 9 shows that the calculated horizontal displacement model is right lateral, which corresponds well with the geological data and the GNSS results. In addition the northern part of the Marmara region

moved downwards, while the southern part moved upwards, as can be seen in Figure 10. This movement also corresponds well with GNSS results at DUMT. Consequently, there is an apparent correlation between the InSAR, GNSS and Coulomb stress modelling results, which contribute to the identification of the Izmit earthquake characteristics.

Acknowledgements

The SAR data have been provided by ESA within the C1F.29006 project and the GPS data have been provided by TUBITAK.

References

1. Sengör, A., Tüysüz, O., Imren, C., Sakinç, M., Eyidogan, H., Görür, N., Rangin, C. (2005). The North Anatolian fault: A new look. *Annu. Rev. Earth Planet. Sci., 33*, 37-112.

2. Karaman, M. E. (2001). Yapısal jeoloji ve uygulamaları, Akdeniz Üniversitesi, Mühendislik Fakültesi, Jeoloji Bölümü.

3. Kalkan, E. and S. Kunnath (2008). "Relevance of absolute and relative energy content in seismic evaluation of structures." Advances in Structural Engineering **11**(1): 17-34.

4. Ozmen, B. (2000). Damage due to August 17, 1999 Izmit Bay Earthquake, Technical Report, Turkish Earthquake Foundation, TDV/DR 010–53.

5. AFAD (2011). Izmit Depremi (17 Agustos 1999) Raporu. Ankara, Turkiye, T.C.Basbakanlık Afet ve Acil Durum Yonetimi Deprem Dairesi Baskanlıgı, Ankara**:** 100.

6. Hamiel, Y. and Y. Fialko (2007). "Structure and mechanical properties of faults in the North Anatolian Fault system from InSAR observations of coseismic deformation due to the 1999 Izmit (Turkey) earthquake." Journal of Geophysical Research: Solid Earth **112**(B7).

7. Bos, A., S. Usai and W. Spakman (2004). "A joint analysis of GPS motions and InSAR to infer the coseismic surface deformation of the Izmit, Turkey earthquake." Geophysical Journal International **158**(3): 849-863.

8. Reilinger, R., S. Ergintav, R. Bürgmann, S. McClusky, O. Lenk, A. Barka, O. Gurkan, L. Hearn, K. Feigl and R. Cakmak (2000). "Coseismic and postseismic fault slip for the 17 August 1999, M= 7.5, Izmit, Turkey earthquake." Science **289**(5484): 1519-1524.

9. Çakir, Z., de Chabalier, J.-B., Armijo, R., Meyer, B., Barka, A., & Peltzer, G. (2003). Coseismic and early post-seismic slip associated with the 1999 Izmit earthquake (Turkey), from SAR interferometry and tectonic field observations. *Geophysical Journal International, 155*(1), 93-110.

10. Bürgmann, R., S. Ergintav, P. Segall, E. H. Hearn, S. McClusky, R. E. Reilinger, H. Woith and J. Zschau (2002). "Time-dependent distributed afterslip on and deep below the Izmit earthquake rupture." Bulletin of the Seismological Society of America **92**(1): 126-137.

11. Peltzer, G. and P. Rosen (1995). "Surface displacement of the 17 May 1993 Eureka Valley, California, earthquake observed by SAR interferometry." Science **268**(5215): 1333.

12. Bock, H. (1978). Introduction to rock mechanics, Dept. of Civil and Systems Engineering, James Cook University of North Queensland.

13. Massonnet, D., M. Rossi, C. Carmona, F. Adragna, G. Peltzer, K. Feigl and T. Rabaute (1993). "The displacement field of the Landers earthquake mapped by radar interferometry." Nature **364**(6433): 138-142.

14. Pritchard, M. and M. Simons (2006). "An aseismic slip pulse in northern Chile and along-strike variations in seismogenic behavior." Journal of Geophysical Research: Solid Earth **111**(B8).

15. European Space Agency. (2007). "InSAR Principles." Retrieved 19 December, 2014, from http://www.esa.int/esapub/tm/tm19/TM-19_ptA.pdf.

16. Blewitt, G., M. B. Heflin, K. J. Hurst, D. C. Jefferson, F. H. Webb and J. F. Zumberge (1993). "Absolute far-field displacements from the 28 June 1992 Landers earthquake sequence." Nature **361**(6410): 340-342.

17. Arnadóttir, T. and P. Segall (1994). "The 1989 Loma Prieta earthquake imaged from inversion of geodetic data." JOURNAL OF GEOPHYSICAL RESEARCH-ALL SERIES- **99**: 21,835-821,835.

18. Japan Association of Remote Sensing. (1996). "Ground Positioning Data." Retrieved 4 April, 2015, from http://wtlab.iis.u-tokyo.ac.jp/~wataru/lecture/rsgis/rsnote/cp6/cp6-8.htm.

19. Stein, R. S. and M. Lisowski (1983). "The 1979 Homestead Valley earthquake sequence, California: Control of aftershocks and postseismic deformation." Journal of Geophysical Research: Solid Earth **88**(B8): 6477-6490.

20. Stein, R. S., G. C. King and J. Lin (1994). "Stress triggering of the 1994 M= 6.7 Northridge, California, earthquake by its predecessors." Science **265**(5177): 1432-1435.

21. Toda, S., J. Lin and R. S. Stein (2011). "Using the 2011 M w 9.0 off the Pacific coast of Tohoku Earthquake to test the Coulomb stress triggering hypothesis and to calculate faults brought closer to failure." Earth, planets and space **63**(7): 725-730.

22. Atzori, S. and S. Salvi (2014). "SAR Data Analysis in Solid Earth Geophysics: From Science to Risk Management." Land Applications of Radar Remote Sensing, Edited by F. Holecz, P. Pasquali, N. Milisavljevic and D. Closson, InTech, ISBN: 980-953.

23. Ferretti, A., C. Prati and F. Rocca (2001). "Permanent scatterers in SAR interferometry." Geoscience and Remote Sensing, IEEE Transactions on **39**(1): 8-20.

24. Lu, Z. (2007). "InSAR imaging of volcanic deformation over cloud-prone areas–Aleutian Islands." Photogrammetric Engineering & Remote Sensing **73**(3): 245-257.

25. Feigl, K. L., F. Sarti, H. Vadon, S. McClusky, S. Ergintav, P. Durand, R. Bürgmann, A. Rigo, D. Massonnet and R. Reilinger (2002). "Estimating slip distribution for the Izmit mainshock from coseismic GPS, ERS-1, RADARSAT, and SPOT measurements." Bulletin of the Seismological Society of America **92**(1): 138-160.

26. Ergintav, S., R. Bürgmann, S. McClusky, R. Cakmak, R. Reilinger, O. Lenk, A. Barka and H. Özener (2002). "Postseismic deformation near the Izmit earthquake (17 August 1999, M 7.5) rupture zone." Bulletin of the Seismological Society of America **92**(1): 194-207.

27. King, G. C., R. S. Stein and J. Lin (1994). "Static stress changes and the triggering of earthquakes." Bulletin of the Seismological Society of America **84**(3): 935-953.

APPENDIX A

15ASRC
List of Presentations & Posters

List of Presentations

Abstracts are listed in alphabetical order of first author

Name of Presenter	Names of all authors	Title
Ruken Alac Barut	Ruken Alac Barut, John Trinder, Chris Rizos	Investigation of the Izmit Earthquake with Interferometric SAR, Global Navigation Satellite System (GNSS) Positioning and Geophysical Seismic Modelling
Stuart Anderson	Stuart Anderson	Radar scattering properties of satellite wakes and their utility for space situational awareness
Andrew Ash	Andrew Ash	A perspective on current UK SSA Research
Jeff Ayton	Jeff Ayton	Astrobiology and life sciences, Human Biology and Medicine
Rhea Barnett	Rhea Barnett, Colin Waters	Relationship between field-aligned and geomagnetic induced currents
Stephen Bathgate	Stephen Bathgate, Rajesh Ganesan, Marcela Bilek and David McKenzie	A plasma thruster using a magnetic nozzle with a HIPIMS plasma source
Annalea Beattie	A. Beattie, L. Offer, I. H. Mogosanu, J. G. Blank, K. A. Campbell, J. Pollock, K. Hodgson, A. Phelps, K. Silburn,	NASA Spaceward Bound New Zealand 2015: Advancing Astrobiology Curriculum Via Teacher-Scientist Collaboration in the Taupo Volcanic Zone
Vickie Bennett	Vickie Bennett	Planetary samples from the Early Earth: New revelations from the oldest terrestrial rocks
Russell Boyce	Russell Boyce	Near-Earth Space Physics : the science to underpin Space Situational Awareness
Russell Boyce	Russell Boyce and Carol Oliver	Preparing for the mid-term Decadal Plan review - results of a survey of views from the space science community
Courtney Bright	Courtney Bright, Rounak Manoharan, Siddharth Pandey, Hilbert van Pelt, Jai Vennik	Venus Atmospheric Pathfinder Research Vehicle: A Mission Concept Study
Courtney Bright	Courtney Bright, Sean Tuttle, Andrew Neely	Stereolithographic 3D Printed Nozzles for Cold Gas Propulsion Experiments
Tim Broadbent	Tim Broadbent, Jason Held	Solving the Mission Operations Problem
Melrose Brown	M. Brown, R. Boyce, D. Griffin, P. Lorrain, I. Dimitrijevic, A. Ramana, C. Benson, A. Lambert, M. Polo, S. Oberst, S. Tuttle, D. Lingard, I. Cartwright, G. Hu, M. Young, T. Teske, G. Colosi, B. Jamali, J. Horridge, G. Dall'Armi-Stoks	Buccaneer Risk Mitigation Mission
James Bultitude	James Bultitude, Tim Broadbent, Yiwei Han, Lily Qiao, Joon Wayn Cheong, Barnaby Osborne	Attitude Determination and Control System for UNSW's QB50 Cubesat
Iver Cairns	Iver H. Cairns	Solving the "Type II Solar Radio Burst Problem" and Predicting Space Weather
Christopher Capon	Christopher Capon	Development of a coupled PIC-DSMC method for the study of objects in a charged space environment
Graziella Caprarelli	G. Caprarelli, A. White, R. Orosei.	Mars Australian Remote Virtual Experiment Laboratory (MARVEL)

Name of Presenter	Names of all authors	Title
Brett Carter	Brett Carter, Endawoke Yizengaw, Chin Lin, Rezy Pradipta, Robert Norman, Tzupang Tseng, James Bennett, Rebecca Bishop, Matthew Francis, Michael Terkildsen, Keith Groves, Ronald Caton and Kefei Zhang	The 2015 St. Patrick's Day superstorm: Effects in the near-Earth space environment and impacts on technologies
Brett Carter	Brett Carter, Endawoke Yizengaw, Rezy Pradipta, Alexa Halford, Robert Norman and Kefei Zhang	On the vulnerability of the equatorial region to geomagnetically induced currents
Manuel Cervera	Manuel Cervera, Harris	TID wavelength control of disturbance features in VI and QVI ionograms
Christine Charles	Christine Charles and Rod Boswell	Plasma propulsion as a vehicle for science in space and in the laboratory
Joon Wayn Cheong	Joon Wayn Cheong, Barnaby Osborne, Jannick Habets	Effect of Self-shadowing and Attitude on Cubesat Solar Power Generation: A Case Study on UNSW EC0 QB50 Cubesat
TJ Chin	TJ Chin, Matthew Tetlow, Mark Rutten	Robust Space Object Detection
Aditya Chopra	Aditya Chopra, Charles H. Lineweaver	Is Habitability Constrained by Biology? The Case for a Gaian Bottleneck
Rowena Christiansen	Rowena Christiansen	Update of the Australian Resuscitation Council Cold Injuries Guideline – Results of a Literature Review
Jonathan Clarke	Jonathan Clarke, Waldie, M. Cooper, S. George, S. Houlahan, G. Murphy, K. Silburn, D. Sprigg and M. Sprigg	The performance of field science in a simulated space suit: stromatolite identification by geologists and non geologists
Daniel V. Cotton	Daniel V. Cotton, Jonathan P. Marshall, Kimberly Bott, Lucyna Kedziora-Chudczer, Jeremy Bailey	Carrying a Torch for Dust in Binary Star Systems
William Crowe	William Crowe, Nathan Kinkaid, John Olsen, John Page	Opportunistic flyby characterisation of Earth passing asteroids
William Crowe	William Crowe, Nathan Kinkaid, John Olsen, John Page	Cooperative estimation of asteroid mass
Martin Cupak	M. Cupak, P. A. Bland, M. C. Towner, R. M. Howie, J. P. Paxman, E. K. Sansom, H. Devillepoix, G. K. Benedix, S. J. Tingay, M. J. Galloway and T. Jansen-Sturgeon	Desert Fireball network: Handling of the multi terabyte data
Julie Currie	Julie Currie, Prof. Colin Waters, Prof. Fred Menk, Murray Sciffer	SuperDARN Backscatter During Intense Geomagnetic Storms
Luke Daly	L. Daly , P. A. Bland , L. V. Forman , P. W. Trimby , S. Moody , L.Yang , H.W. Liu , S. P. Ringer and M. Saunders	Early solar system events revealed by analysis of tiny nuggets
Andrew Dempster	Andrew Dempster	Off Earth Mining
Hadrien Devillepoix	Hadrien Devillepoix	A satellite survey with the Desert Fireball Network
Keira Doherty	Keira Doherty, Yao Xiong Loo, Nicole Blinco, Liam Waldron, and Jonathon Clarke	Photovoltaic Power System Design for a Mars Analogue Research Station
Kerrie Dougherty	Kerrie Dougherty	Space-related Research and Innovation in the Australian Defence Scientific Service
Zheyuan Du	Zheyuan Du, Linlin Ge, Xiaojing Li and Alex Hay-Man Ng	Atmospheric Correction over Ordos region based on Differential Interferometry And Persistent Scatterer Interferometry

Name of Presenter	Names of all authors	Title
Lucy V Forman	L. V. Forman, P. A. Bland, J. Smith, J. Paxman	Looking for a Needle in a Haystack: The Search for Extralunar Fragments in Apollo 14 Soils
Lewis Freeland	Lewis Freeland, Michael Terkildsen	The symmetry of halo Coronal Mass Ejections as a quantitative predictor for severe space weather at Earth
Robert S. Fuller	Robert S. Fuller	Stellarium Skycultures as an aid to K-6 Science Syllabus Cross-cultural Understanding of Indigenous Astronomy
George Georgevits	George Georgevits	Detection of Kuiper Belt Objects by Stellar Occultation
Adam Gilmour	Adam Gilmour	A Space Academy to inspire the next generation of Space Engineers
Eamonn Glennon	Eamonn Glennon, Joon Wayn Cheong, Mr Kevin Parkinson, Andrew Dempster	Qualifying the Kea GPS Receiver for UNSW's EC0 CubeSat
Alice Gorman	Alice Gorman	"Is it wrong to wish on space hardware?" Exploring emotional attachments to spacecraft
Carla Guedes	Carla Guedes and Duane Hamacher	Meteor Traditions of the Torres Strait Islanders and other Melanesian Cultures
Thomas Haber	T. Haber, M. D. Norman, V. C. Bennett and F. Jourdan	Constraining the bombardment history of Moon with a set of Apollo 16 impact melts rocks
Jacob Hacker	Jacob Hacker, Nikita Sardesai, Martin Losekamm, Adam Vigneron	Legal and Political Implications of Future On-Orbit Servicing Missions
Duane Hamacher	Duane Hamacher, Robert Fuller, Trevor Leaman, Carla Guedes, John South, William Stevens, Michelle Gantevoort, and Robert Pankhurst	An Introduction to Sydney Aboriginal Astronomy
Trevor Harris	Trevor J Harris, Adrian D Quinn	The DSTO Ionospheric Sounder Replacement for JORN
Andrew Heitmann	Andrew Heitmann, Robert Gardiner-Garden, Andrew MacKinnon, Iain Reid, Bruce Ward	Preliminary observations of ionospheric disturbances using 2D angle-of-arrival estimation on oblique incidence soundings
Jason Held	Jason Held, Daniel Bunker, Tim Broadbent	Parabolic flight testing results for DragEN Electrodynamic Tether Deployer
Gail Higginbottom	Gail Higginbottom	Origins of Standing Stone Astronomy in Britain
Gabriela Hobbs	G.N. Hobbs and S. M. Coleman	The Case for Mining Asteroids
Steven Hobbs	S.W. Hobbs, D. J. Paull and J. D. A. Clarke	A Comparative Analysis of Terrestrial and Martian Gullies: Evidence for Erosion by Complex, Multi-Agent Processes
Tyler Hobson	Tyler A. Hobson, I. Vaughan L. Clarkson, Travis Bessell, Mark Rutten, Neil Gordon	Initial Orbit Determination using Minimal Imagery and Constrained Trajectories
Jonti Horner	Jonti Horner, Bruna Contro, Robert Wittenmyer & Jonathan Marshall,	The Structure of the 'Asteroid-belt' Analogue Around HR8799
Anthony Horton	Anthony Horton, Lee Spitler, Matthew Colless, Michael Ashley, Joss Bland-Hawthorn, Russell Boyce, Tamara Davies, Roger Franzen, Karl Glazebrook, Jon Lawrence, Raymond Norris, Christopher Power, Jordi Puig-Suari, Sam Reisenfeld, Emma Ryan-Weber	Australian Space Eye: Ultra-faint astronomical imaging from a CubeSat
Robert M. Howie	Robert M. Howie, Jonathan Paxman, Philip A. Bland, Martin C. Towner	Deploy Your Own Desert Fireball Network Observatory
Trevor Ireland	Trevor R. Ireland	Hayabusa Mission Update
Moriba Jah	Moriba Jah	Perspective on current US SSA research

Name of Presenter	Names of all authors	Title
Ingo Jahn	I. Jahn, C. Manzie, D. Buttsworth, A. Paull	Aerodynamics and Control Optimal Design for Hypersonic Vehicles
Eriita Jones	Eriita Jones, Graziella Caprarelli, Franklin Mills	The Thermophysical Properties of Impact Crater Ejecta and Floor Materials on Mars
Eriita Jones	Eriita Jones	Shallow transient liquid water on Mars and its implications for life: Lessons from the Phoenix Lander and Curiosity Rover
Dhiren Kataria	Dhiren Kataria	Enhanced performance low resource in-situ sensors for space missions
Dhiren Kataria	Dhiren Kataria, Anasuya Aruliah, Alan Smith, Robert Wicks, Rahil Chaudery, Andrew Malpuss, Gethyn Lewis	Nanosatellites for in-situ studies of the Earth's ionosphere and thermosphere – exploiting the QB50 mission opportunity for Space Weather science
Lucyna Kedziora-Chudczer	Lucyna Kedziora-Chudczer, Daniel V. Cotton, David J. Kedziora and Jeremy Bailey	Observations of H3+ Molecular Emissions in Jupiter's Aurora
Piers Koefoed	P. Koefoed, Y. Amelin, Q-Z. Yin, M. E. Sanborn, M. Huyskens	U-Pb dating of the oldest known planetary meteorite: The achondrite Asuka 881934
Alexey Kondyurin	Alexey Kondyurin	Large size space construction for space exploitation
Ed Kruzins	Ed Kruzins	Options for Australian Payloads and Cubesats with NASA
Daniel Kucharski	Daniel Kucharski, James Bennett	The interaction between the Earth's magnetic field and the spinning satellites
Vickal Kumar	Vickal V. Kumar, Zahra Bouya, Murray Parkinson, David Neudegg, Phillip Maher	On the prediction of foF2 using 10.7 cm solar flux and Kp index
Andrew Lambert	Andrew Lambert and Manual C. Polo	Progress in Passive Optical Tracking Using the Falcon Telescope Network
Trevor Leaman	Duane Hamacher and Trevor Leaman	Animals in Australian Aboriginal Astronomical Traditions
Bo Li	B. Li, Iver H. Cairns, J.T. Gosling, G. Steward, M. Francis, D. Neudegg, H. Schulte in den Baumen, P.R. Player, A.R. Milne	Mapping magnetic field lines between the Sun and Earth
David Lingard	D. Lingard, M. Rutten, I. Carwright, R. Earl, A. Dempster, E. Glennon, K. Parkinson, R. Boyce, M. Brown	Australian Participation in the Biarri Cubesat Missions
Qingxiang Liu	Qingxiang Liu, Linlin Ge, Chun Tung Chou and Xiaojing Li	Damage Detection for 25 April 2015 Nepal Earthquake with Satellite Synthetic Aperture Radar Intensity and Coherence results
Tharika Liyanage	Tharika Liyanage, Jochen Brocks	Searching for the (hydrocarbon) skeleton key: Using biomarkers to find evidence of the first animals
Ronald Maj	Ronald Maj, Iver Cairns	Quasi-thermal noise spectroscopy and dust detection in Earth's ionosphere
Naomi Mathers	Naomi Mathers	The Advanced Instrumentation and Technology Centre (AITC): A National Facility Supporting Astronomy and Space Activities in Australia
Darren May	Darren May	An Update on Defence's SSA Activities
Troy McCann	Troy McCann, Stan Skafidas, Robert Mearns, Anton Tarasenko, Martin Lawrence	The University of Melbourne Space Program – Launching Melbourne into the final frontier
Dan Meehan	Dan Meehan	Ionospheric Research in Defence
Stavros Melachroinos	Stavros Melachroinos, Tao Li, Thomas Papanikolaou	Developing an Australian GNSS analysis capability for augmented Precise Point Positioning
Frederick Menk	Frederick Menk and Colin Waters	Magnetoseismology: Ground-based remote sensing of Earth's magnetosphere
Christopher Miller & Yilser Kabaran	Christopher Miller, Yilser Kabaran, Nathan Kinkaid	A review of steering with Rocker Bogie chassis design

Name of Presenter	Names of all authors	Title
Franklin Mills	F.P. Mills, K.L. Jessup, A.C. Vandaele, A. Mahieux, E. Marcq, B. Sandor, A. Stolzenbach, and F. Lefèvre	Post-Venus Express: An Overview of Current Issues in Understanding the Composition and Chemistry of Venus' Mesosphere
David Netherway	David Netherway and Robert Gardiner-Garden	On Power Received via Oblique HF Ionopheric Propagation
Patrick Neumann	Patrick R C Neumann, Marcela M M Bilek, David R McKenzie	Pulsed Cathodic Arc Spacecraft Propulsion Systems
Craig O'Neill	Craig O'Neill and Siqi Zhang	The role of core-differentiation in ejection of a Moon-forming disk
Sebastian Oberst	Sebastian Oberst, Iain Cartright, Timothy Teske, Doug Griffin, Sean Tuttle, Andrew Lambert, Russell R. Boyce	Sensitivity to micro-vibrations: damping of thin curved flexible space structures
Brian J. O'Brien	Brian J. O'Brien FTSE	From Antarctic Auroras to Nanodust on the Moon, 60 Years of Glorious Entertainments in Space Science: A Tribute to Professor Harry Messel
Carol Oliver	Carol Oliver, Martin Van Kranendonk and Tara Djokic	An innovative approach to astrobiology education in the online environment
Siddharth Pandey	Siddharth Pandey, Sean Tuttle, John Young	Computational study of the effect of Mars surface atmosphere induced thermal convection within horizontal gap enclosures on surface heat transfer characteristics within a Mars rover.
Siddharth Pandey	Siddharth Pandey, Jonathan Clarke	Spaceward Bound India 2016: Taking Astrobiology to the Roof of the World
Subhash Dadaji Pawar	Subhash Dadaji Pawar	Comparison of Air ion variation in winter season at urban station Sangli (17° 4' N 74° 25' E) and rural station Ramanandnagar (17° 4' N 74° 25' E) India
Lenard Pederick	Lenard Pederick, Manuel Cervera	Modelling the Interference Environment in the HF Band
Michael Phillips, Brian Luc	Michael Phillips, Brian Luc, Stuart Bartlett, Thomas Dixon and Elias Aboutanios	Development of a low-cost Software-Defined-Radio based student groundstation
Robert Pidgeon	R.T.Pidgeon, R.E Merle, M. L. Grange and A. A. Nemchin	Dating late thermal events on the Moon from the annealing of radiation damage in zircon
Brooke Porteous	Brooke Porteous and Duane Hamacher	Astronomical and Seasonal knowledge within Torres Strait Islander Art
Sana Qaisar	Sana U. Qaisar, Sean L. Tuttle, Mike J. Ryan,	Systems Engineering Essentials for Small Satellite Missions
Li Qiao	Li Qiao, Andrew G Dempster, Wayne L Hargreaves	Experience gained from Satellite Design Projects
Sam Reisenfeld	Sam Reisenfeld	The Communication System of the Australian Space Eye: Ultra-faint Astronomy Imaging from Space
Matthew Richardson	Matthew Richardson	If you build it, will they come? An Analysis of Price and Demand in the Launch Industry
Jay Ridgewell	Jay Ridgewell, Emma Donnelly	Getting cash for communication
Chris Rizos	Chris Rizos, Yong Li, Wei Jiang	A Real-time Precise Navigation System for UAV Applications
Nicholas Robinson	Nicholas Robinson	Optimal Path Planning for a SLAM-based Navigation System for Small UAVs
Mark Rutten	Mark Rutten and Neil Gordon	SSA Research in DST Group
Roy Sach	Roy Sach	Outer Space: Debris and Deceit?
Eleanor Sansom	E. K. Sansom, P. A. Bland, M. C. Towner, J. P. Paxman, R. M. Howie, M. Cupak, M. J. Galloway, G. K. Benedix	The Expansion of the Desert Fireball Network
Joachim M. Schmidt	J. M. Schmidt and Iver H. Cairns	Demonstration of a Viable Quantitative Theory for Interplanetary Type II Radio Bursts
Jack Scott	Jack Scott	SBAS for Australia and New Zealand

Name of Presenter	Names of all authors	Title
Aramesh Seif	Aramesh Seif, Kefei Zhang, Brett Carter, Robert Norman, and Suqin Wu	Characterizing Daytime GHz Scintillation at Equatorial Regions Using GNSS Radio Occultation Measurements
Michael Smart	Prof. Michael K. Smart, Mr Dawid Preller, Mr Adriaan Schutte	A Reusable Launch System for Small Satellites
Harrison Steel & Michel Fathallah	Harrison Steel, Michel Fathallah	Development and testing of a Complete, Sub-$1000 2U CubeSat Prototype
Samira Tasnim	Samira Tasnim and Iver H. Cairns	A Generalized Theory for the Evolution of Angular Momentum and Azimuthal Magnetic Fields in the Ecliptic Heliosphere
Ross Taylor	Ross Taylor	Why Can't a Planet be more like a Star
Anne Unewisse	Anne Unewisse, Manuel Cervera, Trevor Harris and Andrew Cool	High Frequency and 630 nm Airglow Observations of Travelling Ionospheric Disturbances over Adelaide, Australia
Martin Van Kranendonk	Martin Van Kranendonk	Early Earth and the making of Mankind: Astrobiology in our own backyard
Ba-Ngu Vo	Ba-Ngu Vo	Stochastic Geometry for Space Situational Awareness (SSA)
James Waldie	James Waldie, David Green, Dava Newman, Jonathan Scott, Simon Evetts	Initial Operational Assessment of the Gravity Loading Countermeasure Skinsuit on the International Space Station
Haiyang Wang	Haiyang Wang and Charles H. Lineweaver	Elemental Devolatilization Patterns of Material in the Solar System
Bruce Ward	B.D. Ward, R. Gardiner-Garden, A. Heitmann	ELOISE – Towards an enhanced understanding of ionospheric variability and its impact on radio wave propagation
Jonathon Wasiliev	Jonathon Wasiliev and Craig O'Neill	Viscosity Formulations and the effect of uncertain parameters
Kefei Zhang	Zhang K., Wang X., Wu S., Yuan Y., Manning T., Norman R., He C., Le Marshall J, Kaplon J., Rohm W., Bosy J. and Kealy A.	Towards an advanced near real-time tropospheric water vapour platform using the Australian NPI for weather forecasting
Siqi Zhang	Siqi Zhang, Craig O'Neill	Thermal evolution of the Moon modelled by core-mantle coupling

Posters

Posters are listed in alphabetical order of first author

Name of Presenter	Names of all authors	Title
Peter Connery	Peter Connery	65° South – The mischarted Flight of Yuri Gagarin
Steven Hobbs	S. W. Hobbs, J. D. A. Clarke and K.A. Campbell	Astrobiology With Mars'Obot: Identifying Microbial Life Forms Using Ground Based Remote Sensing
Steven Hobbs	S.W. Hobbs, J.D.A. Clarke, S. Pandey, M. Van Kranendonk, D. Willson, C.E. Coleman-Jennings	A4 Rover Proposal: A Small Planetary Science Rover for Geologic and Astrobiology Investigations for Mars Surface Exploration
Jonti Horner	Jonti Horner, James Gilmore, Dave Waltham	The Influence of Jupiter and Mars on Earth's orbital evolution
Jonti Horner	Horner, J., Pepper, J., Soutter, J., Hart, R. and the KELT Science Team	The Kilodegree Extremely Little Telescope (KELT): Searching for Transiting Exoplanets in the Northern and Southern Sky
Jonti Horner	Jonti Horner, Patryk Sofia Lykawka	2001 QR322 – an update on Neptune's first unstable Trojan companion
Taofiq Huq Noor	Taofiq Huq Noor, Nathan Kinkaid	Preliminary Design of an Asteroid Flyby Mission using CubeSat Technology
David Ivers	David Ivers, Denis Winch	Analysis of daily variations from simultaneous Swarm constellation magnetic data & Intermagnet data
Dhiren Kataria	M. Trichas, M. Gibbs, R. Harrison, J. Davies, D. Kataria, R. Bentley, L. Green, J. Eastwood	Carrington-L5: The Next Generation Space Weather Operational Mission
John Lam	John Lam, Shannon Green, Daniel Sheratt	Development and Testing Platform for the UNSW EC0 Cubesat
Samuel Matthews	Samuel Matthews, Craig O'Neill	Geodynamics of Venusian-type planets
Shannon McConachie	Shannon McConachie, Penelope King, Liane Loiselle and Les Kinsley	Thermal (mid-) infrared laboratory studies of materials found in meteorites
Franklin Mills	F.P. Mills, M. Shunmuga Sundaram, M. Allen, and Y.L. Yung	Potential Impacts of Heterogeneous Chemistry on Venus' Mesosphere
Christian Renggli	C.J. Renggli, P.L. King, R.W. Henley	A thermochemical comparison of metal transport, speciation and condensation in a lunar volcanic gas and a terrestrial volcanic gas
Marian Selorm Sapah	Marian Selorm Sapah, Yuri Amelin, Trevor Russell Ireland	Petrography, Chemistry and Chronology of Refractory Inclusions in NWA 4502
Martin Towner	Martin C. Towner, Philip A. Bland, Robert M. Howie, Jonathan Paxman, Ellie K. Sansom,Trent Jansen-Sturgeon, Hadrien Devillepoix	Initial Results From The Desert Fireball Camera Network: Meteorites On The Ground
Yang Zhao	Yang Zhao, Kefei Zhang, James Bennett, Jizhang Sang and Suqin Wu	A Method for Improving Two-line Element Outlier Detection Based on a Consistency Check